P-1

THE INTERNATIONAL HYDROGRAPHIC REVIEW

VOL. 31 · Nº 1
MAY 2025

IHO
International Hydrographic Organization

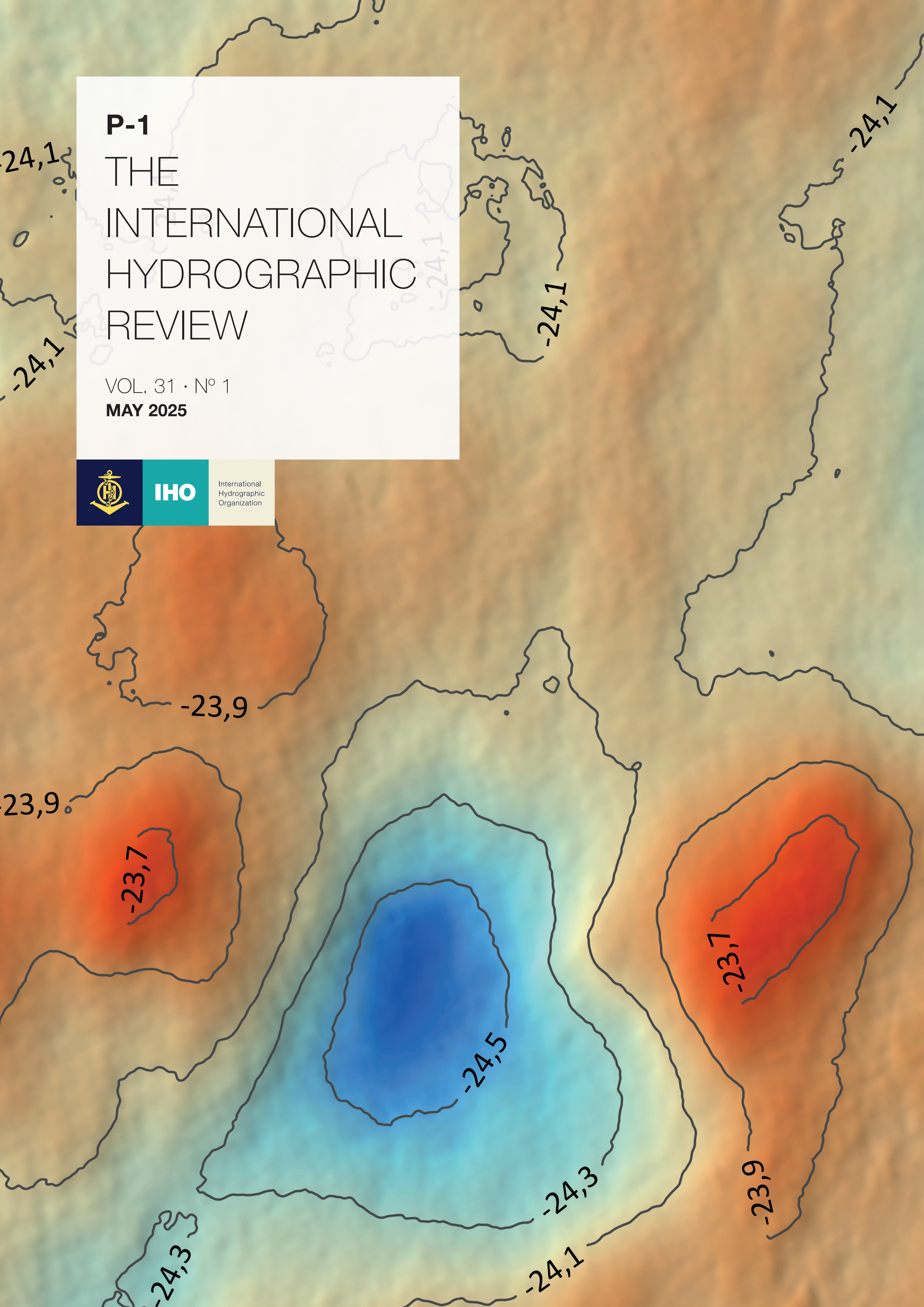

P-1

THE INTERNATIONAL HYDROGRAPHIC REVIEW

VOL. 31 · Nº 1

MAY 2025

International Hydrographic Organization

International Hydrographic Organization
Vol. 31 · Nº 1 — May 2025

Cover image

The cover image illustrates the bathymetry of the Kwinte area, derived from a comprehensive long time series of bathymetric data. Situated on the Belgian part of the North Sea, this area has been found to be remarkably stable. It thus serves as a natural reference area for the quality control of multibeam echosounder bathymetry and backscatter measurements. This topic is described in further detail in the related article by Samuel Deleu & Marc Roche (pp. 120–128).

Open Access Policy

This journal provides immediate open access to its content on the principle that making research freely available to the public supports a greater global exchange of knowledge.

About the Journal

The International Hydrographic Review (IHR) is an international scientific journal publishing peer-reviewed papers on all aspects of hydrography and associated subjects, ranging from the latest technical developments and significant events to book reviews and historical recollections. The IHR was first published in 1923 and since then has been published regularly.

Editorial

Welcome to the first issue of the 31st volume of The International Hydrographic Review (IHR).

Patrick Westfeld

The acquisition, processing, analysis and interpretation of data from all the world's seas, rivers and lakes is facilitated by hydrography, which thus enables a comprehensive understanding of our waters and paves the way for their safe and sustainable use. This is also impressively demonstrated by each of the 15 papers in this issue. Be it the exploration of the impact of measurement uncertainty on digital bathymetric model quality, or the mapping of submarine landslide susceptibility or the investigation of the barriers that women prevent them from pursuing a career in the field of hydrography – this issue is once again packed with a variety of scientific research papers, technical reports as well as notes on the work of our hydrographic community.

The IFHS Student Award 2024 was awarded to Julia Swedenklef of the University of Plymouth (United Kingdom). We are delighted that she has accepted our invitation to present her award-winning work on the topic Slippery slopes in the South Sandwich Islands: A GIS based approach to submarine landslide susceptibility mapping in the form of an invited scientific article (pp. 12–27).

The present issue comprises a total of five peer-reviewed scientific articles: Bahareh Mohammadivojdan et al. explore the impact of measurement uncertainties on digital bathymetric models (pp. 28–50), which form the fundamental basis for safe navigation of waters. The authors present a processing pipeline for modelling these uncertainties, with a view to improving the quality of the resulting models. Emily Harrex & Emily Tidey present a concise analysis of the role of women in hydrography within the South-West Pacific region (pp. 52–64). Their research focuses on the underrepresentation of women in hydrography, with a focus on the barriers that hinder the career progression of women in this field. The performance of "Desktop in the Cloud" processing software is the subject of an investigation by Brian R. Calder & Brian Miles (pp. 66–74). This is particularly exciting in light of the fact that the processing of hydrographic data no longer relies exclusively on local computers. Instead, there has been an increasing tendency for individual processing steps or entire process sequences to be migrated to cloud-based solutions. In their scientific assessment, Andre A. Araujo & Nicholas Hedley also address the benefits of novel, innovative technologies for handling hydrographic data, in this case the advantages of a tabletop augmented reality interface for analytical 3D bathymetric data visualization (pp. 76–100). The study by Shivani Seepersad & Dexter Davis proposes a probabilistic maritime risk assessment model for the identification of areas with high hazard potential, such as narrow waterways and turning zones (pp. 102–118). This aims to provide guidance for the management of maritime safety in Small Island Developing States.

The most recent HYDRO Conference, organised by the German Hydrographic Society, held in November 2024, was a resounding success. This event, which was hosted on the Baltic Sea coast, saw hydrographic professionals from around the globe present the latest advances in hydrography and its impact on marine surveying, navigation, maritime safety, environmental protection and sustainable development. In this issue of the IHR, we are publishing four of these contributions as conference papers. Samuel Deleu & Marc Roche present the Kwinte area, a natural reference area for the quality control of multibeam echosounder bathymetry and

ISSN print: 0020-6946
DOI prefix: 10.58440
URL: https://ihr.iho.int/

Publisher:
International Hydrographic Organisation
4b Quai Albert 1er
98011 Monaco

Editorial Board:
https://ihr.iho.int/editorial-team/

backscatter measurements on the Belgian part of the North Sea (pp. 120–128). Xavier Lurton is proposing approaches that would simplify the assessment of the environmental impact of hydrographic echosounders (pp. 130–138). Cloud and AI technologies are revolutionizing hydrography, state Jann Wendt et al. and presenting TrueOcean, an ocean data platform contributing to this development. (pp. 140–146). Hans Visser presents the improvements to the Fugro Marinestar GNSS precise point positioning algorithm (pp. 148–151).

The latest issue of IHR concludes with five notes and technical reports. These include an evaluation of the potential of a new underwater time-of-flight laser scanning system (Annika L. Walter, pp. 152–164), an analysis of the challenges and solutions involved in harnessing private sector data for the Ocean Decade (Peter Burger & Laura Meyer, pp. 166–170), a report on hydrographic surveying in extremely extreme conditions (Barry Grinker & Ariel Tarcic, pp. 172–182), an investigation into the precision of hydrographic data collected in the Persian Gulf (Nader Pasandeh et al., pp. 184–194), and an overview of ocean bathymetry advancements (Murtaza Taak et al., pp. 196–204).

On behalf of the Editorial Board, I hope that you will enjoy reading this new issue of the IHR!

Dr Patrick Westfeld
Chief Editor, IHR

https://doi.org/10.58440/ihr-31-1-e01

Content

Notes / Technical reports

INVITED ARTICLE

Slippery slopes in the South Sandwich Islands: A GIS based approach to submarine landslide susceptibility mapping

Author
Julia Swedenklef[1]

Preamble

Julia Swedenklef from the University of Plymouth (United Kingdom) is the winner of the IFHS Student Award 2024 for her Bachelor's thesis on "Slippery slopes in the South Sandwich Islands: A GIS based approach to submarine landslide susceptibility mapping". The following article summarises her award-winning work.

Abstract

Submarine landslides pose significant hazards due to their potential to generate destructive tsunamis, making their study crucial for risk assessment and mitigation. These mass wasting events are particularly prevalent in submarine volcanic island settings where oversteepened slopes, seismic activity, and oceanic processes can precondition slopes for failure. However, landslide susceptibility in such environments remains poorly understood, especially in remote oceanic regions where high-resolution data is difficult to obtain. This is particularly true for the South Sandwich Islands, a remote volcanic arc in the Southern Atlantic Ocean, which is known to be susceptible to landslide occurrence and tsunami generation, yet landslide distribution and susceptibility in this area have not been previously investigated. This study presents the first detailed landslide inventory and statistical susceptibility model focused on the South Sandwich Islands, integrating shipboard bathymetry data with multiple geologic, geomorphological and oceanographic factors using the frequency ratio (FR) approach. The resulting landslide susceptibility map exhibited good performance, with area under the curve values of 0.76 and 0.78 for success and prediction rates (PR), respectively. The results identify northward current velocity as the most influential factor preconditioning slopes for failure (PR = 3.43), and slope (PR = 1.40) and aspect (PR = 1) as the least influential. This study increases our understanding of landslide occurrence patterns and causal factors, thereby providing a foundation for improved hazard assessments aimed at mitigating the risks posed by landslide-induced tsunamis in the South Sandwich Islands and comparable submarine volcanic environments. Moreover, this study showcases the effectiveness of integrating geospatial datasets within the FR statistical modeling framework to investigate hazards in data-limited marine regions.

Keywords
frequency ratio model · submarine landslides · landslide susceptibility mapping · South Sandwich Islands · bathymetric data

✉ Julia Swedenklef · swdej2@gmail.com

[1] University of Plymouth, Plymouth PL4 8AA, United Kingdom

https://doi.org/10.58440/ihr-31-1-a07

Resumé

Les glissements de terrain sous-marins présentent des risques importants en raison de leur potentiel à générer des tsunamis destructeurs, ce qui rend leur étude cruciale pour l'évaluation et l'atténuation des risques. Ces phénomènes de perte de masse sont particulièrement fréquents dans les environnements d'îles volcaniques sous-marines où les pentes trop raides, l'activité sismique et les processus océaniques peuvent préconditionner les pentes à la rupture. Cependant, la susceptibilité aux glissements de terrain dans de tels environnements reste mal comprise, en particulier dans les régions océaniques éloignées où il est difficile d'obtenir des données à haute résolution. C'est particulièrement vrai pour les îles Sandwich du Sud, un arc volcanique isolé dans l'océan Atlantique Sud, connu pour être sujet aux glissements de terrain et à la formation de tsunamis, mais dont la répartition et la vulnérabilité n'ont jamais été étudiées auparavant. Cette étude présente le premier inventaire détaillé des glissements de terrain et le premier modèle statistique de vulnérabilité axé sur les îles Sandwich du Sud, intégrant des données bathymétriques recueillies à bord de navires avec de multiples facteurs géologiques, géomorphologiques et océanographiques en utilisant l'approche du rapport de fréquence (FR). La carte de susceptibilité aux glissements de terrain (LSM) qui en résulte a montré de bonnes performances, avec des valeurs de surface sous la courbe (AUC) de 0,76 et 0,78 pour les taux de réussite et de prédiction, respectivement. Les résultats identifient la vitesse du courant portant au nord comme le facteur le plus influent préconditionnant les pentes à la rupture (PR = 3,43), et la pente (PR = 1,40) et l'aspect (PR = 1) comme les moins influents. Cette étude nous permet de mieux comprendre les schémas d'occurrence des glissements de terrain et leurs causes, et fournit ainsi une base pour améliorer les évaluations des risques visant à atténuer les risques posés par les tsunamis induits par les glissements de terrain dans les îles Sandwich du Sud et les environnements volcaniques sous-marins comparables. En outre, cette étude démontre l'efficacité de l'intégration de jeux de données géospatiales dans le cadre de modélisation statistique de RF pour étudier les risques dans les régions marines où les données sont limitées.

Resumen

Los corrimientos submarinos de tierra suponen un peligro significativo por su potencial para generar tsunamis destructivos, lo que hace su estudio crucial para la evaluación y mitigación de riesgos. Estos fenómenos de erosión masiva son particularmente frecuentes en entornos de islas volcánicas submarinas, donde las pendientes excesivamente pronunciadas, la actividad sísmica y los procesos oceánicos pueden predisponer las laderas a corrimientos. Sin embargo, la susceptibilidad a los corrimientos de tierra en estos entornos sigue estando poco estudiada, especialmente en regiones oceánicas remotas donde es difícil obtener datos de alta resolución. Esto es particularmente cierto en el caso de las Islas Sandwich del Sur, un remoto arco volcánico en el Océano Atlántico Sur, conocido por ser susceptible a los corrimientos de tierra y la generación de tsunamis, pero no se había estudiado previamente la distribución de corrimientos de tierra y la vulnerabilidad de esta área. Este estudio presenta el primer inventario detallado de corrimiento de tierras y un modelo estadístico de vulnerabilidad centrado en las Islas Sandwich del Sur, integrando datos batimétricos de buques con múltiples factores geológicos, geomorfológicos y oceanográficos usando el enfoque de Relación de Frecuencias (FR). El mapa de vulnerabilidad a corrimientos (LSM) resultante mostró un buen rendimiento, con valores de área bajo la curva (AUC) de 0,76 y 0,78 para los índices de éxito y predicción, respectivamente. Los resultados identifican la velocidad de la corriente hacia el norte como el factor más influyente que precondiciona las laderas para los corrimientos (PR = 3,43), y la pendiente (PR = 1,40) y el aspecto (PR = 1) como los menos influyentes. Este estudio aumenta nuestra comprensión de los patrones de los corrimientos de tierra y los factores causales, proporcionando así una base para mejorar las evaluaciones de peligro destinadas a mitigar los riesgos de los tsunamis generados por los corrimientos de tierra en las Islas Sandwich del Sur y entornos volcánicos submarinos comparables. Además, este estudio muestra la eficacia de integrar conjuntos de datos geoespaciales en el marco del modelo estadístico FR para investigar los peligros en regiones marinas con datos limitados.

1 Introduction

1.1 Background

Submarine landslides represent a significant geological hazard due to their potential to generate destructive tsunamis, particularly in volcanic island settings where slope oversteepening and seismic activity contribute to their occurrence (Gallotti et al., 2020). Submarine volcanic flank collapse has the potential to cause great devastation. Historical examples highlight the devastating consequences, such as landslide-induced tsunamis on Oshima-Oshima (Japan, 1741, ~2000 casualties), Mt. Unzen (Japan, 1792, ~14,500 casualties), and Ritter Island (Papua New Guinea, 1888, >1500 casualties) (Karstens et al., 2020). The remote South Sandwich Islands, an active volcanic arc located in the Southern Atlantic Ocean, is particularly susceptible to landslide occurrence, and the impacts from tsunamis originating here have been recorded globally (Dragani et al., 2008). Despite this risk, landslide susceptibility in this region remains understudied, highlighting the need for focused research.

This study aims to address this gap by conducting the first comprehensive landslide inventory mapping and susceptibility modelling assessment for the South Sandwich Islands. The primary objectives are: (1) to create a detailed landslide inventory map by identifying and categorizing past landslide events using shipboard multibeam bathymetric data, and (2) to develop a landslide susceptibility model by integrating the landslide inventory with various geomorphic, geophysical, and oceanographic causative factors. The Frequency Ratio (FR) statistical approach will be used to calculate the ratio between landslide occurrence and non-occurrence for different classes of causal factors (Lee & Pradhan, 2007). This method is well-suited for data-scarce regions as it primarily relies on mapping past landslides and relating them to available regional datasets. This study is based on the assumption that landslide occurrence is both dependent on landslide causative factors, and that future landslides will occur under the same conditions of past landslides (Lee & Talib, 2005; Getachew & Meten, 2021). Throughout this study, the term "landslide" will be used to encompass various forms of sediment mass movement, such as slumps, debris flow, slips, or slides, all of which result in the formation of a characteristic scar in the bathymetry.

By enhancing the understanding of landslide dynamics and susceptibility in the South Sandwich Islands, this study will provide a baseline for future research and inform regional hazard assessment and mitigation strategies. The landslide inventory database and susceptibility map generated in this research will serve as valuable resources for researchers and policymakers involved in mitigating the risks posed by landslide-induced tsunamis in this remote oceanic region.

1.2 Study area

1.2.1 Physiographic and geological setting

The South Sandwich Islands are a 350 km long volcanic arc located in the remote South Atlantic Ocean, approximately 760 km south-east of South Georgia (Allen & Smellie, 2008). This intra-oceanic arc was formed by the subduction of the South American tectonic plate beneath the Antarctic plate (Hogg et al., 2021; Leat et al., 2014). The main tectonic features in the region include the South Sandwich Trench, marking the subduction zone, the volcanic arc itself comprising the islands, and the East Scotia Ridge back-arc spreading center (Leat et al., 2003). The islands are volcanically active, with various volcanoes exhibiting eruptions within the time frame of historical record (Bristol Island, 1956; Protector Shoal, 1962; Saunders Island, 1995–1998; Montagu Island in 2001–2007 (Leat et al., 2013)). The bathymetry of the arc is marked by steep volcanic flanks and seamounts, making the region particularly susceptible to slope instability and mass wasting processes. Historical records also indicate that the area has experienced significant seismic activity, with earthquakes occurring at various depths and displaying complex temporal patterns (Jia et al., 2022). These seismic events, combined with the oversteepening of volcanic slopes, can trigger slope failures and contribute to landslide hazards.

1.2.2 Oceanographic setting

In addition to the active tectonic processes, the South Sandwich Islands are situated in a dynamic oceanographic setting influenced by the Antarctic circumpolar current (ACC). This powerful eastward-flowing current encircles Antarctica and is comprised of several fronts, shown in Fig. 1. The Southern Boundary (SB) of the ACC flows northeastward through the region, generating strong currents, turbulence, and mixing patterns that can affect seafloor sedimentation and slope stability (Thorpe & Murphy, 2022; Nicholson et al., 2020; Collins et al., 2022). The complex interaction between active volcanism, seismicity, steep submarine slopes, and the influence of the ACC creates an environment particularly prone to submarine landslides and mass wasting processes.

2 Methodology

A methodology workflow was created as in Fig. 2, detailing key steps taken to generate results. The following Sections 2.1–2.7 provide a more detailed overview as to how methodological steps were undertaken.

2.1 Data collection and organization

Data for the susceptibility mapping was compiled from various sources including a 100 m resolution Digital Elevation Map (DEM) and its derivatives (Leat et al., 2014), modelled sediment thickness, gravity anomaly, magnetic anomaly, current velocity at

https://doi.org/10.58440/ihr-31-1-a07

1000 m depth, and historical earthquake events. All data were resampled to 100 m to match the DEM resolution. Table 1 compiles the causative factors with the data time scale, resolution, and source.

The DEM was used for landslide identification and mapping. It was converted to a red relief image map (details in Section 2.2) to aid visual detection of landslides by identifying headwalls, sidewalls, and deposit areas. The 3D visualization and 2D profile tool in QGIS were also used to identify/confirm possible landslides. A total of 342 landslides were identified and randomly split into 80 % for modelling and 20 % for validation. Data processing was done using QGIS, Excel and IBM SPSS.

2.2 Preparing Red Relief Image Map (RRIM)

Using the methods of Chiba et al. (2007), a Red Relief Image Map (RRIM), was created to aid landslide identification. The main benefit of using the RRIM approach is that it distinguishes concave and convex features (valleys vs ridges), unlike a slope map which is the more commonly used technique for landslide mapping. RRIM depicts features with greater steepness as appearing redder and features that are more downward than the surroundings as darker. This was done by overlaying a topographic openness map with a white to red colour scale on a greyscale slope map.

2.3 Landslide classification scheme

Identified landslides were classified from A–E based on the clarity of headwalls and sidewalls, adapted from Chang et al. (2021). This scheme assigns confidence levels to account for the limited resolution and challenges of visual identification of landslides over large time scales. The classification scheme used is described in Fig. 3.

2.4 Database for landslide causative factors

Landslide susceptibility analysis requires a comprehensive spatial database comprising of a landslide inventory and various factor layers known to influence slope instability. In this study, ten causative factors (Table 1) were selected based on data availability and their significance in previous landslide susceptibility studies, both for submarine (Dyer et al., 2022; Du et al., 2022; Masson et al., 2006; Conforti & Letto, 2021; Innocenti et al., 2020) and terrestrial (Acharya & Lee, 2018; Alkhasawneh et al., 2013; Borrell et al., 2016; Genene & Meten, 2021; Getachew & Meten, 2021; Islam et al., 2022; Mersha & Meten, 2020; Mirnazari et al., 2014) environments. All factor layers were compiled in QGIS as raster datasets with a consistent projection (WSG84 UTM Zone 24S) and a cell size, and sub divided into a number of classes depending on the range of the data.

2.5 Collinearity analysis

A collinearity analysis was performed to exclude highly correlated factors and avoid biasing the results (Conforti & Letto, 2021). Pearson correlation

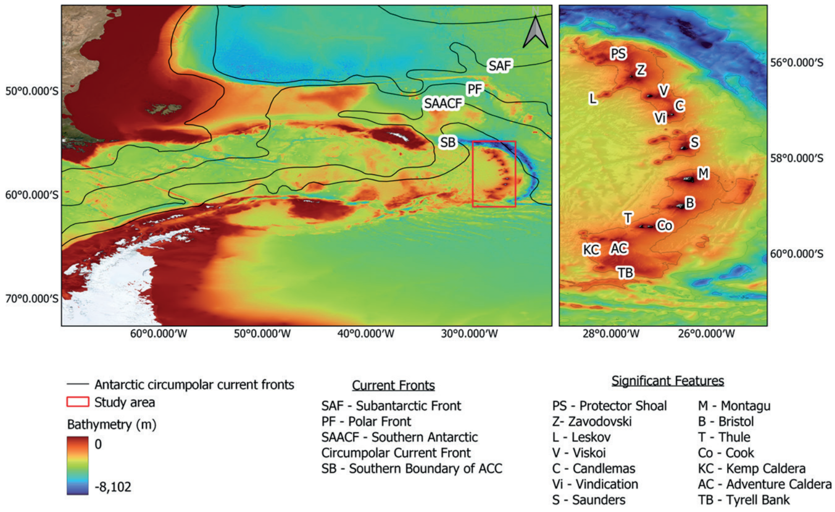

Fig. 1 Map of the South Sandwich Islands study area, showing the ACC fronts, significant bathymetric features, and geographic context. ACC front data from Orsi & Harris (2019) and bathymetry data from GEBCO (2023).

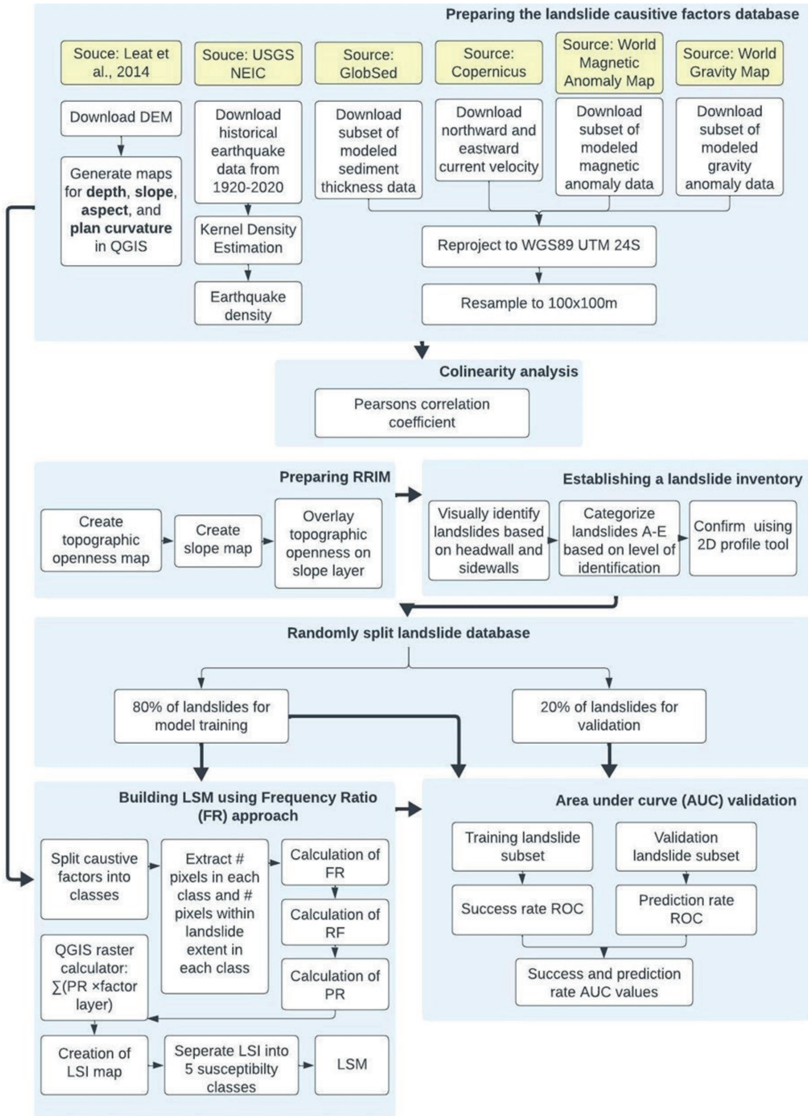

Fig. 2 Workflow diagram illustrating the key methodological steps followed in this study for landslide inventory mapping.

Table 1 Summary of the causative factors used in the landslide susceptibility modeling, including their respective time scales, resolutions, and data sources.

Factor	Time scale	Resolution	Source
Depth	2014	100 m	Leat et al. (2014)
Slope	2014	100 m	Derived from Leat et al. (2014)
Aspect	2014	100 m	Derived from Leat et al. (2014)
Plan curvature	2014	100 m	Derived from Leat et al. (2014)
Sediment thickness	2019	10 km	GlobSed (Straume et al., 2019)
Bouguer gravity anomaly	2012	5 km	Bureau Gravimétrique International
Magnetic anomaly	2015	5 km	World Digital Magnetic Anomaly Map (Choi et al., n.d.)
North/east current velocity	2020—2022	7 km	Copernicus Marine Service (CMEMS, 2023)
Earthquake Density	1920—2020	100 m	U.S. Geological Survey (USGS, 2017)

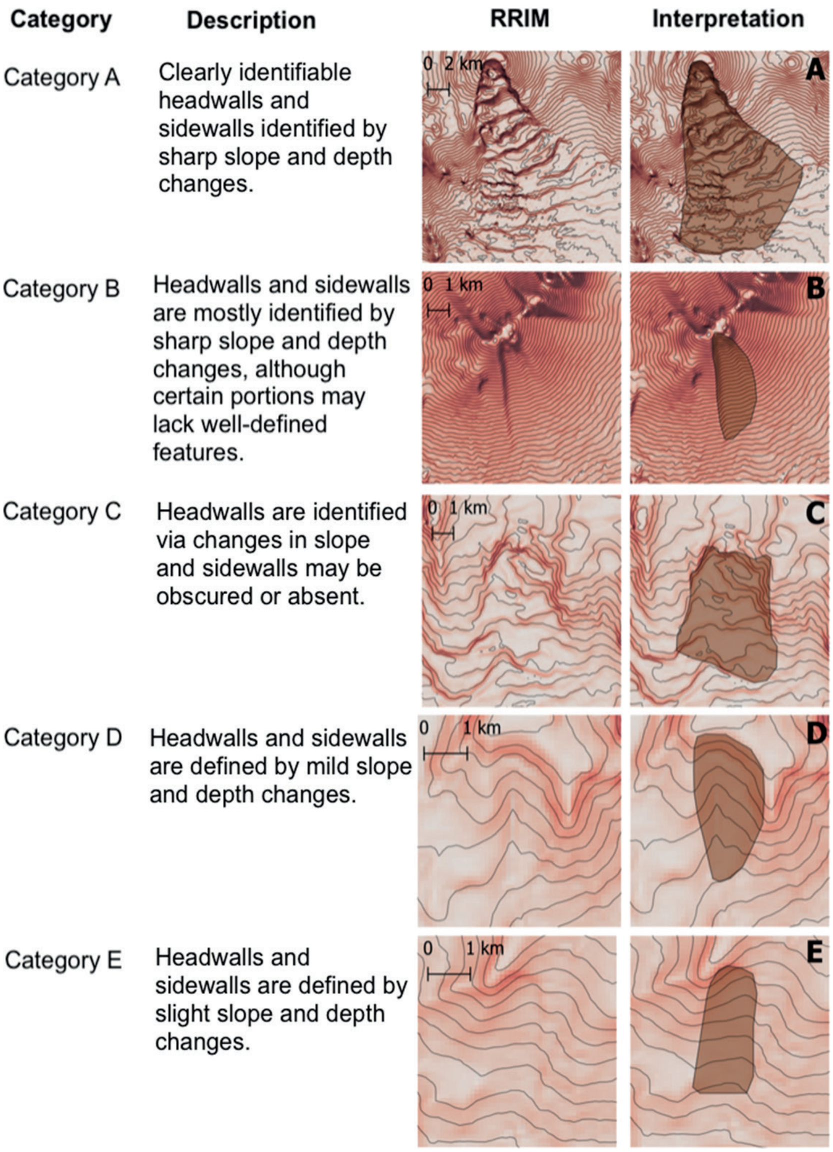

Fig. 3 Landslide classification scheme used for categorizing submarine landslides in the study area, adapted from Chang et al. (2021). Example features for each category are shown on the RRIM alongside interpretations of landslide extents with 50 m contour lines.

coefficient was used to detect collinearity among the ten factors. Factors with coefficients exceeding 0.7 were considered correlated and removed from further analysis.

2.6 Frequency ratio model

The frequency ratio (FR) model is a simple bivariate statistical method often used in landslide susceptibility mapping with reliable results (Silalahi et al., 2019; Acharya & Lee, 2018; Genene & Meten, 2021; Mirnazari et al., 2014; Oh, Lee & Hong, 2017; Rahman et al., 2020; Amaliah et al., 2021). The FR method calculates the ratio of landslide occurrence to non-occurrence for each class of the causative factors. In this study, the landslide inventory database was divided into a training subset (80 % of the data) for constructing the susceptibility model and a validation subset (remaining 20 %) for assessing the model's predictive capability. For each factor layer, the number of pixels in each class was extracted, along with the number of pixels within the training landslide regions for that class.

The FR value for each class was calculated using the formula below (Thapa & Bhandari, 2019):

$$FR_{in} = \frac{A/B}{C/D} \tag{1}$$

where

A: Number of landslide pixels for individual class *i* within each factor *n*

B: Total number of pixels in landslide regions over study area

C: Number of pixels in each class *i* of each factor *n*

D: Total number of pixels in the study area

An FR value greater than 1 indicates a higher probability of landslide occurrence for that class. To standardize the FR values within the range of 0 to 1, the relative frequency (RF) was derived using the following formula (Youssef et al., 2023):

https://doi.org/10.58440/ihr-31-1-a07

$$RF_{in} = \frac{FR_{in}}{\sum FR_{in}} \tag{2}$$

The causative factor layers were then reclassified with their respective RF values. Next, the weight, or prediction rate (PR), of each factor was calculated to assess its relative importance:

$$PR = \frac{RD_{max} - RF_{min}}{RF_{min}(RF_{max} - RF_{min})} \tag{3}$$

Using the raster calculator in QGIS, the landslide susceptibility index (LSI) was computed by summing the products of each factor's PR and reclassified RF layer:

$$LSI = \sum (PR \times \text{factor layer}) \tag{4}$$

The LSI represents the relative landslide susceptibility, with higher values indicating higher susceptibility. The LSI values were categorized into five classes (very low, low, medium, high, and very high) using Jenks natural breaks, generating the final landslide susceptibility map (LSM) from the training subset.

2.7 Area under curve validation

The LSM's accuracy was assessed using area under the curve (AUC) derived from success and prediction rate receiver operating characteristic (ROC) curves using IBM SPSS software. Success rate evaluates the model's efficiency in capturing known landslides (training subset). Prediction rate calculates the percentage of independent landslides captured by the susceptibility map, indicating the ability to predict "unknown" landslides. This is done using the validation landslide subset that was not used in the model (Genene & Meten, 2021).

3 Results

3.1 Landslide inventory map

A total of 342 landslides were identified throughout the study site, primarily concentrated on the upper slopes of volcanoes and seamounts. The majority of landslides were classified into category B (106 landslides), followed by D (73), C (69), A (68), and E (21). The average area of landslides in the South Sandwich Islands is 6,200 km^2. There is a concentration of small landslides not associated with volcanoes in the deep region north of Protector Shoal. The most significant landslide event is documented on the southern side of the Protector Shoal, spanning 7,620 km^2.

The distribution of mapped landslides across the entire study site is shown in Fig. 5, with the training and validation landslides indicated by yellow and green, respectively. The general pattern of landslide occurrence 6 indicates that landslides tend to occur on the upper slopes of volcanic islands and seamounts. A deviation from the pattern of landslides occurs on the Visokoi Island where there is an absence of landslides, instead, an erosion pattern is present.

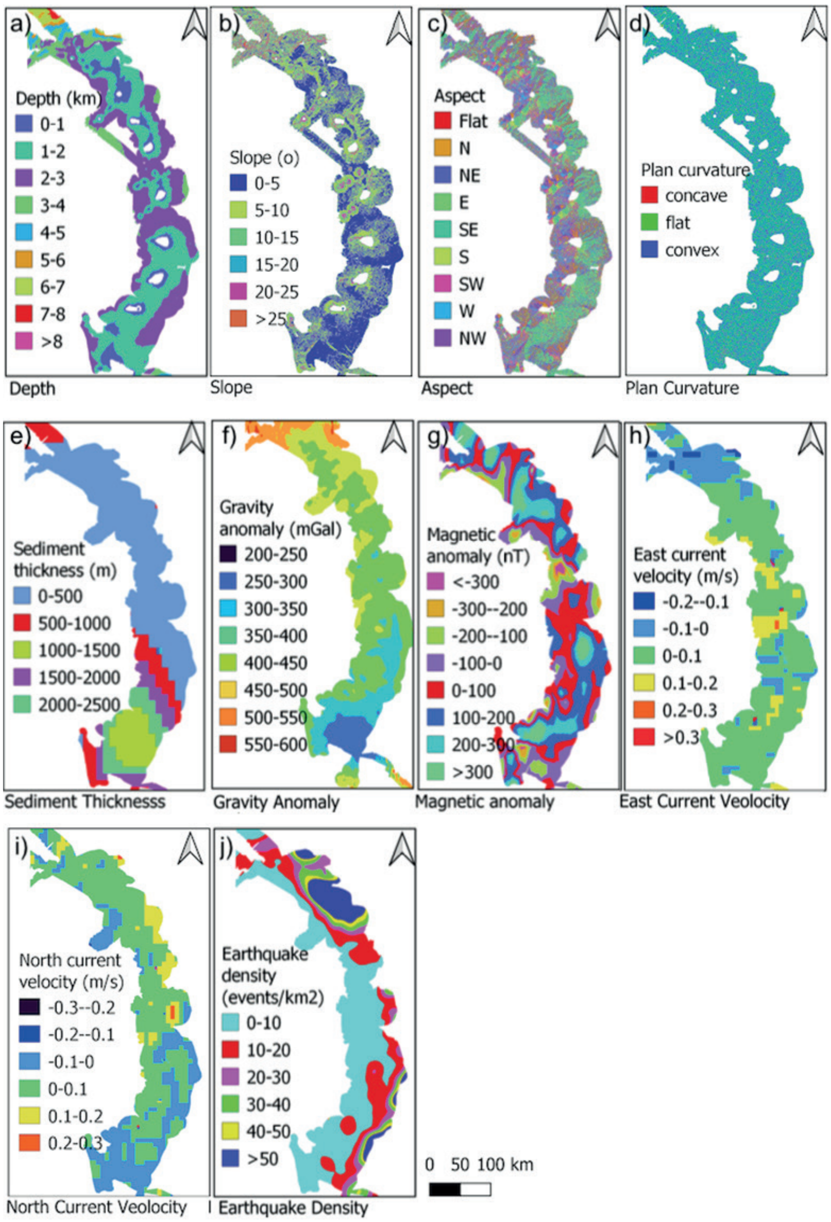

Fig. 4 Categorized maps of the ten causative factors used in the landslide susceptibility modeling: (a) slope, (b) aspect, (c) depth, (d) plan curvature, (e) sediment thickness, (f) Bouguer gravity anomaly, (g) magnetic anomaly, (h) eastward current velocity, (i) northward current velocity, and (j) earthquake density.

3.2 Detection of collinearity between causative factors

The Pearson correlation test confirmed no strong collinearity among the causative factors, with all correlation coefficients between -0.7 and 0.7 (Appendix, Table 3). Therefore, all ten factors were included in the landslide susceptibility model.

3.3 Relationship between landslide occurrence and causative factors

The FR model approach outlined in Section 2.6 enabled a comprehensive analysis of the relationship between landslide occurrence and the ten selected

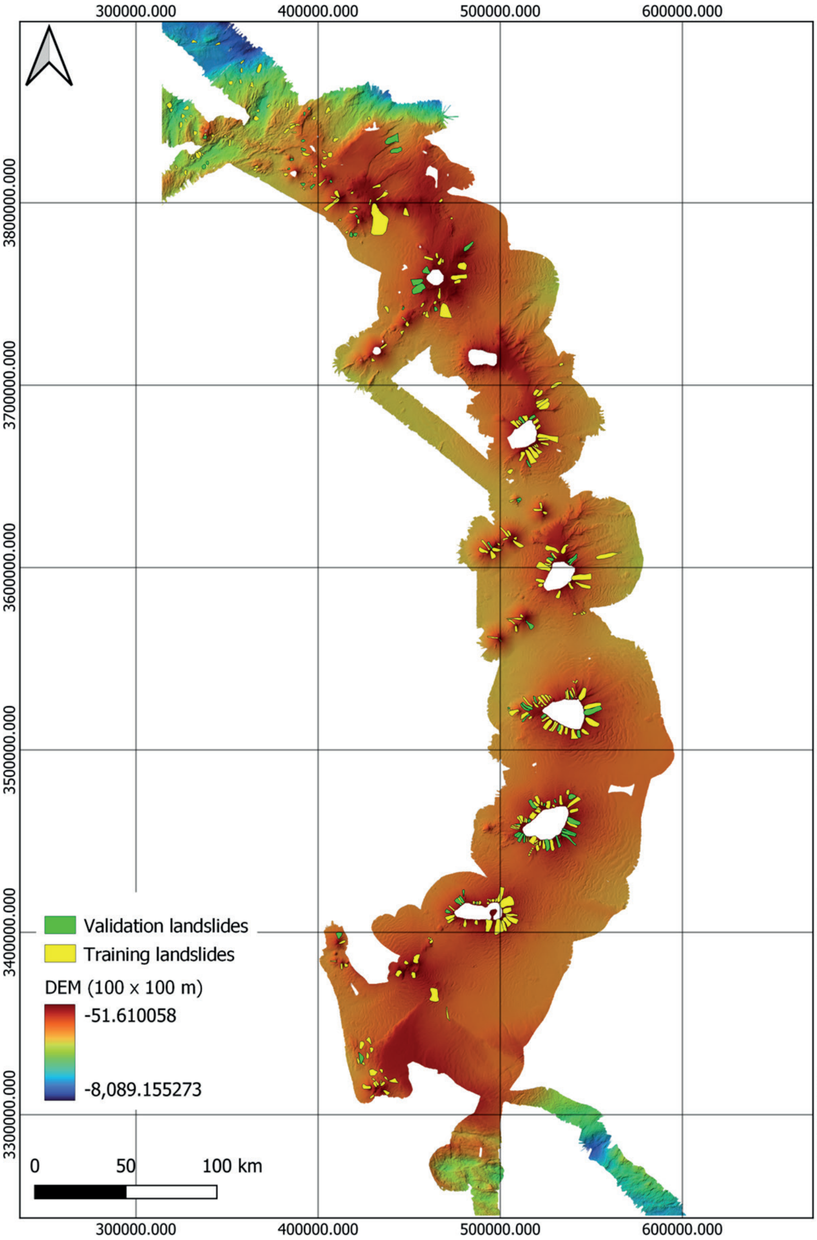

Fig. 5 Distribution of mapped landslide extents in the study area, divided into training (80 %) and validation (20 %) subsets, overlaid on the digital elevation model (DEM) of the South Sandwich Islands.

causative factors in the South Sandwich Islands region. Fig. 6 graphically represents the FR values, with the red dashed line indicating when the classes exhibit a higher propensity for landslide occurrence (FR > 1). Table 4 in the Appendix shows the full table of FR, RF and PR values.

Northward current velocity emerged as the most significant factor, with the 0.2–0.3 m/s class exhibiting the maximum FR value of 4.55, indicating high relative landslide susceptibility under these strong northward flow conditions. For eastward currents, the 0.1-0.2 m/s class demonstrated the maximum FR value of 1.27. As anticipated, most landslides occurred within 1000 m depth (FR = 4.27), with the 1000–2000 m class also exhibiting elevated susceptibility (FR = 1.12), and no slides were detected below 6000 m depth. Additionally, areas with earthquake densities greater than 10 events/km^2 were significantly more susceptible, peaking at 40–50 events/km^2 (FR = 24.21).

Surprisingly, slope angle did not show the expected increasing susceptibility trend on steeper slopes. Instead, the 15–20° class had the highest FR value of 2.54. While aspect overall was found to be the least significant (Fig. 7), the south-facing slopes were the only classes found to have higher landslide susceptibility. Additionally, positive magnetic anomalies (>0 nT, FR up to 3.28) were generally associated with higher landslide occurrences, except for values less than -300 nT which also showed elevated susceptibility (FR = 1.11). The Bouguer gravity anomaly data showed greater association between landslide occurrence and positive gravity anomaly values, with the 350–400 mGal class having an FR value of 2.50.

Increased sediment thickness correlated with higher landslide susceptibility with the 2000–2500 m class having the highest FR value of 4.29. Finally, the 'flat' curvature class (values between -0.05 and 0.05) had an FR value of 1.018, just exceeding the higher susceptibility threshold of FR > 1 and is a relatively minor factor for the LSM.

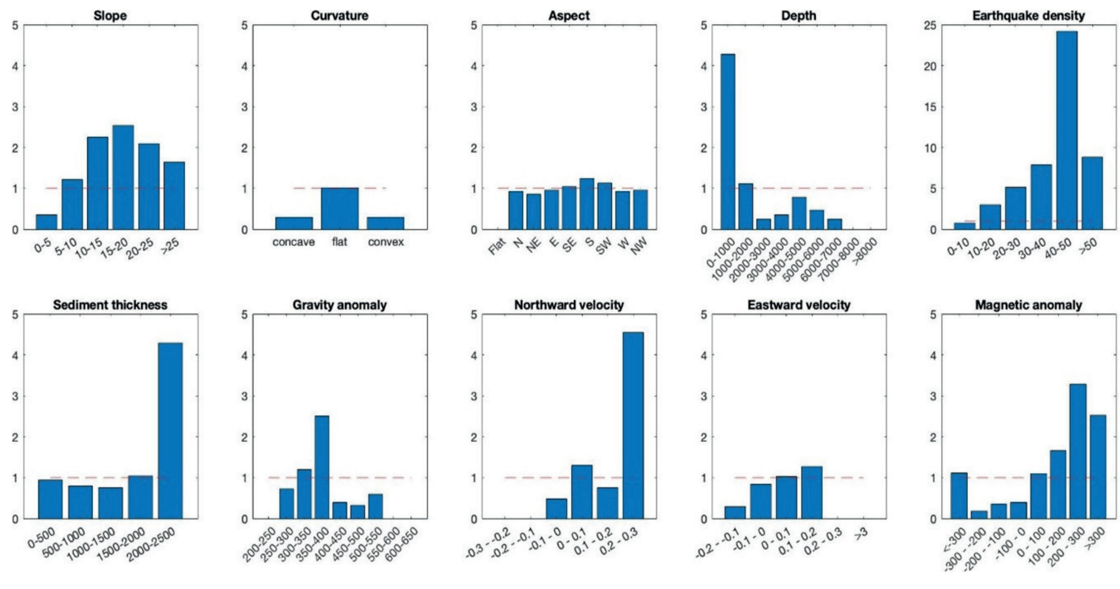

Fig. 6 Bar charts representing the FR values for each class of the ten causative factors, with the red dashed line indicating values greater than 1, which signify higher landslide susceptibility.

Table 2 Area coverage and percentage of mapped landslides within each landslide susceptibility class (very low, low, medium, high, and very high) in the final landslide susceptibility map.

Class	Area (km²)	Percentage of area	Percentage of landslides (%)
Very low	1,620,206	3.04	0.30
Low	19,844,137	37.26	18.04
Medium	12,947,584	24.31	6.73
High	13,955,485	26.20	33.33
Very high	4,897,613	9.19	41.59

3.4 Prediction rate of factors

The significance of each factor to landslide occurrence is given by the PR values (Youssef et al., 2023). Northward current velocity was found to be the most significant factor for determining landslide susceptibility, followed by depth, eastward current velocity, earthquake density, sediment thickness, curvature, and gravity anomaly. The least significant factors were aspect, slope, and magnetic anomaly. A scatterplot of the PR values for each factor is shown in Fig. 7.

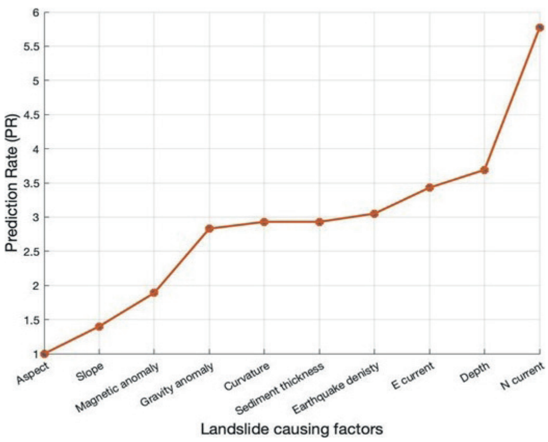

Fig. 7 Scatterplot showing the overall weight or PR of each causative factor in determining landslide susceptibility, based on the FR modeling approach.

3.5 Landsliide susceptibility map

The LSI values computed by the frequency ratio model ranged from 81 to 612. The LSI values were classified into five categories (very low, low, medium, high, and very high susceptibility) using the Jenks natural breaks method. This classification technique optimally represents clustered patterns by minimizing within-group variance while maximizing between-group variance (Chen et al., 2013). The area coverage and percentage of mapped landslides within each susceptibility class are presented in Table 2. The 'very low' class covered the smallest area (3.04 %) and contained only 0.3 % of total landslides, while the 'high' and 'very high' classes encompassed a substantial 74.92 % of landslides despite accounting for 35.39 % of the study area. This distribution aligns with the expectation that higher susceptibility areas should capture a greater proportion of historical landslide events.

The resulting LSM is shown in Fig. 8. As anticipated, 'high' to 'very high' susceptibility areas are concentrated around the upper slopes of volcanic islands and seamounts, where steeper terrain is more prone to slope failures. Visually, the LSM exhibits some harsh geometric patterns likely due to the coarse resolutions of certain input datasets. For example, a rectangular section in the southern end of the study area is characterized as 'high susceptibility'; however, no landslides have occurred in that region. This pattern corresponds to the spatial distribution of the sediment thickness factor layer, suggesting that the model may have assigned excessive weight to this parameter in certain areas due to its coarse resolution.

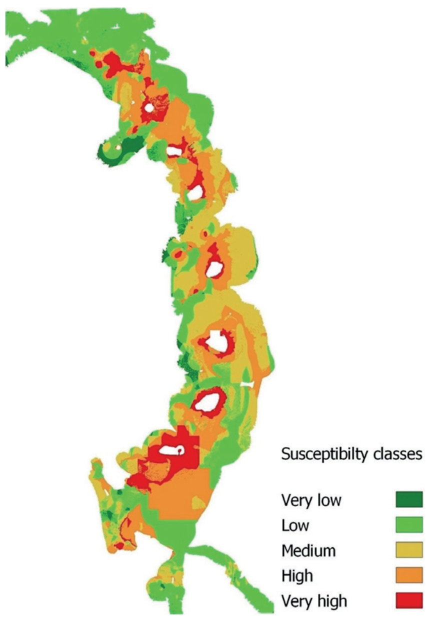

Fig. 8 LSM of the South Sandwich Islands, generated using the FR model and classified into five susceptibility classes.

Additionally, while the LSM indicates 'very high' susceptibility on the upper slopes of Visokoi Island, no landslides were detected in this area during inventory mapping. Instead, a gully feature, potentially formed by glacial erosion, was observed. This discrepancy highlights the importance of interpreting the LSM in conjunction with field observations and other relevant data.

3.6 Model validation

Model validation was performed using AUC derived from ROC curves for success rate and prediction rate scenarios. An AUC of 0.5 represents a random prediction, while a value of 1 indicates perfect classification. Fig. 9 shows the success rate (black) and prediction rate (blue) ROC curves for the landslide susceptibility model developed in this study. The corresponding AUC values are 0.759 for the success rate and 0.784 for the prediction rate, suggesting good overall performance in capturing both known and unknown landslide events.

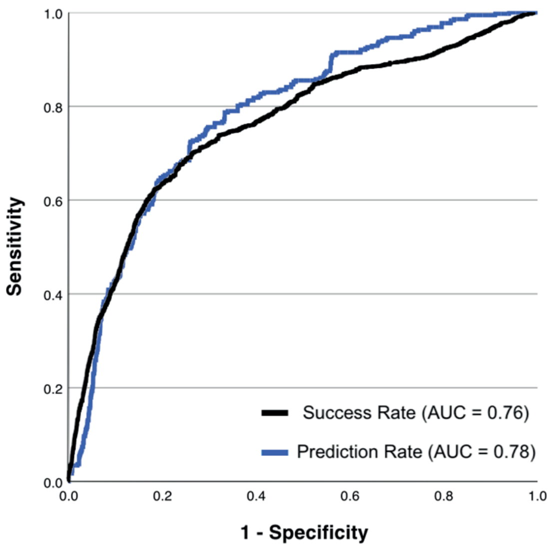

Fig. 9 ROC curves for assessing the performance of the landslide susceptibility model, showing the success rate (black) for the training landslides and the prediction rate (blue) for the validation landslides, with their respective AUC values.

4 Discussion

4.1 Landslide inventory map

This analysis is constructed around the theory that future landslides are likely to occur under similar conditions as past landslides, therefore, the landslide inventory map is a crucial factor in this analysis. The majority of landslides were concentrated on the upper slopes of volcanic islands and seamounts, reflecting the influence of steep terrain and surface processes on slope failure dynamics. This pattern aligns with observations from other volcanic island and seamount settings, where the steepness of upper slopes, erosion from underwater currents which tend to be stronger near the surface, and ongoing volcanic and seismic activity contribute to heightened instability. (e.g., Dyer, 2022; Avdievitch & Coe, 2022; Chang et al., 2021).

A notable deviation from this pattern was observed in the area north of Protector Shoal, where a concentration of smaller landslides not directly associated with volcanic edifices was identified. This cluster may be indicative of the influence of regional oceanographic processes, such as strong bottom currents or sediment transport mechanisms, in triggering slope failures in this region. Further investigation into the local sedimentological and hydrodynamic conditions could shed light on the specific causal factors responsible for this landslide distribution.

The classification scheme employed in this study provides a valuable framework for quantifying the confidence levels associated with each identified landslide feature. By assigning categories based on the clarity of headwalls and sidewalls, this approach acknowledges the inherent challenges and uncertainties involved in visual landslide detection, particularly in areas with limited resolution data. The distribution of landslide categories revealed that the majority fell within categories B and D, indicating a moderate level of confidence in their identification. This finding underscores the need for caution in interpreting the results and highlights the potential for both false positives (misidentified features) and false negatives (unidentified actual landslides) within the inventory.

4.2 Landslide susceptibility map

Examination of the ROC analysis results show that the LSM supplied good success and prediction rate with AUC values of 0.76 and 0.78, respectively (Fig. 9). Approximately 81.6 % of mapped landslides occurred in areas classified as medium to very high susceptibility, aligning with the assumption that future landslides will occur under similar conditions as past events. This indicates that the FR method is a reliable and robust method for predicting landslide susceptibility within the study area.

The selection of landslide causative factors and their relative importance values significantly impact the accuracy of the susceptibility model. While the influence of predisposing factors on landslide distribution has been extensively studied in terrestrial environments (Alkhasawneh et al., 2013; Genene & Meten, 2021; Islam et al., 2022; Mersha & Meten, 2020; Mirnazari et al., 2014), investigations into submarine landslide susceptibility mapping are less common (Conforti & Letto, 2021; Shan et al., 2021). In this study, the influence of each factor was assessed using the PR as an extension of the FR method. The findings suggest that while all factors positively contributed to the LSM, their relative importance in the model construction varied. Notably, the northward current velocity emerged as the most influential factor, with a PR value of 5.8, followed by depth (PR = 3.7) and eastward current velocity (PR = 3.4).

The results support previous research linking high current velocities to submarine landslide occurrence by promoting slope oversteepening (Nicholson et al., 2020; Du et al., 2022). However, the identification of current velocity as the most influential factor in susceptibility mapping is a novel finding. A plausible explanation lies in the study area's proximity

https://doi.org/10.58440/ihr-31-1-a07

to the ACC. The South Sandwich Islands are situated near the ACC's SB, which flows northeastward through the region (Thorpe & Murphy, 2022). The ACC's strong currents can erode and transport sediments, leading to the accumulation of unstable deposits on over-steepened slopes, pre-conditioning them for failure (Clare et al., 2016; Stoecklin et al., 2017). This process may be exacerbated by seismic activity, which can trigger slope collapse. Notably, Nicholson et al. (2020) demonstrated that the ACC, specifically the subantarctic front, directly influences the location, magnitude, and frequency of landslides in the Falkland Islands, located 1500 km from the present study site. The combination of current velocity data and modeled sediment thickness in this study provides compelling evidence for a similar ACC-driven mechanism governing landslide dynamics in the South Sandwich Islands, and merits further investigation.

Depth was the second most important factor, with nearly all slides occurring above 1000 m, despite more than 90 % of the study area being located below this depth range, which is consistent with the decreasing influence of waves and currents at greater depths and sediment accumulation on upper slopes. This result supports results previously found in submarine landslide studies (Borrell et al., 2016; Dyer, 2022; Du et al., 2022).

Surprisingly, slope, which is typically a crucial factor in both terrestrial and submarine studies (e.g., Reichenbach et al., 2018; Innocenti et al., 2020), was among the least significant. While the correlation between susceptibility and slope is site-specific, depending on the unique variables present in a given study area, a greater occurrence of landslides is generally expected with increasing slope angle. In this study, the highest susceptibility occurred on slopes between 15-20°, decreasing for steeper slopes. A similar outcome was reported by Avdievitch & Coe (2022), who suggested two possible explanations: either there is truly a lower frequency of landslides on steeper slopes, or the apparent decrease in susceptibility is due to undetected landslides, resulting from a lack of observable scarps or limited spatial coverage. Prancevic et al. (2020) theorized that smaller-scale landslides tend to occur on steep slopes, limiting the number of larger-scale, and thus more detectable, landslides that would otherwise be expected.

The resolution of the input datasets used for the causative factor maps has a direct impact on the quality and accuracy of the resulting landslide susceptibility model. In this study, all the modelled causative factor layers had coarse resolutions, ranging from 5–10 km (Table 1). These coarse resolutions can introduce inaccuracies into the LSM. For example, the LSM exhibits rectangular patterns in certain areas that correspond to the spatial distribution of the sediment thickness layer, suggesting the model may have assigned excessive weight to this parameter. Similarly, the current velocity layers, while still providing valuable information, may not fully capture localized flow patterns and seafloor interactions that could influence landslide susceptibility. Ideally, higher resolution data would be used for all causative factors to better represent the complex interactions and terrain variability within the study area, however, primary data collection in this remote region can be difficult and costly.

Overall, this study has successfully created a reliable and accurate landslide susceptibility map for the spatial prediction of future landslides in the South Sandwich Islands. While comparisons to other LSM studies can be challenging due to differences in time scales, data resolution and availability, and predisposing factors (Conforti & Letto, 2021), this study achieves AUC values (0.76 and 0.78) consistent with the typical range of 0.7 - 0.9 reported for other submarine landslide studies (Innocenti et al., 2020; Dyer et al., 2022). Terrestrial LSM studies often achieve higher AUC values (>0.80), likely due to greater data availability and resolution (Acharya & Lee, 2018; Amaliah et al., 2021; Genene & Meten, 2021; Rasyid, Bhandary & Yatabe, 2016). An advantage of this study is the use of PR values to indicate the significance of each causative factor, an approach employed by few other FR studies.

4.3 Limitations of the study

Despite the advantages of this study, these results must be interpreted with caution and some limitations should be acknowledged. Firstly, regarding landslide identification, the resolution of the multibeam bathymetric data (100 m) is sufficient for identifying large-scale landslides but may have prevented the detection of smaller-scale events. This limitation could be a contributing factor to the relatively low significance of the slope factor in the susceptibility model, as explained previously.

Furthermore, the landslide inventory does not distinguish between failure mechanisms or source and deposit areas. Different failure types may be influenced by varying factors, and there could be considerable differences in environmental conditions between source points and deposits, which the LSM does not account for (Collico et al., 2020).

The varying resolutions of causative factor layers, particularly the coarse modelled data for Bouguer gravity anomaly and magnetic anomaly (5 km), current velocity (7 km) and sediment thickness (10 km) data, introduce uncertainties and decrease model accuracy by failing to capture localized patterns. Additionally, the absence of lithology data, a highly significant factor in many studies, is a limitation of this research.

These limitations highlight the need for higher-resolution data, a deeper understanding of failure mechanisms and sediment characteristics. Addressing these limitations could significantly improve the accuracy and reliability of landslide susceptibility assessments in the South Sandwich Islands region.

5 Conclusion

This study represents the first comprehensive assessment of submarine landslide susceptibility in the remote South Sandwich Islands region of the Southern Atlantic Ocean. By integrating a detailed landslide inventory map with various geomorphic, geophysical, and oceanographic causative factors, a landslide susceptibility model was developed using the FR statistical approach. The resulting LSM provides valuable insights into the spatial distribution of landslide hazards in this understudied volcanic arc environment.

The key findings of this research highlight the critical influence of current velocity, depth, and seismicity on slope instability in the South Sandwich Islands. Notably, northward current velocity emerged as the most significant causative factor, likely attributed to the region's proximity to the Antarctic Circumpolar Current. This finding emphasizes the importance of considering regional oceanographic patterns in assessing submarine landslide susceptibility.

While the LSM demonstrated good performance, with AUC values of 0.76 and 0.78 for success and prediction rates respectively, several limitations must be acknowledged. The coarse resolutions of certain input datasets, such as current velocity, sediment thickness, and gravity/magnetic anomalies, introduced uncertainties and potential biases in the model output. Additionally, the lack of distinction between failure mechanisms and source/deposit areas in the landslide inventory may have impacted the model's accuracy. Despite these limitations, the LSM provides a valuable baseline for understanding landslide dynamics and susceptibility in this remote region. The findings of this study can inform future research efforts, hazard assessments, and risk mitigation strategies related to landslide-induced tsunamis in the South Sandwich Islands and other similar volcanic arc settings.

References

Acharya, T. D. and Lee, D. H. (2018). Landslide Susceptibility Mapping Using Relative Frequency and Predictor Rate along Araniko Highway. *KSCE Journal of Civil Engineering, 23*(2), pp. 763–776. https://doi.org/10.1007/s12205-018-0156-x

Alkhasawneh, M. Sh., Ngah, U. K., Tay, L. T., Mat Isa, N. A. and Al-batah, M. S. (2013). Determination of Important Topographic Factors for Landslide Mapping Analysis Using MLP Network. *The Scientific World Journal*, pp. 1–12. https://doi.org/10.1155/2013/415023

Allen, C. S. and Smellie, J. L. (2008). Volcanic Features and the Hydrological Setting of Southern Thule, South Sandwich Islands. *Antarctic Science, 20*(3), pp. 301–308. https://doi.org/10.1017/s0954102008001156

Amaliah, R., Soma, A. S., Mappangaja, B. and Mambela, F. (2021). Analysis of the Landslide Susceptibility Map Using Frequency Ratio Method in sub-sub-Watershed Mamasa. *IOP Conference Series: Earth and Environmental Science, 886*(1), pp. 012088–012088. https://doi.org/10.1088/1755-1315/886/1/012088

Avdievitch, N. N. and Coe, J. A. (2022). Submarine Landslide Susceptibility Mapping in Recently Deglaciated Terrain, Glacier Bay, Alaska. *Frontiers in Earth Science, 10*. https://doi.org/10.3389/feart.2022.821188

Borrell, N., Somoza, L., León, R., Medialdea, T., Gonzalez, F. J. and Gimenez-Moreno, C. J. (2016). GIS Catalogue of Submarine Landslides in the Spanish Continental Shelf: Potential and Difficulties for Susceptibility Assessment. *Advances in Natural and Technological Hazards Research*, pp. 499–508. https://doi.org/10.1007/978-3-319-20979-1_50

Chang, Y., Mitchell, N. C. and Quartau, R. (2021). Landslides in the Upper Submarine Slopes of Volcanic Islands: The Central Azores. *Geochemistry, Geophysics, Geosystems, 22*(10). https://doi.org/10.1029/2021gc009833

Chen, J., Yang, S. T., Li, H. W., Zhang, B. and Lv, J. R. (2013). Research on Geographical Environment Unit Division Based on the Method of Natural Breaks (Jenks). *ISPRS – International Archives of the Photogrammetry, Remote Sensing and Spatial Information Sciences, XL-4/W3*, pp. 47–50. https://doi.org/10.5194/isprsarchives-xl-4-w3-47-2013

Chiba, T., Suzuki, Y. and Hiramatsu, T. (2007). Digital Terrain Representation Methods and Red Relief Image Map, a New Visualization Approach. *Map, Journal of the Japan Cartographers Association*, 45(1), pp. 27–36. https://doi.org/10.11212/jjca1963.45.27

Choi, Y., Dyment, J., Lesur, V., Garcia Reyes, Catalan, M., Ishihara, T., Litvinova, T., Hamoudi, M., the WDMAM Task Force*, and the WDMAM Data Providers** (n.d.) *World Digital Magnetic Anomaly Map*. Version 2.1. http://www.wdmam.org (accessed 25 February 2025).

Clare, M. A., Hughes Clarke, J. E., Talling, P. J., Cartigny, M. J. B. and Pratomo, D. G. (2016). Preconditioning and Triggering of Offshore Slope Failures and Turbidity Currents Revealed by Most Detailed Monitoring yet at a fjord-head Delta. *Earth and Planetary Science Letters, 450*(450), pp. 208–220. https://doi.org/10.1016/j.epsl.2016.06.021

Collico, S., Arroyo, M., Urgeles, R., Gràcia, E., Devincenzi, M. and Peréz, N. (2020). Probabilistic Mapping of earthquake-induced Submarine Landslide Susceptibility in the South-West Iberian Margin. *Marine Geology, 429,* p.106296. https://doi.org/10.1016/j.margeo.2020.106296 References

Collins, M. A., Hart, T., Hogg, O. T., Collins, M. A., Hollyman, P. R., Liszka, C. M., Stewart, H. A. and Trathan, P. N. (2022). South Sandwich Islands – An understudied isolated Southern Ocean archipelago. *Deep Sea Research Part II: Topical Studies in Oceanography, 201*, pp. 105121–105121. https://doi.org/10.1016/j.dsr2.2022.105121

Conforti, M. and Letto, F. (2021). Modeling Shallow Landslide Susceptibility and Assessment of the Relative Importance of Predisposing Factors, through a GIS-Based Statistical Analysis. *Geosciences, 11*(8), p. 333. https://doi.org/10.3390/geosciences11080333

Dragani, W. C., D'Onofrio, E. E., Grismeyer, W., Fiori, M. M. E., Violante, R. A. and Rovere, E. I. (2008). Vulnerability of the Atlantic Patagonian coast to tsunamis generated by submarine earthquakes located in the Scotia Arc region. Some numerical experiments. *Natural Hazards, 49*(3), pp. 437–458. https://doi.org/10.1007/s11069-008-9289-4

Du, X., Sun, Y., Song, Y., Xiu, Z. and Su, Z. (2022). Submarine Landslide Susceptibility and Spatial Distribution Using Different Unsupervised Machine Learning Models. *Applied sciences, 12*(20), pp. 10544–10544. https://doi.org/10.3390/app122010544

Dyer, A. S., Mark-Moser, M., Duran, R. and Bauer, J. (2022). Offshore Application of Landslide Susceptibility Mapping Using Gradient Boosted Decision Trees: A Gulf of Mexico Case Study. *Research Square*. https://doi.org/10.21203/rs.3.rs-2070041/v1

Gallotti, G., Zaniboni, F., Pagnoni, G., Romagnoli, C., Gamberi, F., Marani, M. and Tinti, S. (2020). Tsunamis from Prospected Mass Failure on the Marsili Submarine Volcano Flanks and Hints for Tsunami Hazard Evaluation. *Bulletin of Volcanology, 83*(1). https://doi.org/10.1007/s00445-020-01425-0

GEBCO (2023). The GEBCO_2023 – Grid a continuous terrain model of the global oceans and land. NERC EDS British Oceanographic Data Centre NOC. https://doi.org/10.5285/f98b053b-0cbc-6c23-e053-6c86abc0af7b

CMEMS (2023). *Global Ocean Physics Reanalysis.* E.U. Copernicus Marine Service Information (CMEMS), Marine Data Store (MDS). https://doi.org/10.48670/moi-00021

Genene, A. and Meten, M. (2021). Landslide Susceptibility Mapping Using GIS-based Information Value and Frequency Ratio Methods in Gindeberet area, West Shewa Zone, Oromia Region, Ethiopia. *Research Square*. https://doi.org/10.21203/rs.3.rs-219331/v1

Getachew, N. and Meten, M. (2021). Weights of Evidence Modeling for Landslide Susceptibility Mapping of Kabi-Gebro locality, Gundomeskel area, *Central Ethiopia. Geoenvironmental Disasters, 8*(1). https://doi.org/10.1186/s40677-021-00177-z

Hogg, O. T., Downie, A.-L., Vieira, R. P. and Darby, C. (2021). Macrobenthic Assessment of the South Sandwich Islands Reveals a Biogeographically Distinct Polar Archipelago. *Frontiers in Marine Science, 8.* https://doi.org/10.3389/fmars.2021.650241

Innocenti, C., Battaglini, L., D'Angelo, S. and Fiorentino, A. (2020). Submarine landslides: mapping the susceptibility in European seas. *Quarterly Journal of Engineering Geology and Hydrogeology, 54*(1). https://doi.org/10.1144/qjegh2020-027

Islam, F., Riaz, S., Ghaffar, B., Tariq, A., Shah, S. U., Nawaz, M., Hussain, M. L., Amin, N. U., Li, Q., Lu, L., Shah, M. and Aslam, M. (2022). Landslide susceptibility mapping (LSM) of Swat District, Hindu Kush Himalayan region of Pakistan, using GIS-based bivariate modeling. *Frontiers in Environmental Science, 10.* https://doi.org/10.3389/fenvs.2022.1027423

Jia, Z., Zhan, Z. and Kanamori, H. (2022). The 2021 South Sandwich Island *M* w 8.2 Earthquake: A Slow Event Sandwiched Between Regular Ruptures. *Geophysical Research Letters, 49*(3). https://doi.org/10.1029/2021gl097104

Karstens, J., Kelfoun, K., Watt, S. F. L. and Berndt, C. (2020). Combining 3D seismics, eyewitness accounts and numerical simulations to reconstruct the 1888 Ritter Island sector collapse and tsunami. *International Journal of Earth Sciences, 109*(8), pp. 2659–2677. https://doi.org/10.1007/s00531-020-01854-4

Leat, P. T., Day, S. J., Tate, A. J., Martin, T. J., Owen, M. J. and Tappin, D. R. (2013). Volcanic Evolution of the South Sandwich Volcanic arc, South Atlantic, from Multibeam Bathymetry. *Journal of Volcanology and Geothermal Research, 265*, pp. 60–77. https://doi.org/10.1016/j.jvolgeores.2013.08.013

Leat, P. T., Fretwell, P. T., Tate, A. J., Larter, R. D., Martin, T. J., Smellie, J. L., Jokat, W. and Bohrmann, G. (2014). Bathymetry and Geological Setting of the South Sandwich Islands Volcanic Arc. *Antarctic Science, 28*(4), pp. 293–303. https://doi.org/10.1017/s0954102016000043

Leat, P. T., Smellie, J. L., Millar, I. L. and Larter, R. D. (2003). Magmatism in the South Sandwich Arc. *Geological Society, London, Special Publications, 219*(1), pp. 285–313. https://doi.org/10.1144/gsl.sp.2003.219.01.14

Lee, S. and Pradhan, B. (2006). Landslide Hazard Mapping at Selangor, Malaysia Using Frequency Ratio and Logistic Regression Models. *Landslides, 4*(1), pp. 33–41. https://doi.org/10.1007/s10346-006-0047-y

Lee, S. and Talib, J. A. (2005). Probabilistic Landslide Susceptibility and Factor Effect Analysis. *Environmental Geology, 47*(7), pp. 982–990. https://doi.org/10.1007/s00254-005-1228-z

Masson, D. G., Harbitz, C. B., Wynn, R. B., Pedersen, G. and Løvholt, F. (2006). Submarine landslides: processes, triggers and hazard prediction. *Philosophical Transactions of the Royal Society A: Mathematical, Physical and Engineering Sciences, 364*(1845), pp. 2009–2039. https://doi.org/10.1098/rsta.2006.1810

Mersha, T. and Meten, M. (2020). GIS-based Landslide Susceptibility Mapping and Assessment Using Bivariate Statistical Methods in Simada area, Northwestern Ethiopia. *Geoenvironmental Disasters, 7*(1). https://doi.org/10.1186/s40677-020-00155-x

Mirnazari, M., Javad, J., Ahmad, A., Baharin, B., Mojaradi, M., Barat, B., Sattari, S. and Farshid, F. (2014). Using Frequency Ratio Method for Spatial Landslide Prediction. *Research Journal of Applied Sciences, Engineering and Technology, 7*(15), pp. 3174–3180. https://doi.org/10.19026/rjaset.7.658

Nicholson, U., Libby, S., Tappin, D. R. and McCarthy, D. (2020). The Subantarctic Front as a Sedimentary Conveyor Belt for Tsunamigenic Submarine Landslides. *Marine Geology, 424*, p. 106161. https://doi.org/10.1016/j.margeo.2020.106161

Oh, H.-J., Lee, S. and Hong, S.-M. (2017). Landslide Susceptibility Assessment Using Frequency Ratio Technique with Iterative Random Sampling. *Journal of Sensors*, pp. 1–21. https://doi.org/10.1155/2017/3730913

Orsi, A. H. and Harris, U. (2019). *Fronts of the Antarctic Circumpolar Current - GIS data*. Ver. 1, Australian Antarctic Data Centre. https://data.aad.gov.au/metadata/antarctic_circumpolar_current_fronts (accessed 25 February 2025).

Prancevic, J. P., Lamb, M. P., McArdell, B. W., Rickli, C. and Kirchner, J. W. (2020). Decreasing Landslide Erosion on Steeper Slopes in Soil-Mantled Landscapes. *Geophysical Research Letters, 47*(10). https://doi.org/10.1029/2020gl087505

Rahman, G., Rahman, A. U., Bacha, A. S., Mahmood, S., Moazzam, M. F. U and Lee, G. L. (2020). Assessment of Landslide Susceptibility Using Weight of Evidence and Frequency Ratio Model in Shahpur valley, Eastern Hindu Kush. *Natural Hazards and Earth System Sciences Discussions*, pp. 1–19. https://doi.org/10.5194/nhess-2020-167

Rasyid, A. R., Bhandary, N. P. and Yatabe, R. (2016). Performance of Frequency Ratio and Logistic Regression Model in Creating GIS Based Landslides Susceptibility Map at Lompobattang Mountain, Indonesia. *Geoenvironmental Disasters, 3*(1). https://doi.org/10.1186/s40677-016-0053-x

Reichenbach, P., Rossi, M., Malamud, B. D., Mihir, M. and Guzzetti,

F. (2018). A review of statistically-based landslide susceptibility models. *Earth-Science Reviews, 180*, pp. 60–91. https://doi.org/10.1016/j.earscirev.2018.03.001

Shan, Z., Guo, F., Lai, X. and Xiao, J. (2021). Assessment of Submarine Landslide Susceptibility in the Sea Area of Zhoushan. *IOP Conference Series: Earth and Environmental Science, 734*(1), pp. 012023–012023. https://doi.org/10.1088/1755-1315/734/1/012023

Silalahi, F. E. S., Pamela, Arifianti, Y. and Hidayat, F. (2019). Landslide susceptibility assessment using frequency ratio model in Bogor, West Java, Indonesia. *Geoscience Letters, 6*(1). https://doi.org/10.1186/s40562-019-0140-4

Stoecklin, A., Friedli, B. and Puzrin, A. M. (2017). Sedimentation as a Control for Large Submarine Landslides: Mechanical Modeling and Analysis of the Santa Barbara Basin. *Journal of Geophysical Research, Solid Earth, 122*(11), pp. 8645–8663. https://doi.org/10.1002/2017jb014752

Straume, E. O., Gaina, C., Medvedev, S., Hochmuth, K., Gohl, K., Whittaker, J. M., Abdul Fattah, R., Doornenbal, J. C. and Hopper, J. R. (2019). GlobSed: Updated Total Sediment Thickness in the World's Oceans. *Geochemistry, Geophysics, Geosystems, 20*(4), pp. 1756–1772. https://doi.org/10.1029/2018gc008115

Thapa, D. and Bhandari, B. P. (2019). GIS-Based Frequency Ratio Method for Identification of Potential Landslide Susceptible Area in the Siwalik Zone of Chatara-Barahakshetra Section, Nepal. *Open Journal of Geology, 9*(12), pp. 873–896. https://doi.org/10.4236/ojg.2019.912096

Thorpe, S. E. and Murphy, E. J. (2022). Spatial and Temporal Variability and Connectivity of the Marine Environment of the South Sandwich Islands, Southern Ocean. *Deep Sea Research Part II: Topical Studies in Oceanography, 198*, p.105057. https://doi.org/10.1016/j.dsr2.2022.105057

USGS (2017). *Advanced National Seismic System (ANSS) Comprehensive Catalog*. U.S. Geological Survey. https://doi.org/10.5066/F7MS3QZH

Youssef, B., Bouskri, I., Brahim, B., Kader, S., Brahim, I., Abdelkrim, B. and Spalevi V. (2023). The Contribution of the Frequency Ratio Model and the Prediction Rate for the Analysis of Landslide Risk in the Tizi N'tichka Area on the National Road (RN9) Linking Marrakech and Ouarzazate. *CATENA, 232*, pp. 107464–107464. https://doi.org/10.1016/j.catena.2023.107464

https://doi.org/10.58440/ihr-31-1-a07

Appendix

Table 3 Pearson correlation coefficient matrix for assessing collinearity among the ten causative factors used in the LSM.

		1	2	3	4	5	6	7	8	9	10
1	Slope	1									
2	Aspect	0.06	1								
3	Depth	-0.17	-0.02	1							
4	Plan curvature	0.00	0.00	0.01	1						
5	Sediment thickness	-0.17	-0.01	0.13	0.00	1					
6	Bouguer gravity anomaly	-0.08	0.09	0.20	0.00	-0.28	1				
7	Magnetic anomaly	-0.05	-0.06	0.10	0.00	0.01	0.08	1			
8	Northward current	0.04	-0.09	0.04	0.00	-0.36	0.20	0.12	1		
9	Eastward current	-0.10	0.00	0.02	0.00	0.15	0.29	-0.14	-0.11	1	
10	Earthquake density	-0.08	-0.11	0.08	0.00	-0.18	-0.11	0.22	0.19	-0.22	1

Table 4 Frequency ratio (FR), relative frequency (RF), and prediction rate (PR) values calculated for each class of the ten causative factors, color-coded based on the susceptibility to landslide occurrence.

Date layers	Class	% Class-pixels	% Landslide-pixels	FR	RF	PR
Slope (degrees)	0–5	51.383	18.36	0.357	0.035	1.398
	5–10	26.583	32.13	1.209	0.12	
	10–15	11.595	26.086	2.25	0.223	
	15–20	5.644	14.311	2.536	0.251	
	20–25	2.713	5.677	2.093	0.207	
	>25	2.082	3.436	1.65	0.163	
Plan curvature	concave (<-0.05)	1.3	0.379	0.292	0.182	2.932
	flat (-0.05-0.05)	97.496	99.265	1.018	0.634	
	convex (<0.05)	1.204	0.355	0.295	0.184	
Aspect	Flat	0	0	0	0	0
	North	12.817	11.907	0.929	0.116	
	Northeast	12.155	10.372	0.853	0.106	
	East	13.598	12.984	0.955	0.119	
	Southeast	13.122	13.746	1.048	0.13	
	South	11.686	14.49	1.24	0.154	
	Southwest	10.726	12.103	1.128	0.14	
	West	11.996	11.034	0.92	0.114	
	Northwest	13.899	13.365	0.962	0.12	

Depth (m)	-1000 < x ≤ 0	9,556	40.796	4.269	0.57	3.693
	-2000 < x ≤ -1000	39.09	43.619	1.116	0.149	
	-3000 < x ≤ -2000	36.285	9.031	0.249	0.033	
	-4000 < x ≤ -3000	7.885	2.821	0.358	0.048	
	-5000 < x ≤ -4000	3.16	2.489	0.788	0.105	
	-6000 < x ≤ -5000	1.749	0.806	0.461	0.062	
	-7000 < x ≤ -6000	1.742	0.438	0.252	0.034	
	-8000 < x ≤ -7000	0.529	0	0	0	
	-∞ < x ≤ -8000	0.004	0	0	0	
Density of earth-quake (number of earthquake events per km²)	0 < x ≤ 10	71.578	54.671	0.764	0.015	3.053
	10 < x ≤ 20	13.368	39.725	2.972	0.06	
	20 < x ≤ 30	5.768	29.525	5.119	0.103	
	30 < x ≤ 40	3.335	26.282	7.88	0.158	
	40 < x ≤ 50	1.625	39.338	24.207	0.487	
	50< x ≤ ∞	4.326	38.137	8.815	0.177	
Sediment thickness (m)	0 < x ≤ 500	63.501	59.607	0.939	0.12	2.927
	500 < x ≤ 1000	19.998	15.887	0.794	0.102	
	1000 < x ≤ 1500	9.019	6.81	0.755	0.097	
	1500 < x ≤ 2000	4.432	4.627	1.044	0.134	
	2000 < x ≤ 2500	3.049	13.068	4.286	0.548	
Bouguer gravity	200 < x ≤ 250	0.005	0	0	0	2.833
	250 < x ≤ 300	2.725	1.97	0.723	0.126	
	300 < x ≤ 350	9.845	11.758	1.194	0.208	
	350 < x ≤ 400	25.16	63.057	2.506	0.437	
	400 < x ≤ 450	44.359	17.392	0.392	0.068	
	450 < x ≤ 500	17.489	5.58	0.319	0.056	
	500 < x ≤ 550	0.406	0.243	0.598	0.104	
	550 < x ≤ 600	0.009	0	0	0	
	600 < x ≤ 650	0.002	0	0	0	

https://doi.org/10.58440/ihr-31-1-a07

Northward current (m/s)	-0.3 < x ≤ -0.2	0.467765725	0	0	0	5.77
	-0.2 < x ≤ -0.1	0.99421193	0	0	0	
	-0.1 < x ≤ 0	30.602	14.827	0.484	0.068	
	0 < x ≤ 0.1	59.842	77.760	1.299	0.183	
	0.1 < x ≤ 0.2	7.740	5.805	0.750	0.106	
	0.2 < x ≤ 0.3	0.352	1.605	4.551	0.642	
Eastward current (m/s)	-0.2 < x ≤ -0.1	0.973	0.283	0.291	0.080	3.432
	-0.1 < x ≤ 0	19.238	16.090	0.836	0.245	
	0 < x ≤ 0.1	68.594	70.163	1.023	0.299	
	0.1< x ≤ 0.2	10.616	13.462	1.268	0.371	
	0.2 < x ≤ 0.3	0.497	0	0	0.0	
	x > 0.3	0.079	0	0	0.0	
Magnetic anomaly (nT)	-∞ < x ≤ -300	2.032	2.264	1.114	0.105	1.894
	-300 < x ≤ -200	5.088	0.927	0.182	0.017	
	-200 < x ≤ -100	15.615	5.412	0.347	0.033	
	-100 < x ≤ 0	27,621	10.722	0.388	0.037	
	0 < x ≤ 100	26.086	28.721	1.101	0.104	
	100 < x ≤ 200	14.156	23.536	1.663	0.157	
	200 < x ≤ 300	6.247	20.48	3.278	0.31	
	300 < x ≤ ∞	3.155	7.937	2.516	0.238	

Author's biography

Julia Swedenklef earned her Bachelor's degree in Ocean Exploration and Surveying from the University of Plymouth in 2024. Throughout her studies, she developed an interest in the process of combining bathymetric data with geological datasets, which led to her dissertation on landslide susceptibility mapping for the South Sandwich Islands. Currently, Julia works at Jan De Nul, where she conducts hydrographic and topographic surveys to support dredging and land reclamation projects. In this position she is further expanding her practical knowledge of survey equipment and reinforcing her passion for processing and analyzing unique datasets.

Julia Swedenklef

PEER-REVIEWED ARTICLE

Enhancing digital bathymetric models by advanced measurement uncertainty analysis

Authors

Bahareh Mohammadivojdan[1], Frederic Hake[3], Felix Lorenz[2], Jan Ole Böllert[4], Robert Weiß[2], Thomas Artz[2], Ingo Neumann[1] and Hamza Alkhatib[1]

Abstract

Accurate Digital Bathymetric Model (DBM)s are essential for ensuring safe navigation on waterways, yet they heavily depend on precise underwater measurements and robust modeling techniques. However, measurements taken in underwater environments are highly susceptible to uncertainties due to challenging environmental conditions and unknown underwater geometries, complicating the evaluation of both measurements and resulting models. This paper explores the impact of measurement uncertainty on DBM quality and presents a systematic pipeline for modeling these uncertainties to improve the reliability of resulting models. The methodology comprises of two primary stages. A detailed measurement uncertainty model is developed in the first stage based on error propagation principles. This model accounts for multiple uncertainty sources ranging from instrument accuracy to environmental influences. In the second stage, we implement a simulation-based approach to evaluate the influence of these uncertainties on the final DBM. To this end, we have developed a survey simulator that simulates a Multi-Beam Echo Sounder (MBES) system and generates realistic measurement uncertainties. The integration of these uncertainties as observation weights during the modeling process enhances model accuracy and reliability. The effectiveness and practicality of the proposed method are confirmed through validation in a controlled simulation environment with known geometry and uncertainties. The results underscore not only the technical benefits of incorporating measurement uncertainty in surface modeling but also highlight its critical importance in ensuring navigational safety through high-quality, reliable DBMs.

Keywords

DBM · surface model · MBES · uncertainty modelling · uncertainty budget

✉ Bahareh Mohammadivojdan · mohammadivojdan@gih.uni-hannover.de

[1] Leibniz University Hanover, Geodetic Institute, Hannover, Germany

[2] Federal Institute of Hydrology, Koblenz, Germany

[3] Allsat GmbH, Hannover, Germany

[4] Saxon State Ministry of Infrastructure and Regional Development, Dresden, Germany

https://doi.org/10.58440/ihr-31-1-a09

Resumé

Des modèles numériques de bathymétrie (MNB) précis sont essentiels pour garantir la sécurité de la navigation sur les voies navigables, mais ils dépendent fortement de mesures sous-marines précises et de techniques de modélisation robustes. Cependant, les mesures prises dans des environnements sous-marins sont très sensibles aux incertitudes dues à des conditions environnementales difficiles et à des géométries sous-marines inconnues, ce qui complique l'évaluation des mesures et des modèles qui en résultent. Cet article explore l'impact de l'incertitude des mesures sur la qualité des MNB et présente un pipeline systématique pour modéliser ces incertitudes afin d'améliorer la fiabilité des modèles obtenus. La méthodologie comprend deux étapes principales. Dans un premier temps, un modèle détaillé d'incertitude de mesure est développé sur la base des principes de propagation des erreurs. Ce modèle tient compte de multiples sources d'incertitude, allant de la précision des instruments aux influences environnementales. Dans un deuxième temps, nous mettons en œuvre une approche basée sur la simulation pour évaluer l'influence de ces incertitudes sur le MNB final. À cette fin, nous avons développé un simulateur de levé qui simule un système de sondeur multifaisceaux (SMF) et génère des incertitudes de mesure réalistes. L'intégration de ces incertitudes sous forme de pondérations d'observation pendant le processus de modélisation améliore la précision et la fiabilité du modèle. L'efficacité et la praticité de la méthode proposée sont confirmées par une validation dans un environnement de simulation contrôlé avec une géométrie et des incertitudes connues. Les résultats soulignent non seulement les avantages techniques de l'intégration de l'incertitude de mesure dans la modélisation de surface, mais aussi son importance cruciale pour garantir la sécurité de la navigation grâce à des MNB fiables et de haute qualité.

Resumen

Los Modelos Batimétricos Digitales (DBM) precisos son esenciales para garantizar la seguridad de la navegación por las vías navegables, pero dependen mucho de la precisión de las mediciones submarinas y de la solidez de las técnicas de modelado. Sin embargo, las mediciones tomadas en entornos submarinos son muy susceptibles a las incertidumbres debidas a las difíciles condiciones ambientales y a las desconocidas geometrías submarinas, que complican la evaluación tanto de las mediciones como de los modelos resultantes. Este artículo explora el impacto de la incertidumbre de las mediciones en la calidad de los DBM y presenta una vía sistemática para modelar estas incertidumbres para mejorar la fiabilidad de los modelos resultantes. La metodología consta de dos fases principales. En la primera fase se desarrolla un modelo detallado de incertidumbre de las mediciones basado en los principios de propagación de errores. Este modelo tiene en cuenta múltiples fuentes de incertidumbre desde la precisión de los instrumentos hasta las influencias ambientales. En la segunda etapa, implementamos un enfoque basado en simulaciones para evaluar la influencia de estas incertidumbres en el DBM final. Para ello, hemos desarrollado un simulador de levantamientos que simula un sistema de Ecosonda Multihaz (MBES) y genera incertidumbres de medición realistas. La integración de estas incertidumbres como confianza de las observaciones durante el proceso de modelado mejora la precisión y fiabilidad del modelo. La efectividad y viabilidad del método propuesto se confirman mediante la validación en un entorno de simulación controlado con geometría e incertidumbres conocidas. Los resultados subrayan no sólo los beneficios técnicos de incorporar la incertidumbre de las mediciones en el modelado de superficies, sino también su importancia crítica para garantizar la seguridad de la navegación mediante DBM de alta calidad y fiables.

1 Introduction

Accurate and reliable DBMs are needed for safe navigation in waterways. This is especially important for Germany– a leading global economic and export nation that relies heavily on its inland and maritime shipping routes to connect industrial hubs to seaports and ensure access to international markets. Its waterways, which connect the North and Baltic Seas and are central to Europe, are vital to the European waterway network, supporting trade and transport safety (BFG, 2013). Nowadays, with the capabilities of sonar-based systems such as MBES, it is possible to sample underwater topography in high spatial resolution and density. These systems measure both location and depth, generating Point Cloud (PC) comprising millions of points in a short time. Although high-resolution measurements are associated with greater detail and raise expectations regarding the detection of fine structures and higher accuracy, assumptions about the precision of such data can be misleading, as each measurement is subject to both vertical and horizontal uncertainties. The International Hydrographic Organization (IHO) provides guidelines to ensure safety and guarantee a minimum level of accuracy for users in order to standardize the quality of DBMs (IHO, 2022).

To create DBMs, we rely on raw measurements from which outliers have been removed. However, this process makes it difficult to produce a high-quality DBM because the source data are not always as accurate as required. Bathymetric measurement uncertainty depends on both the survey system and survey conditions. A survey system is, in essence, a multi-sensor system composed of several sensors (e.g., MBES, IMU, GNSS, etc.). The error budget is influenced by various factors related to the system and measurement set up (e.g. sensor installation, georeferencing, measurement track, speed, etc.) Hare et al. (2011). Additionally, further inaccuracies may be introduced during the modeling process itself, for example due to model approximation errors, limitations in the chosen surface representation, or the presence of noise and outliers in the input data. This raises two questions: if we closely examine the measurement process and its surrounding conditions, can we quantify these inaccuracies or estimate the uncertainties involved? And how might this information enhance the final model?

1.1 Uncertainty of bathymetry surveys

A realistic estimate of the measurement uncertainties is crucial for evaluating their impact on final products, such as DBM. This information is invaluable not only for assessing model quality but also for applications such as measurement planning and bridge risk management (Eakins & Taylor, 2010; Hare et al., 2011). Extensive research has focused on detecting and modeling the source of errors in bathymetric surveys. For example, Hare (1995) developed an algorithm to predict the uncertainty of bathymetry surveys by considering various influencing factors. He accounted for the total depth error by including errors from the sounder system, roll, pitch, heave, refraction, dynamic draught, and water level. Moreover, the total error budget should also incorporate errors from the positioning system, relative transducer-sounding position, heading, and the relative antenna-transducer position (Hare, 1995). Today Precise Differential Global Positioning System (PDGPS) are used for positioning, which replaces the errors associated with dynamic draught and water level with the uncertainty of the GNSS solution. The law of propagation of variances can be applied to integrate different sources of uncertainty and derive estimates of Total Propagated Uncertainty (TPU), separating it into a vertical component – Total Vertical Uncertainty (TVU) – and a horizontal component – Total Horizontal Uncertainty (THU) (Hare, 1995; Hare et al., 2011). However, it is important to note that position and depth errors should not be considered as inherently coupled. In complex underwater environments, especially in areas with abrupt morphological changes, even small horizontal deviations can cause significant apparent depth discrepancies. Thus, while the TPU model provides an overall estimate of uncertainty, it does not fully account for morphology-driven effects. Therefore, in addition to considering the combined TPU, a separate and independent assessment of TVU and THU is necessary to properly characterize the measurement uncertainties. Many researchers have contributed to this model to account for more error sources e.g. doppler frequency shift, baseline decorrelation when using frequency modulated pulse (Haji Mohammadloo et al., 2018, 2019). The quality of uncertainty model, was researched by (Haji Mohammadloo et al., 2018; Tengku Ali et al., 2022; Abubakar & Poerbandono, 2023). However, due to lack of ground truth on underwater geometry, validation of the quality of the developed models still remains under-researched.

1.2 Modeling and quality of DBM

The accuracy of the DBM depends on both the quality of the source data and the modeling technique employed. Since every measurement inherently carries some uncertainty, these uncertainties propagate into the final bathymetric model. The modeling approach can range from a simple grid-based representation to a complex 3D mathematical surface. Numerous studies have focused on spatial data modeling. Choosing the suitable modeling technique, depends on the characteristics of the PC such as its size, distribution, density and regularity. Although MBES PCs are typically dense, they are non-homogeneous and contain some gaps. Consequently, many modeling techniques are unable to handle large datasets with high variability and spatial gaps. In practice, simpler grid representations are frequently used for these data (Maune et al., 2007), where each cell is assigned a single value derived from various

 https://doi.org/10.58440/ihr-31-1-a09

interpolation techniques. Common methods include splines, kriging, nearest neighbor, minimum curvature, modified Shepard's method, Inverse Distance Weighting (IDW), Triangulated Irregular Network or artificial intelligence (Lorenz et al., 2021; Maune et al., 2007; Wlodarczyk-Sielicka et al., 2016). Each method has its strength and is chosen based on the specific circumstances of the dataset (Yang et al., 2004; Rishikeshan et al., 2014). An appropriately chosen interpolation technique not only reduces computational cost by limiting mesh nodes to local neighborhoods, but can also mitigate the influence of measurement noise by averaging over multiple observations. This often results in smoother and more realistic surface representations. However, the accuracy of the final model remains sensitive to factors such as cell size, point density, topographic variability within each cell, and the interpolation strategy chosen. In addition, unlike hierarchical or global surface models that can incorporate broader spatial dependencies, grid-based approaches may be limited in their ability to capture complex structures if the local window is too restrictive.

A DBM can be derived based on global functions. For example, Bisquay et al. (1998) and Bottelier et al. (2005) use Kriging to interpolate the underwater geometry by exploiting the correlation among data points. However, this method is computationally expensive, and to achieve reliable estimates, the underlying trend in the data must be modeled separately (Mohammadivojdan et al., 2020). Alternatively, a DBM can be derived based on a mathematical model, representing a continuous global surface– such as traditional polynomial surfaces or free-form surfaces, like B-splines and non-uniform rational B-splines (Piegl, 1997; Bureick et al., 2016). For a global surface approximation, Arnold & Shaw (1993), Bjørke & Nilsen (2009) and Mohammadivojdan et al. (2021), employ a coarse-to-fine strategy in building the surface. A hierarchical surface model can overcome specific challenges posed by high-density, high-noise, and nonhomogeneous distribution of MBES measurements. In this context, Mohammadivojdan et al. (2024) utilize a hierarchical B-spline surface model – namely, the Multilevel B-spline Approximation (MBA) model introduced by (Lee et al., 1997) – which adapts to varying topographies and efficiently handles data gaps.

Furthermore, various survey configurations and operational setups also impact the accuracy of DBMs. These setups influence point density and distribution, which in turn affect modeling error. Maleika (2013) investigated the influence of factors such as vessel speed, swath width, track configuration, and measurement density on model quality (Maleika et al., 2012). Since there is no ground truth on the underwater geometry, it is challenging to precisely estimate the DBM accuracy. To quantify the modeling error, several statistical approaches are available, including cross-validation, split-sample and jack-knifing, and bootstrapping (Paquet, 2010; Erdogan, 2009; Mohammadivojdan et al., 2021). These approaches evaluate the model's predictive performance by testing it on data that were not used during the estimation process, ensuring that the model generalizes well to new, unseen data. By partitioning the data into subsets or repeated resampling, these techniques estimate the variability and reliability of the model's predictions, providing a robust assessment of its accuracy and potential biases. However, it is important to note that in the absence of ground truth, both training and test subsets are affected by similar random noise characteristics inherent to MBES systems. As a result, while these methods can provide insight into the internal consistency and robustness of the model, they may not fully reflect the absolute modeling error, especially in high-noise environments.

1.3 Contribution

The objective of this study is to quantify the uncertainty of a DBM and explore how incorporating uncertainty information can improve their accuracy and reliability. We achieve this by developing a comprehensive uncertainty model that quantifies the uncertainties inherent in bathymetric measurements. We employ a Monte-Carlo-based approach for error propagation, which provides a computationally straightforward way to account for complex, non-linear relationships and non-standard probability distributions. Unlike classical error propagation methods, our approach avoids intricate mathematical derivations while still offering a detailed representation of the uncertainties affecting our measurements. This work focuses on creating a DBM from outlier-cleaned raw data using a mathematical surface, specifically employing the MBA approach. Our goal is to explore how uncertainty information can enhance this model. Our approach is to incorporate uncertainty data as weights within the adjustment process, to assess its impact on model quality. However, a major challenge is the lack of real-world cases with known ground truth; without precise knowledge of the true underwater geometry, it is difficult to definitively evaluate the model's accuracy. To overcome this, we developed a simulation environment that generates a known geometry based on a precise mathematical model representing the ground truth. Within this controlled environment, we simulate both the measurement process and its corresponding uncertainties. This setup allows us to obtain measurements that include uncertainties while retaining complete knowledge of the true geometry, thereby enabling a better understanding of how uncertainty affects the model.

Recognizing that a single simulation scenario is insufficient for drawing reliable conclusions, we conducted a comprehensive Monte-Carlo simulation experiment, repeating the entire process multiple times. In each iteration, both the geometry and the associated uncertainties are simulated, and two versions of the DBM are generated: one that incorporates the uncertainty information to improve the model, and one that does not. This comparative approach enables us to evaluate the impact of incorporating uncertainty on the model's accuracy and reliability. Ultimately, we identify the optimal model and generate additional outputs – such as Confidence Intervals (CI) and uncertainty maps – that provide a clearer picture of the model's precision. This paper is organized in three parts. Part 1 describes the development of the uncertainty model and the hydrographic survey system used in our experiment, as well as the model's validation (Sections 2 and 3). Part 2 presents the survey simulator (Section 4). Part 3 details the data processing, modeling algorithm, the Monte-Carlo experiment, and the resulting analysis (Section 5).

2 Description of the uncertainty model

According to the Guide to the Expression of Uncertainty in Measurements (GUM), to estimate uncertainty of a measured value *Y*, we should establish the functional relationship between the target value *Y* and all the other quantities (X_1, X_2, …, X_N) contributing in the measurement process (ISO, 1995)

$$Y = f(X_1, X_2, .., X_N) \tag{1}$$

If the input variables are uncorrelated, the combined measurement uncertainty $u_c(Y)$ of a target quantity *Y* can be calculated from the standard uncertainties of the input quantities $u_i(X)$ as follows (Schwarz, 2020a):

$$u_c(Y) = \sqrt{\sum_{i=1}^{n}(c_i \cdot u(X_i))^2} \tag{2}$$

wherein,

c_i – Sensitivity coefficient, defined as $c_i = \partial f / \partial x_i$

$u(x_i)$ – Standard uncertainty of the input quantity x_i

n – Number of input quantities

The uncertainty u_c is propagated from the uncertainties of the inputs using a first-order Taylor series expansion (linear approximation). The sensitivity coefficient is derived from the partial derivative of the functional model (*Y*=f(*X*)) with respect to the input quantities, which indicates the effect of each input quantity on the final results. This represents the case where functional model is linear and no correlation is assumed between the input parameters.

The concept of GUM, defines a CI around a measured value called *expanded uncertainty*. The true value of the measurand is expected to lie within this interval. Mathematically, it is represented as:

$$U(Y) = k \cdot u(Y) \tag{3}$$

where *k* is the coverage factor, determined based on the desired Confidence Level (CL). Thus, the final measurement result can be expressed as:

$$Y \pm U(Y) \tag{4}$$

2.1 Establishing the measurement model

In this case, the measurement model is the solution of the coordinates in the target coordinate system. The goal is to derive the absolute coordinates of the waterbed from the raw measurement data collected by the installed sensors. This derivation occurs in multiple steps and is relative to different reference systems.

Step 1 – Deriving coordinates within Transducer coordinate system (T-Frame): Coordinates in the T-Frame are derived based on transducer measurements (range *r*, beam angle *θ*) as follows:

$$\begin{bmatrix} X_T \\ Y_T \\ Z_T \end{bmatrix} = \begin{bmatrix} 0 \\ r \cdot \sin(\theta) \\ -r \cdot \cos(\theta) \end{bmatrix} \tag{5}$$

Step 2 – Transforming into Ship's coordinate system (B-Frame): In the B-Frame, the *X*-axis runs along the ship's length (positive toward the bow), and the *Z*-axis points toward the zenith of the ship. The *Y*-axis corresponds to the port side direction. The origin of this coordinate frame is the ship's Center of Gravity (CoG). Coordinates in B-Frame are obtained by a 6DOF transformation: first, the coordinates in T-Frame are rotated based on mounting angles of the transducer with respect to the ship body frame (denoted by *α*, *β*, and *γ*), and then they are translated based on the coordinate difference between the transducer's reference point and the ship's CoG. This translations in XYZ($\Delta X_{T\text{-}B}$, $\Delta Y_{T\text{-}B}$, $\Delta Z_{T\text{-}B}$) are determined in a vessel offset survey.

$$\begin{bmatrix} X_B \\ Y_B \\ Z_B \end{bmatrix} = \mathbf{R}(\alpha, \beta, \gamma) \cdot \begin{bmatrix} X_T \\ Y_T \\ Z_T \end{bmatrix} + \begin{bmatrix} \Delta X_{T-B} \\ \Delta Y_{T-B} \\ \Delta Z_{T-B} \end{bmatrix} \tag{6}$$

Step 3 – Transformation from B-Frame into the Local topocentric coordinate system (LL-Frame): Measurements from the Global Navigation Satellite System (GNSS) sensor are obtained in the LL-Frame, which has globally defined axes: The Y-axis points toward geographic north, and the Z-axis runs parallel to the plumb line, pointing toward the local zenith. The translation values in XYZ($\Delta X_{B\text{-}LL}$, $\Delta Y_{B\text{-}LL}$, $\Delta Z_{B\text{-}LL}$), are based on the coordinate differences between the ship's CoG and reference point of the GNSS antenna. Due to the axis orientation in the UTM system, α_H is introduced, which results from the heading according to $\alpha_H = 90° - H$. The rotation is based on the measured heading α_H, pitch *P* and roll *R* by Inertial Measurement Unit (IMU).

$$\begin{bmatrix} X_{LL} \\ Y_{LL} \\ Z_{LL} \end{bmatrix} = \mathbf{R}(\alpha_H, P, R) \cdot \begin{bmatrix} X_B \\ Y_B \\ Z_B \end{bmatrix} + \begin{bmatrix} \Delta X_{B-LL} \\ \Delta Y_{B-LL} \\ \Delta Z_{B-LL} \end{bmatrix} \tag{7}$$

Step 4 – Combining with GNSS Measurements: The final coordinates are obtained by combining the transformed coordinates in LL-Frame with the GNSS measurements

https://doi.org/10.58440/ihr-31-1-a09

from the GNSS:

$$\begin{bmatrix} X \\ Y \\ Z \end{bmatrix}_{Final} = \begin{bmatrix} X_{LL} \\ Y_{LL} \\ Z_{LL} \end{bmatrix} + \begin{bmatrix} X_{GNSS} \\ Y_{GNSS} \\ Z_{GNSS} \end{bmatrix} \tag{8}$$

This generalized formulation describes the measurement system illustrated in Fig. 1 and applicable to different sensor types and fields of application.

2.2 Identifying influencing factors

Once the measurement model has been established, the next crucial step is to identify all elements that influence the accuracy of the final quantity. These factors arise from the sensors themselves – including their quality and the reliability of the source data – environmental conditions, and the definition of the chosen reference frames. In the case of an MBES, not only must uncertainties in measured range and angle be considered, but also indirect influences such as variations in sound speed at different depths, the transducer's opening angle, pulse length, beam bandwidth, and heave. In addition, the precise alignment of the sensors relative to one another and the careful definition of reference points play a vital role in ensuring accurate results. The main factors influencing bathymetric measurement uncertainty are illustrated in Fig. 2. For a deeper discussion of each uncertainty source, its overall impact, and the methodologies to quantify it, readers are referred to (Hare, 1995) and (Wirth, 2011).

2.3 Uncertainty estimation

With the measurement model established and the relevant influencing factors identified, the next step is to estimate the uncertainty of the target quantity via error propagation. Classical GUM propagation (refer to Eq. 2) involves computing the derivatives of the measurement model for all influencing parameters. However, because our measurement model is highly nonlinear, the classical approach is suboptimal. For complex systems, an alternative solution is to use Monte Carlo Method (MCM), as described in GUM (ISO, 1998). MCM offer several advantages: it overcomes the limitations of classical GUM propagation – which assumes small uncertainties and relies on a first-order Taylor expansion – and it accommodates any Probability Density Function (PDF) of input parameters, thereby extending the analysis beyond the constraints of normal distributions. The outcome of MCM is not just a standard uncertainty, it also gives a complete uncertainty distribution.

To estimate uncertainties using MCM, it is first necessary to identify the PDF corresponding to each influencing factor. MCM is based on performing a large number of simulated random experiments, and its validity is ensured when a sufficient number of trials are conducted. Typically, the number of samples ranges from 1,000 to 1,000,000 (e.g., m = 100,000 in Alkhatib et al. (2009) and m = 1,000,000 in

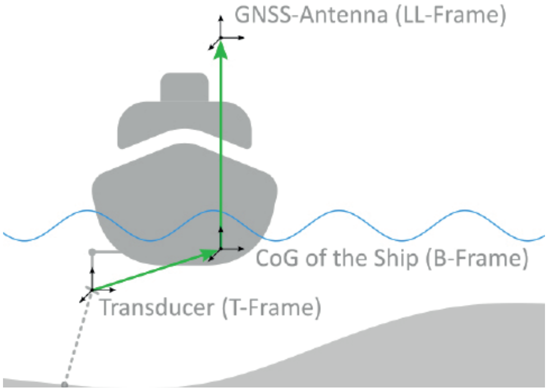

Fig. 1 Illustration of measurement system, sensors, and the defined coordinate frames.

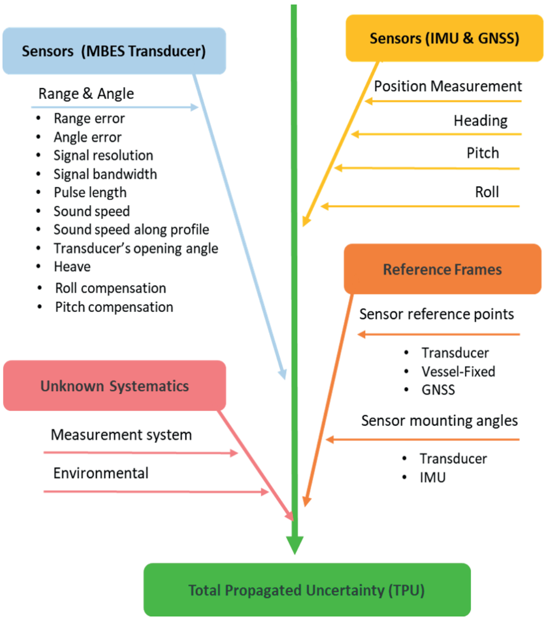

Fig. 2 The influencing factors on bathymetric measurement uncertainty.

Schwarz (2020b)). Due to its computational intensity, it is imperative to optimize the number of samples to achieve a balance between computational efficiency and result accuracy (ISO, 1998; Schwarz, 2020b).

The outcome of MCM is the PDF of the parameter of interest, which represents the combined measurement uncertainty. The three-dimensional expanded uncertainty, at a 95 % CL, is defined as the TPU. As specified by the IHO (2022), the TPU consists of two components: TVU and THU. The TVU is extended uncertainty in vertical dimension (σ_{Height}). Similarly, THU is a two-dimensional uncertainty for the North and East dimensions (σ_{North}, σ_{East}). For normally distributed, one and two-dimensional variables, The IHO defines an expansion factor of 1.96 and 2.45, respectively. Known systematic deviations U_c can also be incorporated. TVU is calculated as:

$$TVU = 1.96 \cdot \sqrt{\sigma^2_{Height} + U^2_{sys.V}} \tag{9}$$

and THU is calculated as:

$$THU = 2.45 \cdot \sqrt{\sigma^2_{East} + \sigma^2_{North} + U^2_{sys.H}} \tag{10}$$

3 Validation of the uncertainty model

To assess the functionality of our model and validate its performance, we use real data. Although the systems and configurations of measurement instruments may vary across different vessels, their underlying principles remain similar. In this study, we focus on a specific measurement system – the Uwe Jens Lornsen (UJL; Fig. 3). We developed the measurement model for UJL according to Section 2.1, and for a specific measurement campaign, a complete uncertainty model is also established.

3.1 Details of the measurement system

The survey vessel UJL (Fig.3) is a survey vessel operated by the Elbe-North Sea (Tönning) Waterways and Shipping Office (WSA). Built in 1993, its primary tasks include monitoring and depth surveying of maritime navigation channels along the Schleswig-Holstein West Coast to ensure safe and efficient navigation. Additionally, UJL is used for surveying structures, harbors, and dredging areas. To perform these tasks, the UJL uses a Kongsberg EM2040C dual-head multibeam echo-sounding system with two permanently installed transducers. For spatial referencing, a satellite-based positioning system – comprising PDGNSS with an integrated navigation sensor system (INS), including a Seapath 330+ and a motion reference unit (MRU 5+) – is used. The location of the sensors on UJL is shown in Fig. 4.

The primary sampling sensors used on UJL is MBES. Two MBES are mounted perpendicularly to the vessel, enabling a profile-based scanning of the seafloor. For efficient scanning, these two echo sounders are oriented along the port–Back Board side (BB) and Star Board side (STB) and tilted at 37° relative to the ship's baseline. In addition to the dual-head system, a third hydroacoustic sensor – a Single Beam Echo Sounder (SBES) – is used to measure the central depth at the vessel's nadir using various frequencies. Note that the SBES was used exclusively for navigation support and was not involved in the bathymetric data processing or experimental analysis.

Fig. 3 Image of survey vessel UJL (WSA, 2023).

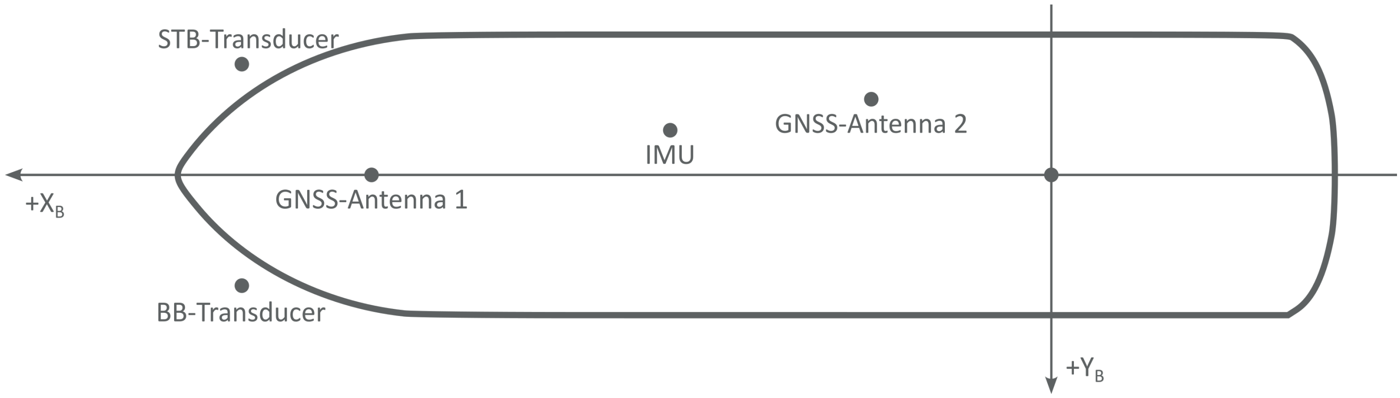

Fig. 4 Schematic layout of the sensor configuration on the UJL survey vessel.

https://doi.org/10.58440/ihr-31-1-a09

The UJL was used in 2019 for a measurement campaign of the man-made Kiel Canal (Fig. 5), conducted by the Elbe Nordsee Waterways and Shipping Office (Tönning). A 300 m long measurement swath was used as test data. In the selected section of the campaign, both flat areas and structured regions characterized by small bed load transport bodies (dunes), embankments, and leaps across flow direction were observed. The riverbed in this area typically consists of rock, silt, and gravel; water depths reach up to 13 m. The 'equal angular' measurement mode produces 256 measurement points per ping, with an across-track distance of around 0.06 m near nadir and 0.4 m in the remote swath areas. Near the vessel's nadir, the point density is approximately 45 points per square meter, decreasing to 15 points per square meter in the outer regions. Based on the vessel's speed and the chosen sampling rate, the pings have a typical along track distance of 0.35 m.

The test area exhibits varying effects on the measurement uncertainty due to the combination of high-water depth with partly shallow areas characterized by sediment and partly sloping embankments. The geometry of the observation configuration changes significantly – for example, the measured distance, the angle of incidence, and consequently, the size of the measurement footprint varies considerably. Furthermore, different structures such as small dunes or leap areas provide distinct backscattering properties, each influencing the measurement uncertainty in a unique way.

3.2 Uncertainty model for UJL

All sensors deliver the raw data in their specific sensor coordinate frame. To retrieve a 3D PC in the target reference frame, the measurements must first be transformed to a consistent vessel reference frame and then to the target reference frame. Section 2.1 outlines the methodology for calculating the seafloor coordinates for a single transducer. Following this methodology, we establish the measurement model for UJL, where the target coordinate system here is ETRS89/DREF91 (realization 2016) with UTM projection.

A detailed list of the key parameters and their corresponding uncertainty values, as incorporated into our uncertainty modeling, is presented in Table 1. For those parameters marked with "e.g.", the listed values are representative examples from the dataset and are not treated as fixed. Instead, they are dynamically estimated per observation within the simulation, using established models such as the geometric range uncertainty model of Hare (1995) and Wirth (2011), which incorporate relevant factors like slant range, beam angle, and sound speed variability. For more details on each uncertainty source and the methods used to quantify them, readers are referred to Hare (1995) and Wirth (2011).

Here, we assume normal distribution for all parameters considered, as listed in Table 1. In this approach, input parameters are assumed to be statistically uncorrelated. Nevertheless, correlations that naturally arise through the functional relationships between variables are implicitly captured by the Monte Carlo Simulation process. The different variations of the input parameters propagate through the nonlinear system model, and their mutual effects on the target variables (X, Y, Z coordinates) are reflected in the output's distribution. The uncertainties are calculated separately for each coordinate component, providing individual uncertainty values for the East, North, and Height components. Following the MCM, 1000 simulations were performed, resulting in 1000 solutions for each point and its East, North, and Height components. The PDF of one example measurement point's coordinate solutions is illustrated in Fig. 6 as an example. A normal distribution has been estimated for each component and shown with red lines in Fig. 6. The calculated coordinates align well with the Normal distribution curve, with no significant deviations observed. Therefore, we use standard deviation corresponding to a CL of 68 % to determine uncertainties of each component (σ_{East}, σ_{North}, σ_{Height}). These uncertainties are then used to calculate TPU values (Eqs. 9 and 10).

Fig. 7 illustrates the results of the MCM uncertainty calculation with 95 % CL for each measurement point. Here, uncertainties are expressed at a 95 % CL, in accordance with the definition of TPU (see Eqs. 9 and 10). The previously calculated standard uncertainties (at 68 % CL) are used as the basis for this propagation. Fig. 7a shows the height uncertainties for the first 100 profiles within the measurement swath, while Fig. 7b presents the horizontal uncertainties. These figures include measurements from both BB and STB transducers, with coordinates color coded according to their calculated TVU and THU. The color scale is provided in the legend. In the height component, uncertainties vary significantly within a single profile, ranging from 9 cm directly under the ship to 29 cm for the outer transducer beams. This variation aligns with the expectation that measurement uncertainty increases with greater measured distances and larger beam angles. Additionally, a slight increase in uncertainty is observed in the direct nadir area. This increase in TVU is mainly due to limitations in signal resolution. At nadir, where the acoustic path is shortest and perpendicular, pulse duration plays a dominant role in depth resolution. Similarly, horizontal uncertainty increases with distance from the vessel due to larger beam footprints and weaker signal returns at steeper angles. In outer swath areas, small errors in angle or range are amplified, leading to greater horizontal position uncertainty. However, the range of the horizontal uncertainty values differs considerably from that of the height uncertainties, varying from 0.55 m near the nadir to 1.28 m in the outer beams. This confirms that horizontal uncertainty is generally higher than height uncertainty.

Table 1 Uncertainty values and influencing parameters for MBES, IMU, and GNSS.

Influencing parameter	Value	Uncertainty symbol	Uncertainty value
		Related to MBES	
Angle measurement θ	-	σ_θ	e.g. 0.002 deg
Range measurement error r	-	σ_r	e.g. 0.12 m
Sound speed along profile v_m	1469 m/s	σ_{vm}	0.123 m/s
Surface sound speed v_s	1468 m/s	σ_{vs}	0.048 m/s
Speed over ground v_{SOG}	2 m/s	σ_{vSOG}	0.101 m/s
Spatio-temporal variations of sound speed Δv	-	$\sigma_{\Delta v}$	0.01 m/s
Signal bandwidth	15 kHz	-	-
Pulse length Δt_{imp}	0.015 s	$\sigma_{\Delta timp}$	0.05 s
Definition of the ground	-	U	0.03 m
MBES Pitch compensation Pk	-	σ_{Pk}	0.11 deg
MBES Roll compensation Rk	-	σ_{Rk}	0.05 deg
Heave	-	-	0.05 m
		Related to IMU & GNSS	
Heading α	-	σ_α	0.064 deg
Pitch P	-	σ_P	0.054 deg
Roll R	-	σ_R	0.054 deg
X_{GNSS}, Y_{GNSS}, Z_{GNSS} (PDGNSS)	-	$(\sigma_X, \sigma_Y, \sigma_Z)_{PDGNSS}$	(0.005,0.005,0.013) m
X, Y, Z (Position)		$(\sigma_X, \sigma_Y, \sigma_Z)_{Pose}$	e.g. (0.143,0.147,0.014) m
		Related to reference frames	
$\{X_0, Y_0, Z_0\}_{GNSS}$	-	$\sigma_{\{X0, Y0, Z0\}GNSS}$	0.005
$\{X_0, Y_0, Z_0\}_{Ship}$	-	$\sigma_{\{X0, Y0, Z0\}Ship}$	0
$\{X_0, Y_0, Z_0\}_{Transducer}$	-	$\sigma_{\{X0, Y0, Z0\}Transducer}$	0.005
Transducer mounting angles (α, β, γ)	-	$\sigma_{\{\alpha, \beta, \gamma\}Transducer}$	(0.1,0.1,0.1) deg
IMU mounting angles	-	$\sigma_{Mount,Pitch}$, $\sigma_{Mount,Roll}$	0.02 deg

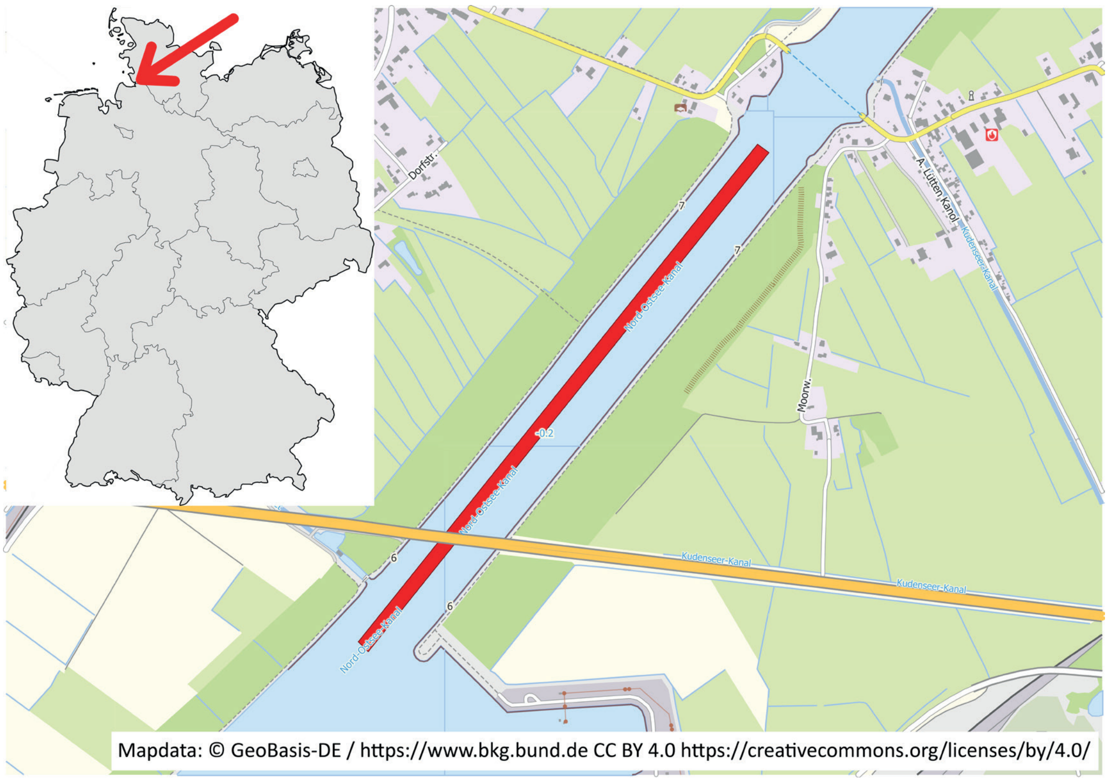

Fig. 5 Survey area of Kiel Canal. The 300 m long measurement swath used as test data.

https://doi.org/10.58440/ihr-31-1-a09

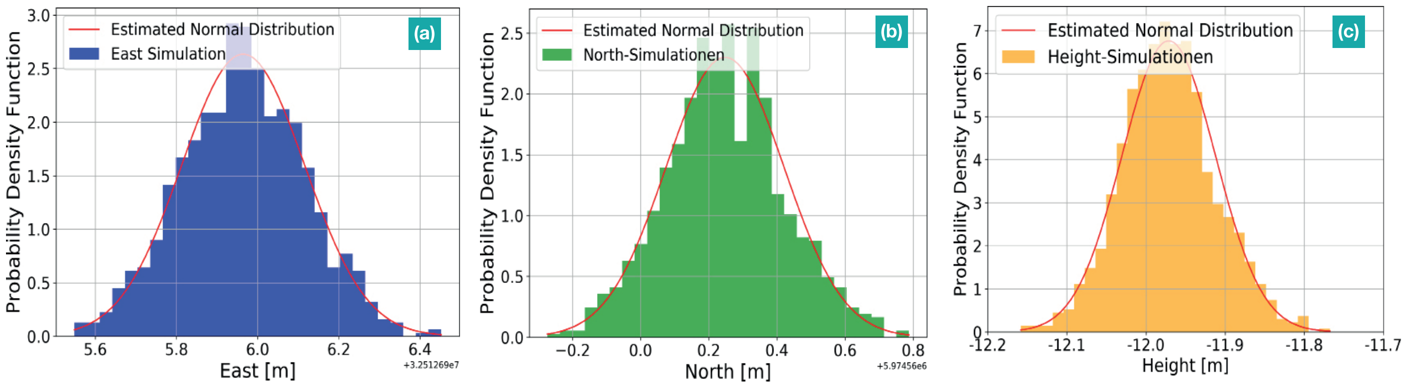

Fig. 6 PDF of East, North, and Height components for one point. The PDF results from 1000 MCM simulations. Red lines represent the fitted normal distribution.

3.3 Discussion of TPU modelling results

To validate the results of the uncertainty analysis, we compared our MCM results with those obtained using the classical GUM approach and those estimates from the commercial software QINSy (version 8.18.3; QPS, 2025), which is used as the data acquisition software on UJL. In this software, the offsets in the vessel frame and the measurement data from the sensors are converted into a 3D PC as projected points in the official reference frame. In addition, other attributes recorded by the sensors are included so that a TPU value per beam can also be determined and specified. The exact procedure for determining the TPU by QINSy is not known, but tests and comparisons suggest that the procedure is similar to the methods described in (Hare, 1995; Wirth, 2011). Nonetheless, it is presumed that QINSy's TPU estimations meet hydrographic standards and provides combined standard uncertainties with 95 % CL.

According to IHO, each survey must comply with a defined "maximum allowable uncertainty" for both vertical and horizontal measurements. For vertical uncertainties, permissible limits at a 95 % CL are computed based on depth-dependent b and depth-independent a parameters, as well as the actual depth d (Eq. 11). These parameters differ according to the survey order as described in IHO (2022). Furthermore, the S-44 standard defines maximum permissible horizontal uncertainties; for example, the maximum horizontal uncertainty THU_{max} allowed for Special Order surveys is set to 2 m (IHO, 2022).

$$TVU_{max} = \sqrt{a^2 + (b \cdot d)^2} \tag{11}$$

Fig. 8 presents the TVU of measurement points for a single representative profile to illustrate the structure and variation of the uncertainty with respect to beam angle relative to the ship's vertical axis (Fig. 8a) and lateral distance (Fig. 8b). While this profile is not intended to be statistically representative of the full dataset, it provides a clear example of the underlying trend. The plots compare solutions from the classical GUM approach, MCM, and QINSy. The uncertainties for BB and STB transducers are shown with similar color. Fig. 8 additionally illustrates the maximum permissible vertical uncertainty TVU_{max} for the Special Order and Exclusive Order survey as defined by the IHO (2022), for a mean depth of 12 m. The uncertainties computed via MCM follow the expected pattern shown in Fig. 7a. As shown in Fig. 8a, TVU increases exponentially with respect to the beam angle, while Fig. 8b shows a more linear increase in TVU with lateral distance from the vessel. The lowest uncertainties occur at distances of 12–15 m from the ship, corresponding to beam angles of 48–53° from the ship's normal. This effect is primarily attributed to limitations in vertical resolution caused by pulse duration. The nadir beams, pointing directly downward, rely almost exclusively on the two-way travel time of the acoustic pulse to determine depth. Consequently, any uncertainty in echo detection, especially when longer pulse durations are used, directly translates into vertical measurement uncertainty. While side beams are more affected by geometric distortion due to effects such as decreasing signal intensity and increasing footprint resulting from beam divergence, nadir measurements are more sensitive to temporal resolution. Additionally, the nadir represents a transition zone between the BB and STB swaths. Here, overlapping beams from both swath edges – where positional and angular uncertainties are typically higher – may interact, compounding the overall uncertainty in this central region. While all three solutions exhibit similar trends, differences exist. The classical GUM approach does not capture the nadir effect seen in MCM results. Since both methods are based on measurement model described by Wirth (2011), only minor discrepancies are expected. These variations likely stem from differences in user-defined input parameters, highlighting their role in uncertainty analysis. Compared to QINSy's uncertainties, the relative variation aligns, but our uncertainty model appears to account for similar factors with differing absolute impacts. All three predicted uncertainties are below TVU_{max} for the Special Order survey. In Fig. 8, we observe that the outer-beam uncertainty of the BB transducer exceeds the Exclusive Order threshold defined by the IHO S-44 standard. According to S-44 standards, the TVU is expected to increase with water depth, following a depth-dependent model (IHO, 2022). However, the measurement campaign analyzed in this study was conducted in a relatively uniform depth environment, with an average depth of approximately 13 meters. As a result, the data do not capture a wide range of depth-induced variability in TVU. Future work in more bathymetrically diverse areas may provide further insight into this relationship.

Fig. 9 presents estimated THU for the same profile measurement. It compares the results from MCM, GUM, and QINSy's THU values. The uncertainties for BB and STB transducers are shown with similar color. Fig. 9 also shows the maximum permissible horizontal uncertainty THU_{max} for the Special Order survey as defined by the IHO (2022), represented by the dotted line.

Compared to height uncertainty, horizontal uncertainty is substantially higher. The uncertainty profile also differs, showing no increased uncertainty in the nadir. The comparison across methods reveals minimal differences between GUM and MCM results. To highlight this, Fig. 9b provides a close-up of the nadir region's uncertainty results. The MCM solution is noisier due to its reliance on simulation rather than linearization, as with the classical GUM method. Larger deviations appear in comparison with the QINSy solution. Particularly in this profile, in the nadir region, QINSy's uncertainty values are roughly 20 cm lower than those from GUM and MCM. Conversely, QINSy's uncertainty increases more significantly in the outer beams. In average the difference between our uncertainty model (both realizations MCM and GUM) and QINSy, along the profiles and for all the 3000 measured profiles, is around 17 cm. This suggests that positional uncertainty influences are modeled differently across methods, and further investigation into QINSy's calculation approach would be required to fully understand these discrepancies.

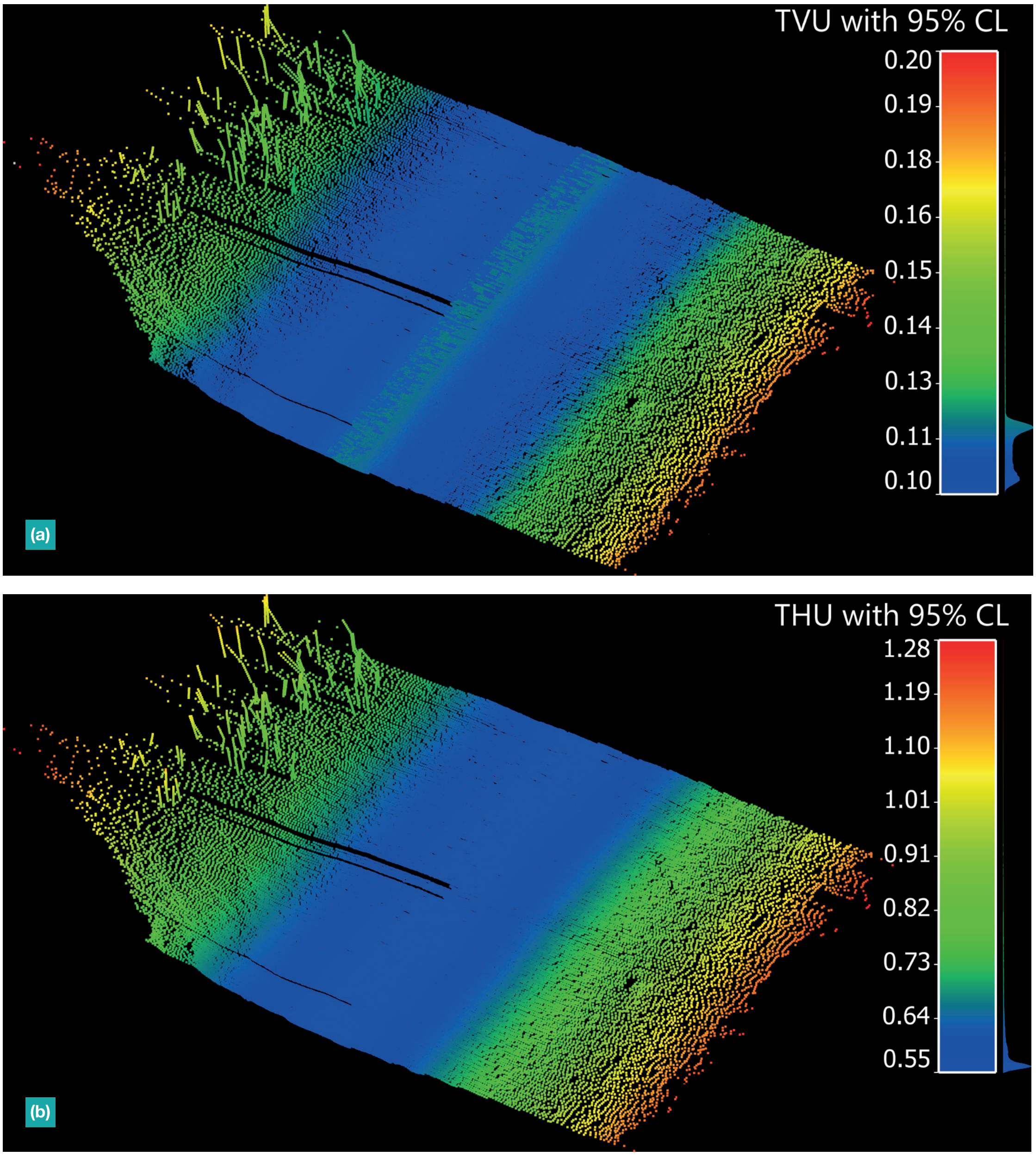

Fig. 7 The results of the MCM uncertainty estimation with 95 % CL for the first 100 profiles: (a) TVU of the first 100 profiles with CL of 95 %. (b) THU of the first 100 profiles with CL of 95 %.

https://doi.org/10.58440/ihr-31-1-a09

All three predicted uncertainties remain below the THU_{max} threshold defined for Special Order surveys; however, at the swath boundaries, they exceed the stricter 1-meter limit specified for the Exclusive Order.

This research primarily focuses on uncertainty solutions derived from MCM. To assess the plausibility of the estimated TPU values, we analyze the overlap area where the BB and STB transducers record measurements simultaneously. This region offers a valuable opportunity to validate the model's accuracy. The two independent transducers measure the same physical surface in this region under slightly different conditions. Since the modeled uncertainty is expressed at the 95 % CI, we expect that, statistically, approximately 95 % of the measurements from one transducer should fall within the confidence interval predicted by the model using the measurements from the other transducer. Moreover, although the two transducers are internally similar, they are physically separate sensors with independent mounting setups. Small differences in mounting geometry, alignment, and calibration introduce slight variations between their measurements. This diversity further strengthens the validation, as it ensures that the comparison is not perfectly redundant but reflects realistic measurement variability. Fig. 10 presents the overlap area beneath the ship for one profile to evaluate height measurement uncertainty. The uncertainty, estimated using the MCM, is expressed as CI around the absolute height measurements. Fig. 10 demonstrates that a majority of the measurements from each transducer fall within the CI of the other. In Fig. 10a, 87.69 % of the BB transducer's readings align with the confidence bounds of the STB transducer, while in Fig. 10b, 87.48 % of the STB transducer's measurements fall within the BB transducer's CI. Although these percentages do not reach the expected 95 % threshold, they suggest that the overlap area is well-represented by repeated measurements. In just this one presented example, the sample size in the overlap region may not be sufficient to make definitive claims regarding the 95 % CL. We observed similar coverage for other profiles as well. Moreover, as the both transducers operate independently, their different setups could influence their measurements. Despite these factors, the observed overlap percentages provide reasonable validation of the estimated CIs.

The overlap area is also analyzed to assess position uncertainty. Since position uncertainty results from a quadratic combination of uncertainties in the East and North components, it is represented as a two-dimensional confidence region. Consequently, each measured point's uncertainty is expressed as a confidence ellipse. Fig. 11 illustrates the overlap area for position measurements, highlighting the confidence ellipses for points recorded by the BB. The semi-major and semi-minor axes correspond to East and North uncertainties, respectively, with no assumed correlation. As depicted, all STB transducer measurements fall within the

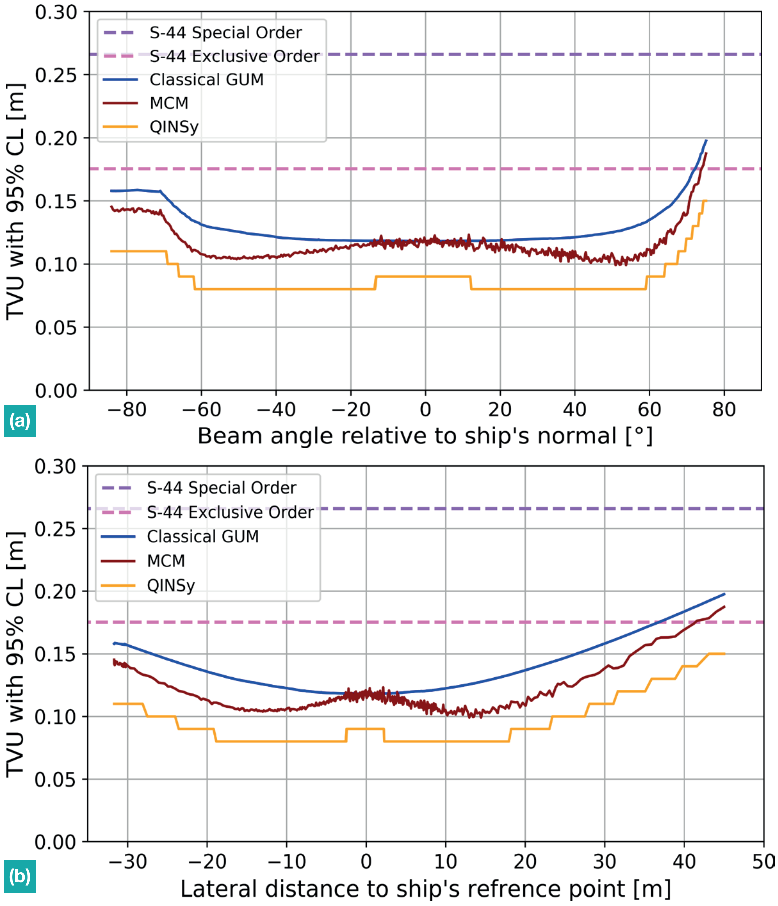

Fig. 8 Extended uncertainty in height for the first profile Measurement with 95 % CL (TVU): (a) TVU versus beam angle relative to ship's vertical. (b) TVU versus lateral distance from ship.

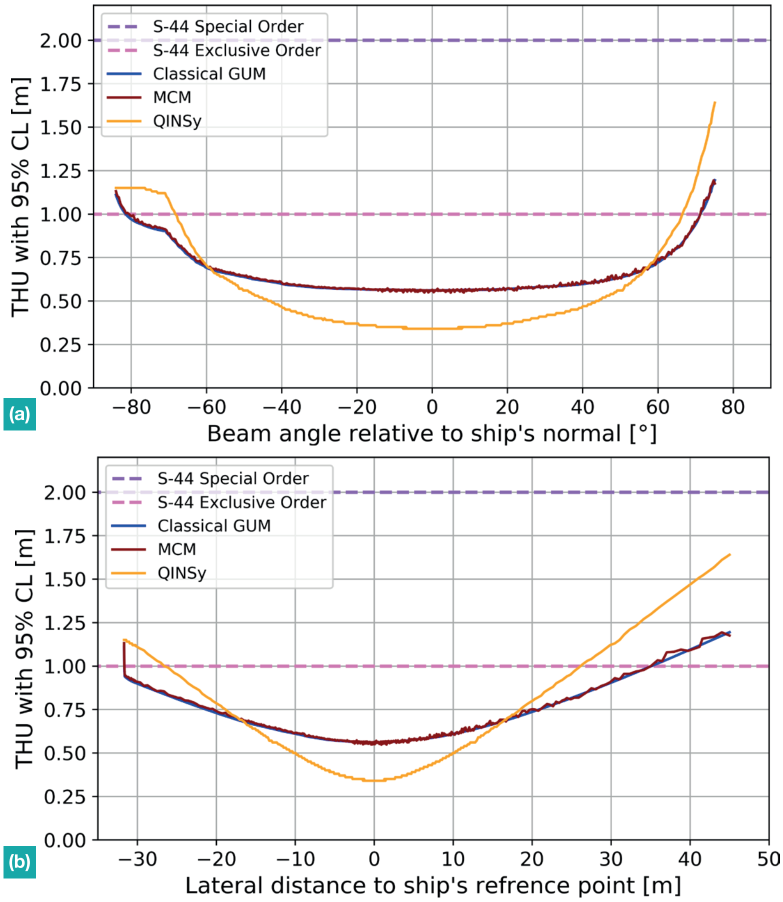

Fig. 9 Extended two-dimensional uncertainty for North and East dimensions of the first profile measurement with 95 % CL (THU): (a) THU versus beam angle relative to ship's vertical. (b) THU versus lateral distance from ship.

BB transducer's confidence ellipses. Unlike the height component, the 2D position measurements achieve a full 100 % overlap within their respective confidence ellipses. This result reinforces the reliability of the position uncertainty estimates obtained through MCM.

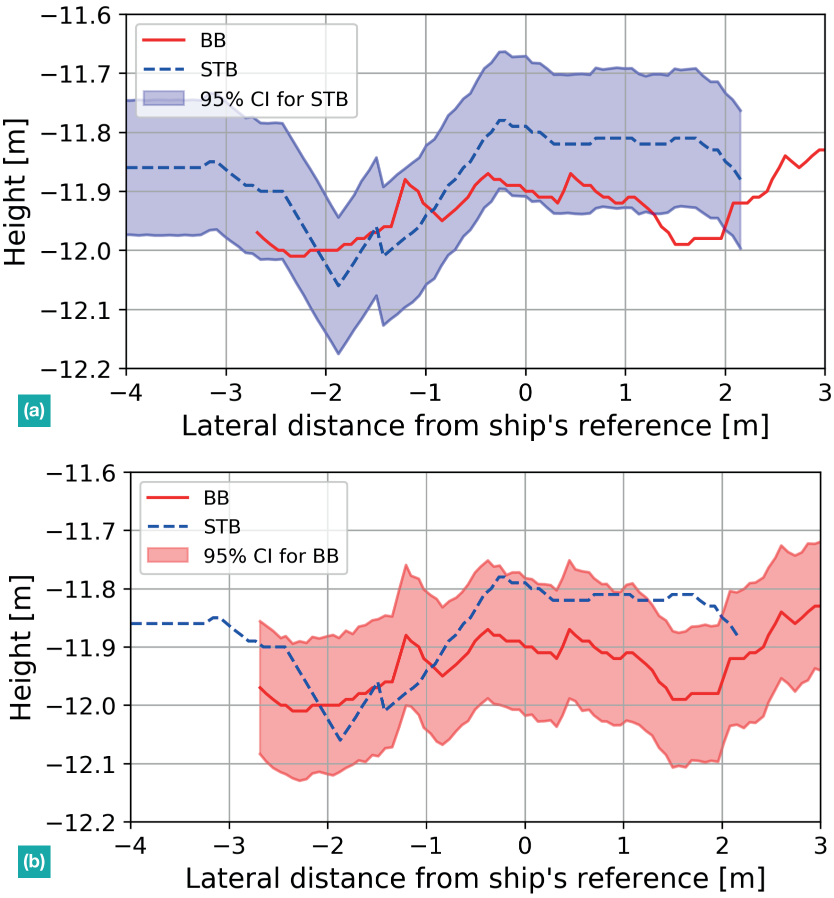

Fig. 10 Measured heights by STB and BB transducers versus their estimated 95 % CI in the overlapping measurement area beneath the ship. (a) CI of the STB transducer. (b) CI of the BB Transducer.

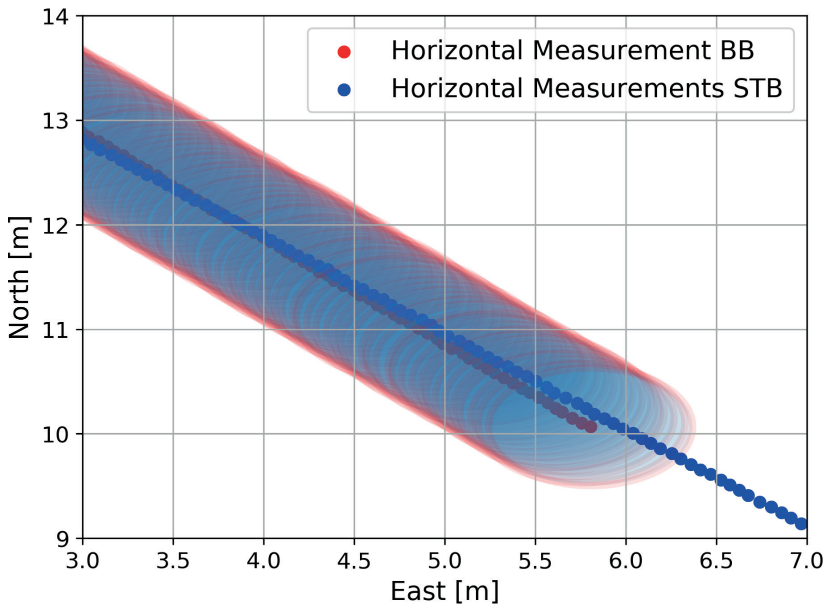

Fig. 11 Measured horizontal coordinates by STB and BB transducers with their corresponding confidence ellipses of overlapping measurement area beneath the ship. East and North are reduced for visualization.

It should be noted that there is no definitive ground truth for either the underwater geometry or the measurement uncertainty. Overall, the overlap analysis supports the validity of the developed uncertainty model. Comparisons with alternative methods further strengthen confidence in the reliability of the estimated TPU values. While systematic differences exist between models, their overall patterns remain consistent. Despite the observed systematic differences between uncertainty model and the commercial software, these deviations do not diminish the usefulness of our results. Since the primary goal of this analysis is to derive weights for the subsequent modeling step, the absolute magnitude of uncertainty is less critical than its relative distribution. The derived uncertainty values are used to construct normalized weights, directly informing the modeling process. Thus, these systematic variations will not negatively influence the outcomes in the second part of this paper. The weighting approach ensures that the subsequent analyses remain robust, as differences in the absolute uncertainty levels do not significantly affect our conclusions or the modeling accuracy presented in the later sections.

A potential empirical approach to characterizing measurement uncertainty in MBES systems would be to perform repeated high-density surveys over a flat and stable area, followed by the generation of a high-resolution averaged gridded surface. Deviations of individual measurements from this reference surface could then be used to estimate the distribution of random errors. Although not explored in the present study, such methods may provide valuable validation or calibration data for future uncertainty modeling.

A key approach to further evaluating this model is through simulation. In the next steps, we use the developed uncertainty model to simulate the ground truth, measurement process, and their corresponding uncertainties, assessing its applicability and reliability.

4 Survey simulator

A major drawback in estimating uncertainties for bathymetric measurements is the unknown geometry of the waterbed. A synthetic dataset is used in this study to overcome this issue. The main idea is to employ a mathematically defined surface to simulate realistic bathymetric measurements. The ground truth surface is defined based on MBA approach by Lee et al. (1997). Our MBA surface is constructed using a set of predefined hierarchical B-Spline functions and is exported as a 3D-PC with equidistant point spacing of 1 cm (Fig. 12).

The simulation environment is implemented in Python using standard libraries like NumPy (Harris et al., 2020) and PyVista (Sullivan & Kaszynski, 2019). Four steps are required to generate a realistic simulated 3D-PC of a waterbed:

1. Transform the generated 3D-PC into a mesh using Delaunay triangulation (Delaunay, 1934).
2. Compute Cartesian coordinates by intersecting

https://doi.org/10.58440/ihr-31-1-a09

the beams of the echo sounder with the mesh of the waterbed using ray-tracing.
3. Calculate the range and beam angle between the sensor and intersected coordinates on the seabed.
4. Predict realistic uncertainties for the obtained coordinates by forward modeling based on the uncertainty model developed in Section 3, using the parameters described in Table 1.

After creating the original 3D point cloud with a resolution of approximately 1 cm, a Delaunay triangulation mesh with the same resolution (1 cm) was generated. The next step is to compute the coordinates of the simulated measurements on the waterbed. The measurement beams are generated according to the chosen sensor, with equidistant angular steps in the field of view of 120°, and the central beam is directed vertically downward. The environment is assumed to be uniform, and no refraction of the acoustic wave is considered, as is generally valid in shallow water areas. Therefore, each ray is treated as a straight line starting from the transducer in the direction of the beam. The intersection of the beam with the seabed surface is determined using ray-tracing; in cases of multiple intersections, the closest one is selected.

One drawback of using a triangulated mesh for the simulation is the occurrence of triangulation error, which is the difference between the generated ground truth surface and the meshed grid used for beam intersection. This error is intrinsic to the process of converting a smooth, continuous surface (the "ground truth") into a mesh made up of flat, polygonal facets. The error is most pronounced in regions with significant curvature, as the exported points in the triangulation are connected by planar triangles.

The magnitude of this error is influenced by several factors, including the curvature of the original surface, the density of the mesh, and the quality and arrangement of the triangles. In areas with high curvature, flat triangles struggle to capture the intricate details of the surface, resulting in larger errors. While the error can be mitigated by reducing point spacing (thereby increasing mesh density), this approach increases computational cost and memory usage. While the error can be mitigated, it remains present and must be considered in the analysis. The error in Z-direction was eliminated by recalculating the Z value at the determined XY location using the original B-Spline functions, ensuring that the simulated coordinates exactly follow the surface. The reprojection process eliminates XY triangulation errors by fixing the original X and Y coordinates and recomputing the Z value based on the true B-spline surface. Thus, only the Z-coordinate is corrected, and no residual XY positional error remains after reprojection. In addressing triangulation errors, recalculating the mesh coordinates using original surface functions, like B-Splines, offers a powerful method to enhance accuracy. This technique specifically targets errors in one or more dimensions by leveraging the precise mathematical representation of the surface from which the mesh is derived. Subsequently, the range and beam angles are recalculated using the sensor's position, and uncertainties are then predicted. The triangulation error and the projection principle are illustrated in Fig. 13.

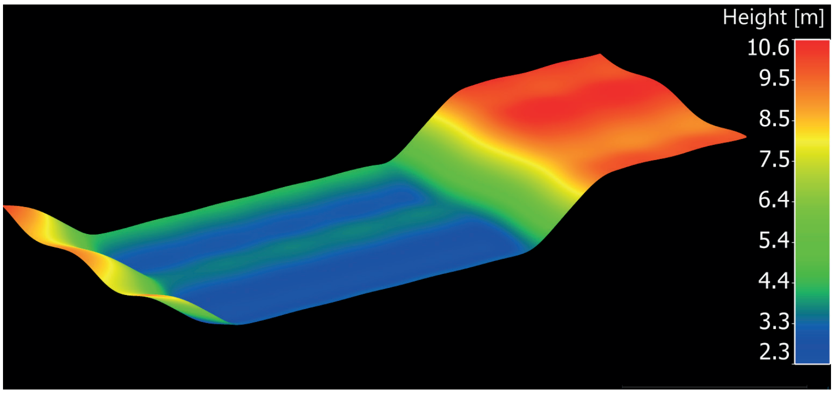

Fig. 12 Simulated geometry as a point cloud. The points are color-coded by the height in meter.

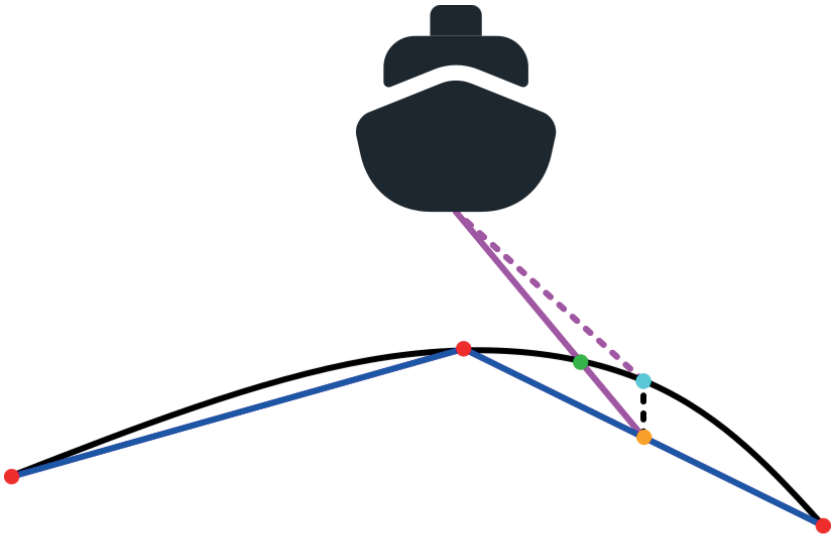

Fig. 13 Triangulation error due to discrepancies between the curved surface and the mesh. The simulated surface is shown in black, the exported point cloud in red dots, and the mesh from Delaunay triangulation in blue. The intersection of the beam (solid magenta line) with the mesh results in the orange point. The desired and true intersection with the surface is shown in green. To eliminate the error in the Z-direction, the orange point is projected onto the surface in the Z-direction and shown in cyan. Subsequently, the beam is recalculated to the new point, which is indicated by the dashed magenta line.

For the simulation in this study, a surface with dimensions of 80 m by 20 m and a total variation in Z-direction of 8 m is used. Four parallel trajectories are simulated to capture the entire area and to generate overlapping regions. The trajectories have an average height above the surface of 12 m above the surface and are spaced 20 m apart. The simulated surface and trajectories are shown in Fig. 14. A profile view of a random realization of the simulated measurements is shown in Fig. 15. The overall workflow of the algorithm is presented in Fig. 16.

After intersecting the beam pattern at every sensor position with the surface and recalculating the Z-value, the resulting beam angle and range readings are error-free. Realistic uncertainties are then added using the parameters and methods described

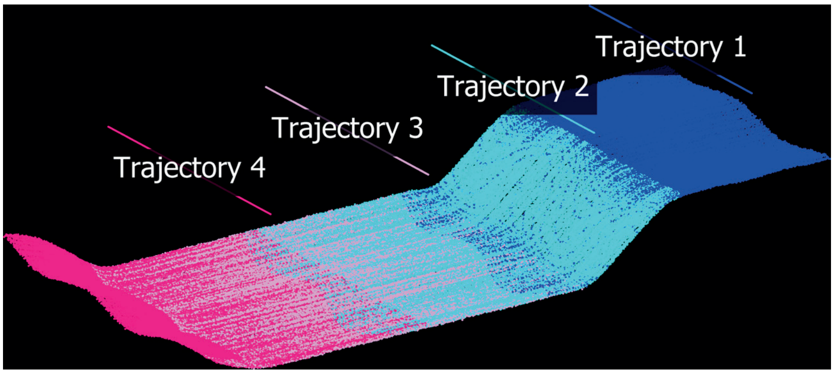

Fig. 14 Simulated measurements along with the four chosen trajectories for the vessel.

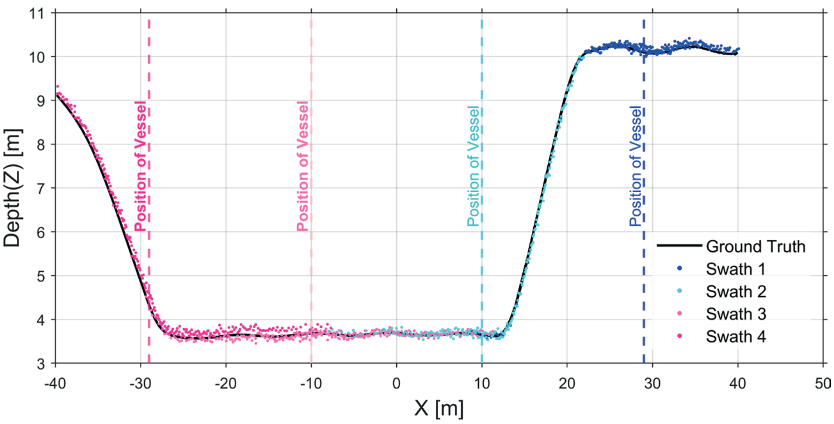

Fig. 15 Profile view of simulated measurements for one realization. The simulated measurements corresponding to different trajectories of the vessel are shown with different colors.

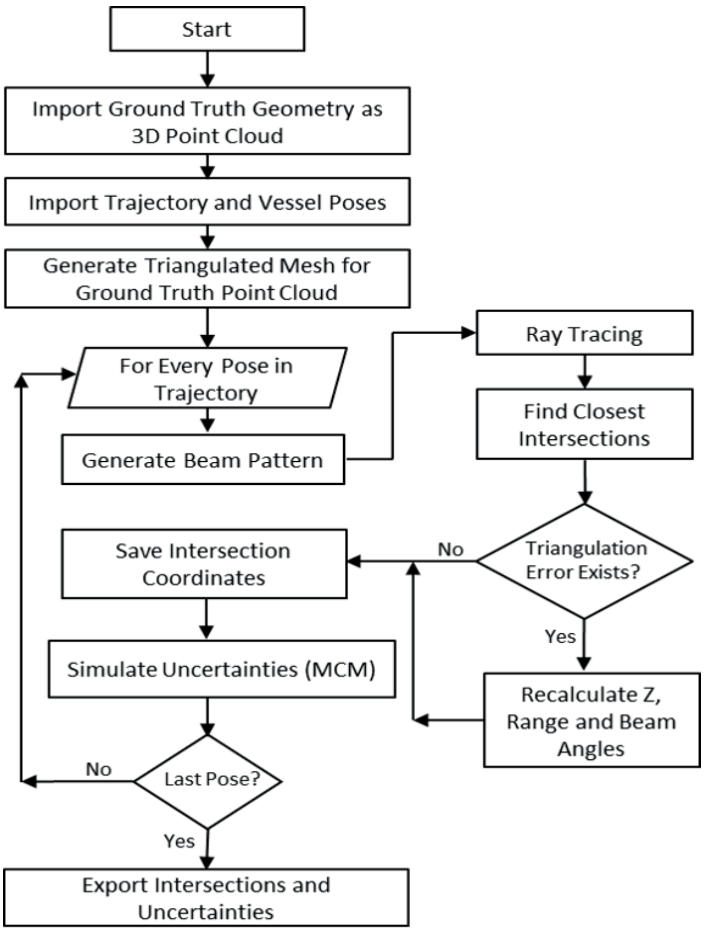

Fig. 16 General algorithm adopted in survey simulator.

in Section 3. This is performed within a Monte-Carlo simulation loop with 1,000 iterations, yielding 1,000 individual realizations for every simulated measurement. This approach facilitates a detailed analysis of the uncertainty budget, the distribution of the uncertainties, and the identification of specific ways to enhance model accuracy and reliability.

5 Measurement uncertainty and DBM

Our goal in this research is to explore how uncertainty information can be used to improve DBMs. To achieve this, we developed a simulation environment in which a known geometry is created using a precise mathematical model representing a theoretical seabed. Within this controlled environment, we simulate the measurement process while incorporating our developed uncertainty model. This setup allows us to obtain measurements that include uncertainties while retaining complete knowledge of the geometry, thereby enabling a detailed analysis of the impact of uncertainty on the final DBM.

The core idea is to integrate the estimated uncertainty information into the modeling process. For this purpose, we first clarify the type of surface model we are focusing on.

5.1 Surface model

Considering the potential complexity of underwater geometry and the characteristics of MBES data – such as high resolution, large volumes, and potential gaps – we require a method that efficiently handles these challenges while minimizing computational complexity. To achieve this, we represent the surface as a 2.5-dimensional (2.5D) model, expressed as:

$$z_0 = f(x_0, y_0) \tag{12}$$

where (x_0, y_0, z_0) represents a point on the surface.

To model this surface, we adapt MBA by Lee et al. (1997). The MBA method is based on hierarchical tensor product B-spline surfaces. Any point on the surface is a linear combination of control points and cubic basis functions. The B-Spline surface is defined by a grid of control points, denoted as $\mathbf{\Phi}$, which lies parallel to the XY-plane. The positions of these control points are predefined on the grid, serving as the basis for constructing the surface representation. To approximate the surface $f(x,y)$, it is necessary to determine the unknown elements of $\mathbf{\Phi}$. This problem is structured as a linear Gauß-Markov Model (GMM), as expressed in Eq. 13 Mohammadivojdan et al. (2024). In this formulation, $\mathbf{z}$ represents the observation vector, while $\mathbf{v}$ denotes the residual vector. The matrix $\mathbf{A}$ is a full-rank design matrix, and $\mathbf{\Phi}$ is the vector of unknown parameters.

$$\mathbf{z} + \mathbf{v} = \mathbf{A}\phi \tag{13}$$

The $\mathbf{\Phi}$ can be estimated by minimizing the sum of the squared residuals, according to Eq. 14. If

https://doi.org/10.58440/ihr-31-1-a09

the assumption is that the observations are equally weighted and uncorrelated, the weight matrix **P** will be an identity matrix. If information about the uncertainty of the observations is available, this **P** is derived as the inverse of the Variance-Covariance Matrix **Σ** of the observations, allowing the model to account for varying observation uncertainties. In Eq. 15, $\mathbf{\Sigma}_z$ represents the Variance-Covariance Matrix of the observations, structured as follows:

$$\hat{\phi} = \left(\mathbf{A}^T\mathbf{P}\mathbf{A}\right)^{-1}\mathbf{A}^T\mathbf{P}\mathbf{z} \tag{14}$$

$$\mathbf{\Sigma}_z = \begin{bmatrix} \sigma_{z_1}^2 & 0 & 0 & 0 \\ 0 & \sigma_{z_2}^2 & 0 & 0 \\ \vdots & \vdots & \ddots & 0 \\ 0 & 0 & \cdots & \sigma_{z_n}^2 \end{bmatrix} \tag{15}$$

The assumption that observations remain uncorrelated is still maintained. Incorporating the weight matrix in this way enhances the robustness of the parameter estimation, ensuring a more reliable solution while accounting for observational uncertainties.

It should be noted that GMM does not directly estimate a posteriori variance factor $\hat{\sigma}_0^2$ (cf. Benning, 2011, p. 144). Therefore, for evaluating the adjustment, $\hat{\sigma}_0^2$ is estimated based on $\hat{\Phi}$ the updated residuals $\hat{\mathbf{v}}$ as follows:

$$\hat{\mathbf{v}} = \mathbf{A}\hat{\phi} - \mathbf{z} \tag{16}$$

$$\hat{\sigma}_0^2 = \frac{\hat{\mathbf{v}}^T\mathbf{P}\hat{\mathbf{v}}}{n-u} \tag{17}$$

where n is the number of observations and u is the number of unknowns.

5.2 Monte-Carlo simulation experiment

To assess the impact of incorporating uncertainties in the model estimation process, we utilize our survey simulator (see Section 4). However, a single simulation scenario is insufficient for drawing reliable conclusions; therefore, we conduct a Monte-Carlo simulation experiment, in which the entire process is repeated multiple times. By analyzing a large number of iterations, we derive more robust inferences and assessments.

In each iteration, both the geometry and the associated uncertainties are simulated and the data are modeled using MBA. Two versions of the model are generated: one that integrates uncertainty information into the estimation process and another that does not. This comparative approach allows us to assess the effect of incorporating uncertainty on model accuracy and reliability. After numerous repetitions, we determine the optimal model and extract additional insights, such as CIs or uncertainty maps, providing a clearer understanding of the model's precision. Fig. 17 illustrates the general algorithm for the adopted Monte-Carlo simulation experiment. In this algorithm, N represents the number of Monte-Carlo iterations, which is set to 1,000 in our study.

5.3 Results and discussion

In the initial step, the focus is on evaluating model quality and associated errors in an ideal scenario assuming no measurement error is present. Although the ground-truth geometry described in Section 4 was generated using MBA functions, and the simulated data were also modeled with an MBA approach, the resulting model does not exhibit zero error. Even in the absence of simulated measurement noise, the estimated surface retains some inaccuracy. This is because the ground-truth surface was generated using a multi-layered MBA construction to introduce local deviations, while the subsequent surface approximation used a selected model complexity without reverse-engineering the original structure. Therefore, a residual modeling error naturally remains even in the absence of simulated measurement noise. This effect is expected and is analogous to real-world modeling situations where the true surface structure is unknown. These inaccuracies can arise in the simulation step or the modeling step; the simulated point cloud inherently exhibits variations in

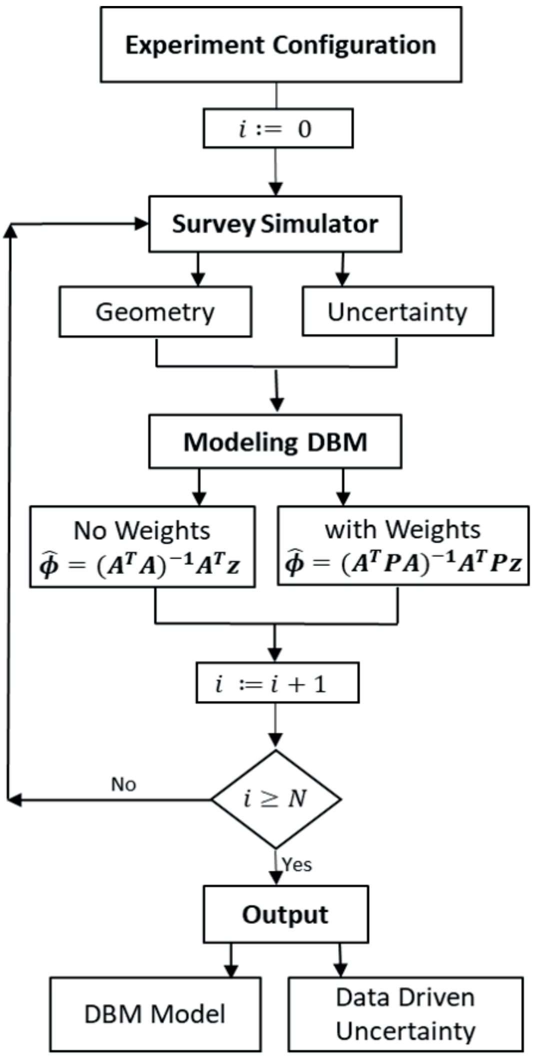

Fig. 17 The general algorithm for the Monte-Carlo simulation experiment.

point density and spatial distribution due to survey parameters, including sensor specifications, water depth, vessel speed, measurement angles, and the underlying geometry of the waterbed. Consequently, these factors result in a non-uniform distribution of data points, inevitably affecting the final model. Additionally, selecting an appropriate model complexity is critical; an excessive number of control points might lead to overfitting, especially if the dataset includes noise or outliers. Thus, choosing the optimal model complexity requires carefully balancing smoothness against accuracy.

To assess model quality, we can look into model error as the spatial distance between the modeled point cloud and the ground truth, either represented as a 3D distance or separately along the *X*, *Y*, and *Z* axes. Of particular interest are the distribution, mean, and Root Mean Squared Error (RMSE) of this error. Fig. 18 illustrates the simulated PC generated by the survey simulator under conditions with zero measurement uncertainty. The points are color-coded according to the magnitude of the 3D model error, representing the distance between the estimated model and the ground truth. The mean model error in this scenario is 0.1 mm, with an RMSE of 3 mm, confirming that, despite being small, a model error clearly exists.

In the experiment, each point in the simulated dataset ends up with 1,000 realizations along the *X*, *Y*, and *Z* components. For each component, we compute the uncertainty value σ, defined as the standard deviation corresponding to the 68 % CL of the distribution. As described in Section 4, the uncertainties are simulated based on the developed uncertainty model in Section 2. Convergence of the Monte Carlo simulations was assessed by monitoring the stability of the estimated mean and standard deviation over increasing numbers of iterations. Statistical metrics stabilized after approximately 800–1,000 iterations, confirming that 1,000 simulations were sufficient. The selected surface modeling approach (MBA) represents a 2.5D model. Like other 2.5D DBMs, its primary emphasis lies on uncertainty in the vertical *Z* direction. To better visualize and evaluate the impact of vertical uncertainties, we chose uncertainty values of approximately (0.02, 0.02, 0.06) m for position (X_{Pose}, Y_{Pose}, Z_{Pose}) components, respectively. Notice that ratio of the positional uncertainty to vertical one is lower than the real data in the simulation. This was done to minimize the influence of large horizontal positioning errors and better isolate and assess the effect of the modeling process on the vertical (z) component, which was the main focus of this study. The horizontal uncertainties were kept at low levels to avoid masking or distorting the analysis of vertical uncertainty propagation. Fig. 19 illustrates these uncertainties separately for each component (*X*, *Y*, and *Z*) and for each point individually. Fig. 19 provides an *XY* view of the simulated data points, color-coded according to uncertainty magnitude. It clearly shows that the uncertainty in the *Z* component (height) is dominant compared to *X* and *Y*. In Fig. 19d we see the combined standard uncertainty of the MC simulations. In which the uncertainty is calculated as,

$$\sigma_{XYZ} = \sqrt{\sigma_X^2 + \sigma_Y^2 + \sigma_Z^2} \tag{18}$$

It is important to note that the difference between this uncertainty measure and the TPU values is that TPU refers specifically to extended uncertainties, which are calculated by Eqs. 9 and 10.

This uncertainty information is utilized to construct the weight matrix required for the GMM adjustment. It's important to note that the MBA model is essentially a 2.5D representation, with parameters estimated by minimizing errors specifically in the *Z*-direction. MBA inherently cannot fully capture or exploit the complete 3D structure of positional uncertainties. This modeling simplification may lead to some loss of fidelity, particularly when significant horizontal errors are present. Consequently, for constructing the weight matrix, we primarily use the estimated uncertainty σ_Z as shown in Fig. 19c (refer to Eq. 15). However, in reality – as well as in our simulations – uncertainty exists in all three spatial dimensions. Even though the MBA model does not explicitly estimate parameters in the X and Y directions, uncertainties in these dimensions can still impact model quality. For this reason, we also explore a scenario in which observations are weighted based on the combined uncertainty σ_{XYZ}. In total, we consider three scenarios in our analysis:

- Case 1: No weighting applied during adjustment
- Case 2: Observations weighted based only on vertical uncertainty σ_Z (Eq. 15)
- Case 3: Observations weighted using full 3D uncertainty σ_{XYZ} (Eq. 18)

Comparing these three scenarios allows us to assess not only the general effectiveness of applying uncertainty-based weights but also whether including full 3D uncertainties can meaningfully improve our results for a model inherently focused on vertical accuracy.

Here, we further investigate the Monte-Carlo simulation results, specifically examining the detailed distribution of errors. We consider both the adjustment quality and the difference between the estimated

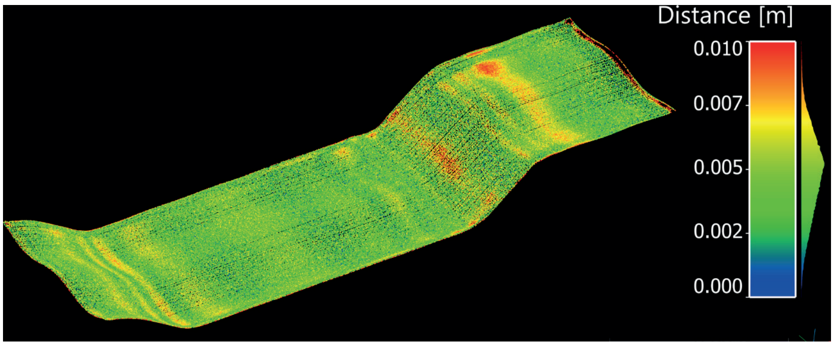

Fig. 18 Simulated PC color-coded by the magnitude of 3D model error (distance between modeled points and ground truth geometry). Simulation performed with zero measurement uncertainty.

https://doi.org/10.58440/ihr-31-1-a09

model and ground truth. The adjustment quality is evaluated using the residual differences between observations and the estimated model, quantified by root of a posteriori variance factor $\hat{\sigma}_0$ (see Eq. 17). These error distributions are presented in Fig. 20.

The gray histogram represents the distribution of simulated errors, specifically the vertical (*Z*-direction), distances between simulated points and the ground truth. This distribution is approximately normal, with an RMSE of 0.09 m. The error distributions from all three modeling scenarios align closely with the simulated error distribution, indicating that each scenario effectively captures the error structure. Furthermore, all three adjustment scenarios yield very similar values for the a-posteriori variance factor: 0.081 m, 0.087 m, and 0.078 m for Cases 1, 2, and 3, respectively. These nearly identical values suggest that the application of weights, whether based solely on vertical uncertainty or combined 3D uncertainty, does not significantly impact the overall adjustment quality.

We further assess model quality by evaluating the difference between the estimated model and the ground truth, specifically the vertical (*Z*-direction), quantified by RMSE of these errors σ_{Model}. Fig. 21 presents the corresponding distributions of these errors for all three cases. In each scenario, the model error is consistently less than half of the a-posteriori variance factor $\hat{\sigma}_0$, indicating that the estimated model gives a much better estimation of the ground truth. The unweighted scenario (Case 1) has the largest error, with $\sigma_{\text{Model}} = 0.044$ m, and its distribution shows clear asymmetry, suggesting the presence of bias. Introducing weighting significantly reduces the error and improves symmetry in the distribution. Case 2, weighted by vertical uncertainty σ_Z, achieves the smallest model error, $\sigma_{\text{Model}} = 0.023$ m, demonstrating a narrower and more symmetric distribution. Case 3, weighted by full 3D uncertainty σ_{XYZ}, also shows substantial improvement over the unweighted case ($\sigma_{\text{Model}} = 0.032$ m), although its error reduction is slightly less pronounced than in Case 2. These quantitative results are summarized in Table 2. These results highlight that applying uncertainty-based weighting enhances model quality by reducing bias and improving error symmetry. Interestingly, the slightly better performance of Case 2 compared to Case 3 might stem from the inherent nature of the MBA approach as a 2.5D modeling method, which primarily optimizes vertical accuracy. Although considering full 3D uncertainties (Case 3) clearly benefits the model, the inherent vertical emphasis of the MBA model means that its greatest accuracy gains come specifically from weighting by vertical uncertainties. This improves overall results in terms of distribution characteristics, and error symmetry. These subtle improvements in modeling accuracy, summarized in Fig. 21, underscore the importance of selecting appropriate uncertainty weighting – even when ground-truth data are unavailable and biases might otherwise remain unnoticed.

Table 2 Summary of results for Monte-Carlo simulation. is root of "a-posteriori variance factor" (see Eq. 17) and σ_{Model} is RMSE of difference between the estimated model and the ground truth.

	Error [m]		
	Case 1	Case 2	Case 3
$\hat{\sigma}_0$	0.081	0.087	0.078
σ_{Model}	0.044	0.023	0.032

We further leverage the Monte-Carlo simulation results to create CI, enabling us to produce a detailed assessment of model quality. Each simulated realization generates slight variations in modeled values at each point, and by analyzing these variations, we can derive a meaningful CI. Fig. 20 illustrates a CI with a 95 % CL. The figure shows an *XY* view of the modeled area, with each point color-coded according to the length of its CI.

Comparing this CI map to the uncertainty distribution in Fig. 22, we observe an interesting difference: while the original uncertainties are highest near the edges of each survey swath – primarily due to unfavorable measurement angles – the modeled CIs are actually lower in these boundary regions. This apparent discrepancy arises because the boundaries of adjacent swaths overlap, providing redundant observations that help reduce the uncertainty and improve modeling accuracy, despite initially poorer measurement quality due to higher incidence angles. Thus, these overlapping areas offer enhanced information density, resulting in a higher-quality model with smaller uncertainties, even where individual measurements originally exhibited higher uncertainty.

These CI maps highlight areas with sufficient data coverage and indicate critical regions where data reliability might otherwise be overlooked. This provides users with a powerful visual tool for decision-making, aiding in strategic interpretation and effective risk identification. The generated CI maps have several practical applications. For survey planning, realistic simulation of measurement uncertainty allows surveyors to predict coverage quality, identify areas where higher uncertainties are expected, and optimize survey parameters such as vessel routes, ping rates, and swath overlap. In terms of confidence mapping, the method produces detailed spatial uncertainty maps that incorporate both measurement and modeling errors, allowing users to generate IHO S-44 compliance layers or internal quality indicators for the delivered bathymetric products. Furthermore, for real-time QA/QC, the approach could be adapted to provide near real-time estimates of expected uncertainty during data acquisition. This would allow operators to dynamically adjust survey settings if quality thresholds are not being met.

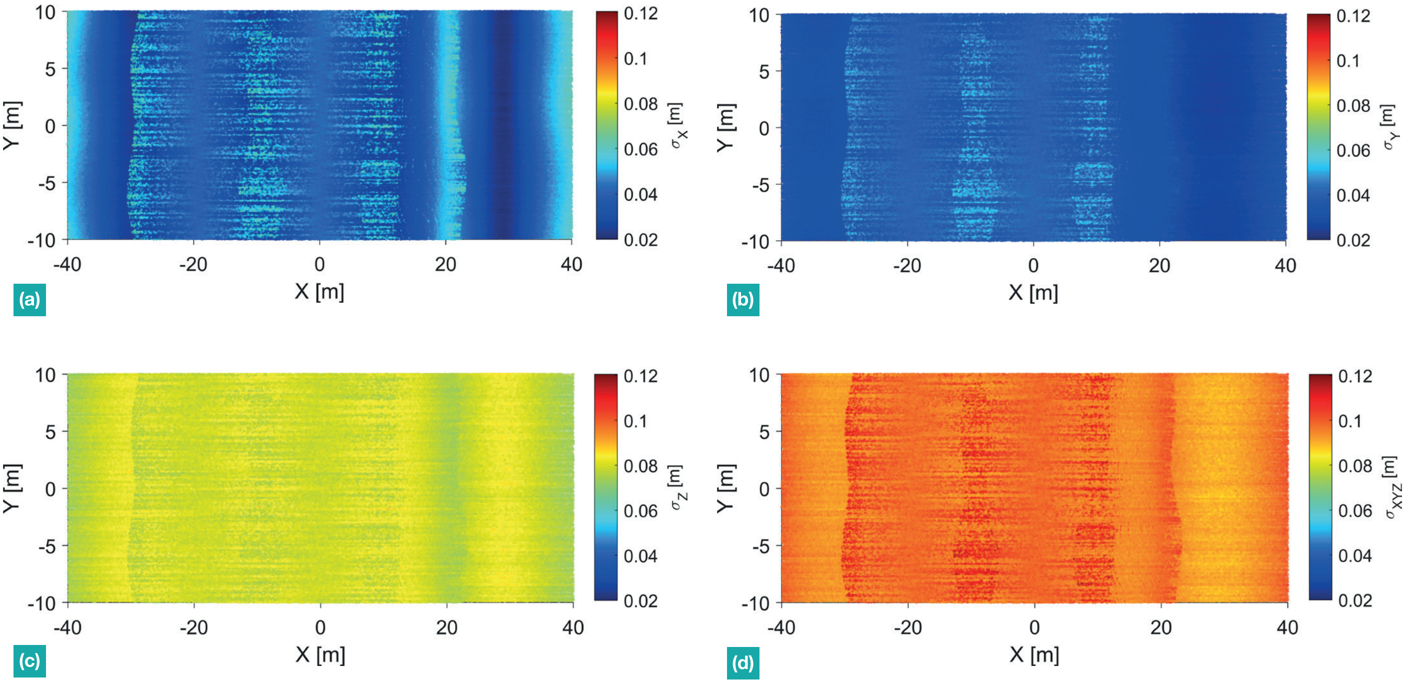

Fig. 19 Estimated uncertainties for each point in Monte-Carlo simulation: (a) uncertainty σ_X in X (Mean = 0.03 m), (b) uncertainty σ_Y in Y (Mean = 0.03 m) and (c) uncertainty σ_Z in Z (Mean = 0.08 m) and (d) combined uncertainties σ_{XYZ} (Mean = 0.09 m) for each point.

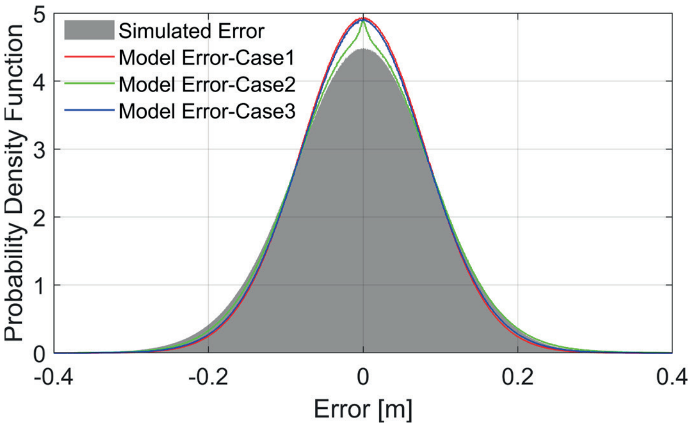

Fig. 20 Histogram of errors after Monte-Carlo simulation. Error measure here is the difference between observations and the estimated model.

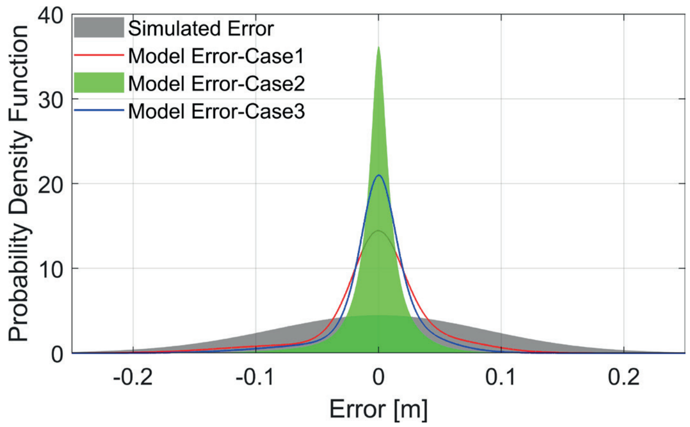

Fig. 21 Histogram of errors after Monte-Carlo simulation. Error measure here is the vertical difference between the estimated model and the ground truth.

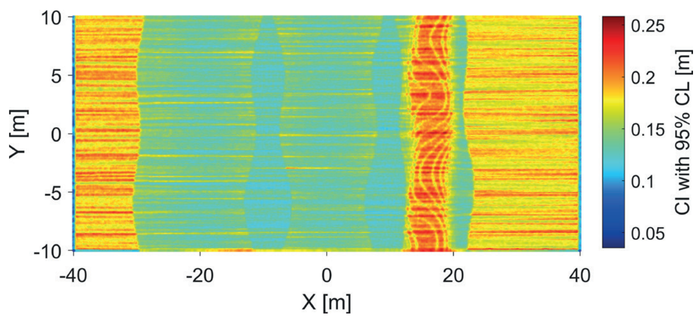

Fig. 22 CI map with a 95 % CL of the model derived from Monte-Carlo simulations. Each point is color-coded according to the magnitude of its CI, highlighting regions of high and low model uncertainty.

https://doi.org/10.58440/ihr-31-1-a09

6 Conclusion

This study is divided into two parts. In the first part, we developed and evaluated a model to predict uncertainties for a hydrographic survey system. Although the measurement model was designed for a specific survey vessel, the underlying concept and workflow are adaptable to other systems equipped with MBES. Our analysis involved defining uncertainty measures according to classical GUM guidelines and conducting extensive Monte-Carlo simulations. The results indicated strong agreement between the two methods, confirming their consistency. However, MCM offers notable advantages over the classical approach, which is less effective for highly nonlinear measurement models and requires complex partial derivatives, MCM accommodates various PDF distributions and provides uncertainty estimates directly as a complete PDF, enabling more extensive analysis. To validate our developed uncertainty model, we compared its results to those obtained from a commercial software solution. Although the overall uncertainty patterns were generally compatible, systematic deviations were observed, likely due to differences in model parameters and assumptions. These discrepancies, however, do not compromise the primary goal of generating relative weights for subsequent modeling steps, ensuring that the later analyses remain robust and reliable.

In the second part of the study, we developed a survey simulator to generate measurements that incorporate uncertainties derived from our model. This controlled environment allowed us to validate the modeled data against known ground-truth values. Using a Monte-Carlo experiment, we assessed the quality of DBMs by incorporating uncertainty information to weight observations during modeling. The results demonstrated that integrating accurate uncertainty information improved the overall accuracy and reliability of the models. Although the numerical improvements may be subtle, they significantly enhance confidence in the resulting models. Additionally, the uncertainty data facilitated the creation of quality maps accompanying the DBMs, which effectively highlight regions of varying reliability and provide practical guidance for future survey planning and data interpretation. The generalizability of the simulation framework depends on the validity of the underlying physical models for uncertainty estimation (e.g., Hare, 1995; Wirth, 2011). Significant variations in measurement conditions or system behavior may require adjustment of simulation parameters or model structures to maintain accuracy.

While in this study we used synthetic surfaces to provide a precisely controlled ground truth, future work should explore the application of the proposed uncertainty modeling framework to real-world surfaces derived from dense MBES surveys. This would allow evaluation of model performance under more realistic and complex seabed conditions.

Further investigation of this experiment using a full 3D surface model is recommended. While the MBA model effectively represents 2.5D surfaces, it does not fully capture or propagate full 3D positional uncertainties. This limitation may constrain the fidelity of uncertainty integration, particularly in environments with strong three-dimensional variability. Further investigation using a full 3D surface model and comprehensive 3D uncertainty propagation is recommended. The application of a comprehensive 3D model, along with full-scale 3D uncertainties, has the potential to yield more profound insights into the manner in which uncertainty information influences model performance and accuracy. This analysis could more effectively reveal the benefits of incorporating uncertainties directly into the modeling process.

References

Abubakar, A. A. and Poerbandono, P. (2023). Effectiveness of vertical error budget model for portable multi-beam echo-sounder in shallow water bathymetric survey. *IOP Conference Series: Earth and Environmental Science, 1245*(1):012041. https://doi.org/10.1088/1755-1315/1245/1/012041

Alkhatib, H., Neumann, I. and Kutterer, H. (2009). Uncertainty modeling of random and systematic errors by means of Monte Carlo and fuzzy techniques. *Journal of Applied Geodesy, 3*, pp. 67–79. https://doi.org/10.1515/JAG.2009.008.

Arnold, J. and Shaw, S. (1993). A surface weaving approach to multibeam depth estimation. *Proceedings of OCEANS'93. II*–95.

Benning, W. (2011). *Statistik in Geodäsie, Geoinformation und Bauwesen* (4. Aufl.). Berlin, Offenbach: Wichmann.

BFG (2013). *Neue Entwicklungen in der Gewässervermessung*. Kolloquium am 20./21. November 2012 in Koblenz. – Veranstaltungen 5/2013, Koblenz, Mai 2013, 104 S. https://doi.org/10.5675/BfG_Veranst_2013.5

Bisquay, H., Freulon, X., De Fouquet, C. and Lajaunie, C. (1998). Multibeam data cleaning for hydrography using geostatistics. *IEEE Oceanic Engineering Society. OCEANS'98. Conference Proceedings (Cat. No.98CH36259)*. pp. 1135–1143. https://doi.org/10.1109/OCEANS.1998.724413

Bjørke, J. T. and Nilsen, S. (2009). Fast trend extraction and identification of spikes in bathymetric data. *Computers & Geosciences 35*, pp. 1061–1071. https://doi.org/10.1016/j.cageo.2008.05.009

Bottelier, P., Briese, C., Hennis, N., Lindenbergh, R. and Pfeifer, N. (2005). Distinguishing features from outliers in automatic Kriging-based filtering of MBES data: a comparative study. In P.

Renard and H. Demougeot-Renard (Eds.), *Geostatistics for environmental applications* (pp. 403–414). Berlin and Heidelberg: Springer. https://doi.org/10.1007/3-540-26535-x_ 34

Bureick, J., Alkhatib, H. and Neumann, I. (2016). Robust Spatial Approximation of Laser Scanner Point Clouds by Means of Free-form Curve Approaches in Deformation Analysis. *Journal of Applied Geodesy, 10*, pp. 27–35. https://doi.org/10.1515/jag-2015-0020

Delaunay, B. (1934). Sur la sph6re vide: Bull, Acad. Science USSR VII, Clas. *Sci. Mat. Nat*, pp. 793–800.

Eakins, B. W. and Taylor, L. A. (2010). Seamlessly integrating bathymetric and topographic data to support tsunami modeling and forecasting efforts. *Ocean globe*, pp. 37–56.

Erdogan, S. (2009). A comparision of interpolation methods for producing digital elevation models at the field scale. *Earth Surface Processes and Landforms, 34*: pp. 366–376. https://doi.org/https://doi.org/10.1002/esp.1731

Haji Mohammadloo, T., Snellen, M. and Simons, D. G. (2018). Multi-beam echo-sounder bathymetric measurements: Implications of using frequency modulated pulses. *The Journal of the Acoustical Society of America, 144*, pp. 842–860. https://doi.org/10.1121/1.5050816

Haji Mohammadloo, T., Snellen, M., Amiri-Simkooei, A. and Simons, D. G. (2019). Assessment of reliability of multi-beam echo-sounder bathymetric uncertainty prediction models. *Proceedings of the 5th Underwater Acoustics Conference and Exhibition*, pp.783–790, Crete, Greece.

Hare, R. (1995). Depth and Position Error Budgets for Mulitbeam Echosounding. *The International Hydrographic Review, 72*(2), https://journals.lib.unb.ca/index.php/ihr/article/view/23178 (last accessed 4 May 2025).

Hare, Rob, Eakins, B. W. and Amante, C. J. (2011). Modelling Bathymetric Uncertainty. *The International Hydrographic Review, 6*. https://journals.lib.unb.ca/index.php/ihr/article/view/20888 (last accessed 4 May 2025).

Harris, C. R., Millman, K. J., van der Walt, S. J., Gommers, R., Virtanen, P., Cournapeau, D., Wieser, E. et al. (2020). Array programming with NumPy. *Nature* (Springer Science and Business Media LLC), *585*, pp. 357–362. https://doi.org/10.1038/s41586-020-2649-2

IHO (2022). *Standards for Hydrographic Surveys* (ed. 6.1). IHO Special Publication S-44, International Hydrographic Organization, Monaco. https://iho.int/uploads/user/pubs/standards/s-44/S-44_Edition_6.1.0.pdf (last accessed 4 May 2025).

ISO/GUM (1995). *Guide to the Expression of Uncertainty in Measurement*. Standard, International Organization for Standardization, Geneva, CH.

ISO/GUM (1998). *Guide to the Expression of Uncertainty in Measurement (GUM) – Supplement 1: Numerical Methods for the Propagation of Distributions*. Standard, International Organization for Standardization, Geneva, CH.

Lee, S., Wolberg, G. and Shin, S. Y. (1997). Scattered data interpolation with multilevel B-splines. *IEEE transactions on visualization and computer graphics, 3*, pp. 228–244.

Lorenz, F., Artz, T., Brüggemann, T., Reich, J., Weiß, R. and Winterscheid, A. (2021). Simulation-based evaluation of hydrographic data analysis for dune tracking on the River Rhine. *PFG–Journal of Photogrammetry, Remote Sensing and Geoinformation Science, 89*(2), pp.111–120.

Maleika, W. (2013). The influence of track configuration and multibeam echosounder parameters on the accuracy of seabed DTMs obtained in shallow water. *Earth Science Informatics, 6*, pp. 47–69. https://doi.org/10.1007/s12145-013-0111-9

Maleika, W., Palczynski, M. and Frejlichowski, D. (2012). Effect of Density of Measurement Points Collected from a Multibeam Echosounder on the Accuracy of a Digital Terrain Model. In J.-S. Pan, S.-M. Chen and N. T. Nguyen (Eds.), *Intelligent information and database systems* (pp. 456–465). Berlin: Springer. https://doi.org/10.1007/978-3-642-28493-9_ 48

Maune, D. F., Kopp, S. M., Crawford, C. A. and Zervas, C. E. (2007). *Digital elevation model technologies and applications: The DEM users manual*. Bethesda, MD: American Society for Photogrammetry and Remonte Sensing, ASPRS.

Mohammadivojdan, B, Alkhatib, H., Brockmeyer, M., Jahn, C.-H. and Neumann, I. (2020). *Surface Based Modelling of Ground Motion Areas in Lower Saxony*. Institutionelles Repositorium der Leibniz Universität Hannover. https://doi.org/10.15488/9344

Mohammadivojdan, B., Brockmeyer, M., Jahn, C.-H., Neumann, I. and Alkhatib, H. (2021). Regional Ground Movement Detection by Analysis and Modeling PSI Observations. *Remote Sensing, 13*, 2246. https://doi.org/10.3390/rs13122246

Mohammadivojdan, B., Lorenz, F., Artz, T., Weiß, R., Hake, F., Alkhatib, Y., Neumann, I. and Alkhatib, H. (2024). Robust algorithm for automatic surface-based outlier detection in MBES point clouds. *Marine Geodesy, 48*(2), pp. 141–172. https://doi.org/10.1080/01490419.2024.2408684

Paquet, R. (2010). Estimation of interpolation error in DEMs using statistical methods. *FIG Congress 2010 – Facing the Challenges–Building the Capacity*.

Piegl, L. (1997). *The NURBS Book* (2nd ed.). Berlin and Heidelberg: Springer. https://doi.org/10.1007/978-3-642-59223-2

QPS (2025). *QPS QINSy.* https://qps.nl/qinsy/ (last accessed 10 March 2025).

Rishikeshan, C. A., Katiyar, S. K. and Vishnu Mahesh, V. N. (2014). Detailed Evaluation of DEM Interpolation Methods in GIS Using DGPS Data. *2014 International Conference on Computational Intelligence and Communication Networks*, pp. 666–671. https://doi.org/10.1109/CICN.2014.148

Schwarz, W. (2020a). Methoden zur Bestimmung der Messunsicherheit nach GUM – Teil 1. *AVN Allgemeine Vermessungs-Nachrichten*, pp. 69–86.

Schwarz, W. (2020b). Methoden zur Bestimmung der Messunsicherheit nach GUM – Teil 2. *AVN Allgemeine Vermessungs-Nachrichten*, pp. 211–219.

Sullivan, C. B. and Kaszynski, A. (2019). PyVista: 3D plotting and mesh analysis through a streamlined interface for the Visualization Toolkit (VTK). *Journal of Open Source Software, 4*, 1450. https://doi.org/10.21105/joss.01450

Tengku A., Afrizal, T., Abbas, M. A., Mustafar, M. A., Said, M. S. M., Hashim, N. M. and Sulaiman, S. A. (2022). Investigating the Vertical Uncertainty in MBES Measurements. *2022 IEEE 18th International Colloquium on Signal Processing & Applications (CSPA)*, pp. 431–435. https://doi.org/10.1109/CSPA55076.2022.9781857

Wirth, H. (2011). *Messunsicherheiten in der Gewässervermessung* [Tech. rep.]. BfG-Bericht 1734.

Wlodarczyk-Sielicka, M., Lubczonek, J. and Stateczny, A. (2016). Comparison of selected clustering algorithms of raw data obtained by interferometric methods using artificial neural networks. *2016 17th International Radar Symposium (IRS)*, pp. 1–5. https://doi.org/10.1109/IRS.2016.7497290

WSA (2023). *Peilschiff Uwe Jens Lornsen*. Wasserstraßen- und Schifffahrtsamt Elbe-Weser. https://www.wsa-elbe-nordsee.wsv.de/Webs/WSA/Elbe-Nordsee/DE/1_Wasserstrassen/4_SchiffeMaschinenwesen/UJLornsen/ujlornsen_node.html (last accessed 5 January 2024).

Yang, C.-S., Kao,S.-P., Lee, F.-B. and Hung, P.-S. (2004). Twelve different interpolation methods: A case study of Surfer 8.0. *Proceedings of the XXth ISPRS* congress, pp. 778–785.

Authors' biographies

Bahareh Mohammadivojdan received her M. Sc. in Geodesy and Geoinformatics from Leibniz University Hannover in 2019 and is currently a researcher at the Geodetic Institute of the same university. Her work focuses on engineering geodesy and geodetic data analysis, with research interests including mathematical surface approximation, uncertainty modeling, and the analysis of geospatial data for hydrographic and topographic applications. https://orcid.org/0000-0002-0648-1162

Bahareh Mohammadivojdan

Dr.-Ing. Frederic Hake pursued his studies in the field of geodesy and geoinformatics at Leibniz University Hannover. He was employed at the Geodetic Institute, Leibniz University Hannover, where he completed his doctorate in 2024, undertaking research in the field of damage detection in buildings using machine learning techniques. Since 2024 he has been employed by Allsat GmbH, where he has been engaged in a number of activities, including the monitoring of ground movements and the infrastructural monitoring of risk structures. https://orcid.org/0000-0001-7424-2270

Frederic Hake

Felix Lorenz graduated with an M. Sc. degree in Geodesy and Geoinformation from the University of Bonn in 2016. Currently he is working in the Department Geodesy and Remote Sensing of the Federal Institute of Hydrology in Germany as a member of the hydrographic survey working group. He gathered knowledge and experience in the field of dune tracking as a member of the research and development project MAhyD (morphodynamic analyses using hydroacoustic data). In his current position he works consulting the German Waterways and Shipping Administration concerning hydrographic data analysis and sensor specifications.

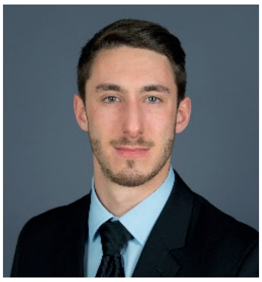

Felix Lorenz

Jan Ole Böllert

Jan Ole Böllert studied Geodesy and Geoinformatics at Leibniz University of Hannover. He graduated with a Master Thesis on "Uncertainty Modelling of Echosounder Measurements". Since 2024 he is employed at the Saxon State Ministry of Infrastructure and Regional Development (SMIL) in Dresden for a technical traineeship for civil service in surveying..

Robert Weiß

Dr.-Ing. Robert Weiß graduated as geodesist from TU Dresden (Germany) in 2003. He investigated the comparability of water surface levels derived from tide gauges, GNSS stations at tide gauges and satellite altimetry and completed his PhD with the topic 'Detection and description of sea level and its changes in the area of the German Bight' in 2012. He has been working in the Federal Institute of Hydrology in Koblenz since 2005. His current work focuses on the evaluation of new sensors, measurement and evaluation methods in the context of digital terrain modeling, such as the analysis of red and green ALS flights.

Thomas Artz

Dr.-Ing. Thomas Artz graduated as geodesist from the University of Bonn. He conducted research in the field of Very Long Baseline Interferometry, Earth Rotation and Terrestrial Reference Frames and completed his PhD on Subdaily Earth Rotation Variations in 2011. Since 2022 he is head of the department of Geodesy and Remote Sensing at the Federal Institute of Hydrology in Koblenz. His department conducts R&D for geodetic and remote sensing tasks regarding the federal waterways in Germany and consults the German Waterways and Shipping Administration as well as the Federal Ministry for Digital and Transport in these research fields.

Ingo Neumann

Univ.-Prof. Dr.-Ing. Ingo Neumann received his Dipl.-Ing. and Ph.D. in Geodesy and Geoinformatics at the Leibniz Universität Hannover in 2005 and 2009, respectively. Since 2012, he has been a Full Professor in the field of Engineering Geodesy and Geodetic Data Analysis at the Geodetic Institute of Leibniz Universität Hannover. His research areas are: artifical intelligence, adjustment theory and uncertainty models, multi-sensor systems, quality assessment, geodetic monitoring, terrestrial laser scanning, and automation of measurement processes. He is active in national and international scientific associations and an official delegate of the German and International Organization of Standardization (DIN and ISO). https://orcid.org/0000-0001-9110-7345

Hamza Alkhatib

PD Dr.-Ing. Hamza Alkhatib studied Surveying Engineering at Karlsruhe Institute of Technology (KIT). He earned his PhD in 2007 from the University of Bonn with a dissertation on "Monte Carlo methods and their applications to satellite gravity missions". Since 2007, he has been leading the research group for Expert-based Data Analysis and Quality Processes at the Geodetic Institute of Leibniz University Hannover. In 2020, he completed his Habilitation on "Advanced Methods and Algorithms for Computer-based Geodetic Data Analysis. His research focuses on machine learning, Bayesian modeling, Monte Carlo methods, and uncertainty quantification in geodetic data analysis. https://orcid.org/0000-0002-4480-1067

https://doi.org/10.58440/ihr-31-1-a09

PEER-REVIEWED ARTICLE

Breaking Waves: A snapshot of women in hydrography in the South-West Pacific

Authors

Emily Harrex[1] and Emily Tidey[1]

Abstract

Only 25 % of qualified hydrographers are women. Here we present a case-study of South-West Pacific women in hydrography from three perspectives: 1) women in hydrography, 2) hydrographic employers, and 3) an undergraduate. Results show the largest barrier is the lack of information about hydrography in schools and universities. Other findings indicate challenges such as a culture of stereotyping, not enough "champions", discrimination, and time away. Recommendations include better promotion of the profession, developing role-models and industry considerations. Suggested further research directions encourage the expansion of the case-study to include high-school children and staff, and women in hydrography beyond our region.

Keywords

women in hydrography · case-study · South-West Pacific · diversity · barriers · questionnaire · career path

Resumé

Seulement 25 % des hydrographes diplômés sont des femmes. Nous présentons ici une étude de cas sur les femmes travaillant dans le domaine de l'hydrographie dans le sud-ouest du Pacifique, sous trois angles différents: 1) les femmes dans l'hydrographie, 2) les employeurs dans le domaine de l'hydrographie et 3) une étudiante universitaire. Les résultats montrent que le principal obstacle est le manque d'informations sur l'hydrographie dans les écoles et les universités. D'autres conclusions mettent en évidence des défis tels que la culture des stéréotypes, le manque de «champions», la discrimination et les absences prolongées. Les recommandations comprennent une meilleure promotion de la profession, la mise en place de modèles et la prise en compte des spécificités du secteur. Les orientations suggérées pour les recherches futures encouragent l'élargissement de l'étude de cas afin d'inclure les élèves et le personnel des lycées, ainsi que les femmes travaillant dans le domaine de l'hydrographie au-delà de notre région.

✉ Emily Tidey · emily.tidey@otago.ac.nz

[1] School of Surveying, University of Otago, Dunedin 9016, New Zealand

https://doi.org/10.58440/ihr-31-1-a04

Resumen

Sólo el 25 % de los hidrógrafos cualificados son mujeres. Presentamos un ejemplo de estudio de mujeres en la hidrografía del Pacífico Sudoccidental desde tres perspectivas: 1) las mujeres en la hidrografía, 2) los empleadores hidrográficos y 3) una estudiante universitaria. Los resultados muestran que el mayor obstáculo es la falta de información sobre hidrografía en las escuelas y universidades. Otros hallazgos indican desafíos como una cultura de estereotipos, la falta de suficientes "campeonas", la discriminación y las ausencias. Las recomendaciones incluyen una mejor promoción de la profesión, el desarrollo de modelos de conducta y consideraciones industriales. Se sugieren nuevas direcciones de investigación, como la ampliación del ejemplo de estudio para incluir alumnos y personal de instituto, y a las mujeres en la hidrografía de fuera de nuestra región.

1 Introduction

Hydrographic surveying is a field that historically, and currently, has a high level of male involvement. This research project, 'Breaking Waves', is a case-study that investigated women in hydrography in the South-West Pacific and the barriers faced by these women during their studies and careers. The work focuses on the experiences of women and other professionals in hydrography.

For this research, the term "hydrographer" refers to all people involved in the work of hydrographic surveying or hydrography; "the branch of applied sciences which deals with the measurement and description of the physical features of oceans, seas, coastal areas, lakes and rivers, as well as with the prediction of their change over time, for the primary purpose of safety of navigation and in support of all other marine activities, including economic development, security and defence, scientific research, and environmental protection." (IHO, 2023b). "Women" refers to those who identified as "female" in our questionnaire responses and in other analysis. "Surveying" has been used as this is common in Aotearoa New Zealand but may be "geomatics" in other countries (e.g. as in Gagnon, 1996 (Canada); Krawczyk, 2002 (Poland); Abd-Elrahman et al., 2019 (USA); Trinder & Fraser, 2019 (Australia)).

1.1 Background

Only a small body of research and information about women in hydrography exists. One of the main sources is the International Hydrographic Organization (IHO). In April 2021, the IHO and the Canadian Hydrographic Service (CHS) set up the Empowering Women in Hydrography (EWH) project with aims to empower women and to see more women in hydrographic leadership positions (IHO, 2024, 2023a). In 2022, EWH surveyed IHO Member States and found that women hold 20 % of leadership roles and make up approximately 25 % of total staff in hydrographic offices (IHO, 2024). Through the EWH initiative, articles published in the International Hydrographic Review (IHR) journal have highlighted issues with safety equipment designed on a "Reference Man" as well as unsuitable living quarters and equipment design (Stewart et al., 2022). Considerations of the phenomenon of "The Leaking Pipeline" in hydrography – where women face career progression barriers and leave the profession at higher rates than their male colleagues – has also been emphasised by Bhatia et al. (2022). Recommendations include leadership, collaborative efforts and policy changes both specific to hydrography (Steward et al., 2022), but also across all Science, Technology, Engineering, and Mathematics (STEM) fields (Bhatia et al., 2022).

Other EHW publications indicate similarities around the world. From 1980–83 Cormier (who worked as part of the CHS) studied Geomatics Technology with 4 other female students (20 %; Cormier, 2021), while in 2023 in Aotearoa New Zealand, first author Emily Harrex had 18 % female classmates in her Bachelor of Surveying final year class. The Hydrographic and Oceanographic Service of the Chilean Navy (SHOA) saw women cartographers in the mid-1960s, and the first female participant in hydrographic officer training in 2010, with 12 graduates by 2020 (SHOA, 2022). In Aotearoa New Zealand the Royal New Zealand Navy (RNZN), which has a hydrography division, undertook a Women at Sea Pilot Study in 1986 with 13 participants (Air Force Museum, 2021).

Historically, hydrography was a task primarily carried out by navies for safety of navigation. Today, while navies still play a role, economic reforms mean that government agencies partnered with private companies are now responsible for nautical charting in Australia and New Zealand and there are many other hydrographic companies working in other fields such as oil and gas, research, construction and environmental monitoring (S+SNZ, 2024).

Current research primarily focuses on specific information (e.g. career-paths, safety, historical involvement) about women involved in hydrography. This case-study adds a variety of responses from women at different stages of their careers, employer information, and a student voice from the South-West Pacific – a region that has not yet featured specifically in EWH publications in the IHR. This regional investigation does not intend to represent the global state of women in hydrography or a detailed history (see earlier publications mentioned that contain more information on this), hence the use of wording 'case-study' and 'snapshot' throughout. In Section 5 we discuss future research ideas, and the hope that this 'snapshot' it is a useful baseline that could be expanded on by others around the world.

1.2 Snapshot framing

This snapshot of women in hydrography was captured through three main "lenses" for an undergraduate project during 2023:

1. That of women in hydrography in the South-West Pacific;
2. From employers at hydrographic companies and firms in Aotearoa New Zealand; and,
3. From first author Emily Harrex, a final-year undergraduate surveying student in 2023.

To gather our information, we sent out 56 questionnaires to women in hydrography and their employers (see Appendix), undertook further investigations through online searches and background reading, and analysed recurring themes that arose.

1.3 Scope of research

This case-study presents a point in time, snapshot view of women in hydrography in the South-West Pacific, thus, the research was constrained. There are three main points to note:

1. The location of interest was the South-West Pacific region. This includes Aotearoa New Zealand, Australia, and the Pacific Islands. This setting was a natural choice given the need to restrict our study to an undergraduate project size and scope, and our location, and was aided by an active Empowering Women in Hydrography Group (49 members at the time of the case-study), in the South-West Pacific.
2. The demographic is women currently working in the hydrographic industry in the region. This a small population to begin with; as an indication of women in hydrography in the region, we consulted the record of women hydrographers certified by the FIG/IHO/ICA recognised Australasian Hydrographic Surveyors Certification Panel (AHSCP). The most recent list of those certified shows that only 5 of 96 certified Level 1 surveyors were women (5 %) and 3 of 77 were certified Level 2 (4 %) at the time of our study in 2023 (AHSCP, 2025). This group was too small to focus on, so we worked with the SWP Empowering Women in Hydrography Group.
3. We approached hydrographic operating companies in Aotearoa New Zealand sourced through membership of the Australasian Hydrographic Society (AHS), which numbered seven at the time of the questionnaire. We did not include independent contractors or those unknown to the Society membership.
4. The targeting of participants in 2. and 3. prior mean that our approach used a combination of convenience and purposive sampling. While this may result in biases from the selection process, it is nevertheless useful as a preliminary case-study and for qualitative research, particularly allowing "focusing on specific people with rare knowledge or experiences" (Ahmed, 2024).
5. Diversity is a broad topic, and many approaches can be taken to investigate elements of workplace diversity. This research looked specifically at gender.

2 Methods

This case-study used a mixed methods approach on questionnaire results and further investigations to determine recurring themes and link our findings, discussion and recommendations for future work.

2.1 Questionnaires

Questionnaires form a large component of this case-study. The first was a general questionnaire of 26 questions to women working in hydrography who were part of the Empowering Women in Hydrography South-West Pacific Group, to gather their demographic information, personal experiences and opinions (Appendix A1). The second questionnaire of seven questions was aimed at hydrographic companies in Aotearoa New Zealand and asked for employers' experiences and opinions (Appendix A2). The questionnaires used multichoice and open text responses. Both questionnaires are included in an appendix to this manuscript. For both, University of Otago Category B Ethics approval was gained and the university's Qualtrics system was used to collect responses during April 2023. Margin of error calculations were not used due to our targeted sampling approach and small sample size (Webster, 2021). This means that care must be taken when analysing the small numbers of responses, which are instead used as a wider thematic steer for this case-study.

The responses to both questionnaires were analysed with graphs of quantifiable data from multichoice answers, and conventional and summative content analysis on open text responses (Hsieh & Shannon, 2005). Conventional analysis enabled us to start with no predetermined themes, and to see what arose as we worked through the texts. We used word clouds for summative and visual analysis by pasting text answers into *wordclouds.com*, along with user-defined rules such as the removal of keywords from the question being analysed, consistent font and colour, and removal of words that only appear once. The result was a series of graphical outputs highlighting word frequency through size and shading of words displayed in the resulting word clouds (Figs. 3, 8, 9 and 12). Note that these word clouds are not a statistical analysis but are used to indicate any key themes in the responses, which we then analysed further (following the recommendation by McNaught & Lam (2010)). Not all questions asked are included in the results discussed in this manuscript, but all were used to guide the following further investigations.

https://doi.org/10.58440/ihr-31-1-a04

2.2 Education and career investigations

Further investigations were guided by responses from the questionnaires. A common theme across many answers was that there needed to be more information and support at schools and universities. Another common theme was that there were not enough examples of women hydrographers working on the job, so further investigations looked at the information available on the internet to people who may be looking at surveying as a career. This included websites such as Careers NZ, The New Zealand Curriculum Online, New Zealand Women in STEM, and the University of Otago School of Surveying website and determining what information regarding surveying and hydrographic surveying was available and how easy this information was to find. Information about what was found and not found on these sites was recorded. Any information mentioning women in hydrography or surveying was noted.

3 Results

3.1 Women in hydrography questionnaire

From 49 members of Empowering Women in Hydrography South-West Pacific group, 24 questionnaire responses were received (response rate of 49 %). For context, recent studies indicate average response rates of 44.1 % in education research (Wu et al., 2022), 48–68 % in broader research (Holtom et al., 2022), 38–76 % in medical research (Toy & Guris, 2022). For our questionnaire, it would not be appropriate to consider the margin of error as our targeted sampling (Section 1.3) means we have not selected our participants truly at random, and our small sample size would make any calculations where responses are ≤15 for a single category misleading (Webster, 2021).

All of our respondents identified as female, were aged between 21 and 60, and have been working in hydrography between zero and 30 years. Of these people, 88 % were employees, and 11 of these provided work email addresses when given an option at the end for further contact. The remaining responses were students, employers and others. The distribution of responses is shown in Figs. 1 and 2.

Fig. 3 shows a word cloud with the responses to question six: "How and why did you get into hydrographic surveying?". The most common words are "projects", "university" and "management", then "job", "working" and "geology". In full answers, these words were used in the context of learning on the job or project. Many respondents had an interest in the ocean and ended up in hydrography after taking certain university papers or joining the Navy. This begins a theme across 42 % of responses to this question as well as featuring in other question responses (Q11, Q12, Q13): many people did not know about, or set out to study and work specifically in hydrography, but rather discovered the field along the way. In question six, respondents used comments such as *"it wasnt [sic] on purpose, it just happened", "I was looking for a job that was local that had some relation to my studies", "By accident, found a job…"*.

3.1.1 Diversity

To assess perceptions of diversity in the workplace, we asked the questions shown in Fig. 4 which shows 14 people (61 %) believed they worked in a gender diverse environment and 9 (39 %) thought they did not. When asked to choose on a continuum (1–5) the perceived importance of gender diversity is in the workplace from not (1/5) to extremely (5/5) important, everyone said it was moderately (3/5) to extremely (5/5) important. The following question asked for an explanation. In these responses common themes were seen, such as gender diversity bringing different approaches, creating more balanced workplaces,

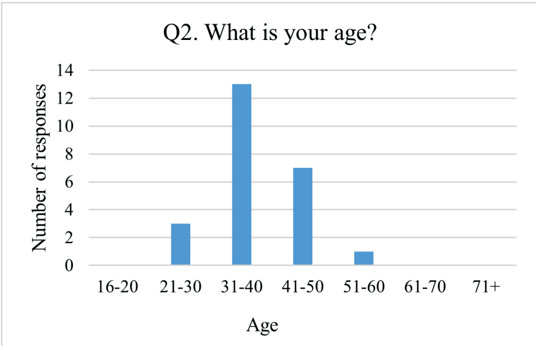

Fig. 1 Results from Q2.

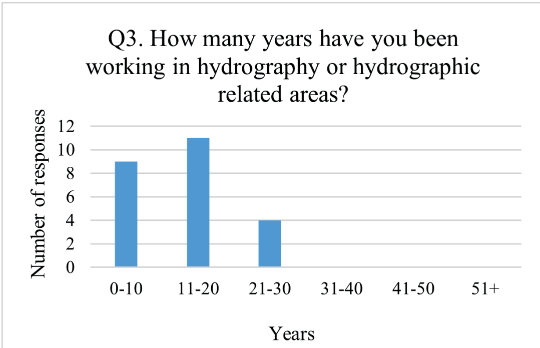

Fig. 2 Results from Q3.

Fig. 3 Results from Q6: How and why did you get into hydrographic surveying?

and that all benefit.

We asked people what percentage of hydrographers they have worked with have been women. Fig. 5 shows that (74 %) 0–10 % and 11–20 % were the most common answers, and no-one has worked with more than 50 % women. In further questions 21 people (95 %) would like to see more women in hydrography and 19 (85 %) think it is important to increase the number of women in hydrography as it brings "*skills, knowledge and experiences to a team… increased collaboration, consultation… [and] knowledge sharing*". 4 people (17 %) said this was not an important focus and 1 was concerned about "*interpersonal issues*" if there were more women.

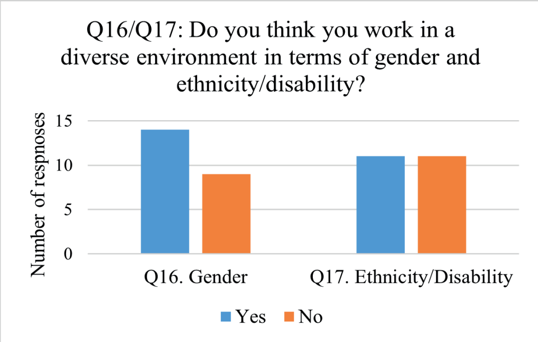

Fig. 4 Results from Q16 and Q17.

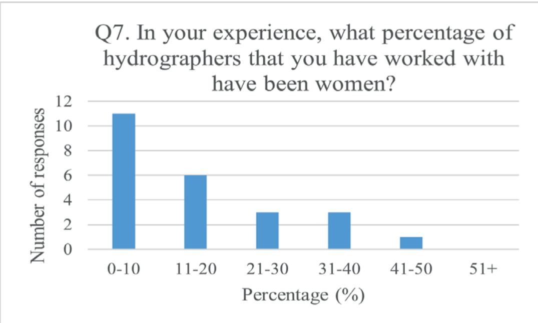

Fig. 5 Results from Q7.

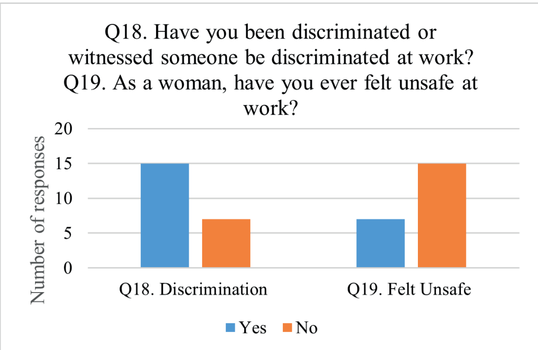

Fig. 6 Results from Q18 and Q24.

3.1.2 Barriers

The IHO states that 25 % of people qualified in hydrography are women (IHO, 2023a). Respondents were asked why they thought this was. A common theme across responses was there is little exposure to hydrography for people in high school or university. Many people also said that gender stereotypes still exist, and that hydrography can be marketed as a "male" profession. Fig. 7 shows barriers that prevent women from pursuing a career in hydrography.

The "other" option was chosen by two people who mentioned aspects such as: no interest from women, women being guided into teaching, nursing, and designing, childcare, not being able to work due to cultural issues and being told there are not enough/ suitable facilities for women.

Safety and workplace sexism are two of the barriers identified. Further questions asked participants if they had witnessed or experienced discrimination, and if they had ever felt unsafe at work. These results are shown in Fig. 6 where the results of questions were a mirror reflection of each other showing our female participants have encountered discrimination more than they have felt unsafe while working. It is important to note the limits of our small sample size here again – nevertheless it is concerning as our respondents were from at least 11 companies, so with a result of 15/24 for this case-study we can say that it has occurred in more than one workplace.

If respondents felt comfortable, they were asked to describe their experiences. Responses showed that encounters with discrimination and feeling unsafe tend to occur when working offshore or in the field, rather than in an office environment. In terms of safety, all responses explained issues of unwanted

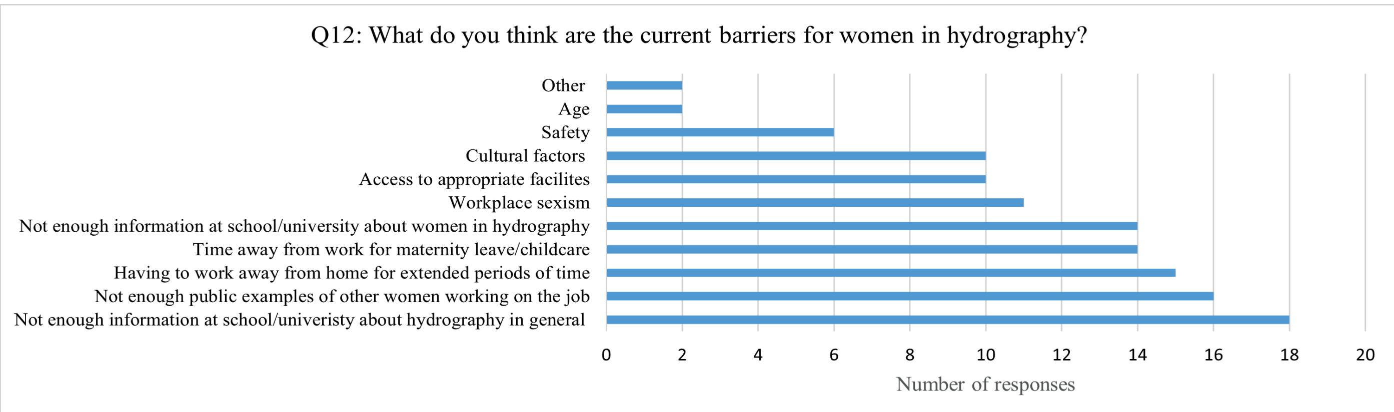

Fig. 7 Results from Q12.

https://doi.org/10.58440/ihr-31-1-a04

Fig. 8 Results from Q21: What have you found challenging about being a woman in hydrography?

Fig. 9 Results to Q15: What changes do you think could be made/what do you think could be done to help increase the number of women in hydrography?

sexual attention and harassment.

When asked what their experience as a woman working in hydrography had been almost all respondents spoke well of their experiences and said that they have felt supported. However, several people highlighted that work has also come with negative experiences. One person wrote the following statement in response to the challenges they had encountered: "*Besides the unwanted sexual attention, [the challenge has been] getting my voice heard in a room of white old men*".

Fig. 8 shows the most common words included in the responses to the question "What have you found challenging about being a woman in hydrography?" were "working" and "men". Aside from this, other prominent words include "culture" and "assumptions". These words were used in the context of working with men who assume the woman is not in charge of the survey team and a culture where women always have to justify themselves. When asked how they had overcome or worked through the challenges they had described, respondents mentioned "*doing the best you can*", "*gaining different experiences*", "*showing that you have the right experience*" for the job as well as trying to highlight the "*cultural changes*" needed.

3.1.3 The future

We finished our questionnaire with inquiries on the future and ways that hydrography can be better promoted to women. When asked: "What would you like to see change in the workplace to be able to help improve the experience of others?" responses alluded to a need for more understanding and support within organisations. Many respondents wrote that they would like to see stereotypes broken with an understanding of what people are good at, irrespective of their gender. "Appropriate" is also a word that appeared many times and respondents linked this back with their responses to Q12 when 42 % identified "access to appropriate facilities" as a current barrier for women in hydrography. Specific examples indicate this is during field operations. For the future they state the need to change: "*Working long days on the water with no appropriate toilet facilities on small boats.*" perhaps by "*Encourage[ing] a break throughout the day at appropriate facilities if we are close by.*"

Fig. 9 highlights a need for there to be more information and support for people at high school and university. "Opportunities" and "awareness" were commonly used words along with "career" and "support". These words are used in the context of increasing awareness for high school and university students, providing more opportunities for women at this level but also for those already working in the industry. "Champions" was a word used in some responses.

3.2 Employer questionnaire

The responses to the employer questionnaire provide a snapshot of data from seven different companies. All respondents were male and were department

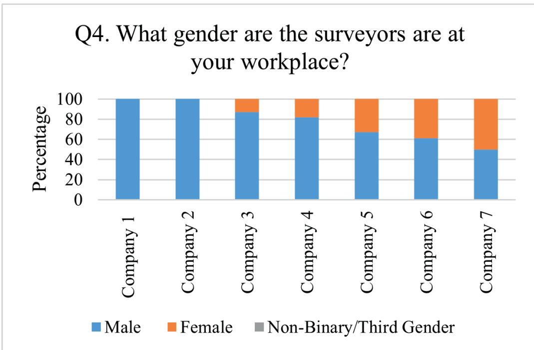

Fig. 10 Results from Q4.

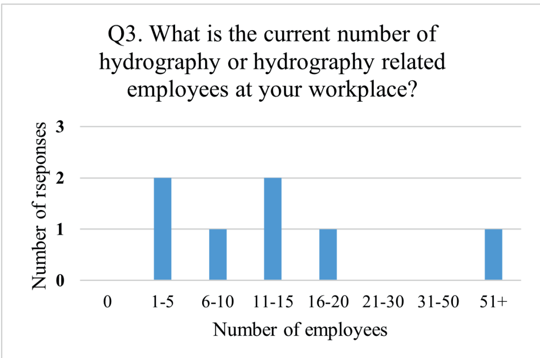

Fig. 11 Results from Q3.

Fig. 12 Results from Q7: What plans, initiatives, or strategies help to create a more diverse workspace?

managers, CEOs, or managing directors for their companies. To understand the diversity of their different workplaces, we asked the total number of surveyors by gender (i.e. also including land surveyors; Fig. 10) and the current number of hydrography or hydrography-related employees at your workplace (Fig. 11).

The results show that of the companies questioned, two have an entirely male surveying team, four have survey teams where female members are between 13–39 % and one company has an even split of male and female surveyors (though note that this company only has two surveyors: one male and one female!). No company has more female surveyors than male surveyors. Most companies questioned have between one and 20 hydrographic employees.

We asked "Do you recruit and employ people with diversity (not just gender) in mind?" and "As an employer do you work to create a more diverse workplace?", all respondents answered in the affirmative to these two questions. Six respondents said that they work to create a more diverse workspace (one did not answer).

Fig. 12 shows the most common words used in response to how employers work to create a more diverse workplace. Here, "inclusion" and "principles" are the most frequently used words. Looking at the full written responses, these words relate mainly to company diversity and inclusion policies and principles.

3.3 Student hydrographer

Similarly to many questionnaire participants, first author Emily Harrex did not know about hydrography at school. She learned about surveying in general during her last year of high school when a careers advisor – who had personal links to the School of Surveying – that suggested the subject to her. Once at university, it took several years until Emily Harrex learned more about, and had the option to, study hydrography as part of her degree. Like many of our participants she too never "planned" to study hydrographic surveying and has instead "fallen into it". In 2024 she started employment as an offshore surveyor in Europe.

On talking informally with fellow university students, it seems most either considered fields such as architecture or engineering before settling on surveying, have family members or friends who are surveyors, or were recommended studying surveying by a career advisor. It was also common to hear of young women who had investigated surveying while in high school, but decided that it was a job for men and continued looking at other career options. Emily Harrex's 2023 final year surveying class is male dominated. Of 50 students, 9 are female (18 %). The smaller hydrographic-specific surveying class typically has 30 or fewer students, and in her year there were 5 females (17 %).

3.4 Education and career investigations

As questionnaire responses mentioned that there needs to be more information and support at schools and universities, information was gathered from the perspective of a high school student curious about hydrography and looking online at their options for careers and study. The use of the Google search engine occurred in September 2023 on the first author's computer directly after wiping the browser history to attempt unbiased search pathways.

The curriculum resources section of the New Zealand Curriculum Online website was the first result of the Google search "resources for Year 13 career choices" (MoE, 2021). The link "resources to explore job ideas" was followed, opening a "jobs by interest" option, which opened a document that broke down potential interests into possible industries and jobs. A search of the document for "surveyor" returned three results. A surveying job was classified under the interest heading of architectural and technical design. "Quantity surveyor" and "building surveyor" were options under the construction interest heading. A search of the document for "hydrographer", "hydrography" and "cartography" returned no results. As "surveying" is not a subject taught explicitly at high school we also used a Google search of "geography related careers" returned a list of 24 professions that had been pulled from sources across the internet. "Cartographer" was the first option. "Surveyor" was also an option at number 18 on the list. It is possible some high-school students may learn of surveying through this route.

For high school students in Aotearoa New Zealand, the Careers New Zealand website is a primary source of information when investigating career options (Careers New Zealand, 2022). On this website you can search for different careers. A search of "hydrographer", "hydrographic" and "hydrography" all returned "surveyor" as the only career option. A search for "hydrographic surveyor" again returned "surveyor" along with nine other options, including building surveyor, civil engineer, naval architect, marine engineer, and ship's master. Using the link to "surveyor" we find "hydrographic surveyor" is mentioned on the page. However, it is located 80 % of the way down the page, and after the list of sources and references. Given most people read around 20 % (Nielsen, 2008) of a webpage, it is likely most people will not see this.

With these searches not providing much information about women in hydrography, or hydrography at all, a broader Google search was made for "women in STEM". The first site to appear was the New Zealand Women in STEM website (WISTEM, n.d.). Under the "engineering" tab there was some information about women in surveying but nothing specific to hydrography. The information was in the form of a video, with women talking about their experiences and a typical day in the life of a surveyor. This is a great source of information for high school students but is perhaps something that students are not aware of if they don't explicitly search for it.

A further source of information investigated was the University of Otago School of Surveying website. The "About Surveying" page provides an overview of research skills and interests that staff have. Hydrographic Surveying is included in this list. The "Study Surveying" page is comprehensive and talks through the entire Bachelor of Surveying degree. The word "hydrographic surveying" is included throughout this page, often in lists with other surveying pathways. Under these two headings, there is no description of what hydrographic surveying or indeed what any other branch of surveying is. The only blurb about hydrographic surveying is included under the "Research at Surveying" heading. This is not an intuitive place for high school students to discover information about different aspects of surveying. Another observation is that there are very few photos of students studying surveying or people working in surveying jobs.

Most of the information presented above relates to land-based surveying careers. There is little information accessible to high school students about hydrographic surveying and it seems that a high school student considering a career in STEM would be very unlikely to come across the career of hydrography during career investigations.

A knowledgeable person may look online for hydrographic qualifications and so come across the IHO Special Publication C-47 'Training Courses in Hydrography and Nautical Cartography', which contains entries for Australia and New Zealand. In Australia it highlights naval training, and for New Zealand lists the degree options at the University of Otago (IHO, 2011). This document did not come up in our searches. The document "List of Recognized Hydrography Programmes" from the FIG/IHO/ICA International Board of Standards of Competence for Hydrographic Surveyors and Nautical Cartographers (IBSC; IBSC, 2024) shows the Royal Australian Navy Cat B course and no others in the South-West Pacific. The region does also contain the Australasian Hydrographic Surveyors Certification Panel (AHSCP), and the document indicates that there was once Cat A training in Australia and New Zealand, but that these courses are no longer recognised (i.e. certified by the IBSC).

4 Discussion

Case-study results have highlighted the challenges and barriers faced by women in hydrography as shared by those working in the profession, those in leadership positions and from the perspective of a student. The targeted sample size means that interesting results have been gained from a group that can share their unique knowledge and experiences, providing a baseline of understanding that now needs to be scaled to provide international and robust statistical analysis. Here we consider each of our study lenses to form our "snapshot" of women in hydrography in the South-West Pacific.

4.1 Women in hydrography

There is a lack of gender diversity in hydrography. Interestingly, in our respondents there is a gap between those who support there being more women in hydrography (95 %) and those who believe it is an important focus (85 %), suggesting other areas of importance for four participants. The reported experiences of our women in hydrography demonstrate the importance of gender diversity with responses highlighting a need to create balanced workplaces that call on different perspectives and utilise the strengths and skills that women bring to the hydrographic industry.

There are multiple instances of women suggesting a lack of promotion of hydrography as a career with many women "falling" into studying hydrography. One said they ended up in hydrography "*by accident, [when I] found a job when I was at university*". These responses highlight a need for better information and awareness of hydrography at high school and university, especially for young women. This lack of information is further emphasised by the barriers identified. The largest barrier to entry, in the opinion of our women hydrographers, was a lack of information about hydrography in schools and universities. The biggest change these women want to see is improvement in publicity about hydrography as a career for both men and women. Crucially, this requires support for those already in the profession too, with one respondent raising the point: "*If women feel they are better supported and have the same opportunities as men, they are more likely to encourage more women into the industry*.". Therefore, there should be more support both for women in the industry and for those looking at hydrography as a career option. Following the lack of information and role models, Fig. 7 shows time away from home and maternity or childcare considerations as another barrier. This indicates a need to consider all aspects of the hydrographic profession – including the many roles that are not offshore for long periods, and perhaps the continuing development of remote operating facilities – and how these are portrayed in current information about the career.

Discrimination is a factor 15 of our women respondents had experienced or witnessed while working at more than one workplace, which was more than the seven who had felt unsafe at work. This may demonstrate that some physical safety matters such as inadequate PPE, inadequate quartering and unsuitable equipment design (Stewart et al., 2022) are starting to be addressed, or are 'easier' to begin to resolve than less visible aspects such as discrimination or unwanted sexual attention. The questionnaire responses showed that these negative experiences tend to occur more in offshore or field situations and should be of concern to employers who have legal and moral obligations to their staff regardless of their location.

Despite these challenges, we perceive the overall experience of the women respondents as positive with some feelings of frustration. This frustration is captured by one respondent who said, "*I have found the constant interrogation of my skills and experience the most challenging*". More specifically having to "*answer questions on often random details of a system/ piece of equipment/ process that someone chooses as a 'test' for me before I can get on with the job*". Several women spoke of the constant interrogation of their skills being one of the biggest challenges and suggests an underlying culture of stereotypes considering "men's" or "women's" jobs.

4.2 Hydrography employers

The employer questionnaire findings add a different perspective to the topic of women in hydrography. Notably these employer responses do not include any women, confirming the IHO identified gender imbalance in management and leadership positions (IHO, 2023a). This finding alone highlights a need for investigation of the underlying factors that contribute to fewer women holding these positions, likely to include aspects such as historical training of male hydrographers (Section 1.1), gender stereotyping (as in Fox-Turnbull et al. (2023) and Huddleson (2017)) and time away from work for maternity leave and childcare (with associated issues such as the leaky pipeline as in Bhatia et al. (2022) and Jackson (2021) and return-to-work challenges as in Green (2023)). The under-representation of women in hydrographic leadership positions may influence women already working in hydrography as well as women looking to pursue a career in hydrography. This relates to the idea of "champions" mentioned throughout the individual questionnaire responses, in Emily Harrex's discussion with fellow students, and the quotable "if you can see it you can be it". If women do not see other women holding leadership roles within hydrographic organisations, it may be that women do not see value in or want to strive for these positions. In terms of high school students, if they do not see women in hydrography leadership positions, they may conclude it is a job for men only. The impact and significance should not be underestimated.

The composition of different workplaces is varied. In our responses, most companies have a relatively small number of hydrographic employees and either none or a smaller percentage of women. The company with an even split of males and females could be somewhat misleading as there are only two staff. Every employer said that they work to create more diverse and inclusive spaces and that the use of diversity and inclusion policies helps this. Hopefully shedding light on the challenges and barriers faced by women will inspire employers to revisit their policies and consider more ways in which they can better support their entire existing, and future, team. Additionally, the development and use of thoughtfully updated policies should promote further diversity in workplaces.

4.3 Student considerations

Comments from first author Emily Harrex indicate that while she was a minority as a female in a male-dominated degree, she nevertheless felt well supported and respected by both staff and peers. On mandatory summer work experience she reported never finding being a woman an issue and that she was lucky to undertake summer work in an office of a land surveying firm where about 40 % of the team were women. The use of the word "lucky" indicating the value placed by students on working in a company with different ratios to their university classes.

It is disheartening that the overall women surveying undergraduate numbers experienced by Emily Harrex in the 2020's reflects what Cormier experienced when studying Geomatics Technology in 1980, showing little growth or change over this time (Cormier, 2021). In the case of SHOA in Chile, it is suggested that the inclusion of women in hydrography has been slow due to the lack of universities courses (SHOA, 2022). Would more hydrographic courses help increase the number of women in hydrography? Not necessarily. There is already a lack of women in surveying/geomatics courses, so it seems improving the gender ratios in existing courses is the first most important step.

The sustained ratio of just under 20 % women in Emily Harrex's smaller, optional, hydrographic class is interesting. One suggestion for this is the possible influence of the fact that the hydrographic surveying lecturer is one of only three women lecturers out of 17 academic staff in the School of Surveying, perhaps filling one of the aforementioned "champion" roles for undergraduates.

When searching online for information for students interested in hydrography, the resulting lack of presence, or small amount of promotion of the profession is obvious. It is notable that this is the result of 'knowledgeable' searches, so the profession must do more to share what it does on a wider scale, particularly to school students.

The IBSC currently recognise 55 hydrography programmes, and nine nautical cartography programmes worldwide (IBSC, 2024). Many of these are naval

https://doi.org/10.58440/ihr-31-1-a04

programmes which may not accept civilian students. There are currently no non-naval, residential (i.e. not online) programmes in the South-West Pacific. The lack of training options in the region (and indeed worldwide) may also be a contributor to the lack of awareness regarding hydrography as a career path.

4.4 Snapshot

Through its many lenses, this case-study shows an overall lack of information and awareness about hydrographic surveying that leads on to the lack of women in training, hydrographic employment and leadership positions. Those women in the industry generally enjoy their profession, although more is needed to continue improvements in aspects of safety, culture and making "champions" visible. It is hoped that this small-scale investigation can be used to generate hypotheses for more wide-scale, and thus more rigorous, understanding of the challenges for women in hydrography.

4.5 Recommendations

Encouraging more women to become involved in hydrography and seeing more women in hydrographic leadership positions is no small feat. We think it will require sustained focus, improved training and collaboration in the following three elements:

Promotion of the hydrographic industry: More work is needed to develop and align marketing approaches from hydrographers (individuals and companies), universities, and surveying bodies. Revisiting websites using a student "lens" would be an easy win, in many cases requiring only small additions or updating of text about hydrography, and the inclusion of diverse photos. The use of graduate profiles of all genders is encouraged. Engagement with related professions is also recommended, to showcase hydrography to those in fields such as teaching, sciences and geography. This is recommended as many current surveying students have a direct link to someone who knows the profession. Our findings also indicate the need to show the many options available to work as a hydrographer, so that time away from home and maternity and childcare considerations do not become a barrier wherever possible.

Hydrographic "champions": Develop ways to demonstrate to young people that hydrography is not targeted or designed for one gender. This might involve working on greater visibility of women hydrographers, including women who manage work and other responsibilities such as being a parent. Professional bodies seem a logical place to showcase these people, with recognition through awards, presentations and articles.

Hydrographic industry considerations: As shown in our questionnaire results, continuing to improve facilities and safety for women is important, but focus should also be on ensuring discrimination and stereotyping is monitored and acted upon. Fostering safe ways for staff to report concerns and considering policies such as questionnaires to gauge the well-being of employees, or project wrap-ups that also consider how empowering women in hydrography was incorporated into jobs are recommended.

5 Future research

As an undergraduate project, sample size limited our investigation. For future research we suggest:

1. Interact with high school careers advisors to determine the information they receive regarding career options and how they make students aware of different pathways, including hydrography. If guests are invited to the school what professions are most usually engaged with and how could hydrography be added?
2. Consider students in their final years of high school to determine which professions students hear about most and what resources they are using to investigate career options after school.
3. Investigate the number of women in university surveying classes over time to gain context on the fluctuations of enrolments and compare these with other related STEM subjects such as engineering. Find out how students come to surveying, and any barriers they have faced so far.
4. This research is specific to the South-West Pacific region and companies in Aotearoa New Zealand. We hope as a 'snapshot' it is a useful beginning that could be expanded by others around the world, thus increasing sample size and allowing robust statistical analysis to take place. Those wishing to build upon the questionnaire in this case-study should consult the appendix.

6 Conclusions

Breaking Waves was a project investigating the topic of women in hydrography and the barriers that prevent women from pursuing a career in this field. This research has been conducted to provide a case-study or "snapshot" of women in hydrography through three different lenses:

1. That of women in hydrography in the South-West Pacific;
2. From employers at hydrographic companies and firms in Aotearoa New Zealand; and,
3. From Emily Harrex, first author of this article, a final-year undergraduate surveying student in 2023.

Through questionnaires and further investigations, we have found there is a lack of information in schools and universities regarding hydrography, as well as surveying in general. This was identified as the largest barrier to women choosing hydrography as a career. Women in the hydrographic industry expressed a desire to see more awareness and promotion of hydrography in schools and universities. Further investigations confirmed this lack of easily accessible information for students investigating career options.

Other challenges highlighted by women include a culture of stereotyping within the industry, not enough "champions" or public examples of women in hydrography, and having to work away from home for extended periods of time. In addition, more women who responded to the questionnaire had experienced discrimination at work than had felt unsafe, both highlighting important concerns (discrimination and safety), but possible areas of recent progress (safety).

Employers of hydrographic companies highlighted a lack of women in CEO, department manager or managing director roles, particularly as all respondents to this questionnaire were male. All respondents indicated they work to create inclusive and diverse workplaces, and that the use of policies relating to these matters helps.

Recommendations for acting on our findings include better promotion of the profession, developing role-models and industry considerations. Suggested research directions enable others to build on this project and continue to empower and encourage women in hydrography.

Acknowledgements

Kia ora, thank you to everyone who has responded to the questionnaires. Your contribution to this project is highly valued and greatly appreciated.

Thank you to the Australasian Hydrographic Society (AHS) for their generous support in recognition of this project – Emily Harrex was one of the 2023 winners of the AHS Education Award and presented findings at both the NZ Region of the AHS and S+SNZ conferences in 2023.

Thank you to three anonymous reviewers who gave feedback which greatly improved this manuscript.

References

Abd-Elrahman, A., Barnes, G., Benjamin, A., Britt, K., Dewitt, B., Hochmair, H. H., Smith, S. and Wilkinson, B. (2019). Geomatics Education at the University of Florida: A Case Study of Challenges and Adaptation. *Surveying and Land Information Science, 78*(1), pp. 5–16.

Ahmed, S. K. (2024). How to choose a sampling technique and determine sample size for research: A simplified guide for researchers. *Oral Oncology Reports, 12.* https://doi.org/10.1016/j.oor.2024.100662

AHSCP (2025). *Australasian Hydrographic Surveyors Certification Panel (AHSCP) – List of Current Certified Professionals in Hydrographic Surveying. Geospatial Council of Australia*. Geospatial Council of Australia, Deakin West, Australia. https://geospatialcouncil.org.au/wp-content/uploads/2025/02/250225Current-Certified.pdf (last accessed 8 March 2025).

Air Force Museum (2021). *Wāhine Toa: Women in Defence.* Air Force Museum of New Zealand, Christchurch, New Zealand. https://www.airforcemuseum.co.nz/whats-on/wahine-toa-women-in-defence/ (last accessed 27 April 2025).

Bhatia, S., Biron, A., Imahori, G. and Stewart, H. (2022). The Empowering Women in Hydrography Project - Fix Your Leaking Pipeline. *The International Hydrographic Review, 28*, pp. 181–196. https://doi.org/10.58440/ihr-28-n09

Careers New Zealand (2022). *Job Profiles.* New Zealand Government. https://www.careers.govt.nz/jobs-database/ (last accessed 2 January 2025).

Cormier, J. (2021). A Career as a Woman with the Canadian Hydrographic Service. *The International Hydrographic Review, 26,* pp. 127–134. https://ihr.iho.int/articles/a-career-as-a-woman-with-the-canadian-hydrographic-service/ (last accessed 2 January 2025).

Fox-Turnbull, W. H., Moridnejad, M., Docherty, P. D. and Cooper, J. (2023). Influencing factors on women in connection with engineering in New Zealand: a triad of lenses. *Int J Technol Des Educ, 34*, 1045–1066. https://doi.org/10.1007/s10798-023-09854-6

Gagnon, P. (1996). From surveying to geomatics evaluation of education needs to adapt to a new paradigm (a canadian perspective). *GEOMATICA, 50*(3).

Green, S. (2023). *It shouldn't be this hard to return to work after maternity leave.* The Spinoff, New Zealand. https://thespinoff.co.nz/society/16-03-2023/it-shouldnt-be-this-hard-to-return-to-work-after-maternity-leave (last accessed 2 January 2025).

Holtom, B., Baruch, Y., Aguinis, H. and A Ballinger, G. (2022). Survey response rates: Trends and a validity assessment framework. *Human Relations*, 75(8), 1560–1584. https://doi.org/10.1177/00187267211070769

Hsieh, H.-F. and Shannon, S. E. (2005). Three Approaches to Qualitative Content Analysis. *Qualitative Health Research, 15*(9), 1277–1288. https://doi.org/10.1177/1049732305276687

IBSC (2024). *List of Recognized Hydrography Programmes* (last update 1 January 2024). FIG/IHO/ICA International Board on Standards of Competence for Hydrographic Surveyors and Nautical Cartographers (IBSC), International Hydrographic Organization, Monaco. https://iho.int/uploads/user/Inter-Regional%20Coordination/IBSC/MISC/IBSC-ProgrammeDatabase.pdf (last accessed 8 March 2025).

IHO (2011). *Training Courses in Hydrography and Nautical Cartography* (7th ed.). IHO Special Publication C-47, International Hydrographic Organization, Monaco. https://iho.int/uploads/user/pubs/cb/c-33/C47E-SEPT09-UPDATED-APRIL11.pdf (last accessed 8 March 2025).

IHO (2023a). *Empowering Women in Hydrography*. International Hydrographic Organization, Monaco. https://iho.int/en/basic-cbsc-ewh (last accessed 2 January 2025).

IHO (2023b). *Hydrographic Dictionary* (last change 10 July 2023). IHO Special Publication S-32, International Hydrographic Organization, Monaco. https://portal.iho.int/iho-ohi/S32/ (last accessed 2 January 2025).

IHO (2024). *Empowering Women in Hydrography: A Transformative Three-Year Journey Towards Gender Equality.* International Hydrographic Organization, Monaco. https://iho.int/en/empowering-women-in-hydrography-a-transformative-three-year-journey-towards-gender-equality (last accessed 8 March 2025).

Jackson, K. (2021). *Why do female engineers discontinue their construction careers* (Master Thesis). Southern Institute of Technology, Invercargill, New Zealand. https://www.researchbank.ac.nz/server/api/core/bitstreams/f32ced9d-1e65-404e-a4d8-aa7f4d5455ee/content (last accessed 2 January 2025).

Krawczyk, A. (2002). Proposal of Redefinition of the Terms Geomatics and Geoinformatics on the Basis of Terminological Postulates. *ISPRS International Journal of Geo-Information, 11*(11), p. 557. https://doi.org/10.3390/ijgi11110557

McNaught, C. and Lam, P. (2010). Using Wordle as a Supplementary Research Tool. *The Qualitative Report, 15*(3), pp. 630–643.

MoE (2021). *Career Education.* New Zealand Curriculum Online – Career Education, Ministry of Education, New Zealand. https://nzcurriculum.tki.org.nz/Curriculum-resources/Career-education (last accessed 2 January 2025).

Nielsen, J. (2008). *How Little Do Users Read?* Nielsen Norman Group, Dover, USA. https://www.nngroup.com/articles/how-little-do-users-read/ (last accessed 2 January 2025).

S+SNZ (2024). *Hydrography Stream*. Survey and Spatial New Zealand (S+SNZ), Wellington, New Zealand. https://www.surveyspatialnz.org/Article?Action=View&Article_id=187 (last accessed 2 January 2025).

SHOA (2022). The Participation of Women in Hydrographic Activity in Chile. *The International Hydrographic Review, 27*, pp. 113–119. https://doi.org/10.58440/ihr-27-n01

Stewart, H., Imahori, G., Biron, A. and Bhatia, S. (2022). Empowering Women in Hydrography – Safety First! *The International Hydrographic Review, 27*, pp. 121–131. https://doi.org/10.58440/ihr-27-n02

Toy, S. and Guris, R. J. D. (2022). How to conduct survey-based research. *Anaesthesia, 78*, pp. 902–905. https://doi:10.1111/anae.15943

Trinder, J. C. and Fraser, C. S. (2012). Geomatics: The case for a change of name of a discipline in the academic context. *Australian Surveyor, 39*(2), pp. 87–91. https://doi.org/10.1080/00050326.1994.10441599

Webster, W. (2021). *Your guide to margin of error.* Experience Management Platform, Qualtrics, North Sydney, Australia. https://www.qualtrics.com/en-au/experience-management/research/margin-of-error/ (last accessed 9 March 2025).

WISTEM (n.d.). *Engineering.* NZ Women in STEM. http://www.womeninstem.co.nz/engineering.html (last accessed 2 January 2025).

Wu, M., Zhao, K. and Fils-Aime, F. (2022). Response rates of online surveys in published research: A meta-analysis. *Computers in Human Behavior Reports,* 7. https://doi.org/10.1016/j.chbr.2022.100206

Appendix

A.1 Questionnaire for women in hydrography

A.1.1 Demographic and basic information

Q1. What is your age? [Options: 16-20, 21-30, 31-40, 41-50, 51-60, 61-70, 71+, Prefer not to say]
Q2. What is your gender? [Options: Male, Female, Non-binary / Third gender, Prefer not to say]
Q3. How many years have you been working in hydrography or hydrographic-related areas? [0-10, 11-20, 21-30, 31-40, 41-50, 51+]
Q4. What are you? [A students, An employer, An employee, Other (Please Specify)
Q5: What are your job title and main responsibilities? If not applicable, what is your involvement with hydrography? [Open text answer]
Q6: How and why did you get into hydrographic surveying? [Open text answer]

A.1.2 Personal experiences and opinions

Q7: In your experience, what percentage of hydrographers that you have worked with have been women? (Rough estimate only) [0-10 %, 11-20 %, 21-30 %, 31-40 %, 41-50 %, 51 %+]
Q8: Do you believe it is important for there to be a focus on increasing the number of women in hydrography? [Yes, No]
Q9: On a scale of 1 to 5, 1 being not at all important and 5 being extremely important, how important do you think it is to have gender diversity in the workplace? [1. Not at all important, 2. Slightly important, 3. Moderately important, 4. Very important, 5. Extremely important]
Q10. Please explain your answer to question 9.
Q11. The International Hydrographic Organization (IHO) states that only 25 % of people qualified in hydrography are women. Why do you think this is?
Q12. What do you think are the current barriers for women in hydrography? (Select as many as you want) [Age, Safety, Workplace sexism, Access to appropriate facilities, Time away from work for maternity leave/childcare, Having to work away from home and family for extended periods of time, Cultural factors, Not enough information at school/university about hydrography in general, Not enough information at school/university about females in hydrography, Not enough public examples of other females working on the job, Other (Please explain).
Q13. What changes do you think could be made/what do you think could be done to help increase the number of women in hydrography? [Open text answer]
Q14. Would you like to see more women in hydrograph? [Yes, No]
Q15. Please explain your answer to question 14.
Q16. In your opinion, do you think you work in a diverse work environment in terms of gender? [Yes, No]
Q17. In your opinion, do you think you work in a diverse work environment in terms of other factors such as ethnicity or disability? [Yes, No]
Q18. Have you ever been discriminated against at work, or witnessed someone else be discriminated against? [Yes, No]
Q19. <Conditional question based on Q18 answer> In the previous question, you said you have been discriminated against at work, or witnessed someone else be discriminated against. If you feel comfortable, please describe your experience [Open text answer]

A.1.3 Your experience as a female

If you are a female, here are some additional questions for you to answer. These questions are optional, but your experiences and thoughts are greatly valued for this research.

If you are not a female or do not wish to answer these questions, you can click the next arrow to skip to the last questions of the survey.

Q20 What has your experience as a woman working in hydrography been? [Open text answer]

Q21 What have you found challenging about being a woman in hydrography? [Open text answer]

Q22 How have you overcome or worked through those challenges? [Open text answer]

Q23 What would you like to see change in the workplace to be able to help improve the experience of others? [Open text answer]

Q24 As a woman in hydrography have you ever felt unsafe at work? [Yes, No]

Q25. <Conditional question based on Q24 answer> In the previous question, you said that as a woman in hydrography, you have felt unsafe at work. If you feel comfortable, please describe your experience. [Open text answer]

A.1.4 Final questions

Q26 If you have any other comments, experiences, or thoughts on this topic that you would like to share, please write these below.

Please provide your contact details if you are interested in being available for future questioning.

A.2 Questionnaire for hydrographic employers

Q1. What is your gender? [Options: Male, Female, Non-binary / Third gender, Prefer not to say]

Q2. What is your title or position in your organisation? [Surveyor, Party Chief, Project Manager, CEO / Managing Director, Other (Please specify)

Q3. What is the current number of hydrography or hydrography related employees at your workplace? [0, 1-5, 6-10, 11-15, 16-20, 21-30, 31-50, 51+]

Q4. How many surveyors are at your workplace? [Text answer for: Male, Female, Non binary / Third gender]

Q5. Do you recruit and employ people with diversity (not just gender specifically) in mind? [Yes, No]

Q6. As an employer do you work to create a more diverse workspace? [Yes, No]

Q7. What plans, initiatives or strategies help to achieve a more diverse workplace? [Open text answer]

Please provide your contact details if you are interested in being available for future questioning.

Authors' biographies

Emily Harrex

Emily Harrex is a Hydrographic Surveyor at Reach Subsea. She graduated from the University of Otago in 2023 with a Bachelor of Surveying, where she completed her final-year research project Breaking Waves: A Snapshot of Women in Hydrography. Since graduating, she has worked offshore in Europe and Australia in the offshore energy industry, and in support of nautical charting efforts.

Emily Tidey

Emily Tidey is a Senior Lecturer in the School of Surveying at the University of Otago. She has a MSc with Distinction in Hydrography from the Cat A programme at the University of Plymouth and has worked internationally as an Offshore Hydrographic Surveyor for Fugro. Today, she teaches undergraduate students hydrographic surveying and land survey methods, and researches the intersection of hydrography with studies in the marine environment. She is interested in underwater mapping, including the use of low-cost GNSS and multi-frequency multibeam systems.

https://doi.org/10.58440/ihr-31-1-a04

PEER-REVIEWED ARTICLE

Performance of "Desktop in the Cloud" processing software deployment

Authors

Brian R. Calder[1] and Brian Miles[1]

Abstract

Deploying desktop hydrographic software in the cloud as virtual PCs has been suggested as a bridging technology to fully cloud-aware processing solutions. We investigate the processing performance of such a system, examining different compute resources and storage options in a variety of operations, with an on-premises server as control. Our results demonstrate that all "desktop in the cloud" (DitC) deployments are slower than the control. A software requirement for a tightly integrated GPU can also significantly increase costs. These observations suggest that while feasible, this form of DitC is a sub-optimal model for implementing a cloud-based hydrographic data processing system.

Keywords

bathymetry · processing performance · cloud-based bathymetric processing · CUBE · Desktop in the Cloud

Resumé

Le déploiement de logiciels hydrographiques de bureau dans le cloud sous forme de PC virtuels a été suggéré comme une technologie de transition vers des solutions de traitement entièrement compatibles avec le cloud. Nous étudions les performances de traitement d'un tel système, en examinant différentes ressources de calcul et options de stockage dans diverses opérations, avec un serveur sur site comme contrôle. Nos résultats démontrent que tous les déploiements de « bureau dans le cloud » (DitC) sont plus lents que le contrôle. L'exigence logicielle d'un GPU parfaitement intégré peut également augmenter considérablement les coûts. Ces observations suggèrent que, bien que réalisable, cette forme de DitC n'est pas un modèle optimal pour la mise en œuvre d'un système de traitement de données hydrographiques basé sur le cloud.

Resumen

Se ha sugerido el despliegue de software hidrográfico de escritorio en la nube como PC virtuales como tecnología puente hacia soluciones de procesamiento totalmente en la nube. Investigamos el rendimiento de procesamiento de un sistema de este tipo, examinando diferentes recursos informáticos y opciones de almacenamiento en una variedad de operaciones, con un servidor local como control. Nuestros resultados demuestran que todos los despliegues de "escritorio en la nube" (DitC) son más lentas que el control. El requisito de software para una GPU estrechamente integrada también puede aumentar significativamente los costes. Estas observaciones sugieren que, aunque es factible, esta forma de DitC es un modelo subóptimo para implementar un sistema de procesamiento de datos hidrográficos basado en la nube.

✉ Brian R. Calder · brc@ccom.unh.edu

1 University of New Hampshire, Center for Coastal and Ocean Mapping, Durham, NH, U.S.A

 https://doi.org/10.58440/ihr-31-1-a03

1 Introduction

There are, potentially, significant benefits to staging and processing hydrographic data using cloud computing resources (defined as: computation, storage, networking, and related compute infrastructure located in many geographic locations and owned and operated by a third party that sells access to this infrastructure for a particular period of time). Assuming that the data can be delivered to the cloud efficiently (a process that is becoming increasingly possible at reasonable cost with the advent of services such as Starlink[1] and OneWeb[2] with marine support), the cloud offers essentially infinite storage and processing capacity (limited primarily by ability to pay), and especially scalability of compute, with appropriately adapted algorithms. Applied appropriately, these characteristics could provide an alternative processing modality for high-density hydrographic data with potential benefits such as better data discovery, easier data management, and faster processing due to the inherently distributed and networked nature of cloud-based systems. Performance of data processing is still a fundamental problem for modern hydrography, and is limited by current desktop-focused software, especially in assuming a fixed hardware model, in contrast to the cloud.

The cloud is, however, a very different environment from traditional desktop computing, and has both different economics and attendant design trade-offs. For example, data ingress is typically free, but data egress is usually not, and therefore there is a significant driver for processing to follow the data into the cloud; the processing must then adapt to the distinctly different compute environment within the cloud if it is to be successful, efficient, or (ideally) both. (The cloud, for example, provides fine-tuned compute resources from a very wide palette of options, separation of compute from graphics and storage, virtual networks, and the option for resilience by design and massively parallel compute.) It is therefore not obvious that current generation non-distributed (i.e., running on a single workstation or server) desktop hydrographic data processing software is well adapted to the cloud, having been designed for a more conventional desktop computing environment with fast locally attached storage, integrated high-performance graphics resources, and exclusive control over data.

Getting data into the cloud is relatively simple, and well understood, and is therefore not treated here. One proposed means to process those data in the cloud is to take current generation hydrographic software and simply set up a "virtual PC" in the cloud ("Desktop in the Cloud", DitC). Most cloud providers allow for either a managed virtual PC (e.g., in Amazon Web Services[3] (AWS), WorkSpaces[4]) or a bare server which can be configured to the user's preference (e.g., in AWS, an Elastic Cloud Compute[5] (EC2) instance). A variety of storage systems can also be configured from object storage (e.g., AWS Simple Storage Service[6], S3), to file-level storage (e.g., AWS Elastic File Store[7] (EFS) or FSx for Windows), or block-level storage (e.g., AWS Elastic Block Store[8], EBS), along with a variety of more specialized systems such as Lustre (Schwan, 2003), a scalable, distributed, high performance file system, typically used for high-performance computing. There are therefore many different combinations of storage and compute that can be used to configure a DitC system, and the trade-offs can be distinctly different in the cloud than on the desktop, primarily because the resources are usually shared so that someone else's use patterns can affect the performance that can be achieved.

We therefore propose here an experiment to gather real-world data for the performance of DitC systems using current generation hydrographic data processing software and cloud services. This focuses on the early-stage compute required for data processing, including data conversion, time-series processing (e.g., motion compensation, TPU estimation), and grid construction. Using AWS as a test base for convenience (all major cloud vendors have analogous compute, storage, and networking offerings), we detail two separate configurations of compute (one managed, one bare), and four different types of storage, using a real-world dataset from NOAA's Ocean Exploration program for test. In addition, we consider an on-premises compute solution as a control, except that we use a rack-mount server and remote storage (in three different configurations) to match as well as possible the conditions in the cloud, and therefore attempt to illustrate the difference that control over resource contention (locally) provides to performance. In addition, these experiments allowed us to estimate total costs to process the test data, and therefore gain some insight into the economics of DitC processing.

2 Methods

Although many cloud providers exist, to reduce the complexity of comparison and without prejudice

[1] https://www.starlink.com (accessed 24 February 2025).

[2] https://oneweb.net (accessed 24 February 2025).

[3] https://aws.amazon.com/ (accessed 24 February 2025).

[4] https://aws.amazon.com/workspaces-family/ (accessed 24 February 2025).

[5] https://aws.amazon.com/ec2/ (accessed 24 February 2025).

[6] https:/aws.amazon.com/s3/ (accessed 24 February 2025).

[7] https://aws.amazon.com/efs/ (accessed 24 February 2025).

[8] https://aws.amazon.com/ebs/ (accessed 24 February 2025).

Table 1 Configuration for compute resources used in the experiment.

Category	AWS Workspaces	AWS EC2	On premises control
Instance name	Graphics Instance	G4ad.2xlarge	N/A
CPU	8 vCPUs	8 vCPU AMD EPYC 7R32	24 core[2] AMD Threadripper 3960x
GPU	Unspecified[1]	AMD Radeon Pro V520 MxGPU	2x NVidia RTX 3080
Main memory	16 GB	32 GB	128 GB
GPU memory	4 GB	8 GB	8 GB
Local storage	100 GB[3]	300 GB NVMe	1 TB PCIe NVMe
Network	10 Gb/s	10 Gb/s	2x10 Gb/s[4]

Notes to the table:

1. The GPU being used is not specified in the AWS documentation, and may not be consistent.
2. Each core supports two thread execution units.
3. The WorkSpaces instance provides a 100 GB disc partition for the operating system, and a second 100 GB partition for data. The connection technology is not specified but is likely EBS.
4. The two network interfaces are bonded for performance and are connected directly to the Storage Area Network (a NetApp FAS2650) in the same server room as the computer.

we select here Amazon Web Services (AWS) as the host platform for the experiments. In the following, all resources, compute and storage, were deployed in AWS Availability Zone[9] us-east-2c to avoid cross-zone transfers (which can incur performance penalties and increase costs). The experiment conducted here consists of multiple replicates of a given set of computing tasks (Section 2.4) associated with hydrographic data processing, applied to a series of combinations of different compute resources (Section 2.1) and storage technologies (Section 2.2). The same dataset (Section 2.3) and processing software (Section 2.5) were used throughout. To mitigate caching effects, and for consistency, a standard procedure (Section 2.6) was used in each instance.

2.1 Compute resources

The broad classes of computation available are a hosted workstation (AWS WorkSpaces), and a fully configurable server (AWS EC2). In each case, a system with configuration typical for desktop processing workstations was selected, including a dedicated GPU, which was found to be required for the software used for processing. AWS accounts did not, at the time of the experiment, generally provide the ability to turn on GPU instances due to limited availability. A special request was made to allow for a single 8 vCPU instance with attached GPU to be turned on for these experiments. An on-premises control was established using a rack-mounted

Table 2 Storage configurations by compute resource used during the experiment.

Category	AWS Workspaces	AWS EC2	On premises Control
File storage	FSx for Windows[1]/SSD	FSx for Windows/SSD	SMB[2]
File storage	FSx for Windows/HDD	FSx for Windows/HDD	N/A[3]
Block storage	N/A[4]	EBS GP3[5] SSD	iSCSI SSD
Block storage	N/A	EBS IO2[6] SSD	iSCSI HDD
Block storage	N/A	EBS ST1[7] HDD	N/A
Local	Unknown (prob. EBS)[8]	N/A	NVMe

Notes to the table:

1. FSx for Windows is a Windows-based file server providing file-level services for Windows clients using Microsoft-specific drivers and services (i.e., SMB). This is recommended by AWS for Windows clients over the EFS service (which uses NFS4 to serve the data).
2. Server Message Block, a Microsoft protocol used for a number of purposes, including file sharing and data transport. This is supported natively by the SAN filer heads.
3. The on-premises control environment does not use spinning hard disc drives for file-level storage.
4. The two network interfaces are bonded for performance and are connected directly to the Storage Area Network (a NetApp FAS2650) in the same server room as the computer.
5. EBS GP3 is a storage technology that is balanced between I/O performance and bandwidth.
6. EBS IO2 is a storage technology that is biased towards I/O performance (i.e., a guaranteed number of operations per second).
7. EBS ST1 is a legacy technology using spinning hard discs rather than solid-state discs; it is dramatically less expensive than SSD-based options.
8. The connection technology is not clear; note (see 4 above) that user-supplied EBS volumes cannot be mounted in WorkSpaces.

[9] https://aws.amazon.com/about-aws/global-infrastructure/regions_az/ (accessed 24 February 2025).

https://doi.org/10.58440/ihr-31-1-a03

physical server. This provides a proxy to the cloud environment so that the comparison is closer than would be obtained through a true desktop machine. The details of the configurations are given in Table 1.

2.2 Storage resources

Cloud storage is available in at least four basic classes: object store (S3), file-level store (EFS, or FSx for Windows), block-level store (EBS), and locally attached storage (typically NVMe discs). Within these broad classes, there are often different service guarantees (e.g., guaranteed number of I/O operations per second, bandwidth, latency, etc.). For the experiment here, five cloud technologies were selected, and three on-premises configurations. Default parameters, where options were available, were used. On-premises storage was provided through a network connection to the Storage Area Network (SAN) controller[10] in the same server room as the computer, on a dedicated network. Table 2 provides the details for the options by compute resource (not all storage types are available on each compute resource).

2.3 Dataset

A dataset was provided by NOAA's Ocean Exploration program, collected by the NOAA Ship Okeanos Explorer. EX2203 (Hoy et al., 2022), Fig. 1, was an early expedition in 2022 that contains data from shoreline to the Puerto Rico trench (approx. 6,500 m depth). For simplicity, 228 of the total 577 files were used to focus on the area around Puerto Rico, rather than the very long transit to the area. The total dataset is approximately 75 GB of Kongsberg Discovery KMALL files (Kongsberg, 2024). This data is publicly available through the NOAA National Centers for Environmental Information[11] bathymetric data portal.

2.4 Computational tasks

Three primary compute tasks were used, simulating the early-stage non-interactive processing of multibeam echosounder (MBES) data. First, data in manufacturer's format was converted into the processing software's internal data format. To assess network and storage contention, three models of data layout were considered:

1. "Read". The source data is held on the indicated external storage media and written to the internal disc on the compute resource.
2. "Write". The source data is held on the internal disc on the compute resource and written to the indicated external storage media.
3. "Roundtrip". The source data is held on, and written to, the indicated external storage media.

Second, first-stage data processing was conducted. This typically includes all time-series adjustments and computations for the data, for example applying

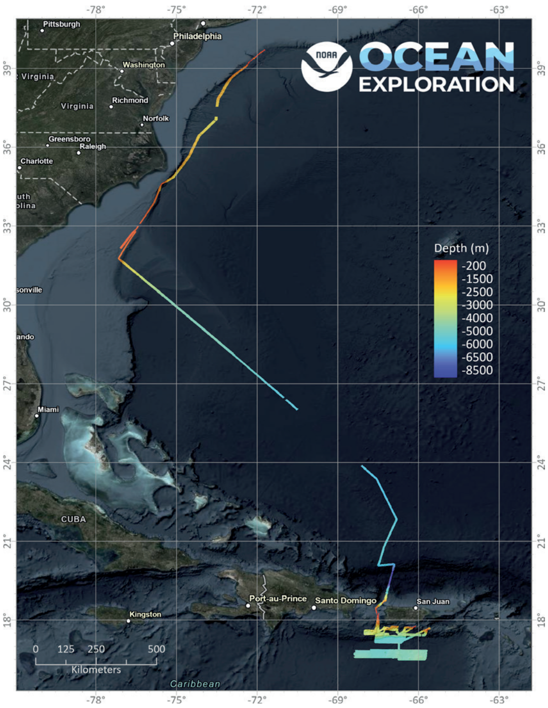

Fig. 1 Example dataset, EX2203, from NOAA's Ocean Exploration program. The last 228 files around the Puerto Rico trench were used for performance testing. Figure courtesy of Shannon Hoy, NOAA Ocean Exploration.

motion effects and static offsets (if not done by the sonar in real-time), adding corrected positioning information, computing uncertainties, etc. In each case, the manufacturer's data was converted onto the indicated external storage, and the software's project directory was placed alongside.

Finally, grid construction was conducted. To test the differences in data access patterns and computation load, two methods were used: a simple weighted average grid, and the CUBE data processing algorithm (Calder & Mayer, 2003). In all instances, the source data and product files were stored on the indicated external media. For the CUBE algorithm, the default configuration ("Deep") in the processing software was used, except that the hypothesis resolution method was set to "Number of Soundings", which should minimize computational load and storage access.

2.5 Software

Given availability and experience, but without prejudice, QPS Qimera[12] was selected for processing (version 2.4.9). Although Qimera has a Linux version, the Windows binary was used since this is more typical in the desktop environment (Linux-based cloud resources are cheaper and might otherwise be preferred, see Section 4). The software was installed separately on each compute resource used and licensed through a stand-alone (virtual machine) license for the cloud resources, and via a license

[10] A NetApp FAS2650 high-availability SAN system (i.e., two cross-connected filer heads for redundancy) was used with 7,200 rpm SAS-attached SATA hard discs for bulk storage with NetApp FlashCache (SSD) front-end cache; 12 GB SAS-attached SSDs were used for pure SSD storage.

[11] https://www.ncei.noaa.gov/access/metadata/landing-page/bin/iso?id=gov.noaa.ngdc:G01034 (accessed 24 February 2025).

[12] https://qps.nl/qimera/ (accessed 24 February 2025).

server in the on-premises environment. Care was taken throughout to ensure that the license was activated immediately before and deactivated immediately after each computation event, since shutting down a cloud compute resource and restarting it results in a different hardware configuration and invalidates the license (this difficulty is addressed in Section 4).

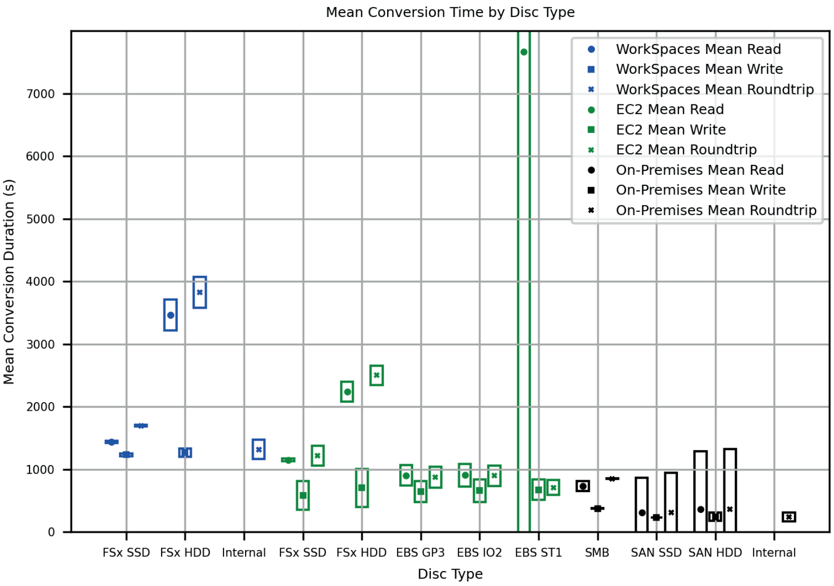

Fig. 2 Data conversion performance (from manufacturer’s format to internal processing format) for WorkSpaces managed virtual PC (blue), EC2 server (green), and on-premises control (black), for each of the 12 compute/storage combinations, and read/write/roundtrip data management plans. Ten replicates of each experiment were run to generate 95 % CI limits, which are shown at rectangles (of arbitrary width) about the mean.

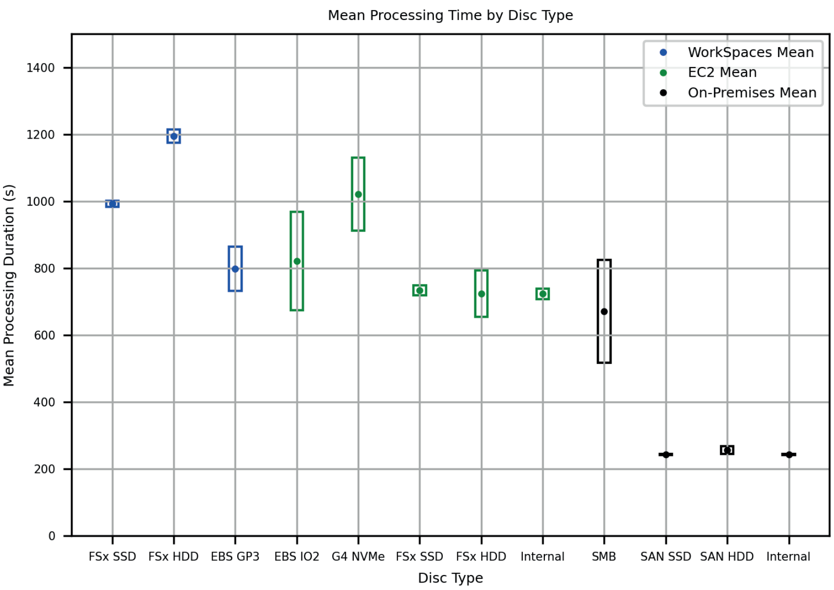

Fig. 3 Data processing performance (time series processing) for WorkSpaces managed virtual PC (blue), EC2 server (green), and on-premises control (black) for each of the 12 compute/storage combinations. Ten replicates of each experiment were run to generate 95 % CI limits, which are shown at rectangles (of arbitrary width) about the mean.

2.6 Experimental procedure

The Cartesian outer product of the compute resources, storage resources, and experiments in Sections 2.1, 2.2, and 2.3 result in a total of 68 configurations. Each configuration was tested ten times to provide some statistical basis for comparison. In each test, the processing log timestamps from Qimera were used to assess elapsed “wall clock” time for the process and were recorded to the nearest millisecond.

For each compute resource, a new installation of Qimera was used. For conversion, the test data were staged on the appropriate storage resource, and then converted into ten separate projects, to minimize cache effects.

For processing, the test data were copied to the storage resource to be used for processing and converted once into a blank Qimera project. Qimera was completely stopped to ensure that the project was closed, after which it was renamed “EX2203_Unprocessed”. This was subsequently copied ten times with distinct names (“EX2203_01” to “EX2203_10”). Each project was then processed in turn.

Finally, for grid construction, each of the ten processed projects was opened in Qimera, and all 228 source files were selected before creating a 150 m resolution Dynamic Grid using the weighted average algorithm with default parameters. A 150 m Dynamic Grid was then constructed using the CUBE algorithm as outlined in Section 2.3.

For each configuration, the arithmetic mean, standard deviation, median, and 95 % confidence interval (based on a Student’s t-statistic (Kendal et al., 1994, sec. 16.10) with $\upsilon = 9$ degrees of freedom) were computed from the times recorded.

3 Results

The results of the data conversion experiment are shown in Fig. 2, color-coded by computational resource, and organized by storage resource on the horizontal axis. The results of the “read”, “write”, and “round-trip” experiments are shown to the left, center, and right of the storage resource marking on the horizontal axis. Vertical boxes around the mean indicate the 95 % CI (note that this reflects the variability of the timings only, since timings cannot be negative).

The results demonstrate that there are significant differences in performance between the computational technologies, with the EC2 instances generally faster than the WorkSpaces instances, with local performance better than either. The storage technology also has a statistically significant role in overall performance for a given computational resource with solid-state drives generally being better, often by a factor of 2–3. The “write” performance (i.e., reading the raw file from local store and writing to the indicated storage technology) is generally better than either “read” or “round-trip” performance, perhaps indicating a more aggressive caching policy on write within the

https://doi.org/10.58440/ihr-31-1-a03

cloud. Somewhat surprisingly, the "round-trip" performance (i.e., reading and writing to the same external storage technology) is not heavily penalized in these tests. Standard advice from the software manufacturer is not to write and read from the same disc due to bandwidth limitations; in the cloud, this appears not to be a significant concern. Finally, the on-premises storage performance seems to suggest some form of read caching, since there is a significantly longer run on the first experiment, which then resolves more quickly for subsequent runs. This is not observed in the cloud-based experiments, most likely because the shared nature of the resources means that cache contents are not preserved between runs.

The results of the data processing experiment are shown in Fig. 3, color-coded by computational resource, and organized by storage resource on the horizontal axis. Vertical boxes around the mean indicate 95 % CI.

The general performance results are consistent with those of the data conversion step (Fig. 2), with the EC2 instance generally faster than the WorkSpaces instance, and the on-premises control faster than either. There is a performance penalty for spinning hard-disc storage for cloud-based systems (although not as much as for the data conversion task), but not for the on-premises system, and surprisingly the performance of all variants of EBS storage for EC2 show no consistent difference, suggesting that the usage pattern here does not match the "performance optimized" (IO2) EBS instance type, which is more expensive than the "general purpose" GP3 store; the similar performance of the "internal" (NVMe) disc on the EC2 instance suggests that it might also be implemented through an EBS mount. The on-premises performance, apart from when using SMB as the data transport, is much more consistent than cloud-based equivalents, most likely due to lower contention for the bandwidth and storage compute available on the local SAN. The SMB transport for on-premises compute is backed by the same SAN arrays and storage processors but is anomalous in performance. This is most likely due to poor interactions between the data access patterns from Qimera for this operation and the transport fabric (e.g., many small files are being accessed, so the overhead in negotiation for initial access overwhelms the protocol). This behavior also likely explains the relatively poorer performance in FSx storage in the cloud, which uses the same transport.

The results of the gridding comparison are shown in Fig. 4, color-coded by computational resource, and organized by storage resource on the horizontal axis. The results of the weighted average and CUBE processing are arranged to the left and right, respectively of the vertical mark for each storage resource. Vertical boxes around the mean indicate 95 % CI.

The results clearly indicate the performance penalty for mechanical (i.e., spinning hard-disc) storage, with performance approximately 4–5 times slower than

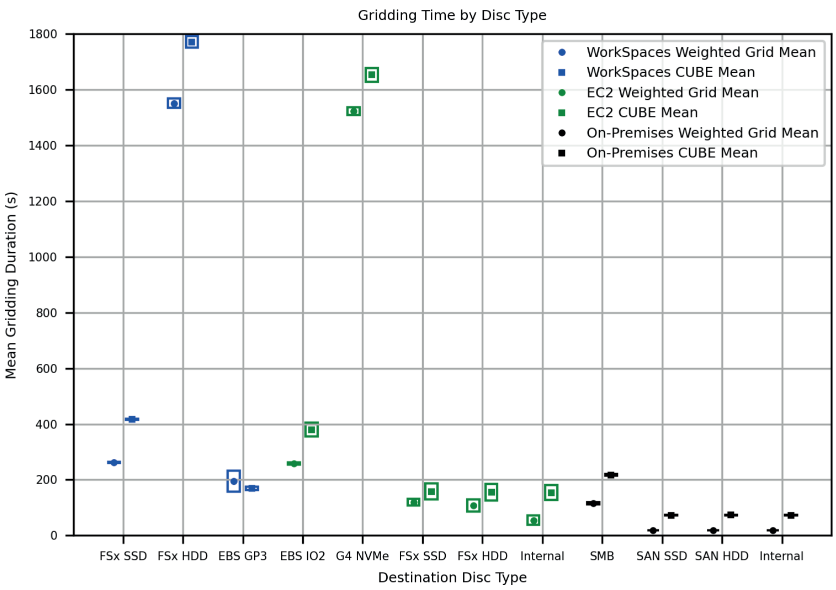

Fig. 4 Spatial processing performance (grid construction using simple weighted mean, or CUBE processing) for WorkSpaces managed virtual PC (blue), EC2 server (green), and on-premises control (black) for each of the 12 compute/storage combinations, and two different algorithms. Ten replicates of each experiment were run to generate 95% CI limits, which are shown at rectangles (of arbitrary width) about the mean.

for the solid-state storage on the same transport, dominating the compute costs. Since grid computation is something that is done frequently in many modern hydrographic data processing workflows, this is a significant concern for practical performance of the overall system. There is also a small performance effect by cloud compute resource, with the EC2 instance generally faster than the WorkSpaces; the on-premises performance is, however, significantly better (in the statistical sense), and much more consistent, likely due to lower resource contention. Finally, there is a clear performance penalty for use of SMB network filesystem both on-premises and in the cloud (i.e., using FSx-mounted storage). There is a trade-off between performance and ease of data management (e.g., to allow data to be shared between multiple simultaneous users) when considering the difference between SMB and EBS resources, to which we return in Section 4.

4 Discussion

The results here clearly demonstrate that there is a statistically significant difference in performance for desktop processing systems deployed in the cloud as a function of the compute resource used and the storage technology attached. In some cases, the difference can be of order 4–5 times slower. There are clear winners and losers. Spinning-disc storage, for example, generally induces a performance penalty, while EC2 compute instances have generally better performance for most compute tasks, potentially because it is possible to attached better (EBS) storage compared to the SMB-based storage used by WorkSpaces virtual desktop environments. The choice between solid-state storage technologies is less clear and may be due more to the transport fabric than the technology. For example, the different types of optimizations applied to EBS storage (e.g., general purpose GP3 relative to I/O optimized IO2) appear to have little influence on performance, but there is a statistically significant performance difference between the use of EBS storage (typically using something like iSCSI transport) and a managed service such as FSx for Windows (a Windows-based file server using SMB as transport).

There is a practical benefit to a file-based store (e.g., EFS or FSx for Windows), however, in that it can be simultaneously shared between users, while block-based store (e.g., EBS) can only be mounted to a single compute resource at any one time (although it can be moved between uses). For data management purposes, then, it might be beneficial to use FSx as primary storage, although the question of whether the continual performance penalty is an acceptable trade-off will be implementation dependent. (Note that the use of FSx here is nominally equivalent to a Windows file server holding data in a local network and sharing it to desktop workstations, a common hydrographic data processing practice. Although not covered by these results, it is likely that similar levels of performance penalty would be observed in this configuration.)

Although the results here argue against DitC as a cloud implementation strategy for hydrographic data processing on the basis of performance, they do allow for recommendations for technology selection if DitC is required. The best overall performance was observed with an EC2 instance (at least a g4ad.2xlarge in AWS terms, with a dedicated GPU) using GP3 EBS storage. If a managed solution is required, a WorkSpaces instance with graphics and FSx for Windows using SSD backing store would be recommended. Note, however, that there are additional requirements to use FSx, since the underlying managed Windows file server needs to have an Active Directory (AD) domain controller available to provide authentication services. This can be an existing domain controller if one exists, or a managed domain controller provided by AWS. This adds an IT management burden, and potentially significant additional costs.

Using cloud services changes the cost structure for data processing: instead of buying physical hardware (or provisioning virtual hardware), a one-time fixed/capital cost, the compute resources and storage are effectively rented, making them a variable/operational cost. Most cloud providers charge for compute by time, with some premium structure for performance of a given compute resource, and for storage by the byte with additional costs for provisioned bandwidth, input-output operations per second (IOPS), etc. It can, therefore, be difficult to estimate the actual costs for cloud services except *post facto* and even then, the costs will rapidly go out of date. We have therefore opted to consider only relative costs here, rather than absolute. Although we have not conducted a full accounting, we note that EC2 instances were less expensive than WorkSpaces (which incur a management cost and require an AD controller to be present), and FSx storage was more expensive than EBS due to both management overheads and licenses for Microsoft products, which is built into the pricing structure. For comparison, however, the estimated cost to hold data for a survey in the cloud for a nominal 90-day processing effort and provision processing resources for it is about the same as buying a new desktop PC, monitors, and storage for each survey, and archiving it at 90 days. Cloud services are not, necessarily, cheaper than desktop alternatives.

A component in this cost is the licensing model employed by current desktop software. Motivated by the model of licensing per seat on physical machines, the license is typically either tied to specific hardware, or is checked out from a separate server on the local network as required. In the cloud, neither model is ideal. Each time an instance is restarted it has equivalent but potentially physically distinct hardware associated, and therefore will invalidate any active license previously installed. The user is therefore left with two options: leave the instance running even when not in use, which incurs significant costs, or actively manage the licenses by deactivating and activating over each restart, which incurs significant management overhead and is inherently fragile. The alternative of running a license server continuously as part of the deployment also incurs computing costs (even though the license server can be very low powered), increases complexity, and is expensive unless amortized over many processing resources. Although the challenges of deploying hydrographic data processing software to the cloud are predominantly technical, the issue of a cloud-friendly licensing (and revenue) model should not be underestimated.

Similarly, the necessity for a tightly coupled CPU and GPU in the compute resource, a norm for desktop systems, in not ideal in the cloud. In the desktop environment, each computer can be expected to have a fast CPU, a dedicated GPU, and locally attached high-speed storage (e.g., a NVMe SSD); processing software can assume this will always be the case and therefore casually require GPU resources, even to boot. None of the processing done here requires GPU support, however, and therefore the assumption that a GPU will always be attached results in a requirement for very expensive and limited availability cloud compute resources with an attached GPU that is never actually used. In the cloud, it would be significantly better to separate out the GUI portion of the software from the computational portion and deploy these separately. This would allow optimization of resources, and therefore cost reduction.

One of the major advantages of the cloud

 https://doi.org/10.58440/ihr-31-1-a03

environment is flexibility (of compute, storage, networking, etc.) which is not a feature of the desktop environment, and therefore is generally not well utilized by desktop software. Modern processing software might be able to take advantage of multiple cores within a single processor, for example, or hyper-threading on a single core, but because the hardware is assumed static it cannot scale beyond the number of cores available (which is often quite limited in cloud systems, the expectation being that the system should scale to multiple communicating compute resources instead). Desktop software cannot, therefore, scale in the way allowed and encouraged by a cloud environment, and consequently achieves limited benefit from cloud deployment; hydrographic data processing tools must be recast as distributed systems (i.e., using algorithms and data structures designed to enable computation to be run on many dozens if not thousands of computation nodes in parallel) to take full advantage of the scalability potential of cloud computing infrastructure. Similarly, the pricing structure of cloud systems depends strongly on details of the hardware and software environment chosen. It is more expensive to use Intel or AMD hardware and Microsoft software, for example, than ARM hardware and Linux software. Unless software vendors allow for architectural and operating system flexibility, they are passing on unnecessary costs to end users that might be significant, making such limited solutions less competitive.

Supporting multiple operating systems and CPU architectures is not trivial, of course, but can be simplified by separating computation engines from user-facing GUIs as well as through the use of containerization technologies such as Docker[13] to package and distribute computation engines. In containerized deployments the entire computational environment required for a deployment is packaged into an image that can be launched on multiple compute resources as required (e.g., using a container orchestration system such as AWS Elastic Container Service[14], Elastic Kubernetes Service[15], or standalone Kubernetes[16]) to scale well and maintain guarantees of availability. For software vendors there might even be a benefit to providing a containerized deployment of their system in that it would avoid many configuration variabilities that cause difficulties with installation and operation of complex software systems.

Finally, we note that the cloud is a moving target in the sense that old compute resources are retired regularly with newer, more powerful services being brought online to replace them. Services are also regularly retired or replaced. This makes it a challenging environment in which to operate and means that the results provided here may only be a snapshot of the performance capabilities of DitC. It is expected, however, that there will always be limitations to the benefits possible, and that truly benefiting from the advantages of the cloud will require development of a cloud-native processing chain that takes advantage of modern techniques such as containerization, microservices, and dynamic scaling of compute and storage resources.

5 Conclusions

These experiments examine the concept of "Desktop in the Cloud", meaning the deployment of current generation non-distributed hydrographic processing software into a cloud environment, in this example Amazon Web Services, to provide remotely accessible computation for ocean mapping data. The evidence is that while this can work, it may not be either cost or time efficient compared to a desktop deployment and therefore, assuming a cloud data processing strategy is desired, it is likely not a good choice. There are also statistically and practically significant performance variations depending on the compute resources and storage technologies selected.

This work quantified the differences for three common tasks (converting data to processing format, initial time-series processing, and grid construction) and showed that computation time can be 4-5 times longer with inappropriate storage technology selection, and that some basic assumptions of desktop deployment (e.g., that you should not read source data, and write processed data, to the same disc) do not necessarily apply in the cloud.

The work also demonstrated limitations for DitC due to assumptions that are valid for the desktop but not for the cloud. Particularly, desktop licensing models are difficult, expensive, or both to support in the cloud, and an assumption of fixed hardware with tightly coupled GPU and storage require cloud-based resources that are poorly utilized by the software. The assumption of fixed hardware (valid for desktop but not for cloud) also intrinsically limits the scalability of computation with DitC, a key benefit of cloud-based deployment.

These results strongly suggest that while DitC is possible, the real benefit to cloud-based hydrographic data processing will only be achieved with specifically designed, cloud-native distributed algorithms and processing software.

Acknowledgements

The authors gratefully acknowledge the funding provided by NOAA Ocean Exploration Cooperative Institute (under the CloudMap program) and through grant NA20NOA4000196 (Continuation of the Joint Hydrographic Center) which supported this work. Use of particular services and service providers in

[13] https://www.docker.com (accessed 24 February 2025).

[14] https://aws.amazon.com/ecs/ (accessed 24 February 2025).

[15] https://aws.amazon.com/eks/ (accessed 24 February 2025).

[16] http://kubernetes.io/ (accessed 24 February 2025).

the course of this work does not represent endorsement on the part of the authors, University of New Hampshire, or NOAA.

References

Calder, B. R. and Mayer L. A. (2003). Automatic Processing of High-Rate, High-Density Multibeam Echosounder Data. *Geochem., Geophys., and Geosystems (G3)*, *4*(6). https://doi.org/10.1029/2002GC000486

Hoy, S., Peliks, M., Freitas, D., Gillespie, T., Wilkins, C., Hoel, P., Ferrante, C., Wu, L. Ruby, C. and Egan, K. (2024). Mapping Data Acquisition and Processing Summary Report. *EX-22-03: Puerto Rico Mapping and Deep-Sea Camera Demonstration (Mapping and Tech Demonstration)*. https://doi.org/10.25923/hczc-e213

Schwan, P. (2003). Lustre: Building a file system for 1000-node clusters, *Proc. 2003 Linux Symposium*.

Kongsberg (2024). *Kongsberg Discovery, EM datagrams on *.kmall format*. Kongsberg Document Number 410224. https://www.kongsbergdiscovery.online/sis/kmall/html/index.html (accessed 1 October 2024).

Kendall, M., Stuart, A. and Ord, J. K. (1994). Kendall's *Advanced Theory of Statistics* (6th ed, Vol. 1), Hodder Arnold, London.

Authors' biographies

Brian R. Calder

Brian R. Calder graduated MEng and PhD in Electrical and Electronic Engineering from Heriot-Watt University, Scotland in 1994 and 1997 respectively, and joined the Center for Coastal and Ocean Mapping and NOAA-UNH Joint Hydrographic Center at the University of New Hampshire in 2000, where he is currently a Research Processor and Associate Director. At CCOM his research interests have focused primarily on processing of bathymetric data for hydrographic applications, the assessment and use of uncertainty in hydrography, and systems for volunteer bathymetric data collection, processing, and use.

Brian Miles

Dr. Miles is trained as a software engineer and physical geographer. His hydrographic research focuses on distributed cloud processing of bathymetric data as well as the development and maintenance of standards-based, machine-readable data formats for the representation and validation of bathymetric datasets. His past research has focused on ecohydrology modeling in urbanized and forested watersheds; this work included developing tools to support reproducible ingest and transformation geospatial data, as well as model calibration and uncertainty estimation using HPC resources. He has current and prior experience in software engineering, Internet of Things, environmental monitoring, and geospatial data storage and analysis. As a software engineer, Dr. Miles is focused on translating research codes and algorithms into deployable software artifacts supported by robust documentation, automated testing, continuous integration, observability, fault tolerance, and scalability.

https://doi.org/10.58440/ihr-31-1-a03

PEER-REVIEWED ARTICLE

An empirical assessment of tabletop augmented reality interfaces for analytical hydrographic data use versus conventional desktop 3D visualization

Authors
Andre A. Araujo[1,2] and Nicholas Hedley[1]

Abstract

This paper explores hydrographic practitioners' ability to perceive the spatial structure and relationships of 3D bathymetric visualizations in tabletop augmented reality (AR) interfaces versus similar 3D data visualized using conventional desktop computer monitors. A two-phased experiment was carried out to compare the performance of two groups of participants, where both used a tabletop AR interface and a desktop monitor to view and perform a set of perceptual and interpretation tasks with identical visualizations of bathymetric datasets. The findings of this intentionally exploratory study are that the AR interface has the potential to offer advantages regarding spatial perception and depth of understanding.

Keywords
bathymetric data · seafloor data visualization · visualization interfaces · augmented reality

Resumé

Cet article étudie la capacité des professionnels de l'hydrographie à percevoir la structure spatiale et le rapport entre les visualisations bathymétriques en 3D dans les interfaces de réalité virtuelle et augmentée (RA) par rapport à des données tridimensionnelles similaires, visualisées sur des écrans d'ordinateurs classiques. Une expérience en deux phases a été menée afin de comparer les performances de deux groupes de participants, qui ont tous deux utilisé une interface de réalité virtuelle augmentée et un moniteur fixe, pour visualiser et effectuer une série de tâches de perception et d'interprétation avec les même affichages de jeux de données bathymétriques. Les résultats de cette étude menée à titre expérimental, montrent que l'interface de réalité virtuelle augmentée peut offrir des avantages en termes de perception spatiale et de compréhension.

✉ Andre A. Araujo · andre_araujo@sfu.ca
[1] Simon Fraser University, Department of Geography, Spatial Interface Research Lab, Burnaby, BC V5A 1S6, Canada
[2] Marinha do Brasil, Directorate of Hydrography and Navigation, Brazilian Navy Hydrographic Centre, Niterói-RJ, CEP 24048-900, Brazil

 https://doi.org/10.58440/ihr-31-1-a05

Resumen

Este artículo explora la capacidad de los profesionales hidrográficos de percibir la estructura espacial y relaciones de las visualizaciones batimétricas 3D en interfaces de realidad aumentada (AR) de sobremesa frente a datos 3D similares visualizados mediante monitores de ordenador de sobremesa convencionales. Se llevó a cabo un experimento en dos fases para comparar el rendimiento de dos grupos de participantes, en el que ambos utilizaron una interfaz de AR de sobremesa y un monitor de sobremesa para ver y realizar un conjunto de tareas de percepción e interpretación con visualizaciones idénticas de conjuntos de datos batimétricos. Las conclusiones de este estudio intencionadamente exploratorio son que la interfaz de AR tiene el potencial de ofrecer ventajas en percepción espacial y profundidad de comprensión.

1 Introduction

Hydrography is experiencing one of the most agitated periods in its history, where the demand for more accurate and fast-updated bathymetric data is growing (Pe'eri & Dyer, 2018; Kastrisios et al., 2023). Driven by ambitious projects such as the "Nippon Foundation – GEBCO Seabed 2030 Project" (Mayer et al., 2018), which has mapped about 20 % of the world's ocean floor and seeks to complete the whole ocean mapping by the year 2030, multiple technologies have been developed and incorporated into hydrographic surveys (Ferreira et al., 2022), increasing the level of complexity and workload. At the same time, the hydrographic data production systems have faced the challenge of migrating to new international standards, the IHO S-100 Universal Hydrographic Data Model, that will require straightforward access to high-quality digital geospatial information to support marine activities (Ponce, 2019; Jonas, 2021). As new sensor technologies and data outputs have emerged, so too have a range of spatial interface technologies and research. Technologies, such as any degree of mixed reality (Milgram & Kishino, 1994) offer significant potential to provide users of geospatial data with new ways to perceive, explore, communicate, and experience underwater environments through interface technologies that can both immerse us in data and, through them, immerse us in the spaces they represent (Hedley, 2017; Speicher et al., 2019; Rokhsaritalemi et al., 2020, Hedley & Lochhead, 2020, Çöltekin et al., 2020, Lochhead & Hedley, 2021).

1.1 Background

Many national governments are signatories to the International Maritime Organization's International Convention for the Safety of Life at Sea (SOLAS; IMO, 1974), reflecting their commitment to ensuring maritime safety through the publication of nautical charts, navigational publications, and supporting services. Therefore, each national Hydrographic Office (HO), or national hydrographic service, is responsible for producing and updating their countries' official nautical documents and establishing policies governing this work (Maia et al., 2017). These efforts are supported by data from hydrographic surveys conducted by government institutions and authorized researchers operating within national jurisdictional waters. The data collected are typically stored in centralized databases, serving as the foundation for generating and maintaining nautical products (National Centers for Environmental Information, 2024).

Each HO has policies and directives on evaluating and using bathymetric data (Maia, Florentino and Pimentel, 2017). Some choose to use automatic systems and algorithms (Calder & Mayer, 2003; Pe'eri & Dyer, 2018; Wölfl et al., 2019), but it is common practice for experienced hydrographic analysts to verify it in some offices (Le Deunf et al., 2020). Visualizing the data is one of the main ways the analyst verifies, manipulating the data set through peripherals such as a keyboard and mouse and using computer screens to display the images. The verification predominately consists of repetitive manual tasks seeking to identify failures in acquiring raw data and processing errors that alter the acquired bathymetry (Masetti et al., 2022). During verification, the analyst uses one or more specific software for bathymetric data processing, ordinarily available on the market (Value Market Research, 2021). These programs, developed by companies based on the guidelines published by the International Hydrographic Organization (IHO), offer various data verification tools (Langhorst, 2022). This way, traditional 2D planar media was consolidated, adding pseudo-3D visualization features and using computer monitors and presentation room projector screens.

If, a few decades ago, the methods of acquiring and processing bathymetric data were limited to a few options, in recent years, hydrographic practices, led by a worldwide effort to develop systems, sensors, and alternative techniques for depth measurement, have increasingly seen the emergence and expansion of automated and autonomous technologies (Smith Menandro & Cardoso Bastos, 2020; Masetti et al., 2022). This growth in the production of bathymetric data has led hydrographic surveys to generate enormous amounts of information from multiple sources (Holland et al., 2016; Jonas, 2023), which requires adequate processing, analyzing, and managing (Wlodarczyk-Sielicka & Blaszczak-Bak, 2020; Le Deunf et al., 2023). Software for acquiring, processing, and managing bathymetric data has developed significantly to adapt to the reality of activities carried out in hydrography, seeking to respond to current demands and bringing efficiency (Langhorst, 2022).

In parallel to this evolving landscape of hydrographic sensors and data production, new spatial interface technologies such as augmented reality (AR) and mixed reality (MR) have begun to attract attention for their potential to allow inherently 3D/4D data to be viewed and experienced in 3D and 4D. Thus, holding the potential to transform how hydrographic data is perceived and interpreted. These immersive technologies offer novel ways to visualize complex datasets by presenting information in three dimensions and allowing users to interact with data spatially. Their integration into hydrographic workflows may offer advantages in terms of spatial awareness, depth perception, and task performance, particularly in contrast to conventional 2D desktop interfaces.

Interface technologies are essential as they act as the conduit through which users interact with and interpret complex data visualizations. These technologies determine how information is displayed and influence user engagement, comprehension, and decision-making processes. Empirical studies on their potential influence are crucial because they provide evidence-based insights into how different interface designs affect user perception, cognitive load, and overall usability. By understanding these impacts, designers can create more effective and intuitive visualizations that serve diverse user needs, ultimately enhancing the ability to derive meaningful insights from data (Few, 2024).

Specifically, in bathymetric data analysis, interface technologies are fundamental in enabling the effective visualization and interpretation of complex underwater terrain data. High-resolution bathymetric maps, essential for marine navigation, environmental monitoring, and resource management applications, rely heavily on sophisticated visualization tools. These tools must present data in an accessible and intuitive manner, allowing users to explore and manipulate the data effectively.

Research has shown that advanced data acquisition methods, such as single-beam and multi-beam echo sounders (SBES), significantly enhance the accuracy and efficiency of underwater mapping. These technologies produce detailed and reliable bathymetric data, but their complexity necessitates robust interface technologies to manage and interpret the information accurately. For instance, multi-beam echo sounders (MBES) are favored for their ability to cover large, high-resolution areas. However, they require sophisticated interfaces to process and visualize the vast data collected (Araujo & Hedley, 2023; Li et al., 2023).

Empirical studies on these technologies are crucial to understanding their impact on user perception and usability. Effective interface design can reduce cognitive load and improve the accuracy of data interpretation, which is particularly important in fields that rely on precise and timely information. By continually evaluating and refining these technologies based on empirical evidence, we can enhance the overall effectiveness of bathymetric data analysis, ensuring that users can make well-informed decisions.

While different methods and interface options exist for viewing bathymetric data, the hydrography community continues to follow the 2D paradigm in which displayed marine information resembles traditional paper nautical charts, even in the most recent chart-plotters. However, there has been growing discussion around the benefits of presenting hydrographic information in more immersive and familiar forms, similar to those found in video games, through 3D visualization or AR-based environments (Hedley and Lochhead, 2020, Lochhead and Hedley, 2021, Jonas, 2023). The emergence and development of new data products and new spatial interface technologies may significantly support the ability of a range of operational stakeholders to perceive and interpret multidimensional bathymetric data. Therefore, there is a need to investigate the potential of emerging tools and interfaces to improve bathymetric data visualization.

1.2 Research objectives and questions

This exploratory research aims to investigate and quantify potential changes in perception and task performance when transitioning the visualization of raw bathymetric data from conventional interfaces to tabletop AR interfaces. This study seeks to uncover underlying patterns and relationships by employing exploratory research methods. It specifically addresses three overarching questions. First, it investigates whether perceptual outcomes differ when users visualize data in AR versus conventional interfaces, particularly regarding users' abilities to identify spatial features and interpret spatial relationships within hydrographic datasets. Second, it assesses task performance by comparing accuracy and speed across both platforms. Third, the study explores the suitability of AR interfaces for daily hydrographic data analysis, identifying affordances users perceive as beneficial and pinpointing characteristics that users find challenging or detrimental for effective data visualization and operational integration. Ultimately, this research aims to identify critical factors and variables influencing user experience and performance, providing a foundation for subsequent research to pursue more targeted studies of contributing factors in the geometry and dimensionality of 3D/4D hydrographic and bathymetric data, interface parameters, visualization features, individual differences, and venue characteristics. Our work aims to be a catalyst for these future studies and contributing to the development of improved visualization techniques for bathymetric data interpretation.

https://doi.org/10.58440/ihr-31-1-a05

2 Related work

In recent decades, the hydrographic community has successfully migrated its nautical products from analog to electronic models, producing them consistently and standardized based on the standards published by the IHO (Ponce, 2019). The databases could also add object and attribute data to the traditional bathymetric data, stimulating the use of Geographic Information Systems (GIS) as part of the hydrographers' toolset (Lekkerkerk, 2018).

However, these digital variants have mainly followed the printed models, maintaining that the presentation is two-dimensional (Jonas, 2023). In other words, the entire creation and later use of nautical charts continue to be essentially visualized in 2D displays, occasionally employing aids of perspective renderings of data on screens like pseudo-3D representation. Over time, the influence and limitations of the IHO standards, especially the IHO S-57 Transfer Standard for Digital Hydrographic Data, may be one of the reasons why different methods and interface options for viewing bathymetric data, such as new 3D interactive visualization interfaces, were not being exploited and taken advantage of (Alexander et al., 2007; Ward et al., 2008; Duan et al., 2021).

Since hydrographic data survey technologies inherently generate 3D data (Bleisch, 2012), tools that provide 3D data processing and 3D data visualization are vital to support interpretation. Modern data processing software has offered features that allow the visualization of a set of bathymetric data from different perspectives, taking advantage of interactive features, where the 3D impression is received through rotation of the model on the computer screen (Lütjens et al., 2019), contributing to the perception and understanding of spatial information.

2.1 Augmented reality

AR is a technology in which information (virtual objects) is superimposed onto the real world directly in front of observers (Milgram & Kishino, 1994; Azuma, 1997). Essentially, AR 'augments' views of reality by integrating virtual computer-generated content into the user's view of their physical environment. This allows users to interact with digital elements as if they were part of the real world, providing an enriched and interactive experience (Azuma, 1997; Hedley, 2017). AR interfaces are made possible by three main ingredients: tracking of real-world surroundings; registration of virtual objects to the real world - when a virtual piece of furniture in an AR application is precisely positioned and aligned within a user's physical room, matching its real-world location, orientation, and scale; and rendering virtual content into views of the real world - made visible by a range of display technologies (Hedley, 2017). Tracking is especially crucial for 3-D applications that involve user interaction with virtual spaces, as it provides the system with real-time spatial information about the user's position and orientation. Accurate and low-latency tracking ensures that virtual content remains stably aligned with the real world, preserving immersion and usability (Billinghurst et al., 2015). In AR, tracking determines the positions of real-world objects, allowing digital objects to be registered to them. This can be done using fiducial markers and computer vision software, where unique patterns are recognized, and their orientation and position relative to the camera's viewpoint are calculated. This enables the AR software to render virtual objects at the correct location and alignment, a method commonly used in tangible AR (Shelton & Hedley, 2002, 2004).

AR systems could use monocular, binocular, and biocular presentations (Kitamura et al., 2014, 2015). A binocular system presents the information using two optical trains, one for each eye. In contrast, a biocular system has only one optical train, and the aperture is large enough to simultaneously observe both eyes.

AR capability can be achieved through combinations of sensors and cameras integrated with display and interaction devices, computer vision software, and thoughtful interface design. Different designed implementations can offer advantages for specific applications (Van Krevelen & Poelman, 2010). Advances in camera, GPS, accelerometer, and display technologies in mobile devices have led to using tablets and smartphones as AR displays (Hedley, 2017). Smartphones and tablets are among the most accessible devices, using their cameras and screens to display AR content (with the metaphor of an AR 'lens'), thus bringing AR applications to a broad audience. Head-mounted displays (HMDs) can arguably provide a more immersive experience by filling the user's entire field-of-view (FOV) with augmented views of reality. Optical see-through HMDs allow users to see the real world directly with digital content superimposed, making them ideal for applications requiring high interaction with the physical environment, such as medical or industrial uses (Carmigniani et al., 2011). Video see-through HMDs, which capture the real world with cameras and display the combined content on screens within the headset, offer better integration of digital elements but may encounter latency issues. Improvement and evolution of wearable virtual reality (VR) devices have increased considerably over the past few years. Devices such as the Meta Quest 3 can be loaded with standalone VR and AR software to enable unwired VR and AR experiences (Speicher et al., 2019). Furthermore, progress in camera and computer vision technology has resulted in increased performance with inside-out tracking by these headsets (for position and context as a basis for registration), enabling users to use the same headset for immersive VR and 'pass-though AR and 'pass-through mixed reality (MR), using the outward-facing cameras on these devices.

2.2 Rationale for choice

This research aims to fill a gap in the ocean data research community. While early work has been done to integrate AR with seafloor data visualization (Palmese & Trucco, 2008), work to study whether such interfaces support effective hydrographic practice is almost nonexistent to date.

Comparing tabletop AR interface visualization with conventional desktop 3D monitor visualization is essential for understanding the advantages and limitations of each approach in bathymetric data interpretation. A tabletop AR interface is an interactive visualization platform where virtual 3D content is overlaid onto a real-world surface, such as a physical table, through the use of AR technology. Typically, users wear AR head-mounted displays (HMDs) or utilize handheld devices, enabling them to see and manipulate virtual objects appearing as if they are physically present on the tabletop. Traditional desktop 3D monitors offer high-resolution displays and familiar interfaces, while tabletop AR interfaces potentially enhance spatial awareness and interaction by integrating digital information with the physical environment (Jo et al., 2021; Turhan & Gümüş, 2022). This comparative analysis aims to determine whether the immersive and interactive nature of AR provides significant improvements in user perception and task performance. Identifying these differences is crucial for developing practical visualization tools that enhance data interpretation accuracy and efficiency, ultimately leading to better decision-making in fields relying on precise bathymetric data.

This comparison is the first step toward a comprehensive and systematic empirical evaluation of mono versus stereo AR and stereo AR versus stereo VR. By establishing a baseline understanding of how AR interfaces compare to traditional 3D monitors, we can design more effective experiments to explore the nuances of stereoscopic visualization. Subsequent studies will delve into the impact of depth perception, spatial awareness, and user interaction on task performance and perception, providing a holistic view of these advanced visualization technologies. The insights from this research will inform the development of optimized visualization tools tailored to specific applications and user needs, enhancing the effectiveness and usability of AR and VR systems in various professional and scientific domains.

3 Empirical methods and materials

This study investigates whether tabletop AR interfaces may enhance perception and task performance in interpreting raw bathymetric data compared to conventional desktop 3D visualizations. It uses exploratory methods to examine how interface type influences user experience, accuracy, and efficiency. The central hypothesis is that users interacting with bathymetric data through a tabletop AR interface may demonstrate improved spatial perception and task performance – such as accuracy and efficiency in interpretation – compared to users using a conventional desktop 3D visualization interface. Findings aim to inform future research and support the development of more effective bathymetric visualization techniques.

3.1 Study procedure

This study employed two 3D visualization interfaces with distinct visual cues to investigate their effects on subjects' data perception. The motor aspects of interaction with 3D visualizations were not considered in this project, as the processing and analysis of bathymetric data – routinely performed by hydrographic analysts – require substantial manipulation of the viewpoint. In other words, bathymetric data are not processed or analyzed from a static, single perspective. Since the participants' motor activity, such as actions for navigating the terrain, was not measured, we utilized typical control devices, such as a computer mouse, to interact with the visualizations.

The study involved the following steps: Participants navigated to a designated survey website[1]. They read and agreed to a consent form outlining the survey's terms, their rights and protections, and contact information for inquiries. Participants completed a survey comprising 52 questions, which included checking boxes, ranking options, and providing short answers, using both desktop and mobile device-based data visualization tools.

The recorded data included participants' responses to the online questionnaire. This data was securely stored in an SFU-supported facility, protected by passwords and encryption. The information collected during the study was kept confidential and used solely for research purposes. No raw survey data was shared with commercial partners, though graphical summaries of aggregated data might have been included in academic publications. No participant names were collected, ensuring no participants were identifiable. The study did not collect any identifying information about participants, ensuring their privacy was maintained. There were no foreseeable risks to participating in this survey. Participants performed simple tasks involving viewing and interpreting 3D data visualizations while sitting at a desk in DHN's regular office, using everyday devices such as a typical desktop computer, smartphone, or tablet with a camera. Participation in the study was voluntary and unpaid.

The experiment was divided into two identical phases, Interface DT and Interface AR, with the execution order alternating between the groups involved. The first group performed tasks using the standard desktop interface (Interface DT) and the augmented reality interface (Interface AR). Conversely, the second group performed the same tasks but started with Interface AR before using Interface DT. Given the use of two datasets in the research, two questionnaire

[1] https://www.surveymonkey.com/ (last accessed 30 March 2025).

https://doi.org/10.58440/ihr-31-1-a05

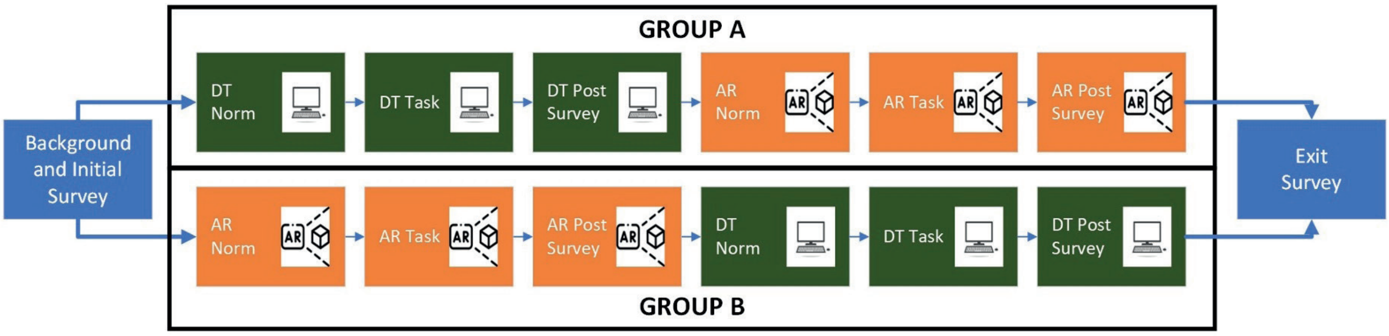

Fig. 1 Experimental layout.

versions were created (A and B), with the order of model use reversed. Consequently, the experiment was conducted in four distinct configurations: Group A, Group B, Group A (inverted), and Group B (inverted).

After consenting to the form, the volunteer is invited to complete a background/operational survey. Following a familiarization period, the experiment begins using one of the interfaces. The volunteer identifies and compares pre-selected points from visualized bathymetric data. A researcher monitors each task, measuring the time it takes to complete it and recording the volunteers' answers during the AR interface phase. During the DT interface phase, the volunteers answer the questions independently.

Upon completing all tasks, the volunteer is invited to answer a post-experiment questionnaire regarding their experience. Then, the volunteer visualizes another 3D model using the other interface and performs identification and comparison tasks with different pre-selected bathymetric data points, manipulating the device to obtain the answers.

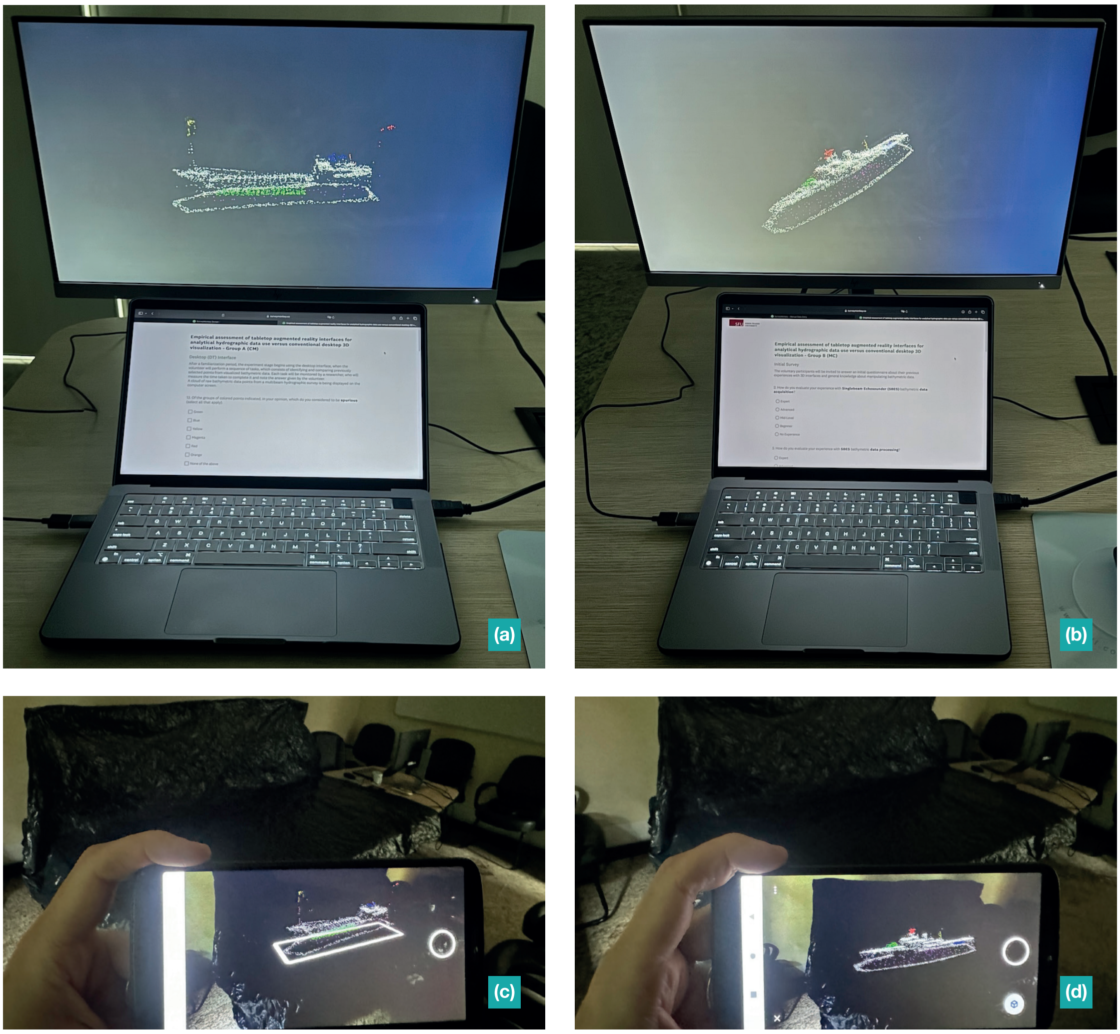

Fig. 2 2 DT Interface GB Church model (a), DT Interface HMCS Mackenzie (b), AR Interface GB Church model (c), AR Interface HMCS Mackenzie (d).

After completing all tasks with the second interface, the volunteer is invited to answer a second post-experiment questionnaire about their experience. Upon completing both stages of the experiment (desktop and AR interfaces), the volunteer responds to a final reflective questionnaire comparing the two stages (Fig. 1).

3.2 Display interface technologies used

Two interfaces were used to view and manipulate the 3D models: the desktop interface (Interface DT) and the augmented reality interface (Interface AR; Fig. 2).

The desktop interface consisted of a flat-screen monitor and a standard mouse placed on a table. Participants were seated during interaction. Using the mouse's three buttons, users could rotate, translate, and zoom in and out on the model.

The AR interface, by contrast, used a handheld mobile device (smartphone) to project the 3D model onto the same table in augmented reality. Participants remained standing and were free to move around the table to explore the model from different perspectives. The device's touchscreen allowed for the model's rotation, translation, and scaling (Fig. 3). However, because the 3D content was anchored to the tabletop, rotation along axes parallel to the table's surface was limited.

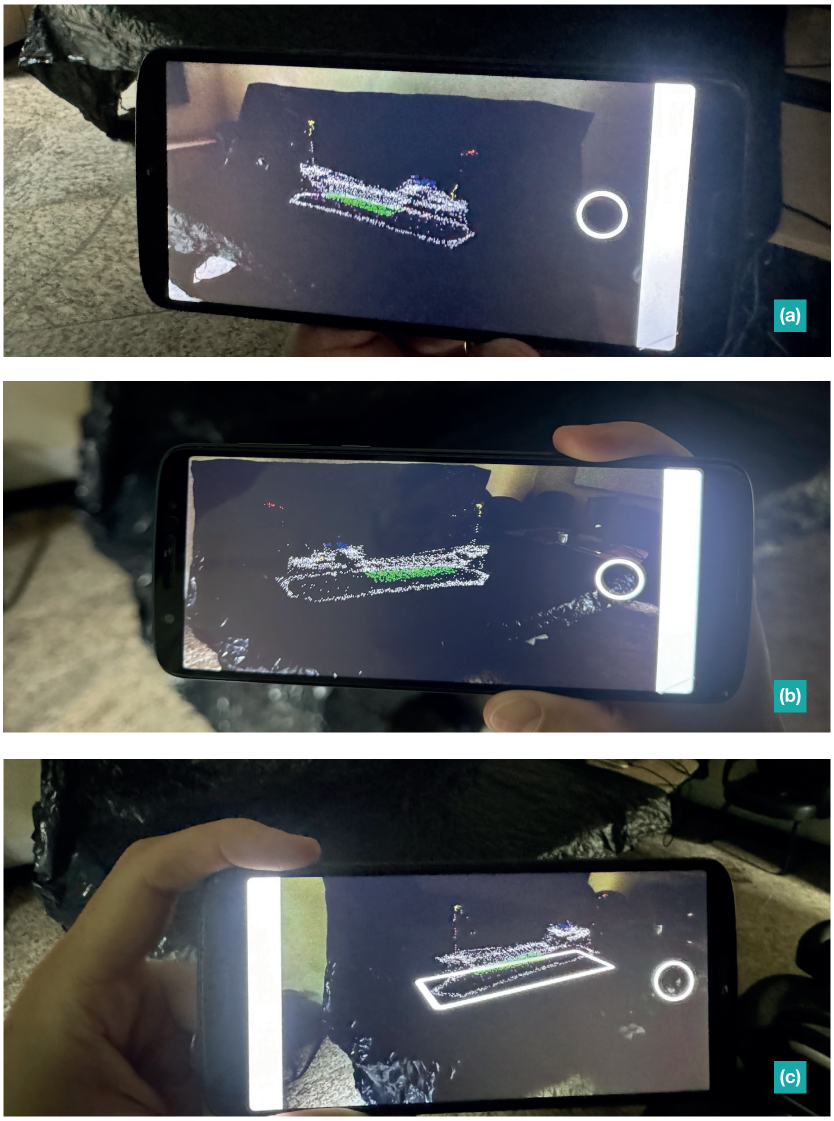

Fig. 3 The 3D AR bathymetric data visualization, seen registered to a desk covered in a blackout sheet, viewed through a handheld mobile device in the hydrographic office configured to conduct this study (a, b, c).

3.3 Bathymetric data used

The experiment used bathymetric data collected from two sunken ships, MV GB Church and HMCS Mackenzie, near Sidney, in October 2019. Using a Kongsberg EM2040P MkII multibeam echosounder aboard the CSL Heron survey boat, owned by the Canadian Hydrographic Service, several survey lines were acquired in each ship's area. The settings included high-density beam spacing, dynamic dual swath, 300 kHz frequency mode, high-resolution water phase data, and a survey speed of around 6 knots (Gomes de Araujo, 2024). These datasets provided the foundational background for the experimental tasks. Both datasets were employed for both interfaces but were only used once per subgroup. Consequently, each subgroup observed a change in the dataset when transitioning from one interface to another.

In point cloud format (.txt), the raw data were imported into CloudCompare software — an open-source software designed to visualize, process, and analyze 3D point cloud data - for preparation (Figs. 4a and 5a). The preparation process involved selecting and coloring specific point groups to capture the attention of the experiment participants (Figs. 4b and 5b). Excess data surrounding the ships' hulls, such as seabed data, was excluded to reduce the total number of points and lighten the files (Figs. 4c and 5c). Additionally, it was necessary to reduce the resolution of both models to accommodate Sketchfab.com's AR visualization limitations. The Sketchfab.com platform – an online platform that enables users to publish, explore, share, and embed interactive 3D models and visualizations, supports VR and AR, allowing users to experience 3D content in immersive environments without the need for specialized software – was also utilized to convert the point cloud models (in LAS file format) to AR file format (GLTF), which was subsequently used in the experiment.

In both models, six groups of points were selected, with each group assigned one of the following colors: blue, red, yellow, green, orange, and magenta. These colors were chosen for their optimal contrast against a black background. The criteria for selecting the points were as follows:

a) One group of points represented spurious data incorrectly acquired by the acquisition system or data typically filtered or excluded during processing. This group was used to test the participant's ability to identify whether the data was accurate.
b) In both models, two vertically adjacent groups of points, not necessarily part of the ship's structure,

 https://doi.org/10.58440/ihr-31-1-a05

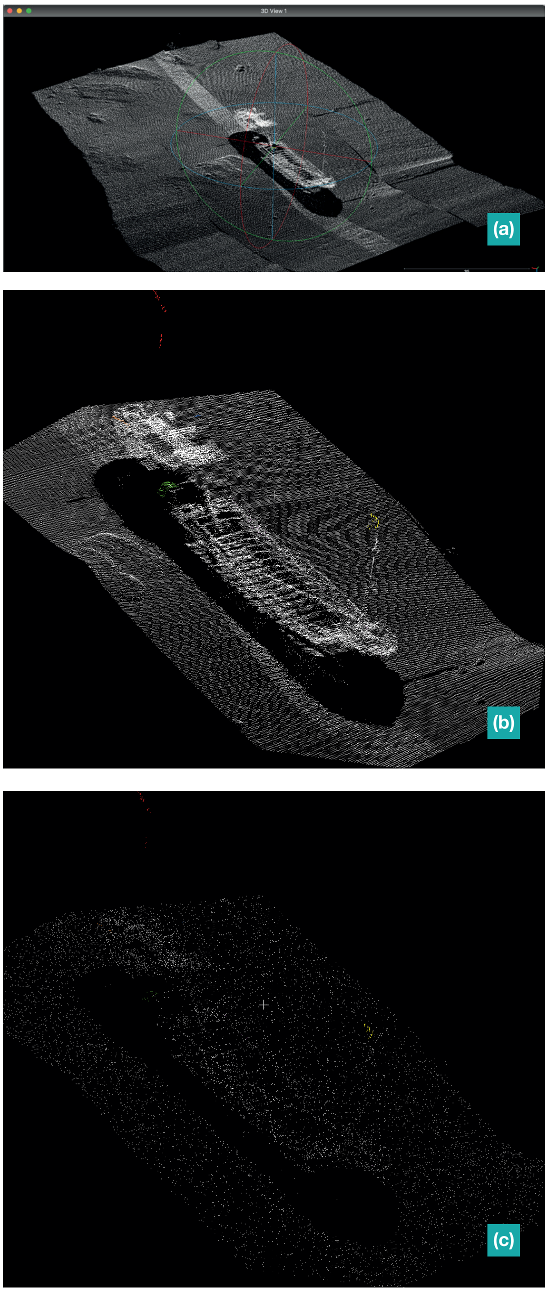

Fig. 4 (a) GB Church Point Cloud Raw; (b) GB Church Point Cloud Color; and (c) GB Church Point Cloud Sample.

were colored red and yellow. These groups were chosen to compel participants to observe the model from a side view.

c) Lastly, three groups of points represented features of the ship's structure. These groups were selected to assess the participants' ability to perceive small features of the model.

3.3.1 GB Church

The G.B. Church was the Artificial Reef Society of British Columbia's (ARSBC) first project, initiated in 1989 and completed over two years. The ship was sunk in August 1991 in Princess Margaret Marine Park near Sidney on Vancouver Island. Preparation involved stripping the vessel down to the steel, creating diver access points, and removing hazardous materials to ensure diver safety. The sinking site, chosen for its flat sandy bottom and proximity to dive shops, met all coast guard and navigation requirements. The G.B. Church quickly became a habitat for marine life like octopus and wolf eels, demonstrating the positive impact of artificial reefs on ecosystems and reducing diver traffic on natural and historical sites (Artificial Reef Society of British Columbia, 2024).

In this model (Fig. 4), the red and yellow groups of points represented data that were not considered spurious but were not part of the ship's structure. The magenta group of points represented spurious data. The blue, green, and orange groups represented features of the ship's structure.

3.3.2 HMCS Mackenzie

The lead ship of her class, HMCS Mackenzie, was built by Canadian Vickers Limited in Montreal and commissioned on 6 October 1962. Over 23 years, Mackenzie operated in the Pacific with the Second Canadian Destroyer Squadron and Training Group Pacific, participating in various exercises. After 30 years of service, she was decommissioned on 3 August 1993 and sold to the Artificial Reef Society of BC. She was scuttled near Rum Island on 16 September 1995 (Artificial Reef Society of British Columbia, 2024).

In this model (Fig. 5), the orange group of points represented spurious data. All the other groups represented features of the ship's structure.

3.4 Participants

Participation in this study was entirely voluntary. Participants could choose not to participate without any impact on their employment, partnerships, or services they currently receive.

The participants were 42 volunteer hydrographer analysts and Cartographic Engineers from the Brazilian Navy Hydrographic Office in Rio de Janeiro, Brazil. Their education background ranged from technical to advanced degrees, with professional experience spanning from newly arrived analysts to those who have served for several years at the Hydrographic Office. Their expertise varies from junior to senior levels, and their analytical specialization differs based on the equipment used, such as single-beam or multi-beam sonar systems. Data collection took place in May and June 2024. Participants were recruited via personal contact and were questioned about their experience with 3D visualization and bathymetric data before testing. While all participants had some prior experience with 3D visualization applications, not all had experience with the specific 3D geographical data used in this study. None were familiar with the presented bathymetry models.

The sample was deliberately chosen to explore the performance of experienced users with hydrographic expertise, focusing on perception, identification, and classification tasks. The participants represented

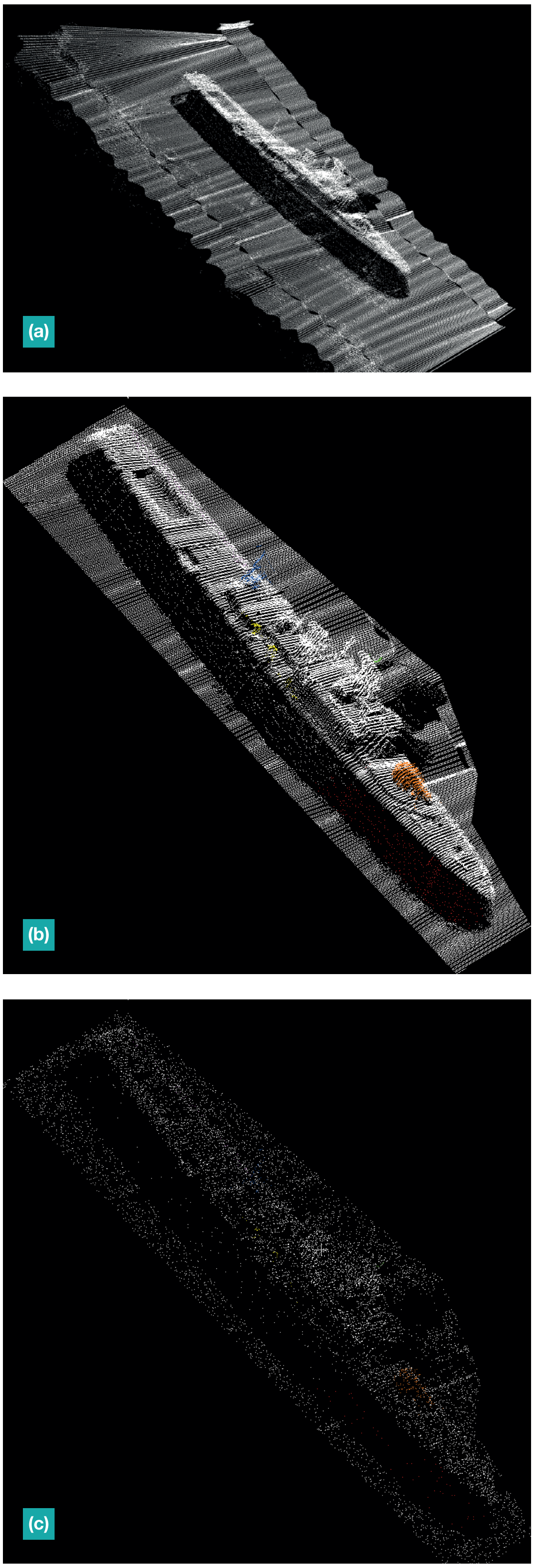

Fig. 5 (a) HMCS Mackenzie Point Cloud Raw; (b) HMCS Mackenzie Point Cloud Color; and (c) HMCS Mackenzie Point Cloud Sample.

nearly all analysts from the BN Hydrographic Office. To balance the order of interface use, participants were divided into two groups (A and B), ensuring an equal number of participants for each interface. All subjects had normal or corrected vision and no motor or movement restrictions.

Both groups had identical experimental conditions, including lighting, temperature, and other environmental factors. Participants consented to the experimental procedure and participated voluntarily, with the option to withdraw at any time. They were instructed to perform tasks with maximum attention and told that precision in answering was more important than speed, though their completion time to answer each question in each task phase would still be recorded.

Due to the anonymous nature of the survey, participants could not withdraw their responses once submitted.

3.5 Background and operational survey

Before the experiment, participants were asked to complete a self-assessment questionnaire to evaluate their prior experience with 3D interfaces and bathymetric data manipulation. Responses were rated across five levels: expert, advanced, mid-level, beginner, and no experience. The questionnaire included the following 11 items:

- How do you evaluate your experience with Single beam Echosounder (SBES) bathymetric data acquisition?
- How do you evaluate your experience with SBES bathymetric data processing?
- How do you evaluate your experience with Multibeam Echosounder (MBES) bathymetric data acquisition?
- How do you evaluate your experience with MBES bathymetric data processing?
- How do you evaluate your experience with bathymetric data feature classification?
- How do you evaluate your experience with desktop 3D data visualization?
- How do you evaluate your experience with Augmented Reality (AR) 3D data visualization?
- How do you evaluate your experience with Virtual Reality (VR) data visualization?
- How do you evaluate your experience with 2D computer or console games?
- How do you evaluate your experience with 3D computer or console games?
- How do you evaluate your experience with AR games?

3.6 Normalization phase

Each task battery began with a normalization phase to minimize disparities in interface handling skills. This familiarization stage allowed participants to practice using the control devices for both the desktop and AR interfaces. Participants were instructed on how to interact with a generic bathymetric dataset containing randomly placed markers. They then practiced manipulating this dataset for three minutes using a mouse and keyboard (for the desktop interface) or the touchscreen of a mobile device (for the AR interface).

https://doi.org/10.58440/ihr-31-1-a05

3.7 Tasks, scoring and response confidence

The following section outlines the tasks assigned to participants, along with their corresponding item numbers in each questionnaire:

a) Q13 (DT Interface) and Q29 (AR Interface) – Of the groups of colored points indicated, which do you consider spurious (select all that apply)?
b) Q15 (DT Interface) and Q31 (AR Interface) – Of the groups of colored points indicated, which do you consider part of the sunken ship (select all that apply)?
c) Q17 (DT Interface) and Q33 (AR Interface) – Which of the groups of colored points indicated is closest to the sea surface (shallowest depth), regardless of whether the data is spurious?
d) Q19 (DT Interface) and Q35 (AR Interface) – How many crane booms can you identify on the ship?
e) Q21 (DT Interface) and Q37 (AR Interface) – How many masts can you identify on the ship?
f) Q23 (DT Interface) and Q39 (AR Interface) – How would you classify the type of shipwreck?

Tasks a) and b) were scored individually for each group of colored points, resulting in scores ranging from 0 (all incorrect) to 6 (all correct). The remaining four tasks were scored based solely on correct responses.

After completing each task, participants rated their confidence in their responses on a seven-point scale (1 = "Not confident at all" to 7 = "Extremely confident"). This additional measure aimed to provide deeper insights into user certainty, helping to identify potential biases and improve the predictive value and validity of the findings.

3.8 Post survey

Following the completion of all tasks, participants answered a post-experiment questionnaire to evaluate their experience using both interfaces. Questions focused on ease of use for each interface and included:

a) Rate your ease of perceiving the horizontal position of the selected points in raw MBES data using AR / DT data visualization interfaces.
b) Rate your ease of perceiving the vertical position (depth) of the selected points in raw MBES data using AR / DT data visualization interfaces.
c) Rate your ease of identifying whether the selected points are considered spurious data in raw MBES data using AR / DT data visualization interfaces.
d) Rate your ease of identifying whether the selected points belong to the structure of the sunken ship in raw MBES data using AR / DT data visualization interfaces.

3.9 Exit survey

After completing both stages of the experiment (desktop and AR environment), volunteers responded to a final reflective questionnaire with comparison questions between the stages performed. For the first four questions, participants indicated whether one of the two interfaces was better or whether there was no difference. The questions included:

a) Did either of the two interfaces (desktop or AR) provide a clearer understanding of the spatial horizontal positioning of the groups of colored points in each task?
b) Did either of the two interfaces (desktop or AR) provide a clearer understanding of the spatial vertical positioning (depth) of the groups of colored points in each task?
c) Did either of the two interfaces (desktop or AR) make identifying parts of ships, such as masts and crane booms, easier?
d) Did either of the two interfaces (desktop or AR) support a more straightforward inspection (exploration) of the dataset?
e) Do you think the AR bathymetric data visualization prototype you just used would be useful in the everyday hydrographic office workflow?
f) In your opinion, which affordances of the AR interfaces do you perceive to support hydrographic office data operations best?
g) In your opinion, which characteristics of AR-based data visualization do you perceive to undermine hydrographic data visualization or present challenges that need to be overcome?
h) Is there any other feedback you would like to share about these DT/AR interfaces in your workflow?

4 Results

4.1 DT interface vs. AR interface: Background and operational survey

4.1.1 Hydrographic experience

The pie chart titled "Hydrography Experience" represents the distribution of responses to five questions about different aspects of hydrography experience:

a) How do you evaluate your experience with Single Beam Echosounder (SBES) bathymetric data acquisition?
b) How do you evaluate your experience with SBES bathymetric data processing?
c) How do you evaluate your experience with Multibeam Echosounder (MBES) bathymetric data acquisition?
d) How do you evaluate your experience with MBES bathymetric data processing?
e) How do you evaluate your experience with bathymetric data feature classification?

From this data, the most common experience levels are "Advanced" and "Beginner," which account for 25 % of the respondents. "No Experience" is also significant, accounting for 19 % of the respondents. Mid-Level experience is held by 18 % of the respondents. The "Expert" level is the least common, with 13 % of respondents rating themselves as such.

This distribution indicates a diverse range of expertise among the respondents, with a notable portion having significant experience (Expert and Advanced combined account for 38 %) and another considerable portion with minimal to no experience (No Experience and Beginner combined account for 44 %).

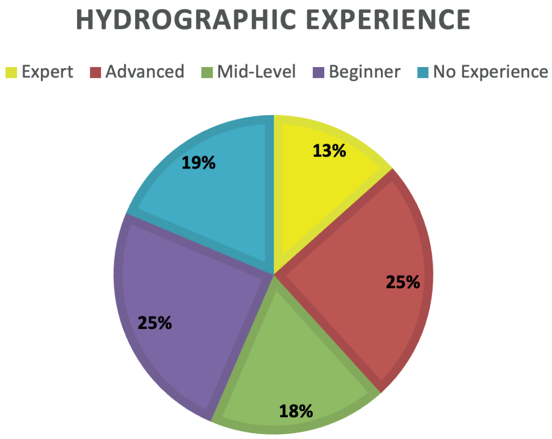

Fig. 6 Hydrographic experience results graph.

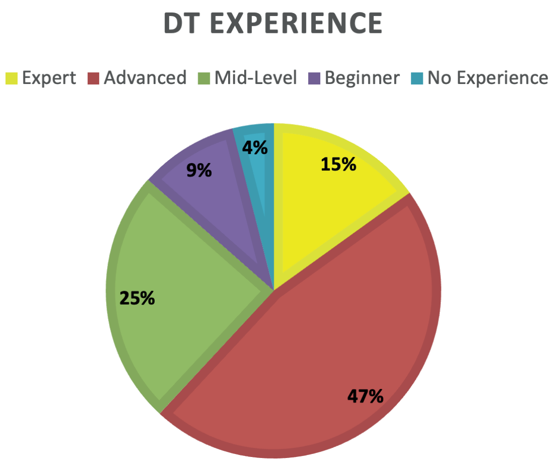

Fig. 7 Desktop interface experience results graph.

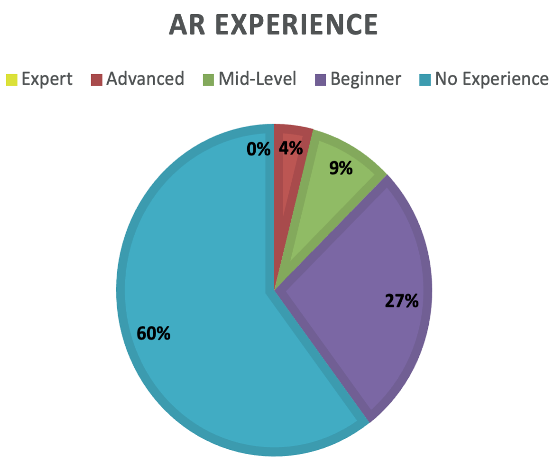

Fig. 8 Augmented reality experience results graph.

4.1.2 Desktop interface experience

The pie chart titled "Desktop Interface Experience" represents the distribution of responses to three questions about experience with desktop interfaces:

a) How do you evaluate your experience with desktop 3D data visualization?
b) How do you evaluate your experience with 2D computer or console games?
c) How do you evaluate your experience with 3D computer or console games?

This data shows that the most common experience level is "Advanced," making up 47 % of the respondents. Mid-Level experience is also significant, accounting for 25 % of the respondents. The "Expert" level is held by 15 % of the respondents. The "Beginner" level is relatively low, with 9 % of respondents rating themselves as such. "No Experience" is the least common, with only 4 % of respondents. This distribution indicates that most respondents have significant experience with desktop interfaces (Advanced and Expert combined account for 62 %). A smaller portion has minimal to no experience (Beginner and No Experience combined account for 13 %).

4.1.3 AR interface experience

The pie chart titled "AR Interface Experience" represents the distribution of responses to three questions about experience with augmented and virtual reality interfaces:

a) How do you evaluate your experience with Augmented Reality (AR) 3D data visualization?
b) How do you evaluate your experience with Virtual Reality (VR) data visualization?
c) How do you evaluate your experience with AR games?

From this data, it can be observed that most respondents have no experience, accounting for 60 %. A significant portion of respondents are beginners, accounting for 27 %. Only 9 % of respondents have a mid-level experience. There are no respondents with advanced or expert-level experience. This distribution indicates that most respondents have little to no experience with AR and VR interfaces (No Experience and Beginner combined account for 87 %). Only a tiny fraction have mid-level experience, and no respondents have advanced or expert experience.

4.2 DT interface vs. AR interface: Task score

4.2.1 Description of the graphs

The box and whisker plots presented utilize a specific color code to represent different elements of the data:

a) Orange Boxes: Represent the interquartile range (IQR) of the data, which is the range between the first and third quartiles. The box itself shows where the central 50 % of the data points lie.
b) Red Horizontal Lines Inside the Box: Represents the median value of the data set. This line divides the box into two parts, indicating that half of the data points are above this value and half are below.
c) Black Whiskers: These lines extend from the edges of the box to the minimum and maximum values within 1.5 times the IQR from the quartiles. They indicate the spread of the data outside the interquartile range.

https://doi.org/10.58440/ihr-31-1-a05

d) Blue Horizontal Lines: Represent the average (mean) values of the data sets. These lines provide an additional measure of central tendency, helping to compare the mean values across different questions.

e) Grid Lines: The grid lines in the background help to visually align the data points for easier comparison across different questions.

This color code allows for clear and detailed visualization of the statistical properties of the data, making it easier to identify central tendencies, variability, and the overall distribution of response times for both DT and AR interface questions.

The box and whisker in the graph of Fig.9 are organized according to the corresponding task or question they represent, as indicated by their labels (e.g., Q13, Q29, Q15). Questions that refer to the same task are grouped accordingly – such as Q13 and Q29, which represent the same question presented in different interface conditions (e.g., desktop vs. AR). This arrangement allows for a direct visual comparison of participant performance or response values across equivalent tasks under different visualization modes. Consistent ordering makes interpreting variations in scores, medians, and confidence levels between interfaces easier.

4.2.2 Comparing questions 13 (Q13 – DT Interface) and 29 (Q29 – AR Interface) – Of the groups of colored points indicated, which do you consider spurious (select all that apply)?

The data for Q13 is centered around a high score, with most values ranging between 0.67 and 1.00. Similarly, the distribution of Q29 data closely mirrors that of Q13, with most values falling within the 0.67 to 1.00 range. Both Q13 and Q29 have an identical median value of 0.83, indicating the same central tendency for both datasets. The first and third quartiles for Q13 and Q29 are identical, demonstrating similar dispersion and range within the middle 50 % of the data. The average score for Q13 is 0.80, while Q29 has a slightly lower average of 0.79, suggesting a similar overall performance across both datasets. Both datasets exhibit a consistent range from 0.67 to 1.00 and lack any outliers, indicating stable scoring patterns without extreme variations.

The data for Q13 and Q29 are remarkably similar regarding central tendency, dispersion, and overall distribution. Both questions yield high scores concentrated around the same values, suggesting that respondents perceive the aspects consistently measured by Q13 and Q29. This similarity underscores the reliability and uniformity in responses to these questions.

The Neyman Confidence Intervals for Q13 and Q29 are similar, with Q29 having a slightly higher and more precise mean estimate. Both intervals overlap significantly, suggesting that the central tendencies of these datasets are very close to each other.

4.2.3 Comparing questions 15 (Q15 – DT Interface) and 31 (Q31 – AR Interface) – Of the groups of colored points indicated, which do you consider part of the sunken ship (select all that apply)?

The data for Q15 is concentrated around a high score, with most values ranging between 0.67 and 1.00, indicating a central tendency towards the upper end of the scoring scale. Similarly, the data for Q31 displays a comparable distribution, with scores predominantly falling within the same range and showing a central tendency towards higher values. Q15 and Q31 share an identical median value of 0.83, highlighting their similar central tendencies. The first and third quartiles for both questions are also the same, demonstrating comparable dispersion and range within the middle 50 % of the data. The average score for Q15 is 0.82, while for Q31, it is slightly lower at 0.81, indicating a similar overall performance in both datasets. Both datasets exhibit the same range from 0.50 to 1.00 and lack any outliers, reflecting consistent scoring patterns without extreme variations.

The data for Q15 and Q31 are strikingly similar

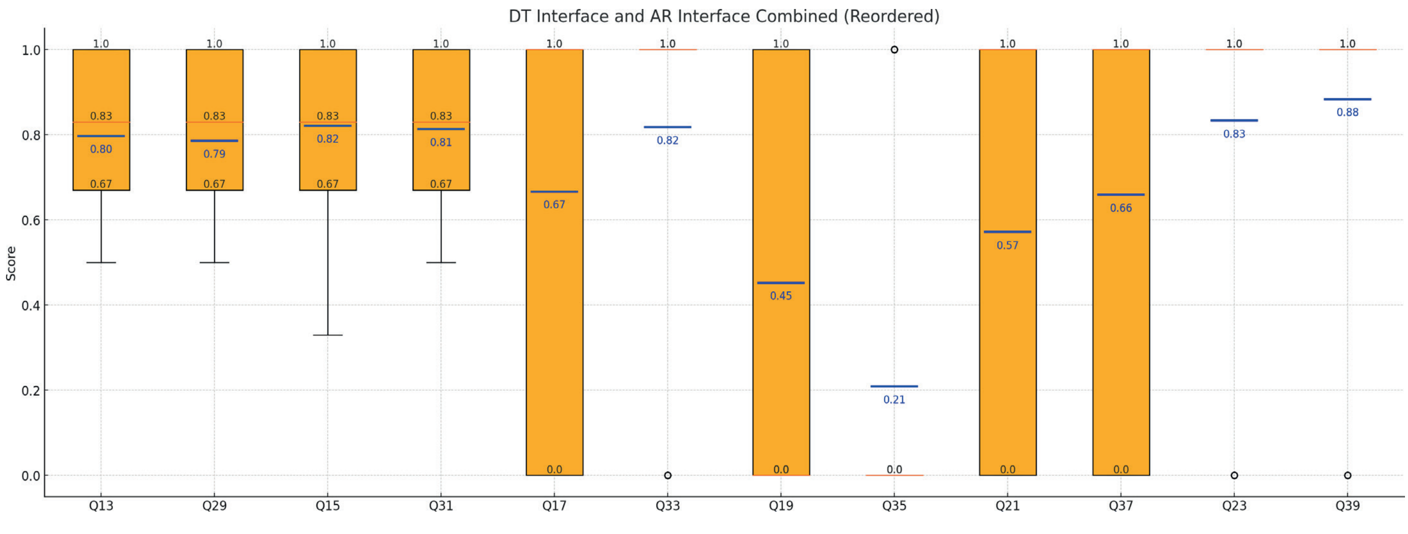

Fig. 9 DT and AR interfaces score.

in central tendency, dispersion, and overall distribution. Both questions have high scores concentrated around similar values, reflecting consistent responses. This consistency suggests that the respondents perceive the aspects measured by Q15 and Q31 similarly, underscoring the reliability and uniformity of their answers.

The Neyman Confidence Intervals for Q15 and Q31 have a similar central tendency, but Q15 suggests a slightly higher mean than Q31. The CI for Q31 is narrower, suggesting a more precise estimate of the mean for Q31 compared to Q15.

4.2.4 Comparing questions 17 (Q17 – DT Interface) and 33 (Q33 – AR Interface) – Which of the groups of colored points indicated is closest to the sea surface (shallowest depth), regardless of whether the data is spurious?

The data for Q17 exhibits a bimodal distribution, with scores concentrated at the lowest (0.00) and highest (1.00) values, suggesting a polarized perception among respondents. In contrast, the data for Q33 is highly skewed towards the highest score, with the majority of values being 1.00 and a few low scores, indicating a strong tendency towards the upper end of the scale. The first quartile for Q17 is at 0.00, and the third quartile is at 1.00, indicating wider dispersion and a bimodal nature. Conversely, Q33 has both quartiles at 1.00, showing no dispersion and a strong skew towards the highest score. The average score for Q17 is 0.66, whereas for Q33, it is higher at 0.82, indicating a more positive overall performance.

Both datasets share the same range from 0.00 to 1.00 and lack outliers. However, their distribution patterns differ, with Q17 being bimodal and Q33 strongly skewed towards the top. This comparison highlights the varying perceptions of the aspects measured by Q17 and Q33. Q17's bimodal distribution suggests a divided perception among respondents, while Q33's skew towards the highest score indicates more uniformly positive responses.

The Neyman Confidence Interval for Q33 suggests a higher and more precise mean than Q17. The intervals indicate a significant difference in the central tendencies of these datasets, with Q33 having a higher mean and a narrower confidence interval.

4.2.5 Comparing questions 19 (Q19 – DT Interface) and 35 (Q35 – AR Interface) – How many crane booms can you identify on the ship?

The data for Q19 exhibits a bimodal distribution, with scores concentrated at the lowest (0.00) and highest (1.00) values, indicating polarized responses among respondents. Conversely, the data for Q35 is highly skewed towards the lowest score, with the majority of values being 0.00 and a few high scores, suggesting a strong tendency towards the lower end of the scale.

Q19 has a median of 1.00, while Q35 has a median of 0.00, reflecting a central tendency towards the highest score for Q19 and the lowest score for Q35. The first quartile for Q19 is at 0.00, and the third quartile is at 1.00, indicating wide dispersion and a bimodal nature. In contrast, Q35 has both quartiles at 0.00, showing no dispersion and a strong skew toward the lowest score. The average score for Q19 is 0.59, whereas for Q35, it is significantly lower at 0.12, indicating a more positive overall performance for Q19.

Both datasets share the same range from 0.00 to 1.00 and lack any outliers, but their distribution patterns differ significantly. Q19 displays a bimodal distribution with significant scores at both extremes, suggesting polarized responses among respondents. In contrast, Q35 shows a strong skew towards the lowest score, indicating predominantly negative responses. This comparison highlights the differing perceptions of the aspects measured by Q19 and Q35, with Q19 receiving more balanced responses and Q35 indicating a tendency towards dissatisfaction.

The Neyman Confidence Interval for Q19 suggests a higher mean compared to Q35. There is no overlap between the intervals, indicating that the central tendencies of these datasets are significantly different, with Q19 having a higher mean and a slightly wider confidence interval.

4.2.6 Comparing questions 21 (Q21 – DT Interface) and 37 (Q37 – AR Interface) – How many masts can you identify on the ship?

The data for Q21 exhibits a bimodal distribution, with scores concentrated at the lowest (0.00) and highest (1.00) values, indicating polarized responses among respondents. Similarly, the data for Q37 shows a bimodal distribution with scores concentrated at both extremes, suggesting a divided perception among respondents. Q21 and Q37 have a median value of 1.00, reflecting a central tendency towards the highest score. Both questions' first and third quartiles are 0.00 and 1.00, respectively, indicating wide dispersion and a bimodal nature. The average score for Q21 is 0.61, while for Q37, it is slightly higher at 0.66, suggesting a marginally more positive overall performance. Both datasets share the same range from 0.00 to 1.00 and lack any outliers, with similar distribution patterns. This comparison highlights the consistent nature of respondent perceptions for the aspects measured by Q21 and Q37.

The Neyman Confidence Interval for Q37 suggests a higher mean compared to Q21. There is some overlap between the intervals, indicating that the central tendencies of these datasets are similar. However, Q37 has a higher mean and a slightly narrower confidence interval than Q21.

4.2.7 Comparing questions 23 (Q23 – DT Interface) and 39 (Q39 – AR Interface) – How would you classify the type of shipwreck?

The data for Q23 is highly skewed towards the highest score, with the majority of values being 1.00,

https://doi.org/10.58440/ihr-31-1-a05

indicating a strong tendency towards the upper end of the scale. Similarly, the data for Q39 shows a strong skew towards the highest score, with most values at 1.00, reflecting a preference for the upper end of the scale. Q23 and Q39 have a median value of 1.00, indicating a central tendency towards the highest score. The first and third quartiles for both questions are 1.00, showing no dispersion and a strong skew toward the highest score. The average score for Q23 is 0.86, while for Q39, it is higher at 0.93, suggesting a slightly more positive overall performance. Both datasets share the same range from 0.00 to 1.00 and lack any outliers, but their distribution patterns are highly skewed towards the top. This comparison highlights the uniformity in respondent perceptions for the aspects measured by Q23 and Q39.

The Neyman Confidence Interval for Q39 suggests a higher and more precise mean than Q23. There is significant overlap between the intervals, indicating that the central tendencies of these datasets are pretty similar. Nonetheless, Q39 has a slightly higher mean and a narrower confidence interval than Q23.

4.3 DT interface vs. AR interface: Time-elapsed

This section presents a comparative analysis of time-elapsed statistics for two groups of questions: the DT Group (Q13, Q15, Q17, Q19, Q21, Q23) and the AR Group (Q29, Q31, Q33, Q35, Q37, Q39).

The DT Group's time-elapsed statistics reveal considerable variability across different questions. For instance, Q13 exhibits a median time of 81.0 seconds, with an interquartile range (IQR) spanning 29.5 to 134.0 seconds and an average of 90.05 seconds. In contrast, Q23, after removing outliers, shows a median of 27.5 seconds, an IQR from 8.25 to 39.25 seconds, and an average of 46.12 seconds. Other questions in this group, such as Q15 and Q17, display medians ranging from 29.0 to 43.0 seconds, with averages between 39.69 and 57.31 seconds.

The AR Group exhibits a more consistent pattern in response times. For example, Q29 shows a median time of 70.0 seconds, with an IQR from 41.0 to 109.0 seconds and an average of 92.67 seconds. Similarly, Q31 and Q35 have medians of 47.0 and 49.0 seconds, respectively, with averages around 57.62 and 59.93 seconds. The ranges in this group, such as 8 to 317 seconds for Q29 and 1 to 259 seconds for Q39, indicate substantial variability but are generally more controlled than the DT Group.

The median time-elapsed for the DT Group tends to be higher in Q13 (81.0 seconds) and lower in other questions (27.5 to 43.0 seconds). In contrast, the AR Group exhibits a more consistent range of medians (31.0 to 70.0 seconds).

The DT Group shows broader IQRs for questions like Q13 (104.5 seconds) and Q15 (64.0 seconds), indicating greater variability. The AR Group has narrower IQRs, suggesting more consistent responses within each question.

The average time-elapsed is relatively similar between the groups. The DT Group's Q13 (90.05 seconds) and the AR Group's Q29 (92.67 seconds) have the highest averages. Other questions in both groups exhibit average times between 37.81 and 59.93 seconds.

The ranges in the DT Group are more extreme, particularly in Q13 (1 to 243 seconds) and Q23 (1 to 95 seconds without outliers). Although the AR Group also has wide ranges, such as 8 to 317 seconds for Q29 and 1 to 259 seconds for Q39, the variability is generally more controlled.

4.3.1 Time-elapsed – Neyman Confidence Intervals

Based on the provided statements and the analysis of the Neyman confidence intervals, here is a summary and critique for each comparison pair within the DT Group and AR Group:

The Neyman confidence intervals for Q13 and Q29 are similar, with both intervals overlapping substantially. This indicates that the time-elapsed data for both questions have similar central tendencies and variability, making them comparable.

Both Q15 and Q31 datasets exhibit similar means and variability, but Q15 (173) and Q31 (20) are significant outliers. Despite the similarities in distributions, the presence of these outliers highlights deviations from the central tendencies in both datasets.

The Neyman confidence intervals for Q17 and Q33 overlap, suggesting some similarity in their distributions. However, Q17 shows more variability compared to Q33. The individual times Q17 (42) and Q33 (22) are consistent with their respective datasets, as they fall within the confidence intervals.

The overlapping confidence intervals for Q19 and Q35 indicate some similarity in their distributions. However, Q35 shows slightly more variability compared to Q19. The individual times Q19 (10) and Q35 (115) are outliers, indicating significant deviations from the central tendencies.

The confidence intervals for Q21 and Q37 also

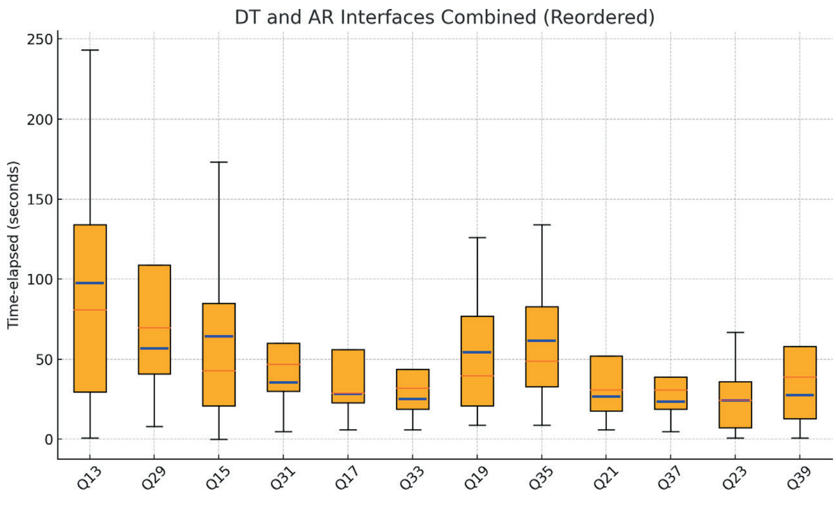

Fig. 10 DT and AR interfaces time.

overlap, suggesting similar distributions. However, Q37 shows more variability compared to Q21. The individual times Q21 (14) and Q37 (8) are outliers, indicating significant deviations from the central tendencies.

For Q23 and Q39, the overlapping confidence intervals indicate similarity in their central tendencies. However, the Q23 dataset shows much higher variability than the Q39 dataset. The individual time Q23 (29) is consistent with its dataset, while Q39 (67) is an outlier, highlighting the difference in the presence and impact of outliers.

The comparisons consistently show that datasets within both groups (DT and AR) have overlapping confidence intervals, indicating similar central tendencies. Variability differences are noted within each comparison, highlighting how some datasets exhibit a greater spread in the data.

4.4 DT interface vs. AR interface: Response confidence

In both groups, the majority of participants reported high confidence levels. Group DT (Desktop Interface) showed higher confidence levels than Group AR (AR Interface). Conversely, Group AR reported higher medium confidence levels than Group DT. Both groups exhibited similar low confidence levels, with a slight increase in Group AR. This suggests that the Desktop interface may foster greater extreme confidence, while the AR interface tends to produce more medium confidence responses (Fig.11).

4.5 DT interface vs. AR interface: Post-survey

4.5.1 Rate your ease of perceiving the horizontal position of the selected points in raw MBES data using DT / AR data visualization interfaces

The DT interface received higher "Very Easy" ratings than the AR interface, indicating that more participants found the DT interface very easy to use. However, the "Easy" ratings favored the AR interface. Both interfaces were very close when combining "Easy" and "Very Easy" ratings, with a slight preference for AR.

The standard deviation for "Easy" and "Very Easy" ratings was higher, indicating more response variability. The average rating for "Easy" and "Very Easy" was almost identical between the DT and AR interfaces.

The "Normal" ratings were fairly close between the two interfaces, with a slight preference for DT. The "Difficult" ratings were slightly higher for the AR interface, and the "Very Difficult" ratings were very close, with a slight preference for DT. The combined "Difficult" and "Very Difficult" ratings were also close, with a slight preference for the AR interface.

Overall, participants rated the AR interface slightly higher for ease of use in the "Easy" and "Very Easy" and "Difficult" and "Very Difficult" categories. In contrast, the DT interface was preferred slightly more for "Normal" ratings.

Table 1 DT (Question 25) vs. AR (Question 41) post-survey results.

	DT Interface (Q25)	AR Interface (Q41)
Very Easy	4	1
Easy	14	18
Normal	14	12
Difficult	8	10
Very Difficult	2	1

4.5.2 Rate your ease of perceiving the vertical position (depth) of the selected points in raw MBES data using DT / AR data visualization interfaces.

The AR interface's "Easy" and "Very Easy" ratings are slightly higher than the DT interface's. The DT interface's "Normal" ratings are close but slightly favor the AR interface. The DT interface's "Difficult" and "Very Difficult" ratings are identical.

Table 2 DT (Question 26) vs. AR (Question 42) post-survey results.

	DT Interface (Q26)	AR Interface (Q42)
Very Easy	5	11
Easy	26	22
Normal	8	6
Difficult	3	3
Very Difficult	0	0

The average rating for "Easy" and "Very Easy" is nearly identical, with a slight preference for AR, while "Normal" ratings show a slight preference for DT. The "Difficult" and "Very Difficult" ratings are the same for both interfaces. The standard deviation for "Easy" and "Very Easy" is low, indicating consistent responses. "Normal" ratings also show low variability, and "Difficult" and "Very Difficult" ratings have no variability since they are identical for both interfaces.

Overall, participants rated the AR interface slightly higher for ease of use in the "Easy" and "Very Easy" category. In contrast, the DT interface was somewhat preferred for "Normal" ratings, with no difference in the "Difficult" and "Very Difficult" category.

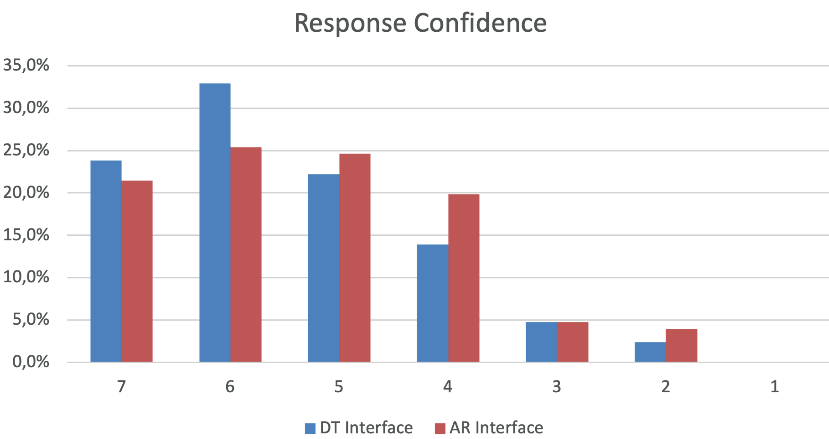

Fig. 11 DT and AR interfaces time.

https://doi.org/10.58440/ihr-31-1-a05

4.5.3 Rate your ease of identifying whether the selected points are considered spurious data in raw MBES data using AR / DT data visualization interfaces.

The AR interface's "Easy" and "Very Easy" ratings are slightly higher than those of the DT interface, while the DT interface's "Normal" ratings are higher than those of the AR interface. Similarly, the AR interface's "Difficult" and "Very Difficult" ratings are slightly higher than the DT interface's.

Table 3 DT (Question 27) vs. AR (Question 43) post-survey results.

	DT Interface (Q27)	AR Interface (Q43)
Very Easy	0	2
Easy	12	13
Normal	20	16
Difficult	6	9
Very Difficult	4	2

The average rating for "Easy" and "Very Easy" is higher for the AR interface, the "Normal" rating is higher for the DT interface, and the "Difficult" and "Very Difficult" ratings are higher for the AR interface. The standard deviation for "Easy" and "Very Easy" is relatively low, indicating consistent responses, while the "Normal" rating shows more variability. The "Difficult" and "Very Difficult" ratings have low variability.

Overall, participants rated the AR interface slightly higher for ease of use in the "Easy" and "Very Easy" and "Difficult" and "Very Difficult" categories. In contrast, the DT interface was preferred for "Normal" ratings.

4.5.4 Rate your ease of identifying whether the selected points belong to the structure of the sunken ship in raw MBES data using AR / DT data visualization interfaces.

The AR interface has higher "Easy" and "Very Easy" ratings than the DT interface, while the DT interface has higher "Normal" ratings. The AR interface has higher "Difficult" and "Very Difficult" ratings.

The average rating for "Easy" and "Very Easy" is higher for the AR interface, the "Normal" rating is higher for the DT interface, and the "Difficult" and "Very Difficult" ratings are higher for the AR interface. The standard deviation for "Easy" and "Very Easy" is relatively low, indicating consistent responses, while the "Normal" rating shows more variability. The "Difficult" and "Very Difficult" ratings also have more variability, indicating a more comprehensive range of responses.

Overall, participants rated the AR interface higher for ease of use in the "Easy" and "Very Easy" and "Difficult" and "Very Difficult" categories. In contrast, the DT interface was preferred for "Normal" ratings.

Based on post-survey results, most participants rated tasks in the AR interface as either "Easy" and "Very Easy" or "Difficult" and "Very Difficult". In contrast, tasks in the DT interface were predominantly rated as "Normal".

Table 4 DT (Question 28) vs. AR (Question 44) post-survey results.

	DT Interface (Q28)	AR Interface (Q44)
Very Easy	1	4
Easy	14	15
Normal	23	14
Difficult	2	6
Very Difficult	2	3

4.6 Exit survey

Based on exit-survey results, most participants preferred the desktop interface for spatial horizontal positioning, identifying parts of ships, and inspecting (exploring) the dataset, with fewer finding no difference and the least preferring the AR interface. However, for spatial vertical positioning (depth), preferences were similar between the desktop and AR interfaces, with a slight majority favoring the desktop (Fig.12).

4.6.1 AR bathymetric data visualization prototype usefulness

The results of the question asking the participants' opinion about the usefulness of the AR bathymetric data visualization prototype used in the experiment in everyday hydrographic office workflow show that a significant majority (90 %) believe the prototype would be useful. However, 82.5 % think it requires refinements. Only a few (7.5 %) are unsure about the prototype's usefulness. Another small portion (7.5 %) believes the prototype is useless (Fig.13).

4.6.2 Open-ended question: In your opinion, which affordances of the AR interfaces do you perceive to best support the hydrographic office's data operations?

By the answers to the question, the volunteers indicate that, in their opinion, the affordances of AR interfaces that best support the hydrographic office's data operations include the practicality of viewing data anywhere without needing to be at the collection site and the ease of sharing data instantly by uploading it to the cloud. AR provides a better definition of data discrimination, especially in vertical viewing, and offers freedom of action with familiar image manipulation for mobile users. It enhances simulation and training, improves visualization, and provides contextual information, making distinguishing and understanding features easier. The ability to manipulate the 3D model and the improved top view of the model are also notable benefits. AR supports spatial interaction and user mobility, allowing for better viewing angles and different locations outside the office. It

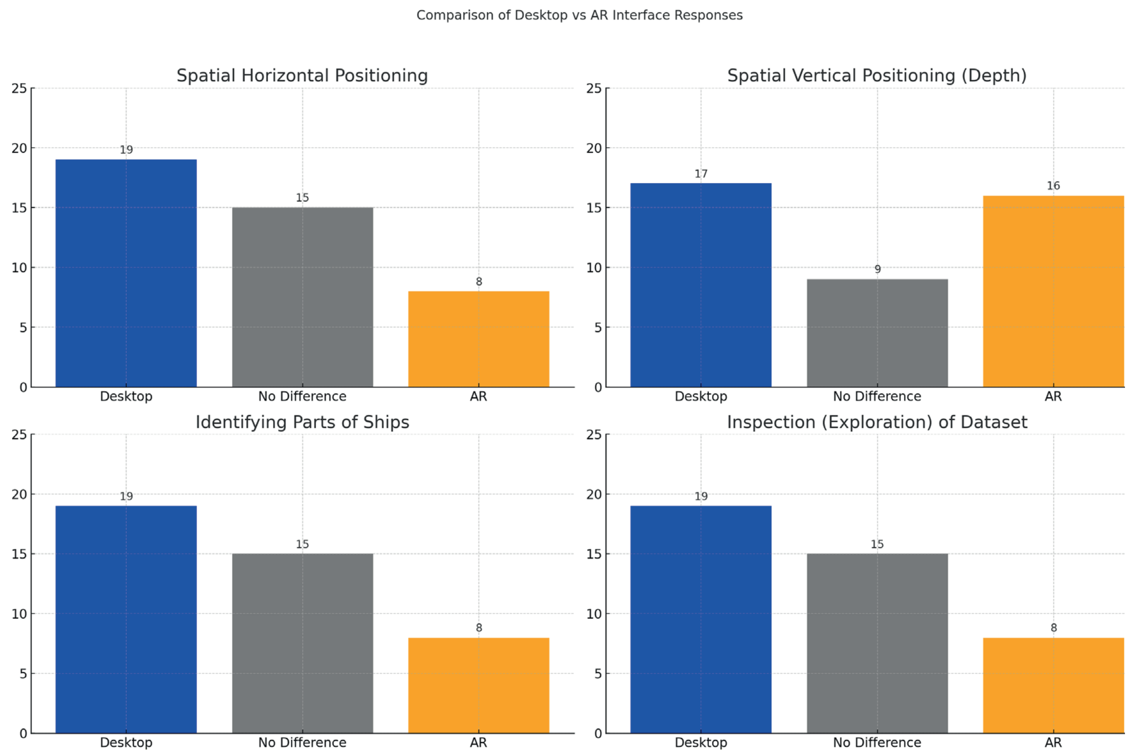

Fig. 12 Exit survey results graph.

facilitates group visualization and interaction, serves as an alternative tool for visualization and display of results, and enhances collaborative experiences—the anchoring on the surface aids in understanding vertical points and terrain behavior. AR interfaces offer greater mobility, making them useful anywhere, and can motivate data analysis by transforming tasks into interactive experiences and overlaying contextual information onto the user's environment.

4.6.3 Open-ended question: In your opinion, which characteristics of AR-based data visualization do you perceive to undermine hydrographic data visualization or to be challenges that need to be overcome?

By the answers to the question, the volunteers indicate that, in their opinion, the challenges and characteristics of AR-based data visualization that may undermine hydrographic data visualization include the need for a specific environment with proper lighting to ensure clear viewing and the impact of ambient brightness and reflections. Users highlighted issues with the size and resolution of the points in point clouds and the limited ability to zoom in on parts of the object. Screen size is challenging, especially when mobile devices have low color contrast and reduced zoom capacity. Accessibility and maneuverability of devices and the longer time required to analyze data were also noted as concerns. The need for user training, familiarization with AR devices, and the infrastructure costs for acquiring and maintaining the technology were identified as significant barriers. Additionally, the dependency on a reference surface, the necessity to maintain environmental control, and the higher reliability and ease of data manipulation in desktop interfaces compared to AR were mentioned. Overall, the need for a specific physical space and environment, high costs, and adequate contrast and lighting are significant challenges that must be addressed to improve AR-based hydrographic data visualization.

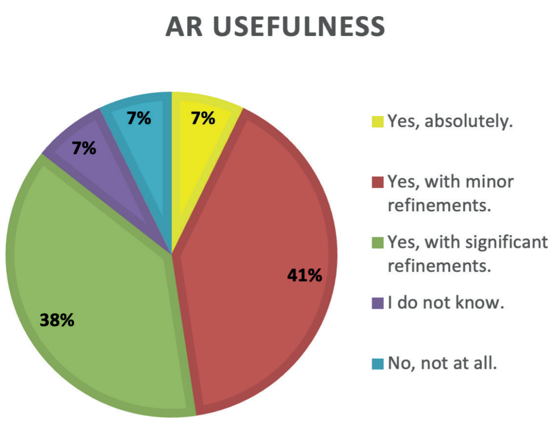

Fig. 13 AR usefulness results graph.

4.6.4 Open-ended question: Is any other feedback would you like to share about these DT / AR interfaces in your workflow?

By the answers to the question, the volunteers indicate that, in their opinion, feedback on the DT/AR interfaces includes the need for options to change vertical exaggeration and axis presentation to identify the grid. While AR might not be practical for large volumes of work, it could benefit specific visualizations at data collection sites, mainly where desktop

https://doi.org/10.58440/ihr-31-1-a05

infrastructure is unavailable. Using a headset with AR devices was suggested for enhanced interaction. However, AR requires specific physical space, which may not align with the typical hydrographic office setup, making it more suitable for visualizing particular cases rather than everyday data analysis. There were calls for functionality to vary the size of cloud points, change scale, adjust color bands, and use larger screens or headsets for better visualization. AR's 3D viewing capability made data interpretation more straightforward, and its potential for training and education was highlighted. It was also suggested that the tool be expanded to VR. Although the DT interface was favored for broad model viewing due to its higher resolution and dark background, AR was preferred for detailed viewing of small features. While adjustments are needed to make AR viable for hydrographic environments, it could significantly impact bathymetric data analysis and other hydrographic services.

4.7 Study's limitations

This research presents several limitations that should be considered when interpreting the findings. First, as an intentionally exploratory study, the primary objective was to identify patterns and generate insights rather than to produce statistically generalizable results. The sample size was limited to the number of qualified personnel available at the Brazilian Navy Hydrographic Office. The study was conducted using only the materials and mobile devices available at the hydrographic office, reflecting a low-cost, practical approach but restricting the range of interface technologies and display configurations that could be tested. The AR prototype used was also an early-stage model, which may not reflect the usability or responsiveness of more mature commercial systems. Furthermore, time constraints required that each participant complete the tasks within a limited time window, potentially impacting the depth of exploration and the accuracy of responses. Lastly, the absence of standardized usability questionnaires, such as SUS (System Usability Scale), and the exclusive use of descriptive statistics limit the study's capacity to offer stronger inferential conclusions. These aspects are important considerations for future research aiming to build upon this initial investigation.

5 Discussion

Beyond the quantitative findings, the qualitative feedback collected in this study provided valuable context for interpreting the observed differences between the AR and desktop interfaces. Participants' reflections offered insights into how the tabletop AR interface influenced their spatial perception and task performance—core aspects of the study's central hypothesis. Comments frequently highlighted the clarity of spatial relationships and the sense of immersion when using AR, suggesting potential advantages in perceiving depth and navigating complex structures. At the same time, participants noted challenges such as the novelty of the interface, the need for more familiarization time, and occasional discomfort or instability when handling the device. This feedback offered a nuanced understanding of how users experienced each interface, revealing factors that may affect usability and adoption in operational settings. By capturing user attitudes and contextual observations that quantitative measures alone cannot fully explain, the qualitative data enriched the overall analysis and pointed to important considerations for future interface development and research.

5.1 Background experience

Based on the distribution of experience levels in desktop interfaces, most volunteers participating in the experiment will likely possess significant proficiency and familiarity with desktop interfaces. Specifically, with 62 % of respondents identifying as either "Advanced" or "Expert", it was reasonable to expect a high baseline level of performance and understanding of complex data visualization tasks among the volunteers. Likewise, low performance was expected when using the AR interface since most volunteers had little or no experience.

5.2 Tasks score

Due to the results of the scores, both the Desktop and Augmented Reality interfaces are perceived positively for visualizing and analyzing 3D Bathymetric data models, with high central tendencies towards the upper end of the scoring scale. The data collected in the background survey initially suggested that volunteers would have a high baseline level of performance and understanding of complex data visualization tasks. It was also expected that their performance would be lower when using the AR interface, given that most volunteers had little or no prior experience with it. However, the results partially contradicted these expectations, as the performances turned out to be similar across both conditions.

The AR interface, in particular, shows slightly higher average scores and less dispersion in several questions (Q29, Q31, Q33, Q37 and Q39), suggesting a marginally better overall performance when they need to perceive the horizontal or vertical position of the points, whether they are spurious data or not, including whether they are part of the ship's structure. Together, these findings suggest that while both DT and AR interfaces are effective, the AR interface may offer a more consistent and enhanced user experience for specific tasks such as perceiving the spatial positioning of points, identifying spurious data, and distinguishing elements of the ship's structure.

5.3 Tasks time-elapsed

In the analyses of time elapsed during tasks, the DT Group demonstrated higher variability and more extreme values in response times, particularly for questions like Q13 and Q15, questions that ask the volunteer to consider whether the colored points are spurious or part of the sunken ship. By contrast, the AR Group exhibits more consistent and narrower distributions, suggesting a more uniform user experience with AR interfaces. Again, contrary to what one might expect from performance, in terms of speed, both interfaces presented comparable duration times. The greater experience with the DT interface on the part of the volunteers did not translate into a shorter analysis time, just as the lesser experience with the AR interface did not translate into a more extended analysis time either.

The analysis uses Neyman confidence intervals to compare datasets within and between the DT and AR groups, highlighting distribution similarities and identifying significant outliers.

5.4 Post-survey and exit-survey

The desktop (DT) interface was generally preferred for spatial tasks, particularly horizontal positioning, identifying parts of ships, and dataset exploration. This preference indicates that participants found the desktop interface more reliable and manageable for these specific tasks, probably due to familiarity, or convention. However, the preference was well-balanced when considering vertical positioning.

The AR interface received polarized responses about the overall task difficulty ratings, with participants rating tasks as either "Easy" and "Very Easy" or "Difficult" and "Very Difficult". This polarization may suggest that while some participants found the AR interface highly intuitive and efficient for specific tasks, others struggled significantly. On the other hand, the DT interface received predominantly "Normal" ratings, indicating a more consistent and moderate user experience.

Some possible explanations for why participants might rate AR and DT interfaces differently regarding ease of use, might include immersion, familiarity, learning curve, cognitive load, and user preferences.

5.4.1 Unpacking the potential benefits of AR and being mindful of subtleties

AR provides a more immersive and interactive experience, which could make perceiving points more straightforward and intuitive. One of the most powerful characteristics of AR is its ability to bring digital 3D objects, such as bathymetric data visualizations, into everyday spaces and robustly anchor them to physical surfaces using tracking, registration, and rendering. This spatial integration means that 3D data is no longer confined to a 2D display interface but can be seamlessly combined with the real-world workspace, particularly the hydrographic desk workspace. This integration leverages the importance of proprioceptive cues, which have been demonstrated to enhance geographic learning in the earliest examples of AR (Singh & Ahmad, 2024).

The significance of AR lies in its ability to combine virtual and real 3D spaces, providing perceptual benefits for users. By experiencing digital content within a real-world proprioceptive context, users of robust AR visualization systems can achieve higher "Easy" and "Very Easy" ratings, reflecting their opinions and reinforcing the intuitive nature of AR. This integration not only enhances productivity and data interpretation but also creates more interactive and immersive work experiences (Shelton & Hedley, 2002, 2004).

It is also worth commenting on the fact that AR visualization experiences can take several forms, and be achieved using a variety of spatial computing-enabled display devices. In this particular case, we used simple natural feature tracking via the Sketchfab application, which is made accessible by the use of a hand-held Android mobile device (smartphone). Using such a configuration allows the user to use a phone (or, for that matter, a tablet) function as a 'lens' through which the user may view the real world, 'augmented' with virtual content (in this case, the point clouds of the GB Church and HMCS MacKenzie). An alternative to this approach would be to use an AR-enabled head-mounted display. Such as a Meta Quest 3 with pass-through MR or pass-through AR. While the 3D virtual content (point cloud visualization) would stay the same, the user's experience of it would be through the headset attached to their head. And, because the headset optically fills the user's field of view (typically using a gasket around the 'goggles'), the user's only field of view is augmented. This contrasts an 'AR lens' metaphor using smartphones and tablets - where the user can see both AR views through the device, at the same time as the unmodified view of the real world all around. The head-mounted pass-through AR or MR approach may feel more elegant and integrated (and hands-free). At the same time, the AR lens approach may be more cost-effective and deployable by using everyday phones and tablets owned by users. The hand-held nature of the AR lens mode may also reinforce the proprioceptive function of the user experience by providing additional skeleto-muscular force-feedback that further calibrates the user's spatial perception of visualizations based on vision and vestibular feedback. Quantifying the potential impact of different AR interface configurations on spatial perception and interpretation of the bathymetric datasets would be an interesting project to build upon the current work.

5.4.2 Familiarity with DT Interfaces

Background results showed that participants are more accustomed to DT interfaces for standard or routine tasks, which could explain their preference to rate the tasks as "Normal". In other words, the familiarity and traditional use of DT interfaces might make them more comfortable with regular or less challenging tasks. On the other hand, background results showed that participants are less accustomed to AR, which could result in difficulties while handling the mobile device, resulting in higher ratings in the "Difficult" and "Very Difficult" category. This raises an interesting question for future work: Would the

https://doi.org/10.58440/ihr-31-1-a05

performance differ if participants had equal previous experience?

5.4.3 Learning curve and adaptability

The AR interface might have a steeper initial learning curve but offers superior ease of use once participants become accustomed to it, leading to higher ratings in the "Easy" and "Very Easy" categories. Participants also highlighted this issue that needs to be overcome to properly implement the interface in the routine activities of a hydrographic office.

The more familiar DT interface might have a lower learning curve but lacks AR's advanced visualization capabilities, making it preferred for everyday tasks but less effective for both "Difficult" and "Very Difficult" tasks.

5.4.4 Visual and cognitive load

AR interfaces can reduce cognitive load by providing a more natural and intuitive visualization, making it easier to grasp simple and complex spatial relationships (Keller et al., 2021; Teng et al., 2023). This could explain higher ratings for both "Very Easy" and "Very Difficult" tasks. For tasks that are not too simple or too complex (i.e., everyday tasks), the DT interface might be seen as more efficient and straightforward, resulting in higher "Normal" ratings.

5.4.5 User preferences and biases

The novelty and innovative appeal of AR might bias participants to rate it higher for ease of use in both simple and complex scenarios. Conversely, some participants might be biased towards traditional DT task interfaces due to long-term usage and comfort.

5.4.6 Open-ended questions

The volunteers provided largely coherent answers to the open questions. Both responses highlighted the practicality and mobility of AR in hydrographic data operations and agreed on AR's potential to enhance collaborative experiences. However, there were conflicting opinions. Some of the reasons for these differing views could be varying levels of prior experience with AR technology, differences in personal preferences for visualization methods, and the specific contexts in which individuals have used hydrographic data. Additionally, discrepancies in the perceived ease of use and the effectiveness of AR tools for particular tasks might have contributed to these differing opinions.

5.4.7 Different experiences and backgrounds and exposure to technology

According to the background survey results, although the volunteers are part of a selected group that includes hydrographers and Cartographic Engineers, they have, at some level, diverse professional experiences, educational backgrounds, and familiarity with 3D visualization technologies (Desktop and AR). These factors all influence their perceptions and opinions. For example, those with more AR experience were more aware of its benefits and limitations, such as the need for specific environmental conditions or high costs. For instance, in the first answer, some volunteers emphasize the ability to view and interact with data using AR interfaces in various environments. In contrast, some highlighted in the second answer the necessity for specific environments, such as the need for proper lighting and controlled environments for effective AR visualization, noting that AR's mobility and flexibility come with certain environmental constraints.

Likewise, those who have used DT interfaces extensively may have different insights than those new to it. Experienced users might appreciate the practical benefits more, while novices might focus on the challenges and learning curve (Unwin, 2020).

5.4.8 Specific roles and responsibilities and perceived value and impact

As the recruitment process did not restrict the organization's rank or function for survey participants, volunteers probably included personnel from different ranks (it is impossible to be sure due to the anonymized aspect of the survey). Their specific organizational roles can shape an individual's opinions (Hewes, 2019). For instance, a data analyst might focus on AR's technical challenges, while a manager might emphasize its strategic benefits for operations.

Likewise, individuals might perceive the value and impact of AR differently based on how directly it affects their work. Those who see immediate benefits in efficiency and visualization might be more favorable, whereas those who encounter obstacles might be more critical.

5.4.9 Personal preferences, comfort levels, bias, and subjectivity

Individual comfort levels with new technology can vary. Some might find AR interfaces intuitive and easy to use, while others might struggle with transitioning from traditional methods. For example, the second text suggests that desktop interfaces offer higher reliability and ease of data manipulation than AR. Also, personal biases and subjective preferences can shape how individuals perceive the advantages and disadvantages of AR technology. These biases can be based on previous experiences with similar technologies or general attitudes toward technological innovation. For example, the first answer highlighted familiar image manipulation and ease of use for mobile users. In contrast, the second answer emphasized the need for user training and familiarization with AR devices.

5.4.10 Users value AR differentially

People may value or prioritize aspects of AR technology differently. Some might focus on its potential for improving data visualization and collaboration, while others might concentrate on technical challenges and usability issues. For example, both answers discuss the impact of AR on data visualization and interaction. The first answer mentions AR facilitating group visualization and interaction, emphasizing AR's advantages in providing spatial interaction and contextual information. The second answer points out challenges related to screen size, resolution, and zoom capacity, which are critical to effective visualization.

In summary, while the desktop interface was preferred for specific spatial tasks due to its perceived reliability and ease of use, the AR interface elicited mixed reactions, suggesting it might offer significant benefits for some users while posing challenges for others. This could point to the AR interface's potential for high usability in optimal conditions and highlight areas where user experience can be inconsistent and needs improvement.

5.4.11 Using experience empirical study of hydrographic AR, to inform the design of future AR-enabled hydrographic workspaces

Finally, and with an eye to future work also, some comments on the nature of the AR workspace. The AR 'workspace' background for our empirical work was a conventional tabletop desk space with a black cloth draped over it. This homogenous dark background was used to make the fine points of the point cloud perceivable (Figs. 4 and 5) and so that users were focused on the characteristics of the 3D point cloud in AR (and to avoid the potential for visual dissonance between real-world background and virtual AR overlays). We intentionally started with this basic configuration (plain background) since the present study was focused on basic task performance and specialized user audience reception and feedback rather than an investigation of visual dissonance (which will be engaged in future work).

Indirectly, the current study helps to raise a number of questions and opportunities for the future design of AR workspaces. Evolving from the homogenous dark workspace backgrounds to intentionally gridded workspace backdrops may offer to strengthen the proprioceptive function and depth cues and the potential to improve judgments of orientation, position, and dimensions of structures in 3D hydrographic point clouds. To this end, we have already begun developing prototypes of these workspaces (Fig. 14).

We believe a map table or workspace designed specifically for AR use, equipped with a gridded surface, could provide strong perceptual, spatial, and proprioceptive cues to support hydrographic interpretation. Future work to enhancing these aspects of the AR-enhanced hydrographic workspaces may aid users in accurately interpreting complex data, thereby improving overall performance and user satisfaction. This could lead to AR-enhanced hydrographic map tables in land-based facilities and in the command spaces of vessels. Future research will pursue this.In summary, the desktop (DT) interface was generally preferred for its familiarity, ease of use, and reliability in routine spatial tasks – particularly those involving horizontal positioning, ship feature identification, and dataset exploration. Its lower learning curve and consistent performance made it effective for everyday hydrographic analysis. However, it lacked the immersive and spatially intuitive (proprioceptive) qualities of the AR interface. While less familiar to most participants, the tabletop AR interface showed potential advantages in spatial perception and depth understanding, especially in tasks requiring complex 3D interpretation. Participants using AR tended to show more consistent performance and slightly improved accuracy despite mixed perceptions of ease of use. Challenges associated with the AR interface included its novelty, device handling, and a steeper learning curve. Still, for tasks involving spatial complexity and immersion, AR appears to offer perceptual and proprioceptive benefits that desktop displays cannot easily replicate. These findings suggest that each interface brings distinct strengths and limitations, and their use may be best optimized according to task type, user experience level, and operational context.

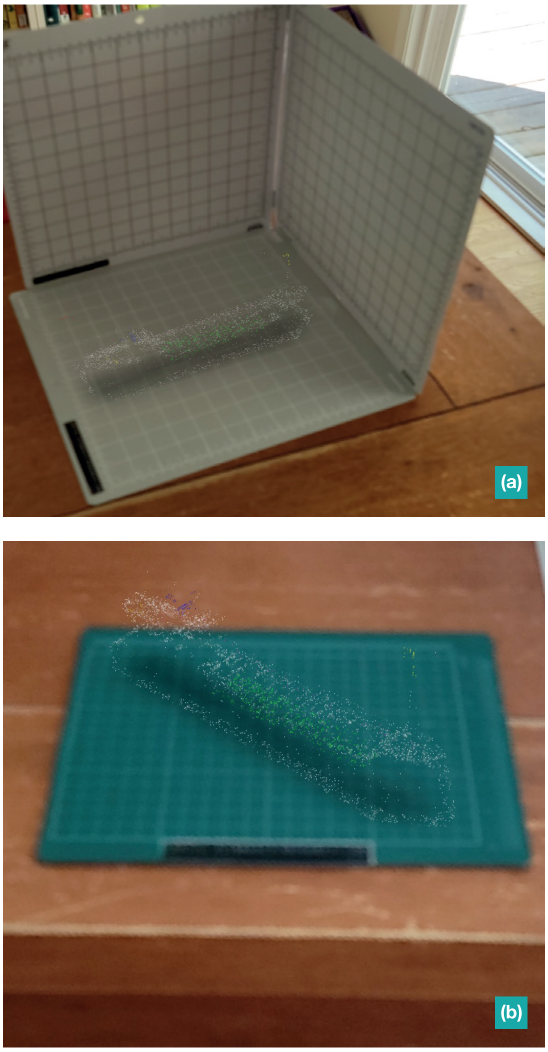

Fig. 14 AR workspace prototypes.

 https://doi.org/10.58440/ihr-31-1-a05

6 Conclusion

In conclusion, this study has provided new, valuable insights into the comparative effectiveness of tabletop AR interfaces and conventional desktop computer monitors for hydrographic practitioners' perception and interpretation of 3D bathymetric visualizations. Through a comprehensive two-phased experiment, we assessed participants' performance across both interface types as they engaged in a series of perceptual and interpretive tasks using identical bathymetric datasets.

The findings indicate that while both interfaces support the visualization of 3D bathymetric data, the AR interface may offer advantages in terms of spatial perception and depth understanding. Participants using the AR interface demonstrated slightly improved accuracy and more uniform completion times, particularly in tasks requiring detailed spatial structure analysis and depth perception. This suggests that the ability of AR to combine 3D digital data visualizations with everyday spaces offers proprioceptively powerful user experiences that may enhance hydrographic data use and interpretation nature of AR, coupled with its ability of AR to provide an intuitive and engaging visualization environment, this may enhance the user's ability to comprehend complex 3D spatial relationships.

Despite its widespread use and familiarity among practitioners, the desktop monitor was not more effective in facilitating an in-depth understanding of 3D bathymetric structures than an AR interface. Despite the limitations of the restricted field of view inherent to small mobile devices, the AR displays allowed participants to perform satisfactorily, highlighting the interface's ability to overcome the challenges faced in accurately interpreting 3D data.

These results underscore the potential of tabletop AR interfaces as a tool for hydrographic analysis, offering a promising alternative to traditional desktop-based methods. By enabling a more natural and effective interaction with 3D visualizations, AR may enhance the analytical capabilities of hydrographic practitioners, leading to more precise and informed decision-making in maritime navigation, resource management, and environmental monitoring.

Future research should explore the integration of AR interfaces with other advanced visualization and interaction technologies and the long-term impacts of AR adoption on hydrographic practices. Further exploration of how to prepare everyday spaces to maximize the proprioceptive strengths of experiencing hydrographic data visualizations via AR, should be explored. This might lead to an ability to create standardized AR hydrographic data viewing bays like "hydrographic AR holodecks". Finally, investigating user training and the development of standardized guidelines for AR interface design could further optimize the benefits observed in this study, ensuring broader and more effective application across the hydrographic community.

These findings align with emerging research in spatial interface technologies, which has shown that immersive environments such as AR and VR can enhance users' spatial awareness and interpretation of complex 3D data. Studies in geospatial and environmental visualization (Çöltekin et al., 2020; Hedley, 2017) have similarly reported that AR-based systems can support a more intuitive understanding of spatial structures when compared to flat-screen displays. In hydrography and marine science, preliminary work has begun to explore mixed reality to improve data communication and situational awareness (Jonas, 2023; Araujo & Hedley, 2023). This study contributes to that growing body of research by offering empirical evidence from a professional context, reinforcing the value of AR as a practical and effective tool for hydrographic analysis.

References

Alexander, L., Brown, M., Greenslade, B., Pharaoh, A. (2023). Development of IHO S-100 – The new IHO geospatial standard for hydrographic data. *The International Hydrographic Review, 29*(1), pp. 164-169. https://doi.org/10.58440/ihr-29-a18

Araujo, A. A. and Hedley, N. (2023). Bathymetric data visualization – A review of current methods, practices and emerging interface opportunities. *The International Hydrographic Review, 29*(2), pp. 150–163. https://doi.org/10.58440/ihr-29-2-a29

Artificial Reef Society of British Columbia (2024). GB Church. https://artificialreefsocietybc.ca/g-b-church.html (last accessed 9 June 2024).

Artificial Reef Society of British Columbia (2024). Mackenzie. http://www.artificialreefsocietybc.ca/mackenzie.html (last accessed 9 June 2024).

Azuma, R. T. (1997). A Survey of Augmented Reality. *Presence: Teleoperators and Virtual Environments, 6*(4), pp. 355–385. https://doi.org/10.1162/pres.1997.6.4.355

Billinghurst, M., Clark, A. and Lee, G. (2015). A Survey of Augmented Reality. *Foundations and Trends® in Human–Computer Interaction, 8*(2–3), pp. 73–272. https://doi.org/10.1561/1100000049

Bleisch, S. (2012). 3d Geovisualization – Definition and Structures for the Assessment of Usefulness. *ISPRS Annals of the Photogrammetry, Remote Sensing and Spatial Information Sciences, I–2*, pp. 129–134. https://doi.org/10.5194/isprsannals-I-2-129-2012

Calder, B. R. and Mayer, L. A. (2003). Automatic processing of high-rate, high-density multibeam echosounder data: Multibeam Echosounder Data. *Geochemistry, Geophysics, Geosystems, 4*(6). https://doi.org/10.1029/2002GC000486

Carmigniani, J. et al. (2011). Augmented reality technologies, systems and applications. *Multimedia Tools and Applications, 51*(1), pp. 341–377. https://doi.org/10.1007/s11042-010-0660-6

Çöltekin, A. et al. (2020). Extended Reality in Spatial Sciences: A Review of Research Challenges and Future Directions. *ISPRS International Journal of Geo-Information, 9*(7), p. 439. https://doi.org/10.3390/ijgi9070439

Duan, J., Wan, X. and Luo, J. (2021). A review of universal hydrographic data model. *Survey Review, 53*(377), pp. 183–191.

Ferreira, I. O. et al. (2022). State of art of bathymetric surveys. *Boletim de Ciências Geodésicas, 28*(1), p. e2022002. https://doi.org/10.1590/s1982-21702022000100002

Few, S. (2024). *Data Visualization for Human Perception*. Interaction Design Foundation - IxDF. https://www.interaction-design.org/literature/book/the-encyclopedia-of-human-computer-interaction-2nd-ed/data-visualization-for-human-perception (last accessed 8 June 2024).

Gomes de Araujo, L. (2024) *Potential of emerging tools and interfaces, like mixed reality, to improve the visualization and interpretation of multidimensional bathymetric data*. M.Sc. thesis. Center for Coastal and Ocean Mapping, University of New Hampshire, Durham, NH. https://ccom.unh.edu/user/3048/publications (last accessed 30 March 2025).

Hedley, N. (2017). Augmented Reality. In D. Richardson et al. (Eds.), *International Encyclopedia of Geography: People, the Earth, Environment and Technology.* Oxford, UK: John Wiley & Sons, Ltd, pp. 1–13. https://doi.org/10.1002/9781118786352.wbieg0961

Hedley, N. and Lochhead, I. (2020). Turning 3D data surveys of intertidal zones into new modes of 3D visualization, simulation and spatial interface experiences. *Int. Arch. Photogramm. Remote Sens. Spatial Inf. Sci., XLIII-B4-2020*, pp. 791–794, https://doi.org/10.5194/isprs-archives-XLIII-B4-2020-791-2020

Hewes, R. P. and Patterson, A. M. (2019). *Making the Shift from Technical Expert to Organizational Leader.* American Management Association. https://www.amanet.org/articles/making-the-shift-from-technical-expert-to-organizational-leader/ (last accessed 12 June 2024).

Holland, M., Hoggarth, A. and Nicholson, J. (2016). Hydrographic processing considerations in the "Big Data" age: An overview of technology trends in ocean and coastal surveys. *IOP Conference Series: Earth and Environmental Science, 34*, p. 012016. https://doi.org/10.1088/1755-1315/34/1/012016

International Maritime Organization (IMO) (1974). *International Convention for the Safety of Life At Sea,* 1 November, 1184 UNTS 3. https://www.refworld.org/docid/46920bf32.html (last accessed 11 July 2023).

Jo, Y. et al. (2021). Ultrahigh-definition volumetric light field projection. *Optics Letters, 46*(17), p. 4212. https://doi.org/10.1364/OL.431156

Jonas, M. (2021). IHO's Role in the Ocean Decade. *Marine Technology Society Journal, 55*(3), pp. 17–20.

Jonas, M. (2023). New horizons for hydrography. *The International Hydrographic Review, 29*(1), pp. 16–24. https://doi.org/10.58440/ihr-29-a01

Kastrisios, C. et al. (2023). Increasing Efficiency of Nautical Chart Production and Accessibility to Marine Environment Data through an Open-Science Compilation Workflow. *ISPRS International Journal of Geo-Information, 12*(3), p. 116. https://doi.org/10.3390/ijgi12030116

Keil, J. et al. (2021). Creating immersive virtual environments based on open geospatial data and game engines. *KN-Journal of Cartography and Geographic Information, 71*(1), pp. 53–65.

Kitamura, A. et al. (2014). Distribution of Attention in Augmented Reality: Comparison between Binocular and Monocular Presentation. *IEICE Transactions on Electronics, E97.C*(11), pp. 1081–1088. https://doi.org/10.1587/transele.E97.C.1081

Kitamura, A. et al. (2015). Comparison between Binocular and Monocular Augmented Reality Presentation in a Tracing Task. *The Journal of the Institute of Image Information and Television Engineers, 69*(10), pp. J292–J297. https://doi.org/10.3169/itej.69.J292

Langhorst, L. (2022). How to Choose the Right Hydrographic Processing Software: Key Considerations Before Investing. *Hydro International*, 22 March. https://www.hydro-international.com/content/article/how-to-choose-the-right-hydrographic-processing-software (last accessed 15 February 2023).

Le Deunf, J. et al. (2020). A Review of Data Cleaning Approaches in a Hydrographic Framework with a Focus on Bathymetric Multibeam Echosounder Datasets. *Geosciences, 10*(7), p. 254. https://doi.org/10.3390/geosciences10070254

Le Deunf, J. et al. (2023). Automating the Management of 300 Years of Ocean Mapping Effort in Order to Improve the Production of Nautical Cartography and Bathymetric Products: Shom's Téthys Workflow. *Geomatics, 3*(1), pp. 239–249. https://doi.org/10.3390/geomatics3010013

Lekkerkerk, H.-J. (2018). Hydrographic Surveying: Where Do We Stand? *Hydro International.* https://www.hydro-international.com/content/article/hydrographic-surveying-where-do-we-stand (last accessed 22 February 2022).

Li, Z. et al. (2023). Exploring modern bathymetry: A comprehensive review of data acquisition devices, model accuracy, and interpolation techniques for enhanced underwater mapping. *Frontiers in Marine Science, 10*, p. 1178845. https://doi.org/10.3389/fmars.2023.1178845

Lochhead, I., Hedley, N. (2021). Designing Virtual Spaces for Immersive Visual Analytics. *KN J. Cartogr. Geogr. Inf., 71*, pp. 223–240. https://doi.org/10.1007/s42489-021-00087-y

Lütjens, M. et al. (2019). Virtual Reality in Cartography: Immersive 3D Visualization of the Arctic Clyde Inlet (Canada) Using Digital Elevation Models and Bathymetric Data. Multimodal *Technologies and Interaction, 3*(1), p. 9. https://doi.org/10.3390/mti3010009

Maia, P., Florentino, C. and Pimentel, V. (2017). Fluxo de dados hidrográficos para a produção de documentos náuticos. *XXVII Congresso Brasileiro de Cartografia e XXVI Exposicarta*, Rio de Janeiro-RJ, pp. 6–10. https://www.researchgate.net/publication/333678399 (last accessed 18 November 2022).

Masetti, G. et al. (2022). Effective Automated Procedures for Hydrographic Data Review. *Geomatics, 2*(3), pp. 338–354. https://doi.org/10.3390/geomatics2030019

Mayer, L. et al. (2018). The Nippon Foundation—GEBCO Seabed 2030 Project: The Quest to See the World's Oceans Completely Mapped by 2030. Geosciences, 8(2), p. 63. https://doi.org/10.3390/geosciences8020063

Milgram, P., & Kishino, F. (1994). A taxonomy of mixed reality visual displays. *IEICE TRANSACTIONS on Information and Systems, 77*(12), pp. 1321–1329.

National Centers for Environmental Information (2024). *Hydrographic Surveys and Data Collection*. https://www.ngdc.noaa.gov (last accessed 8 June 2024).

National Oceanic and Atmospheric Administration (2024). *Nautical Charts*. https://www.nauticalcharts.noaa.gov (last accessed 8 June 2024).

Palmese, M. and Trucco, A. (2008). From 3-D Sonar Images to Augmented Reality Models for Objects Buried on the Seafloor. *IEEE Transactions on Instrumentation and Measurement*, 57(4), pp. 820–828. https://doi.org/10.1109/TIM.2007.913703

Pe'eri, S. and Dyer, N. (2018). Automated Depth Area Generation for Updating NOAA Nautical Charts. *Hydro International*, pp. 27–29.

Ponce, R. (2019). Multidimensional Marine Data: The next frontier for Hydrographic Offices. *The International Hydrographic Review, 22*. https://ihr.iho.int/articles/multidimensional-marine-data-the-next-frontier-for-hydrographic-offices/ (last accessed 30 March 2025).

Rokhsaritalemi, S., Sadeghi-Niaraki, A. and Choi, S.-M. (2020). A Review on Mixed Reality: Current Trends, Challenges and Prospects. *Applied Sciences, 10*(2), p. 636. https://doi.org/10.3390/app10020636

Shelton, B. E. and Hedley, N. R. (2002). Using augmented reality for teaching Earth-Sun relationships to undergraduate geography students. *The First IEEE International Workshop Agumented Reality Toolkit,. First IEEE International Augmented Reality Toolkit Workshop*, Darmstadt, Germany: IEEE, p. 8. https://doi.org/10.1109/ART.2002.1106948.

Shelton, B. E. and Hedley, N. R. (2004). Exploring a cognitive basis for learning spatial relationships with augmented reality. *Technology, Instruction, Cognition and Learning, 1*(4), p. 323.

Singh, G. and Ahmad, F. (2024). An interactive augmented reality framework to enhance the user experience and operational skills in electronics laboratories. *Smart Learning Environments, 11*(1), p. 5. https://doi.org/10.1186/s40561-023-00287-1

Smith Menandro, P. and Cardoso Bastos, A. (2020). Seabed Mapping: A Brief History from Meaningful Words. *Geosciences, 10*(7), p. 273. https://doi.org/10.3390/geosciences10070273

Speicher, M., Hall, B. D. and Nebeling, M. (2019). What is Mixed Reality? in *Proceedings of the 2019 CHI Conference on Human Factors in Computing Systems. CHI '19: CHI Conference on Human Factors in Computing Systems*, Glasgow Scotland Uk: ACM, pp. 1–15. https://doi.org/10.1145/3290605.3300767

Teng, J. et al. (2023). Machine learning-based cognitive load prediction model for AR-HUD to improve OSH of professional drivers. *Frontiers in Public Health, 11*, p. 1195961. https://doi.org/10.3389/fpubh.2023.1195961

Turhan, B. and Gümüş, Z. H. (2022). A Brave New World: Virtual Reality and Augmented Reality in Systems Biology. *Frontiers in Bioinformatics, 2*, p. 873478. https://doi.org/10.3389/fbinf.2022.873478

Unwin, A. (2020). Why is Data Visualization Important? What is Important in Data Visualization? *Harvard Data Science Review, 2*(1). https://doi.org/10.1162/99608f92.8ae4d525.

Value Market Research (2021). *Global Hydrographic Acquisition Software Market Report*. https://www.valuemarketresearch.com/report/hydrographic-acquisition-software-market (last accessed 13 October 2022).

Van Krevelen, D. W. F. and Poelman, R. (2010). A Survey of Augmented Reality Technologies, Applications and Limitations. *International Journal of Virtual Reality, 9*(2), pp. 1–20. https://doi.org/10.20870/IJVR.2010.9.2.2767

Ward, R., Alexander, L., Greenslade, B. and Pharaoh, A. (2008). IHO S-100: The New Hydrographic Geospatial Standard for Marine Data and Information. *Canadian Hydrographic Conference, 425*. https://scholars.unh.edu/ccom/425 (last accessed 30 March 2025).

Wlodarczyk-Sielicka, M. and Blaszczak-Bak, W. (2020). Processing of Bathymetric Data: The Fusion of New Reduction Methods for Spatial Big Data. *Sensors, 20*(21), p. 6207. https://doi.org/10.3390/s20216207

Wölfl, A.-C. et al. (2019). Seafloor Mapping – The Challenge of a Truly Global Ocean Bathymetry. *Frontiers in Marine Science, 6*, p. 283. https://doi.org/10.3389/fmars.2019.00283

Authors' biographies

Lieutenant Commander Andre A. Araujo holds a B.Sc. in Naval Science from the Brazilian Naval College and a graduate diploma in hydrography from the Directorate of Hydrography and Navigation (DHN, Brazil), recognized as an IHO Category A educational program. He earned a Master of Science degree in Geography from Simon Fraser University (SFU, Canada), where he researched "Bathymetric data visualization using extended reality in applied hydrographic operations environments." From 2015 to 2021, he served at DHN, where he developed extensive expertise in hydrographic surveying. Following the completion of his Master's degree in 2024, he resumed his professional activities at DHN, where he is currently posted.

Andre A. Araujo


Nicholas Hedley

Dr. Nicholas Hedley is an Associate Professor of geovisualization and spatial interface research in the Department of Geography at Simon Fraser University, Canada. He is a multi-disciplinary spatial visualization and spatial interface designer/developer/applied scientist and also the founding director of the Spatial Interface Research Lab at SFU. His primary interests are in 3D/4D geographic visualization, spatial interface research, spatial reality capture, and applying these methods to challenging geographic phenomena. His work also involves designing 4D geovisual analysis and simulation, to facilitate powerful ways to characterize, visualize, experience, and interact with geographic data.

https://doi.org/10.58440/ihr-31-1-a05

PEER-REVIEWED ARTICLE

Integrating data-limited techniques for maritime risk assessment in Small Island Developing States

Authors
Shivani Seepersad[1] and Dexter Davis[1]

Abstract
Maritime navigation is critical for the economic development of Small Island Developing States, yet resource constraints often hinder comprehensive risk assessments. This study developed a probabilistic risk assessment method using publicly available data, including historical traffic patterns and port call logs, to identify turning zones and traffic routes. The Monte Carlo approach and Poisson distribution were used to simulate traffic events, with vessels assumed to drift within a one-hour period. Overlapping safety zones were identified as potential candidates for drifting collisions, and fault tree analysis was used to calculate causation probabilities. The study results highlight port approaches, narrow waterways and turning zones as areas with the highest incident probability, followed by areas to the north of Trinidad and, separately, to the north of Tobago. This scalable model provides actionable insights, aiding policymakers and maritime professionals in prioritising resources and mitigating navigation risks.

Keywords
Monte Carlo simulation · probabilistic analysis · Geographic Information Systems (GIS) · drifting collisions · Small Island Developing States

Resumé
La navigation maritime est essentielle au développement économique des petits Etats insulaires en développement (PEID), mais le manque de ressources empêche souvent de réaliser des évaluations complètes des risques. Cette étude a permis de développer une méthode d'évaluation probabiliste des risques à partir de données accessibles au public, notamment les historiques des flux de trafic et les registres des escales portuaires, afin d'identifier les zones de rotation et les axes de trafic. La méthode de Monte Carlo et la distribution de Poisson ont été utilisées pour simuler les événements de trafic, les navires étant supposés dériver dans un délai d'une heure. Les zones de sécurité qui se chevauchent ont été identifiées comme des zones potentielles de collisions par dérive, et une analyse par arbre des causes a été utilisée pour calculer les probabilités de causalité. Les résultats de l'étude mettent en évidence les approches portuaires, les voies navigables étroites et les zones de rotation comme étant les secteurs présentant la plus forte probabilité d'incident, suivies des secteurs situés au nord de Trinité et, séparément, au nord de Tobago. Ce modèle évolutif fournit des informations exploitables, aidant les décideurs politiques et les professionnels du secteur maritime à hiérarchiser les ressources et à atténuer les risques liés à la navigation.

✉ Shivani Seepersad · dawn@seepersad.org
[1] Department of Geomatics Engineering and Land Management, The University of the West Indies, St. Augustine, The Republic of Trinidad and Tobago.

https://doi.org/10.58440/ihr-31-1-a06

Resumen

La navegación marítima es crítica para el desarrollo económico de los Pequeños Estados Insulares en Desarrollo (PEID), pero las limitaciones de recursos suelen dificultar la realización de evaluaciones de riesgo completas. Este estudio ha desarrollado un método probabilístico de evaluación de riesgos usando datos de dominio público, incluyendo patrones históricos de tráfico y registros de escalas portuarias, para identificar zonas de giro y derrotas de tráfico. Se usó el enfoque de Monte Carlo y la distribución de Poisson para simular los sucesos de tráfico, suponiendo buques a la deriva dentro de un periodo de una hora. Se identificaron solapes en las zonas de seguridad como posibles candidatos para colisiones a la deriva, y se usó el análisis de árbol de fallos para calcular las probabilidades de causalidad. Los resultados del estudio destacan los aproches a puertos, las vías navegables estrechas y las zonas de giro como las áreas con mayor probabilidad de incidentes, seguidas por las zonas al norte de Trinidad y, por separado, al norte de Tobago. Este modelo escalable proporciona información práctica que ayuda a los creadores de políticas y a los profesionales marítimos a priorizar recursos y mitigar los peligros para la navegación.

1 Introduction

Maritime navigation forms the backbone of economic stability, social development, and disaster resilience for Small Island Developing States (SIDS). These nations, often characterised by geographic isolation and limited terrestrial resources, rely critically on maritime transport to sustain vital industries, facilitate international trade, and ensure the timely delivery of essential goods and services, particularly in natural disasters. While crucial, this dependence on maritime activity inherently introduces navigational risks, underscoring the need for robust risk assessment and mitigation strategies. International maritime conventions, including the United Nations Convention on the Law of the Sea (UNCLOS; UN, 1982), the International Convention for the Safety of Life at Sea (SOLAS; IMO, 1974), and the International Convention for the Prevention of Pollution from Ships (IMO, 1973, 2025), advocate for coastal States to conduct comprehensive risk assessments to minimise the occurrence of maritime incidents and safeguard both human life and the marine environment.

Maritime incidents, however, persist within SIDS despite these obligations, often resulting in significant negative consequences, including economic losses, environmental damage, and loss of life. For instance, on 21 February 2010, the container ship Angeln capsized and sank 2.5 miles south-west of Vieux Port, Saint Lucia, after taking on water and developing a starboard list. While all 12 crew members were rescued, losing the vessel led to significant economic consequences, including salvage costs and the removal of 230 tons of bunker fuel (IMO, 2010). On 19 July 1979, the oil tankers Atlantic Empress and Aegean Captain collided approximately 10 miles off the coast of Tobago during a tropical rainstorm. Both vessels caught fire and began leaking oil immediately after the collision, resulting in the tragic loss of several crew members. The Atlantic Empress ultimately spilt an estimated 287,000 tonnes of oil, marking it the largest ship-source spill ever recorded (ITOPF, 2025). On 11 March 2023, the Calypso 2, a charter vessel, foundered in the coastal waters of Anguilla, resulting in the loss of two lives and being listed as a very serious marine casualty (IMO, 2024). More recently, on 7 February 2024, the tank barge Gulfstream spilt heavy fuel oil off the coast of Tobago, resulting in a Tier 2 oil spill (Trinidad and Tobago Guardian, 2024). The National Oil Spill Contingency Plan of Trinidad and Tobago categorises a Tier 2 oil spill as a medium-sized spill that can significantly impact the surrounding area. It requires regional or national support to ensure an adequate spill response (MEEA, 2013).

The Greater Caribbean Region (GCR), encompassing a diverse array of SIDS, exemplifies the challenges and vulnerabilities of maritime activity in such contexts. Within this region, Trinidad and Tobago (T and T), an archipelagic nation situated off the northeastern coast of Venezuela, serves as a microcosm of the broader maritime landscape, sharing maritime characteristics, governance frameworks, and environmental vulnerabilities. Like major Caribbean ports such as Kingston (Jamaica), Freeport (Bahamas), and San Juan (Puerto Rico), T and T's Gulf of Paria and the waters off Chaguaramas experience relatively high vessel density, diverse maritime activities (Sánchez & Wilmsmeier, 2009), and navigational hazards (NGA, 2024). Vessel tracking platforms like Marine Traffic indicate that shipping density, vessel composition, and transit patterns in T and T are comparable to trends observed throughout the region, reinforcing the applicability of a standardised risk assessment framework (MarineTraffic, 2025). Recent hazardous sea alerts issued in T and T, St. Vincent and the Grenadines, Grenada, Antigua and Barbuda, and the British Virgin Islands highlight the frequent occurrence of rough seas, long-period swells, and high surf warnings, which threaten vessel stability, disrupt port operations, and complicate oil spill response efforts (Loop News, 2024). SIDS lack the infrastructure to handle extreme weather (Muñoz & Ötker, 2018), increasing the risk of ship accidents and cargo delays. Additionally, the Institute of Marine Affairs (IMA) study identifies T and T's Gulf of Paria as a high-risk zone for ship-source pollution, where rough seas can intensify oil spill dispersal and complicate response strategies, similar to high-traffic areas across the region (Singh et al., 2015). From a governance perspective, T and T operates under the same regulatory frameworks as the broader Caribbean maritime sector, ensuring standardised risk mitigation approaches. The Caribbean Memorandum of Understanding on Port State Control (CMoU on PSC) establishes uniform vessel inspection protocols, preventing substandard operations through compliance with SOLAS, MARPOL, and the International Convention on Standards of Training, Certification and Watchkeeping for Seafarers (STCW; IMO, 1978) regulations (CMoU, 2020). The Caribbean Shipping Association (CSA) and the Caribbean Community (CARICOM) also facilitate regional cooperation on port efficiency, vessel monitoring, and sustainability initiatives (CSA, 2024). The dynamic maritime environment, shared governance structures, and risk management frameworks demonstrate that T and T's maritime space is representative of regional conditions, reinforcing its suitability as a case study for risk assessment methodologies applicable to the SIDS of the GCR.

Drifting collisions, a specific type of maritime incident which this study defines as the collision of a drifting vessel with another moving vessel, pose a significant risk within T and T's waters. Several documented incidents highlight the potential severity of such events. In February 2009, a luxury yacht went adrift along the northern coastline of Trinidad, near Blanchisseuse, during heavy rains, resulting in one fatality (Trinidad and Tobago Express, 2009). In September 2018, the partially submerged MV Treasure Queen II drifted near Pier II along the north-western coastline of Trinidad (Trinidad and Tobago Guardian, 2018). In December 2020, during rough seas, a deep-sea fishing boat drifted towards land near the south-eastern coastline in Speyside (Trinidad and Tobago Express, 2020). In May 2021, a drifting vessel, suspected to be a migrant boat, was discovered near Belle Garden Beach in south-eastern Tobago (LoopTT, 2021). In March 2022, a trawler overturned and drifted for over two hours off the western-coastline of Tobago (Trinidad and Tobago Newsday, 2022). As previously mentioned, in February 2024, the Gulfstream tanker caused a Tier 2 oil spill after drifting to Tobago's northern coastline (Trinidad and Tobago Newsday, 2024). These incidents, along with other reported occurrences involving SOLAS vessels (Rambarran, 2021) underscore the need for practical risk assessment and mitigation measures to address drifting collisions and enhance maritime safety in T and T. Historical data indicate that the northern and north-western coastlines of Trinidad, as well as waters surrounding Tobago, are particularly susceptible to such incidents. The recurrence and severity of these events – often occurring under rough sea conditions or as a result of equipment failure – highlight gaps in existing monitoring and predictive frameworks. They also emphasize the necessity for a locally adapted, data-efficient model capable of estimating where and how drifting collisions are most likely to occur. This study addresses that need by developing a probabilistic risk assessment model that simulates drifting events and estimates incident probabilities using publicly available data.

Traditional maritime risk assessment methodologies, such as those outlined in the International Organization for Marine Aids to Navigation (IALA) risk management toolbox and the OpenRisk Toolbox, often present significant challenges for SIDS due to their reliance on combinations of extensive expert judgment, proprietary datasets (e.g., AIS data, high-resolution bathymetric data), and specialised software, training and consultancy services. These requirements can be prohibitively expensive and resource-intensive for SIDS, limiting their capacity to implement such methodologies effectively. To address these challenges, this study proposes an alternative maritime risk assessment model tailored explicitly to the resource-constrained environments of SIDS, focusing on estimating the probability of drifting collisions. The model minimises data requirements by utilising publicly available data sources, including historical traffic pattern images, port call logs, and open-source traffic pattern images, while maintaining predictive accuracy. By incorporating a Monte Carlo simulation approach and fault tree analysis (FTA) within a Geographic Information System (GIS), the model enables the calculation of localised causation probabilities of maritime incidents and facilitates the construction of statistical scenarios for annual incident probability estimations.

The development and validation of this model within the context of T and T's maritime domain provide valuable insights for other SIDS facing similar challenges. The model's reliance on publicly available data and adaptability to varying maritime environments enhance its scalability and replicability. It offers a practical and cost-effective solution for maritime risk assessment in resource-constrained settings. The findings of this study contribute to a deeper understanding of maritime risks and empower policymakers, researchers, and maritime stakeholders to prioritise interventions and develop effective strategies for mitigating drifting collisions and enhancing overall maritime safety within SIDS regions.

2 Literature review

The Aids to Navigation Requirements and Management – Risk Management working group of IALA (IALA, 2025) surveyed maritime authorities worldwide to identify the risk assessment methodologies commonly used in their operations. Eighty-one

https://doi.org/10.58440/ihr-31-1-a06

responses were received, some requiring further clarification from the respective authorities. Among the usable results, 28 respondents mentioned the Simplified IALA Risk Assessment (SIRA), 21 cited the IALA Waterway Risk Assessment Program (IWRAP), ten referenced the Ports and Waterways Safety Assessment (PAWSA MK II), and two mentioned the Simulation and Analysis Model for Safety of Navigation (SAMSON). The hydrographic risk assessment approach developed by Land Information New Zealand (LINZ) was not included as a response in this survey but has been utilised by hydrographic authorities in the South-West Pacific to prioritise resources for charting. This study reviews the applicability of these tools within resource-constrained environments such as SIDS. It examines key factors such as the availability of expert judgment, access to proprietary datasets derived from automatic identification systems (AIS) and historical vessel incident databases, the role of navigational hazard data, and the need for specialised training and consultancy. The probabilistic frameworks underlying these approaches are evaluated, and complementary methods, such as Monte Carlo simulations and FTA within a GIS are examined to develop a maritime risk assessment approach tailored for SIDS.

The Simplified IALA Risk Assessment (SIRA) was the most widely used maritime risk assessment tool among the maritime authorities that completed the survey. Developed by IALA, SIRA provides a structured and resource-efficient method for conducting small-scale risk assessments based on industry best practices. It requires minimal resources for implementation and relies on stakeholder engagement and expert judgment to identify potential hazards, assess their likelihood and severity, and develop mitigation strategies. This approach offers national authorities a practical framework for initial risk assessments, particularly in resource-constrained environments. As data availability and resources improve, authorities are encouraged to transition to more advanced tools, like IWRAP and PAWSA, that apply scientifically rigorous approaches, incorporating robust data analysis, theoretical modelling, simulation techniques, and expert judgment to assess the probability and consequences of maritime incidents (IALA, 2022c).

The IWRAP is a computer-based tool for calculating the probabilities of collisions, groundings and allisions. It models waterways using geometric and bathymetric data, and analyses AIS-based traffic volumes and compositions. Annual incident probabilities are derived using causation factors, calibrated against historical data and informed by expert judgment. While IWRAP provides a robust framework for estimating probabilities, its application can be limited by its reliance on proprietary datasets and licensing requirements (IALA, 2022a). IWRAP does not quantify the consequences of incidents, and it is often complemented by tools like the Ports and Waterways Safety Assessment (PAWSA). PAWSA incorporates about forty experts' qualitative inputs during a two-day workshop to evaluate the broader consequences of maritime incidents and derive overall risk indices and options for mitigation (IALA, 2022b).

Using a comprehensive voyage database, the SAMSON model calculates accident probabilities by identifying potentially dangerous situations, termed exposures. These exposures are categorised based on traffic types, such as route-bound (e.g., merchant vessels and ferries), non-route-bound traffic (e.g., fishing or recreational vessels), and specific accident scenarios. Accident frequencies are determined by multiplying the calculated exposures by casualty rates, which are derived from global datasets, including historical accident data from Lloyd's List Intelligence. This approach enables SAMSON to estimate the probability of various maritime incidents, such as collisions, groundings, and fires. SAMSON also serves as a strategic tool for policymaking and contingency planning by evaluating the potential impact of safety measures on casualty frequencies. However, its reliance on proprietary voyage datasets and the need for expert judgment can limit its accessibility, particularly for resource-constrained environments (MARIN, n.d.).

Within the LINZ method, the likelihood of an incident at sea is determined by analysing vessel traffic density acquired from AIS data and identifying hazards that could result in loss of life and/or pollution. These consequences are represented spatially within a GIS and combined with likelihood using weighting factors to calculate risk. This methodology, fully documented by Riding & Rawson (2015) for GIS implementation, aims to produce a heat map across the entire waterway to prioritise resource allocation effectively. However, the method requires extensive representation of waterway features within a GIS and relies on expert judgement – resources that are not always readily available within SIDS.

The framework underpinning these probabilistic maritime risk assessment approaches is based on the formula $NC = NA \times PC$ where NC is the geometric probability, NA represents the geometric number of vessel encounters assuming blind navigation, and PC denotes the causation probability of such incidents (Fujii, 1971; MacDuff, 1974). This review highlighted the challenges of applying existing maritime risk assessment approaches in resource-constrained environments. Traditional approaches like IWRAP, SIRA, PAWSA, SAMSON, and the LINZ method, as well as those utilising Monte Carlo simulation techniques rely on combinations of extensive proprietary datasets, licensing requirements, and costly training or consultancy fees. It should be noted that risk assessment methods are designed to achieve different objectives, and therefore, results across methods are not always directly comparable. Table 1 presents a comparative summary of the reviewed methodologies. It contrasts each model based on key factors such as data requirements, reliance on expert judgment,

Table 1 Applicability of maritime risk assessment models in resource-constrained environments.

Model	Data requirements	Expert judgment	Implementation cost	Analytical depth
SIRA	Low (basic charts, stakeholder input)	Low (few experts required)	Medium (training)	Qualitative
IWRAP	High (terrestrial AIS data, bathymetry, historical incidents)	Low (at least one trained expert required)	Medium to high (training and software license)	Quantitative
PAWSA	Medium (charts, information related to 24 risk factors)	Very high (40 experts, workshops)	High	Qualitative
SAMSON	High (global voyage databases)	Medium	Medium to high (consultancy fee)	Quantitative
LINZ	High (GIS layers, AIS data)	Medium to high	Medium to High	Quantitative
Proposed Model	Low (public traffic images, port calls, open data)	Low to medium (root cause data, software expertise)	Low	Quantitative

implementation cost, and suitability for SIDS. This comparison illustrates that while tools like IWRAP and SAMSON offer high analytical precision, they may not be feasible in regions with limited access to proprietary AIS datasets, large expert panels, or budgetary capacity for training and consultancy. SIRA remains highly applicable to such regions; however, it is intended primarily as a basic tool to identify risk control options. In contrast, the proposed model prioritises simplicity, accessibility, and probabilistic analysis, making it especially suitable for small maritime administrations operating with minimal resources.

2.1 Estimation of the geometric number of incident candidates

Monte Carlo simulations estimate NA by dynamically modelling vessel traffic patterns and simulating ship domains to identify and count potential incident candidates. By incorporating probabilistic inputs such as encounter angles, vessel speeds, and traffic density, these simulations replicate real-world scenarios to identify critical encounters. To model discrete events such as vessel encounters, Monte Carlo techniques are adaptable to various probability distributions, including normal and Poisson distributions. Applications of Monte Carlo simulations in maritime contexts include Przywarty (2008), who employed Poisson processes to identify critical encounters, and Goerlandt & Kujala (2010), who used traffic scenarios to estimate incident probabilities. Recent advancements highlight the versatility of Monte Carlo methods, such as integrating them with machine learning models (Vukša et al., 2022) or semi-Markov processes (Bogalecka & Dabrowska, 2023). Despite these innovations, their application in resource-constrained environments such as SIDS remains limited due to similar challenges, including extensive data and computational resource requirements.

2.2 Estimation of the causation probability

FTA is a deductive method that models the sequence of events leading to incidents. It begins with a top event, such as a collision, and traces its root causes through a hierarchical structure of basic events connected by logic gates. Probabilities are assigned to these basic events, enabling the calculation of the top event probability (Haugen & Kristiansen, 2023). FTA was chosen for this study because it is simple to construct, data-efficient, and adaptable to resource-constrained contexts like SIDS. Its structured framework facilitates the integration of human, technical, and environmental factors into the model, aligning with the study's goal of developing a practical and replicable methodology for SIDS. The reliability and versatility of FTA have been extensively validated, as highlighted by the National Aeronautics and Space Administration (NASA) Office of Safety and Mission Assurance (NASA 2002), underscoring its effectiveness in modelling complex systems and quantifying failure probabilities. Causation probabilities in the FTA model are influenced by human errors (e.g., inattentiveness), technical failures (e.g., equipment malfunctions), and environmental conditions (e.g., low visibility) (IALA, 2009). These factors are modelled using historical data from the public domain, such as incident reports and records from national authorities. Unlike Bayesian Networks (BNs), which require extensive conditional probabilities and datasets, FTA allows for simplified assumptions without compromising analytical accuracy.

Traffic events simulated using the Monte Carlo technique do not account for the impact of risk mitigation measures which are globally recognised as critical safety measures that significantly reduce collision probabilities. For instance, pilotage in regions like the Great Belt and Turkish Straits has been demonstrated to reduce incident risks by up to 59 times. The causation factor value can be adjusted accordingly to incorporate the effect of these measures (IMPA, 2022). In addition to pilotage, other risk reduction measures, such as operational procedures, are widely recognised as effective in enhancing maritime safety. However, the literature has not extensively quantified their precise impact on incident probabilities. When using IWRAP, IALA recommends adjusting the causation factor value based

https://doi.org/10.58440/ihr-31-1-a06

on historical incident data to align model outputs with observed accident frequencies. IALA further advises that any adjustments to the causation factor should be documented to ensure transparency and reproducibility in risk assessments. While this approach is not strictly scientific, it serves as a practical solution in the absence of a more precise method (IALA, 2024).

This review highlighted the challenges of applying existing maritime risk assessment approaches in resource-constrained environments. Traditional approaches, such as IWRAP, SIRA, PAWSA, SAMSON, and the LINZ method, as well as those utilising Monte Carlo simulation techniques to assess NA, relied on combinations of extensive proprietary datasets, licensing requirements, and costly training or consultancy fees. It is worth noting that risk assessment methods are designed to achieve different objectives, and therefore, results across methods are not always directly comparable (Seepersad et al., 2020).

3 Methodology

This study addresses the limitations of traditional maritime risk assessment tools by leveraging publicly accessible data and structured modelling techniques to enhance accuracy and scalability. The methodology provides a computationally efficient and representative framework for modelling vessel movements, making it particularly suitable for resource-constrained environments. The methodology integrates Monte Carlo simulations to estimate the geometric number of drifting collision candidates (NA) and FTA to model causation probabilities (PC), unifying these components within the probabilistic framework (NC = NA × PC).

3.1 Data collection and sources

To address the challenge of limited AIS data, this methodology incorporated an alternative approach using traffic pattern images published on open-source platforms such as Marine Traffic. These images substitute AIS data from terrestrial or satellite systems when unavailable, ensuring maritime traffic modelling remains possible. For such cases, port call logs for one month can be analysed to estimate the frequency of vessel arrivals. The resulting data can then be scaled to represent an annual dataset, assuming no significant seasonal variations in traffic patterns. This scaling approach, also utilised in IWRAP, is designed for computational efficiency, enabling streamlined analysis without requiring complete year-round datasets (IALA, 2024). Historical data on vessel incidents were gathered through correspondence with the Navigational Aids Officer at the Maritime Services Division of T and T (Rambarran, 2021) and supplemented by reports from local newspapers. Human, technical, and environmental factors required for developing the fault tree were sourced from existing literature, including environmental data from the T and T Meteorological Office website. The modelling process was facilitated using ArcGIS Pro version 3.1.2, which utilizes the Model Builder environment and the integrated Python 3.9 interpreter for spatial analysis. ArcGIS Pro offers monthly subscription options, making it accessible and cost-effective for resource-constrained applications.

3.2 Simulation of the geometric number of drifting collision candidates

The process of modelling vessel movements to identify the geometric number of drifting collision candidates consists of eight major steps. These steps are summarised in Table 2. Fig. 1 depicts traffic patterns for 2023 obtained from MarineTraffic (2025), which were analysed to identify commonly utilised traffic routes for each port, with AIS data used as an alternative when available. Turning zone boundaries along these routes were delineated and stored as individual records in a polygon feature class, ensuring that each traffic route and related turning zones were uniquely identified. A random selection of traffic event identifiers was performed to ensure a diverse sample of vessel movements (refer to step 1 in Table 2). At this stage, a traffic event was a randomly selected vessel transit instance, identified from traffic pattern images or AIS data. After selection, each event was assigned a simulated departure time, navigation trajectory, and time-based movement data using probabilistic modelling techniques. By the end of the process, each traffic event had a complete profile – including spatial path, temporal dynamics, and safety domain – suitable for collision risk analysis. Departure times were modelled using a Poisson process, where the transit frequency (λ) was calculated based on the number of traffic events over a 24-hour epoch as shown in Eq. 1 below and step 2 in Table 2.

$$\lambda = \frac{N}{T \times 3600} \tag{1}$$

where

λ: event rate (events per second)

N: total traffic events

T: epoch duration (24 hours)

Vessel movement through turning zones was simulated by generating waypoints within the predefined boundaries and connecting them to form continuous transit paths. Each vessel's navigation trajectory was determined by sequentially linking these waypoints (refer to step 3 in Table 2). The inter-arrival times were generated using an exponential distribution to reflect the assumption that vessel departures occur independently at a constant rate. This was implemented using the inverse transform sampling method, where the time between successive departures was calculated as shown in Eq. 2 below and step 4 in Table 2.

$$t_i = \sum_{j=1}^{i} y_i \quad (2)$$

where
t_i: timestamp of the i^{th} event
y_i: inter-arrival time (randomly generated using $\lambda = \frac{N}{T\times 3600}$, where $Uj\sim U(0,1)$ is a uniformly distributed random variable, ensuring that inter-arrival times follow an exponential pattern

The timestamps naturally spanned 17 days due to the cumulative nature of inter-arrival times and the total number of randomly selected traffic events. In real-world scenarios, however, factors such as port congestion, scheduling constraints, and environmental conditions can influence departure times, meaning vessel movements may not always adhere strictly to an exponential distribution. If structured scheduling or external constraints impact vessel traffic, alternative approaches, such as empirical distribution modelling, may be required.

Fig. 2a illustrates the simulation of a single traffic event, including the associated turning zone boundaries along a randomly selected route. Fig. 2b presents the density of traffic events after the simulation was completed. A comparison of Figs. 2b and 1 reveal similar traffic distributions. Differences in the spatial distribution of maritime traffic along the south-eastern shoreline of Trinidad are attributed to offshore installations constructed after this study, including the Galeota Port Expansion and the East Coast Marine Area (ECMA) platforms and facilities associated with British Petroleum Trinidad and Tobago's (BPTT)'s gas fields. Notably, the colour coding in Fig. 1 represents traffic density relative to global patterns, whereas Fig. 2b is scaled to the local simulation.

Following vessel track generation, feature classes were joined into a unified dataset for analysis. Track points were placed at 1,000-meter intervals to ensure that safety buffers along the same route did not overlap, simplifying the spatial representation of vessel movements (refer to step 5 in Table 2).

Table 2 Summary of the traffic event simulation process.

Step	Description	Formulae / tool used
1. Identify traffic routes and turning zones	Analyse traffic pattern images or AIS data to identify common traffic routes and turning zones. Store results in a polygon feature class and assign unique identifiers.	ArcGIS Pro: General tools were used to digitise vessel routes and turning zones as polygons. Unique IDs allow tracking of individual traffic events.
Random selection of traffic events	Randomly select traffic event identifiers from the feature class.	ArcGIS Pro – SubsetFeatures_ga: Randomly selects a subset of traffic events, introducing stochastic variation into the simulation.
2. Simulate departure times	Simulate vessel departure times using a Poisson process. Random inter-arrival times are calculated using an exponential distribution with a rate λ.	Python 3.9: Used to simulate random departure intervals based on a Poisson process. Formula: $\lambda = \frac{N}{T\times 3600}$, where λ: event rate (events per second) N: total traffic events T: epoch duration (24 hours)
3. Generate vessel trajectories	Generate waypoints within turning zones and connect the waypoints to form vessel tracks.	ArcGIS Pro – CreateRandomPoints_management: Creates waypoints in turning areas. ArcGIS Pro – PointsToLine_management: Connects the waypoints to form vessel trajectories.
4. Compute event timestamps	Compute timestamps using the cumulative sum of inter-arrival times to determine event sequence.	Python 3.9: Calculates event timestamps by summing inter-arrival times. Formula: $t_i = \sum_{j=1}^{i} y_i$, where t_i: timestamp of the ith event y_i: inter-arrival time (randomly generated using $y_i = -\frac{ln(1-U_j)}{\lambda}$, where Uj~U(0,1)
5. Generate track points and adjust temporal resolution	Join feature classes and generate points along vessel tracks at 1,000 m intervals.	ArcGIS Pro – Join: Combines relevant spatial and attribute data. ArcGIS Pro – GeneratePointsAlongLines_management: Places points along vessel tracks at specified intervals (1,000 m).
6. Simulate safety zones	Circular buffers representing safety zones were created using Fujii's Ship Domain Theory. The buffer radius was set to 1.6 times the length of the largest vessel in the dataset to account for gaps in ship attribute data.	ArcGIS Pro – Buffer: Constructs circular buffers around each vessel track point. Formula: $R = 1.6 \times L_{max}$, where R: safety zone radius L_{max}: length of the largest vessel in the dataset
7. Identify drifting collision candidates	Identify overlapping safety zones and round timestamps to hourly intervals for computational efficiency in drift collision modeling.	ArcGIS Pro – Spatial Join: Identifies where and when safety zones overlap. Python 3.9: Used to round timestamps to hourly intervals for efficient time-based collision filtering.
8. Merge overlapping safety zones and calculate overlaps	Merge all overlapping safety zones, replace null values, calculate total overlaps, and divide the study area into a 1 km² grid cell.	ArcGIS Pro – Merge: Combines overlapping buffers into single polygons. ArcGIS Pro – Field Calculator (Find and Replace): Cleans null entries. ArcGIS Pro – Fishnet Tool: Creates a 1 km² grid for spatial aggregation of overlap counts.

https://doi.org/10.58440/ihr-31-1-a06

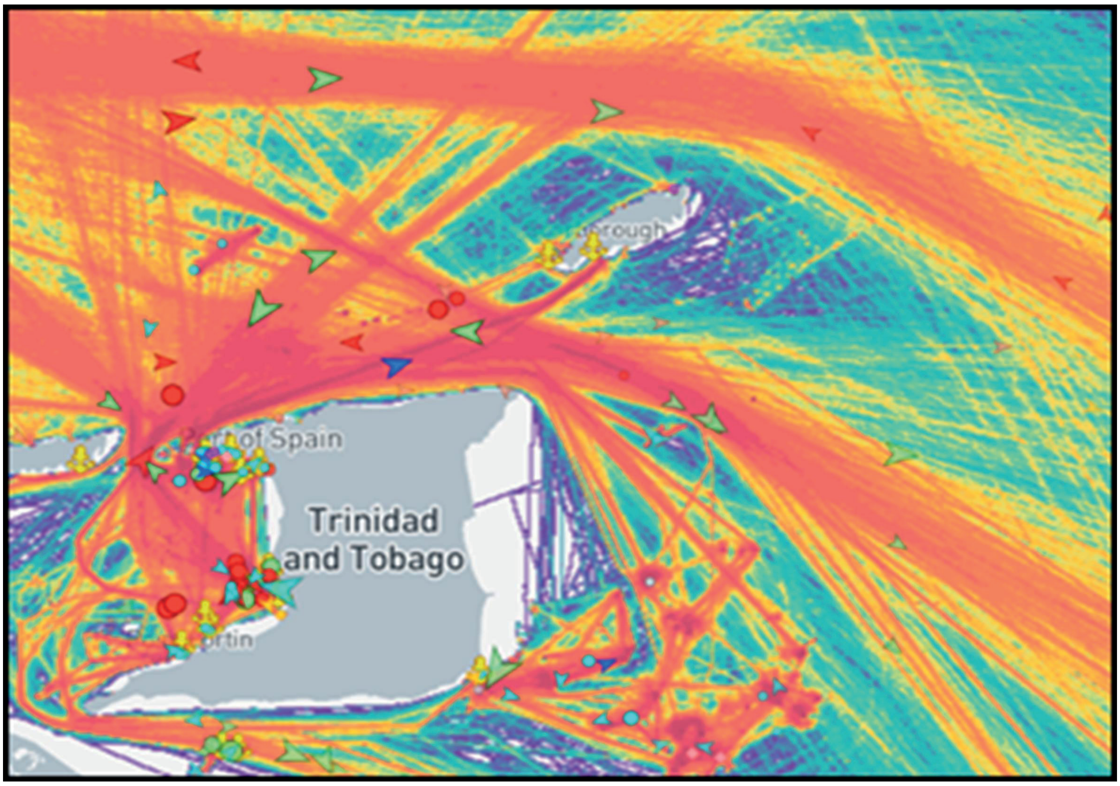

Fig. 1 Vessel traffic pattern for the year 2023 acquired from MarineTraffic (2025).

Timestamps were then adjusted to the nearest hour to more efficiently model vessel drift and potential collisions. Using hourly intervals reduced computational demands while enabling the simulation of traffic volume across multiple shipping routes within T and T's Economic Exclusive Zone (EEZ). Based on Fujii's Ship Domain Theory, safety zones were defined as circular buffers around each vessel position. Due to the uniform circular shape, no distinction was made between inbound and outbound vessel movements at port locations. As shown in Eq. 3 below and step 6 in Table 2, the buffer radius was set to 1.6 times the length of the largest vessel in the dataset to accommodate potential gaps in ship attribute data. For this study, the largest vessel measured 300 meters, resulting in a safety zone radius of 480 meters. This standardisation eliminated the need for vessel traffic attributes defined in AIS data.

$$R = 1.6 \times L_{max} \tag{3}$$

where

R: safety zone radius

L_{max}: length of the largest vessel in the dataset

Overlapping safety zones were analysed to identify drifting collision candidates (refer to step 7 in Table 2). To consolidate results, all overlapping safety zones were merged into a single dataset, and the annual number of overlaps per square kilometre was computed to quantify potential drifting collision hotspots (refer to step 8 in Table 2). The study area was then divided into a standardised 1 km² grid, ensuring that all spatial data layers remained aligned. The spatiotemporal resolution employed was deemed sufficient for capturing broader vessel movements associated with drifting, aligning with the scope of this analysis. While higher-resolution hydrodynamic data could improve the model, the selected approach prioritises scalability and computational feasibility without imposing excessive processing requirements.

3.3 Estimation of the causation probability

Historical incident reports obtained from the Maritime Services Division of T and T, alongside newspaper articles, were analysed to identify the causes of maritime incidents. These causes were categorised using the framework of causation factors outlined by IALA (2009). The probabilities associated with each cause contributing to a failed evasive manoeuvre are presented below.

- Based on historical incident data from 2018 to 2024, provided by Rambarran (2021), and national newspapers, the probability of human error aboard SOLAS-compliant vessels was estimated at 0.6 per year.
- Environmental risks, such as hazardous seas and reduced visibility, were assessed using national meteorological bulletins (2020–2022) (T and T Meteorological Service, 2025), and local interviews. Hazardous sea conditions were evaluated geographically (see Fig. 3a). Based on expert interviews, reduced visibility due to squalls was estimated to occur twice per month and last 18 minutes per event, with an annual probability of 0.0008.

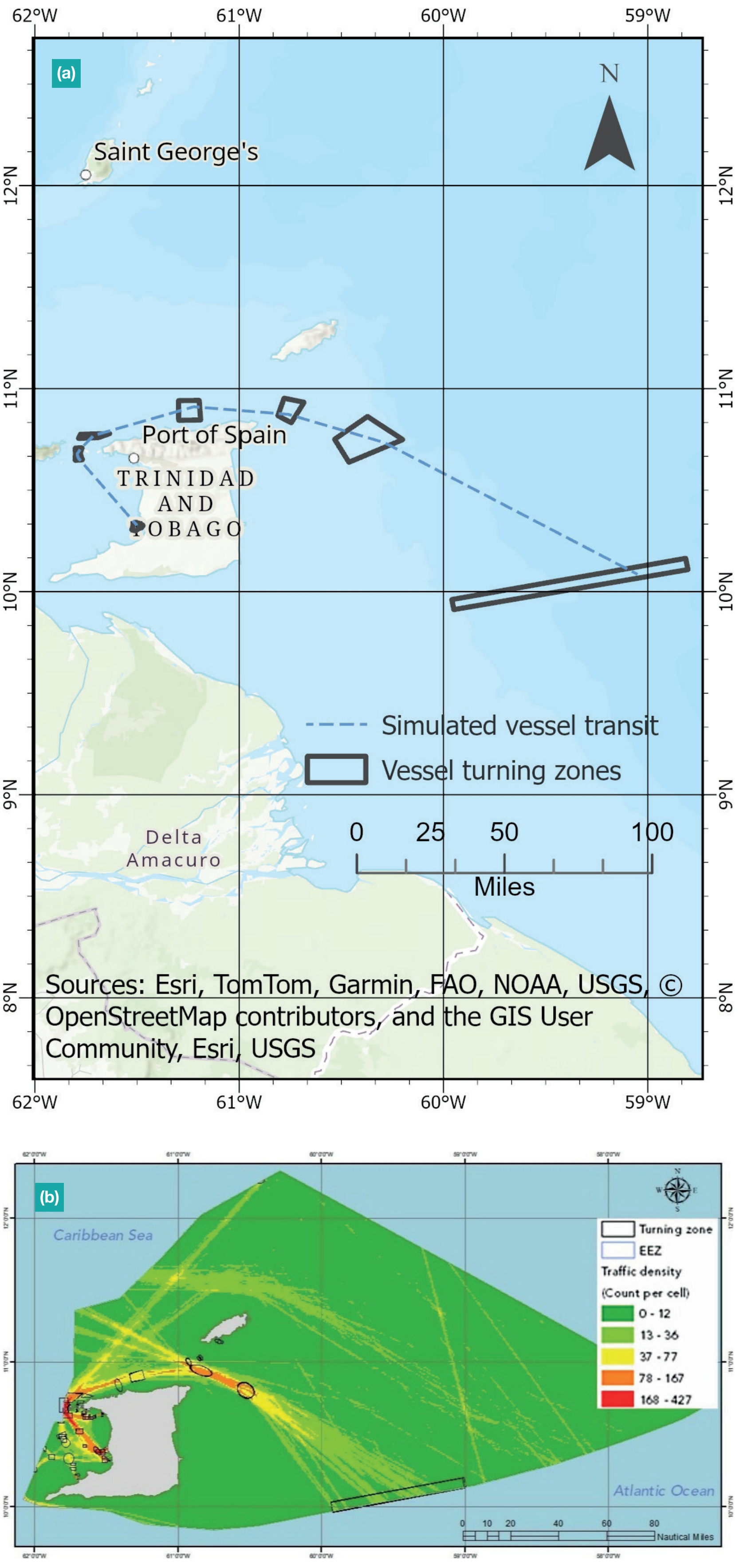

Fig. 2 One simulated traffic event and the related turning zones (a) and simulated traffic events for 17 days of simulated time (b).

- The Port State Control of Trinidad and Tobago, supported by the United States Coast Guard, assigns ship risk profiles based on type, age, Flag State, and historical detention records, following principles aligned with the Paris Memorandum of Understanding. Detention probabilities from inspections were used to estimate the probability of undesired scenarios resulting from technical deficiencies. Between 2005 and 2021, 2,031 ships were inspected, with 16 detentions, resulting in an annual average detention probability of 0.941 over the 17 years (CMoU, 2024).
- Human failure to address onboard deficiencies was modelled using a causation probability of 0.00001, based on Kirwan's (1994) research on operator performance for well-designed tasks, as cited in the relevant literature on the IALA webpage. This value represents the probability of failure to repair the drifting scenario before the occurrence of the undesired event.
- The probability of Marine Aids to Navigation (AtoN) failure was calculated using IALA standards for Category 1 AtoN, which require 99.8 % availability (equivalent to one day of downtime annually) (IALA, 2004). This results in a failure probability of 0.0027, applied spatially to AtoN nominal ranges (see Fig. 3b) listed in the Pub 110: List of Lights, Radio Aids, and Fog Signals (NGA, 2024).

Except for hazardous sea conditions and the failure of Marine Aids to Navigation (AtoN), all assessed probabilities were applied across the entire EEZ of T and T rather than being confined to specific navigational zones. The figures below illustrate the spatial variation in probability for hazardous sea conditions (Fig. 3a) and areas susceptible to AtoN failure (Fig. 3b). Fig. 3a illustrates the spatial variation in the probability of hazardous sea conditions within T and T's maritime domain. The probability values are color-coded, with green areas representing very low probabilities and red areas indicating very high probabilities. Notably, hazardous sea conditions are most prominent along the northern nearshore coastlines, where wave energy and meteorological factors contribute to greater risks. These conditions have critical implications for maritime safety, as they increase the likelihood of vessel instability, loss of maneuverability, and failed evasive maneuvers in emergency situations. Fig. 3b depicts the locations of marine aids to navigation (black dots) and their nominal operational ranges (yellow shaded areas) (MOWT, 2024). The yellow zones indicate the spatial extent of navigational aid coverage where necessary to ensure safe passage for vessels operating within these waters, especially in poor visibility conditions.

The fault tree shown in Fig. 4 below was modelled after Haugen (1991) and utilised the following Boolean logic to calculate causation probabilities:

$$P_C = [AB] + [CD] + [EF] \tag{4}$$

https://doi.org/10.58440/ihr-31-1-a06

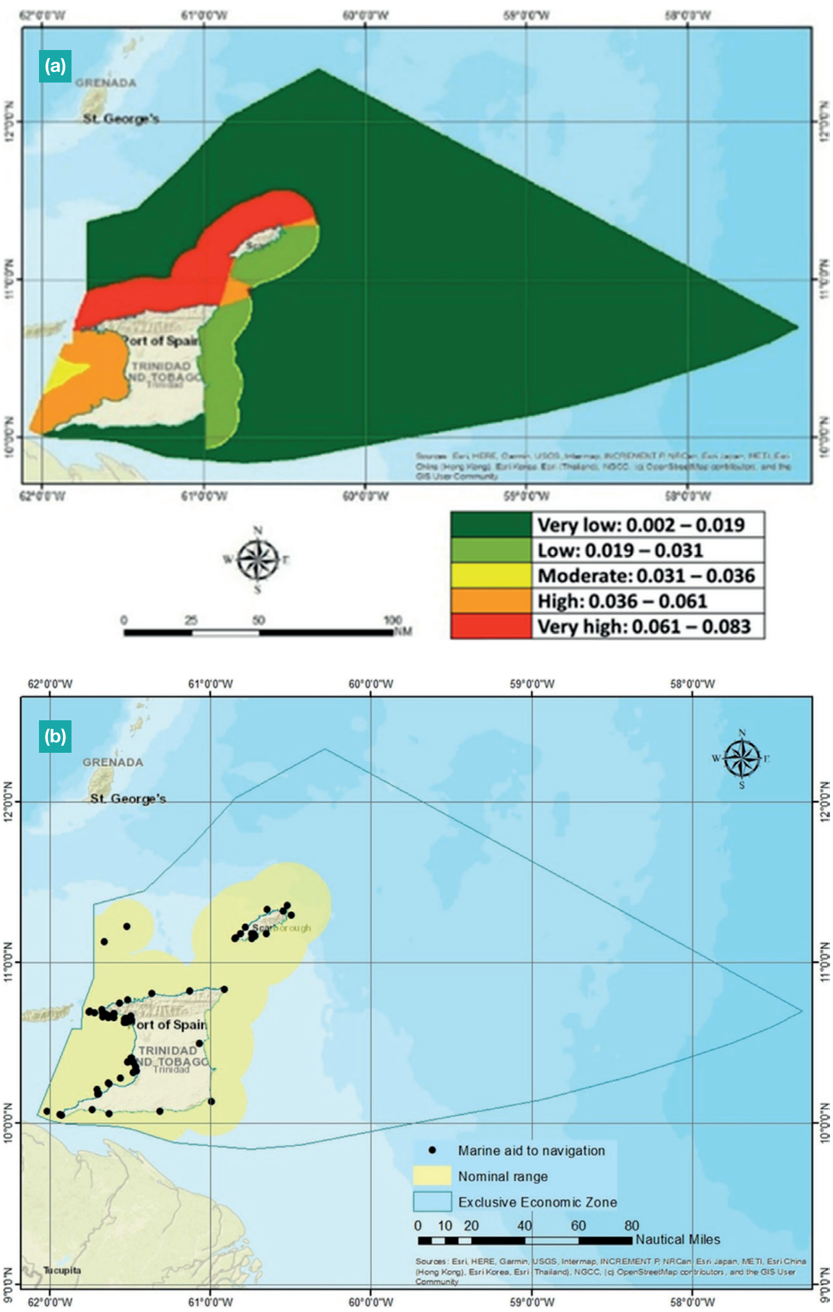

Fig. 3 (a) Probability of hazardous sea conditions. (b) Areas susceptible to the failure of Marine Aids to Navigation.

3.4 Assumptions

Simulation of the geometric probability of drifting collisions assumed a Poisson distribution for vessel departures, with inter-arrival times generated using exponential sampling. A fixed drift duration of one hour was applied, and circular safety zones were defined with a radius of 480 m (1.6 × vessel length). Overlapping safety zones within the same hourly interval were counted as collision candidates. A uniform spatial resolution of 1 km² and temporal resolution of one hour were used to optimise computational efficiency. The causation probability fault tree assumed independent contributions from human, technical, and environmental failures. Probabilities were based on incident data, IALA publications, and expert estimates. Human and technical risks were uniformly applied, while environmental risks were spatially modelled. These inputs represent a static snapshot; causation probabilities may change over time due to regulatory, technological, or operational shifts.

4 Results

This section presents key findings from the Monte Carlo simulations that estimate the geometric number of drifting collision candidates (NA) and the causation probability (PC) estimated using the FTA.

4.1 The geometric number of drifting collision candidates based on the Monte Carlo approach

Fig. 5 illustrates the geometric number of annual drifting collision candidates generated using the Monte Carlo simulation approach. The calculation involves counting the number of overlapping safety zones of vessels operating within the same hour, indicating the potential for drifting collision scenarios. An overlap between safety zones indicates that two vessels are operating within a proximity that would not allow sufficient time or space to take evasive action if one were to become disabled and begin drifting, thereby creating a realistic potential for collision. The spatial distribution of overlapping safety zones can support decision-making by identifying where limited safety resources should be prioritised and by informing regulatory measures aimed at preventing drifting collisions in high-risk zones.

4.2 The causation probability based on the fault tree analysis

The Monte Carlo simulation and fault tree analysis did not explicitly account for the effectiveness of existing risk control measures such as pilotage and operational procedures. As a result, adjustments to the causation factor values (refer to Fig. 6) were necessary to improve alignment between the modelled probability of drifting collisions and observed historical patterns. Studies have shown that pilotage can reduce incident risk by up to 59 times in areas such as the Great Belt and the Turkish Straits. Using this benchmark, the causation factor was initially reduced by a factor of 59 to reflect the mitigating impact of pilotage in the study area. The effectiveness of local operational procedures has not been explicitly quantified in the literature. To account for these additional controls, a further reduction was applied using a combination of trial and error, expert judgment from individuals familiar with local maritime operations, and calibration based on historical data. This process resulted in a total causation factor reduction of 65 times. This approach of adjusting the causation factor to reflect local conditions and bring model outputs into closer agreement with historical incident data is consistent with the methodology used in IWRAP, a recognized maritime risk assessment tool developed by IALA.

In this study, the causation factor was adjusted

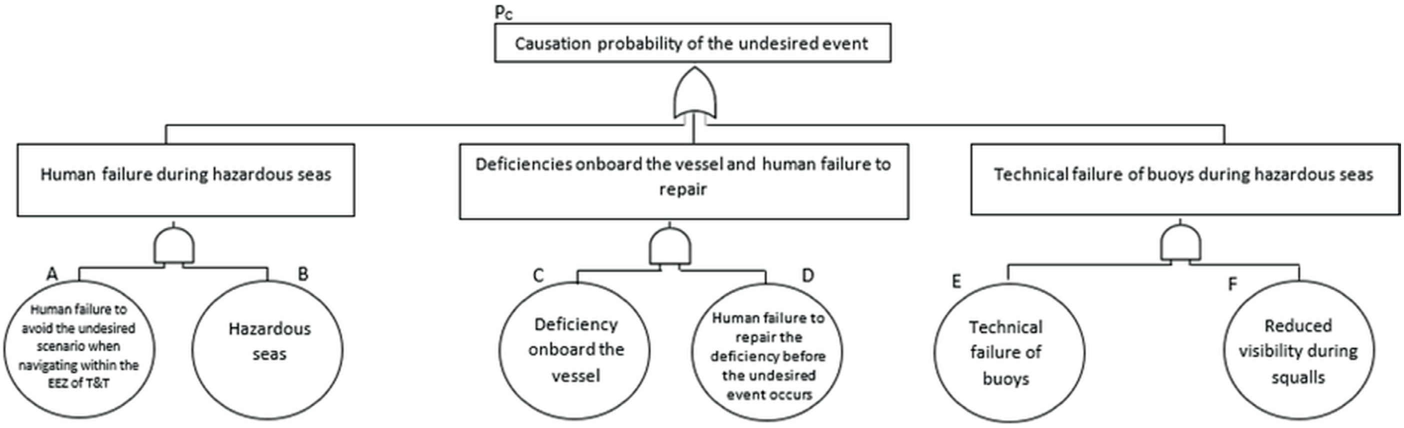

Fig. 4 Fault tree developed to assess the causation probability of undesired maritime events.

with the dual objective of approximating the observed average of 0.6 incidents per year in Trinidad and Tobago's waters and preserving the relative spatial variation in drifting collision probability, particularly the probability of incidents along the northern and north-western coasts of Trinidad and the waters around Tobago, as supported by historical patterns. While the final modelled output does not precisely match the historical incident frequency, it achieves a reasonable balance between the overall incident probability and the geographic distribution of risk. Table 3 presents the mean probability of drifting collisions across the modelled zones, and Fig. 8 depicts the resulting spatial distribution following adjustment for risk control measures.

4.3 Estimation of the probability of drifting collisions

Fig. 7 below illustrates the annual probability of drifting collision candidates, calculated by multiplying the geometric number of drifting collision candidates (refer to Fig. 5) by the causation probability (refer to Fig. 6). The standard deviation data classification method in ArcGIS Pro was used to classify the results, as it highlights deviations from the mean and identifies areas with unusually high or low probabilities of drifting collisions. The mean probability was calculated as 0.014, with areas less than or equal to 0.013853 classified as low probability (≤0.5 standard deviations from the mean). Medium probabilities (0.5 to 1.5 standard deviations) were classified up to 0.03877, while high probabilities (>1.5 standard deviations) reached up to 3.983315. Colour coding was applied to represent these classifications: green indicates probabilities less than 0.5 standard deviations from the mean, orange represents probabilities between 0.5 and 1.5 standard deviations, and red highlights probabilities greater than 1.5 standard deviations. Geographically, the areas around Trinidad marked in red include the northern region, the approach to the Point Lisas port, and an isolated area at approximately 10.5392°N 061.6798°W. Around Tobago, red zones include the approach to the Scarborough port and an isolated area at approximately 11.2254°N 60.9284°W. A large red geographic

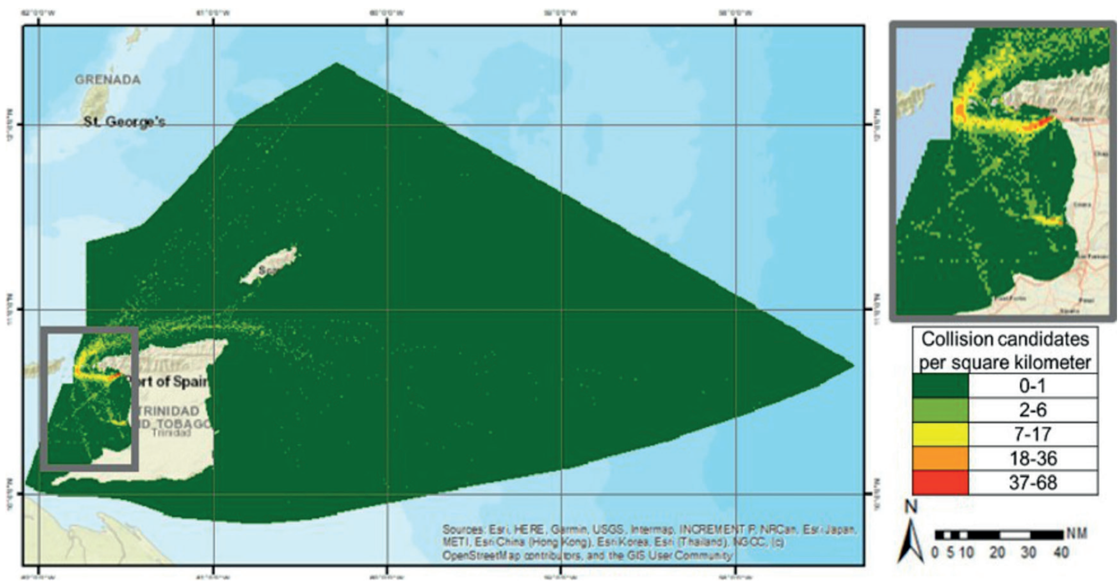

Fig. 5 Frequency of drifting collision candidates per square kilometre.

https://doi.org/10.58440/ihr-31-1-a06

area, indicating significantly elevated probabilities, is located between Trinidad and Tobago. Orange-coloured zones, representing medium probabilities, surround these high-risk areas, including regions within the Gulf of Paria and several areas north of Tobago.

A closer analysis segmented the EEZ into five focus areas, as illustrated in Fig. 8. The data highlights distinct risk profiles across these areas. Area one exhibits generally low probabilities with isolated instances of higher risk. Area two demonstrates the highest variability and overall risk, indicating the need for prioritised risk mitigation strategies. Area three displays stable yet slightly elevated probabilities compared to Area one. Area four shows moderate risks, with distinct pockets of higher probability, while Area five maintains a stable and consistently low-risk profile with minimal variation. To represent the annual drifting collision probabilities for each focus area, the Jenks Natural Breaks classification method was applied. This method ensures an optimised representation of risk distribution by grouping values that are naturally closer together. This method enhances the visual and statistical understanding of spatial risk variations across the EEZ. Table 3 summarises the results of this analysis, providing a comparative overview of the probabilities within each focus area and guiding the prioritisation of risk management efforts. These results support the development of a risk assessment methodology tailored to the specific challenges of SIDS.

4.4 Model validation

To validate the model, simulated traffic patterns were compared with historical traffic data, areas with relatively high probabilities of incidents were compared with those identified by IWRAP, and the overall probability of incidents was compared with historical incident records. The spatial distribution of simulated vessel traffic, generated using Monte Carlo techniques and Poisson-distributed departure times, was visually compared to annual traffic density maps from the MarineTraffic platform. This comparison confirmed that the simulated traffic patterns closely mirrored observed vessel behaviour, particularly along key corridors, port approaches, and turning zones. The visual alignment provided confidence that the simulated vessel activity realistically reflected operational conditions within Trinidad and Tobago's maritime domain. The spatial distribution of drifting collision probabilities was compared with results obtained from IWRAP, a recognised maritime risk assessment tool used to assess navigational risk within the Gulf of Paria (Seepersad et al., 2020). While IWRAP does not directly simulate drifting collisions as defined in this study, the general patterns of high-risk areas identified by both models were consistent. A comparative review of areas one and two, as shown in Fig. 8, alongside the IWRAP results, highlights notable correlations.

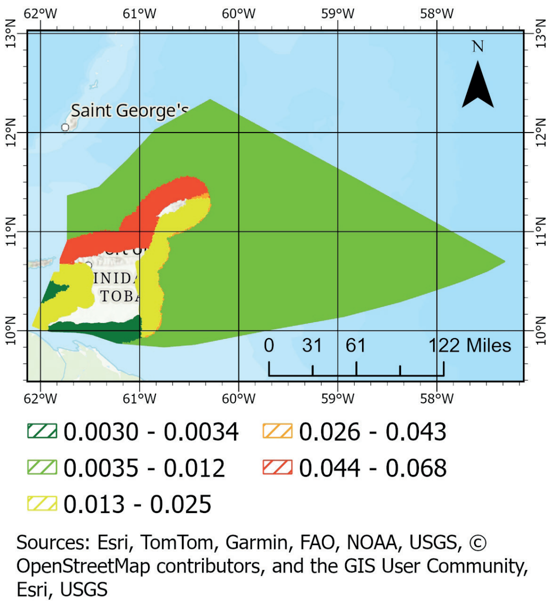

Fig. 6 Adjusted annual causation probability of drifting collisions.

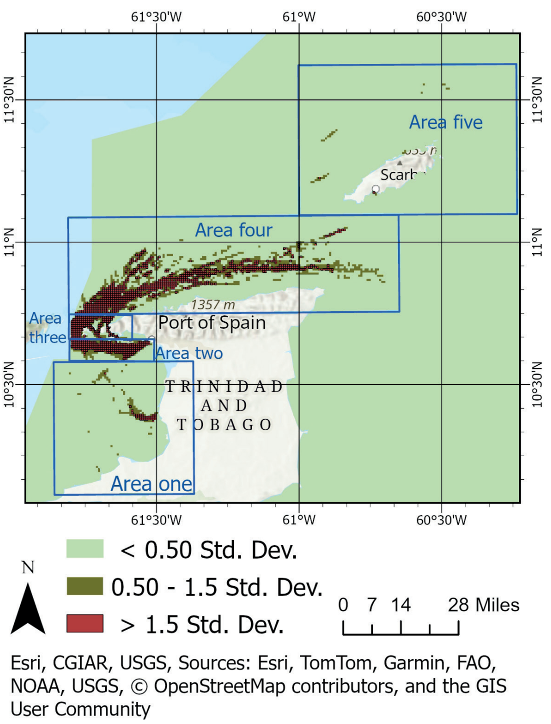

Fig. 7 High-risk areas for drifting collisions identified using the standard deviation data classification method.

Area one corresponds to turning zones within the Gulf of Paria and port approaches along the central to southern coastline. Similarly, area two aligns with port approaches along the north-western coastline. These similarities suggest consistency between the model's outputs and established risk patterns identified by IWRAP.

In terms of historical incident alignment, the literature review and incident records indicate that drifting collisions in Trinidad and Tobago have most frequently occurred along the northern and north-western coastlines of Trinidad, as well as the western, northern, and south-eastern coastlines

Table 3 Annual drifting collision probabilities per focus area.

Area	Minimum probability of drifting collisions	Mean probability of drifting collisions	Maximum probability of drifting collisions	Modal probability of drifting collisions
One	0.01	0.04	0.40	0.01
Two	0.01	0.20	3.98	0.02
Three	0.01	0.20	1.20	0.02
Four	0.01	0.06	0.70	0.02
Five	0.02	0.02	0.04	0.02

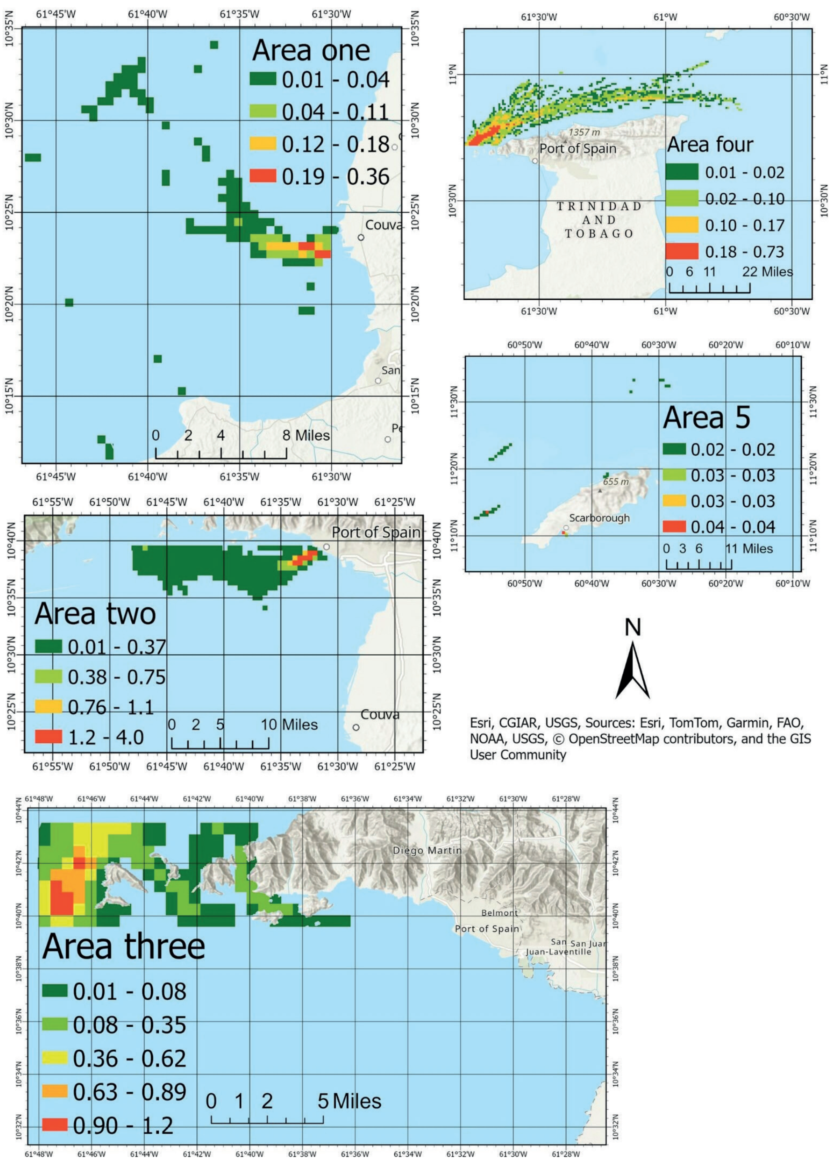

Fig. 8 Probabilities of drifting collision per area based on the Jenks Natural Breaks data classification method.

of Tobago. Notably, the available records do not specify drifting collisions within the Gulf of Paria, except for the northern and north-western areas. However, both this model and the IWRAP results identify the Gulf of Paria as an area of elevated risk. Drifting incidents along the south-eastern coastline of Tobago often involved deep-sea fishing vessels or migrant boats, both of which may lack AIS transponders or deliberately disable them. These characteristics help explain why the modelled results shown in Fig. 8 did not detect incidents in that area, as the simulation relies on observable or estimable traffic patterns. Further analysis of Fig. 8 revealed that area four shows an increased probability of drifting collisions near Tobago's western coastline, while area five exhibits lower but non-negligible risk in the waters north of Tobago, with a notable hotspot near the Port of Scarborough.

Although the model outputs were consistent with known high-risk zones and the general historical incident frequency of approximately 0.6 per year, formal statistical validation techniques such as confidence intervals, error margins, or residual analyses were not applied. This limitation stems from the lack of detailed, georeferenced incident datasets. Future enhancements to the model should incorporate such data, allowing for the use of statistical performance metrics to quantify model accuracy and uncertainty.

5 Discussion

This study addressed a critical gap in maritime risk assessment for SIDS, where limited resources often constrained the adoption of traditional resource-intensive methods. By integrating publicly available data, structured modelling techniques, and geospatial tools, the proposed methodology offered a practical and scalable solution for evaluating maritime risks. Its adaptability to resource-limited contexts ensured alignment with international obligations under frameworks such as SOLAS, MARPOL, and UNCLOS, making it highly relevant to coastal States facing similar challenges.

A notable strength of the methodology lies in its innovative use of alternative datasets, including open-source traffic patterns and historical port call logs, to supplement limited AIS data. This approach aligned with established probabilistic modelling efforts (Przywarty, 2008; Goerlandt & Kujala, 2011), while prioritising accessibility and cost-effectiveness. Furthermore, the integration of Monte Carlo simulations and FTA enhanced the robustness of risk estimation by accounting for probabilistic vessel encounters and causation probabilities. The use of FTA, successfully applied in aerospace and maritime contexts (NASA, 2002; Haugen & Kristiansen, 2023), ensured methodological reliability while maintaining computational feasibility for SIDS.

Another strength of the model lies in its balance between granularity and practicality. While the model

 https://doi.org/10.58440/ihr-31-1-a06

did not simulate highly specific or overly precise results, this was an intentional design choice to prioritise robust risk assessment over predictive precision. Attempting to simulate outcomes with excessive specificity risks introducing errors or overreliance on uncertain data, which could misinform mitigation efforts and resource allocation priorities. Instead, the model focused on identifying broad areas of concern and prioritising risk factors, ensuring that recommendations were actionable, value-laden, and resilient to data uncertainties. This approach underscores the importance of a risk assessment framework that guides mitigation efforts without creating a false sense of precision.

The findings also demonstrated the capability of the methodology to replicate real-world traffic patterns, as evidenced by the alignment between simulated and AIS-derived traffic densities. The safety zone mapping results effectively identified high-risk areas, providing actionable insights for resource allocation and risk mitigation strategies.

Despite its contributions, this study faced several limitations. The model did not fully account for dynamic environmental factors such as meteorological conditions and water currents, which could significantly influence vessel drift and collision probabilities. Future enhancements could incorporate finer-scale hydrodynamic data or employ Bayesian networks for more nuanced analyses. Additionally, the framework specifically targeted drifting collisions, which limited its scope. Expanding the methodology to include other maritime risks, such as groundings or allisions, would enable a more comprehensive assessment of maritime safety. A hydrographic (bathymetry, floor characteristics, tides, etc.) analysis could provide valuable information about grounding avoidance and grounding mitigation.

The simulation assumed existing traffic patterns as the starting point, which may have underestimated overall traffic volumes and, consequently, the number of drifting collisions. This highlights the importance of incorporating dynamic initial traffic conditions in future studies. Furthermore, several simplifying assumptions were made to balance computational efficiency with accuracy, such as constant vessel speeds, omission of ship turning radii, and reliance on the Poisson process for simulating departure times without accounting for seasonal variations. While these simplifications were justified within the study's scope, future research could address them by utilising more detailed data and computational resources.

6 Conclusion

This study developed a resource-efficient methodology for maritime risk assessment tailored to the unique challenges of SIDS. By integrating publicly available data with probabilistic modelling techniques, it provided actionable insights into the spatial variability of risk across the study area, enabling prioritisation of resources to reduce maritime risks. The approach successfully balanced granularity and practicality, focusing on broad risk patterns without over-reliance on precise yet uncertain data. Comparisons with established models, such as IWRAP, validated its robustness, while its flexibility ensures adaptability to other contexts.

Although limitations remain, including simplified assumptions and the exclusion of dynamic environmental factors, the framework offers a scalable foundation for maritime safety management. Future integration of probability values with economic consequence estimates could further enhance decision-making, providing policymakers with interpretable and impactful tools for resource allocation and risk mitigation. This study demonstrates that robust maritime risk assessments can be achieved in resource-constrained environments, advancing the field of maritime safety management.

7 Future works

Future work could extend this study by incorporating an economic valuation of consequences, where probability values are multiplied by potential consequences expressed as dollar values. This approach would enable the calculation of risk per unit area, combining probability and consequence to produce actionable and interpretable risk maps. Addressing the limitations presented in 5.1 could also improve the value of this methodology.

References

Bogalecka, M. and Dabrowska, E. (2023). Monte Carlo simulation approach to shipping accidents consequences assessment. *Water, 15*(10). https://www.mdpi.com/2073-4441/15/10/1824 (last accessed 20 January 2025).

CMoU (2020). *Annual Report 2020*. Caribbean Memorandum of Understanding on Port State Control, Kingston, Jamaica. https://www.caribbeanmou.org/sites/default/files/annual_report_2020.pdf (last accessed 30 January 2025).

CMoU (2024). *Publications.* Caribbean Memorandum of Understanding on Port State Control, Kingston, Jamaica. https://caribbeanmou.org/content/publications (last accessed 30 September 2024).

CSA (2024). *Initiatives on Port Efficiency and Sustainability*. Caribbean Shipping Association, Kingston, Jamaica. https://www.caribbeanshipping.org/ (last accessed 30 January 2025).

Fujii, K. T. Y. (1971). Traffic capacity. *The Journal of Navigation, 27*(4), pp. 543–552, https://doi.org/10.1017/S0373463300022384

Goerlandt, F. and Kujala, P. (2010). Modelling of ship collision probability using dynamic traffic simulation. In B. J. M. Ale, I. A. Papazoglou and E. Zio (Eds.), *Reliability, Risk and Safety* (pp.40–447). Taylor and Francis Group, London. https://www.

researchgate.net/publication/286541864 (last accessed 20 January 2025).

Haugen, S. (1991). *Probabilistic evaluation of frequency of collision between ships and offshore platforms*. [Doctoral dissertation, University of Trondheim].

Haugen, S. and Kristiansen, S. (2023). *Maritime Transportation: Safety Management and Risk Analysis.* CRC Press, Kindle edition, p. 217.

IALA (2004). *Categorisation and Availability Objectives for Short Range Aids to Navigation* (R0130, 3.1 ed.) International Association of Marine Aids to Navigation and Lighthouse, Staint Germain en Laye, France. https://www.iala.int/product/r0130/ (last accessed 20 May 2024).

IALA (2009). *Causation Probability Modelling*. https://www.iala.int/wiki/iwrap/index.php/Causation_Probability_Modelling (last accessed 20 January 2025).

IALA (2022a). *The Use of IALA Waterway Risk Assessment Programme* (G1123, 2.1 ed.). International Association of Marine Aids to Navigation and Lighthouse, Staint Germain en Laye, France. https://www.iala.int/product/g1123/ (last accessed 20 January 2025).

IALA (2022b). *The Use of Ports and Waterways Safety Assessment* (G1124, 2.1 ed.). International Association of Marine Aids to Navigation and Lighthouse, Staint Germain en Laye, France. https://www.iala.int/product/g1124/ (last accessed 20 January 2025).

IALA (2022c). *The Use of the Simplified IALA Risk Assessment Method* (G1138, 2.0 ed.). International Association of Marine Aids to Navigation and Lighthouse, Staint Germain en Laye, France. https://www.iala.int/product/g1138/ (last accessed 20 January 2025).

IALA (2024). *Aids to Navigation Manager Training Level 1 – Use of the IALA Risk Management Tools* (C1003, 3.0 ed.). International Association of Marine Aids to Navigation and Lighthouse, Staint Germain en Laye, France. https://www.iala.int/product/c1003/ (last accessed 30 January 2025).

IALA (2025). *Review of the Risk Management Tools – Global Survey*. International Association of Marine Aids to Navigation and Lighthouse, Staint Germain en Laye, France.

IMO (1973). *International Convention for the Prevention of Pollution from Ships* (MARPOL). International Maritime Organization, London, United Kingdom. https://www.imo.org/en/about/Conventions/Pages/International-Convention-for-the-Prevention-of-Pollution-from-Ships-(MARPOL).aspx (last accessed 30 January 2025).

IMO (1974). I*nternational Convention for the Safety of Life at Sea (SOLAS)*. International Maritime Organization, London, United Kingdom.
https://www.imo.org/en/About/Conventions/Pages/International-Convention-for-the-Safety-of-Life-at-Sea-(SOLAS),-1974.aspx (last accessed 30 January 2025).

IMO (1978). *International Convention on Standards of Training, Certification and Watchkeeping for Seafarers (STCW).* International Maritime Organization, London, United Kingdom.
https://www.imo.org/en/OurWork/HumanElement/Pages/STCW-Convention.aspx (last accessed 30 January 2025).

IMO (2010). *Global Integrated Shipping Information System (GISIS)* (Incident record: C0008290). International Maritime Organization, London, United Kingdom. https://gisis.imo.org/Public/MCIR/Occurrence.aspx?Reference=C0008290 (last accessed 30 January 2025).

IMO (2024). *Global Integrated Shipping Information System (GISIS)* (Incident record: C1000310). International Maritime Organization, London, United Kingdom. https://gisis.imo.org/Public/MCIR/Occurrence.aspx?Reference=C1000310 (last accessed 30 January 2025).

IMO (2025). *Oil pollution: prevention and response*. International Maritime Organization, London, United Kingdom. https://www.imo.org/en/OurWork/Environment/Pages/OilPollution-Default.aspx (last accessed 20 January 2025).

IMPA (2022, November 1). *Maritime pilots and pilotage: Our commitment to safety, pollution prevention and environmental sustainability.* IMO Seminar, International Maritime Pilots' Association, London, United Kingdom. https://www.impahq.org/sites/default/files/content-files/20220916-IMPA%20IMO%20Seminar%202022-FINAL.pdf (last accessed 20 January 2025).

ITOPF (2025). *Atlantic Empress, West Indies, 1979.* ITOPF Ltd, London, United Kingdom. https://www.itopf.org/in-action/case-studies/atlantic-empress-west-indies-1979/ (last accessed 30 January 2025).

Kirwan, B. (1994). *A guide to practical human reliability assessment* (1st ed.). CRC Press. https://doi.org/10.1201/9781315136349

Loop News Caribbean (2024). *Rough seas affecting coastlines across the Caribbean*. https://www.loopnews.com/content/rough-seas-affecting-coastlines-across-the-caribbean/ (last accessed 30 January 2025).

MacDuff, T. (1974). The probability of vessel collisions. *Ocean Industry, 9*(9). https://trid.trb.org/View/26999 (last accessed 20 January 2025).

MarineTraffic (2025). *AIS vessel tracking map*. Kpler Holding SA, Brussels, Belgien. https://www.marinetraffic.com/en/ais/home/centerx:-60.2/centery:10.2/zoom:8 (last accessed 30 January 2025).

MARIN (n.d.). SAMSON*: Safety assessment models for shipping and offshore in the North Sea*. Maritime Research Institute Netherlands, Wageningen, The Netherlands. https://www.marin.nl/en/about/facilities-and-tools/software/samson (last accessed 20 January 2025).

MEEA (2013). *The National Oil Spill Contingency Plan of Trinidad and Tobago.* Ministry of Energy and Energy Affairs, Government of the Republic of Trinidad and Tobago, Port of Spain, Republic of Trinidad and Tobago.

MOWT (2024). *Aids to Navigation Operational Plan for All Areas.* Maritime Services Division, Ministry of Works and Transport, Government of the Republic of Trinidad and Tobago, Port of Spain, Republic of Trinidad and Tobago.
https://www.mowt.gov.tt/MOWT/media/General/Documents/Maritime%20Forms/Navigational%20Plan/Maritime-Services-Division-Aids-to-Navigation-Operational-Plan-for-all-areas.pdf (last accessed 30 January 2025).

Muñoz, S. and Ötker, I. (2018). *Building resilience to natural disasters in the Caribbean requires greater preparedness.* International Monetary Fund, Washington, D.C., USA. https://www.imf.org/en/News/Articles/2018/12/07/NA120718-Building-Resilience-to-Natural-Disasters-in-Caribbean-Requires-Greater-Preparedness (last accessed 2 April 2025).

NGA (2024). *List of Lights, Radio Aids, and Fog Signals* (Publication number 110). Maritime Safety Office, National

Geospatial-Intelligence Agency, Springfield, USA. https://msi.nga.mil/api/publications/download?key=16694312/SFH00000/NIMA_LOL/Pub110/Pub110bk.pdf&type=view (last accessed 27 March 2025).

NASA (2002). *Fault Tree Handbook with Aerospace Applications* (1.1 ed.). NASA Office of Safety and Mission Assurance, National Aeronautics and Space Administration, Washington, D.C., USA. https://www.mwftr.com/CS2/Fault%20Tree%20Handbook_NASA.pdf (last accessed 20 January 2025).

Przywarty, M. (2008). Probabilistic model of ships' navigational safety assessment on large sea areas. *Proceedings of the 16th International Symposium on Electronics in Transport,* Ljubljana, Slovenia. https://www.researchgate.net/publication/387019707_Probabilistic_model_of_ships_navigational_safety_assessment_on_large_sea_areas (last accessed 20 January 2025).

Rambarran, T. (2021). *Correspondence on vessel incidents* [unpublished]. Maritime Services Division, Ministry of Works and Transport, Government of the Republic of Trinidad and Tobago, Port of Spain, Republic of Trinidad and Tobago.

Riding, J. and Rawson, A. (2015). *LINZ Hydrography Risk Assessment Methodology Update* (report number 15NZ322, issue 03). Land Information New Zealand (LINZ), Wellington, New Zealand. https://iho.int/uploads/user/Inter-Regional%20Coordination/WEND-WG/WENDWG%20Repository/SWPRHP-Hydrography-Risk-Assessment-Methodology.pdf (last accessed 7 April 2025).

Sánchez, R. J. and Wilmsmeier, G. (2009). Maritime sector and ports in the Caribbean: The case of CARICOM countries. CEPAL – *Serie Recursos naturales e infraestructura, 140.* https://www.researchgate.net/publication/259871293_Maritime_sector_and_ports_in_the_Caribbean_the_case_of_CARICOM_countries (last accessed 2 April 2025).

Seepersad, D., Greenland, A., Eriksson, O. F. and Miller, K. (2020). Benefits of assessing risk in maritime navigation using IALA and LINZ methods. *The International Hydrographic Review, 23.* pp. 7–33. https://ihr.iho.int/articles/benefits-of-assessing-risk-in-maritime-navigation-using-iala-and-linz-methods/ (last accessed 20 January 2025).

Singh, A. et al. (2015). *Assessment of Ship-Source Pollution in the Gulf of Paria.* Institute of Marine Affairs (IMA). https://www.ima.gov.tt/publications/ (last accessed 30 January 2025).

Trinidad and Tobago Express (2009). *Dead man found aboard drifting yacht.* https://trinidadexpress.com/news/local/dead-man-found-aboard-drifting-yacht/article_38fe4033-0ec8-503c-a4b3-bc0ff916f32a.html (last accessed 20 January 2025).

Trinidad and Tobago Guardian (2018). *Treasure Queen II now a hazard*. https://www.guardian.co.tt/news/treasure-queen-ii-now-a-hazard-6.2.666682.a3e5b88a3f (last accessed 20 January 2025).

Trinidad and Tobago Guardian (2020). *Castara fishermen rescue drifting deepsea vessel.* https://www.guardian.co.tt/news/castara-fishermen-rescue-drifting-deepsea-vessel-6.2.1332650.f61392fad6 (last accessed 20 January 2025).

Trinidad and Tobago Guardian (2024). *PM weighing foreign help if oil spill worsens*. https://www.guardian.co.tt/news/pm-weighing-foreign-help-if-oil-spill-worsens-6.2.1923219.50bcf5d956 (last accessed 26 March 2025).

Trinidad and Tobago Newsday (2022). Updated: *Five rescued after boat sinks: God saved us from drowning.* https://newsday.co.tt/2022/03/13/updated-five-rescued-after-boat-sinks-god-saved-us-from-drowning/ (last accessed 20 January 2025).

Trinidad and Tobago Meteorological Service (2024). *Satellite imagery.* https://www.metoffice.gov.tt/ (last accessed 30 August 2024).

UN (1982). *United Nations Convention on the Law of the Sea* (UNCLOS). United Nations, United Nations, New York, USA. https://www.un.org/depts/los/convention_agreements/texts/unclos/unclos_e.pdf (last accessed 30 January 2025).

Vukša, S., Vidan, P., Bukljaš, M. and Pavic, S. (2022). Research on ship collision probability model based on Monte Carlo simulation and Bi-LSTM. *Marine Science and Engineering, 10*(8). https://www.mdpi.com/2077-1312/10/8/1124 (last accessed 20 January 2025).

Authors' biographies

Shivani Seepersad is an Advisor to the International Organisation of Marine Aids to Navigation and a PhD candidate in the Department of Geomatics Engineering and Land Management at the University of the West Indies, Trinidad and Tobago. Her doctoral research, titled An Economic Evaluation of Risks due to Maritime Navigation across the Greater Caribbean Region, focuses on maritime safety and risk assessment. She has previously served as a GIS intern at York University, contributing to flood risk modelling for the Greater Toronto Area, and as a GIS technician at Land Information New Zealand on the Niue Hydrographic Risk Assessment. Shivani holds a B.Sc. in Geomatics Engineering (Honours) and an M.Sc. in Geoinformatics (Distinction).

Shivani Seepersad


Dexter Davis

Dexter Davis is Lecturer in the field of surveying, adjustments and geodetic surveying and is also Coordinator of the B.Sc. Geomatics Engineering Programme in the Department of Geomatics Engineering & Land Management, Faculty of Engineering, The University of the West Indies. He is a member of the Institute of Surveyors of Trinidad and Tobago as well as the ASPRS. His research areas include engineering surveying, digital photogrammetry and digital mapping, GNSS, geodesy and geodetic applications and hydrographic surveying. Some of his recent work includes sea level monitoring, low cost and disaster relief mapping and 3D point cloud applications for engineering and digital twins.

https://doi.org/10.58440/ihr-31-1-a06

CONFERENCE PAPER

A natural reference area for the quality control of multibeam echosounder bathymetry and backscatter measurements: The Kwinte area on the Belgian part of the North Sea

Authors

Samuel Deleu[1] and Marc Roche[2]

Preamble

The following work was presented at the Hydrographic Conference HYDRO 2024, 5–7 November 2024, Rostock-Warnemünde, Germany in the oral session *Quality aspects of MBES measurements.*

Abstract

The *Kwinte* area in the Belgian part of the North Sea serves as a site for monitoring the quality of shallow water multibeam echosounder bathymetric and backscatter data. Time series acquired over two decades confirm its bathymetric and sedimentary stability. Included in the Belgian Marine Spatial Plan and freely accessible, the Kwinte area allows for verification of bathymetric data compliance to IHO hydrographic quality standards. The availability of reference backscatter angular responses obtained with a calibrated singlebeam echosounder facilitates cross-calibration of backscatter data, thereby enabling a comparison of backscatter data from diverse array of multibeam echosounders deployed on various vessels.

Keywords

multibeam echosounder · bathymetry · natural reference area · hydrographic quality control · backscatter cross-calibration

✉ Samuel Deleu · samuel.deleu@mow.vlaanderen.be

[1] Flemish Hydrography, Agency for Maritime and Coastal Services, Belgium

[2] Continental Shelf Service, FPS Economy, Belgium

https://doi.org/10.58440/ihr-31-1-c03

1 Introduction

In order to assess the quality of the bathymetric and backscatter (BS) datasets from different multibeam systems and different vessels, a reference area on the Belgian part of the North Sea has been established: the *Kwinte* area. This natural reference area has been included in the Marine Spatial Plan (MSP) 2020–2026[1] for the Belgian Part of the North Sea as a reference area for the calibration and quality evaluation of measuring devices. In practice, all seabed disturbing activities are prohibited inside this area in order to preserve at long term an undisturbed seabed for bathymetric and BS measurements. Extensive survey work by Flemish Hydrography (VH)[2], Continental Shelf Service (COPCO)[3] and other participants to this project has been carried out during the last decade here. Multiple surveys allow to cross check the depths and positioning of the different measurements and to build up a reference bathymetric model of the area.

The purpose of this conference paper is to present the essential information about the *Kwinte* reference area and to show how it can be used for both bathymetry and BS data quality control and calibration. The results were presented during the Hydro 2024 conference in November 2024 in Rostock, Germany.

2 Location

The *Kwinte* reference area lies 17 km from the coast in the gulley between two sandbanks (Fig. 1). It has a length of 1,5 km and a width of 650 m, with depths ranging from 23 to 26 m LAT (Fig. 2). The area is to a large extent flat. Slope breaks affect its southern part. The NW part is shaped by a network of small to medium dunes of 10–30 m wave length. No dunes are observed in the SE part of the larger *Kwinte* area, which is dominated by rounded and irregular hills and depressions of decimetric height forming a typical hillocky morphology, characteristic of the relatively flat gravel areas of the troughs between sandbanks. In the *Kwinte* channel, tidal currents can reach up to 1 m/s during periods of spring tides and remain around 0,5 m/s during neap tides. The sedimentary cover of the *Kwinte* reference area consists of gravelly sand (gS) and sandy gravel (sG) with a high carbonate content exceeding 15 %, due to the abundance of shells. This composition has been verified through four series of Van Veen grab samples and Sediment Profile Imaging (SPI) system images collected from 2001 to 2022.

The *Kwinte* area is defined in the current Marine Spatial Plan (MSP) 2020–2026 and will be kept in the follow-up MSP 2026-2032 as an area where seabed disturbing activities are prohibited. Seabed anthropic alteration cannot be overlooked, as trawling marks are clearly visible on some BS images of the *Kwinte* area. Any impact by human activities (trawls, anchors,

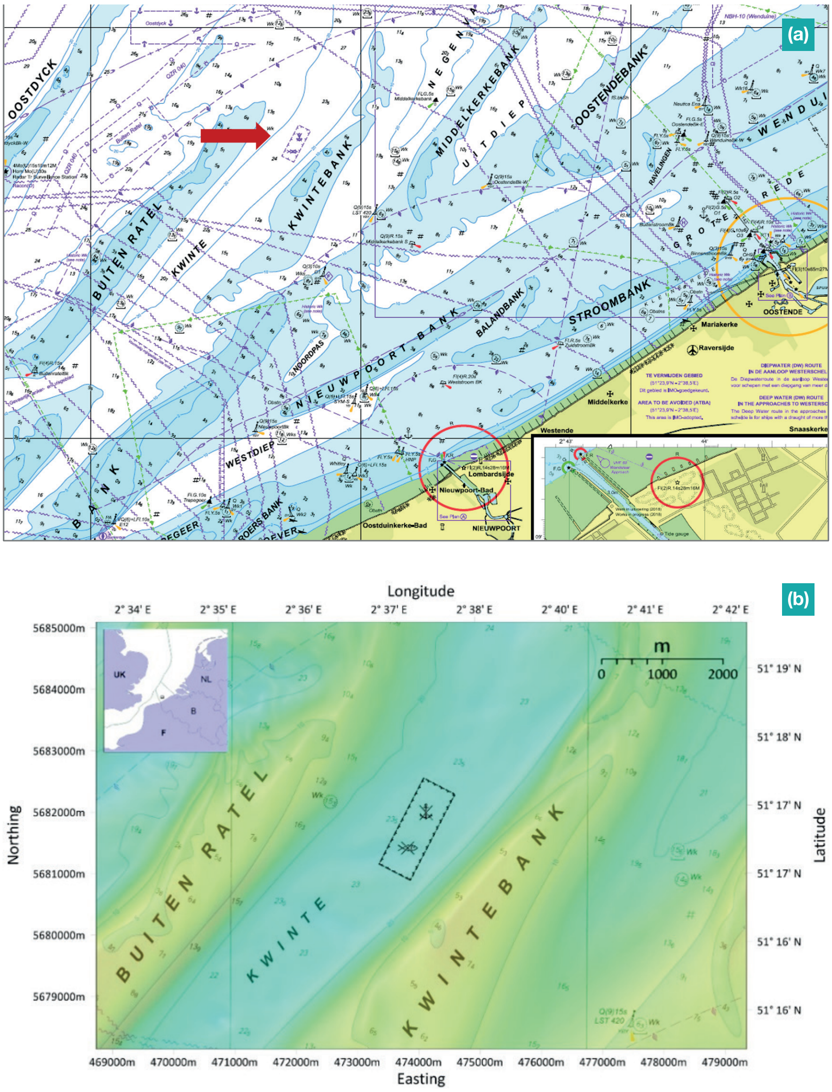

Fig. 1 (a) Location of the *Kwinte* area on the Belgian Continental Shelf (red arrow) and (b) its location relative to the adjacent sandbanks Buiten ratel and Kwintebank.

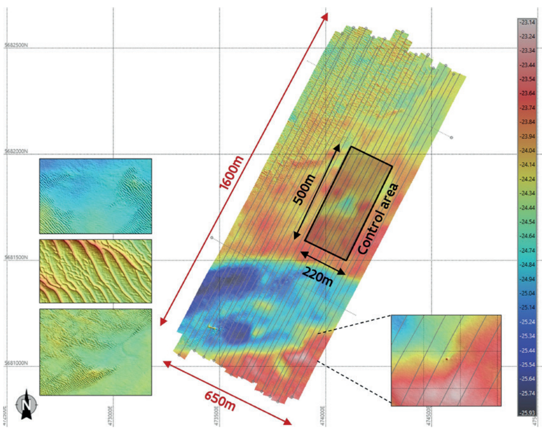

Fig. 2 Example of a typical survey of the *Kwinte* area. The area is 1600 m long and 650 m wide. The small black rectangle represents the control area where calculations are done and whose results are presented in Fig. 6. The rectangle on the bottom right shows the object which is used for position control.

[1] https://www.health.belgium.be/en/environment/seas-oceans-and-antarctica/north-sea-and-oceans/marine-spatial-plan (accessed 15 March 2025).
[2] https://www.agentschapmdk.be/en/flemish-hydrography (accessed 15 March 2025).
[3] https://economie.fgov.be/en/themes/enterprises/offshore-sand-and-gravel (accessed 15 March 2025).

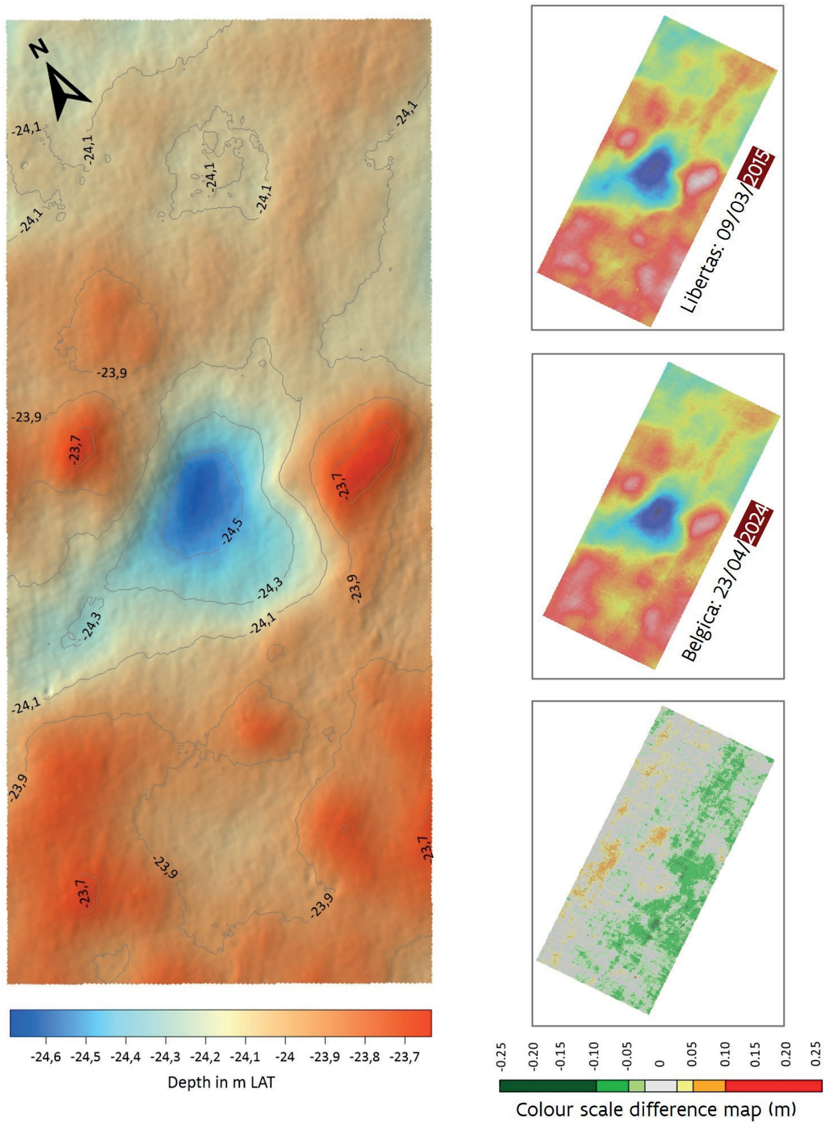

Fig. 3 Bathymetry of the model based on averaging the up to now 45 accepted surveys (image on the left). The images on the right side show one of the oldest accepted surveys from 2015 and one of the most recent accepted surveys from 2024 and the difference map between both revealing the stability of the control area.

Fig. 4 Overview of all the participating vessels until now. All vessels have a dedicated multibeam setup. Their length ranges from 10 m to 100 m.

dredging, ...) on the seabed surface will change the bathymetry and by modifying the sediments, inducing a change of the BS level. This human impact has to be excluded to assess the natural value of the calibration area. During the last few years there has been less impact but nevertheless some fishermen still trawl in the area. A control mechanism by the authorising government has been put in place.

3 History

In 2003, COPCO selected the *Kwinte* area as a reference site for sandy gravels during the development of a supervised acoustic classification system for surficial sediments in the sand extraction areas of the Belgian part of the North Sea. This classification system was based on backscatter (BS) data from a 100 kHz Kongsberg Discovery EM1002 MBES.

Subsequently, as part of monitoring the impact of sand extraction on the marine environment, this small area was considered by COPCO as a control area and measured sporadically. Over the years, it became clear that the *Kwinte* area was very stable, both in terms of bathymetry and BS.

Since 2009, extensive surveys of the *Kwinte* area have been carried out by COPCO and VH using multiple MBESs installed on several vessels, with different setups and at different times. The resulting long time series of bathymetric and BS data demonstrates that the seabed remains remarkably stable throughout the years (Fig. 3). Over a period of 10 years, the *Kwinte* area shows neither significant accretion nor erosion of the seabed. This demonstrated stability gives the *Kwinte* area the status of an ideal natural reference area for controlling the hydrographic quality of bathymetry measurements. Due to the stable seabed in terms of morphology and sedimentology, it is also an ideal reference area for controlling the repeatability of BS measurements done by individual MBES.

In 2023, a collaborative effort with Ifremer (France) on board the HV Sirius enabled the acquisition of reference BS angular responses by employing a single-beam echo sounder (SBES) that had undergone meticulous calibration using reference spheres prior to deployment. The recorded frequencies, ranging from 50 kHz to 400 kHz, encompass a substantial frequency spectrum, including the frequencies typically utilized by shallow-water MBESs. The calibrated BS angular responses resulting from these measurements constitute the reference BS levels that allow the BS from any MBESs operating at comparable frequencies to be calibrated.

Since its incorporation into the MSP 2020–2026, the *Kwinte* area has been maintained as accessible and open, with the objective of encouraging all users of MBES to visit and assess the quality of their data by sharing their measurements with VH and COPCO, fostering a mutually beneficial relationship (Deleu & Roche, 2020).

Contracting survey companies working for VH are obliged to carry out a series of acceptance tests prior to the start of the first survey. Only when they pass the tests successfully, can they start the contract and carry out hydrographic MBES measurements with the used vessel and setup. The final test is a survey on the *Kwinte* area, as it is a very stable and well-known

https://doi.org/10.58440/ihr-31-1-c03

area and gives VH the necessary confidence regarding data quality.

The accessibility of the *Kwinte* area, coupled with the VH contractual imperative to utilize it for hydrographic data quality control, has resulted in a substantial accumulation of bathymetric data collected by a diverse array of MBESs deployed on various Belgian and Dutch vessels (Fig. 4).

Over the past two years, the potential of the *Kwinte* area to evaluate the quality and calibration of BS data has begun to garner attention from numerous surveyors, and this interest is anticipated to escalate in the forthcoming years.

4 Results

4.1 Bathymetry

The effective control area is focused on a sub area within the *Kwinte* area with a demonstrated flat seabed. The mean depth value of this control area (Fig. 2) is around -24.00 m LAT which means that, following the International Hydrographic Organization (IHO) Exclusive Order Limits (using the Matrix Reference; IHO, 2022), the Maximum Allowable Vertical Uncertainty TVU_{max}) is around 0.23 m, using the following formula:

$$\mathrm{TVU}_{\max}(d) = \sqrt{a^2 + (b \times d)^2} \tag{1}$$

Before everything else, datasets are examined on overlap, visible artefacts, spikes, confidence levels, statistical analysis and checked with reference to the TVU of the IHO Exclusive Order Norm. Difference maps are generated to compare each survey with any other survey and with the model (Fig. 5).

After each accepted new survey, the model is updated. A mean value per survey on a small subarea is calculated for each survey and plotted in time with reference to the mean model value and the IHO Exclusive Order Norm limits (Fig. 6). Up until now 45 surveys are accepted, with the first accepted survey being done in 2015. The time span of 10 years does not reveal a trend in bathymetry which ensures us that the area is bathymetric stable. Next to the 45 accepted surveys a number of surveys did not pass the acceptance criteria and are not included in the pipeline of accepted surveys. Some of the reasons up until now are: not enough data points, mean value out of limits IHO Exclusive order, too much noise and

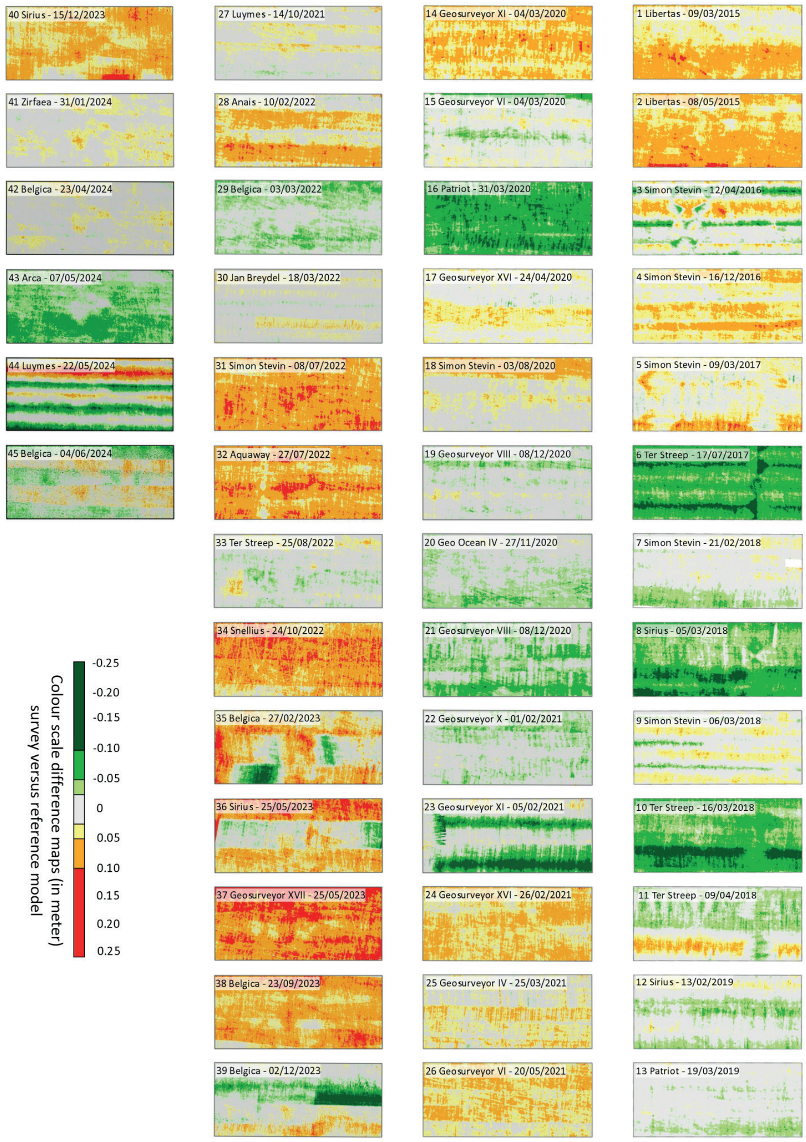

Fig. 5 Difference maps of all of the accepted surveys with reference towards the model. The colour scale ranges from -25 cm (green colours) to +25 cm (red colours).

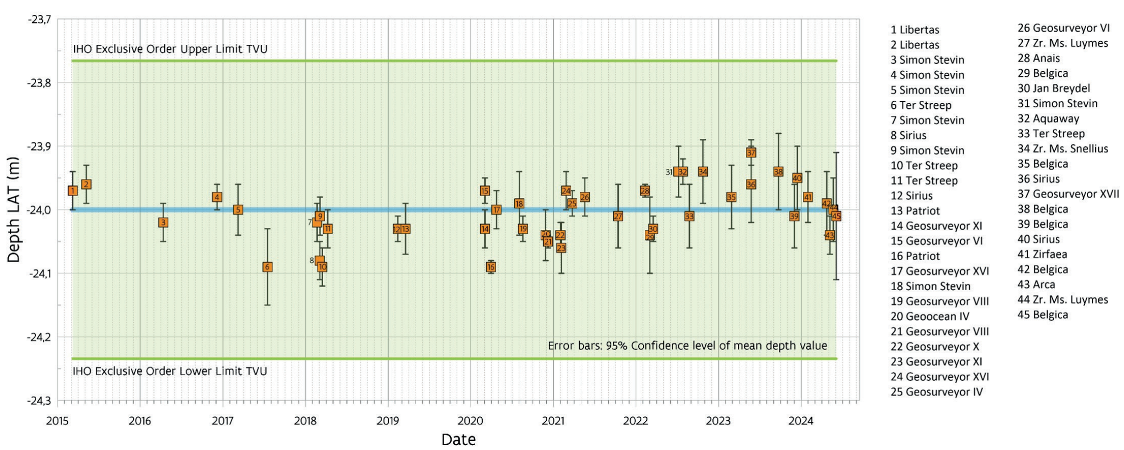

Fig. 6 Bathymetric time series of the mean value of the control area for each survey (orange squares). The blue line represents the overall mean value of the up to now 45 accepted surveys with in green the IHO Exclusive order Upper and Lower TVU limits.

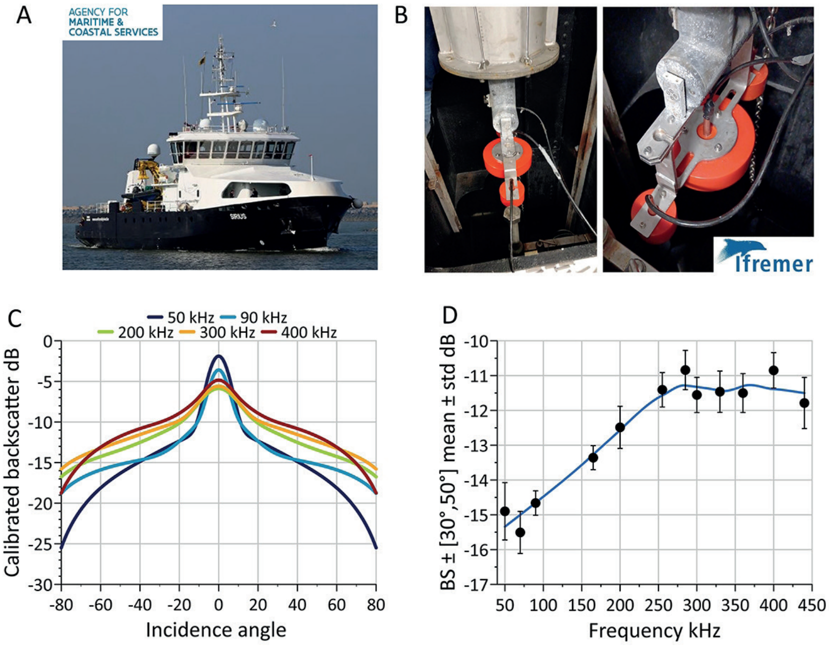

Fig. 7 Acquisition of reference BS data in the *Kwinte* area: (a) HV Sirius; (b) EK80 and pan & tilt system installed in the HV Sirius moonpool, with the three Ifremer EK80 calibrated transducers (ES70 in the middle, ES200 forward and ES333 backward); (c) Resulting reference BS angular response for 50, 90, 200, 300 and 400 kHz; (d) Calibrated BS level in the ±[30°,50°] angular incidence range *versus* frequency.

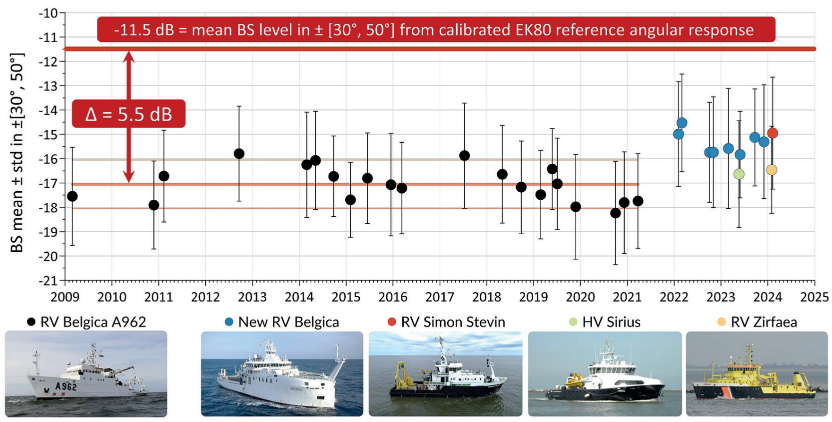

Fig. 8 300 kHz BS time series of the *Kwinte* area. Mean and std in the incidence angle interval ±[30°,50°] with the mean reference level of -11.5 dB given for the same angle interval; BS without compensation, corrected for insonified area and transmission loss.

spikes, too many motion artefacts and bad positioning accuracy.

For each survey, statistics are calculated and a whole table of these is stored to assess the quality of that survey. Some of the used parameters are: 95 % confidence levels, amount of accepted and rejected footprints, hit count, span and differences towards the model. The results of all these analyses determine if a new survey is accepted or not and provides certainty of the quality of the multibeam setup. It is also used as the final control during acceptance tests for survey companies carrying out survey work on the Belgian part of the North Sea for Flemish Hydrography. If the survey does not pass, that specific vessel with that specific multibeam setup cannot be used for survey work until a new survey on the *Kwinte* area is accepted.

In the southern part of the reference area, a clear object can be detected (Fig. 2). Its shape is conical, which makes the shallowest point an ideal control point for horizontal uncertainty. The coordinates of the shallowest point of this object or all accepted surveys are plotted with reference towards the Total horizontal uncertainty (THU) based on the IHO Exclusive Order. This gives a good idea if the used geodetic settings and lever arms are correct.

4.2 Backscatter

MBES BS is commonly used to map habitats and sediments. In the sand extraction areas of the Belgian part of the North Sea, BS has also been used since 1999 as a proxy to monitor changes in the seabed related to dredging activities. However, from 1999 to 2009 the BS remained uncalibrated with poorly controlled quality and repeatability. These shortcomings have prevented the cross-comparability of data collected by different MBES carried by different vessels, limiting the use of BS in monitoring programs to BS time series collected with a single MBES on one vessel.

Since 2013, the Backscatter Working Group (BSWG) has been working to establish practical methods for achieving quality control and calibration of MBES BS data (Lurton et al., 2015). Natural reference areas have emerged as a pragmatic solution to this problem (Eleftherakis et al., 2018). The approach, which relies on the stability of the seafloor of the natural reference area, allows for three main objectives: 1. Cross calibration using reference measurements from a pre-calibrated singlebeam echosounder (SBES); 2. Repeatability assessment through regular MBES measurements in the reference area as part of monitoring programs and 3. Data comparability measurements from different MBES systems by using data collected in the same reference area (Roche et al., 2018).

The *Kwinte* natural reference area, characterized by shallow bathymetry, homogeneous sediment cover and low temporal variability, provides stable and consistent characteristics essential for the BS calibration, quality and repeatability control.

Calibration in a natural reference area requires angular BS response curves (ARC) from measurements made in the same area using a calibrated singlebeam echo sounder (SBES). Through a partnership with Ifremer (France), the reference ARC's were obtained in the *Kwinte* area between May 22 and 25, 2023, using three Kongsberg Discovery (KD) EK80 SBES transducers installed on the HV Sirius, covering frequencies from 50 kHz to 440 kHz (Fig. 7a). The transducers, mounted on a pan-and-tilt device, were deployed in the HV Sirius moonpool (Fig. 7b). A reference sphere was used to calibrate the EK80 transducers. The pan and tilt unit was remotely controlled from the bridge, rotating the transducers between -10° and +75° in 5° increments. The survey covered 18 lines in both directions per frequency, creating a detailed reference library of ARC's for

 https://doi.org/10.58440/ihr-31-1-c03

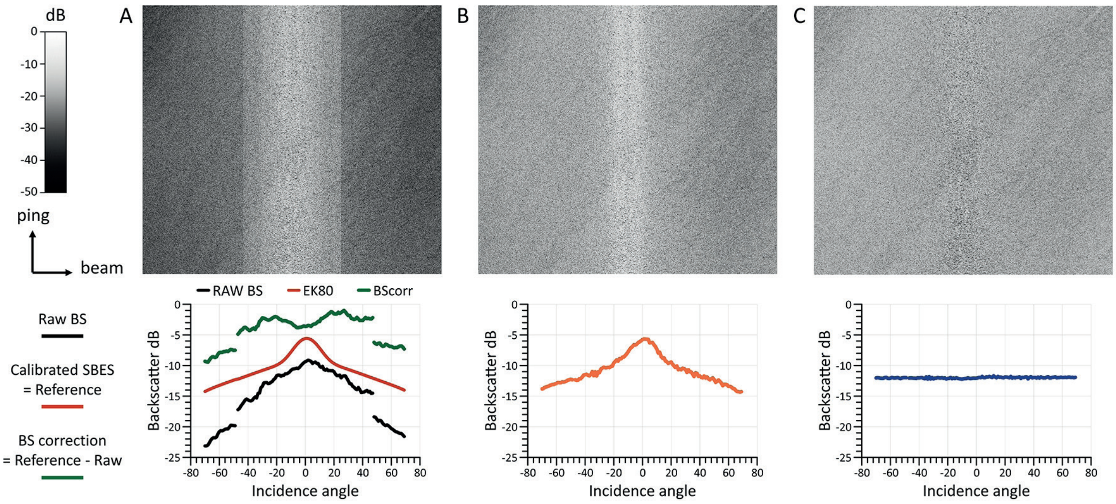

Fig. 9 MBES BS calibration method; visualization in ping beam geometry: (a) Average angular response of raw BS, reference angular response from calibrated SBES and BS calibration correction; (b) BS calibrated and corrected for beam pattern; (c) BS calibrated, corrected for beam pattern and with compensated angular response.

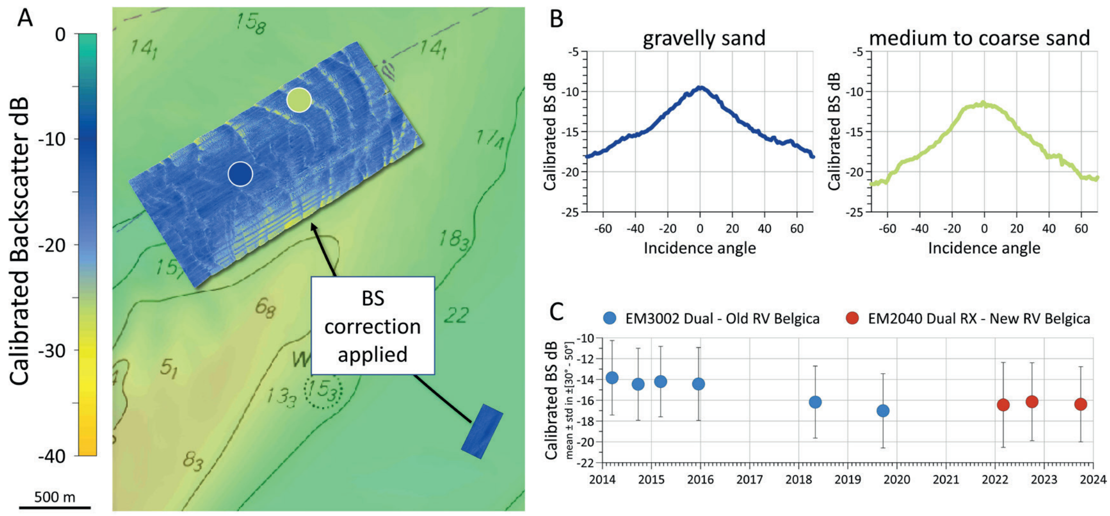

Fig. 10 Example of cross calibration of 300 kHz BS data from a sand extraction monitoring area: (a) Cross-calibration using the BS correction established on the Kwinte subarea and resulting calibrated BS mosaics; (b) Calibrated BS angular responses in two areas of interest; (c) Time series of calibrated BS values (mean ± std in the ±[30°, 50°] angular incidence range), BS data from two different MBES.

the *Kwinte* area (Fig. 7c). These calibrated angular responses serve as a reference for the calibration of the MBES BS (Fezzani & Berger, 2023). For frequencies from 50 kHz to 250 kHz, the average BS level in the ±[30°,50°] angular incidence range varies linearly from -15.5 dB to -11.5 dB. After 250 kHz, the average BS level stabilizes at about -11.5 dB (Fig. 7b). At this angular interval, the reference value for the 300 kHz frequency commonly used for sand extraction monitoring is therefore -11.5 dB.

The BS stability of the *Kwinte* area is a *sine qua non* for its use in calibrating and controlling the BS quality of MBESs. This stability is amply demonstrated by the successive average BS levels recorded from 2009 to 2021 at 300 kHz with the KD EM3002D MBES installed on the former RV Belgica (Fig. 8). In this reference time series, BS levels remain comfortably within ± 1 dB of the overall mean, and no significant trend is observed over the time period considered. Beginning in 2022, a series of measurements were made at 300 kHz with different models of the KD EM2040 MBES carried on different vessels. In the absence of calibration, these BS measurements are not comparable with each other or with previous measurements (Fig. 8).

The mean difference between the average BS level measured by a MBES in the ±[30°,50°] angular incidence range and the reference value of -11.5 dB is an estimation of the metrological accuracy of the MBES in measuring BS at 300 kHz. For measurements made from 2009 to 2011 with the KD EM3002D, this deviation is 5.5 dB. In energy terms, this means that the KD EM3002D measured only 30 % of the expected backscattered energy. With deviations of around 2.5 dB from the reference level, the KD EM2040 systems installed on the new RV Belgica and RV Simon Stevin show much better metrological quality for BS measurements at 300 kHz by measuring 60 % of the expected backscattered energy.

The MBES BS cross calibration process follows a

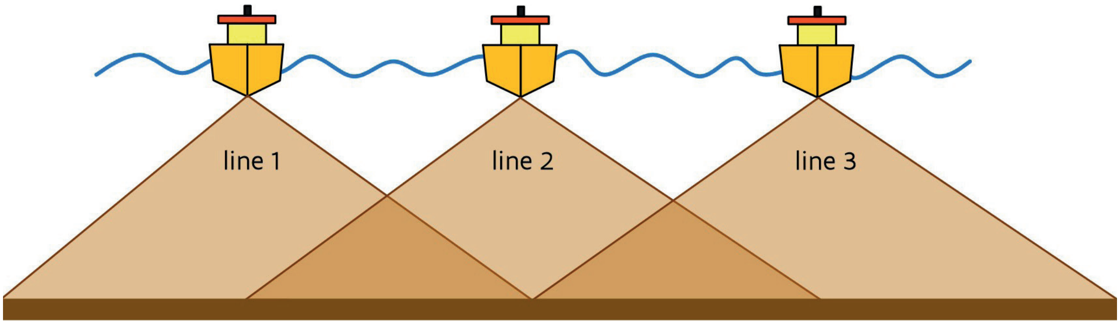

Fig. 11 Preferred line spacing resulting in a 200 % overlap.

systematic approach using Ifremer's *SonarScope*®, an open Matlab software that applies precise correction to each term of the sonar equation. BS measurements taken with the calibrated SBES EK80 guarantee the reference mean Angular Response Curve (ARC).

For each angle of incidence, the calibration corrections to be applied to the MBES BS data correspond to the differences between the MBES measurements and the reference mean ARC from the calibrated SBES EK80. Beam pattern correction is included in the BS correction values relative to the mean reference ARC (Fig. 9a). All BS measurements involved are taken at the same frequency and strictly within the *Kwinte* calculation sub area. The BS calibrated and corrected for the beam pattern keeps the BS angular dependence, which is related to the seabed's characteristics (Fig. 9b). It can be used for analyzing and modeling the angular response across different habitats. The calibration ensures the intercomparability of BS from different MBESs acquired with similar frequencies. A flattening correction is then applied to the calibrated BS corrected for the beam pattern. This correction keeps the calibrated average level of the BS consistent over the entire surveyed area. With no further artefacts, the resulting calibrated BS, corrected for the beam pattern and for the angular response, can be used as a basis for acoustic classification and seabed habitat mapping (Fig. 9c).

As part of the monitoring of the environmental impact of sand extraction in the Belgian part of the North Sea, MBES measurements are systematically carried out at 300 kHz. The stability of the *Kwinte* area and the reference mean ARC from the EK80 calibrated at 300 kHz provide a reliable basis for cross-calibrating all the MBES BS data from different shipborne systems. However, a systematic measurement of the MBES BS of the *Kwinte* sub area during each survey campaign is necessary to take into account the instrumental variation of the BS linked to fluctuations in seawater temperature.

This cross-calibration method has been successfully applied to BS time series from sand extraction monitoring zones. It facilitates the intercomparison of BS data from different MBESs, corrects for instrumental discrepancies and ensures the integrity of the BS data over the long term (Roche et al., 2025). An example of cross calibration of BS data from one monitoring area is presented in Figure 10. Data regularly acquired from the monitoring zone located on the sandbank to the north of the *Kwinte* area have been systematically calibrated using the *Kwinte* subarea survey that is closest in seawater temperature and in time (Fig. 10a). Calibrated and beam pattern corrected BS data can be used to extract angular responses in areas of interest for detailed analysis of acoustic-sediment relationships (Fig. 10b). Mean BS level in the ±[30°,50°] angular range is a reliable proxy for assessing changes in sediment cover. Cross-calibration allows data from different MBES to be considered within the same time series (Fig. 10c).

Currently, cross-calibration is carried out during post-processing, but future advances could allow real-time corrections to be integrated into MBES acquisition systems.

5 Get started yourself and contribute to the project

If you undertake a new survey in the *Kwinte* reference area, please inform VH[4] and COPCO[5] . The recommended procedure is described on our website[6]. It takes about two to three hours to survey the area. We ask to acquire the data with online RTK (Real Time Kinematic) for positioning and we ask to refer the data to LAT (Lowest Astronomical Tide). VH can assist with this, if needed.

A typical survey consists of a set of parallel lines with 200 % overlap (Fig. 11). The aim is to achieve a filled 1 m × 1 m grid after processing. It is important to survey with RTK accuracy or similar and to refer towards Lowest Astronomical tide (LAT).

Once the survey has been carried out and has been processed, please send the complete project to VH[4] and COPCO[5]. All participants will receive feedback on their survey. The data in the control area will be checked towards the IHO Exclusive Order for bathymetry and compared with the model. The

[4] Please send an email at samuel.deleu@mow.vlaanderen.be (subject *Survey Kwinte reference area*).
[5] Please send an email at marc.roche@economie.fgov.be (subject *Survey Kwinte reference area*).
[6] *Kwinte* reference area: https://www.agentschapmdk.be/en/acoustic-reference-area-kwinte (accessed 18 March 2025).

https://doi.org/10.58440/ihr-31-1-c03

delivered datasets will also be checked on artifacts resulting from timing, motion, sound velocity or other problems. If the bathymetric survey is accepted, the participant will be asked for approval to incorporate the results in the mean reference model calculation. If the participant agrees, info regarding the approved survey will be published on the website. A remark here: an accepted survey over the *Kwinte* area does not guarantee that all subsequent surveys with the vessel in other areas are also accepted. This is not the responsibility of the project partners.

For each accepted survey an extensive report is prepared with a description of the results and with reference towards the mean model.

6 Conclusion

The *Kwinte* reference area is a key site for monitoring the quality of bathymetry and BS measurements by MBES. Its stability, sediment composition and protection from seabed disturbance make it an ideal site for ensuring reliable and comparable bathymetry and BS data from MBES systems. Long-term monitoring of the area has confirmed its value as a reliable natural reference site.

Its accessibility and integration into the marine spatial plan reinforces its importance. A policy of free access encourages public and private entities to use it for hydrographic surveys. The *Kwinte* area's accessibility, along with VH's contractual requirement for its use in hydrographic data quality control, has led to a significant collection of bathymetric data from various MBES operated on Belgian and Dutch vessels.

The stability of the bathymetry is a major advantage of the *Kwinte* area. Decades of surveys reveal minimal changes in the elevation of the seabed, allowing for an accurate assessment of instrument performance and repeatability. The consistency of these results between the different MBES configurations makes the *Kwinte* area an essential reference for the validation of bathymetric data, the detection of biases and the refinement of measurement techniques in order to meet international hydrographic standards.

As a stable BS reference, the *Kwinte* area plays a crucial role in ensuring the accuracy, the consistency, the repeatability and the comparability of MBES BS measurements, particularly in the context of seafloor scientific monitoring programs. Long-term BS measurements done with the same MBES demonstrate a remarkable BS level consistency without any trend over more than a decade. This stability ensures that any variations observed in the BS levels can be confidently attributed to instrumental bias rather than real sediment changes. In addition, the reference angular response curves (ARC) derived from calibrated single beam echo sounder (SBES) measurements provide a robust framework for cross-calibrating MBES BS data. The cross-calibration methodology allows the instrumental variations associated with seawater temperature to be taken into account. By systematically surveying the *Kwinte* area during each monitoring campaign, a retrospective calibration of the BS measurements ensures the inter-compatibility of BS data from different MBES. This approach has been successfully applied to sand extraction monitoring areas, allowing the integration of BS data from different MBES into a single coherent time series, thus improving the reliability of seafloor evolution studies.

Currently used for post-processing, this methodology could, in the future, ideally be integrated into MBES acquisition systems to allow real-time calibration.

As research progresses, the *Kwinte* reference area will continue to serve as a reference for high quality, reproducible and scientifically rigorous MBES bathymetric and BS data, reinforcing its essential role in validating MBES data used in hydrography, marine habitat monitoring and sediment dynamics studies.

In practice, the definition, initial assessment, monitoring, and management of a reference area fall under the responsibility of a specific organization or group of stakeholders. However, establishing collectively a network of calibration zones would enhance accessibility for all relevant actors in the field, enabling calibration and repeatability checks of bathymetry and BS for any MBES used in international campaigns and research and monitoring initiatives. Mandating that contractors involved in hydrographic survey, monitoring and mapping programs regularly survey reference areas to calibrate their sonar systems would convey a strong and positive message to the hydrographic and scientific communities. In particular for the BS users community, for which no BS quality scale has yet been established, this requirement would underscore the significance of quantitative BS signal acquisition and processing, marking a significant advancement in this research field.

Acknowledgements

The authors wish to thank their colleagues at VH and COPCO who participated in the project. We would like to warmly thank our colleagues Ridha Fezzani, Arnaud Gaillot and Laurent Berger for their work in calibrating, acquiring, analyzing and producing the *Kwinte* area BS reference angular responses. The authors also thank the participating institutes and companies and the crews of the Hydrographic and Research Vessels involved in acquiring the data presented in this contribution.

References

Deleu, S. and Roche, M. (2020). KWINTE, a Dedicated Quality Control Area in the North Sea with Stable Seabed. Reference Area for Multibeam Bathymetry and Backscatter. *Hydro international, 1*, pp. 18–20.

Eleftherakis, D., Berger, L., Le Bouffant, N., Pacault, A., Augustin, J. M. and Lurton, X. (2018). Backscatter calibration of high-frequency multibeam echosounder using a reference single-beam system, on natural seafloor. *Marine Geophysical Research, 39*, pp. 55–73.

Fezzani, R. and Berger, L. (2023). *Creation of a reference area for backscatter calibration of shallow and medium depth multibeam sounders.* Ifremer internal report, ASTI-2023-300, 24.

IHO (2022). *Standards for Hydrographic Surveys* (ed. 6.1). IHO Special Publication S-44, International Hydrographic Organization, Monaco. https://iho.int/uploads/user/pubs/standards/s-44/S-44_Edition_6.1.0.pdf (accessed 18 March 2025).

Lurton, X., Lamarche, G., Brown, C., Lucieer, V., Rice, G., Schimel, A. and Weber, T. (2015). Backscatter measurements by seafloor-mapping sonars. Guidelines and recommendations. doi:10.5281/zenodo.10089261 200

Roche, M., Degrendele, K., Vrignaud, C., Loyer, S., Le Bas, T., Augustin, J. M. and Lurton, X. (2018). Control of the repeatability of high frequency multibeam echosounder backscatter by using natural reference areas. *Marine Geophysical Research, 39,* pp. 89–104.

Roche, M., Birkenes Lønmo, T. I., Fezzani, R., Berger, L., Deleu, S., Bisquay, H., Gaillot, A., Vanparys, K., Vercaemst, J., Degrendele, K., Barette, F., Fonseca, L., Verstraeten, J., Jensen, K., Echholt Nilsen, K., Montereale Gavazzi, G., Lurton, X., Augustin, J.-M. (2025). Instrumental temperature-dependence of backscatter measurements by multibeam echosounder: findings and implications. *Frontiers in Remote Sensing, Special Issue Multibeam Echosounder Backscatter: Advances and Applications*, accepted 8 May 2025.

 https://doi.org/10.58440/ihr-31-1-c03

CONFERENCE PAPER

Towards a simpler assessment of the environmental impact of hydrographic echosounders

Author
Xavier Lurton[1]

Preamble

The following work was presented at the Hydrographic Conference HYDRO 2024, 5–7 November 2024, Rostock-Warnemünde, Germany in the oral session *Environmental and habitat mapping*.

Abstract

Conducting seafloor-mapping surveys often implies preliminary authorization requests based on the prediction of the field radiated by the sonars to be operated, compared to acceptable thresholds established for concerned marine animals and different risk levels. Applied to multibeam echosounders, risk assessment studies show very moderate risk levels, for objective reasons that are presented here together with some modelling results. Such systematic risk evaluations are redundant since they always concern the same sonars and animal species. It is suggested that regulatory authorities explicitly consider the case of seafloor-mapping echosounders, confirm their limited impact according to current methodologies and standards and, when appropriate, exonerate them from preliminary risk assessment.

Keywords
environmental impact · echosounder · hydrography · marine mammals

✉ Xavier Lurton · xavier.lurton@orange.fr

[1] Consultant in Underwater Acoustics, Locmaria Plouzané, France

 https://doi.org/10.58440/ihr-31-1-c02

1 Introduction

Within the general effort to decrease the impact of man-caused underwater noise on the marine animal populations, the operation of active sonar systems has been, for several decades, more and more subject to regulation and control. The initial concern was the impact of naval sonars on marine mammals; it was then extended to other categories of sonar systems, now including echosounders used for seafloor mapping.

In a number of countries today, programming seafloor-mapping survey cruises (for scientific, industrial or hydrographic purposes) implies a preliminary authorization procedure based on the prediction of the field radiated by the echosounders to be operated, compared to acceptable impact thresholds established for the concerned marine animals (cetaceans in a high majority of cases) and different levels of impact (from disturbance to physical injury). These studies usually conclude to a very moderate risk level (if any), for a number of objective reasons (Lurton & DeRuiter, 2011): most echosounders transmit high-frequency signals in the upper part or beyond the animals' auditory ranges, and attenuating very fast in seawater; the echosounder signals are very short (tens of microseconds to tens of milliseconds) although relatively narrow-band (hence non-impulsive), and are transmitted inside narrow angular sectors (typically 1°); seafloor-surveying sources are intrinsically mobile and insonify very briefly a given point. All these factors determine a sporadic time-space occupation by the echosounder radiation. After comparison with the acceptable thresholds (mainly relevant for cumulated received energy), this logically results in an absence of constraining measures for these systems.

Systematically conducted today, such risk studies are very redundant, since they always concern the same sonar systems which are actually quite few. This obviously causes a waste of time and efforts for both the applicants and the regulatory authorities: for one given echosounder the resulting conclusions are always the same and could have been established once for all through a common preliminary effort involving the regulators and the constructors.

Although the issue of acoustical noise impact on marine life is a real concern today for a number of causes (increase of the shipping traffic, offshore industry and various coastal activities), the specific case of echosounders should be reconsidered. In this respect, it is suggested that the regulatory authorities should explicitly consider the current seafloor-mapping echosounders, confirm their moderate impact according to current methodologies and standards and, when appropriate, exonerate them from preliminary impact studies. This effort could be helped by the echosounders constructors providing the necessary technical background. Such an evolution could be supported by the main actors in the field of ocean mapping (IHO, hydrographic services, public agencies, oceanography institutes…).

The present paper summarizes the fundamentals of the various issues to consider (echosounder radiation properties, currently applicable risk thresholds) and gives a simple (while sufficient) methodology and some practical results providing a basis for the approach recommended above.

2 Context

The impact of anthropogenic acoustic noise upon marine life has been a concern for more than three decades, mainly regarding marine mammals (MM). First alerts came in the 1990s, with the acknowledgement of a number of cetacean strandings caused by naval drills operating medium-frequency active sonars; these events usually concerned odontocetes, and especially beaked whales. This led to a significant effort in scientific research in this field (Southall et al., 2007), as well as first attempts of mitigation and regulation for naval sonars (TNO, 2016). In 2008, a massive stranding of melon-head dolphins trapped in an estuary in Madagascar was interpreted (Southall et al., 2013) as triggered by a distant survey operation by a 12-kHz multibeam echosounder (MBES). This event and its interpretation, causing significant reactions of the public opinion, raised suspicion about the harmfulness of low-frequency MBES, then spreading to other echosounder types. Since then, the extension of regulation and authorization procedures to more and more acoustic sources has been going on, linked to generalized environmental legislation and environment impact assessments (EIA) policies in many countries (e.g. Thomsen et al., 2021). This paper considers, from an engineering point of view, the particular field of seafloor-mapping cruises (for hydrography, science or industry purposes) operating MBES systems.

2.1 Objective quantification of auditory risks

Quantifying the acoustical impact of human activities upon marine life is an extremely wide and complex topic, restricted here to (1) marine mammals and particularly cetaceans (especially affected by acoustic phenomena and scrutinized by public opinion) and (2) multibeam echosounders (i.e. the main tool used today in seafloor mapping and especially hydrography, whose analysis can be extended to other sonar systems).

The acoustical risks quantification implies a specific analysis of the noise field at receiver; the received signals are expressed along dedicated metrics, whose comparison with admissible risk thresholds leads to conclusions about their acceptability and finally to key decisions such as cruise authorization and/or binding application of mitigation measures.

Sound levels received from a noise source are mainly expressed using two fundamental metrics (Southall et al., 2007):

- The Sound Pressure Level (SPL) is the maximum instantaneous value of the received sound pressure. Its use is especially relevant in the case of very-high-power impulsive sources such as explosions. As a sound pressure value, it expresses in dB re 1 µPa.

- The Sound Exposure Level (SEL) is the cumulated signal energy received over a reference period (conventionally 24 hours). It is well adapted to long or repetitive signals whose accumulation leads to a significant impact even for moderate instantaneous levels. Homogeneous to an energy, it expresses in dB re 1 µPa²s.

The auditory risk thresholds must be defined, in the case of marine mammals, according to various parameters:

- The animal species, defining their auditory response and frequency specialization and sensitivity;
- The received signal frequency range and its nature (impulsive or not, intermittent or continuous, wide- or narrow-band…);
- The type of risk to consider (from disturbance to physical injury) and possibly its severity level (Southall et al., 2021).

Marine mammals are classified today (NOAA, 2024) into several hearing groups: low-frequency (LF_c – all mysticetes); high-frequency (HF_c – most odontocetes); and very-high-frequency (VHF_c – some odontocetes). Other mammals (such as sirenians, seals or bears) constitute other specific hearing groups, possibly distinguishing in-air and in-water conditions for the amphibious. They are not considered in the present work; this omission is conservative since they are less sensitive to sound impact than cetaceans.

The distinction between the various auditory groups is based on considerations on their hearing sensitivity at low level with its corresponding frequency dependence, i.e. their audiograms. In order to account for this frequency selectivity, specific weighting curves (named "M-Weighting") are derived from the audiograms; conceptually they can be compared with the "dB-A" or "dB-C" weighting curves well known in human audiology (Houser et al., 2017). Fig. 1 depicts the M-Weighting curves computed for the three cetacean groups according to the latest reviews (NOAA, 2024) compared with the MBES frequency range (12 to 400 kHz).

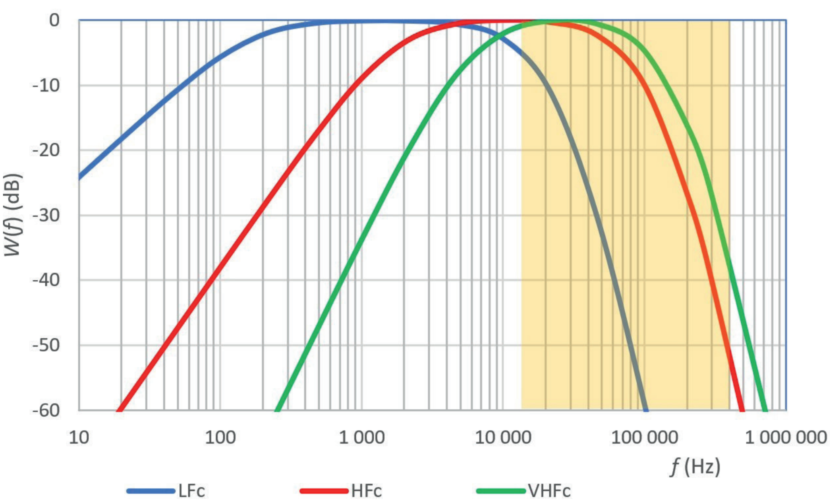

Fig. 1 M-weighting functions for the three auditory classes of cetaceans, plotted vs. frequency. See (NOAA, 2024) for details and discussions. The overall frequency range of current MBESs (12–400 kHz) is superimposed.

2.2 Current standards for risk thresholds

The auditory risk levels associated to the reception of sound may be classified in three categories. *Behavioral impact* is the lowest risk level caused by sound reception. The subject receiving the sound perceives it as significant enough for triggering a reaction (usually of avoidance, but attraction is possible as well) at various levels of severity (Southall et al., 2021). No physiological degradation of the auditory system is involved in this process. The received sound property causing the reaction can be energetic (the instantaneous level, or the cumulated energy), but also linked to its content (a sound can be perceived as having an unpleasant, threatening, intriguing, appealing etc. "character"). Considering the extreme variability and generality of these concepts and their intrinsic subjectivity, no applicable quantified threshold is obtainable today from the scientific literature, although the studies in this domain are many (while these really dedicated to MBES are rather rare, see e.g. Kates-Varghese et al., 2020). It must be mentioned that two classical figures for behavioral thresholds are still in use today (NMFS, 2024): SPL = 160 dB re 1 µPa for impulsive sounds and SPL = 120 dB re 1 µPa for non-impulsive. However, considering that these levels do not depend at all on the noise properties (frequency, duration, spectral content…) neither on the animal species and auditory properties, nor on the exposure conditions, they can hardly be considered as reliable quantitative thresholds based on scientific results and usable as such.

A *Temporary Threshold Shift (TTS)* is a short-term impairment of the auditory system, caused by too intense an exposure to sound. It is commonly experimented in human audition, when a feeling of temporary deafening happens after some overexposure to noise, and disappears after a variable time lag depending on the severity of the overexposure. TTS values available for marine mammals (Finneran, 2015) result from objective measurements conducted in laboratory conditions (as well as for humans and terrestrial mammals).

A *Permanent Threshold Shift (PTS)* is a definitive impairment corresponding to an irreversible degradation of some parts of the auditory system. For obvious ethical reasons it cannot be measured experimentally as a provoked feature, but is extrapolated from measured TTS values (a shift of +20 dB from TTS to PTS is often admitted). Obviously, a PTS may be of various severity levels, classified in human audition from "mild" to "profound hearing loss". In the case of MM risk assessment, the considered PTS threshold corresponds to the smaller permanent shift that can be observed (taken as -3 dB). Hence PTS in

https://doi.org/10.58440/ihr-31-1-c02

Table 1 Values of the various risk thresholds (in SPL or SEL) retained today for PTS or TTS and for the three auditory classes of cetaceans; from (NOAA, 2024).

Threshold types	Cetacean Auditory Group			Units
	LF_C	HF_C	VHF_C	
TTS / Impulsive / Unweighted SPL	216	224	196	dB re 1µPa
TTS / Impulsive / M-weighted SEL	168	178	144	dB re 1µPa^2.s
TTS / Non-Impulsive / M-weighted SEL	177	181	161	dB re 1µPa^2.s
PTS / Impulsive / Unweighted SEL	222	230	202	dB re 1µPa^2.s
PTS / Impulsive / M-weighted SEL	183	193	159	dB re 1µPa^2.s
PTS / Non-Impulsive / M-weighted SEL	197	201	181	dB re 1µPa^2.s

this context does not correspond to a profound impairment of the affected subject, but to the slightest level of detectable injury sequel[1].

The most common criterion used today for acoustical environmental risk assessment is the PTS, due to its objective quantifiability. By definition, behavorial reactions and TTS are temporary issues, stopping after their cause has disappeared.

The latest standards available today have been compiled by NOAA/NMFS based on the state of the art of the available scientific literature (NOAA, 2024; NMFS, 2024). On this basis, Table 1 gives the TTS and PTS values for cetaceans associated to both impulsive and non-impulsive signals (the latter relevant for echosounders).

2.3 Typical requirements for risk assessment studies

The analysis needed for an auditory risk assessment study implies both a statement of the animal species and populations expected to be present on the survey area; a summary of the radiation properties of the sonars to be operated; and finally, a computation of the associated risks based on the threshold limit range determination.

From specialized databases a list must be established of the various expected species with their local density, accounting for seasonality; this makes it possible to determine the relevant risk thresholds to be applied. The sonar information must include the relevant characteristics of the source level and directivity, the frequency range covered, the transmission duration and repetition rate. The cruise program must also be established, including e.g. the planning for transmission sequences and the associated survey speeds. Finally, the insonification risks have to be computed accounting for the relevant sonar properties and applicable thresholds, basically using algorithms such as the one presented in the following. The risk assessment results make it possible to take a decision about the cruise acceptability, either without restrictions or with application of a number of mitigation measures (limitation of the source level, monitoring by specialized marine mammal observers).

2.4 Multibeam echosounders characteristics

Multibeam echosounders are today the most widely used sonar systems for seafloor mapping. We will not propose a detailed description of their working principles, since only their transmitting part (Lurton, 2016) is of interest here: it always consists in a long projector array (several tens of times the acoustic wavelength) installed along the carrier vehicle axis, while relatively narrow across-ship. The purpose is to transmit the echosounder signal within a fan-shaped lobe (Fig. 2) of very wide aperture across-track (significant levels are radiated up to 60–70° on each side of nadir with a fall-off at grazing angles) and very narrow along-track (a 1° magnitude is usual). The transmission process can be split (Fig. 2) into several angular sectors across-track (in order to maximize the available power in each one) and several swaths along-track (to maximize the coverage and sounding density). However, in this angular partition the various sectors do not overlap neither in angle nor in time, so that within a ping sequence a receiving point is insonified only by one sector and one swath.

MBES systems can be declined into several categories according to their frequency range, itself related to their specialization in water depth range. Table 2 gives, for five arbitrary archetypes of MBES (Deep Water 1 & 2, Medium Deep, Continental Shelf, Shallow Water), a set of transmit characteristics derived from various constructors' documentation and expected to be representative of current systems: frequency, source level, angle aperture, pulse duration, total transmission time (in case of multi-sector and multi-swath systems), pulse rate (for a typical water depth value). These figures are given here as representative magnitudes for typical current systems and settings; individual cases may differ from these values. Note that these are rather upper values (e.g. for source levels or pulse durations), in order to stay on the conservative side of the assessment.

The types of signals emitted by seafloor-mapping echosounders show little variety. They are most often CW pulses (a gated sine wave, with some envelope

[1] Note that regulations of human audition protection (e.g. limits of exposure to noisy work environments) are usually not so protective: a permanent hearing loss is considered as significant when exceeding -25 dB.

Table 2 Typical characteristics of several archetypal MBES (Deep Waters 1 & 2, Medium Deep water, Continental Shelf, Shallow Waters): Frequency F (kHz), Source Level SL (in dB re 1 μPa@1m), along-track aperture θ (°), far-field limit range R_{FF} (m), relative level of sidelobes SLL (dB), elementary pulse duration T_P (ms), total duration of one pulse cycle T_T (ms), pulse repetition delay T_R (s), typical water depth H (m) and seawater absorption coefficient α (dB/km). The MBES characteristic values are inspired from various constructors' documentation.

Parameters (units)	MBES Category				
	DW1	DW2	MD	CS	SW
F (kHz)	12	33	70	150	300
SL (dB)	242	237	225	222	220
θ (°)	1	1	1	2	2
R_{FF} (m)	410	149	70	8	4
SLL (dB)	-25	-25	-25	-25	-25
T_P (ms)	50	20	5	2	1
T_T (ms)	400	200	50	10	3
T_R (s)	20	10	2	1	0.2
H (m)	5000	2500	500	200	20
α (dB/km)	1.32	7.96	23.3	44.7	73.1

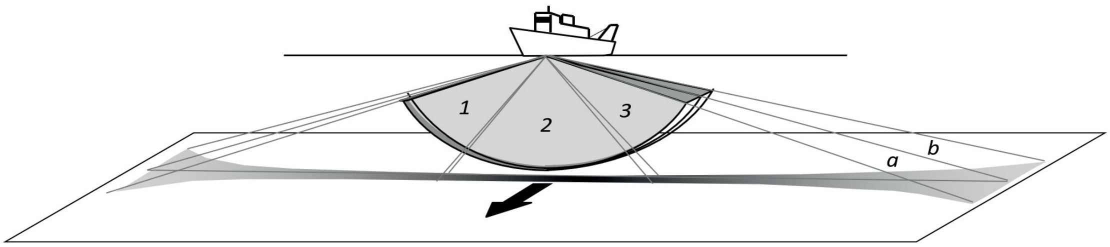

Fig. 2 Simplified insonification geometry for the main lobes of a multibeam echosounder. The transmit array radiates inside one or more narrow fan-shaped sectors, for a progressive coverage of the seafloor by successive swaths along the carrier ship motion. This sketch depicts two transmit sectors along-track (a, b) and three across-track (1, 2, 3).

tapering smoothing the rise and decay); although their duration can be very short (tens of μs to tens of ms according to the operating frequencies) they are still tonal narrow-band signals and are not to be assimilated to impulsive signals such as blasts, shocks or airguns (Finneran & Jenkins, 2012) characterized by a very wide spectral occupation prone to cause specific auditory damages. The FM signals used to increase the operational range of MBES do not show really different properties, and are characterized by slightly longer pulse durations and a usually modest frequency sweep. Hence, risk thresholds evaluated for echosounder signals have to consider them as non-impulsive despite their short durations.

3 Modelling

3.1 Risk threshold range computation

The fundamental formula establishing the risk threshold range R_{RT} for a given configuration (sonar parameters, cetacean group) states the equality between the received SEL and the selected risk threshold value compensated by M-weighting:

$$SEL(R, f) = RT(M_m) - MW(M_m, f) \text{ for } R = R_{RT} \quad (1)$$

written here in decibels, where $SEL(R, f)$ is the cumulated sound exposure level at range R and frequency f of interest for the noise considered; RT is the risk threshold level upon reception, for a MM species and a given risk level (TTS, PPS…); and MW is the M-weighting factor, depending on MM species M_m, and signal frequency f.

3.2 MBES radiation regimes

As for any active sonar source, two main regimes of radiation must be considered for the sound exposure at a given receiver, namely transmission either inside the main lobe or through the lateral sidelobes. This simplifying approach is interesting both for its ease of conceptualization despite a complex radiation geometry (Lurton, 2016) and for its capacity to provide correct magnitudes in an approximate but realistic and conservative way.

Direct Insonification – The most obvious regime is when the receiver is located inside the fan-shaped MBES main lobe radiation pattern (Fig. 3). The source level to consider then is the nominal transmit power of the sonar, and the insonification duration is the pulse length. The SEL value for this "direct" regime expresses as:

$$SEL_D(R, f) = SL + DF + 10\text{Log}T_P - TL(R, f) \quad (2)$$

with

- SL = Sonar Source Level, in dB re 1μPa@1m
- DF = Transmit Directivity Function toward the

 https://doi.org/10.58440/ihr-31-1-c02

receiver. It is simplified here to a constant 0 dB inside the main lobe, and a characteristic relative value (typically -20 to -30 dB) in the sidelobes
- $10\text{Log}T_p$ = energy integration over exposure time T_p
- $TL = 20\text{Log}R + \alpha(f)R$ = transmission loss at range R and signal frequency f, $\alpha(f)$ being the absorption coefficient in dB/m. Note that, at short ranges from the source, a different TL expression accounting for the near-field effect must be considered (see below).

A key particularity of this main-lobe direct-exposure case is that it happens only once (if ever) for a survey line close to a fixed receiver, since the MBES transmit beam is very narrow and intersects only once per ping any point of the nearby medium, accounting for the sonar platform motion ahead. The insonification probability decreases at short ranges and for slow ping rates (and/or high speeds), as it can be shown from an elementary geometrical description (see a sketch in Fig. 3).

Near-field propagation losses in the main lobe – Due to their very long dimension relatively to wavelength making their angular aperture magnitude around 1°, MBES transmit at short ranges in the "near-field" regime (Lurton 2010). Beyond a limit range defined at frequency f as the "Fresnel range" or "far-field range" and given by $R_{FF} = L^2/\lambda$ where L is the array length and λ the signal wavelength, the propagation follows the classical spherical law in $1/R^2$; however, below this limit range the propagation follows a cylindrical variation in $1/R$. The transmission loss writes then under the generalized form:

$$TL(R, f) = 10\text{Log}(R \, x\max(R, R_{FF}(f)) + \alpha(f)R \qquad (3)$$

For a 1° aperture, the Fresnel range $R_{FF}(f)$ equals approximately 400, 150 and 70 m for frequencies 12, 33 and 70 kHz. The near-field effect will be considered only in the computations related to insonification in the main lobe; for the sidelobe radiation the spherical regime is considered.

Sidelobe insonification – Since the sidelobes radiate all over the angular space surrounding the main lobes (in first approximation at a constant level) they are prone to insonify the receiver at each ping whatever its position. If they are considered, in first approximation, to radiate with a roughly constant level (Lurton 2015) there is no angular dependence and the only parameter is then the sonar-receiver range which is prone to change from ping to ping. In the usual seafloor-mapping configuration of an infinite survey line passing by the receiver at a minimum range R_m, it can be shown that the cumulated SEL can be approximated by the expression (Lurton, 2016; NOAA, 2024):

$$SEL_{cum}(R_m) = SL_{SL} + 10\text{Log}_{10}[\pi/V/R_m x T_T/T_r] \qquad (4)$$

with
- SEL_{cum} the SEL cumulated along the survey line
- SL_{SL} the source level provided by the sidelobes;
- V the sonar speed in m/s, assumed constant;
- T_T/T_r the duty cycle, or the ratio of the total transmitted pulse length to the time interval between two ping sequences (see Table 2).

3.3 Model validity: a conservative approach

Although deliberately simplified, the above modelling provides a solid basis for risk assessment studies. The MBES radiation characteristics result from a thorough analysis of more detailed approaches and knowledge (Lurton, 2016). Considering the purpose and the context of EIA studies, it is interesting to remind here three main conservative hypotheses underlying the present methodology:
- The MBES properties are given for high values maximizing their potential impact; in particular the source levels and pulse lengths, without systematically representing *maximum maximorum* values, are taken in their upper range, while in actual situations the systems are operated most of the time at lower power adapted to the local water depth.
- The risk thresholds values, proposed in (NOAA, 2024) and used here, correspond to the lowest detectable levels of impairment, either temporary or permanent.
- The radiation patterns in the vertical plane (for both main lobe and sidelobes) are taken as constant with angle, while they actually decrease significantly at low grazing angles and hence minimize the SEL in the upper water layers.
- The direct exposure case is admitted to happen at least once during the survey line, while this may not be the case (Fig. 3).

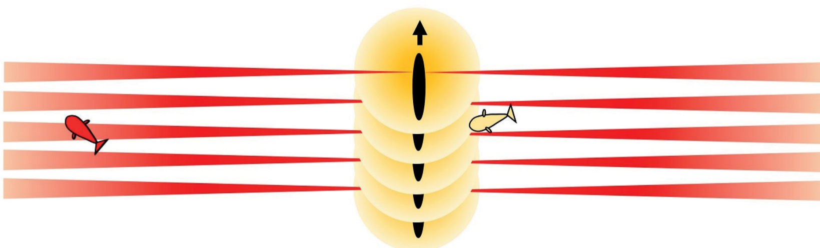

Fig. 3 Horizontal view of the insonification by a MBES during a survey line. The sketch depicts a series of pings along the carrier ship advance. The main lobe (red) is very narrow and has little chances to intercept a receiver. On the other hand, the sidelobe radiation continuum (yellow) strikes the receiver for every ping, but with lower levels and at varying ranges along the survey line.

Two more remarks are to be done about propagation modelling applied here. For the sake of simplicity, the absorption effect in seawater was omitted in actual numerical computations, hence maximizing the predicted SEL values. Conversely, the influence of multipaths propagation is not considered, which minimizes the SEL prediction. However, considering the obtained threshold ranges (Section 4), both

Table 3 PTS threshold ranges in the case of direct insonification inside the main lobe. The result value “0” means that no solution in range can be found since the SEL is then lower than the threshold whatever the range.

MBES	*F* (kHz)	SL (dB)	T (ms)	R_{RT}/LF_c	R_RT/HF_c	R_{RT}/VHF_c
DW1	12	242	50	2 m	2 m	120 m
DW2	33	237	20	0	1 m	50 m
MDW	70	225	5	0	0	1 m
CS	150	222	2	0	0	0
SW	300	220	1	0	0	0

absorption and multipaths are obviously of low influence and neglecting them in first approximation is justified.

4 Computation results for generic representative configuration

4.1 Computation results

The M-Weighted risk thresholds (PTS and non-impulsive criteria) are compared with the SEL from MBES, and the difference is used to compute the risk threshold range R_{RT} (accounting for the near-field effect).

Main lobe insonification – As explained above, in this case the animal is located inside the main lobe and receives one direct ping; the received sound intensity is then at its highest possible value. However, this event is very short and happens only once (if at all; Fig. 3), since the lobe aperture is very narrow and the receiver will very soon be out of it due to the carrier motion (and possibly to its own); conventionally, the number of active pings is taken here equal to unity. The risk threshold ranges are estimated using a combination of Eqs. 1, 2 and 3 above (i.e. including the near-field effect).

Sidelobe insonification – The modelling applied here was chosen to consider the cumulated exposure caused by a survey line passing close to the receiver and described by the model given in (Eq. 4). For multi-sector and/or multi-swath MBES, the effective transmission time to consider for sidelobes cumulates the durations of all the signals transmitted within one ping sequence (T_T in Table 2). For the demonstrative computation presented here, we used a carrier speed of V = 4 m/s (around 8 knots), a sidelobe level by -25 dB below the main lobe, and a duty cycle of T_T/T_R = 1/50.

4.2 Analysis of computation results

For the two configurations presented here (insonification by one ping in the main lobe in Table 3; or by a complete survey line through the sidelobes in Table 4), the threshold ranges are null or negligible in most cases. The only exception happens for the low-frequency echosounders DW1 and DW2 and the VHF cetaceans; still in this case the threshold ranges are quite modest. In all other cases, and despite the conservative hypotheses applied (Section 3.3), the risk thresholds are never reachable.

These limited and simplified results have been presented as an illustration of what is normally obtained from a risk assessment study conducted preliminarily to a survey cruise operating MBES. To summarize, two cases can be considered:

Higher-frequency MBES (above 70 kHz), used for seafloor mapping over the continental shelf (depth smaller than 200 m) and shallow water, as well as prone to be installed on deep vehicles (ROVs and AUVs) cannot cause SELs exceeding the today's admissible thresholds (NOAA, 2024), whatever the cetaceans auditory class. This results from the fact that these sonars transmit at relatively modest levels (compared to lower-frequency systems) and with very short pulses inside a small number of angular sectors. Moreover, beyond 150–200 kHz their frequency is expected to exceed the auditory range of all marine mammals (Fig. 1). It is also reminded that high-frequency sound is submitted to a fast decay when propagating in seawater (magnitudes from 30 dB/km at 100 kHz up to 100 dB/km at 400 kHz); however, the very short ranges obtained in the computation results above do not give the absorption effect a significant role.

Lower-frequency MBES (below 70 kHz), used for mapping the deep ocean and the continental slopes, raise a limited risk, if any. Indeed, they present several negative features: they transmit in the frequency range of higher sensitivity of MMs; their source levels and pulse lengths are usually high, for efficiently mapping deep seafloor; and they are little affected by seawater absorption. However, despite these concerning features, their actual risk of exceeding admissible thresholds (NOAA, 2024) remains negligible for cetaceans of the LF_c and HF_c hearing classes; it is noticeable, while modest, only for the VHF_c cetacean class[2].

5 Discussion

The environmental impact of mapping sonars (mainly echosounders) is regularly questioned nowadays. Consequently, in many countries, conducting scientific or industrial survey cruises implies a preliminary request for an authorization based on the prediction of the field radiated by the sonars to be operated,

[2] It should be noted in this respect that many of the VHF cetacean species are coastal species, with little chances of being submitted to low-frequency MBES survey operations conducted in deep waters.

https://doi.org/10.58440/ihr-31-1-c02

to be compared to the acceptable impact thresholds defined for the concerned marine animals (Section 2.3). Such predictions may exceed the capabilities of many labs or survey companies, especially since the input data (sonar technical information) may be hardly available. It should be much more practical that such studies are conducted once for all by the sonar constructors and/or independent instances and results made available to their customers and to regulators; the purpose is that (1) the surveyors could use these results in their authorization request applications; (2) the regulatory authorities could *a priori* exonerate certain sonar classes or models, considered as impactless based on these results; (3) the constructors could claim some official approval of their products in terms of noise impact. Generally speaking, this should go in the sense of a better transparency about the actual characteristics of echosounders and their potential impact.

It is hence suggested that, following the present study, a specific project of impact prediction of seafloor-mapping sonars is conducted, relying on both previously published modelling works (e.g. Lurton, 2016) completed by some more recent results, jointly with the latest available science regarding the acoustical impact of acoustical systems on marine life (e.g. Southall, 2019) and finally the latest regulatory syntheses (NOAA, 2024). This should not be limited to MBES, but extended to other mapping sonars (single-beam echosounders, side-scan sonars, subbottom profilers) akin to (Ruppel, 2022). In a first step, for every concerned sonar an approximate functional model will be built, in agreement with the constructor who will provide the necessary information needed for an accurate modelling (transmission beam patterns, source levels, pulse characteristics – together with relevant operating modes recommended in survey conditions). The radiation model will then be applied for computing the relevant sound field characteristics (sound pressure level SPL, sound exposure level SEL cumulated along survey lines). The results of the radiation model computations will then be compared to the various threshold values available in the scientific literature and currently applied by regulators. This comparison will lead to conclusions about the predicted impact of the studied system, in the framework of the current scientific knowledge and regulation context; note that the results will be prone to be easily adapted to possible/probable evolutions of the regulatory thresholds.

6 Conclusions

While the impact of man-caused underwater noise on marine life is today a wide topic of concern, the particular case of hydrographic echosounders deserves a special attention. Since their apparition one century ago, these systems have constantly adopted similar specific characteristics making them of low concern for marine life: short narrow-band signals at medium to high frequencies, inside downward-steered narrow sectors. Within this configuration, the animals exposure in main transmission lobe at high level is only sporadic; sidelobe insonification continuously happens but at much lower levels. Hence the chances of exceeding objective risk thresholds (such as PTS defined in particular for marine mammals) appear to be very low, if possible at all. On the other hand, behavioral reactions of animals to echosounding are certainly possible – although no consensus exists today neither on the actual significance of their impact nor even on the possibility that they could be quantified. In this context, enforcing the respect of objective physiological thresholds appears as the best option today.

While limited in its scope and methodology, the work proposed here has presented a general framework for comparing the technical characteristics of today's echosounders and the current knowledge status (often used in a regulatory framework) about risk thresholds applicable to marine mammals. Its clear conclusions are that higher-frequency echosounders (above 70 kHz) cannot reach current thresholds, while lower-frequency systems are possibly of concern for cetaceans of the VHFc class. These conclusions do not significantly differ from those obtained previously for a similar context (Lurton & DeRuiter, 2011) despite the subsequent evolutions in echosounders properties and available scientific knowledge.

Official authorization procedures prior to conducting at-sea operations of echosounders are now enforced in many countries and are applicable to hydrographic, scientific, or industrial contexts, involving predictive studies of the possible risks of these sonar systems to marine fauna. The paradox here is that most of these studies are pointless since, as shown in the present paper, the impact of most hydrographic echosounders as expressed by current risk standards (NOAA, 2024) is negligible. Hence a high number of assessment studies are conducted yearly, always regarding the same echosounders types and models and the same marine species, and always leading to the same conclusions.

What is suggested here is that, in a near future, a concerted effort is dedicated to a systematical evaluation of the objective risk level raised by current echosounders, leading to clear conclusions about the possibility to exonerate certain classes of systems from the current regulatory constraints. This should be a joint effort between the constructors (providing detailed information about the transmission characteristics of their products) and regulators (that should endorse the results of such studies and include them in future regulations), under the scrutiny of independent instances controlling the scientific relevance of such works and ensuring the public dissemination of the results. As a preliminary, the work presented here above has proposed a methodology for such a future task, and hopefully has given first useful magnitude orders and conclusions.

References

Finneran, J. J. (2015). Noise-induced hearing loss in marine mammals: A review of temporary threshold shift studies from 1996 to 2015. *J. Acoust. Soc. Am., 138*, pp. 1702–1726.

Houser, D. S., Yost, W., Burkard, R., Finneran, J. J., Reichmuth, C. and Mulsow, J. (2017). A review of the history, development and application of auditory weighting functions in humans and marine mammals. *J. Acoust. Soc. Am., 141*, pp. 1371–1413.

Kates Varghese, H., Miksis-Olds, J., DiMarzio, N., Lowell, K., Linder, E., Mayer, L., and Moretti, D. (2020). The effect of two 12 kHz multibeam mapping surveys on the foraging behavior of Cuvier's beaked whales off of southern California. *J. Acoust. Soc. Am. 147*(6), pp. 3849–3858.

Lurton, X. (2010). *An Introduction To Underwater Acoustics – Principles and Applications, Second Edition*, Springer-Verlag, Berlin.

Lurton, X. (2016). Modeling of the sound field radiated by multibeam echosounders for acoustical impact assessment. *Applied Acoustics, 101*, pp. 201–221, https://doi.org/10.1016/j.apacoust.2015.07.012

Lurton X. and DeRuiter S. (2011). Sound radiation of seafloor-mapping echosounders in the water column, in relation to the risks posed to marine mammals. *The International Hydrographic Review, 6*, pp. 7–18.

NMFS (2024). *Summary of Marine Mammal Protection Act Acoustic Thresholds*. Silver Spring, Maryland: National Marine Fisheries Service (NMFS), Office of Protected Resources.

NOAA (2024). *Update to: Technical Guidance for Assessing the Effects of Anthropogenic Sound on Marine Mammal Hearing (Version 3.0): Underwater and In-Air Criteria for Onset of Auditory Injury and Temporary Threshold Shifts*. U.S. Dept. of Commer., National Oceanic and Atmospheric Administration (NOAA). NOAA Technical Memorandum NMFS-OPR-71, 182 p.

Ruppel, C. D., Weber, T. C., Staaterman, E., Labak, S. J. and Hart, P. E. (2022). Categorizing Active Marine Acoustic Sources Based on Their Potential to Affect Marine Animals. *J. Mar. Sci. Eng., 10*, 1278. https://doi.org/10.3390/jmse10091278

Southall, B. L., Finneran, J. J., Reichmuth, C., Nachtigall, P. E., Ketten, D. R., Bowles, A. E., Ellison, W. T., Nowacek, D. P. and Tyack, P. L. (2019). Marine mammal noise exposure criteria: Updated scientific recommendations for residual hearing effects. *Aquatic Mammals, 45*, pp. 125–232. https://doi.org/10.1578/AM.45.2.2019.125

Southall, B. L., Nowacek, D. P., Bowles, A. E., Senigaglia, V., Bejder, L. and Tyack, P. L. (2021). Marine Mammal Noise Exposure Criteria: Assessing the Severity of Marine Mammal Behavioral Responses to Human Noise. *Aquatic Mammals, 47*(5), pp. 421–464. https://doi.org/10.1578/AM.47.5.2021.421

Southall, B. L., Bowles, A. E., Ellison, W. T., Finneran, J. J., Gentry, R. L., Greene, C. R., Jr., Kastak, D., Ketten, D. R., Miller, J. H., Nachtigall, P. E., Richardson,W. J., Thomas, J. A. and Tyack, P. L. (2007). Marine mammal noise exposure criteria: Initial scientific recommendations. *Aquat. Mammal., 33*, pp. 411–521.

Southall, B. L., Rowles, T., Gulland, F., Baird, R. W. and Jepson, P. D. (2013). *Final report of the Independent Scientific Review Panel investigating potential contributing factors to a 2008 mass stranding of melon-headed whales (Peponocephala electra) in Antsohihy, Madagascar*. https://iucn-csg.org/wp-content/uploads/2010/03/Southall-Madagascar-ISRP-FINAL-REPORT.pdf (accessed 15 March 2025).

Thomsen, F., Mendes, S., Bertucci, F., Breitzke, M., Ciappi, E., Cresci, A., Debusschere, E., Ducate, C., Folegot, T., Juretzek, C., Lam, F.-P., O'Brien, J. and dos Santos, M. E. (2021). Addressing underwater noise in Europe: Current state of knowledge and future priorities. *Future Science Brief, 7*, European Marine Board, Ostend, Belgium. ISSN: 2593-5232. ISBN: 9789464206104. https://doi.org/10.5281/zenodo.5534224

TNO (2016). *Comparison of ASW sonar risk assessment and mitigation between six different nations – a report by the SDI ASRM Group*. TNO Report R10570.

CONFERENCE PAPER

TrueOcean: How cloud and AI technologies are revolutionizing hydrography

Authors

Jann Wendt[1], Daniel Wehner[1] and Houssem Sadki[1]

Preamble

The following work was presented at the Hydrographic Conference HYDRO 2024, 5–7 November 2024, Rostock-Warnemünde, Germany in the oral session *Data fusion and management.*

Abstract

TrueOcean, developed by north.io GmbH, is an ocean data platform designed to address the complexities of managing, sharing, and analyzing marine data. The platform consolidates diverse sensor data formats into a unified, cloud-optimized format, leveraging scalable cloud infrastructure for efficient storage, processing, and analysis. Key features include the use of the Apache Parquet format for data unification and H3 indexing for efficient geospatial data management. The platform supports collaboration and data sharing through standard protocols like SFTP, RSYNC, WMS, and WFS. Additionally, the Geodata Processing Engine integrates Apache Spark and Kubernetes to enable large-scale data processing. By combining flexible data management, scalable analysis, and robust collaboration tools, TrueOcean serves as a comprehensive solution for marine data stakeholders, facilitating the extraction of actionable insights across various use cases.

1 Introduction

TrueOcean is an ocean data platform that is being developed by north.io GmbH, which is a German based software company. The TrueOcean platform serves as a comprehensive data warehouse designed to simplify data management, sharing, and collaboration. Furthermore, it provides a foundation for data processing and analysis using scalable computational resources, enabling efficient extraction of valuable information directly from raw sensor data.

Managing marine data poses significant challenges due to the absence of standardized data formats for the diverse range of sensors used to acquire it. Common sensor types include multibeam echosounders, side-scan sonars, magnetometers, sub-bottom profilers, as well as lidar, optical, and SAR satellite sensors. Each sensor type can again store data in a different format, such as *.gsf, *.xtf, *.all, or *.s7k for multibeam echosounders. This variety of data formats makes interoperability and scalability difficult (Fig. 1, *Raw Data*). In addition, these formats are not optimized for scalable cloud environments, highlighting the need to unify

✉ Jann Wendt • jwendt@north.io

[1] north.io GmbH, 24118 Kiel, Germany

 https://doi.org/10.58440/ihr-31-1-c04

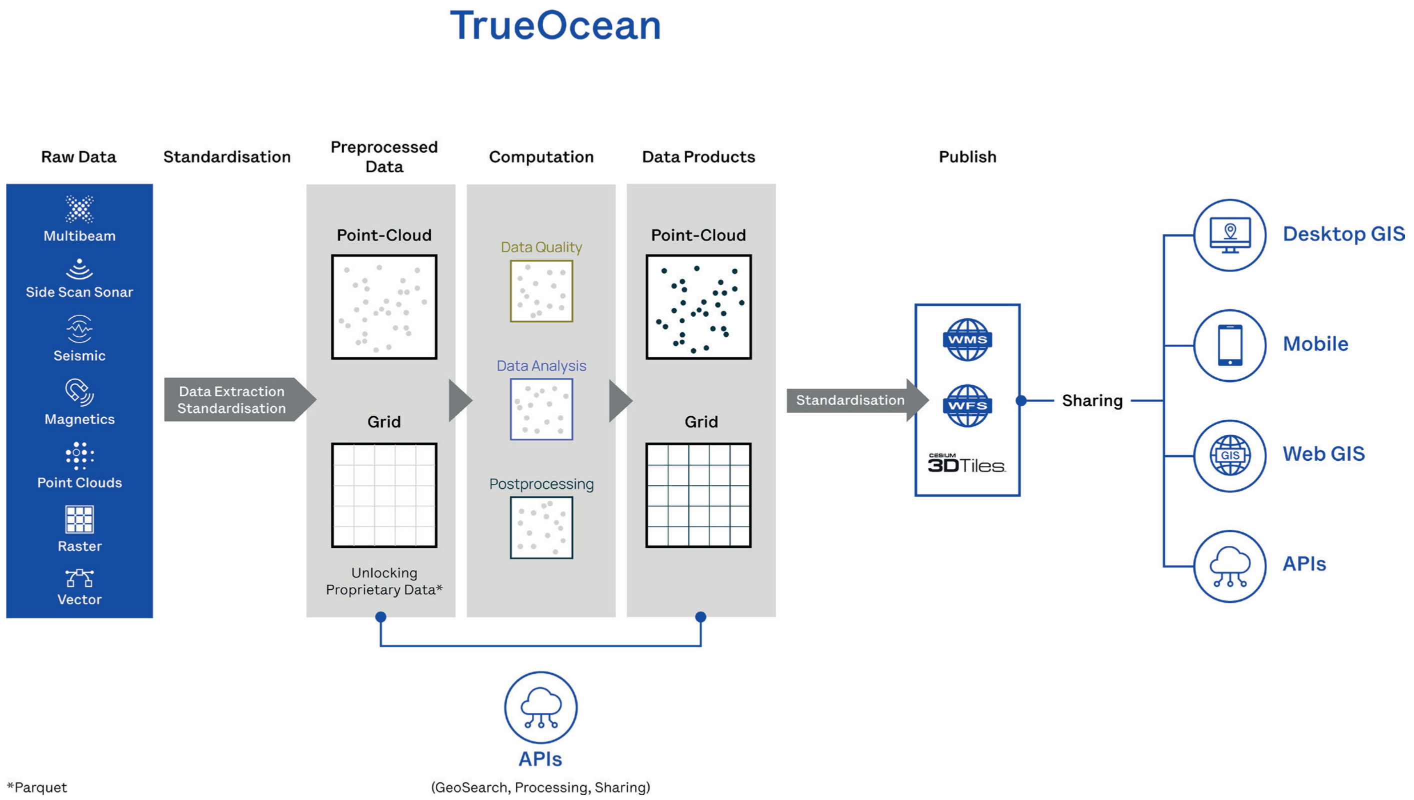

Fig. 1 Overview of the data workflow in the TrueOcean data platform.

various sensor data into a cloud-optimized format for efficient storage and streamlined data handling (Fig. 1, *Preprocessed Data*). Furthermore, proper metadata management is equally important, with alignment to existing standards (ISO, 2019; INSPIRE, 2025) being a critical objective. Another key consideration for marine data, as with any geospatial data, is the visualization of locations on a map. Efficient indexing of geospatial data is essential to make files easy to locate, access, and use within the platform.

Once data is effectively organized, sharing and collaboration typically become the next priorities, given that marine projects often involve multiple stakeholders. TrueOcean facilitates sharing through its built-in map functionality, common protocols like SFTP/RSYNC, as well as via standardized APIs such as Web Map Services (WMS) and Web Feature Services (WFS; Fig. 1, *Publish*).

Unifying data into a cloud-optimized format also enables integration with scalable computing environments, supporting data processing and advanced analysis workflows (Fig. 1, *Computation)*. A unified and open-source data format offers the added advantage of eliminating vendor lock-in, ensuring interoperability across workflows and compatibility with a variety of tools without requiring proprietary software.

By combining functionalities for data management, sharing, collaboration, and scalable processing/analysis, the TrueOcean platform establishes itself as a central hub for accessing marine data and extracting actionable insights for a wide range of use cases.

2 Technology

The TrueOcean platform is designed as a SaaS (Software-as-a-Service) and hence consists of several microservices that interact with each other. These microservices allow for a more flexible structure regarding updates, maintenance, and the implementation of new functionalities. The main technical components regarding the different topics "Data Management", "Data Sharing/Collaboration", and "Processing/Analysis/AI" are described in more detail below.

2.1 Data management

To manage the diverse set of marine data formats from different sensor types, unification of this data is required. Therefore, a microservice denoted as fconv that can convert the data from the different sensor types to a common data format, the Apache Parquet format (Apache Parquet, 2025), is being developed. The Parquet format is chosen as it is optimized for cloud applications, an open-source data format, constantly maintained due to its founding through the Apache Foundation and it is already widely used in the technology industry. The optimization for cloud applications implies a high compressibility, fast query operations for I/O operations, support of complex nested data structures, interoperability with various languages (e.g., Java, Python, Scala) and big data environments (Apache Spark, Hadoop, Hive), leading to efficient usage for parallel computing. In addition to the data format conversion each file that contains geographical coordinates is indexed using H3 indexing. H3 indexing divides the Earth's surface into

Table 1 Supported data formats in the TrueOcean data platform.

Sensor type	Data format
Multibeam Echosounder	*.all, *.kmall, *.s7k, *.gsf, *.xtf, *.raw
Side Scan Sonar	*.jsf, *.sdf, *.sds, *.xtf, *.til
Subbottom Profiler / Seismic	*.segy, *segd
Magnetometer	*.csv, *xlsx, *.txt
Point Cloud	*.las, *.laz, *.pts, *.csv, *.txt, *.xyz
Raster	*.asc, *.tiff, *.gdb
Vector	*.shp, *.gdb, *.kml

a hierarchical grid of hexagons, which provides an efficient and flexible way to index and organize spatial information (H3, 2025). The division into hexagons reduces edge effects compared to traditional square grids, and it is more natural for representing spherical surfaces. A main advantage of H3 is its hierarchical structure, which allows for varying levels of precision. The zoom levels for the size of a hexagon vary between 0.58 m to 1281 km, which refers to the edge length of the hexagon. A list of currently supported data formats by the fconv service is given in Table 1.

Despite the data itself, metadata is also important to align with the FAIR principles (Wilkinson et al., 2016) and make the data findable, accessible, interoperable, and reusable. There exist different metadata standards for geospatial which are in use by different stakeholders. Common standards are INSPIRE (INSPIRE, 2025) and ISO19115 (ISO, 2019). A vocabulary that is developed in the context of the European Commission's "Interoperable Europe" initiative to map the metadata attributes is the GeoDCAT-AP 3.0.0 (GeoDCAT-AP, 2025). While this is not fully implemented into the TrueOcean data platform, the goal is to thrive towards interoperability with these existing metadata standards. An additional standard to discover, browse, and query metadata is the Catalog Services for the Web (CSW) defined by the Open Geospatial Consortium (Catalog Services, 2025). The TrueOcean platform allows to interoperate with this CSW standard.

The TrueOcean platform is designed to be deployed on cloud infrastructure, with the option to also be implemented on on-premises systems. Given that marine survey data can range from gigabytes to several terabytes, a scalable storage solution is essential. For this purpose, the TrueOcean platform utilizes Ceph as its distributed storage system (Ceph, 2025). Ceph is an open-source project known for its scalability, allowing data to be stored across distributed systems. It supports multiple storage types, including object, block, and file storage. Additionally, Ceph offers robust fault tolerance and redundancy, ensuring data integrity and preventing loss. When deployed on appropriate hardware, Ceph can deliver high data throughput, making it well-suited for large-scale data processing and ensuring seamless interoperability within the system. Data can be uploaded to the storage location using several common protocols, including HTTP, SFTP, and RSYNC.

2.2 Sharing and collaboration

Having data organized within the TrueOcean platform, sharing and collaboration are commonly the next steps that are required. The user roles available on the platform, which are admin/member/guest allow for different variations on how to share the data. On the platform the data is organized in projects and user defined folder structures within each project. To share and collaborate on data, users can be invited to the respective project with the intended user rights (e.g., view, edit, download). The intended user rights can be defined on a folder and subfolder level. In addition to an invitation of users, the data can also be shared using the same protocols as for the data upload, which are HTTP, SFTP and RSYNC. When a share is created, the credentials to access the data can be shared by the data owner with whoever the data owner wants (Fig. 2, left). For specific geospatial data types, like raster data, standard protocols like WMS and WFS are available to share the data. Also, external data can be integrated into the TrueOcean platform using the WMS/WFS protocols. The data that is being stored in the projects can also be displayed on maps within the platform. Different maps can be created, like projects (Fig. 2, right), while a map can contain data from different projects and vice versa.

2.3 Data processing and analysis

The processing of large-scale data will be handled by the Geodata Processing Engine, currently under development at north.io. Designed as an independent technological foundation, the Geodata Processing Engine is being developed in respect of interoperability with the TrueOcean platform. As its core, the Geodata Processing Engine combines the technologies of Apache Spark (Apache Spark, 2025) and Kubernetes (Kubernetes, 2025) to distribute computing power and horizontally scale data processing tasks across multiple servers. This combination ensures stable performance while mitigating the limitations of single-server setups, such as constrained hardware capacity, and provides a degree of fault tolerance. Kubernetes streamlines resource management and cloud deployment, offering dynamic resource allocation, automatic scaling, and built-in fault tolerance. Meanwhile, Apache Spark automatically translates user-defined algorithms into optimized, scalable computations, efficiently distributing tasks across available resources. Additionally, the Apache Parquet format, used as the unified data format, is optimized for seamless integration with the Apache Spark framework.

The efficiency of algorithm translation and resource allocation also depends on the data structure itself. To maximize the performance of the Geodata Processing Engine, the system automatically minimizes data shuffling and optimizes data storage arrangements for greater efficiency. Examples of algorithms that are being developed for multibeam echosounders range from preprocessing (e.g., offset corrections, navigation interpolation, georeferencing), to data quality control (e.g., data point density, beam footprints), and analytics (e.g., gradient, sphericity).

3 Use cases

3.1 Offshore: Enhancing data management, sharing, and analysis during acquisition

In offshore geophysical surveys, vast quantities of data are collected from a range of sensors, e.g., multibeam echosounders (MBES), side-scan sonar (SSS), sub-bottom profilers (SBP), magnetometers, and seismic streamers. Managing these datasets in real time is critical for ensuring survey integrity and immediate decision-making.

3.1.1 Data management

Traditional data acquisition methods have often depended on local storage onboard survey vessels. Such setups come with inherent risks including data duplication, limited storage capacity, and the potential for loss during adverse conditions. TrueOcean addresses these challenges by providing a cloud-based data management framework that automates the ingestion of raw data. As data streams in from various sensors, TrueOcean assigns structured metadata tags, ensuring that every dataset is immediately backed up and catalogued. This approach minimizes manual intervention and expedites data retrieval, thereby reducing downtime and enhancing operational efficiency offshore.

3.1.2 Sharing and Collaboration

One of the steady challenges in offshore operations is bridging the gap between the vessel and onshore support teams. With TrueOcean, real-time data synchronization becomes a cornerstone of offshore collaboration. Through secure cloud connections, survey teams can share data instantaneously with remote experts and project managers. This real-time sharing means that preliminary assessments and feedback can be provided even before the survey vessel leaves the area, allowing early detection of data gaps or anomalies. The use of standardized data formats within TrueOcean further facilitates interoperability among various stakeholders, ranging from regulatory bodies to subcontractors, ensuring that the same high-quality data is available to everyone being involved.

The rapid evolution of cloud computing has transformed the way geophysical data is acquired, managed, and interpreted. As surveys grow in scale and complexity, robust platforms like TrueOcean serve as a blueprint for integrating scalable data management, real-time collaboration, and advanced processing techniques into every stage of geophysical operations. This article outlines how offshore operations, onshore validation efforts, and cloud-based processing services can benefit from a unified approach that TrueOcean exemplifies.

3.2 Onshore: Validating, managing, and collaborating on survey data for QA/QC

Once raw data reaches onshore processing centers, the focus shifts from acquisition to a thorough validation process. This stage is crucial for ensuring the integrity and quality of the datasets

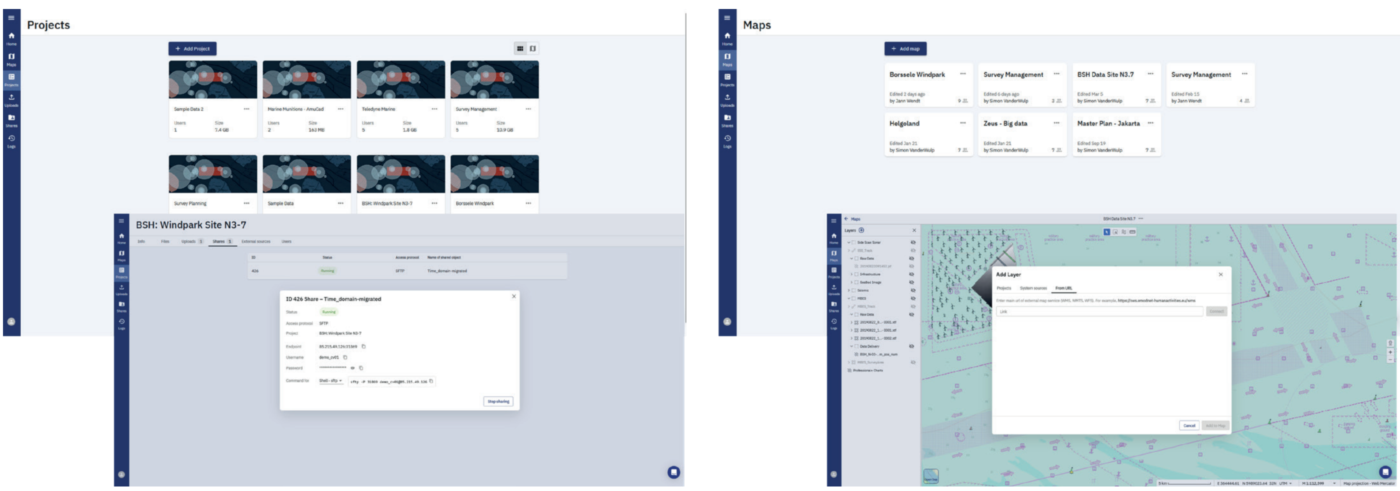

Fig. 2 User interface of the TrueOcean platform showing the projects (left) and maps view (right). In the projects view a sftp share and the corresponding credentials is shown. For the map view the integration of external sources via WMS/WFS is shown.

before they are used for final interpretations and reporting. Here, a cloud-based system modeled after TrueOcean's robust data management protocols plays an indispensable role.

3.2.1 Data management

Onshore operations benefit immensely from a structured, centralized repository for geophysical data. TrueOcean's architecture supports a wide array of industry-standard file formats, ranging from near-seabed sensor formats to sub-seabed formats like SEG-Y seismic files to GeoTIFF raster images and vector files, allowing for the efficient organization and retrieval of complex datasets. The platform allows linking the numerous documents that needs to be prepared by contractors and client to be geotagged and linked to the same area of interest along with sensor files acquired during operations making these available in near real time for all stakeholders of the project to have the same visibility on the progress of the survey but also leverage the platform to expedite decision making for reruns, infills and compliance with contractual agreements by minimizing conflict during any decision making process.

3.2.2 Sharing and collaboration

Historically, data sharing in onshore environments often meant physically transferring hard drives or using disparate data management systems that did not communicate well with one another. TrueOcean's cloud-centric approach allows multiple users to access, annotate, and collaborate on the same datasets simultaneously, regardless of their location. Survey contractors, academic researchers, government agencies, and technical experts can all work on a shared platform, ensuring that every piece of data is scrutinized and validated. Furthermore, integrated version control systems maintain a detailed audit trail of every change made to the data, fostering transparency and facilitating error tracking. This seamless collaboration not only accelerates QA/QC workflows but also builds trust among stakeholders through consistent, documented validation processes.

3.3 Data processing: A scalable cloud solution for geophysical data interpretation

As the demands of geophysical surveys continue to expand, the need for a scalable, cloud-based data processing service becomes paramount. Building on the principles demonstrated by TrueOcean, our upcoming processing service is designed to streamline complex workflows while supporting a broad range of file formats and processing techniques.

3.3.1 Data management

The cloud-based processing service leverages a centralized data repository to handle diverse geophysical file formats detailed in Table 1 and extendable to other file formats depending on the scope of work. By integrating TrueOcean's approach to data management, the service ensures that data,

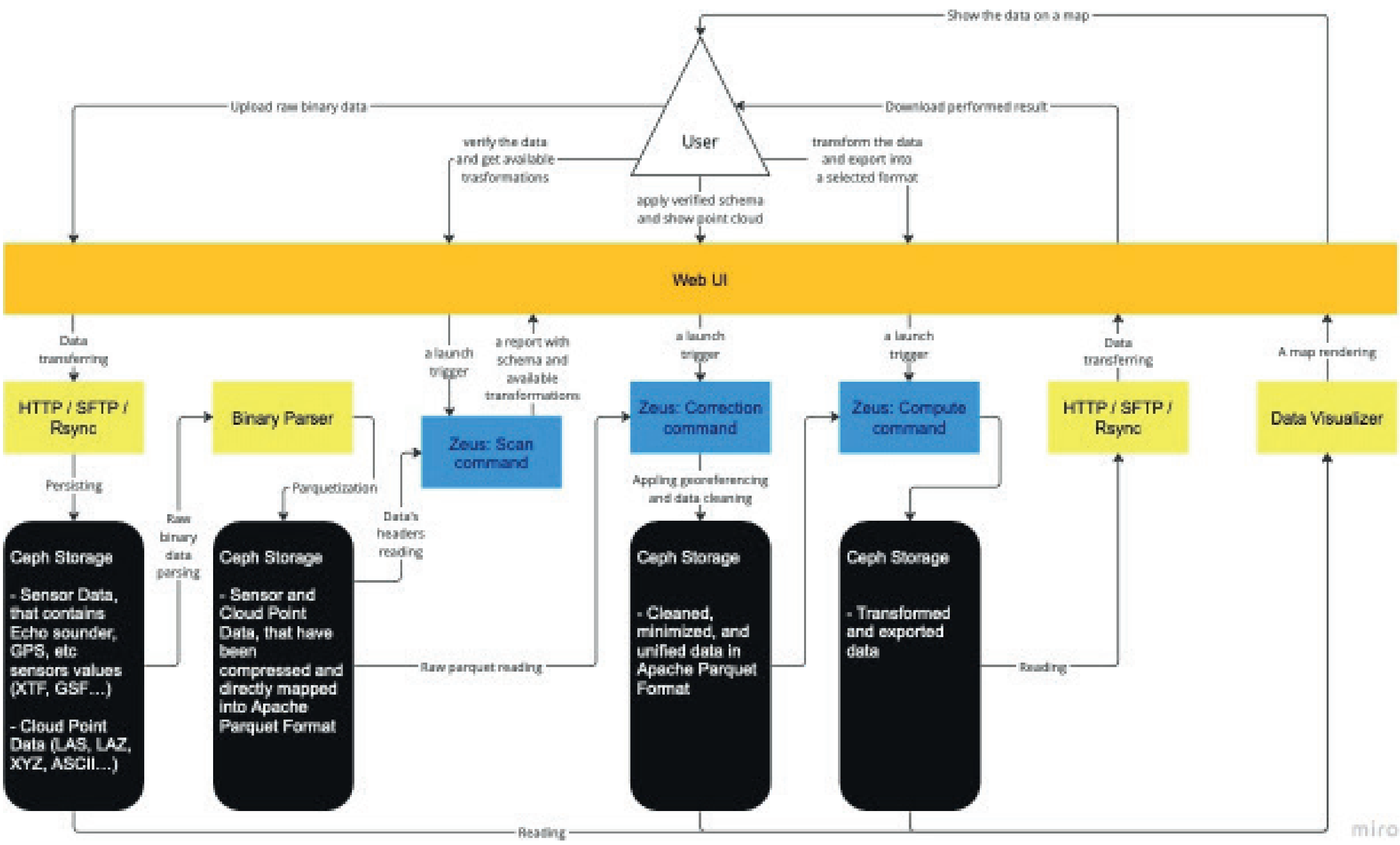

Fig. 3 Schematic overview that illustrates where in the workflow the TrueOcean platform can act as an Ocean Data Warehouse. Different data sources are ingested and unified and forwarded to different user applications.

https://doi.org/10.58440/ihr-31-1-c04

from raw inputs to processed outputs, is stored in a coherent and accessible manner. This organization simplifies not only data retrieval but also the archiving of historical datasets, enabling users to track trends over time or revisit previous survey results with ease. The support for widely recognized file formats coming from near seabed sensors, like S7k, ALL, XTF, Jsf, GSF and sub-seabed formats like SEG-Y, along with formats like XYZ, Geotiff, and SHP underline the system's commitment to interoperability with existing geospatial and survey software.

3.3.2 Sharing and collaboration

A key innovation of the processing service is its web-based dashboard, which exemplifies TrueOcean's commitment to transparency and user empowerment. The dashboard provides stakeholders with real-time insights into processing progress and allows for the secure submission of raw data. Through role-based access controls, the system ensures that every user—from project managers to field engineers—has access only to the data relevant to their responsibilities. This targeted sharing minimizes the risk of data misinterpretation and helps maintain a secure processing environment. Additionally, the service features automated report generation for survey files troubleshooting in PDF, GIS-compatible files, and interactive 3D models. These capabilities facilitate a comprehensive review of survey results without overwhelming users with technical details.

3.3.3 Data processing and analysis

The Geodata Processing Engine will expedite critical tasks such as bathymetric contour generation, seismic visualization, and the creation of data deliverables highlighting quality metrics like TVU, THU and TPU of bathymetric survey and statistical indicators of seabed conditions and morphometric surfaces.

To ensure the efficiency of these tools, we are conducting a comprehensive benchmark testing phase to evaluate the time efficiency and quality enhancements offered by the Geodata Processing Engine compared to traditional processing methods. Preliminary results are promising, aligning with our expectations and providing valuable insights as we rigorously stress-test our architecture to identify and resolve potential issues. This meticulous approach aims to deliver a reliable and resilient solution that meets the evolving demands of the renewable energy sector.

Traditional desktop solutions, while historically reliable, face significant challenges in handling the increasing volume and complexity of data generated by modern sensors. Scaling computational power to accommodate this growth is essential, especially as geophysical scopes of work in the offshore industry become more intricate and keener to simultaneous operations approaches. The Geodata Processing Engine, being integrated into the TrueOcean platform, addresses this challenge by leveraging distributed computing capabilities, allowing for horizontal scaling of tasks. This approach enables the efficient processing and analysis of raw data to actionable deliverables with less turnaround time than its counterpart. In the context of renewable site characterization, timely data processing is crucial for informed decision-making related to permitting, construction design, and logistical planning during the installation and throughout the whole lifecycle of an offshore windfarm, the challenge has become data centric.

4 Conclusion and outlook

The integration of cloud-based platforms into geophysical data workflows signifies a transformative shift in offshore and onshore operations. Platforms exemplifying effective data management, seamless sharing, and advanced processing capabilities within a scalable framework are at the forefront of this evolution. Offshore, real-time data management and analysis not only safeguard data integrity but also enhance operational decision-making. Onshore, structured data management and collaborative validation ensure that each dataset is rigorously vetted before informing critical interpretations. Moreover, cloud-based processing services open new avenues for automated, AI-enhanced data analysis, capable of handling diverse file formats and substantial datasets.

By aligning real-world use cases with these functionalities, it becomes evident that the future of geophysical data management lies in scalable, interoperable systems supporting every stage of the survey lifecycle. As the offshore geophysical industry continues to embrace digital transformation, such platforms will be instrumental in delivering high-quality, actionable insights while maintaining the operational agility required in today's dynamic survey environments.

In addition to these capabilities, addressing the challenge of vast amounts of valuable data stored in isolated archives by Hydrographic Offices and private entities is crucial. Recognizing the potential of these untapped resources, establishing a marketplace for data that has been acquired and resides in silos can facilitate the optimization of survey planning across various regions worldwide by providing access to historical datasets. Consequently, the hard work and resources invested in acquiring these insights are preserved and utilized, preventing them from fading into obscurity.

By transforming dormant data into accessible assets, such initiatives not only enhance the efficiency of future surveys but also honor and leverage past efforts, ensuring that valuable information continues to contribute to advancements in geophysical research and operations.

Acknowledgements

We like to acknowledge the entire team at north.io GmbH for development of technology used for the TrueOcean platform and the Geodata Processing Engine.

References

Apache Parquet (2025). *Apache Parquet Documentation*. The Apache Software Foundation. https://parquet.apache.org/docs/ (last accessed 10 March 2025).

Apache Spark (2025). *Unified engine for large-scale data analytics.* The Apache Software Foundation. https://spark.apache.org/ (last accessed 11 March 2025).

Catalog Services (2025). *OGC Catalogue Services 3.0.* Open Geospatial Consortium. https://www.ogc.org/publications/standard/cat/ (last accessed 10 March 2025).

GeoDCAT-AP (2025). *GeoDCAT-AP 3.0.0.* https://semiceu.github.io/GeoDCAT-AP/releases/3.0.0/ (last accessed 11 July 2022).

Ceph (2025). *Ceph – The Future of Storage™*. Ceph Foundation. https://ceph.io/en/ (last accessed 12 March 2025).

H3 (2025). *H3 indexes points and shapes into a hexagonal grid*. https://h3geo.org/ (last accessed 10 March 2025).

INSPIRE (2025). *Metadata Technical Guidelines.* European Commission, European Union. https://knowledge-base.inspire.ec.europa.eu/metadata-technical-guidelines_en (last accessed 10 March 2025).

ISO (2019). *ISO 19115-1:2014 Geographic information – Metadata. Part 1: Fundamentals*. International Organization for Standardization, ISO/TC 211, 35.240.70. https://www.iso.org/standard/53798.html (last accessed 31 March 2025).

Kubernetes (2025). *Kubernetes Documentation.* The Linux Foundation ®. https://kubernetes.io/docs/home/ (last accessed 11 March 2025).

Wilkinson, M., Dumontier, M., Aalbersberg, I. et al. (2016). The FAIR Guiding Principles for scientific data management and stewardship. *Scientific Data, 3*, 160018. https://doi.org/10.1038/sdata.2016.18

 https://doi.org/10.58440/ihr-31-1-c04

CONFERENCE PAPER

Fugro Marinestar GNSS precise point positioning service enhancements in 2024

Author
Hans Visser[1]

Preamble

The following work was presented at the Hydrographic Conference HYDRO 2024, 5–7 November 2024, Rostock-Warnemünde, Germany in the oral session *New trends in positioning.*

Abstract

The paper shows the improvements in the Fugro Marinestar algorithms in 2024. Using 120 GNSS reference stations uncalibrated phase biases are calculated for GPS, Galileo, BeiDou and Glonass(G4). using triple frequences. Worldwide 95 % position accuracy is 1–1.5 cm for east and north and 3–5 cm for the height. The concept of narrow and wide lanes using three frequencies is explained. Orbit and Clock corrections from third party has been extended with Galileo named XP3. The global convergence time is 29 seconds. Satguard Navigation Message Authentication on G4 has been added. Also new is Atomichron sub nanosecond timing.

Keywords
GNSS · PPP · converge time · accuracy

✉ Hans Visser · hans.visser@fugro.com

[1] Fugro Innovation & Technology BV, Fugro, The Netherlands

 https://doi.org/10.58440/ihr-31-1-c01

1 Introduction

In Fugro's continuous efforts to improve GNSS positioning accuracy, various services making use of the L-band of geostationary satellites have been developed since 1997. Marinestar™ is one of the services that currently provides precise orbit, clock, and phase bias corrections of satellites to marine clients. These corrections enable precise point positioning (PPP) with integer ambiguity resolution (IAR) with almost the same accuracy as traditional real time kinematic (RTK) produces, without using reference stations nearby. The service supports four constellations: GPS, Galileo, BeiDou, and GLONASS, with approximately 120 satellites in total. This article highlights several enhancements to the service achieved in 2024, with a focus on faster convergence, higher accuracy, scintillation mitigation, and anti-spoofing.

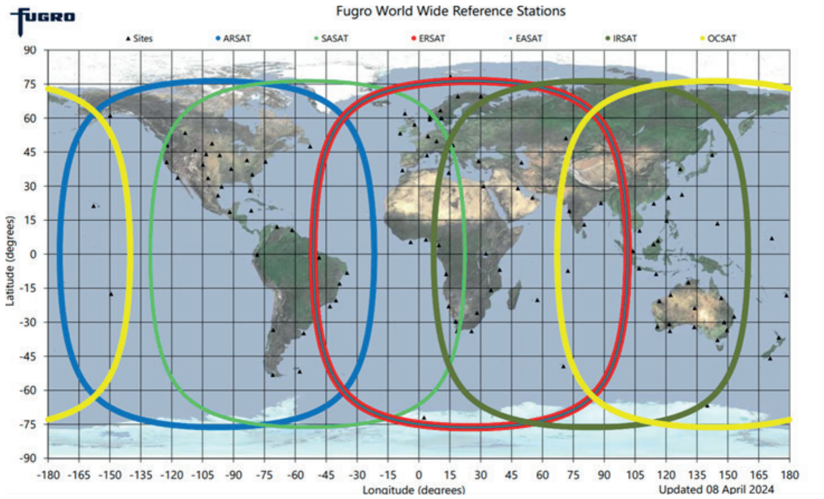

Fig. 1 Overview of L-band satellites and reference stations.

2 Network configuration

The reference network consists of 130 reference stations with Trimble NetR5, NetR9, Alloy and Septentrio PolaRx5 GNSS receivers. Two GNSS manufacturers are used so the orbit and clock calculations can continue if one of the receiver types fail. The orbit and clocks for GPS, Galileo, BeiDou and GLONASS (G4) are calculated in three calculation centres in Norway, Sweden, and Germany. At each location at least two independent computers calculate orbit and clock solutions. There are two network control centres each with a backup to continue to work in case of hurricanes, power, or major internet outages. One of the backups is now cloud-based. Using the cloud improves robustness against local or regional hazards such as for example, hurricanes and power outages.

There are six geostationary L-band satellites with two uplink locations. There is one primary uplink and a backup uplink in case of bad weather, power, or internet outages.

Over the geostationary L-band satellites orbit and clock corrections are sent for G4 and XP3.

3 XP3

Using independent orbit and clock sources from a third-party GPS and GLONASS corrections have been broadcast since 2006. The main purpose of XP is to increase independent solutions for the dynamic position market. In 2024 corrections for Galileo have been added improving the robustness of this independent service considerably against local radio interference and ionospheric scintillation. Adding Galileo increases the average number of satellites from ~15 to ~22 satellites and the addition of Galileo E5ab adds an independent frequency making the solution less sensitive to radio interference.

4 Triple frequency implementation

A significant improvement in 2024 involves the addition of third-frequency phase biases and

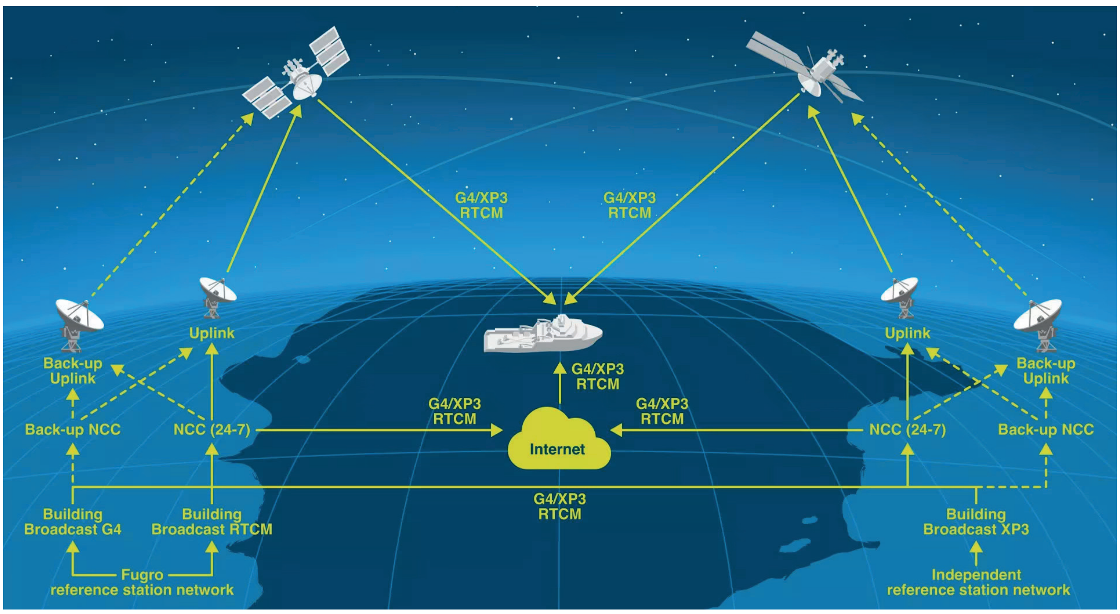

Fig. 2 Schematic overview of redundant GNSS infrastructure.

Table 1 GNSS frequencies (in MHz) and wavelengths (in cm).

Freq.	Band	GPS	Band	Galileo	Band	BeiDou	GPS	Galileo	BeiDou
f1	L1	1575.42	E1	1575.42	B1I	1561.098	19.0	19.0	19.2
f2	L2	1227.60	E5a	1176.45	B2I	1207.14	24.4	25.5	24.8
f3	L5	1176.45	E6	1278.75	B3I	1268.52	25.5	23.4	23.6

Table 2 GNSS wide and narrow lane wavelengths (in cm) adding and subtracting frequencies.

	GPS	Galileo]	BeiDou
f1-f2	86.2	75.1	84.7
f1-f3	75.1	101.1	102.5
f1+f2	10.7	10.9	10.8
f1+f3	10.9	10.5	12.1

Fig. 3 llustration of narrow(yellow) and wide(red) lanes for 2 GNSS satellites.

inter-frequency code biases of Galileo and BeiDou for the Integer Ambiguity resolution to the existing dual-frequency service. This enhancement allows clients to utilize the third frequency GNSS measurements in conjunction with more reliable and intelligent Integer Ambiguity Resolution strategies. This enhancement has been notably contributed to faster convergence and higher accuracy.

From the three frequencies by adding the frequencies L1+L2 and L1+L3 two narrow lanes with wavelengths in the order of 10 cm can be constructed. By subtracting the frequencies L1-L2 and L1-L3 wide lanes with wavelengths of 80 to 100 cm can be made. Combining the lanes using the MLambda integer search technique allows for much faster fixing of the correct ambiguities and thus faster convergence time.

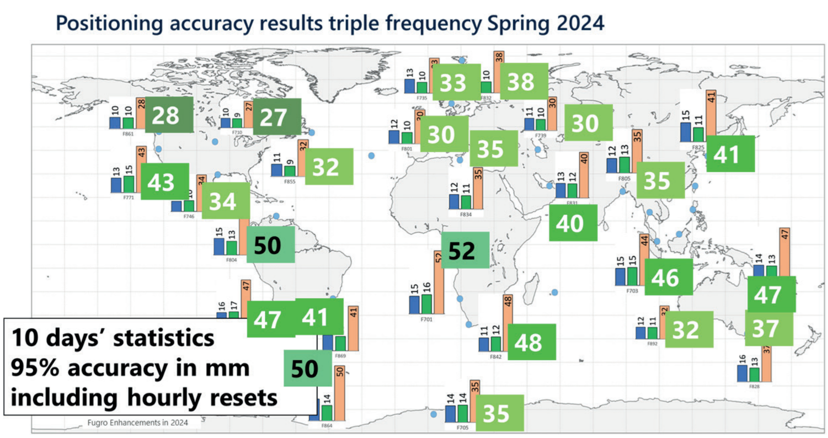

Fig. 4 Positioning accuracy results with triple frequency. North (blue), East (green) and Height (brown).

5 Global position accuracy

Using measurements of 24 globally spread GNSS reference stations for 10 days 95 % north accuracies between 10–16 mm and east 10–15 mm and height 30–50 mm was achieved. Every hour the position calculation was restarted. See Fig. 4.

6 Convergence time

The convergence time is defined as 95 % of the samples are better than 10 cm for height and better than 5 cm for north and east. The convergence time has been reduced from approximately 12 minutes to better than 3 minutes (95 %), while the accuracy has seen a global improvement to 2.5 cm horizontally and 5.0 cm vertically (95 %). Many ideal experimental sites have achieved even higher accuracy, reaching 1.5 cm horizontally and 3.5 cm vertically (95 %), with almost instantaneous convergence (with one minute). See Fig. 5.

Resetting the solutions every hour in a period of 10 days gives nominal 29 seconds for the north and east to be better than 5 cm and 10 cm for height in 95 % of the 240 restarts.

7 Scintillation position improvements

From 2022 until 2027, ionospheric scintillation is experiencing a period of high activity, with an expected peak in 2025. Scintillation is frequently observed near the equator and in the Arctic region, where many of Fugro's clients have ongoing engineering projects. As a result, GNSS measurements are significantly degraded, leading to positioning with much lower accuracy and occasional positioning resets. The largest improvement is by adding BeiDou3 with 36 nominal satellites in 2023 increasing the used GNSS satellites from 30 to 40 satellites. To further improve scintillation handling, Fugro enhanced its PPP engine with various level of quality controls in 2024. These improvements have effectively mitigated or largely reduced the impact of scintillation. Consequently, the position performance is now significantly better than it was before.

https://doi.org/10.58440/ihr-31-1-c01

8 Satguard spoofing mitigation

GNSS signal spoofing represents an intelligent and sophisticated form of signal interference, where malicious actors may employ a device to transmit fake GNSS ephemeris, measurements, or corrections, deceiving a receiver into calculating an incorrect position. Fugro has introduced the authentication service Satguard®, which has the capability to distinguish fake and true signals (i.e. navigation messages and corrections) from the four constellations. The service offers an opportunity to prevent the injection of fake signals into the PPP engine, thereby, ensuring accurate positioning for clients. The raw ephemeris is collected from all reference stations in the world. The ephemeris sources are compared and verified and a hash per ephemeris is created. The hash is a cryptographic code which is used to verify that the ephemeris is original and has not been modified. This checksum is broadcasted over the L-band. Also, the corrections do have a checksum which is broadcast.

The NMEA GGA Station ID is used to show the state of the receiver.

9 Atomichron

As timing is also relevant for offshore operations Fugro has added Satguard® to the timing service. Atomichron timing service is than 1 nanosecond. This is achieved by broadcasting the difference in system time of GPS, GLONASS, Galileo and BeiDou to a Fugro timing standard, which is close to UTC. This precise time can be used in timing operations to prevent time spoofing.

10 Conclusion

The 2024 enhancements to Fugro's GNSS PPP service have significantly advanced its technical capabilities. The integration of triple-frequency phase biases and inter-frequency code biases for GPS, Galileo, and BeiDou has resulted in faster convergence times and higher positioning accuracy. The addition of Galileo corrections to XP3 has increased the robustness of the service against local radio interference and ionospheric scintillation, with the average number of satellites used rising from approximately 15 to 22.

The improved PPP engine, with enhanced quality controls, has effectively mitigated the impact of scintillation, particularly in equatorial and Arctic regions. Furthermore, the introduction of the Satguard® authentication service provides a robust mechanism to detect and prevent GNSS signal spoofing, ensuring the integrity and reliability of positioning data. These technical advancements collectively enhance the precision, reliability, and security of the Marinestar service for marine applications.

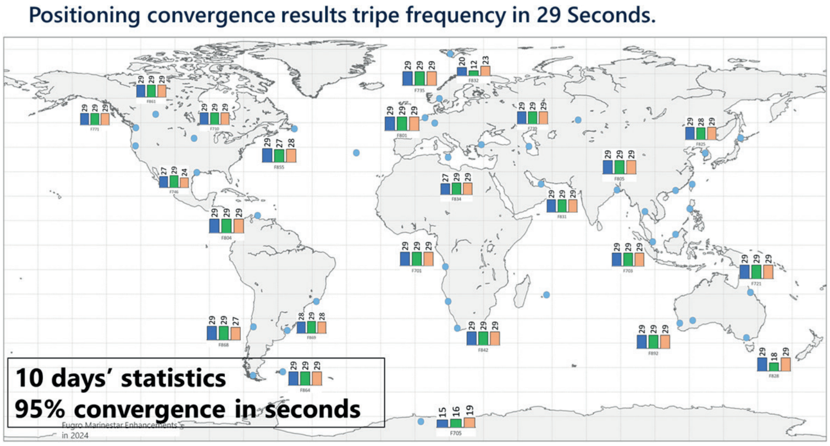

Fig. 5 95 % convergence time in seconds of hourly resets during 10 days.

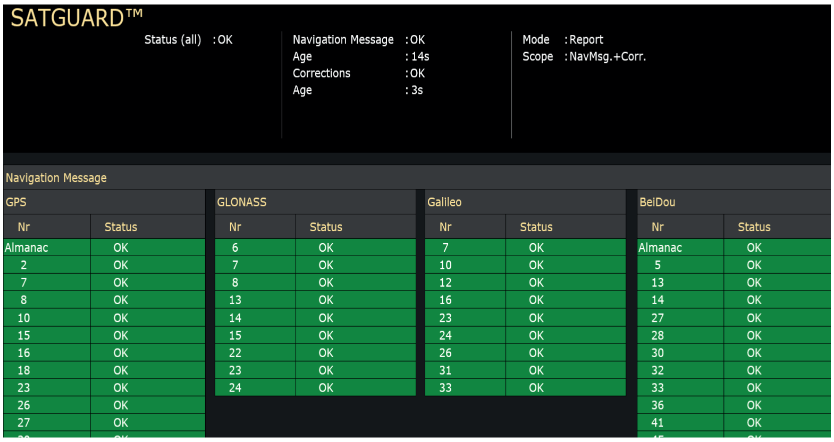

GPS		GLONASS		Galileo		BeiDou	
Nr	Status	Nr	Status	Nr	Status	Nr	Status
Almanac	OK	6	OK	7	OK	Almanac	OK
2	OK	7	OK	10	OK	5	OK
7	OK	8	OK	12	OK	13	OK
8	OK	13	OK	16	OK	14	OK
10	OK	14	OK	23	OK	27	OK
15	OK	15	OK	24	OK	28	OK
16	OK	22	OK	26	OK	30	OK
18	OK	23	OK	31	OK	32	OK
23	OK	24	OK	33	OK	33	OK
26	OK					36	OK
27	OK					41	OK

Fig. 6 Overview of authenticated satellites.

NOTE / TECHNICAL REPORT

Underwater laser scanning: Evaluating the performance of ULi in laboratory environments and presenting first insights from real-world applications

Authors

Annika L. Walter[1], Ellen Heffner[1], Annette Scheider[1] and Harald Sternberg[1]

Abstract

With the global expansion of underwater infrastructure elements, which all require regular inspection, maintenance and repair operations, precise and high-resolution monitoring solutions become crucial. Subsequently, technologies which are able to detect deformations in the range of millimetres, indicating damage at an early stage, are required. Since underwater laser scanning systems are supposed to achieve a much higher accuracy and measurement speed than acoustic techniques, they deliver an enormous potential. However, since water presents physical difficulties to optical systems in terms of turbidity and reachable distance, up to date, only sparse information regarding the performance of an underwater laser scanner and only view estimates about to the actual usability of such a system for corresponding monitoring purposes, are available. For that purpose, the underwater lidar system ULi was tested in two laboratory and one real-world environment. It can be concluded, that (1) man-made and organic structures down to a size of 2.36 mm can be detected at a close-range of ≤ 0.56 m in static laboratory environments, (2) a Böhler star with an arc length of 2.95 mm can be fully resolved at a mid-range of ≤ 8.03 m in static laboratory environments and that (3) the operation of ULi is not suitable for water bodies with a turbidity level of ≥ 6 NTU or a Secchi depth of ≤ 1.10 m.

Keywords

underwater laser scanner · close- and mid-range · laboratory environment · real world environment · level-of-detail · Böhler star · resolution

1 Introduction

The development of the terrestrial laser scanner is considered as a milestone in the enhancement of geodetic measuring instruments (Witte & Sparla, 2015). Through the transition from discrete to continuous area-wise measurements, the terrestrial laser scanner allows to capture entire objects instead of a few object points (Witte & Sparla, 2015). Installed on airborne and land-based platforms, terrestrial laser scanners can collect 3D data in large volumes with an accuracy of better than 1 cm while maintaining an unprecedented resolution and speed (Shan & Toth, 2018). Subsequently, terrestrial laser scanners have become well established surveying techniques for the acquisition of geospatial information. Hence, the retrieved point clouds are not only used to produce digital terrain and 3D city models, but also in the scope of forest management and monitoring, the revamping of industrial installations as well as the documentation of cultural heritage sites (Vosselman & Maas, 2010). Next to the strong interest in capturing 3D objects on the landside, this interest has also been projected onto the water-, particularly the underwater side (Hildebrandt et al., 2008). Here,

✉ Annika L. Walter · annika.walter@hcu-hamburg.de

[1] HafenCity University Hamburg, D-20457 Hamburg, Germany

https://doi.org/10.58440/ihr-31-1-n05

underwater infrastructure elements, such as port facilities, offshore wind turbines, pipelines, submarine cables and drilling platforms, require regular inspection, maintenance and repair (IMR) operations (Nauert & Kampmann, 2023). Driven by the potential to operate terrestrial laser scanners on water-based platforms such as unmanned vehicles or vessels to capture the surrounding environment above water as well as the development of bathymetric laser scanners mounted on for instance drones, the development of laser scanners operating only under water has become a crucial challenge in recent years. Next to the development of systems which are based on the triangulation principle, lately two companies also developed systems based on the Time-of-Flight (ToF) principle (3D at Depth, 2025; Fraunhofer IPM, 2025). Because of the recent development of the ToF Underwater LiDAR System (ULi) by the Fraunhofer Institute for Physical Measurement Techniques (IPM), there are so far no studies which further investigate the suitability of ULi under laboratory as well as under non-laboratory conditions and which assess to which extend this particular underwater laser scanner can be considered as the monitoring solution the worldwide expansion of underwater infrastructure elements requires. To change this subject, ULi is tested in varying environments, including two laboratory basins as well as the river Elbe. For the latter, the multisensory survey vessel of the HafenCity University Hamburg (HCU) is used.

2 State-of-the-art

Over the past decades, different technologies to realize measurements under water have been developed. Subsequently, underwater structures can be captured by using optical technologies such as digital cameras which are commonly used to support the visual inspection carried out by divers (Sun et al., 2021). Related studies to capture coral reefs (Muhammad, 2024) or to document archaeological underwater sites (Calantropio & Chiabrando, 2024), outline two possible applications. Furthermore, an exemplarily study from Ottaviano et al. (2024) shows, that digital cameras can also be mounted on remotely operated or autonomous underwater vehicles which allows the inspection of objects within depths of a few hundred metre. Although digital cameras are cheap and easy to operate, studies also describe that the quality of the retrieved images, including the appearance of colours, is heavily degraded by poor light conditions and turbidity (Wang et al., 2024). In addition, Alsakar et al. (2024) outline, that the restoration and the enhancement of underwater images include subjective as well as objective methods. While the appliance of subjective image quality metrices is time-consuming and cost-intensive, objective image quality assessment techniques apply mathematical and statistical models which - however - also rely on the human visual system. Subsequently, objective measurement parameters are sparse. Therefore, information about underwater structures is commonly gathered by using acoustic technologies such as traditional sonar systems. Related studies involve the underwater inspection of bridge structures (Zhang et al., 2024) and archaeological sites (Lee et al., 2021). The advantage of acoustic systems is, that they are not sensitive to turbidity and thus allow for long operational distances of several thousand metres. The drawbacks are, that those systems measure comparably slow and inaccurate. Hence, only a resolution in the range of centimetres, can be achieved (Lekkerkerk & Theijs, 2011, pp. 58 and 84).

In terms of monitoring tasks for large built underwater structures, especially in shallow-waters, neither cost- and labour-intensive camera operations resulting in heavily degraded images nor slowly operating acoustic systems providing low resolutions, are suitable. Hence, fast operating technologies which are able to detect deformations in the dimension of millimetres, indicating damage at an early stage, are required. Facing the worldwide expansion of underwater infrastructure elements, the demand for a fast, precise and high-resolved monitoring solution becomes even more present (Nauert & Kampmann, 2023). Driven by the high propagation velocity as well as the achievable accuracy and resolution, active optical techniques, such as underwater laser scanners, deliver enormous potentials.

To determine the 3D position of points, underwater laser scanners either use triangulation principles or the ToF method. Besides the varying functionalities, the main differences lie in the achievable scan range and the depth resolution. Hence, McLeod et al. (2013) outline, that triangulation-based laser scanners provide a higher depth accuracy when operating in a range of less than 1 m. Above 2.5 m, ToF laser scanners are generally more accurate. On account of this, the depth resolution of a ToF laser scanner depends on the resolution of the time or the phase measurement and not on the scan distance. Subsequently, systems using the ToF technique offer a greater potential for the usage in turbulent dynamic water bodies where the presence of currents and waves hinder the underwater laser scanner from approaching the object of interest up to a distance of 1 m.

Until now, two companies have developed ToF underwater laser scanning systems. While 3D at Depth developed the ToF operating systems SL3, SL4, SL4n and SL6 (3D at Depth, 2025), the Fraunhofer IPM developed the underwater laser scanner ULi (Fraunhofer IPM, 2025). With the technical specifications provided by the manufacturer, namely a sampling frequency of 100 kHz, a scanning distance in the range of several metres and a precision in the order of sub-millimetre in clear waters (Fraunhofer IPM, 2024), ULi has the potential to meet the demands which come along with the worldwide expansion of underwater infrastructure elements.

3 Sensor Technology

The underwater laser scanner ULi consists of two major components, being a scanning unit and a processing unit.

3.1 Scanning Unit

The waterproof cylindrical housing, illustrated in the Fig. 1, has a diameter of 0.172 m, a length of 0.375 m and can be used in depths of up to 300 m.

To emit short laser pulses in the order of one nanosecond onto the underwater environment and detect the returning light, a green laser with a wavelength of 532 nm and two rotating wedge prisms, allowing for a 44° field of view (FoV), are used. Hence, the distance to the target is determined based on the pulse propagation time. While the laser has a pulse repetition rate of 100 kHz, the rotating prisms allow the entire FoV to be captured without moving the underwater laser scanner. The laser pattern can be set to linear, circular or planar and thus dynamically adapted to the field of application (Fraunhofer IPM, 2024).

3.2 Processing unit

The hardware of ULi involves a processing unit. The backside of the processing unit contains inputs for a pressure sensor cable, a 24 V-DC power supply cable, an ethernet cable and a cable which is connected to the underwater scanning unit. The frontside features a pressure switch, a lock to start the scanner in the 3B mode, a laser-on-lamp indicating whenever the laser is used in the 3B laser mode and a power on / off switch. Hence, the laser scanner can be operated in two different laser modes, being laser class 2M and 3B. Since the laser radiation from the laser class 3B is dangerous for human eyes and skin, an additional pressure sensor is attached to the underwater laser scanner. Consequently, the laser operation in the 3B mode automatically switches off if the water level rises above a pre-defined pressure threshold of 0.7 dbar. This significantly enhances the safety at work. By connecting the processing unit with an ethernet cable to a PC or laptop, the entire operation and data acquisition of the underwater laser scanner can be steered over a graphical user interface (GUI). The GUI indicates the status of the scanning system and allows the user to set different parameters including the pulse rate or the laser pattern. Furthermore, the interface is used to start, record and stop the measurement. The measured data can be analysed by applying a full waveform analysis. Compared to a discrete signal analysis, this approach allows to separate the backscattered light-pulse from those caused by the water surface and particles within the water column. As a result of this separation, unwanted reflections within the signal can be suppressed and topographical data can be extracted (Hydro International, 2024).

Fig. 1 Housing of ULi (Fraunhofer IPM, 2024).

4 Methodological approach

According to the information provided in Sections 2 and 3, ULi has the potential to become the monitoring solution the worldwide expansion of underwater infrastructure elements requires. To assess whether this potential can be realized, the following overall research question arises:

- Which performance and potential offers ULi?

To answer this question, the following sub-research question must be addressed:

- To which extent does the quality of the derived point clouds differ when ULi is tested under laboratory as well as under non-laboratory conditions?

In response to this sub-research question, three case studies were carried out:

- Static laboratory close-range measurements
- Static laboratory mid-range measurements
- Dynamic real-world close-range measurements

5 Case Studies

To evaluate the outcome of ULi, particular with regard to the achievable range and resolution, the conducted studies will be elaborated in the following sub-sections.

5.1 Static laboratory close-range measurements

To evaluate the close-range performance of ULi under laboratory clear water conditions, various static measurements in a test basin of the HCU, were carried out.

5.1.1 Test environment HCU Lab

The measurements were conducted in an already existing small acrylic glass basin with a length of 1.20 m, a width of 0.60 m and a depth of 0.60 m. The basin was filled with water from the tab to a water level of 0.45 m. To ensure a horizontal radiation of the measuring laser and thus a good impact angle on the target, a triangular substructure was established. With this set-up, which is also shown in the Fig. 2a, the distance between the lenses and the opposite end of the basin was approximately

 https://doi.org/10.58440/ihr-31-1-n05

0.56 m. To measure the turbidity of the water within the basin, the multi-sensor oceanographic profiler AML-3 from AML Oceanographic with a stated precision of 0.10 NTU, an accuracy of 0.20 NTU and a resolution of 0.01 NTU, was used (AML Oceanographic, 2025). The profiler indicated an average turbidity of 0.00 NTU, which means that the underwater laser scanner was tested under optimal conditions.

5.1.2 Targets HCU Lab

To assess the suitability of the underwater laser scanner with respect to different tasks, including IMR operations of different infrastructure elements, thirteen targets with varying surface characteristics were placed into the test basin. Hereby, also materials which are particularly used for the construction of underwater infrastructure elements, were selected. Subsequently not only a coated-, a lacquered- and a rusted steel plate, but for instance also two targets made out of wood, which was used in former times for the construction of quay walls and which is still used for the construction of mooring dolphins, were tested. While small targets were directly pressed onto the acrylic glass at the end of the basin, as shown in the Fig. 2b, targets which exceed the height of the basin were held approximately 5 cm in front of the glass rear panel.

As a result, it could not only be investigated whether the underwater laser scanner is suitable for inspection and maintenance operations on rusted quay walls and wooden mooring dolphins, but also to assess how varying surface textures, mainly characterized by their roughness, influence the reflection behaviour of the transmitted laser. Furthermore, the existing cracks, holes, scratches et cetera of the tested materials were used to assess whether ULi can technically be used to detect deformations in the range of millimetres. An overview of all targets and a more thoroughly elaboration can be derived from Walter et al. (2025).

5.1.3 Data acquisition HCU Lab

To conduct the measurements, the settings summarized in the following Table 1, were applied. To ensure that the target would be visible in the data, a maximum distance of 5 m and a skip distance of 0 m was set. Furthermore, the parameter skip pulses was set to 0. Considering that ULi measures 100.000 points per second and skipping none of the pulses, this resulted in a pulse repetition rate of 100 kHz. As the filter was set to adjustment, the green laser was emitted with a strength corresponding to the lowest possible laser class 2M. Hence, the reduction of the laser power increased the safety of work in the laboratory environment. To test the reflectivity behaviour of the different targets, a circular laser pattern, a motor speed of 5 Hz and a radius change speed of 0 Hz was applied. Hence, the laser rotated with a constant speed and at a constant radius on the surface of the target. To scan the entire surface of the targets, the radius change speed was adjusted to 0.01 Hz. In this case, the laser rotated with a firstly increasing and then decreasing radius and therewith captured the entire surface of the selected target. Since the smallest rotation radius occurs when setting the radius to 0.6, this parameter was selected.

The incoming waveforms were directly reviewed in real-time using the Raw Signal Monitor. As it can be seen in the illustrated example in the Fig. 3, the live monitor displays three curves. The red curve refers

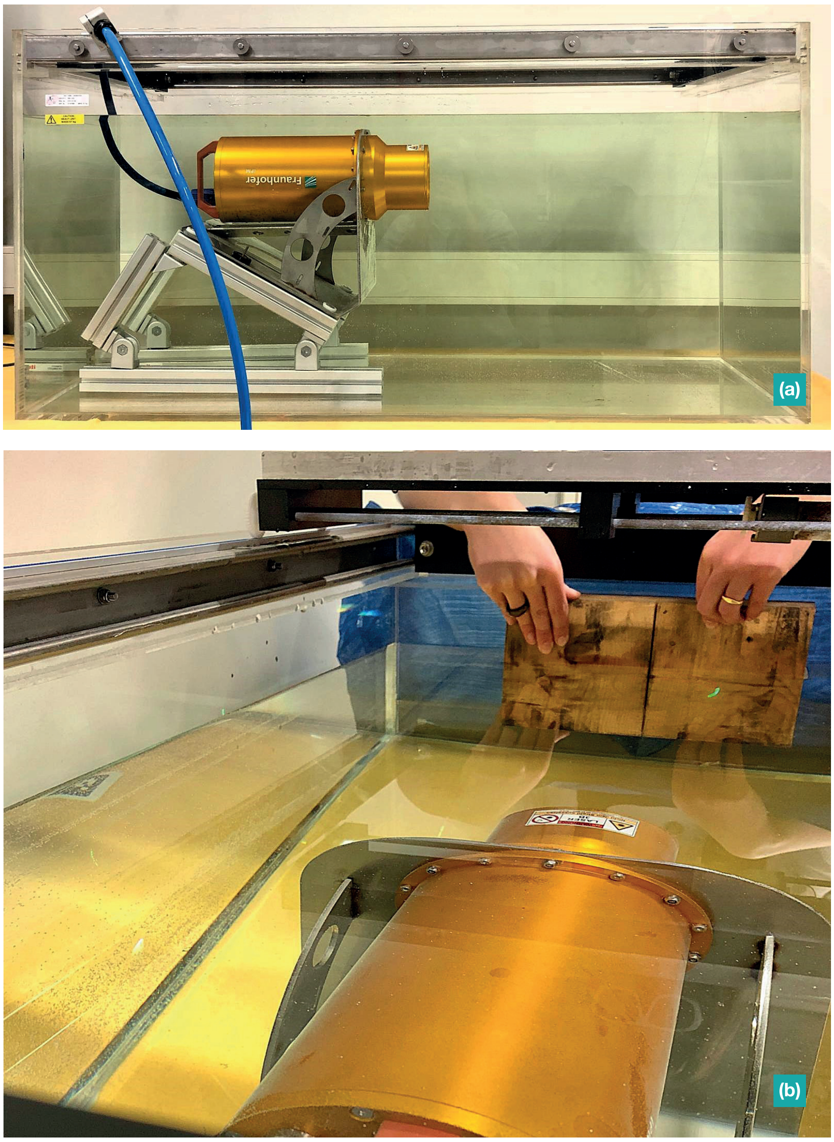

Fig. 2 (a) Test basin with ULi and (b) green laser pointing on wood target at the end of the test basin.

Table 1 Settings of ULi at HCU Lab.

Max distance (m in water)	5
Skip distance (m in water)	0
Skip pulses	0
Filter	adjustment
Laser pattern	circle
Motor speed (Hz)	5
Radius change speed (Hz)	0 (to 0.01)
Radius	0.6

to a fibre reference which is recorded before the light leaves the scanner. Thus, it functions as an internal reference signal. Once the light is transmitted and reflected, it reaches a detector where an avalanche photodiode converts the optical signal into an electrical signal. The electrical signal is split by a ratio of 1:10 between two amplifiers. Subsequently, the signal is strengthened to varying degrees. While the signal, which is attenuated by a factor of 10, is denoted as the sensitive channel and coloured in green, the other signal is denoted as rough or less sensitive channel and coloured in blue. Consequently, the green coloured signal is much more sensible.

In Fig. 3, the first peak of the green coloured curve indicates the reflection of the green laser on the lenses of the scanning unit while the second peak refers to the reflection triggered from the target. To assess the distance between the lenses of the underwater laser scanner and the target, the number of samples between the first and the second peak can be determined. Since each sample has a length of approximately 2.20 cm, the sample difference from the x-axis must be multiplied with this length. The derived product can be used to estimate the distance between the scanner and the target and to verify the curves displayed in the raw signal monitor. In the shown case, the estimated target distance is 0.44 m, which is regarded as realistic.

5.1.4 Results from HCU Lab

The retrieved waveforms were processed in Pulsalyzer and CloudCompare. Pulsalyzer is a proprietary post-processing software solution developed by the Fraunhofer IPM which can be used to review the derived waveforms, assess the associated point cloud and export the data from the proprietary .lidar format into .las files. The .las files can be imported into other point cloud processing software's. For the purpose of this research, the open source point processing software CloudCompare was used.

Overall, the measurements show, that light coloured targets with a shiny smooth surface exhibit a better reflectivity and cause less scattering in comparison to dark coloured, matt and rough surfaces (Walter et al., 2025). The scattering of the point clouds, defined by their thickness, ranged from 6 mm to 48 mm which is significantly higher to what can be typically derived from terrestrial laser scanners. This might be related to the fact that the targets were held by hand and not securely fixed. Three exemplarily point clouds are shown in the Fig. 4 below. Since the water in the test basin was only 0.45 m deep, the increasing radius caused the green laser to be reflected on the calm water surface. This additional reflection is indicated by the horizontal line in all three point clouds. The additional visible concentric circular pattern is a result of the selected scan pattern “Circle”. As it can be seen in the left and in the middle point cloud, the holes within the selected target materials are clearly visible. To determine the diameter of the holes, a digital calliper with a stated resolution of 0.01 mm was used. While the holes in the white lacquered steel plate ranged from 5.20 mm to 6.09 mm, the holes of the black coated steel target ranged from 6.59 mm to 6.71 mm. For organic structures such as the wooden box, elements such as knotholes and grains are mainly recognized by their change in intensity. Nevertheless, the 30 cm long and 2.36 mm wide vertical notch in the centre of the target is visible. Subsequently, the static laboratory measurements show, that the close-range point clouds can be used to identify man-made structures such as drilled holes or cracks as well as organic structures down to the millimetre scale (Walter et al., 2025).

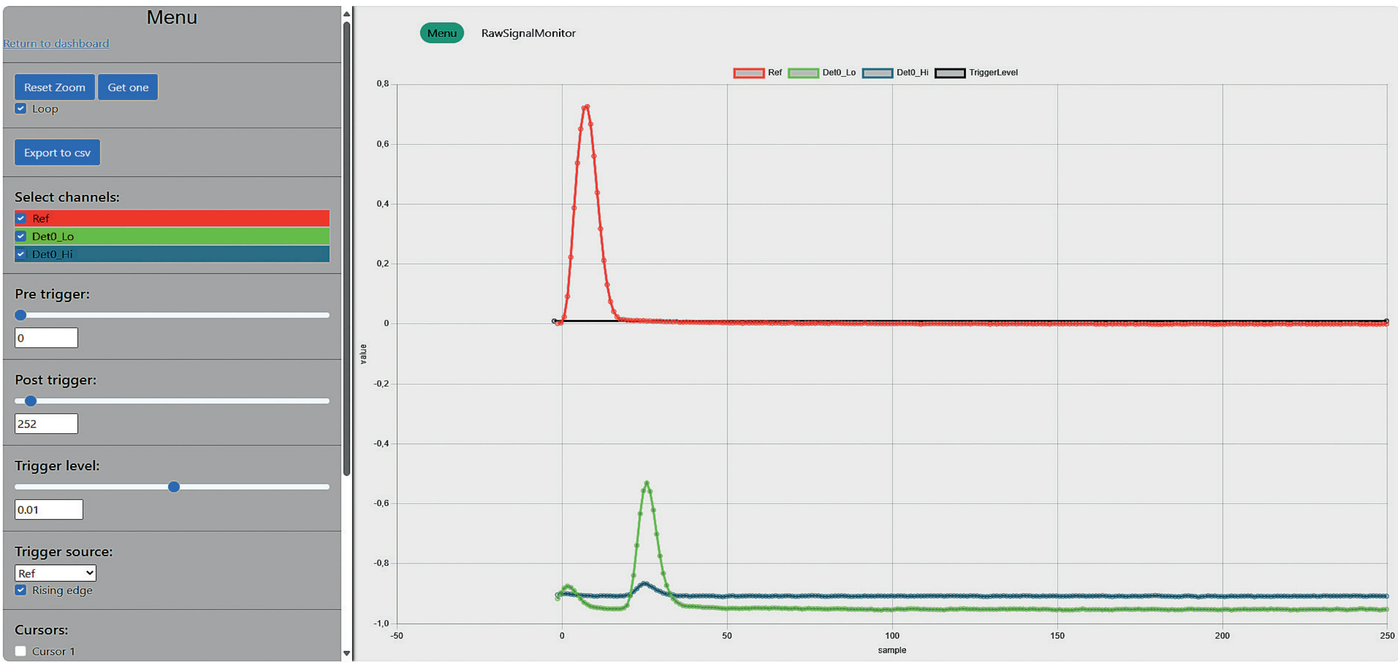

Fig. 3 Raw signal monitor for a white smooth acryl plate target.

5.2 Static laboratory mid-range measurements

To evaluate the mid-range performance of ULi under clear water conditions, additional tests in the laboratory infrastructure of the Institute of Mechanics and Ocean Engineering (MUM) from the Technical University Hamburg (TUHH) were carried out.

5.2.1 Test environment MUM TUHH Lab

The tests were conducted in a 15 m long, 1.50 m wide and 1.60 m deep glass basin which was filled with water from the tab to a water level of 1.20 m. To allow for a maximum possible distance between the lenses and the opposite end of the basin, the underwater laser scanner was placed at one end of the basin. To ensure a horizontal radiation of the measuring laser and thus a good impact angle on the target, a construction made out of aluminium profiles and a tensioning strap was used. As a result, the centre of the lenses was roughly 0.64 m submerged under the water and the distance to the end of the basin was about 9 m. The oceanographic profiler indicated an average turbidity of 0.00 NTU, which means that the underwater laser scanner was again tested under most favourable conditions.

5.2.2 Targets MUM TUHH Lab

To further assess the performance of ULi and to make a conclusive statement about how wide a crack in a material must be to be clearly identified in the point cloud, the achievable resolution was further investigated. From the perspective of the user, the resolution describes the capability of the underwater laser scanner to detect small objects or object parts in a point cloud. Technically, this capability is influenced by the smallest possible angular increment between two successive points as well as the size of the laser spot on the object itself (Boehler et al., 2003). Hence, a test object which comprises small elements or narrow slots on a flat surface can help to determine application-specific resolution capabilities. As a result, a so-called Böhler star was constructed. To determine the best suitable construction material for underwater applications, the results from the first study described in Section 5.1, were examined. By means of that, not only the quality of the derived point cloud, mainly given by its scattering, but also the suitability of the material as such, including its weight and its thickness, were taken into consideration. Conclusively, the material Resopal was selected. To assess the size and the distribution of the rays for the front panel, the beam diameter of ULi and the beam divergence, which the Fraunhofer IPM specified with 2.00 mm at exit and 1.50 mrad respectively, were accounted. An information about the smallest angular increment of ULi was not available. Finally, a Böhler star consisting of 32 rays with a respective opening angle of 11.25° and a size of 1 m × 1 m was designed. The related drawing is shown in the following Fig. 5a. To mill the rays into the front Resopal panel, a S3 Cutter from Zünd with a stated resolution of 0.005 mm and a repetition accuracy of ± 0.03 mm, was used (Zünd, 2023). Since the target had to be stencilled once, it can be assumed that the overall Böhler star was manufactured with a final production quality of 0.20 mm.

If ULi offers a high resolution, driven by small angular increments and a narrow laser spot size, reflections should not only occur on the front, but also on the rear panel. If the reflections on the rear panel are present in the outer regions as well as close to the centre, a very high resolution is achieved (Boehler et al., 2003). Subsequently, the Böhler star can be used to gather resolution information from different ranges. To further investigate the influence that a changing

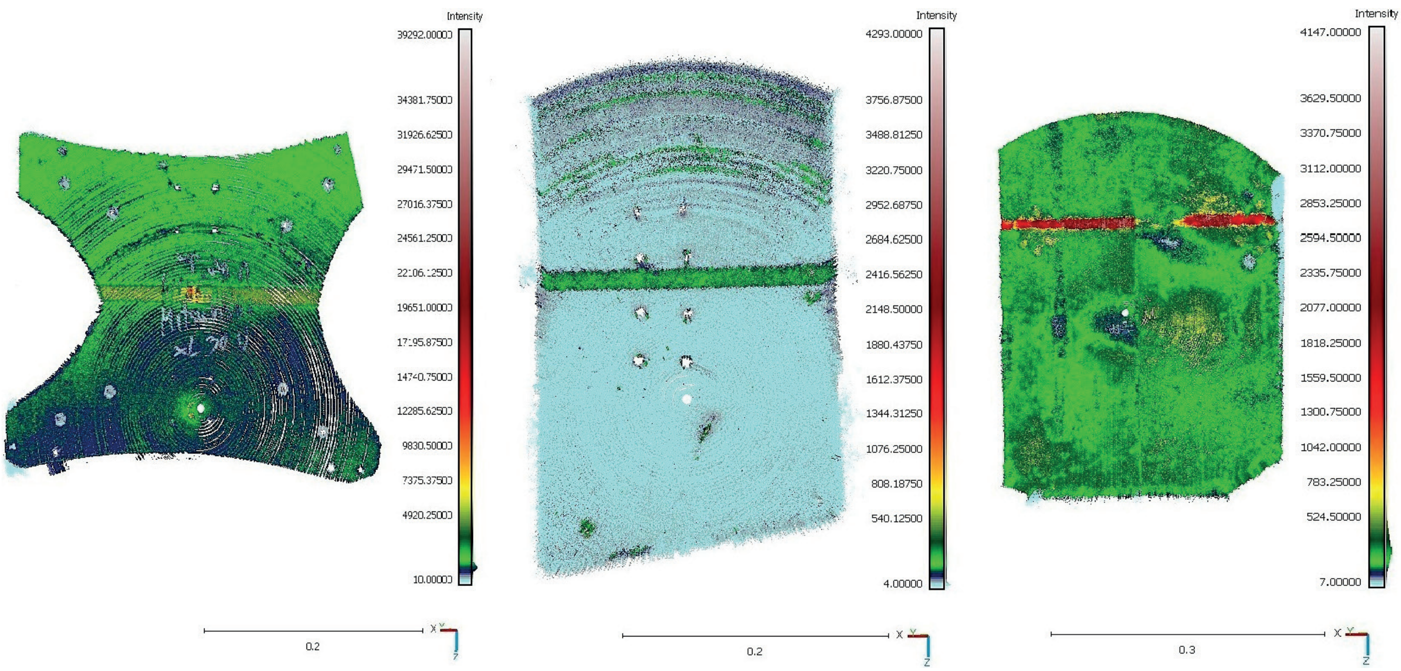

Fig. 4 Point clouds retrieved from a spiral scan and coloured by intensity for a white lacquered steel plate (left), a black coated steel plate (middle) and a wooden box (right).

panel to panel distance might have, the front and the rear panel of the Böhler star were connected by using nine 30 cm long threaded rods. The rods did not only allow to vary the distance between 1.16 cm and 24.90 cm, but also to enhance the overall stability of the Böhler star. The final assembly of all components was done by hand and is illustrated in the Fig. 5b.

5.2.3 Data acquisition MUM TUHH Lab

To acquire the data, the settings summarized in the following Table 2, were used. To determine the resolution of the underwater laser scanner, the Böhler star was positioned in varying distances. Subsequently, the distance between the lenses of ULi and the front panel of the Böhler star reached from a maximum of 8.03 m down to 1.03 m. To minimize the occurrence of noise, caused by reflections from the side walls as well as from the floor of the basin, the parameters "maximum distance" and "skip distance" were adapted. This limitation of recorded data in a specific range drastically decreased the final file size. To enhance the eye safety around the glass basin, the filter level "adjustment" was selected. Subsequently, the green laser did not operate at full power, but was emitted with a strength corresponding to the lowest possible laser class 2M. All other specified parameters are given in the Table 2.

To assess how the distance between the front and the rear panel of the Böhler star would influence the overall resolution of the retrieved point cloud, three scenarios were tested. First, the panels had a maximum distance of 24.90 cm. With this panel distance, the Böhler star was placed in a distance of 8.03 m, 7.03 m, 6.03 m, 5.03 m, 4.03 m, 3.03 m, 2.03 m, 1.53 m and 1.03 m from the lenses of the underwater laser scanner. In the second and third scenario, the panel distance was reduced to 12.50 cm and 1.16 cm respectively and the Böhler star was again scanned in all nine distances.

5.2.4 Results from MUM TUHH Lab

While the waveforms were processed in Pulsalyzer, the retrieved point clouds were further evaluated in CloudCompare. Here, it becomes evident, that a decreasing distance between the front and the rear panel of the Böhler star causes an overall lower scattering of the point cloud, but makes it also more difficult to separate the reflections triggered from the front and the rear panel. The case is also depicted in Fig. 6.

In Fig. 6 (left), the front and the rear panel have a distance of 24.90 cm. As it can be seen, both panels can be clearly separated from each other. While the upper blue coloured low intensity noise of the rear panel refers to reflections caused by the aluminium profiles on which the target was fixed, the remaining blue coloured reflections are caused by the edges of the front and the rear panel where only a part of the signal was reflected from the target. The edge effects do not occur uniformly, but stronger at the surrounding edges of the panels than at the cut-out Böhler star rays. Thus, the edges of the front and the rear panel cause a smearing of the signal. This behaviour is already known from terrestrial laser scanners. Hence, ranging as well as triangulation scanners both produce a variety of wrong points in the vicinity of edges. Since the laser spot cannot be focused to

Table 2 Settings of ULi at MUM TUHH Lab.

Max distance (m in water)	10 (to 3)
Skip distance (m in water)	7 (to 0)
Skip pulses	0
Filter	adjustment
Laser pattern	circle
Motor speed (Hz)	5
Radius change speed (Hz)	0.001 (to 0.01)
Radius	0.6

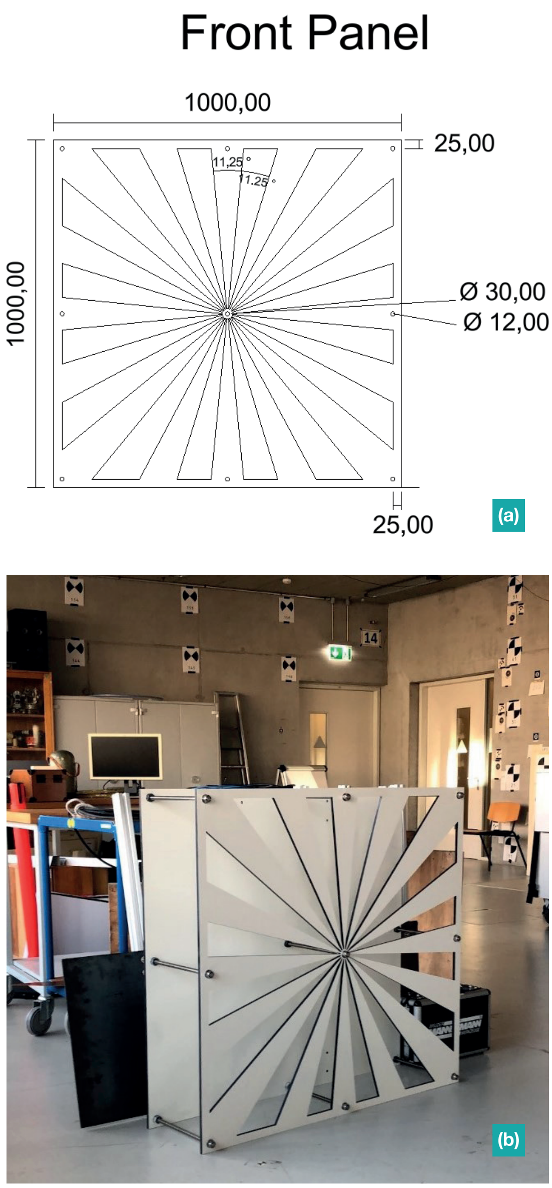

Fig. 5 (a) Construction drawing of the Böhler star with specifications in millimetres and (b) the final constructed Böhler star with a maximum panel to panel distance of 24.90 cm.

https://doi.org/10.58440/ihr-31-1-n05

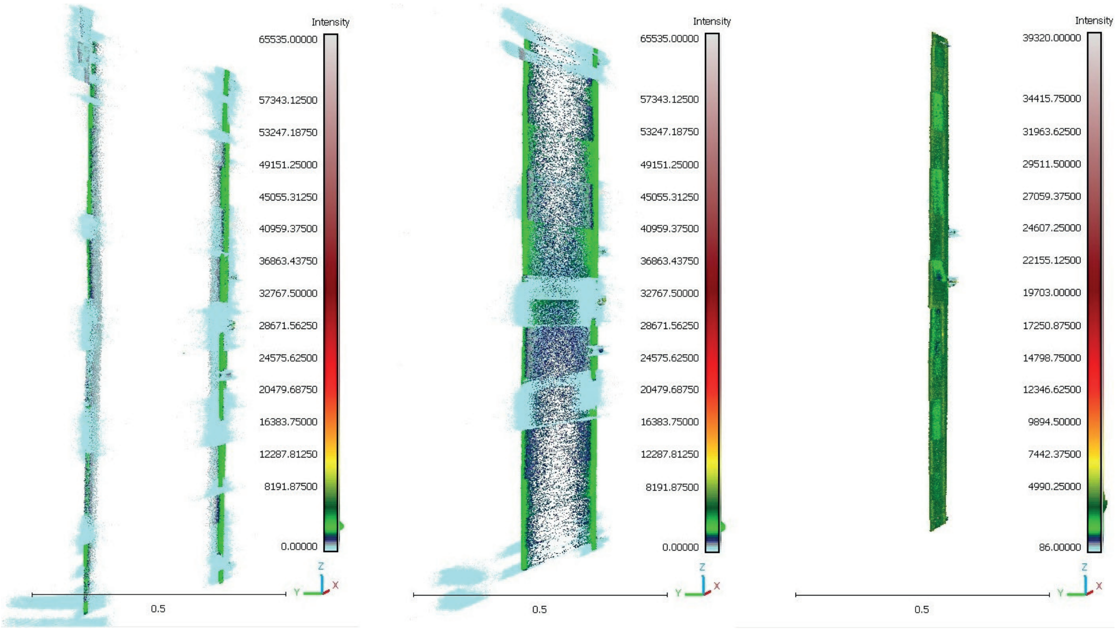

Fig. 6 Lateral view of the point clouds from the front (right) and the rear (left) panel coloured by intensity and retrieved under a scanning distance of 1.03 m and a panel distance of 24.90 cm (left), 12.50 cm (middle) and 1.16 cm (right).

point size, those wrong points are inevitable (Boehler et al., 2003). The outlined effect can also be seen in Fig. 6 (middle), where the front and the rear panel have a distance of 12.50 cm. In addition to the blue coloured noise, this arrangement of the panels causes the occurrence of dark blue coloured mixed-pixels. Mixed-pixels occur whenever two objects, in this case two panels, are spatially adjacent in the range direction. Since the laser spot illuminates both surfaces, the beam cannot distinguish between both surfaces and the reflected signal is integrated (Lichti et al., 2005; Wang et al., 2016). Hence, the resulting point does not lie on either surface and the two surfaces cannot be properly resolved in the point cloud (Schmitz et al., 2020). However, since the mixed-pixels have a lower intensity than the green coloured reflections, the front and the rear panel can still be separated from each other. For a panel distance of 1.16 cm, shown in Fig. 6 (right), the mixed-pixels are more compressed and have a higher density. As a result, the front and the rear panel cannot be accurately separated from each other.

In addition to the noise caused by the edge effects and the occurrence of mixed-pixels, both panels are subject to scattering. To determine the width of the scattering for the front and for the rear panel, the point cloud was segmented. In the process of segmentation, outliers and reflections caused by edge effects were manually removed. The process of cleaning was thoroughly done by the same person and according to the same criteria. Following, a best-fit plane for the point cloud belonging to the front and the point cloud belonging to the rear panel, was computed. To numerically quantify the average deviation of the points from the fitted planes and thus gather an information about the dispersion of the point clouds relative to the plane, the root mean square error (RMSE) of the fitted planes was computed. The results are shown in Fig. 7.

While the horizontal axis indicates the scan distance between the lenses of ULi and the front panel of the Böhler star, derived from a tape measurement, the vertical axis displays the RMSE of the fitted plane. The results for the varying panel distances, being 24.90 cm, 12.50 cm and 1.16 cm are coloured in blue, green and red respectively. While the results retrieved from the front panel are connected by a solid line, the results derived from the rear panel are connected by a dotted line.

When evaluating the first dataset, referring to a panel to panel distance of 24.90 cm, it can be seen that the overall RMSE increases with an increasing scanning distance. Subsequently, the dispersion of the point cloud increases. However, it becomes evident, that the front panel always indicates a higher dispersion than the rear panel. This behaviour applies to all scan distances. For the second data set, where the distance between the front and the rear panel was reduced to 12.50 cm, the computed RMSE for a scan distance of 1.03 m and 1.53 m is larger for the rear than for the front panel. Nevertheless, the differences are marginal and in the range of micro and nano metres. From 2.03 m to 6.03 m scanning distance, the RMSE computed for the front panel is thoroughly higher than for the rear panel. For the last two scanning distances of 7.03 m and 8.03 m, the RMSE is again larger for the rear panel than for the front panel. Subsequently, it seems that both edge cases, being a very small and a very large scanning distance, increase the dispersion on the rear panel. Nevertheless, except for the scanning distance of 5.03 m, where the RMSE difference is with 0.00136 m comparably large, the variations are overall not significant. Since the mixed-pixels were eliminated throughout the manual segmentation and thus not encountered for the plane fitting, the magnitude of the RMSE is comparable to what was derived for the first dataset. For the third dataset, where the distance between the front and the rear panel was set to 1.16 cm, the results are more or less vice-versa to the results from the second dataset. Hence, the RMSE for the two first and the last scanning distance is larger for the front than for the rear panel. For the remaining scanning distances, the behaviour changes and the computed RMSE is larger for the rear panel than for the front panel. Hence, small and large scanning distances increase the dispersion on the front panel. This is exactly opposite to what was observed for the second dataset. Despite of that, the RMSE difference for the front and the rear panel for the third dataset is comparably large. This becomes especially evident for a scanning distance of 4.03 m, where the difference is 0.0023 m. Since Fig. 6 (right) shows, that the third dataset has the least edge effects and an overall low amount of noise, this dataset should also have the lowest RMSE for the plane fitting. Hence, the high RMSE differences can be attributed to the manual segmentation, which was not only conducted on a visual basis, but which was due to the high density of mixed-pixels very difficult. Consequently, the results retrieved from the third dataset should be handled with care and treated with less resilience than the results retrieved from the first and the second dataset.

Despite the occurrence of mixed-pixels and the dispersion of the reflections triggered from the front and the rear panel, the underwater laser scanner was able to completely resolve the rays of the Böhler star. The result can be seen in the following Fig. 8. The upper three images refer to the front panel which was scanned at a distance of 8.03 m and for which the panel distance was 24.90 cm, 12.50 cm and 1.16 cm respectively. During all three scans, the centre of the Böhler star was entirely captured. The examples show, that the rays are resolved until they converge in the centre circle. Here, the length of one arc element is 2.95 mm. Similar, also the projected rays on the rear panel, illustrated by the lower three images in Fig. 8, are entirely captured until the beginning of the centre circle with a diameter of 3 cm. Equivalent results were achieved with decreasing scanning distances. Subsequently, neither the distance between the two panels nor the scanning distance itself significantly influence the depictability of the Böhler star. Following, ULi offers a very high resolution, which is primarily driven by small angular increments and a narrow laser spot size. Since the Böhler star is fully resolved in all tested configurations, another structure with more fine details to fully evaluate the performance of ULi, would be required.

5.3 Dynamic real-world close-range measurements

To evaluate the close-range performance of ULi under real-world conditions, the underwater laser scanner was mounted on the survey vessel DVocean and various measurements in a side channel of the River Elbe were carried out.

5.3.1 Integration of ULi on the survey vessel DVocean

Before the data could be acquired, several preliminary steps, including a mounting on the survey vessel DVocean, an integration into the existing network, the establishment of a time synchronization and the conduction of a calibration, were necessary.

The in-house survey vessel of HCU, the DVocean, has a length of 8.00 m, a width of 2.55 m and a height above the waterline of 2.80 m. To simultaneously collect data from different sensors, the DVocean features three mounting poles – one at the

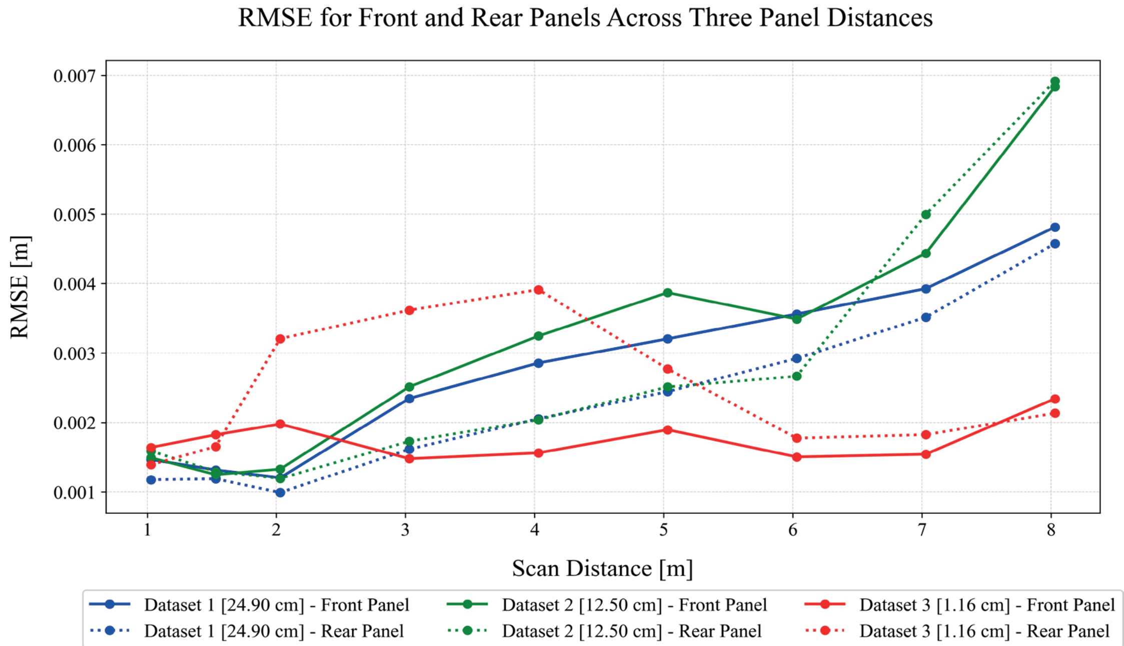

Fig. 7 Root mean square error of the best fit planes for the front and the rear panel of the Böhler star for different panel distances and varying scan distances.

https://doi.org/10.58440/ihr-31-1-n05

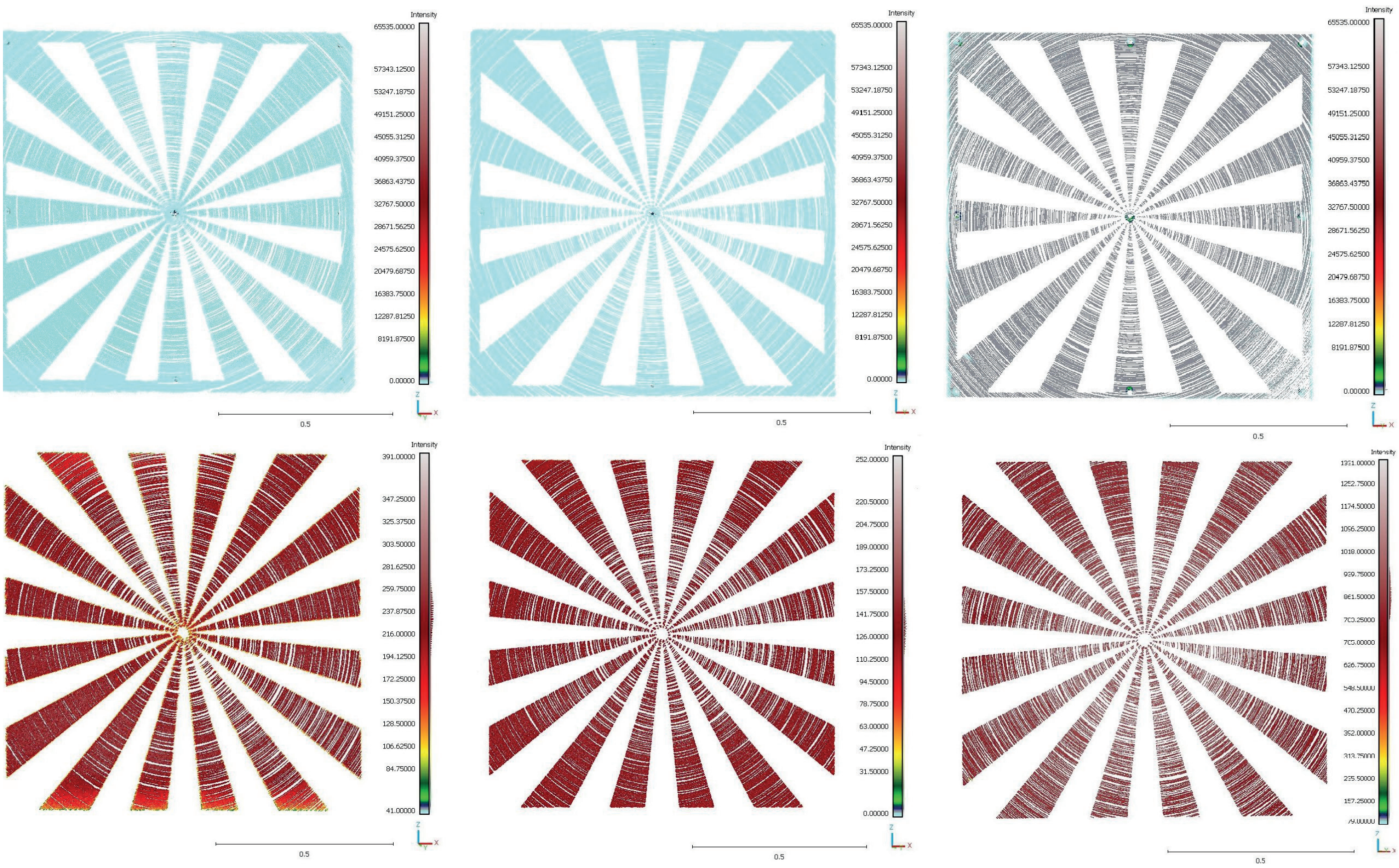

Fig. 8 Point Cloud from front (upper row) and rear (lower row) panel coloured by intensity in a distance of 8.03 m and a panel distance of 24.90 cm (left), 12.50 cm (middle) and 1.16 cm (right).

bow and one on each aft side of the vessel. To accurately capture reflections from infrastructure elements such as bridge foundations or quay walls, ULi was mounted on the port-side pole. To facilitate a flexible mounting and demounting procedure, the Fraunhofer IPM designed a frame, which is also depicted in the Fig. 9a and which can be easily screwed onto the plate of the pole. A quick deployment and retrieval of ULi was achieved by folding down the pole with a leash. To minimize the movement and the vibrations of the pole in the water, caused by environmental factors such as currents, the sensor was stabilized using tensioning straps, which can also be seen in the Fig. 9b.

To integrate the scanner into the existing network on board of the DVocean, a fixed IP address and port were assigned to ULi. The processing unit was connected via ethernet to the main switch of the ship network. Therewith, the collected data could not only be directly reviewed on the screen, but they could also be combined with the trajectory information derived from the motion and position sensors on board. To time-synchronise ULi with the trajectory recording sensors on board, a Precision Time Protocol (PTP) server, utilizing the Pulse Per Second (PPS) signal from the GNSS U-Blox evaluation kit EVK-M8T, was set up on a Raspberry 5. Since PTP hardware timestamping takes the time delay caused by the transmission of messages into account, it provides a more accurate time information in comparison to PTP software timestamping or a Network Time Protocol (NTP). To feed the PTP signal into the network, a Linux running time server on the Raspberry Pi was used. Overall, the PTP hardware timestamping resulted in a mean error and thus in an accuracy of -7.5 ns at ULi.

5.3.2 Calibration of ULi

To calibrate ULi, the position of the housing within the coordinate system of the vessel was determined. Therefore, pre-defined fix points with known coordinates, which are distributed across the vessel, were used. Equipped with a magnetic adapter and a spherical mounted reflector, those fixed based adapter points served as known reference points. To achieve the highest possible accuracy, the known fixed points were measured with a laser tracker from Hexagon. Furthermore, the housing of ULi was geometrically captured with a high-precision hand-held laser tracker from Hexagon. With the help of the 3D transformation parameters, determined from the known fixed points, the reference coordinates from ULi were transformed into the coordinate system of the vessel. A more detailed elaboration of the calibration procedure can be derived from Scheider et al. (2025).

5.3.3 Test environment Elbe

The survey was conducted on 25.10.2024 in the Tiefstackkanal in Hamburg. One key advantage of this location is that a lock separates it from the main channel of the River Elbe, which results in an overall lower sediment and salinity influx. Hence, the location offers clearer water conditions with less turbidity. To numerically verify the turbidity levels, the oceanographic profiler and a Secchi disk were used. While the probe measured a turbidity of 6.00 NTU, the Secchi depth was recorded at 1.10 m. In comparison, measurements taken in the main channel of the River Elbe showed an average turbidity of 8.60 NTU and a Secchi depth of 0.79 m, which confirmed a higher clarity of the water within the Tiefstackkanal.

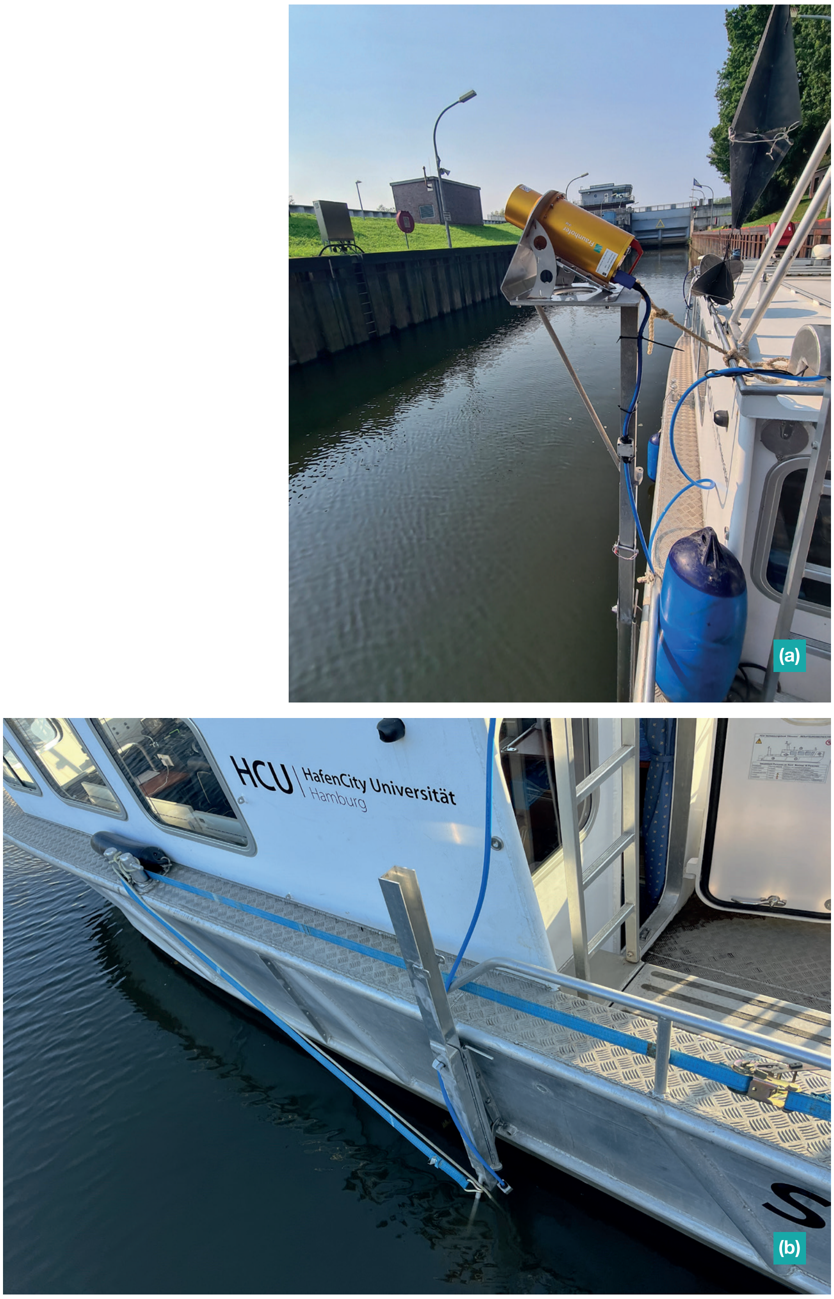

Fig. 9 (a) Mounting of ULi on the port-side pole and (b) stabilization of the pole in the water by tensioning straps.

Table 3 Settings of ULi in the river Elbe.

Max distance (m in water)	5
Skip distance (m in water)	0
Skip pulses	0
Filter	none
Laser pattern	circle
Motor speed (Hz)	1
Radius change speed (Hz)	0.05
Radius	1

5.3.4 Targets Elbe

To particular investigate the performance of ULi with regard to IMR operations and monitoring tasks, a survey along several mooring dolphins, a laying brage and two bridge foundations was conducted. To capture reflections, the DVocean was carefully navigated close to the respective targets. Subsequently, the distance between the underwater laser scanner and the mooring dolphins / laying brage / bridge foundations ranged from 1 m to a maximum of 3 m. Therewith, the targets were situated at a close range and mostly within twice the Secchi depth. To ensure a sufficient point density, the speed of the vessel was reduced to 2 kn and maintained throughout the survey.

5.3.5 Data acquisition in the river Elbe

To acquire the data, the settings summarized in the following Table 3, were used. In contrast to the two laboratory measurements, the filter was set to none. Hence, the green laser operated at its maximum power, corresponding to laser class 3B.

To capture the trajectory of ULi, the raw data from the iXBlue motion sensor Hydrins – in cooperated with the Septentrio AstRx U-3 positioning system on board – was simultaneously recorded using the proprietary iXBlue software MultiLogger.

5.3.6 Results from Elbe

To process the recorded motion data and to smooth the trajectory in areas of GNSS signal outages underneath the bridge, the proprietary software Delph INS was used. Hence, a Kalman Backward- and Forward Filter was applied. The refined trajectory was exported as a text-based ASCII file which contained time, position and orientation data. This file can be imported into Pulsalyzer. However, when reviewing the processed point clouds in CloudCompare, it became evident that neither the mooring dolphins, nor the laying brage nor the bridge foundations, generated any reflection. Subsequently, the underwater laser scanner was not able to detect the targets. Given that the distance between ULi and the targets ranged from 1 m to 3 m and given that the first laboratory study revealed that ULi is able to detect close-range targets, it can be concluded that the turbidity of the water was too high. Therewith, the field test in the Elbe did not deliver any meaningful or reliable results.

6 Conclusion

The first study presented in Section 5 has shown, that the point clouds derived from the underwater laser scanner can be used to identify man-made

https://doi.org/10.58440/ihr-31-1-n05

structures such as drilled holes or cracks as well as organic structures down to a size of 2.36 mm. Nevertheless, the respective measurements exhibited a relatively high scattering up to 48 mm, which varied depending on the used material. Since the maximum distance between the lenses of the scanning unit and the target was less than 0.60 m and since the targets were not securely fixed, but only held by hand, those circumstances probably contributed to the observed high scattering. Meanwhile, the second study revealed, that a 1 m x 1 m large Böhler star is generally suitable to assess the performance of an underwater laser scanner in clear water conditions. Here, the study showed that a level-of-detail down to 2.95 mm can also be retrieved for mid-range measurements and scanning distances of up to 8.03 m. Since the Böhler star was properly fixed, the dispersion of the retrieved point clouds decreased and an overall higher quality could be achieved. Lastly, the third study, conducted under real-world conditions in a side-channel of the river Elbe did not provide any results. Subsequently, it can be said that ULi is not suitable for the operation in water bodies with a turbidity of ≥ 6 NTU or a Secchi depth of ≤ 1.10 m.

Conclusively, it can be said that a static operation of ULi generally allows to resolve structures down to the range of millimetres at close- and mid-range under controlled laboratory circumstances with a turbidity level of 0.00 NTU. Under respective water conditions, ULi is able to detect small-scale damages as cracks and holes down to a size of 2.36 mm. However, since a turbidity level of 0.00 NTU can only be achieved in laboratory environments, the usage of ULi for IMR operations as well as monitoring tasks in real-world environments, is not yet approved.

7 Outlook

To verify the statement of the manufacturer, saying that measurements carried out in clear water offer a sub-millimetre precision, further measurements in laboratory environments with advanced targets, are required. In addition, the retrieved point clouds should be compared with sophisticated ground truth measurements. Therefore, targets should be scanned with a laser tracker before they are submerged into the water. Besides, the laboratory investigations can be extended by using different scanner settings such as the line scan or other incidence angles to get a broader analysis about the resolution capability of ULi. Furthermore, the performance of ULi under even longer scanning distances should be investigated. Following, also dynamic scenarios, should be evaluated. Subsequently, it must be assessed whether a level-of-detail in the range of millimetres or even sub-millimetres can be achieved when not only the underwater laser scanner, but also the targets are moving. For this purpose, possibilities to track the respective trajectories, must be developed. Moreover, the level of turbidity at which the usage of ULi is still feasible, must be further narrowed down. On that account, laboratory environments in which the turbidity level can be precisely steered, are required. Alternatively, further tests in real water bodies, which offer lower levels of turbidity, should be conducted. Respective scenarios could involve measurement campaigns in lakes or natural sea environments with a Secchi depth of more than 2 m. Further tests in the river Elbe are, if at all, only meaningful in spring when less rainfall and a lower amount of leaves decrease the turbidity level. To further evaluate the overall performance of ULi and its suitability for IMR tasks and monitoring solutions, direct comparisons with traditional acoustic instruments, such as a multibeam echosounder or a side-scan-sonar, should be carried out.

Acknowledgements

We would like to thank the head of the HCU model workshop Sven Friedrich for processing the Resopal panels as well as Prof. Dr. Seifried and Dr. Pick from the Institute of Mechanics and Ocean Engineering of the TUHH for providing their test basin for the static laboratory mid-range measurements.

References

3D At Depth (2025). *Technology – 3D at Depth are developers of the world's first truly deepwater LiDAR*. 3D at Depth Inc., Huston, USA. https://3datdepth.com/technology/ (last accessed 7 March 2025).

Alsakar, Y. M., Sakr, N. A., El-Sappagh, S., Abuhmed, T. and Elmogy, M. (2024). Underwater image restoration and enhancement: a comprehensive review of recent trends, challenges, and applications. *Vis Comput, 41*, 3735–3783. https://doi.org/10.1007/s00371-024-03630-w

AML Oceanographic (2025). *Why choose AML for dredging applications…*. AML Oceanographic Ltd., Victoria BC, Canada. https://amloceanographic.com/oceanographic-instrument-configuration-packages/aml-3-with-svp-turbidity-for-dredging (last accessed 7 March 2025).

Bianco, G., Gallo, A., Bruno, F. and Muzzupappa, M. (2011). A comparison between active and passive techniques for underwater 3D applications. *The International Archives of the Photogrammetry, Remote Sensing and Spatial Information Sciences. XXXVIII-5/W16,* pp. 357–363. https://doi.org/10.5194/isprsarchives-XXXVIII-5-W16-357-2011 (last accessed 1 May 2025).

Boehler, W., Bordas Vicent, M. and Marbs, A. (2003). Investigating Laser Scanner Accuracy. *Proceedings of the XIXth CIPA Symposium,* Antalya, Turkey. https://www.cipa-heritagedocumentation.org/wp-content/uploads/2018/11/Boehler-e.a.-Investigating-laser-scanner-accuracy.pdf (last accessed 7 March 2025).

Calantropio, A. and Chiabrando, F. (2024). Underwater Cultural

Heritage Documentation Using Photogrammetry. *Journal of Marine Science and Engineering, 12*(3), p. 413. https://doi.org/10.3390/jmse12030413

Fraunhofer IPM (2024). *Underwater LiDAR System. Optical inspection of underwater infrastructure. Long range, high precision 3D mapping.* Fraunhofer Institute for Physical Measurement Techniques IPM , Freiburg, Germany. https://www.ipm.fraunhofer.de/content/dam/ipm/en/PDFs/product-information/OF/AUS/Underwater-LiDAR-ULi.pdf (last accessed 7 March 2025).

Fraunhofer IPM (2025). *Inspecting underwater infrastructure. Underwater Infrastructure. 3D acquisition and monitoring of large underwater structures using LiDAR.* Fraunhofer Institute for Physical Measurement Techniques IPM , Freiburg, Germany. https://www.ipm.fraunhofer.de/en/bu/object-shape-detection/applications/underwater-laserscanning/underwater-laserscanning.html (last accessed 7 March 2025).

Hildebrandt, M., Kerdels, J., Albiez, J. and Kirchner, F. (2008). A practical underwater 3D-Laserscanner. OCEANS 2008, Quebec City, QC, Canada, 2008, pp. 1–5, https://doi.org/10.1109/*OCEANS.2008*.5151964

Hydro International. (2024). *FGI harnesses Fraunhofer's Lidar tech for maritime surveys.* Geomares, Lemmers, The Netherlands. https://www.hydro-international.com/content/news/fgi-harnesses-fraunhofer-s-lidar-tech-for-maritime-surveys (last accessed 7 March 2025).

Lee, Y.-H., Kim, J.-H., Lee, S.-H. and Kim, S.-B. (2021). Underwater Excavation Records Using Underwater Acoustic Survey: A Case Study in South Korea. *Applied Sciences, 11*(9), 4252. https://doi.org/10.3390/app11094252

Lekkerkerk, H.-J. and Theijs, M.-J. (2011). *Handbook of Offshore Surveying* (Volume III, 2nd ed.). Skilltrade BV. ISBN: 978-90-816591-3-0.

Lichti, D., Gordon, S. and Tipdecho, T. (2005). Error models and propagation in directly georeferenced terrestrial laser scanner networks. *Journal of Surveying Engineering, 131*(4), pp. 135–142.

McLeod, D., Jacobson, J., Hardy, M. and Embry, C. (2013). Autonomous inspection using an underwater 3D LiDAR. *OCEANS 2013*, San Diego, pp. 1–8. https://doi.org/10.23919/OCEANS.2013.6741175

Muhammad, F. (2024). *Simultaneous Underwater Vision based Mapping and Navigation* [Doctoral Dissertation]. Institut Teknologi Bandung.

Nauert, F. and Kampmann, P. (2023). Inspection and maintenance of industrial infrastructure with autonomous underwater robots. *Frontier in Robotic and AI, 10*. https://doi.org/10.3389/frobt.2023.1240276

Ottaviano, E., Testa, A., Rea, P., Saccucci, M., Pelliccio, A. and Ruggiu, M. (2024). Experimental Activity with a Rover for Underwater Inspection. *Actuators, 14*(1), p. 7. https://doi.org/10.3390/act14010007

Scheider, A., Walter, A. L., Heffner, E. and Sternberg, H. (2025). Future challenge in the calibration of high-resolution hydrographic multi-sensor systems. *FIG Working Week 2025*, Melbourne, Australia.

Schmitz, B., Kuhlmann, H. and Holst, C. (2020). Investigating the resolution capability of terrestrial laser scanners and its impact on the effective number of measurements. *ISPRS Journal of Photogrammetry and Remote Sensing, 159*, pp. 41–52. https://doi.org/10.1016/j.isprsjprs.2019.11.002

Shan, J. and Toth, C. K. (2018). *Topographic Laser Ranging and Scanning. Principles and Processing* (2nd ed.). CRC Press.

Sun, K., Cui, W. and Chen, C. (2021). Review of Underwater Sensing Technologies and Applications. *Sensors, 21*(23). https://doi.org/10.3390/s21237849

Vosselman, G. and Maas, H.-G. (2010). *Airborne and Terrestrial Laser Scanning*. Whittles Publishing Ltd. Scotland.

Walter, A. L., Heffner, E., Scheider, A. and Sternberg, H. (2025): Underwater Laser Scanning: Integration and Testing in different environments. *FIG Working Week 2025*, Melbourne, Australia.

Wang, Q., Sohn, H. and Cheng, J. C. (2016). Development of a mixed pixel filter for improved dimension estimation using AMWC laser scanner. I*SPRS Journal of Photogrammetry and Remote Sensing, 119*, pp. 246–258. https://doi.org/10.1016/j.isprsjprs.2016.06.004

Wang, M., Zhang, K., Wei, H., Chen, W. and Zhao, T. (2024). Underwater image quality optimization: Researches, challenges, and future trends. *Image and Vision Computing, 146*. https://doi.org/10.1016/j.imavis.2024.104995

Witte, B. and Sparla, P. (2015). *Vermessungskunde und Grundlagen der Statistik für das Bauwesen*. Wichmann Verlag. Berlin, p. 208.

Zhang, S., Zhu, Y., Xiong, W., Rong, X. and Zhang, J. (2024). Bridge substructure feature extraction based on the underwater sonar point cloud data. *Ocean Engineering, 294.* https://doi.org/10.1016/j.oceaneng.2024.116770

Zünd (2023). *Instruction Manual* (Volume 1). S3 M-800. S300M081210. Product Description, p. 36.

https://doi.org/10.58440/ihr-31-1-n05

NOTE / TECHNICAL REPORT

Harnessing private sector data for the Ocean Decade: Challenges and solutions

Authors

Peter Burger[1] and Laura Meyer[1]

Abstract

The health of the ocean is critical to the well-being of the planet, influencing climate regulation, oxygen production, and the livelihoods of billions of people. Despite the importance of ocean science, significant gaps remain in our understanding of the world's oceans, hindering sustainable ocean governance. This article explores the role of the private sector in ocean data sharing, with a focus on the Bathymetry Data Sharing Guideline developed by the Ocean Decade Corporate Data Group. It highlights the need for private sector engagement in unlocking valuable ocean data, the benefits of data sharing such as data for decision making and ocean management, and the challenges that must be overcome to access privately held ocean data. By enhancing greater collaboration between the private sector and scientific community, this effort supports the broader goals of the United Nation Decade of Ocean Science for Sustainable Development 2021–2030 ('Ocean Decade') and Sustainable Development Goal 14 in promoting sustainable ocean stewardship.

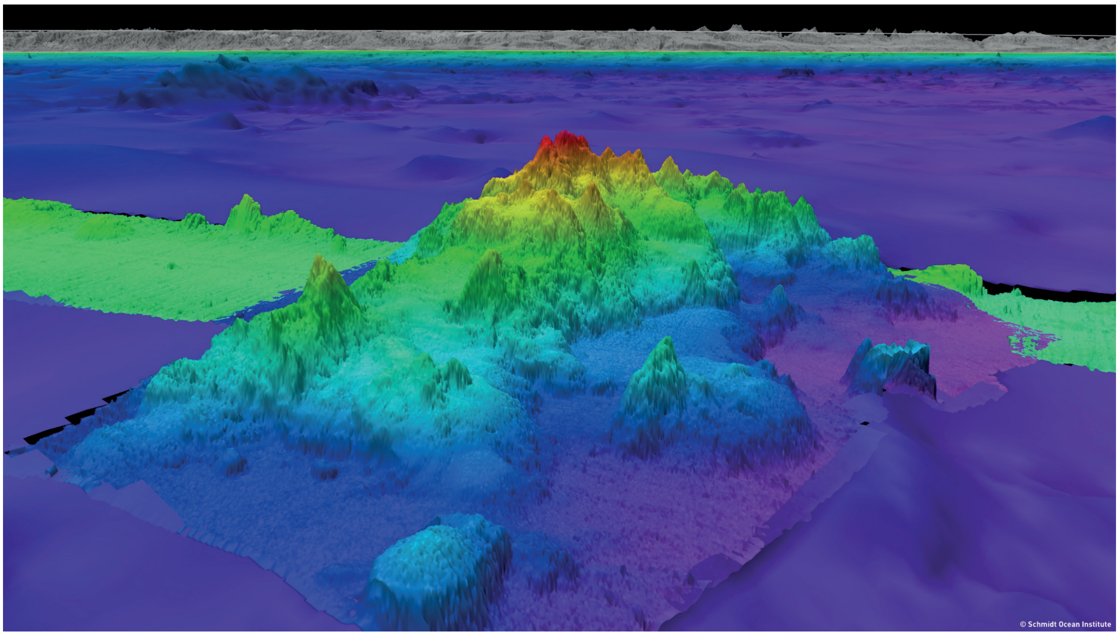

Fig. 1 Seabed photo (Source: Schmidt Ocean Institute).

✉ Peter Burger · p.burger@unesco.org

[1] Ocean Decade Coordination Unit, Intergovernmental Oceanographic Commission of UNESCO

 https://doi.org/10.58440/ihr-31-1-n04

1 Introduction

A healthy ocean is the beating heart of the planet and a vital component of Earth's ecosystem. It regulates the climate, provides over half the planet's oxygen, absorbs significant amounts of heat and CO2, and provides food and livelihoods for over four billion people (Bindoff et al., 2019). However, the escalating consequences of climate change constitute an immediate and significant challenge to global well-being, demanding innovative mitigation strategies (Guan et al., 2023). Without a healthy ocean, biodiversity is severely disrupted, economies suffer, and global climate challenges intensify.

Hence, there is an urgency to better understand the ocean-climate nexus and develop ocean-focused solutions. Despite the importance of ocean science, significant gaps remain in our understanding, hindering sustainable ocean governance (Guan et al., 2023). Identifying and overcoming these gaps with data and information is crucial to addressing the many challenges facing the ocean and coastal areas.

The United Nations Decade of Ocean Science for Sustainable Development 2021–2030 ('Ocean Decade') aims to build bottom-up momentum and action to advance "the science we need for the ocean we want" (UNGA, 2017). Achieving this mission ultimately depends on our ability to have access to "the data we need for the science we want".

Unfortunately, the availability of ocean data is often insufficient to drive critically important research and inform sustainable ocean governance and policies. Overcoming these data gaps requires a massive, coordinated effort that combines the expertise, resources, and commitment of governments, academia, civil society, the private sector, and Indigenous communities (Von Schuckmann et al., 2024).

The private sector has much to gain from a healthy ocean and much to lose from a poorly managed and depleted one. Understanding the ocean and oceanic processes is critical to mitigating development risks and recognizing societal benefits in a sustainable ocean economy. Since industry is one of the beneficiaries of the ocean's shared resources, it has a responsibility to help ensure its longevity.

2 The Ocean Decade as an accelerator for data sharing

Led by the Intergovernmental Oceanographic Commission (IOC) of UNESCO, the Ocean Decade is a multifaceted initiative in support of Sustainable Development Goal (SDG) 14 (UNGA, 2017). It aims to build a common, global framework for ocean science that will help reverse the cycle of decline in ocean health and create improved conditions for sustainable ocean development worldwide.

A key enabler of the Ocean Decade is a wholly mapped ocean. The Nippon Foundation-GEBCO Seabed 2030 Project, underway since 2017, is a collaborative project between The Nippon Foundation and the General Bathymetric Chart of the Oceans (GEBCO) to inspire the complete mapping of the ocean by 2030 and the compilation of all bathymetric data into the freely available GEBCO Ocean Map.

Closing ocean data gaps requires collaboration across sectors. The global ocean economy encompasses a wide range of businesses, including defense and security, shipbuilding, oil and gas, offshore wind, fisheries, aquaculture, shipping, and tourism. While essential, the private industry is at times an overlooked key partner in expanding the pool of ocean data generators and users to fill existing gaps, jointly with governments, governmental institutions, NGOs, and academia.

The global ocean economy encompasses a wide range of businesses, including defense and security, shipbuilding, oil and gas, offshore wind, fisheries, aquaculture, shipping, and tourism. The private industry can help achieve the Ocean Decade's and Seabed 2030 goal to improve the coordination of and access to existing and new global ocean science data. Now more than ever, companies understand that employees, shareholders, customers, and society expect them to contribute to a sustainable future (UNGC, 2015). Businesses must balance short- and long-term stakeholder interests while integrating economic, social, and environmental considerations into decision-making – advancing the goals of the Ocean Decade and Seabed 2030, and ensuring that today's actions do not compromise the next generation's ability to meet their needs. A recent report from Hub Ocean assessed that only 3 % of biodiversity data in OBIS/GBIF was provided by the private sector (HUB Ocean, 2024).

3 A focus on bathymetry

Among all ocean data, bathymetry is a foundational component of any ocean-based research and is essential for developing sustainable solutions to pressing global challenges, including declining ocean health and climate change. Nearly all areas of ocean science, including ocean circulation, tsunami propagation, coastal erosion, coastal flooding, biodiversity monitoring, as well as restoration efforts, require some form of bathymetric data.

Mapping the entire ocean floor is an ambitious task that can only be achieved through international collaboration. At the end of 2024, just over 26 % of the global seabed is mapped, and it is estimated that an additional 15–20 % of the seabed has already been mapped but not yet shared with Seabed 2030 (Fig. 2; Seabed 2030, 2017.). By integrating existing bathymetric data from all sectors into the GEBCO grid, it is estimated that we can chart an additional 15–20 % of the world ocean.

4 The role of the private sector

The private sector holds a vast reservoir of valuable ocean data, actively acquired through activities such as offshore energy exploration, marine infrastructure development, and scientific research. They are actively collecting ocean data in support of resource and infrastructure development projects around the globe. These projects include a wide range of scientific inputs, including metocean measurements, bathymetry, seabed morphology, and biodiversity, among other datasets. These data support the permitting, design, engineering, construction, and operation of marine assets but is generally not shared or made publicly accessible. For the most part, this information is only used once and stored in poorly connected data repositories. Often, these data are considered proprietary by the company that conducted the survey and/or the government that authorized the survey.

Under a partnership between the Ocean Decade and world leading geo-data specialist Fugro, the Ocean Decade Corporate Data Group (CDG) was established in January 2023 (Fig. 3). The group comprises leaders from private sector companies representing a wide variety of marine industries, including fisheries, energy, telecommunications, and marine contractors. This working group focuses on developing frameworks and mechanisms that will accelerate the unlocking and provision of public access to privately held ocean data. The group is co-chaired by Fugro CEO Mark Heine and UNESCO-IOC Executive Secretary Mr. Vidar Helgesen.

Published by the CDG[1] at the end of 2024, the "Bathymetry Data Sharing Guideline" (UNESCO-IOC, 2024) highlights the important opportunities and mutual benefits for industrial companies working in the marine environment to unlock and make their existing and future surveys' bathymetry data publicly available to Seabed 2030. It provides practical guidelines and best practices on how to share their data.

5 The benefits of ocean data sharing

Companies stand to gain from unlocking ocean data stored in their archives and servers. Beyond reputational and environmental, social, and governance benefits, benefits, sharing data enhances stakeholder trust, improves decision-making, and fuels innovation. Making such data publicly accessible contributes to a broader understanding of ocean health, helps identify emerging threats, and supports effective mitigation strategies – all crucial for protecting the marine environment businesses depend on.

Stakeholders like investors, local communities, regulators, and environmental organizations value transparency. Data sharing strengthens these relationships while driving scientific advancements and technological progress. For hydrographic offices (HOs), releasing bathymetric data offers opportunities for global collaboration, supports the Sustainable Development Goals, and enhances access to other valuable datasets – lowering survey costs and benefiting the wider public.

Ultimately, data sharing empowers companies to understand their environmental impacts more clearly, develop targeted mitigation strategies, and position themselves as leaders in the sustainable ocean economy.

6 Hurdles to unlock privately held ocean data

Despite the clear benefits, challenges remain in the widespread sharing of ocean data. Making private-sector data available requires solving several technical, legal, and economic barriers related to information technology infrastructure, data management and processing, intellectual property rights, and other liabilities. The Ocean Decade Corporate

Fig. 2 GEBCO 2024 mapped grid (Source: Seabed 2030).

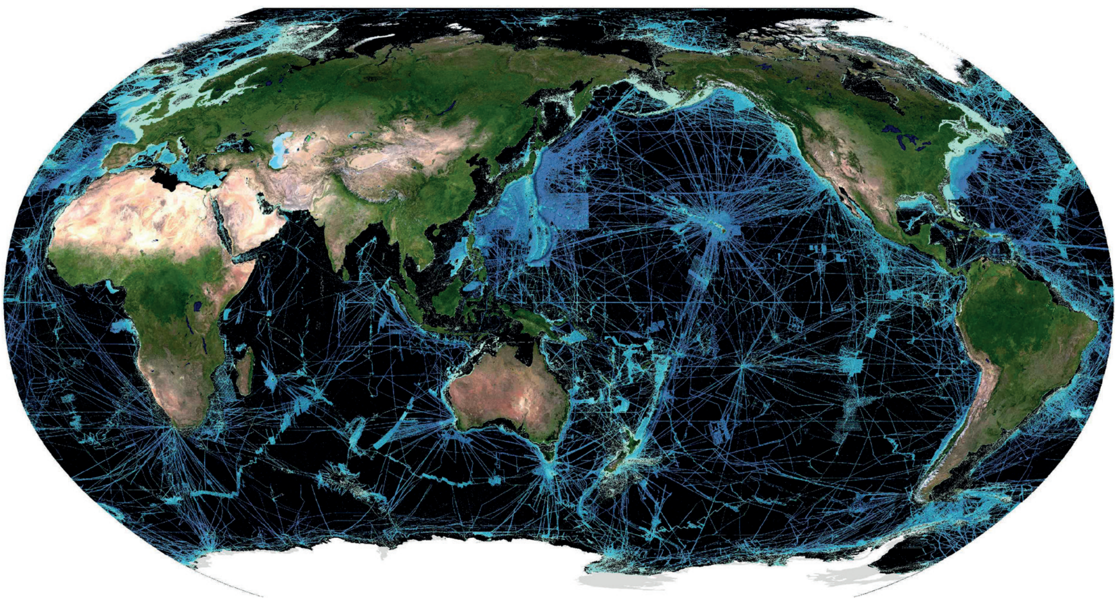

[1] https://oceandecade.org/ocean-decade-corporate-data-group/ (last accessed 16 April 2025).

https://doi.org/10.58440/ihr-31-1-n04

Fig. 3 Group photo Corporate Data Group September 2024, in-person meeting at UNESCO headquarters, Paris France (Source: UNESCO-IOC).

Data Group is focusing on developing solutions to accelerate the unlocking and provision of public access to privately held ocean data, recognizing that collaboration among stakeholders is paramount to overcoming these challenges.

Much of the ocean science data collected by the private sector r has been in national waters or Exclusive Economic Zones (EEZs) with the permission of national governments under various lease arrangements (Fig. 4). In most cases, it is these national governments that ultimately own the data and determine whether to make it publicly accessible. Even when companies are willing to share their data, national governments must approve the release if the data was acquired within their EEZ. However, individual countries have different approaches to allowing and facilitating the sharing of data collected by parties in their territorial and EEZ waters. This difference in approaches can be restrictive and hinder private-sector companies' efforts to unlock and share relevant ocean data they have collected. Despite many national governments' endorsement of the Ocean Decade, as well as their signing up to international conventions, agreements, and frameworks such as Convention on Biological Diversity (CBD, 1992), BBNJ Agreement (UN, 2023), UNCLOS (UN, 1982), that promote data-sharing and public access to data, most have yet to take clear steps to allow public release of private sector ocean science data collected within their jurisdiction.

Outside EEZ waters, data is also collected as part of surveys for submarine telecommunication cables and critical mineral surveys. For the latter, the International Seabed Authority and developers have committed to sharing their bathymetry data with Seabed 2030.

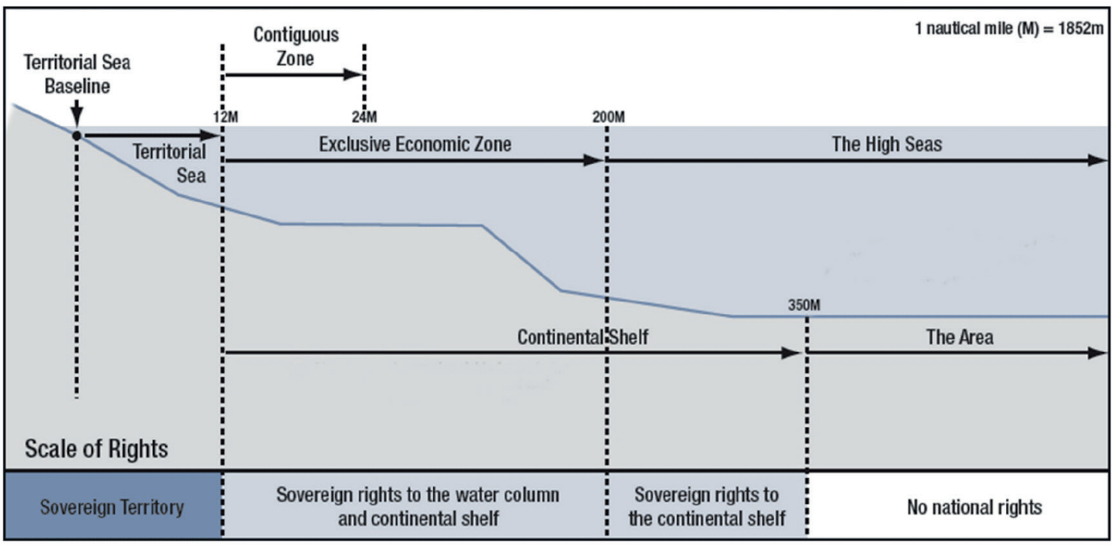

Fig. 4 Maritime Zones (incl. EEZ) (Source: Flanders Marine Institute / VLIZ / Arctic Council, Arctic Marine Shipping Assessment 2009).

7 Policy recommendations

To overcome these challenges, the CDG has developed a policy recommendation for countries to facilitate data sharing in territorial and Exclusive Economic Zone (EEZ) waters. Encouraging countries to implement policies that mandate ocean data sharing for public and private entities operating within their jurisdictions is crucial. This can be achieved by actively incorporating mandatory open data sharing conditions into offshore licensing agreements and permitting processes for public and private parties operating in their national jurisdictions.

To address this a policy recommendation to overcome barriers to data sharing in areas within national jurisdiction that was accepted at the 28th session of the IODE Committee meeting in March 2025. The recommendation urges UNESCO-IOC Member States to support the sharing of data for all-ocean related data collection in their territorial waters and exclusive economic zone through the inclusion of the provisions of the IOC Data Policy and Terms of Use in licensing and permitting within their jurisdictions. This recommendation will be presented for adoption by the 33rd session of the IOC Assembly in June 2025.

8 Conclusion

The private sector has an important role to play in advancing ocean science and sustainable development, not only through ocean technology innovation, but also by facilitating data sharing. Through unlocking and sharing their ocean data, companies can contribute to a healthier ocean, support informed policy-making, and foster innovation. The work of the Ocean Decade, including through its Bathymetry Data Sharing Guideline provides a practical framework for achieving these goals, but overcoming the challenges requires coordinated efforts from all stakeholders.

As we move forward, it is imperative that the private sector, governments, and international organizations work together to ensure that decisions-makers and other stakeholders have access to robust ocean data to support the longevity and health of our ocean.

References

Bindoff, N. L., Cheung, W. W. L., Kairo, J. G., Arístegui, J., Guinder, V. A., Hallberg, R., Hilmi, N., Jiao, N., Karim, M. S., Levin, L., O'Donoghue, S., Purca Cuicapusa, S. R., Rinkevich, B., Suga, T., Tagliabue, A. and Williamson, P. (2019). Changing ocean, marine ecosystems, and dependent communities. In H.-O. Pörtner, D. C. Roberts, V. Masson-Delmotte, P. Zhai, M. Tignor, E. Poloczanska, K. Mintenbeck, A. Alegría, M. Nicolai, A. Okem, J. Petzold, B. Rama and N. M. Weyer (Eds.), *IPCC Special Report on the Ocean and Cryosphere in a Changing Climate* (pp. 447–587). Cambridge University Press. https://doi.org/10.1017/9781009157964.007

CBD (1992). *Convention on Biological Diversity* (adopted 5 June 1992, entered into force 29 December 1993), 1760 U.N.T.S. 69. https://www.cbd.int/doc/legal/cbd-en.pdf (last accessed 16 April 2025).

Guan, S., Qu, F. and Qiao, F.-L. (2023). United Nations Decade of Ocean Science for Sustainable Development (2021–2030): From innovation of ocean science to science-based ocean governance. *Frontiers in Marine Science*, *9*. https://doi.org/10.3389/fmars.2022.1091598

HUB Ocean (2024). *Tides of transparency: A first mapping of industrial ocean data sharing (biodiversity).* Oslo: HUB Ocean. https://sadataproducts.blob.core.windows.net/huboceandatapublic/HUBOcean_TidesOfTransparency_2024.pdf (last accessed 16 April 2025).

OC (2025). Data policy and terms of use (2023). *IOC Information document series, 1548*. The Intergovernmental Oceanographic Commission, Paris, France. https://unesdoc.unesco.org/ark:/48223/pf0000393235.locale=en (last accessed 7 May 2025).

Seabed 2030 (2017). *Our mission.* https://seabed2030.org/our-mission/ (last accessed 16 April 2025).

UN (1982). *United Nations Convention on the Law of the Sea* (adopted 10 December 1982, entered into force 16 November 1994). 1833 U.N.T.S. 397. United Nations, New York, USA. https://www.un.org/depts/los/convention_agreements/texts/unclos/unclos_e.pdf (last accessed 16 April 2025).

UN (2023). *Agreement under the United Nations Convention on the Law of the Sea on the conservation and sustainable use of marine biological diversity of areas beyond national jurisdiction* (adopted 19 June 2023, not yet in force). United Nations, New York, USA. https://www.un.org/bbnjagreement/en (last accessed 16 April 2025).

UNESCO-IOC (2024). *Ocean Decade Bathymetry Data Sharing Guideline* (The Ocean Decade Series, 58). UNESCO. https://oceandecade.org/publications/ocean-decade-bathymetry-data-sharing-guideline/ (last accessed 16 April 2025).

UNGA (2017, December 5). *Resolution A/72/73.* UN General Assembly, United Nations, New York, USA. https://documents.un.org/doc/undoc/gen/n17/421/90/pdf/n1742190.pdf (last accessed 16 April 2025).

UNGC (2015). *Guide to corporate sustainability: Shaping a sustainable future.* United Nations Global Compact, United Nations, New York, USA. https://www.globalcompact.de/migrated_files/wAssets/docs/Nachhaltigkeits-CSR-Management/un_global_compact_guide_to_corporate_sustainability.pdf (last accessed 16 April 2025).

Von Schuckmann, K., Holland, E. A., Haugan, P. and Thomson, P. (2020). Ocean science, data, and services for the UN 2030 Sustainable Development Goals. *Marine Policy, 121*. https://doi.org/104154. 10.1016/j.marpol.2020.104154

NOTE / TECHNICAL REPORT

Surveying in extremely extreme conditions – Dead Sea evaporation ponds

Authors

Barry Grinker[1,2] and Ariel Tarcic[1]

Abstract

Multi beam echo sounder survey systems have many advantages in surveying inshore and offshore areas, lakes and other water bodies, particularly for navigation and engineering purposes. This article describes a project to determine feasibility of using these systems in a very extreme environment. Hypersaline, high temperature Dead Sea evaporation ponds with very shallow depths were surveyed, along with a portion of a feeder canal with an artificial bottom. Results showed that while some aspects of multi beam hydrographic surveying are impossible to achieve or insignificant, with caution and paying particular attention to certain aspects, it is possible to obtain excellent results. The use of multi beam systems in these shallow ponds is clearly advantageous compared to single beam or real-time kinematic GNSS land surveying.

1 Introduction

A local chemical company operates evaporation ponds in their Dead Sea site located in the southern basin of the Dead Sea in Israel. These ponds, fed by a feeder canal from the northern basin, are very shallow, hypersaline water bodies of extremely high temperatures, enhancing rapid evaporation and minerals crystallization. Operation of these ponds demands frequent hydrographic surveying to determine chemical harvesting requirements and results and to calculate required water replenishment volumes.

Until recently, all surveying was conducted either by a Land Surveyor using real-time kinematic (RTK) GNSS or single beam echo sounding, depending upon the depths of the ponds. Both methods produce discontinuous data with limited coverage, requiring much interpolation to fill the data gaps. In a very heterogeneous environment with mineral crystals of various sizes and shapes, randomly spread over the pond bottoms, interpolation results in relatively low accuracy survey products.

This paper describes and elaborates on a three-day campaign, during September 2024, to survey three ponds and a section of the feeder canal using a multi beam echo sounder (MBES) survey system mounted on a small, flat bottomed boat.

2 Aim

The purpose of the survey project was to evaluate the feasibility of using a MBES system in these extreme conditions and, if feasible, to determine whether the advantages in using this method of surveying are cost effective. In addition, and depending upon the final results, the project aimed to produce insight into the methodology of such a survey and any required emphasis on certain aspects to achieve desired results.

3 The project sites

The Dead Sea, lying between Israel and Jordan, is divided into two basins. The northern basin, the larger in area, reaches depths up to approximately 300 m. In 2006, a comprehensive MBES survey was conducted in the northern basin using an ELAC 1050 50 kHz MBES. At the time of that survey, the Dead Sea surface was measured at -421 m below the Mediterranean mean sea level (MSL; Beaudoin et al., 2011).

The southern basin consists today of a number of interconnected evaporation and waste disposal ponds, operated for harvesting various minerals. Fig. 1 shows the general area and the evaporation ponds. On the left is a general picture of Israel and

✉ Barry Grinker · barry57g@gmail.com

[1] Lia Engineering Ltd., Haifa, Israel

[2] Technion – Israel Institute of Technology, Division of Mapping and Geo-Information Engineering, Haifa, Israel

https://doi.org/10.58440/ihr-31-1-n01

the Dead Sea, in the center is an enlargement of the ponds in the southern basin and on the right is an enlargement where the three evaporation ponds, A, B and C, involved in this study, are shown by red dots. In Fig. 2 one can see the feeder canal and in the enlargement the section surveyed in this study.

In each pond a small area was designated for surveying for this feasibility study. In pond A the area surveyed covered 7,500 m^2, in pond B the area surveyed was 16,800 m^2 and in pond C the area planned for surveying was 12,500 m^2. However, in pond C only 4,850 m^2 were actually surveyed due to very shallow depths inaccessible by boat. Fig. 3 shows the area actually surveyed relative to the planned area in pond C.

Evaporation pond A has depths of about 2 m, measured water temperature of 38.8 °C, salinity ranging between 350 PSU (Practical Salinity Units) on the surface to 359 PSU on the bottom, water density averaging 1,286 kg/m^3 and sound speeds of 1,870 m/s at the surface to 1,878.7 m/s on the bottom.

Evaporation pond C has depths less than 1 m, measured water temperature of 38.8 °C, salinity ranging between 377 PSU on the surface to 384 PSU on the bottom, water density averaging 1,313 kg/m^3 and sound speeds of 1,897 m/s at the surface to 1,899.6 m/s on the bottom.

Mud and waste pond B has depths of up to 1.7 m, measured water temperature of 38.8 °C, salinity ranging between 375.7 PSU on the surface to 377 PSU on the bottom, water density averaging 1,310 kg/m^3 and sound speeds of 1,895.7 m/s at the surface to 1,897 m/s on the bottom.

The feeder canal, surveyed near the intake station on the shores of the northern Dead Sea basin, has depths varying according to the pumping schedule. Depths during the survey reached up to 6m, measured water temperature of 34.87 °C at the surface to 34.28 °C on the bottom, salinity averaging 299.9 PSU, water density averaging 1,240 kg/m^3 and sound speeds of 1,820.5 m/s.

Table 1 summarizes the Dead Sea ponds characteristics. The SVP data and graphs of the depth-dependent sound speeds and salinities are given in Fig. 4.

It is clearly evident that in the ponds the salinity increases significantly towards the bottom, consequently resulting in an increase in sound speed. Water temperature does not change significantly due to the very shallow depths so the major influence on sound speed is clearly the salinity. In the feeder canal on the other hand salinity and water temperature have little variation with depth, thus the sound speed has very small and insignificant changes with depth – varying only 0.14 m/s between the surface and 4.5 m depth.

Note that density was calculated according to salinity measurement of the Valeport Swift SVP, using the EOS80 formula suited for regular sea water. The Valeport profiler specifications claim an accuracy of 0.01 kg/m^3 and a resolution of 0.001 kg/m^3. Dead Sea water, having a larger variety of minerals than regular sea water, is expected to have a higher density than that calculated.

Fig. 1 The Dead Sea and the project area.

Fig. 2 Section of the feeder canal surveyed.

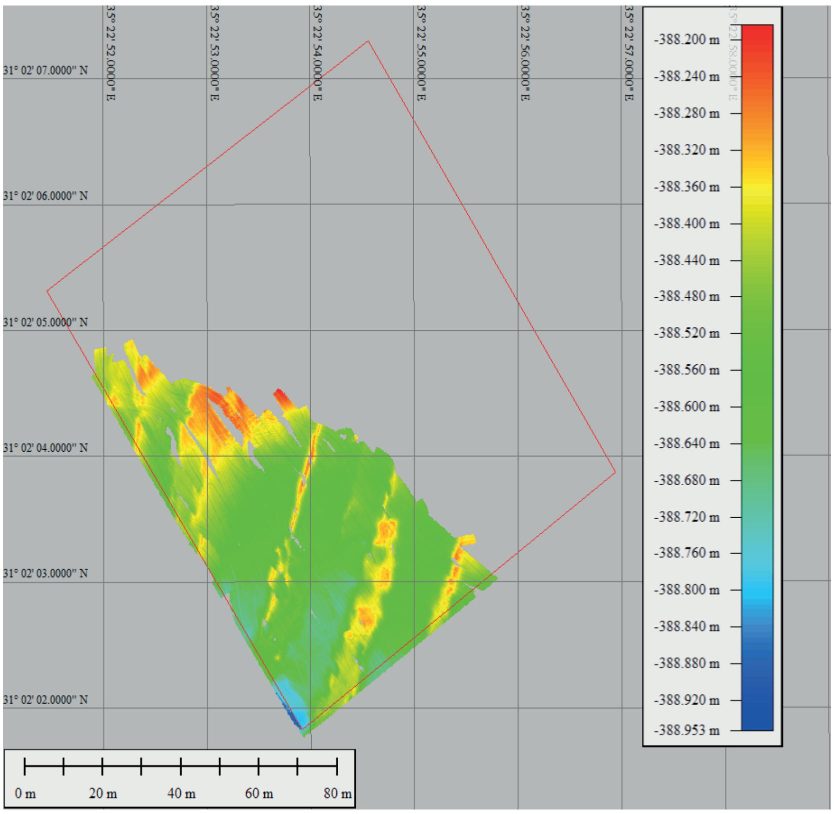

Fig. 3 Pond C survey area.

Table 1 Dead Sea ponds characteristics.

Pond	Maximum depth (m)	Temperature (°C)	Salinity (PSU)	Density (kg/m^3)	Sound velocity (m/s)
A	2	38.8	350–359	1,286	1,870–1,878.7
B	1.7	38.8	375.7–377	1,310	1895.7–1897
C	1	38.8	377–384	1,313	1,897–1,899.6
Feeder Canal	6	34.8	299.9	1,240	1820.5

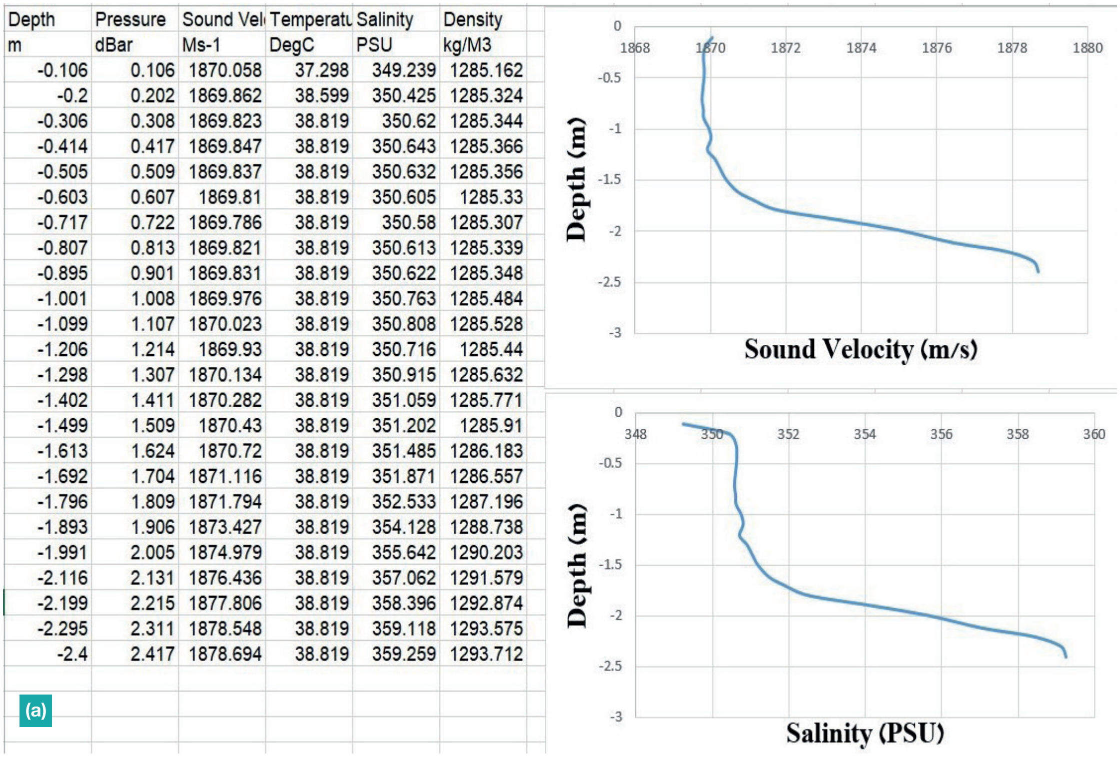

Depth	Pressure	Sound Vel	Temperatu	Salinity	Density
m	dBar	Ms-1	DegC	PSU	kg/M3
-0.106	0.106	1870.058	37.298	349.239	1285.162
-0.2	0.202	1869.862	38.599	350.425	1285.324
-0.306	0.308	1869.823	38.819	350.62	1285.344
-0.414	0.417	1869.847	38.819	350.643	1285.366
-0.505	0.509	1869.837	38.819	350.632	1285.356
-0.603	0.607	1869.81	38.819	350.605	1285.33
-0.717	0.722	1869.786	38.819	350.58	1285.307
-0.807	0.813	1869.821	38.819	350.613	1285.339
-0.895	0.901	1869.831	38.819	350.622	1285.348
-1.001	1.008	1869.976	38.819	350.763	1285.484
-1.099	1.107	1870.023	38.819	350.808	1285.528
-1.206	1.214	1869.93	38.819	350.716	1285.44
-1.298	1.307	1870.134	38.819	350.915	1285.632
-1.402	1.411	1870.282	38.819	351.059	1285.771
-1.499	1.509	1870.43	38.819	351.202	1285.91
-1.613	1.624	1870.72	38.819	351.485	1286.183
-1.692	1.704	1871.116	38.819	351.871	1286.557
-1.796	1.809	1871.794	38.819	352.533	1287.196
-1.893	1.906	1873.427	38.819	354.128	1288.738
-1.991	2.005	1874.979	38.819	355.642	1290.203
-2.116	2.131	1876.436	38.819	357.062	1291.579
-2.199	2.215	1877.806	38.819	358.396	1292.874
-2.295	2.311	1878.548	38.819	359.118	1293.575
-2.4	2.417	1878.694	38.819	359.259	1293.712

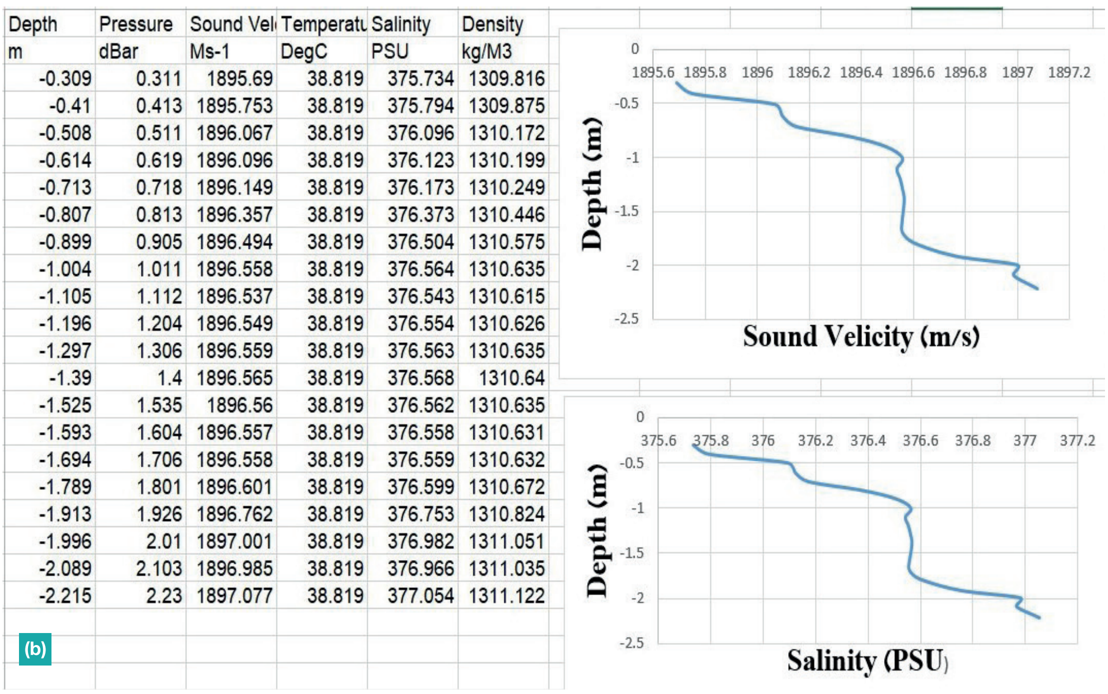

Depth	Pressure	Sound Vel	Temperatu	Salinity	Density
m	dBar	Ms-1	DegC	PSU	kg/M3
-0.309	0.311	1895.69	38.819	375.734	1309.816
-0.41	0.413	1895.753	38.819	375.794	1309.875
-0.508	0.511	1896.067	38.819	376.096	1310.172
-0.614	0.619	1896.096	38.819	376.123	1310.199
-0.713	0.718	1896.149	38.819	376.173	1310.249
-0.807	0.813	1896.357	38.819	376.373	1310.446
-0.899	0.905	1896.494	38.819	376.504	1310.575
-1.004	1.011	1896.558	38.819	376.564	1310.635
-1.105	1.112	1896.537	38.819	376.543	1310.615
-1.196	1.204	1896.549	38.819	376.554	1310.626
-1.297	1.306	1896.559	38.819	376.563	1310.635
-1.39	1.4	1896.565	38.819	376.568	1310.64
-1.525	1.535	1896.56	38.819	376.562	1310.635
-1.593	1.604	1896.557	38.819	376.558	1310.631
-1.694	1.706	1896.558	38.819	376.559	1310.632
-1.789	1.801	1896.601	38.819	376.599	1310.672
-1.913	1.926	1896.762	38.819	376.753	1310.824
-1.996	2.01	1897.001	38.819	376.982	1311.051
-2.089	2.103	1896.985	38.819	376.966	1311.035
-2.215	2.23	1897.077	38.819	377.054	1311.122

Depth	Pressure	Sound Vel	Temperatu	Salinity	Density
m	dBar	Ms-1	DegC	PSU	kg/M3
-0.2	0.202	1897.055	38.819	377.049	1311.11
-0.308	0.31	1896.963	38.819	376.96	1311.023
-0.398	0.401	1896.949	38.819	376.946	1311.009
-0.505	0.509	1898.202	38.819	378.15	1312.196
-0.596	0.6	1898.681	38.819	378.609	1312.65
-0.695	0.7	1899.162	38.819	379.071	1313.106
-0.799	0.804	1899.658	38.819	379.546	1313.576
-0.906	0.912	1899.611	38.819	379.5	1313.531

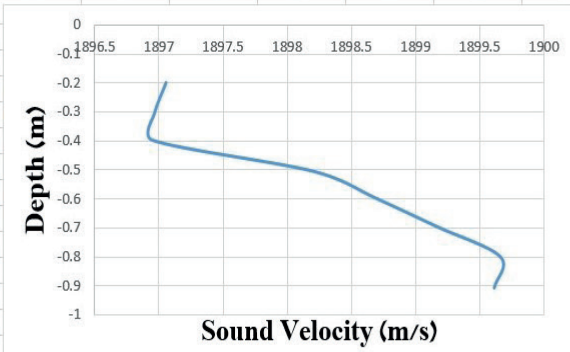

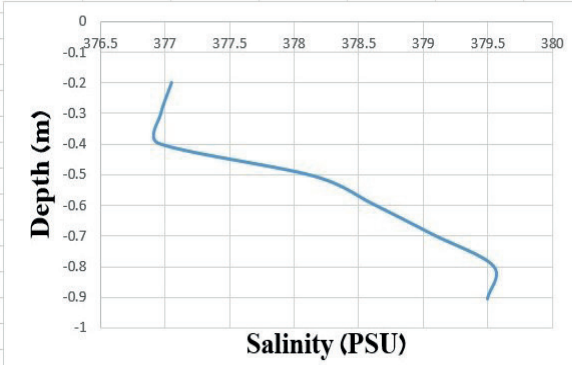

(c)

Depth	Pressure	Sound Ve	Temperatu	Salinity	Density
m	dBar	Ms-1	DegC	PSU	kg/M3
-0.398	0.401	1820.56	34.341	299.521	1240.14
-0.501	0.505	1820.56	34.332	299.521	1240.15
-0.618	0.622	1820.56	34.295	299.498	1240.15
-0.729	0.734	1820.55	34.314	299.496	1240.14
-0.803	0.809	1820.55	34.313	299.5	1240.14
-0.904	0.91	1820.55	34.328	299.507	1240.14
-1.001	1.008	1820.54	34.292	299.477	1240.14
-1.099	1.106	1820.54	34.344	299.497	1240.12
-1.2	1.208	1820.54	34.309	299.477	1240.13
-1.301	1.31	1820.53	34.322	299.473	1240.11
-1.394	1.404	1820.53	34.338	299.478	1240.11
-1.491	1.501	1820.53	34.327	299.478	1240.12
-1.601	1.612	1820.52	34.295	299.451	1240.11
-1.731	1.743	1820.53	34.27	299.445	1240.12
-1.788	1.8	1820.53	34.26	299.436	1240.12
-1.917	1.931	1820.51	34.29	299.439	1240.1
-1.999	2.013	1820.52	34.272	299.433	1240.11
-2.114	2.129	1820.52	34.303	299.453	1240.11
-2.207	2.223	1820.53	34.305	299.456	1240.11
-2.29	2.306	1820.52	34.265	299.43	1240.11
-2.386	2.403	1820.53	34.291	299.45	1240.12
-2.494	2.511	1820.54	34.264	299.441	1240.13
-2.584	2.602	1820.53	34.264	299.436	1240.12
-2.698	2.717	1820.53	34.271	299.436	1240.12
-2.797	2.816	1820.53	34.267	299.437	1240.12
-2.904	2.924	1820.53	34.262	299.428	1240.12
-3.018	3.039	1820.53	34.285	299.442	1240.11
-3.1	3.122	1820.55	34.269	299.447	1240.13
-3.183	3.205	1820.53	34.314	299.451	1240.11
-3.302	3.325	1820.53	34.284	299.44	1240.11
-3.401	3.424	1820.53	34.279	299.434	1240.11
-3.66	3.686	1820.52	34.27	299.413	1240.1
-3.678	3.704	1820.52	34.299	299.431	1240.1
-3.935	3.962	1820.55	34.274	299.446	1240.13
-4.01	4.038	1820.5	34.293	299.408	1240.08
-4.105	4.134	1820.49	34.283	299.384	1240.07
-4.185	4.214	1820.5	34.289	299.402	1240.08
-4.293	4.323	1820.59	34.288	299.479	1240.15
-4.384	4.414	1820.5	34.282	299.395	1240.08

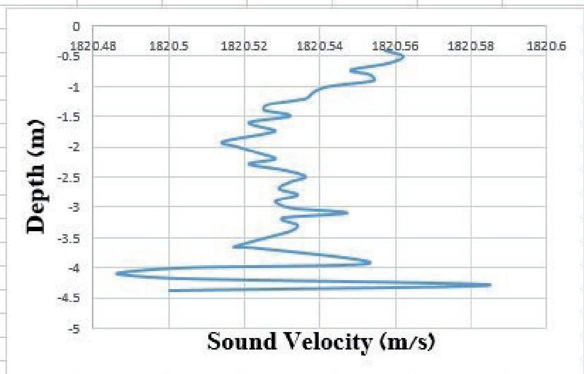

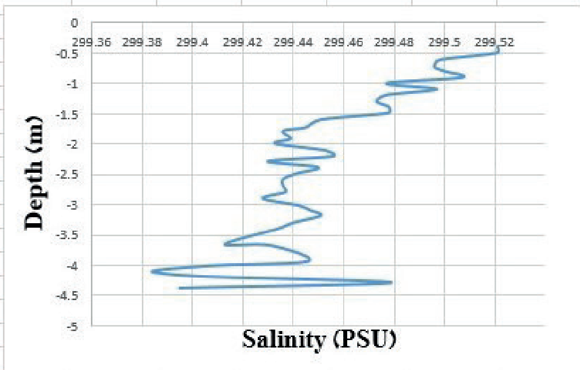

(d)

Fig. 4 SVP data as well as graphs of the depth-dependent sound speeds and salinities: (a) pond A; (b) pond B; (c) pond C; (d) feeder canal.

Fig. 5 The flat bottom survey boat.

Fig. 6 The Portus pole mounted over the side.

Fig. 7 Valeport Swift SVP.

As the title of this paper indicates, these are extremely challenging conditions for conducting a MBES hydrographic survey. Measuring calibration parameters to input into the survey equipment requires instruments suitable for these high salinities and sound speeds. Most instruments are calibrated for regular sea water. For example the AML - 3 LGR SVP (500 m) measures sound speeds between 1,375–1,625 m/s. In addition the very shallow waters and salt mushrooms or muddy bottoms demand much caution during the survey, both for safety reasons and reliable data collection, with noise and acoustic reverberation prevalent.

4 Required results

The main incentive for this project was to obtain a continuous map of the ponds with the highest accuracy possible, in a cost-effective manner. Accuracy would in this case refer to the depiction of the ponds' floors, including both depth relative to a reference level and position, in order to determine mineral harvesting or water replenishment requirements. Certainly, IHO S-44 standards, pertinent mainly though not entirely to navigation, are not relevant in this case with the project being more of an engineering issue rather than one intended for navigation. In addition, depths relative to the ponds' surfaces are more of interest for the site operators than absolute depths, reduced to a chart datum such as the Israel Land Survey Datum (I.L.S.D). Tides are naturally irrelevant in these small ponds.

With this in mind relevant procedures were undertaken, considering restraints due to the extreme environment, to achieve the highest position and depth accuracy and complete coverage of the ponds' floors. For example, during the equipment installation, the use of a portable refrigerator box for all the topside electronics was necessary in order to avoid overheating (air temperature at the site was around 40 °C – certainly extreme). A Patch Test was not conducted since one would be impossible in such shallow waters and the effects of orientation offsets, usually small, could be considered negligible. The Norbit iWBMS suite comes with the IMU mounted on the transducer, eliminating any concern regarding blatant equipment installation errors. Maximum precaution was taken to install the equipment with the best orientation and in the most stable manner possible. The installation of the Norbit Portus Pole, attached to a rigid bracket over the side of the boat, shown in Figs. 5 and 6, contributed to substantially reducing all angular offsets of the IMU and the attached MB transducer.

In addition, requiring depths relative to a practical reference level for operational purposes in the ponds, together with the frequent GNSS spoofing during the campaign, led us to conduct the survey in the following method. Transducer draft was measured at the beginning of each survey and added to the measured and calculated depths below the

https://doi.org/10.58440/ihr-31-1-n01

transducer (DBT) to provide instantaneous depths below the ponds' surfaces (DBW). At the same time, elevations of the ponds' surfaces (negative of course) were recorded from the local tide staffs which are geodetically related to the I.L.S.D. level through a Survey of Israel (SoI) benchmark in the area. Thus, by combining the three measurements, DBT, draft and tide staff reading, the ponds' bottom surface was obtained relative to I.L.S.D for comparison with the land surveyor's GNSS RTK measurements reduced also to I.L.S.D using the SoI's ILUM 2.0 model. In this way we obtained both a practical output for the ponds operators as well as output for quality assessment and accuracy evaluation.

5 Equipment used

For this project we used the Norbit iWBMS survey equipment with frequencies between 200–700 kHz, mounted over the side using a Norbit Portus Pole. The iWBMS comes with a SBG Equinox GNNS/INS embedded system to measure pitch, roll and heave mounted on the transducer and, understanding that the unusual environment would require irregular measuring equipment, a high sound speed calibrated sound velocity sensor (SVS) to measure water sound speed at the sonar head. Navigation and heading data were collected with two GNSS antennae mounted on top of the Portus Pole. In addition, a Valeport sound velocity profiler Swift SVP, calibrated to measure sound speeds up to 1,900 m/s, was used in each survey area prior to commencing the survey.

Figs. 5, 6 and 7 show the survey boat, the pole mounting of the iWBMS and the GNSS antennae and the SVP used.

Data acquisition was obtained on board using QPS Qinsy software and data processing in the office using Qimera.

Control and quality assessment was done by comparing the processed data to point measurements in each area, taken by a Certified Land Surveyor using Leica RTK GNSS. Considering the possibility of soft sediments in some of the ponds, a 7.5 cm radius round disk was attached to the bottom of the survey pole in order to avoid penetration below the sediment surface. Fig. 8 shows the disk attached to the surveyor's pole.

6 Method

The first day of the project, on September 8th 2024, involved mobilization of the boat, preparing and installing the equipment. Heading was calibrated during the GNSS Azimuth Measurement Subsystem (GAMS) setup with position calculations running eight shaped maneuvers until the heading solution reached the system accuracy threshold. Once this was completed the survey team commenced to the feeder canal. After measuring transducer draft using a measuring tape, taking an SVP cast and entering the results into the acquisition software (QPS Qinsy), the team began surveying along 1 km of the canal. The swath angle was set at 150° in order to maximize coverage due to extremely shallow water depth and after testing several frequencies, transducer acquisition frequency of 400 kHz was chosen as it had the best signal to noise ratio. Since it is narrow, only two survey lines were run along the canal, ensuring a large percentage of overlap. Ten RTK GNSS measurements were taken by the Land Surveyor along the survey lines for comparison.

During the canal survey pumping took place changing the absolute water level from time to time. Understanding that the purpose of the survey in this area was not to measure depths, the emphasis was placed on getting a high-resolution picture of the plastic lining on the canal floor. Severe GNSS spoofing during the survey, did not allow the use of RTK height as a reference, hence absolute depths along the canal were unobtainable and the relative depths were used only to produce a picture of the canal's floor. Using the 400 kHz option with a wavelength less than 5mm enabled obtaining excellent resolution. The GNSS spoofing naturally affected the position of the soundings as well, but this was corrected by moving the final DEM into place manually, using conspicuous features along the canal as anchors for the necessary horizontal translation.

The following day, September 9th, began by deploying the survey boat to pond A at the southern end of the southern basin. After measuring transducer draft, taking an SVP cast and entering the results into the acquisition software, the team began surveying along the main survey lines, in a NE–SW direction. Line spacing varied between 3.3 m and 6.5 m, ensuring adequate overlap. Swath angle was 150° and frequency 200 kHz as it had the best signal to noise

Fig. 8 GNSS RTK survey pole with disk.

ratio after testing several frequencies. Thirty-three main survey lines were run with two perpendicular cross check lines, covering 2.4 NM during 1 hour and 20 minutes of surveying at 1.8 knots. After completing the MBES survey, sixteen GNSS RTK measurements were collected by the Land Surveyor, spread around the surveyed area. Fig. 9 shows the survey lines run in pond A, overlaid on the color-coded bathymetry.

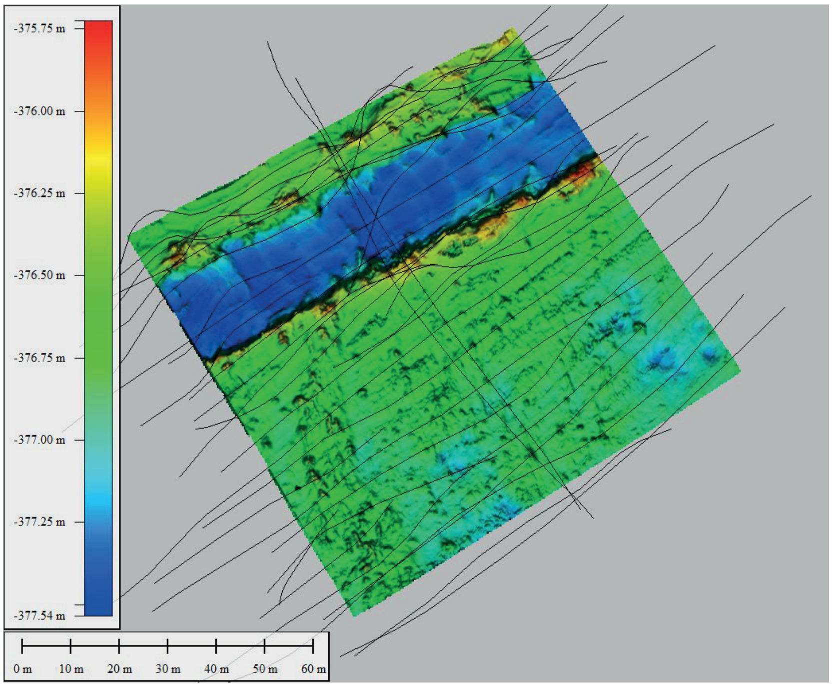

Fig. 9 GNSS RTK survey pole with disk.

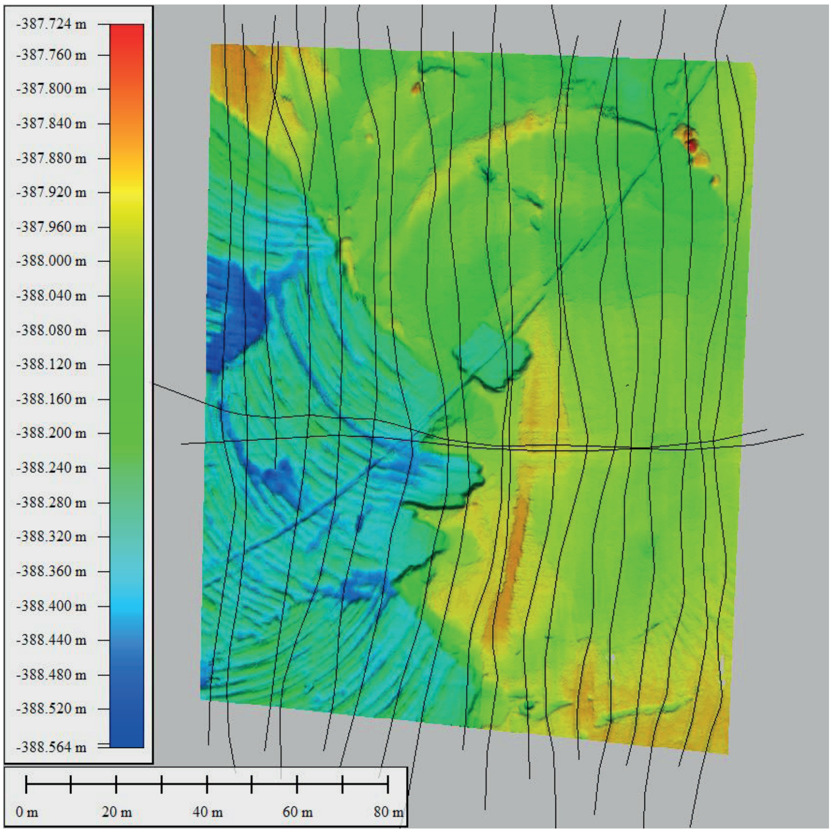

Fig. 10 Pond B survey lines.

The third day of the project, September 10th, began with the survey boat deployed in the mud and waste pond B. Once again, the transducer draft was measured and an SVP cast taken. Nineteen main survey lines were run in a N–S direction with another two perpendicular cross check lines. Line spacing varied between 5 m and 10 m ensuring adequate overlap. Swath angle was 150° and frequency alternated between 200–400 kHz with changes made on board according to the quality of the raw data collected. The frequency changes were made due to extreme water density variations in the survey area, mainly due to different water composition in the dredged canal bottom. The survey lines overall length was 2 NM and the survey took one and a half hours at 1.33 knots. After completing the MBES survey, only three GNSS RTK measurements were taken for quality assessment due to GNSS spoofing during the land survey. Fig. 10 shows the survey lines run in pond B, overlaid on the color-coded bathymetry.

Then the survey boat was transferred to pond C where twenty-four main survey lines were run in a NW–SE direction with another two perpendicular cross check lines. Line spacing varied between 2.2 m and 4.7 m ensuring adequate overlap. Swath angle was 150° and once again the frequency was alternated between 200–400 kHz as deemed pertinent according to the quality of the raw data collected. This was done according to the reasons explained in the previous paragraph, only this time an additional reason was changes in the water composition in the survey area resulting from diverse water densities and temperatures which created some hot and dense water cells within the survey area. The survey lines overall length was 1.3 NM and the survey took one hour at 1.3 knots. After completing the MBES survey, five GNSS RTK measurements were taken for quality assessment. Fig. 11 shows the survey lines run in pond C, overlaid on the color-coded bathymetry.

The RTK GNSS validation measurements undertaken by the land surveyor used the ellipsoid height and the survey of Israel's national undulation model, ILUM 2.0, producing elevations relative to the Israel Land Survey Datum (ILSD). Naturally in the Dead Sea area all elevations are negative.

7 Data processing

After each survey day, raw *.db files were imported into QPS Qimera for preliminary processing and data evaluation using a 20 cm cell size dynamic surface. A SVS – SVP comparison was conducted and IMU data loaded for navigation and attitude post processing in order to achieve better results.

Then after approval of data quality and coverage the data was backed up on two SSD HDD for additional processing in the office where each survey area was deeply cleaned using the cloud point slice editor along with a 3D view of same data. During data processing,

https://doi.org/10.58440/ihr-31-1-n01

Table 2 Dead Sea ponds characteristics.

Pond	Water surface level	Maximum elevation (depth)	Minimum elevation (depth)	Δ (depth range)	Average elevation (depth)
A	-375.435 m	-375.725 m (0.29m)	-377.535 m (2.1m)	181 cm	-376.822 m (1.195m)
C	-387.953 m	-388.183 m (0.23m)	-388.953 m (1.0m)	77 cm	-388.511 m (0.615m)
B	-386.824 m	-387.725 m (0.90m)	-388.564 m (1.74m)	84 cm	-388.115 m (1.321m)

we noticed some GNSS spoofing which could cause an ERS survey to have significant error variations of the *Z*-values in some survey lines (Fig. 12). Therefor it was decided to use sonar depth along with draft and tide staff data instead of RTK height. Elevations were then reduced to ILSD ILUM2 using local tide staff gauges in each pond and UTC time.

The difference between the ellipsoidal height at the beginning of the line and that at the end of the line a couple of minutes later, reached up to 2 m. The survey line is displayed on the map to the left (Fig. 12).

Each dynamic surface was then exported as an ASCII *.xyz file and loaded into Blue Marble's Global Mapper program where it was cropped and transformed to local CRS and exported in the same format as final processed datasets.

8 Results

Post processing involved cleaning the data and preparing a 20 cm grid map of each area. In Table 2 is a summary of the results obtained in the ponds.

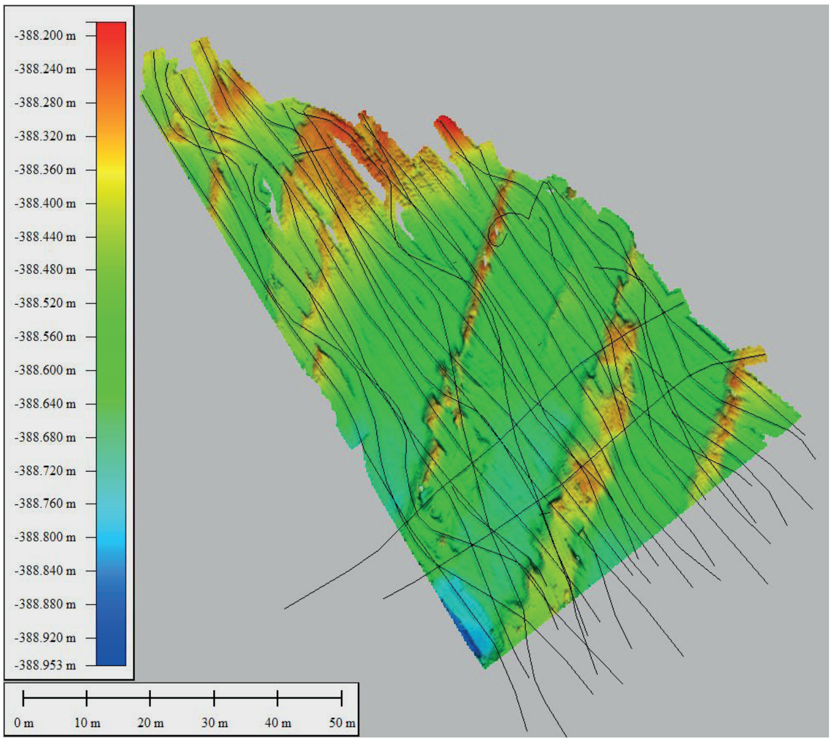

Fig. 11 Pond C survey lines.

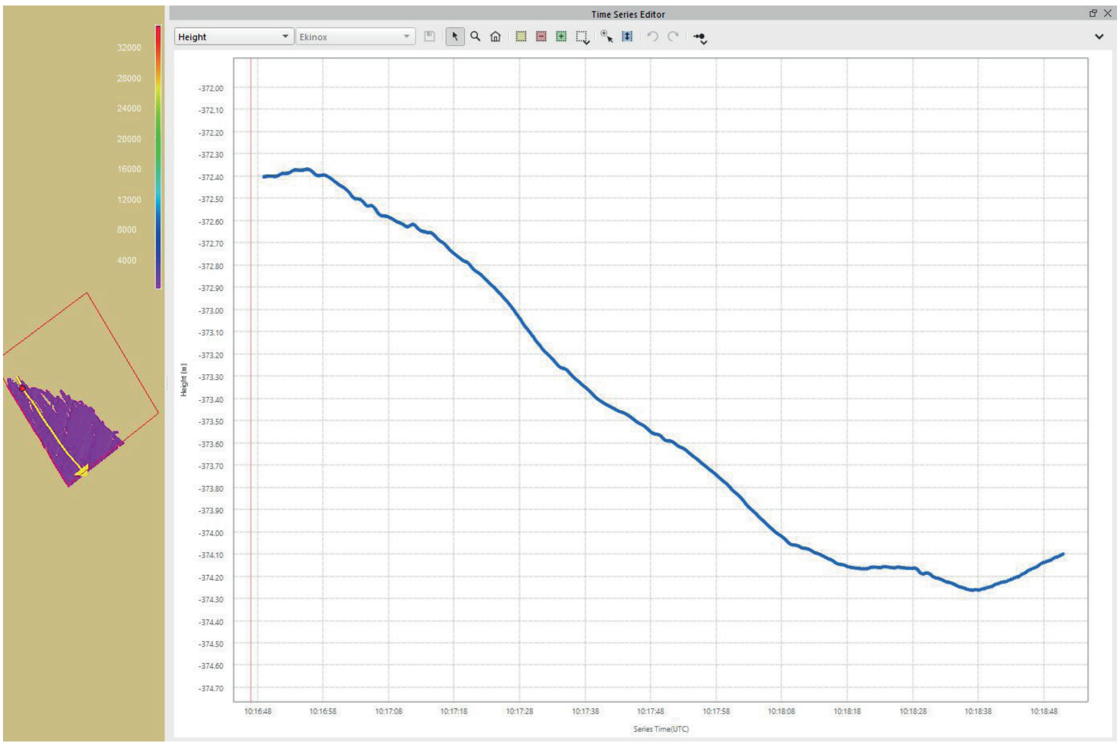

Fig. 12 GNSS RTK ellipsoidal height along a survey line.

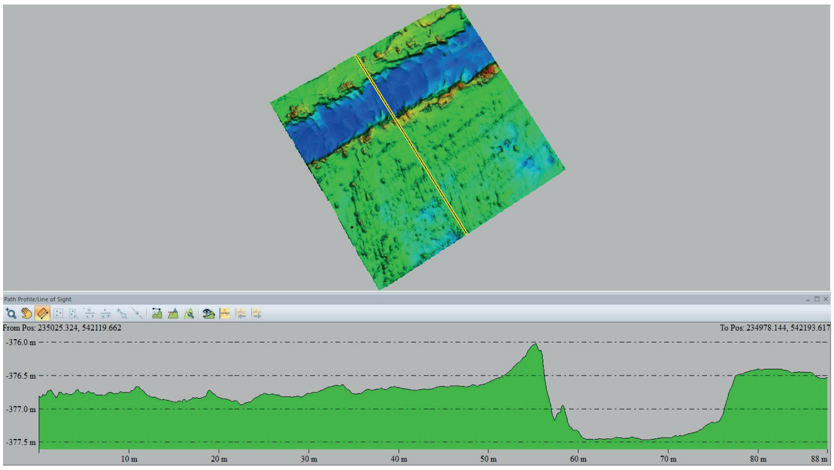

Fig. 13 Pond A bathymetry and cross section.

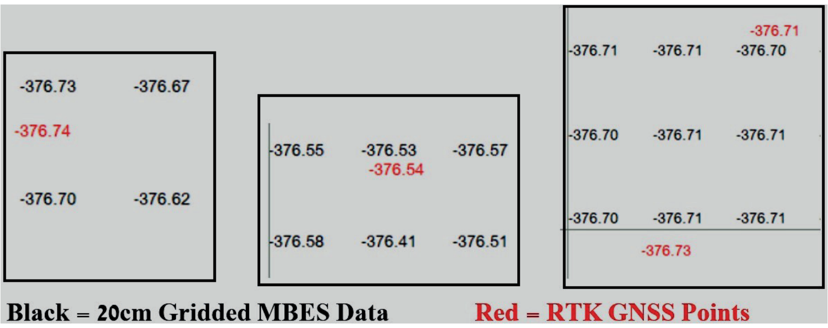

Fig. 14 Pond A MBES – RTK GPS comparisons.

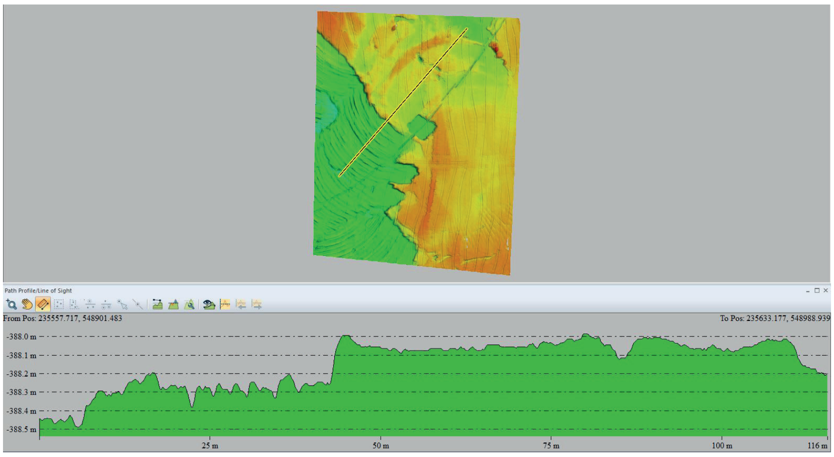

Fig. 15 Pond B bathymetry and cross section.

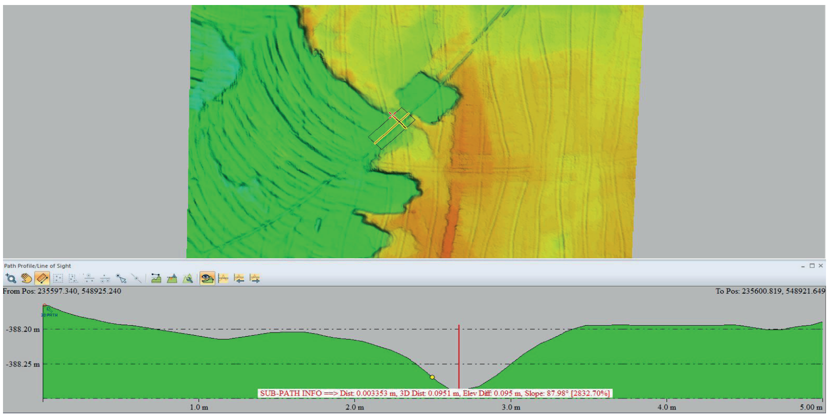

Fig. 16 Cable remanence furrow in pond B.

9 Data analysis

The data was analyzed by visual comparison of the main survey lines with the cross sections at the intersections. In addition, the MBES 20 cm gridded output was compared to the land surveyor's RTK GNSS measurements where available. Where prominent features were observed, their interpretation was validated with the site operators in charge of the ongoing works.

9.1 Pond A

In pond A, a channel, 19 m wide and 1 m deep, is clear evidence of previous harvesting in the area. Fig. 13 shows this channel in a top view and a cross section.

Comparison between the MBES output and the RTK GNSS points shows differences on the order of one or two centimeters, as demonstrated in Fig. 14.

9.2 Pond B

This pond with a muddy bottom was surveyed at 400 kHz in order to obtain the highest resolution possible. Fig. 15 clearly demonstrates signs of dredging in the "deeper" area to the south-west and the smoother "shallower" area to the north east where dredging and waste extraction had yet to be conducted.

Another feature observed here is a shallow 9 cm furrow, remanence of a cable that lay on the muddy bottom which was removed some time prior to the survey (Fig. 16).

In this pond the land surveyor had difficulty discerning exactly when the disk attached to his survey pole reached the bottom. When raising the disk out of the water after taking the measurement, mud covering it indicated that the measurements were taken a little below the surface of the mud. This was validated in the comparisons with the MBES data which were usually shallower than the RTK GNSS points, as shown to the left in Fig. 17 below. In some areas however, the bottom was a little more consolidated and the data was compatible, as shown to the right in Fig. 17.

9.3 Pond C

This pond was only partially surveyed due to part of the planned area being inaccessible by boat. Salt harvesting is evident in Fig. 18 with furrows 20 m wide with depths between 25 cm and 30 cm. The remnant salt ridges running parallel in a NE–SW direction are clearly seen. As in pond A, the MBES – RTK GNSS comparisons show excellent correlation, with differences of 1–2 cm (Fig. 19).

9.4 Feeder canal

As mentioned earlier, the feeder canal was surveyed with the intention of providing a high-resolution picture of the canal's bottom, rather than bathymetry which varies according to the pumping schedule.

Near the intake pumping station P9 close to the

https://doi.org/10.58440/ihr-31-1-n01

shore of the Dead Sea northern basin, the maximum depth reached approximately 6m. Here folds in the plastic sheets lining the bottom are evident, as shown in Fig. 20. These folds change the depths on the order of 6 cm.

In another area, approximately 600 m from the beginning of the canal opposite to the water reservoir, a 30 cm protrusion runs across the entire canal width. This protrusion, demonstrated in Fig. 21, correlates with a concrete beam used to anchor the plastic sheets.

10 Conclusions

The extreme conditions of this project – very shallow, highly saline, warm water with either a very soft or a crystallizing hard, heterogeneous bottom – posed many potential problems. In order to ensure required results, the following procedures needed special attention:

- Choice of suitable vessel and equipment capable of working in this extreme environment.
- Equipment alignment during installation – considering no Patch Test done.
- SVP measurements up to 1,900 m/s conducted in each area, as deep as possible and as close to the bottom as possible, entered into the data collection program prior to beginning each survey.
- Slow survey speed to obtain as much overlap and redundancy as possible – required also for safety in shallow, small ponds.
- Small line spacing distance, considering swath angle used and surveyed area depth, to ensure sufficient overlap.
- Careful real time monitoring of data collection along the survey lines to ensure continuous overlap and no data gaps.
- Continuous monitoring of data quality, including GNSS fixes, throughout the survey – stopping data recording when raw data considered contaminated with errors.
- Frequency adjustment during the survey to obtain the highest resolution and best results possible.

However, certain elements of MBES hydrographic surveying, complex, if at all possible, proved to be negligible and unnecessary in these conditions. These elements, not addressed in the survey, include:

- Patch Test calibration of the equipment – small misalignment angles produce negligible errors in such shallow depths. For example, a 1° angular roll offset would result in a 0.3 mm depth error and 3.5 cm horizontal error at a nominal depth of 2 m in the nadir and 3 cm depth error and 1.7 cm horizontal error at an outer beam of 60°.
- Pitch and roll angles and heave values are very small in a pond limited in size where waves do not develop – their impact on the final results in such shallow waters are negligible (Fig. 22).

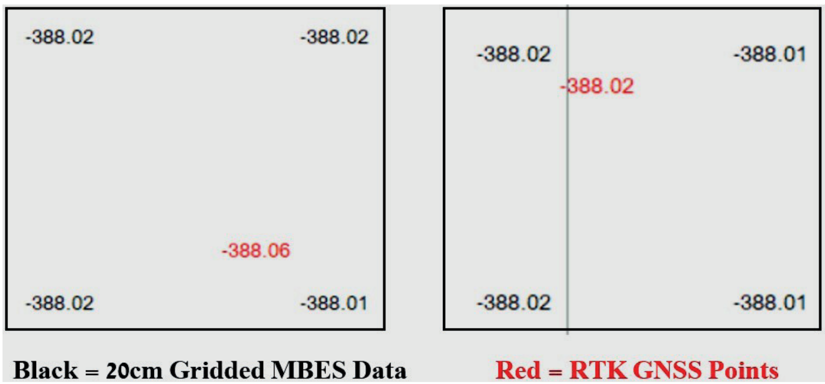

Fig. 17 Pond B MBES – RTK GPS comparison.

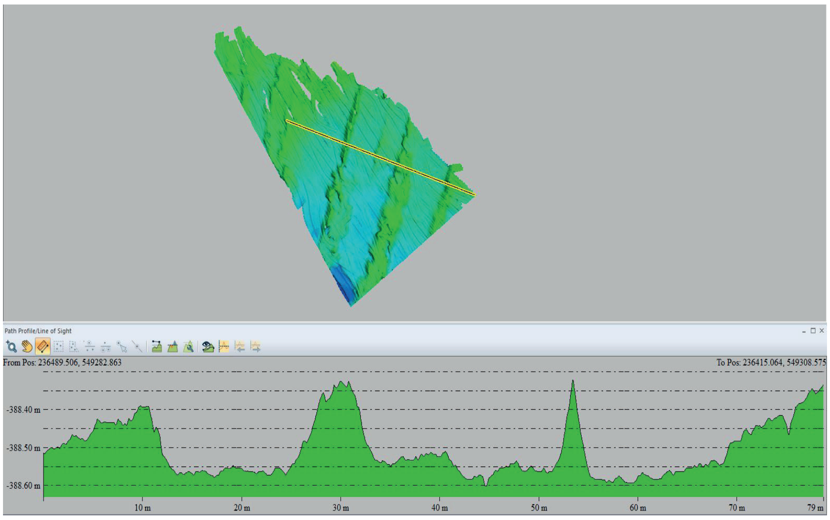

Fig. 18 Pond C bathymetry and cross section.

Fig. 19 Pond C MBES – RTK GNSS comparisons.

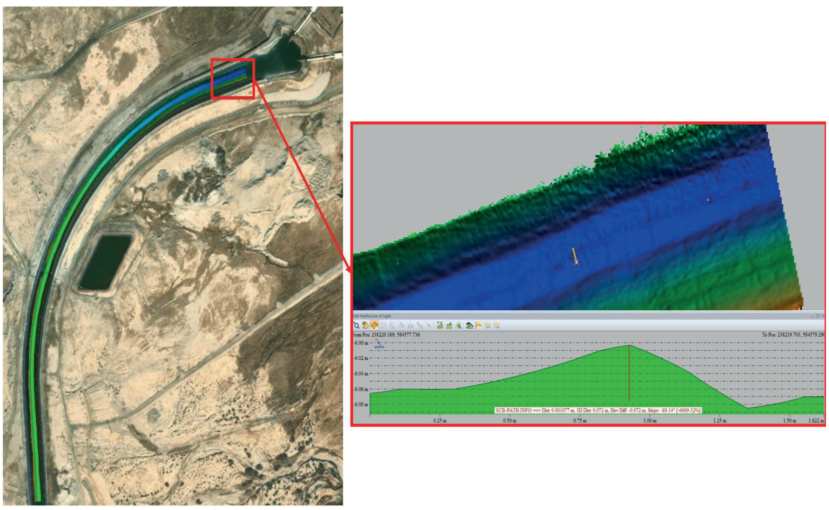

Fig. 20 Plastic sheets near P9.

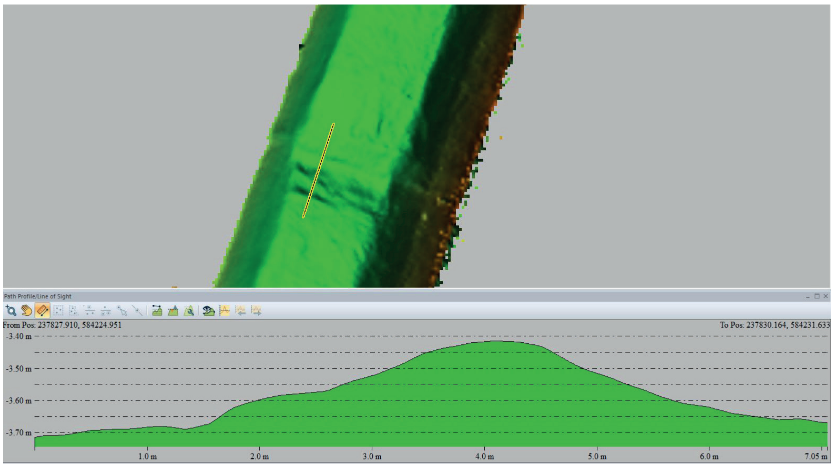

Fig. 21 Concrete beam cross section.

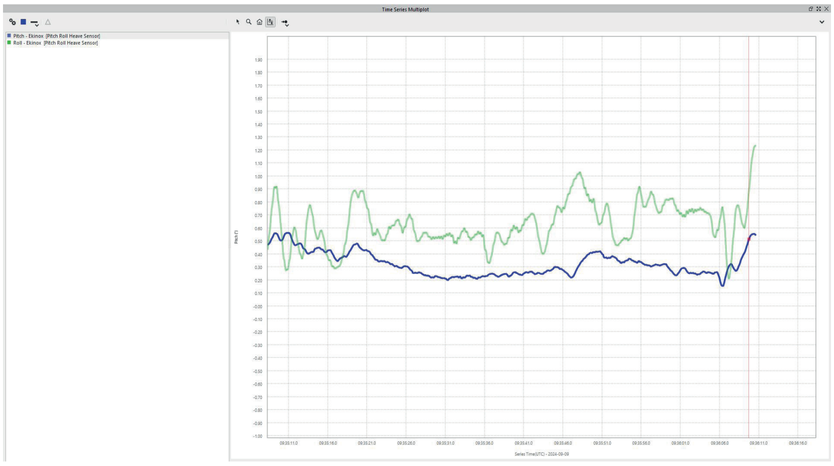

Fig. 22 Typical pitch (blue) and roll (green) values during the survey.

- Horizontal offset measurements – having the GNSS antennae placed on the pole above the transducer makes only the vertical offset calibration relevant. The horizontal offset is determined by the Portus Pole manufacturer.
- Draft measured in each area on each day was the same despite water density differences, probably due to the flat bottomed, small boat.

The results of this project clearly show that MBES surveying in the extreme conditions of evaporation ponds is feasible. Careful attention to critical aspects of hydrographic surveying is essential to obtain required results, while other aspects, less relevant in this case, may be overlooked.

The results show a continuous DEM of the evaporation ponds' substrates, portrayed on a 20 cm grid in this case. In addition, the artificial lining of the feeder canal was clearly seen in the data produced after post processing.

This project gave us an insight into the implications involved in using this technique to monitor the evaporation ponds and the feeder canal. The surveys conducted covered small areas in each pond. Understanding that the chemical company would probably need larger scale surveys, with more extensive coverage in each pool, this project will enable them to estimate costs and time frames for future surveys.

References

Beaudoin, J., Sade, A., Schulze, B. and Hall, J. K. (2011). Dead Sea Multi-beam Echo Sounder Survey. *Hydro International, 15,* pp. 21–23.

https://doi.org/10.58440/ihr-31-1-n01

NOTE / TECHNICAL REPORT

Investigating the precision of hydrographic data by comparing the differences between multi-beam and single-beam echo-sounders (case study: Bushehr port in the Persian Gulf)

Authors

Nader Pasandeh[1], Seyed Shahed Mosavat[2], Sepideh Abadpour[2], Ali Kourosh Niya[1], Bahman Tajfirooz[2], Seyed Mojtaba Zarei[1] and Amir Hossein Kazemi[1]

Abstract

This study examines discrepancies between single-beam and multi-beam data at Bushehr Port, where multi-beam data were processed using mathematical models. Single-beam-derived depths from control points were then interpolated onto these surfaces and compared statistically. The analysis revealed an average depth difference of 0.03 m between the sensors, with a standard deviation of 0.08 m at a 98 % confidence interval, and a root mean square error of 0.21 m. The results confirm that multi-beam surveys with the IHO S-44 standard (Edition 6.1.0), achieve Special Order accuracy while reducing field operation time and costs, and providing more extensive seabed coverage.

Keywords

single-beam echo sounder · multi-beam echo sounder · hydrographic standards · data quality assessment

1 Introduction

Maintaining ports as critical components of the goods transportation network and primary gateways for passenger transport is essential, placing them as pivotal elements of the blue economy (Tajfirouz et al., 2022; Motallebi Korbekandi & Zare Zardeyni, 2022). In this regard, ensuring sufficient navigational depth in ports and waterways for the safe passage of vessels remains a key priority for the relevant authorities. Consequently, the routine monitoring of seabed alterations in ports and maritime channels has become a major focus for planners in national port management and navigation. Accurately identifying waterways and measuring seabed depth and its fluctuations (bathymetry) through the use of advanced tools to update seabed maps is a globally accepted practice (Saeidi et al., 2023). While optical remote sensing tools and satellite imagery have facilitated depth estimation, the effectiveness of this technology is highly dependent on favorable weather conditions, image clarity, and is constrained to shallow, clear (non-turbid) waters (Bandini et al., 2018). Despite advancements in remote sensing technologies, including machine learning algorithms for hydrographic mapping, the accuracy of these depth measurements remains inferior to that achieved using acoustic equipment (Saeidi et al., 2023; Pike et al., 2019). Among acoustic devices, the multi-beam echo sounder (MBES) has gained significant attention in national ports over the last decade. The volume of data captured by MBES is exponentially higher than that of single-beam echo sounders (SBES), providing continuous seabed coverage, which accelerates depth measurement and reduces field operation times (Costa et al., 2009).

✉ Ali Kourosh Niya · alikouroshniya@gmail.com

[1] Port and Maritime Organization, Tehran, Iran

[2] Darya Tarsim Consulting Engineers Co. Ltd., Tehran, Iran

 https://doi.org/10.58440/ihr-31-1-n02

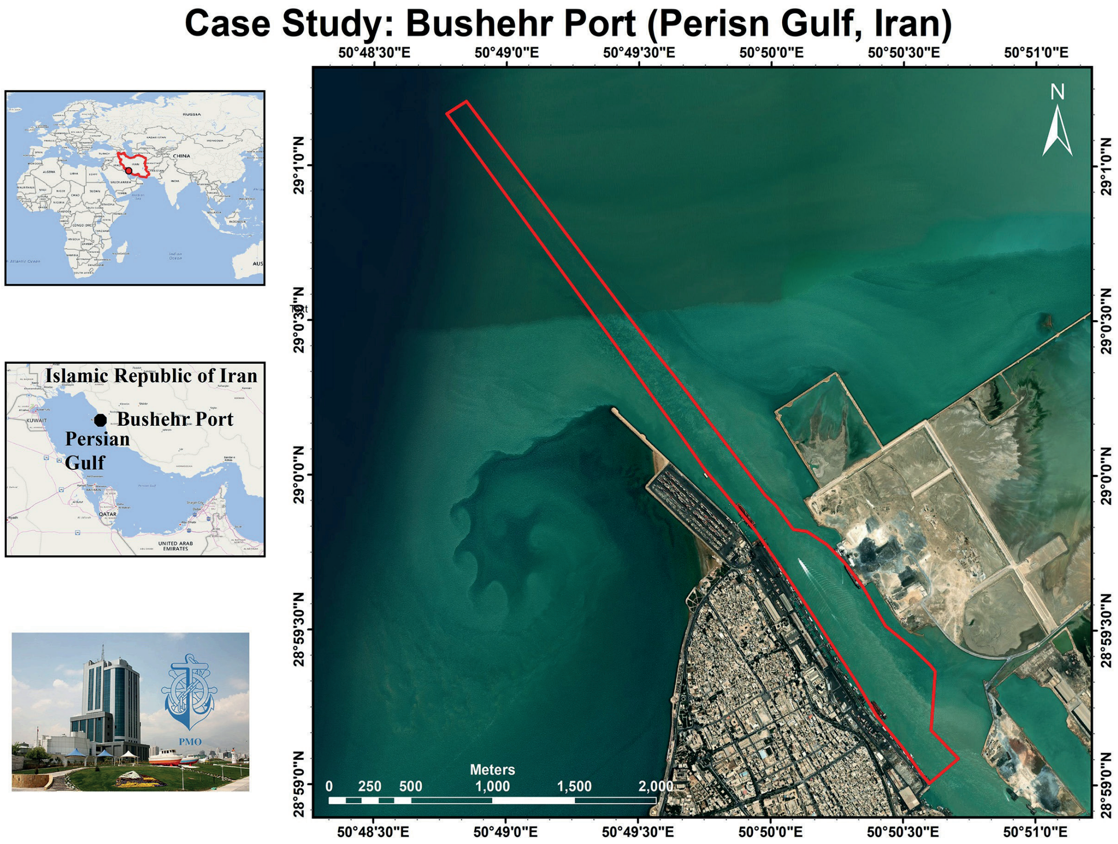

Fig. 1 The study area (red limit) at Bushehr port, Iran (Google Earth image).

However, the accuracy of MBES measurements is not uniform, varying based on multiple factors. In particular, at the edges of survey swaths, refraction errors and other inaccuracies must be addressed. Given that depth data is costly, scarce and considering the dynamic nature of the seabed, detailed analysis and comparison of data from SBES and MBES in existing areas can help clarify the errors in MBES measurements. Notably, limited research has been conducted on comparing SBES and MBES data, largely due to the high costs and difficulty of obtaining such data from two different sensors within a reasonable timeframe. In their thesis, Shamai Gahfarokhi explored various methods for sorting MBES data and different interpolation techniques for surface point elevations, ultimately developing an optimal model for aligning data from MBES and SBES while enhancing the accuracy of surveyed edges (Ghahfarokhi, 2020). A 2021 study in Indonesia evaluated the quality and discrepancies between MBES and SBES data in relation to the IHO S-44 standard (Pratomo & Saputro, 2021). Another study in Australia focused on creating maps of seabed biological habitats using the return energy from both MBES and SBES, though it did not address depth measurement or its accuracy (Parnum et al., 2009). Similarly, a separate study classified seabed materials based on the return energy from MBES devices (Zhi et al., 2014). However, no comprehensive investigation has yet examined the statistical differences, correlations, and three-dimensional surface information derived from MBES and SBES data in Iranian ports. Therefore, this study aims to compare MBES and SBES data in the port of Bushehr.

The primary objectives of the current research are outlined as follows:

1. To evaluate the accuracy of processed MBES data in the Port of Bushehr concerning compliance with the IHO S-44 standard.
2. To compare the processed data from both MBES and SBES concerning adherence to the IHO S-44 standard.
3. To assess the digital elevation models (DEMs) derived from MBES and SBES data.
4. To develop a model for fitting and correlating the differences observed between the MBES and SBES datasets.
5. To analyze the volumetric discrepancies between the two surfaces generated from MBES and SBES data.

Given that the application of MBES in the coastal regions of Iran has only recently commenced, and that the majority of hydrographic activities in the country have historically relied on SBES (INCC, 2020), this research represents a significant advancement in optimizing both costs and time associated with hydrographic operations. Furthermore, the processing and evaluation of MBES performance, including its beam angles and their influence on depth accuracy, will provide valuable insights for other researchers and relevant organizations in the selection and application of this technology in hydrographic projects.

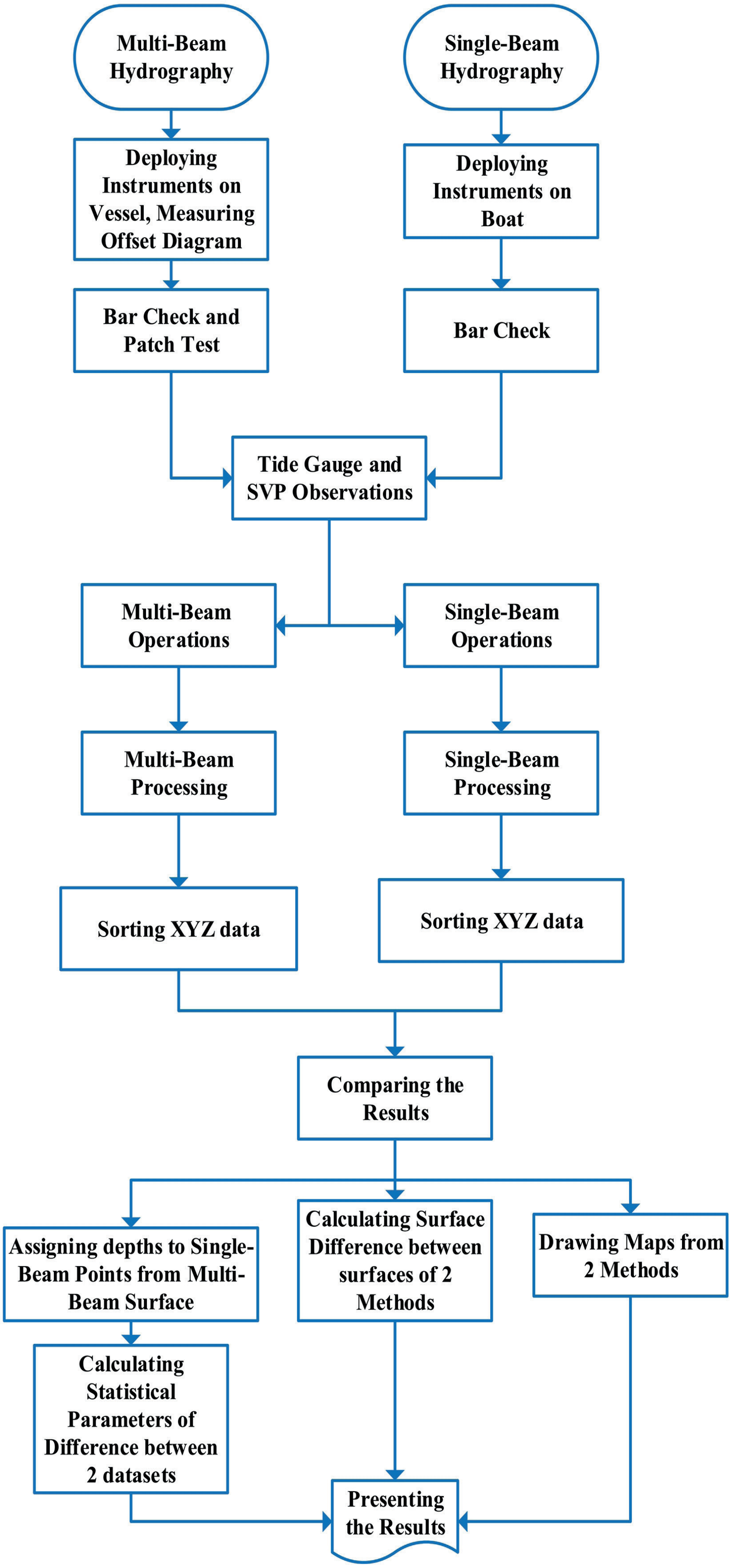

Fig. 2 Research flowchart.

2 Study area

The study area for this research is the Port of Bushehr, situated in the Persian Gulf in southern Iran. This region experiences an average temperature of 25 °C and is characterized by a hot and humid climate, with an annual average precipitation of 206 mm (Sotoudehpour et al., 2020). The Port of Bushehr features a channel and access passage that extends approximately 16 km, facilitating maritime navigation, with continuous and periodic dredging and depth measurements conducted in this channel. The geographical coordinates of the study area range from 28° 57' 30" to 29° 01' 30" north and from 50° 44' 30" to 50° 51' 30" east (Fig. 1).

3 Data

Given the size of the basin and access channel of Bushehr Port, this research focuses on the internal channel area, utilizing depth measurements acquired from both MBES and SBES in the waters surrounding Bushehr Port. This selection is motivated by the flat seabed region and the ongoing dredging activities in the outer section of the access channel. The processed data, which accounts for sound speed, tidal influences, and error corrections, were employed in the analysis. In this study, the reference elevation surface for depth measurements is established based on chart datum, which is closely aligned with the Lowest Astronomical Tide.

4 Methodology

The MBES depth data were processed utilizing average sorting methods in the Hypack Software (version 2017), which were modeled as mathematical procedures. Following this, the depths of SBES data points were linearly interpolated onto these surfaces to derive corresponding depth values. The next phase involved a statistical comparison of these estimates to evaluate the differences between elevation values modeled and those determined in Section 5.6. Subsequently, the selected model was applied to the SB depth data, assessing its compliance with the nominal accuracy as defined by the IHO S-44 standard. Ultimately, a comparison was made between the depth data acquired from both SBES and MBES at Bushehr Port, and maps of the region were generated and analyzed using both datasets. Furthermore, the volumetric difference between the two DEMs was calculated and compared. Fig. 2 presents a flowchart illustrating the research process.

4.1 Corrections and calibration of instruments

4.1.1 Tidal corrections

In both MBES and SBES depth sounding methods, it is essential to concurrently measure the water level in relation to chart datum during hydrographic operations. Figure 3 illustrates the Hypack format used for tide corrections. This simultaneous measurement allows for the determination of elevations at sounding locations on the seabed relative to chart datum using

https://doi.org/10.58440/ihr-31-1-n02

the recorded depths. To achieve this, an automatic tide gauge from the Ports and Maritime Organization, positioned at Bushehr Port, was utilized. The zero level of the tidal staff was calibrated to the benchmark BM-CYDS1014, which has a known elevation above chart datum. The elevation of this benchmark in relation to the chart datum is 4.141 m, establishing the zero level of the tidal staff at 0.75 m above the chart datum. The automatic tide gauge recorded tidal levels every 10 minutes, which were subsequently converted to elevations relative to chart datum during the post-processing phase.

4.1.2 Measuring sound speed in water

Both SBES and MBES operate based on the same physical principles for measuring water depth (Pratomo & Saputro, 2021). The echo sounder emits electrical signals, which are converted into sound waves through a transducer and transmitted into the water. When these sound waves encounter the seabed, they are reflected back to the device. By measuring the time taken for the waves to travel to the seabed and return, the depth *d* in meter, or the distance from the transducer to the seabed can be calculated using the following Eq. 1:

$$d = \frac{v \times t}{2} \tag{1}$$

In Eq. 1, the time t, measured in seconds, is recorded by the echo sounder, while v denotes the speed of sound in water, expressed in m/s. The sound speed varies based on three parameters: the electrical conductivity of seawater (salinity), temperature, and the hydrostatic pressure of the water column (depth). Consequently, it is essential to calibrate the echo sounder at least twice or more per day according to the sound velocity variations using a sound velocity profiler device.

This procedure entails entering the desired sound velocity into the depth sounder during hydrographic surveys. Following this, a sound velocity profile is obtained at different locations over several days (Fig. 4), and adjustments for variations in sound velocity relative to the entered value are applied to the depth measurements during the post-processing phase. Figure 4 illustrates the Hypack format used for sound speed corrections.

4.1.3 Patch test

In the MBES depth sounding method, it is crucial to accurately calculate the static settings of the transducer along the three rotational axes (roll, pitch, and yaw) and the latency between receiving position data from the satellite positioning receiver and the depth sounder to avoid bias errors in the true three-dimensional coordinates of each beam (Gueriot et al., 2000). To compute each of these rotations, data collection must be performed using a specific methodology, which will be detailed subsequently, followed by rotation calculations using the patch test

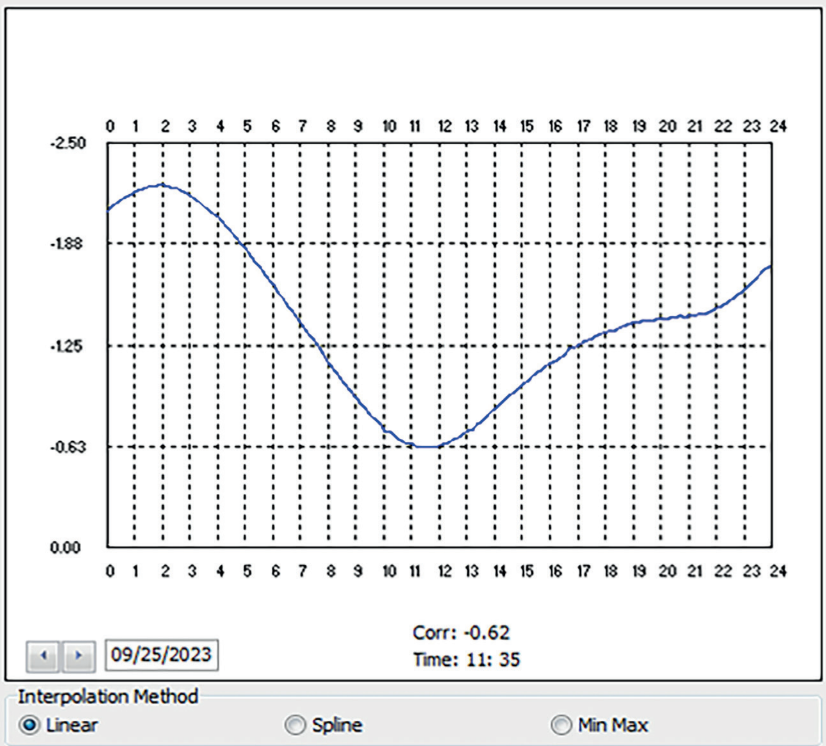

Fig. 3 Water level observations (horizontal in hour, vertical in meter).

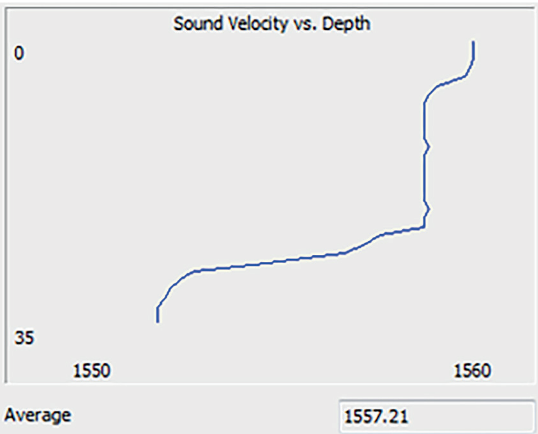

Fig. 4 Sound velocity profile observations in water (horizontal: sound speed, vertical: depth).

module of the hydrographic software.

Roll refers to the misalignment of the vessel's vertical axis in the left-right direction between the transducer and the motion sensor (Xiao, 2003).

Pitch indicates the vertical misalignment of the vessel in the forward-backward direction between the transducer and the motion sensor.

Yaw rotation denotes the horizontal misalignment of the vessel concerning the position of the transducer and the GNSS antenna relative to the vessel's direction of movement.

Latency refers to the misalignment error between the coordinates of the surveyed position and the depth recorded by the echo sounder, arising from a lack of synchronization between the corresponding data received from the transducer and the precise satellite positioning provided by the GNSS receiver.

4.2 SBES depth sounding

In single-beam (SB) depth sounding, the spacing between survey lines in the direction perpendicular to the coastline is established at 10 m, while control lines perpendicular to the main survey lines are set at intervals of 50 m. This method employs a small motorboat equipped with radio systems and differential positioning systems to determine Real-Time Kinematic (RTK) locations. The equipment includes a sound velocity probe, a precise hydrographic echo sounder, and data collection, logging, and processing software. The echo sounders utilized in this study were the Ceeducer Pro and Hydrotrac Odom, operating at a frequency of 200 kHz, with a beam angle of 8 deg and a resolution of 1 cm.

During echo-sounding operations in calm sea conditions, the transducer's index error was addressed in the echo sounders through a bar-check test, and adjustments for sound velocity and water level fluctuations were implemented as part of the post-processing phase. Additionally, the RTK positioning system, provided by the national Continuously Operating Reference Stations (CORS) geodetic service, was employed to enhance the accuracy of positioning data.

4.3 MBES depth sounding

For the collection of MBES data, hydrographic sounding lines were strategically designed along the channel axis to accommodate the approximate depth of the area, ensuring a 30–40 % overlap between adjacent strips. A pilot vessel, named Hamyar 3, from Bushehr Port, was utilized to carry out the MB hydrographic operations.

The hardware employed in this study included the WASSP S3i MBES, with a transducer operating at a frequency of 160 kHz and a beam angle of 120 degrees, as well as a motion sensor (Advanced Navigation), GNSS heading system (Hemisphere), precise satellite positioning system (RTK), SVP-Digi Bar Pro sound velocity meter, and CTD-CastAway environmental sensor.

Upon installation of all equipment on the vessel, their relative positions to one another and the vessel's axis were measured using a total station. The separation values of the sensors were then set into the MBES. To address errors stemming from the rotation and misalignment of the transducer axis, the satellite receiver antenna, and the motion sensor in relation to the survey vessel's center of gravity, a patch test was conducted, and the measured corrections were applied to the MBES through the corresponding software (Whittaker et al., 2011). Furthermore, two quality control tests were incorporated into the MB depth sounding processing using hydrographic software, Hypack: (1) a beam angle test and (2) a statistical comparison of check lines, which are elaborated in Sections 4.3.1 and 4.3.2, respectively.

4.3.1 Beam angle test

The beam angle test assesses the depth-sounding accuracy of the MBES across various angles of incidence (beams) by utilizing a reference surface. In this context, the reference surface consists of SB depth soundings that are perpendicular to one or more multi-beam (MB) hydrographic lines. This procedure enhances the quality and accuracy of the data collected while optimizing the overall volume of data. In the MB surveys, data points corresponding to beam angles less than 45 degrees were considered for analysis. Data from multibeam sonar systems is generally more accurate at angles below 45 degrees compared to wider angles due to factors such as beam spreading, signal-to-noise ratio (SNR), refraction, scattering, and beam angle resolution and ect. For these reasons, data collected at angles below 45 degrees is typically more reliable and accurate for bathymetric mapping and seafloor characterization.

Subsequently, the results from this test were applied to angles ranging from 5 to 45 degrees, using the data obtained from the SB soundings as the reference surface.

4.3.2 Statistical comparison of check lines

Statistical comparison enables the evaluation of MB data against SB depth soundings (check lines). Initially, several MB sounding lines are selected in a flat area with a gentle slope, located near a tide gauge. Perpendicular to these selected lines, SB sounding lines are designed, and hydrographic surveys are conducted separately using the respective systems. Additionally, patch testing and sound velocity profile measurements are performed to apply necessary corrections to the measured depths. This operation is executed using a motorboat and a diesel pilot vessel equipped with various instruments.

Following data collection, the information gathered by the depth-sounding devices is processed using hydrographic software, transforming it into XYZ files within the software environment. After implementing necessary corrections, such as removing outlier data and accounting for tidal influences, all information is entered as final coordinates into the QGIS (ver.3.40) Environment. The data is then converted into maps at the horizontal reference level (WGS84 - 1984 World Geodetic System) and projected in the UTM-39 system. To estimate the elevation corresponding to a point on a map, linear interpolation is calculated.

To evaluate accuracy, it is essential to have data that reflects actual values for which comparison criteria can be established to determine optimal accuracy. Thus, check points must be defined. The SB depth information obtained under comparable conditions in a similar area serves as a representation of the true depth. Assuming that the output of this device is completely reliable, and that the depth recorded for each location accurately reflects the true depth, these coordinates are treated as check points. Given that the ray in SBES depth measurement is directed

https://doi.org/10.58440/ihr-31-1-n02

nearly vertically to the seabed, in an ideal scenario, it would not be affected by refraction and would exhibit no refractive error. In shallow water conditions, where the sea is calm and nearly ideal, the assumption that the data obtained from SBES depth measurement is entirely reliable is accepted for the purposes of this research.

4.3.3 Quality assessment of data

To assess the quality of data acquired from the MBES mapping of the Bushehr harbor channel according to the criteria set forth by the International Hydrographic Organization (IHO) and publication S-44, tools available within hydrographic software were employed. The evaluation of accuracy utilizes the uncertainty criterion, a non-negative value that delineates the range of values within which the correct parameter estimates are likely to fall at a specified confidence level (IHO, 2022). Position uncertainties should be articulated at a confidence level of 95 %. The overall uncertainty (encompassing both random and systematic components) associated with depth measurement surveys is represented by the total propagation uncertainty (TPU), which consists of two parts: horizontal uncertainty (THU) and vertical uncertainty (TVU). The horizontal component serves as a two-dimensional metric capturing all uncertainties pertaining to measurements within the horizontal plane, whereas the vertical component constitutes a one-dimensional metric that accounts for all uncertainties associated with vertical measurements (IHO, 2022).

The errors contributing to an increase in THU can be categorized as follows (Hare et al., 2011):

a) Positioning system uncertainty
b) Range and beam angle uncertainties
c) The uncertainty associated with the ray path model (including the sound speed profile for sonars) and the beam pointing angle
d) The uncertainty in platform heading
e) System pointing uncertainties resulting from sensor misalignment
f) Sensor location
g) Platform motion sensor uncertainties, e.g. roll and pitch
h) Sensor position offset uncertainties
i) Time synchronisation / latency

Furthermore, the factors that lead to an increase in TVU can be enumerated as follows (Hare et al., 2011):

a) Vertical datum uncertainty
b) Vertical positioning system uncertainties
c) Water level measurement uncertainties, including co-tidal uncertainties where relevant
d) Instrument uncertainties
e) Sound speed uncertainties (for sonars)
f) Ellipsoidal / vertical datum separation model uncertainties
g) Platform motion uncertainties, i.e. roll, pitch and heave
h) Vessel draught, settlement and squat (for sonars)
i) Seabed slope (bathymetry systems)
j) Time synchronisation / latency

The mathematical modeling of each of these errors and their impact on overall error has been conducted by Hare (1995). The IHO classifies five orders of accuracy for hydrographic surveys in the 6.1.0 edition of the S-44 standard, providing maximum allowable values for THU and TVU for each order, along with the capability to detect features, as shown in Table 1. The maximum value of TVU is derived from Equation 2.

$$TVU_{\max}(d) = \sqrt{a^2 + (b \times d)^2} \tag{2}$$

where

a denotes a portion of height uncertainty that remains independent of depth,
b signifies a coefficient that reflects a portion of height uncertainty that varies with depth,
d represents the depth.

In coastal regions, the Special Order referenced in Table 1 is employed (IHO, 2022).

4.4 Root mean square error

The root mean square error (RMSE) is defined as the difference between the values predicted by a model and the actual observed values, serving to quantify the error between two datasets. Given that the RMSE represents an average of the existing errors, it serves as a crucial metric for evaluating the overall accuracy of the data. The RMSE for depth is computed using the following equation:

$$RMSE(z.\bar{z}) = \sqrt{\frac{\sum_{i=1}^{n}(z_i - \bar{z}_i)^2}{n}} \tag{3}$$

In Eq. 3, *z* denotes the actual depth value, $\bar{z}$ signifies the estimated depth value, and n indicates the total number of models. Ultimately, the achieved accuracy was compared against the IHO global standard for the nominal accuracy necessary in hydrographic work, ensuring adherence to the required order and the safe navigation of vessels. The differences between the two interpolation methods and the discrepancies between the two digital models derived from MB and SB depth measurements were subsequently evaluated.

5 Results and discussion

This section presents the outcomes of the quality control test for depth sounding, the digital models obtained from SB and MB depth soundings, and the differences between the two digital elevation models (DEMs) derived from these distinct depth sounding methods.

5.1 Quality control test and removal of data with lower confidence levels

The results pertaining to the accuracy test of MB depth sounding at various beam angles, using a reference level, are summarized in Table 2. This table

Table 1 Minimum bathymetry standards for safety of navigation hydrographic surveys.

Criteria	Area description	Depth THU	Depth TVU	Feature detection	Feature Search	Bathymetric coverage
Special order	Areas where under keel clearance is critical	2 m	a = 0.25 m b = 0.0075	Cubic features > 1 m	100 %	100 %

displays the statistical output for beam angles ranging from 0 to 45 degrees on both sides. Assuming the maximum measured depth (accounting for tidal influences) is 15 m, the statistical accuracy across all beam angles up to 45 degrees, at a confidence level of 95 %, varies between 0.17–0.27 m, which complies with the Special Order outlined in the IHO S-44 standard. Consequently, to enhance data quality and minimize the excessive volume of data, the information associated with outside beams, which exhibited lower confidence levels, was excluded. This approach effectively reduces outlier data and accelerates the process of map production and other spatial analyses. Fig. 5 illustrates the statistical test results of the MBES data at a 95 % confidence level in comparison to the SB data. Additionally, as a case in point, the normal probability distribution curves for the test angles of 5 and 45 degrees are depicted in Fig. 6.

Fig. 7 shows the location of quality control tests conducted within the port of Bushehr. Furthermore, Fig. 8 presents the results obtained from several statistical comparisons in hydrographic software across different areas of the project scope.

5.2 Horizontal and vertical uncertainties and object detection

Fig. 9 presents a graphical representation of the two-dimensional horizontal uncertainties, one-dimensional vertical uncertainties, and object detection uncertainties for the MB survey conducted in the Bushehr port channel. These figures illustrate the typical error performance of an MBES system in shallow water. The graphs demonstrate the MB performance using GNSS-RTK for positioning and attitude sensors at a target depth of 15 m. In order to enhance the accuracy of the side beams, depth data within a 90-degree range of the MBES system was employed. Ultimately, based on the initial parameters provided to the hydrographic software, the results from the MB depth measurement are anticipated to meet the criteria for special order accuracy.

5.3 Digital models obtained from two depth measurement methods

The map produced from the SB depth measurements is illustrated in Fig. 10. The data depicted in this figure indicates that the maximum and minimum depths recorded in Bushehr Port are 13.27 m and

Table 2 Statistical test for beam angles.

Beam angle (deg)	Max. outlier (m)	Mean diff. (m)	95 % confidence (m)
0	0.40	0.01	0.17
5	0.40	0.03	0.17
10	0.40	0.06	0.19
15	0.51	0.07	0.22
20	0.68	0.07	0.19
25	0.94	0.07	0.21
30	0.94	0.07	0.21
35	0.88	0.08	0.24
40	0.94	0.10	0.25
45	0.87	0.14	0.27

https://doi.org/10.58440/ihr-31-1-n02

6.05 m, respectively, with the channel's center generally exhibiting depths ranging from 10.5–13.3 m. The length and width of this channel are 6 km and 250 m, respectively. The southern part of the channel is enclosed by berthing areas an artificial island formed from dredged materials. As shown in the figure, the island is currently under development.

In contrast, Fig. 11 showcases the map derived from the MBES measurements. This figure reveals that the maximum and minimum depths recorded are 13 m and 6.11 m, respectively, while the center of the channel typically displays depths between 10.5–13 m.

5.4 Average depth measurement differences

To determine the differences in spot depth measurements within the designated area, a comparison was made between the data collected from SBES and MBES measurements using linear interpolation. This approach involved interpolating the depths measured by the SB method onto the denser surface generated from the MB method, allowing for the assessment of elevation differences at corresponding locations. The average difference observed in the Port of Bushehr is calculated to be 0.03 m.

5.5 Calculation of the difference between two digital surfaces

Following the calculation of point height differences between the two bathymetric methods, we will proceed to evaluate the three-dimensional surface discrepancies resulting from SBES and MBES in the Port of Bushehr. The three-dimensional surface (digital terrain model), was generated through interpolation of surrounding points using QGIS software.

As depicted in Fig. 12, the volume difference between the surfaces obtained from SBES and MBES is found to be 77,835 m³ over an area of 464,511 m², alongside a settled sediment volume of 98,321 m³ across 641,219 m². Specifically, in the 464,511 m² area, the MBES depths are deeper (lower) compared to those measured by SBES, while in the 641,219 m² area, MBES depths are shallower (higher). Consequently, the elevation coordinates derived from SBES are generally deeper than those from MBES, due to the larger volume and area of settled sediment.

In contrast, the study referenced in (Pratomo & Saputro, 2021) indicated that, overall, the elevation coordinates obtained from SBES are shallower than those from MBES. This discrepancy suggests that it is not possible to definitively conclude which method measures depth values more accurately; such outcomes can vary significantly from one region to another. By calculating the volume of the grid – representing the difference between sediment deposition and erosion—and dividing it by the total area, we derive a volume difference of 0.04 m³ per meter, which aligns with the findings of the aforementioned research (Pratomo & Saputro, 2021), indicating the insignificance of this difference.

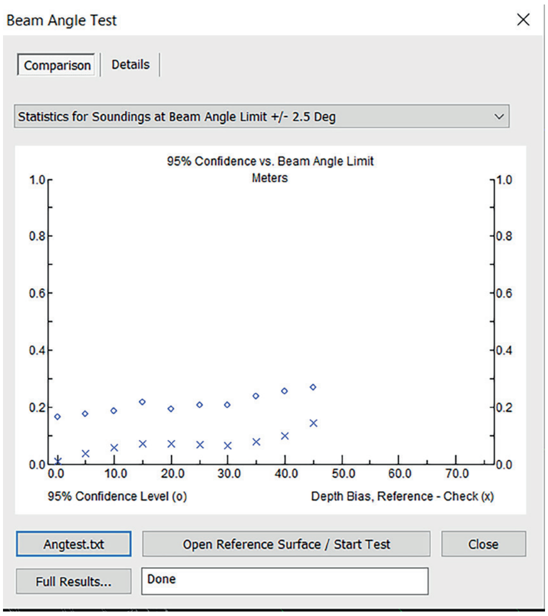

Fig. 5 Extracted values from the statistical test.

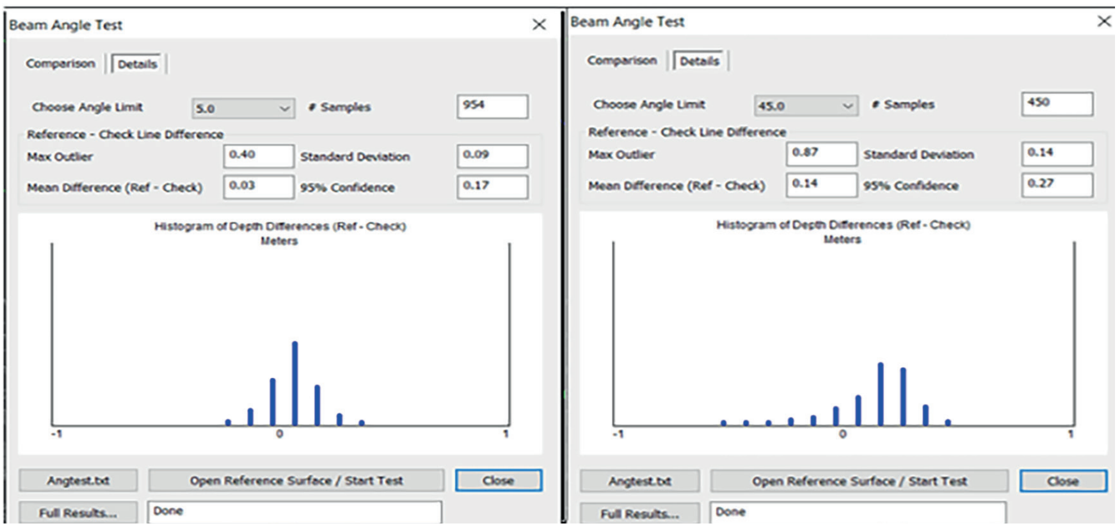

Fig. 6 Statistical values of the beam angle test of the MBES system presented as a histogram.

5.6 Statistical characteristics of the difference between two depth-sounding data

To analyze the statistical characteristics of the differences between the depth-sounding data obtained from the MBES and SBES systems, outlier data were eliminated, and the optimal normal distribution function for the remaining data was identified. In Fig. 13, the red curve illustrates the fitted distribution function, while the green curve represents the theoretical normal distribution. Therefore, it can be stated that

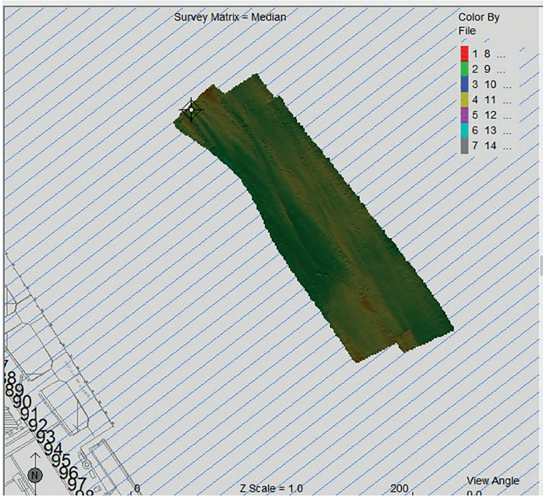

Fig. 7 SB hydrographic lines (perpendicular to jetty) versus MB swath.

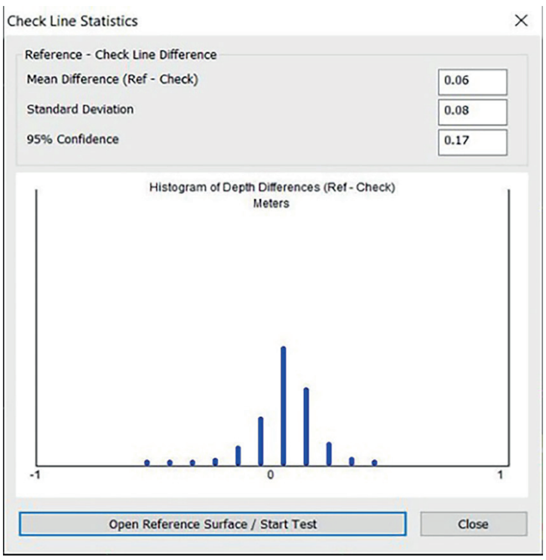

Fig. 8 Statistical test of cross lines (SB versus MB depth measurements).

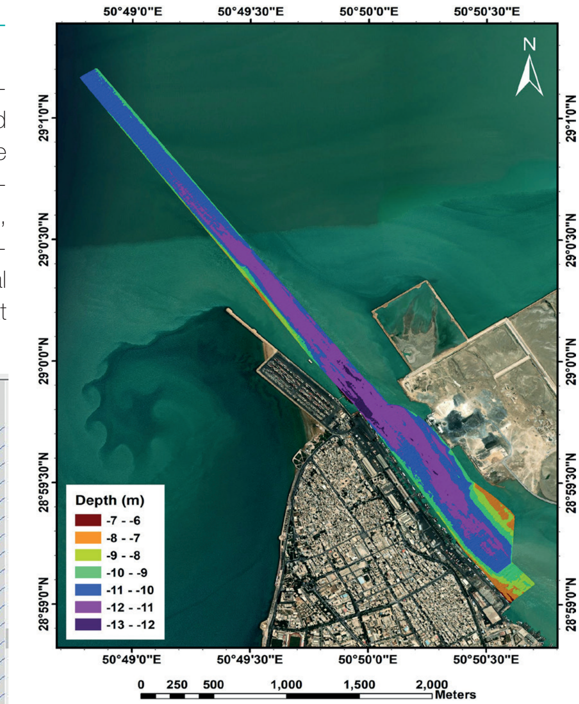

Fig. 10 Color-coded map of single-beam hydrography in Bushehr port.

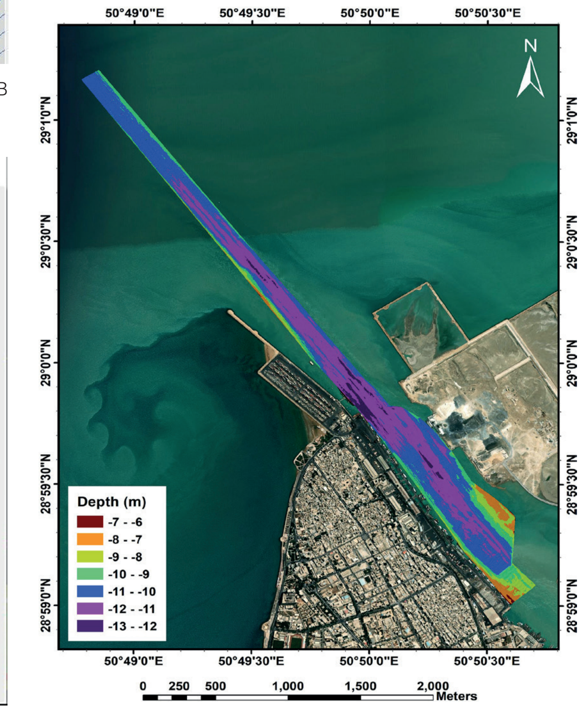

Fig. 11 Color-coded map of multi-beam hydrography in Bushehr port.

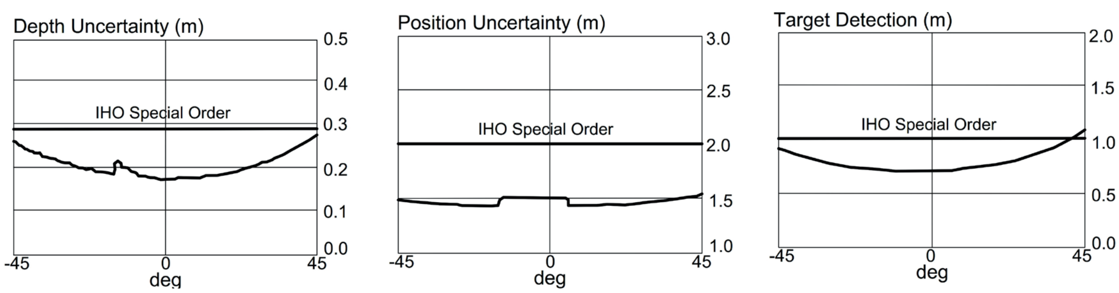

Fig. 9 Uncertainty charts in MB hydrography of Bushehr port.

https://doi.org/10.58440/ihr-31-1-n02

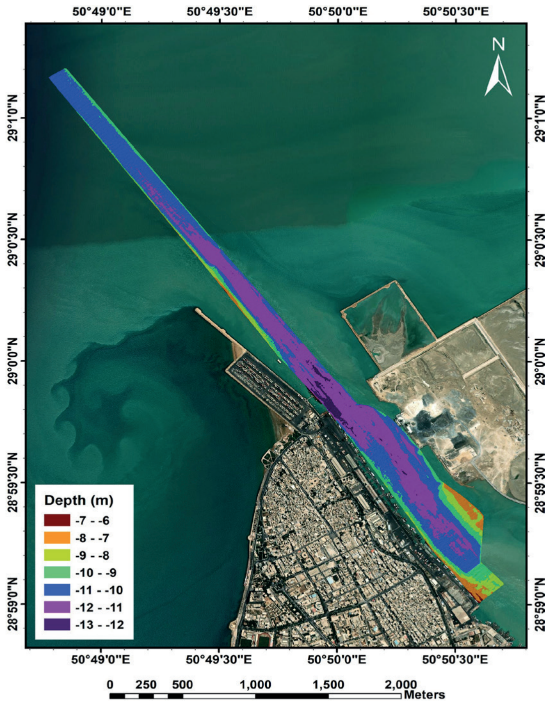

Fig. 12 Difference between the two surfaces obtained from SB and MB depth soundings.

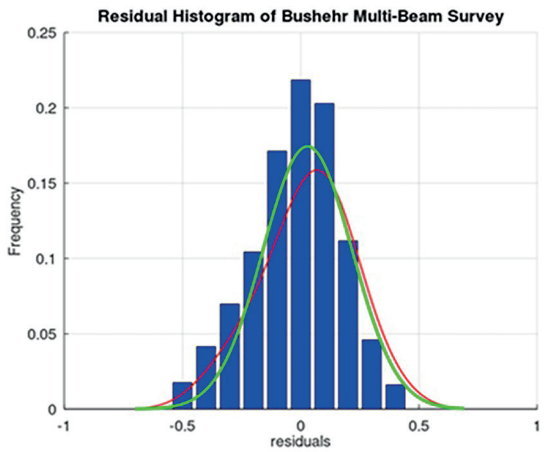

Fig. 13 Fitting normal distribution function to the difference between MB and SB data.

the residuals or the difference between two depth soundings closely approximates a normal distribution and lacks significant systematic errors. It is evident that normal distribution function, characterized by a mean of 3 cm and a standard deviation of 8 cm, provides the best approximation for the differences between the depths measured by MBES and SBES, achieving a 98 % confidence interval.

6 Conclusion and recommendations

Ensuring a safe navigation environment in ports and along coastlines is a critical aspect of maritime transportation in the country. In this study, we demonstrated that implementation of advanced depth sounding equipment, such as MBES, can significantly reduce the volume of field operations by up to 50 %, depending on seabed conditions and topography.

Furthermore, establishing a unified and continuous procedure for seabed mapping using data from MBES – rather than relying on interpolation methods and depth estimation between sounding lines in SB surveys – significantly enhances the accuracy of dredging calculations, sedimentation assessments, and coastal maintenance efforts. Nevertheless, this approach necessitates meticulous control and review of guidelines to mitigate errors and confidence intervals associated with surveys using wider beam angles in MBES.

In the studied area, it was observed that depths obtained from SB surveys are generally deeper than those from MB surveys. However, considering the continuous changes in the seabed, the discrepancies in the measured depths are minimal. Given the ongoing need for periodic sedimentation assessments in Iran's critical ports and channels, future research could concentrate on calculating sedimentation rates utilizing MBES to achieve extensive and continuous seabed coverage.

Acknowledgments

This article is based on the contract for conducting hydrographic surveys in the ports of Bushehr Province, signed between the Marine Affairs Department of the Ports and Maritime Organization and Darya Tarsim Consulting Engineers. The authors would like to express their gratitude to the Marine Affairs Department for their support in facilitating this research. In addition, they express their sincere gratitude to the esteemed anonymous reviewers whose valuable insights and comments have significantly contributed to improving the quality of this study.

References

Bandini, F., Olesen, D., Jakobsen, J., Kittel, C. M. M., Wang, S., Garcia, M. and Bauer-Gottwein, P. (2018). Technical note: Bathymetry observations of inland water bodies using a tethered single-beam sonar controlled by an unmanned aerial vehicle. *Hydrol. Earth Syst. Sci., 22*, 4165–4181.

Costa, B. M., Battista, T. A. and Pittman, S. J. (2009). Comparative evaluation of airborne LiDAR and ship-based multibeam SoNAR bathymetry and intensity for mapping coral reef ecosystems. *Remote Sensing of Environment, 113,* 1082–1100.

Ghahfarokhi, S. S. 2020. *Studying Methods for Improving the Quality of Multi-Beam Echo Sounder Data* (Master's thesis). University of Tehran, Iran.

Gueriot, D., Chedru, J., Daniel, S. and Maillard, E. (2000). The patch test: a comprehensive calibration tool for multibeam echosounders. *OCEANS 2000 MTS/IEEE Conference and Exhibition*. Conference Proceedings (Cat. No. 00CH37158), IEEE, 1655–1661.

Hare, R. (1995). Depth and Position Error Budgets for Mulitbeam Echosounding. *The International Hydrographic Review, 72*(2), https://journals.lib.unb.ca/index.php/ihr/article/view/23178 (last accessed 4 May 2025).

Hare, Rob, Eakins, B. W. and Amante, C. J. (2011). Modelling Bathymetric Uncertainty. *The International Hydrographic Review, 6*. https://journals.lib.unb.ca/index.php/ihr/article/view/20888 (last accessed 4 May 2025).

IHO (2022). *Standards for Hydrographic Surveys* (ed. 6.1). IHO Special Publication S-44, International Hydrographic Organization, Monaco. https://iho.int/uploads/user/pubs/standards/s-44/S-44_Edition_6.1.0.pdf (last accessed 4 May 2025).

INCC (2020). *Hydrographic Surveying Practices in Iran: Transition from SBES to MBES*. INCC Publications, Iranian National Cartographic Center, Tehran, Iran.

Motallebi Korbekandi, M. A. and Zare Zardeyni, A. 2022. Strategies for the Development of Maritime Economy in line with the Goals of a Resistive Economy. *Defense Economics, 6*, pp. 53–81.

Parnum, I., Siwabessy, J., Gavrilov, A. and Parsons, M. (2009). A comparison of single beam and multibeam sonar systems in seafloor habitat mapping. *Proc. 3rd Int. Conf. and Exhibition of Underwater Acoustic Measurements: Technologies and Results, Nafplion, Greece*, pp. 155–162.

Pike, S., Traganos, D., Poursanidis, D., Williams, J., Medcalf, K., Reinartz, P. and Chrysoulakis, N. 2019. Leveraging Commercial High-Resolution Multispectral Satellite and Multibeam Sonar Data to Estimate Bathymetry: The Case Study of the Caribbean Sea. *Remote Sensing, 11,* 1830.

Pratomo, D. and Saputro, I. (2021). Comparative analysis of singlebeam and multibeam echosounder bathymetric data. *IOP Conference Series: Materials Science and Engineering*. IOP Publishing, 012015.

Saeidi, V., Seydi, S. T., Kalantar, B., Ueda, N., Tajfirooz, B. and Shabani, F. 2023. Water depth estimation from Sentinel-2 imagery using advanced machine learning methods and explainable artificial intelligence. *Geomatics, Natural Hazards and Risk, 14,* 2225691.

Sotoudehpour, A., Madadi, A. and Asghari Saraskanrood, S. (2020). Geomorphological Monitoring of Bushehr Port Coastline. *Geographical Researches, 35*, pp. 177–187.

Tajfirouz, B., Saeidi, V., Khalili, H. and Nemati, M. H. (2022). Volume and Rate Estimations of Sedimentation in Amirabad Port During Period 2018-2021. *Journal of Geomatics Science and Technology, 11*, pp. 115–123.

Whittaker, C., Sebastian, S. and Fabre, D. (2011). Multibeam sonar performance analysis value and use of statistical techniques. *The International Hydrographic Review, 5*. https://journals.lib.unb.ca/index.php/ihr/article/view/20878 (last accessed 4 May 2025).

Xiao, S. (2003). *Effects of Vessel Motion on Echo Sounding in Fisheries*. University of Victoria.

Zhi, H., Siwabessy, J., Nichol, S. L. and Brooke, B. P. (2014). Predictive mapping of seabed substrata using high-resolution multibeam sonar data: A case study from a shelf with complex geomorphology. *Marine Geology, 357*, pp. 37–52.

https://doi.org/10.58440/ihr-31-1-n02

NOTE / TECHNICAL REPORT

Ocean bathymetry: Decadal advances, persistent challenges, and future horizons

Authors

Murtaza Taak[1], Muhammad Yasrab[2] and Anas Jamshed[1]

Abstract

The article provides an overview of ocean bathymetry advancements since 2015, which demonstrates how multibeam sonar and satellite-derived bathymetry, along with LiDAR and unmanned systems, improved both ranges and mapping precision. Mapping technology faces multiple obstacles, including data paucity and political barriers, while access to technology remains unequal across nations, so integrated efforts through projects such as Seabed 2030 receive strong emphasis. The article suggests future approaches using artificial intelligence, citizen hydrospatial sciences participation and blockchain technology, which aim to improve access to ocean mapping data while setting maritime safety benchmarks, increase the knowledge, understanding of the hydrospatial domain and sustainable development goals.

Keywords

capacity building · satellite-derived bathymetry · seabed mapping

1 Introduction

Documenting the seabed of specific areas or the ocean, in general, is the foundation of the oceanography fields and the hydrospatial domain (Hains et al., 2022). This scientific field pertains to the introductory study of ocean features, including currents, tides, and waves. It is crucial in applications ranging from the safety of navigation, management of sea resources, monitoring the effects of the sea on marine structures and ecosystems, and assessment of climate change. For the last ten years, new technologies have risen that have brought bathymetric science to another level where surveying the ocean floor becomes precise and detailed.

As said earlier, quality bathymetry data is crucial. From enabling the international maritime business to promoting sustainable fisheries, these data underpin significant determinations in global and local settings. Furthermore, bathymetry is critical to finding viable solutions to even the most burning issues related to climate change because it supplies the primary baseline information required for resolving issues associated with sea-level rise, shoreline shifts, and the effects of storms.

Over the past ten years, significant advances have been achieved concerning new advanced technologies, which include multibeam sonars, satellite-derived bathymetry, and laser imaging detection and ranging (LiDAR). Compartmentalized systems such as autonomous underwater vehicles (AUVs) and unmanned surface vehicles (USVs) have expanded the capabilities of bathymetric and hydrospatial surveys to complex and sometimes dangerous areas. In addition, international projects like the Nippon Foundation-GEBCO (General Bathymetric Chart of the Oceans), Seabed 2030 Project have advanced calls to focus on the worldwide goal of mapping all the world's oceans.

Notwithstanding these developments, some issues have cropped up in organizations. The expensive venture in sea drilling, lack of information on a significant portion of the ocean, and accessibility and technology constraints in developed countries demonstrate that the field is sustainable for further development. This paper reviews the developments associated with ocean bathymetry from 2015 to 2025, discusses the contemporary issues that continue to

✉ Murtaza Taak · petariantaak@gmail.com

1 National School of Hydrography, Pakistan

2 National Hydrographic Office, Pakistan

https://doi.org/10.58440/ihr-31-1-n03

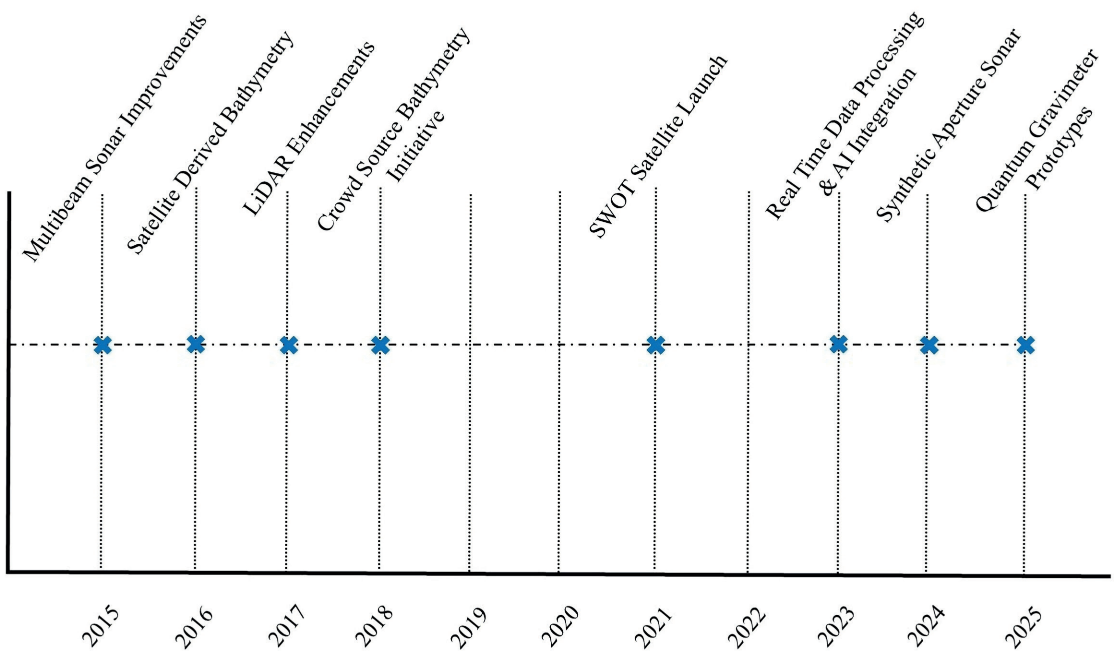

Fig. 1 Technological advancements timeline.

be experienced, and looks ahead to the future of bathymetry based on advances in technology and collaboration for fair sharing of valuable information.

2 Technological advances in ocean bathymetry

2.1 Multibeam sonar systems

Multibeam sonar technology has evolved with advancements that enable high-resolution deep and shallow water mapping. Improvements, especially in signal processing and Data fusion techniques, have made these systems more accurate and efficient (National Research Council, 2015; IHO, 2021b). Current multibeam systems have a wider band and real-time viewing instruments, making it easier to generate accurate terrain during surveys.

2.2 Satellite-derived bathymetry

Satellite-derived bathymetry (SDB) is highly cost-effective technique for mapping coastal and shallow inland waters where water clarity allows. Methods based on points like Real Time (RT) and Direct LiDAR Waveform (DLW) LiDAR have enhanced SDB precision (Ouellette et al., 2023; Zhang et al., 2024). The International Hydrographic Organization (IHO) has been enthusiastic about SDB applications, launching practices like the Ocean Decade Bathymetry Data Sharing Guideline (UNESCO-IOC, 2024). Additional improvements in imagery resolution, especially in cloud penetrations, and more frequent satellite revisit rates have strengthened SDB.

2.3 Autonomous vehicles and remote sensing

Using the autonomous underwater and unmanned surface vehicles have opened up the bathymetric surveys in remote and dangerous areas. Modern AUVs belong to vessels capable of high-resolution seafloor mapping in compliance with standards set by the IHO (Kyoko, 2024; Reithmeier, 2024). New accomplishments include swarm robotics, where several AUVs work jointly, another improvement in navigation, which increases data accuracy when operating in a deep-sea area.

2.4 LiDAR technologies

New airborne and topo-bathymetric LiDAR systems developments improved new shallow nearshore and shallow water mapping where water clarity allows. These cost-effective technologies offer hi-resolution data and are especially useful in locations where sonometer techniques pose challenges (Corcoran & Parrish, 2023; Ekelund, 2023). Newer technologies are green-wavelength, which sees deeper through water columns, and multispectral LiDAR, which acquires other ecological and geological data.

2.5 Crowdsourced bathymetry

Crowdsourced bathymetry (CSB) has, therefore, risen to popularity as one of the economical ways of enhancing global data acquisition. Commercial and recreational vessels can contribute to the bathymetric data under the IHO's CSB initiative (IHO, 2024b; Goddard, 2025). Much progress has been made in integrating mobile apps and onboard data logging systems so that nontechnical people can easily acquire and share good bathymetry data. The question of data quality and data liability remains an issue. However, CSB could be adapted as a tool for reconnaissance, hazard detection and temporary navigational warnings (Hains et al., 2024).

2.6 SWOT satellite missions

Radar interferometry from Satellite Surface Water and Ocean Topography (SWOT) has introduced

Table 1 Mapping technologies.

Technique	Resolution	Application	Limitations	Cost implications	Scalability
Multibeam sonar	High (meters)	Deep-sea mapping	High cost, requires vessel deployment	Expensive and slow due to vessel and operational costs	Scalable for localized high-resolution mapping but costly for global coverage
SDB	Moderate (meters)	Coastal and shallow areas	Limited in deep water, accuracy varies; water clarity dependent	Low by avoiding or minimizing field work to moderate; dependent on satellite access and processing	Highly scalable for large areas, especially in shallow and remote regions
LiDAR	High (centimeters)	Nearshore and coastal mapping	Limited depth penetration; water clarity dependent	Expensive but much faster coverage and weather dependent due to airborne platform and technology costs	Scalable for specific nearshore projects but limited to shallow and clear waters
CSB	Variable	Global data contribution	Data quality, consistency and liability issues	Low and opportunistic, as it leverages existing vessels and voluntary and free contributions	Highly scalable with proper integration and quality controls
SWOT	Moderate (meters)	Large-scale oceanographic features	Limited resolution in coastal areas; water clarity dependent	High initial investment for satellite missions but cost-efficient long-term	Globally scalable, especially for open ocean areas
SAS	Very high (centimeters)	Deep and turbid waters	High equipment cost	Very expensive due to advanced equipment and processing	Scalable for deep and targeted applications but not for widespread use

new techniques in seafloor mapping where water clarity allows. The operation of these missions gives the global coverage and advances the knowledge of major oceanographic characteristics (Fu et al., 2024). Subsequent versions of SWOT are likely to enhance radar altimeters having better resolution and accuracy.

2.7 Synthetic aperture sonar

This work introduces a new technology known as synthetic aperture sonar (SAS), which is seen as a capability-enhancing tool for high-definition seafloor mapping where water clarity allows. SAS systems involve sophisticated signal analysis to capture clear pictures of the seabed, particularly in deep, dark waters. They are most helpful in recognizing objects and topographical formations and are essential for geological and industry use (Kyoko, 2024).

2.8 Real-time data processing and machine learning

With the help of machine learning algorithms, the integration of real-time data processing has challenged the way bathymetric data are analyzed. These technologies allow for automated detection of features, erroneous data correction, and automated modelling, saving time in post-survey data processing (Wu et al., 2021; GEBCO, 2025a).

2.9 Fiber optic sensing for seafloor mapping

In recent years, new developments in fiber optic sensing have demonstrated capability in seafloor mapping. One such system uses distributed acoustic sensing (DAS) to detect seismic and acoustic signals over large distances, which can carry out large-scale bathymetry surveys at a cost (Cheng et al., 2021).

2.10 Deep learning for feature extraction

New learning algorithms have further enriched the possibility of feature extraction from bathymetry data sets. Sparker and boomer can locate underwater structures, sediment types and ecological habitats more efficiently than conventional techniques (Corcoran & Parrish, 2023).

2.11 Hybrid systems

Multimodal solutions integrating sonar, LiDAR, and optical imaging in a single framework are frequently used for successful and efficient surveys in various underwater terrains. These systems take advantage of two or more technologies to give a better insight into the conditions on the ocean floor (Kyoko, 2024). Details of technologies utilized for mapping is mentioned in Table 1.

3 Global initiatives and collaborative efforts

3.1 The Nippon Foundation-GEBCO, Seabed 2030 project

The Global Exploration of the Continuous and Ongoing Processes of the Earth, also known as Seabed 2030, is an initiative led by GEBCO and supported by the Nippon Foundation. This goal is being completed through the cooperation efforts of governments,

 https://doi.org/10.58440/ihr-31-1-n03

commercial organizations, research institutes, technologies and CSB (Jakobsson et al., 2024; GEBCO, 2025a).

3.2 The International Hydrographic Review contributions

In addition, The International Hydrographic Review (IHR) has been instrumental in reporting developments and research findings in bathymetry. IHR articles have pointed to different means to increase knowledge and understanding of the roles of machine learning in data analysis and the applicability of SDB methods at large (Ferreira et al., 2022; Ouellette et al., 2023).

3.3 GEBCO training program

The Training Program of General Bathymetric Chart of the Oceans (GEBCO) aims to strengthen the bathymetry study by building up the qualified human resources of various countries and areas. This effort has resulted in a colossal improvement in seafloor mapping and data integration around the globe (GEBCO, 2025b).

3.4 IHO capacity building initiative

The main objective of the IHO Capacity Building Initiative is to enhance the technical and institutional capacity of under-resourced nations. This program improves developing nations' capacity to engage in bathymetric efforts (IHO, 2023) through capacity building, knowledge transfer and funding support.

3.5 The United Nations Ocean Decade bathymetry data sharing guidelines

As per the Ocean Decade initiative, the IHO has formulated some principles to help different countries share data fairly. Recognizing bathymetry as a global public good, these guidelines are intended to reduce restrictions to this fundamental geospatial dataset and promote global cooperation and openness (UNESCO-IOC, 2024).

3.6 Arctic bathymetric mapping collaboration

Cooperative work in the Arctic, like the International Bathymetric Chart of the Arctic Ocean (IBCAO), has made it possible to map areas that were not mapped before. Such projects are essential for assessing the effects of climate change in Polar Regions (Jakobsson et al., 2024).

3.7 Regional partnerships for SDB and CSB

Organizations in the Caribbean and Pacific have collaborated to advance the use of satellite-derived bathymetry and crowdsourced bathymetry approaches to enhance coastal protection. Such efforts point out the applicability of regional organizations to ending localized bathymetric deficits (Dery, 2024; Thomas et al., 2021). Key initiatives are mentioned in Table 2.

4 Supporting under-resourced nations

4.1 Challenges faced by under-resourced nations

Currently, there are several problems with using the most sophisticated bathymetric resources for many countries, especially for the states of the South and Small Island Developing States. These challenges include high costs, limited technical skills, and limited access to data-sharing networks (Hariram, 2024; GEBCO, 2025b). Most developing countries find it very challenging to fund and conduct large-scale bathymetric surveys. Landlocked countries face difficulties acquiring raw ocean information through various means influencing their interests. Because of technical limitations and insufficient funding, many coastal nations have failed to create coastal mapping

Table 2 Key initiatives.

Initiative	Focus	Impact	Metrics of success
Seabed 2030 project	Global seafloor mapping	Increased international collaboration	Over 26.1 % of the global ocean floor mapped as of June 2024; goal: 100 % by 2030
IHO crowdsourced bathymetry	Data collection via vessels	Expanded dataset, cost-effective mapping	Over 1,500 vessels contributing data; increased bathymetric coverage in shallow and coastal areas
Ocean decade bathymetry guidelines	Data sharing and standardization	Improved global data accessibility	Development of open-access data-sharing frameworks adopted by 50+ nations
SWOT satellite missions	Satellite-based mapping	Enhanced understanding of oceanography	Successful mapping of large-scale oceanographic features with 95 % global surface water coverage achieved
GEBCO training program	Training global bathymetric experts	Strengthened expertise worldwide	Over 120 trainees from 45+ countries completing the program since inception
IHO capacity building initiative	Capacity building in under-resourced nations	Broader participation in bathymetric projects	Delivered 100+ technical workshops and funded 50+ new hydrographic offices in developing nations

initiatives properly. Therefore, some important areas are still not protected against climatic factors, and maritime areas are not secure.

4.2 Capacity-Building Initiatives

For many underdeveloped countries, capacity-building programs are indispensable. The IHO and GEBCO have used training workshops and scholarships to promote human capital by developing local professionals with expertise in hydrography and bathymetry (IHO, 2023; Midford & Østhagen, 2024). Some of the training, including the Nippon Foundation-GEBCO Training Project, has been useful in preparing the participants for the mapping tasks worldwide. For instance, Ghana has benefited from such endeavours; currently, the trained personnel are accruing the upgrade of the bathymetric survey along the coast of Ghana.

4.3 Collaborative data sharing

Understanding and addressing these lapses could be achievable by pulling the plugs in our technological releases that neglect the modern means of making data open access to everyone. The IHO Crowdsourced Bathymetry Initiative and Ocean Decade Guidelines are transparent about using bathymetric data openly for the benefit of all countries (IHO, 2024b; UNESCO-IOC, 2024). An example of the above model is EMODnet (European Marine Observation and Data Network), which works to improve data sharing (IHO, 2024a).

4.4 Financial support mechanisms

Access to international funding sources and cooperation may contribute to the funds required to conduct bathymetric surveys in the least-developed countries. For instance, the World Bank's Blue Economy program has helped finance coast mapping and resilience investment in Mozambique and Bangladesh. They have also facilitated the movement of technology and skills between developed and developing countries (National Research Council, 2015; Jakobsson et al., 2024). Ghana has also partnered with organizations such as the African Union and UNECA (United Nations Economic Commission for Africa) to take the initial form of the development of more contemporary hydrographic offices.

4.5 Leveraging low-cost technologies

Crowdsourced bathymetry and satellite-derived bathymetry are also possible low-cost solutions for Low- and Middle-Income Countries (LMICs). These approaches minimize the use of costly multibeam sonar systems and large survey vessels (Corcoran & Parrish, 2023; Ekelund, 2023). Ghana has recently adopted satellite-based techniques for mapping important coastal areas susceptible to flood and erosion.

4.6 Case Studies

- Fiji's Bathymetric Mapping Initiative: Fiji used international collaborations and crowdsourced bathymetry to enhance its coastal mapping capabilities (IHO, 2024b; Goddard, 2025).
- The Caribbean Region: Support Regional partnerships facilitated scaling of SDB projects utilizing deep learning and cloud technologies improving coastal resilience (IHO, 2024a).
- The African Region: Evaluation of EU international goals reveals that hydrographic capacity development for Africa can provide important backing for port infrastructure expansion and blue economic growth, sustainable fisheries promotion, and stronger maritime security (IHO, 2024a).
- Ghana's Coastal Resilience Program: To mitigate vulnerabilities to climate change and maritime security, Ghana has undertaken projects to improve coastal mapping infrastructure using international aid and satellite-derived bathymetry (Dery, 2024).

5 Persistent challenges

5.1 Data gaps in deep ocean mapping

Even with all technological advances, large swaths of the deep ocean remain unmapped. Due to the high cost and logistical complexity of deep-sea expeditions, progress is hindered (IHO, 2023; Hariram, 2024). Furthermore, the Southern Ocean and areas around the Pacific Ring of Fire pose significant problems because of extreme depths, remoteness and harsh environmental conditions. Unfortunately, these gaps are compounded by the lack of global funding for deep-sea exploration, which leaves many critical ecosystems and geological features unknown (National Research Council, 2015).

5.2 Integration and standardization

Standardization and quality control have been challenging in integrating different datasets from multibeam sonar, SDB, and AUVs. Global data sharing is complicated without uniform data formats (Hankin et al., 2010; IHO, 2023). For example, large-scale mapping projects using these data may be prone to errors due to inconsistent data sets generated by different nations or institutions. To address these discrepancies, we need to develop international standards and automated means to harmonize data.

5.3 Environmental and geopolitical barriers

Some surveys are only feasible within a narrow environmental range, for example, adverse weather, strong currents or rough seas. Meanwhile, access to exclusive economic zones (EEZs) is also restricted by geopolitical conditions, preventing complete mapping. Territorial boundary disputes and restrictions on data collection in sensitive areas continue to hold up progress (National Research Council, 2015; Midford & Østhagen, 2024). The list of current geopolitical barriers and its impact on mapping is mentioned in Table 3.

https://doi.org/10.58440/ihr-31-1-n03

Table 3 Geopolitical barrier.

Region / area	Geopolitical barrier	Impact on mapping initiatives
South China Sea	Territorial disputes among multiple nations	Restricted access to disputed waters; increased tensions and interruptions in mapping efforts
Arctic Ocean	Overlapping territorial claims by Arctic nations	Delays in collaborative mapping; fragmented data collection due to independent efforts
EEZs	Strict regulations on foreign access to EEZs	Gaps in mapping in under-resourced areas; limits on international collaboration
Gulf of Guinea	Piracy and maritime insecurity	Increased costs for security; limited mapping of high-risk regions
Horn of Africa	Piracy and security risks	Disruptions to mapping efforts and restricted access to maritime zones
Indian Ocean	Data sharing restrictions	Limited integration of bathymetric data; challenges for collaborative projects
Eastern Mediterranean	Territorial disputes	Delays in mapping earthquake-prone zones; risks to survey vessels
Red Sea	Conflict and security issues	Limited mapping in conflict zones; challenges for international collaboration
Persian Gulf	International sanctions	Limited access to modern mapping technologies; delays in regional bathymetric progress
Pacific Ring of Fire	Remoteness and geopolitical complexities	Limited access to critical oceanic features; increased costs for deep-sea surveys

5.4 Limited access to advanced technologies

High costs, special training requirements, or unavailability limit the use of advanced bathymetric technologies in many under-resourced nations. However, this limitation maintains the divide in the global bathymetric data, with significant discrepancies in sub-Saharan Africa and parts of Southeast Asia (Hariram, 2024). In addition, these countries face further hurdles due to a lack of infrastructure for processing and keeping large datasets.

5.5 Data privacy and security concerns

While crowdsourced and shared bathymetric data have been increasingly approaching utility for more and more applications worldwide, we are seeing growing concerns with data privacy and security. For example, sensitive coastal and underwater infrastructure data could be vulnerable to misuse or cyber-attacks in geopolitically sensitive regions. To handle them, it is important to develop robust sharing systems of data and security structures (Trice et al., 2021).

5.6 Resource and capacity constraints in bathymetric science

Large-scale bathymetric surveys are associated with high costs, often resulting in uneven resource allocation in which wealthier nations can afford to map areas of present interest. As a result, much of the world, especially in the Global South, remains insufficiently mapped and studied. Equitable progress in bathymetric science (Jakobsson et al., 2024) requires collaborative funding mechanisms and international partnerships.

6 Future horizons

6.1 Artificial intelligence, machine learning and deep learning

AI, machine learning and deep learning will revolutionize automated feature detection and error reduction of bathymetric data. Such technologies will improve data accuracy and shorten processing time (Ferreira et al., 2022; Long et al., 2023). For example, machine learning algorithms are taught to recognize certain seafloor features like underwater ridges and fault lines from large datasets. Additionally, AI-powered automation will facilitate cross-referencing diverse data sets, such as sonar, satellite and LiDAR data, for seamless integration.

6.2 Advances in satellite technology

With improvements in the resolution and spectral capabilities of new satellites to be launched, SDB will be expanded. Given missions of SWOT satellites, such as those of Fu et al. (2024) and Araujo & Hedley (2023), seafloor mapping applications are promising. Satellite technologies on the horizon will enhance polar coverage and other areas with sparse coverage due to high cloud cover, expanding the existing coverage of optical and

Table 4 Steps for integrating blockchain technology.

Step	Description	Actions / examples
Pilot projects for proof of concept	Introduce blockchain technology for secure storage and sharing of bathymetric data in specific initiatives.	Implement blockchain in regional collaborations like the Caribbean or Pacific mapping projects.
Develop interoperability standards	Create protocols for blockchain integration with existing bathymetric platforms.	Collaborate with EMODnet, NOAA, and IHO to establish technical interoperability standards.
Stakeholder training and engagement	Educate hydrographers, researchers, and policymakers about blockchain benefits.	Conduct training workshops with support from IHO and GEBCO initiatives.
Establish data governance policies	Define protocols for data access, permissions, and ethical usage.	Work with international organizations like Seabed 2030 to develop global governance frameworks.
Promote accessibility for under-resourced nations	Ensure blockchain solutions are cost-effective and user-friendly.	Develop open-source blockchain platforms tailored for ease of use by nations with limited technical capacity.
Public-private partnerships	Foster collaborations between governments, research institutions, and private firms.	Encourage companies specializing in blockchain to partner with hydrographic organizations for funding and deployment.
Scale through regional collaborations	Use blockchain platforms for regional data-sharing projects to demonstrate scalability.	Apply blockchain for managing shared datasets across African coastal nations or Southeast Asia.
Long-Term integration	Incorporate blockchain platforms into global bathymetric initiatives for sustained usage.	Embed blockchain as a backbone for data-sharing within initiatives like Seabed 2030 and the GEBCO Training Program

radar-based systems. Hyperspectral imaging and nanosatellite constellations are innovations that will improve data resolution and accessibility for smaller nations and research institutions.

6.3 Expanded use of AUVs and USVs

Multibeam sonar, LiDAR, and optical imaging are hybrid sensors that will find their way onto future AUVs and USVs. These systems will enable comprehensive mapping in complex underwater environments (Constantinoiu et al., 2023; Kyoko, 2024). Their operation in remote areas for extended periods will require advances in autonomous navigation and energy efficiency and will reduce the need for crewed missions. Modular designs will also allow for rapid customization of AUVs and USVs to meet the needs of particular research objectives from deep sea geology to biodiversity assessment in the hydrospatial domain.

6.4 Open data and collaborative platforms

Multinational web-based tools and data releases will stimulate international projects to undertake bathymetric studies. e.g. the IHO collaborates with the GEBCO Strategy 2023–2030 (IHO, 2021a). This white paper also details how data sharing will transition to future platforms based on cloud computing and blockchain technology to enable open and direct data sharing between buyers, suppliers and third parties. This will support data-sharing platforms that facilitate global collaboration and data integrity of ocean bathymetry safely and transparently. The process, explanation and procedure of blockchain technology adoption, are given in Table 4. EMODnet and NOAA's Digital Coast improve engagement by developing interfaces with more up-to-date data feeds to the broader public.

6.5 Emerging sensor technologies

Bathymetric and hydrospatial data collection is poised to be revolutionized by recent innovations in sensor technology, quantum gravimeters and distributed acoustic sensing. For example, quantum gravimeters can detect the minutest differences in gravitational fields and tell us much about seafloor structure (Ekelund, 2023). Quantum gravimeters are revolutionary tools which offer the possibility of making ultra-sensitive measurements of gravitational fields to yield high-resolution seafloor mapping. However, these sensors, developed from these capabilities and advancing fiber optic technologies, will be taken to previously closed-off regions beneath ice shelves and sediments. The pathway to adoption of quantum sensors is mentioned in Table 5.

6.6 Integration of citizen hydrospatial science

The role of the broader citizen science in expanding data coverage will be key to the expanded data collection effort. On the one hand, existing datasets will be significantly augmented through programs encouraging recreational boaters, fishers, and coastal communities to contribute geospatial data (IHO, 2024b; Goddard, 2025;) in the hydrospatial domain. In order to have widespread participation and data validation, emerging tools like mobile applications with user-friendly interfaces will be utilized.

7 Conclusion

Over the past decade, ocean bathymetry has received transformative advances in technology, global

Table 5 Pathway to quantum sensors adoption.

Pathways to adoption	Key steps and actions
Research and development (R&D): Invest in research to improve the robustness, portability, and scalability of quantum sensors.	Increase funding for quantum sensing R&D through national and international research bodies (e.g., EU Horizon, NOAA grants).
Prototype testing in controlled environments: Test initial designs in shallow and known bathymetric environments.	Deploy prototypes in coastal areas for proof-of-concept studies.
Integration with Existing Systems: Develop compatibility with AUVs, USVs, and shipborne platforms.	Equip autonomous and manned survey vehicles with quantum sensors for hybrid mapping projects.
Cost reduction for commercial adoption: Transition from academic prototypes to commercially viable models through private-sector partnerships.	Establish public-private partnerships to scale production and reduce costs.
International collaboration and knowledge sharing: Share findings and successes through global hydrographic forums.	Organize workshops with stakeholders like IHO, GEBCO, and Seabed 2030.

collaboration, and science. With advanced seafloor mapping technologies such as Multibeam sonar, LiDAR, and Satellite-Derived Bathymetry, the scale and precision of mapping have greatly increased, propelling us to map all of the world's oceans. Concurrently, autonomous vehicles and advanced sensor systems have extended human reach into deep marine environments, from the most remote and hostile to the deepest parts of the ocean, providing unique glimpses into deep-sea ecosystems and geological processes.

However, there is much left to be worked on. Ocean regions far from landmasses have data gaps that need more global funding and logistical support. Geopolitical disputes, environmental constraints, and gaps in technological access are among additional barriers that further hinder the completion of a fully mapped seafloor. Overcoming these blockages will depend heavily on active international collaboration, fair resource distribution, and comprehensive capacity-building programs aimed at under-resourced nations.

The field promises to be transformed by nimble technologies such as artificial intelligence, quantum sensors and blockchain-enabled data-sharing platforms. The improvements in oceanographic and hydrospatial data accuracy, uncertainty and accessibility will spur progress in linked multidisciplinary areas such as climate science, maritime safety, marine and hydrospatial resource management. The Seabed 2030 Project and GEBCO's training programs represent best practices in bringing together collective action to achieve scientific goals inclusively and equitably.

When completion of the Gulf (referred to as a metaphor for seabed mapping) is realized, the future of ocean bathymetry, unveiling the mysteries of the seafloor, relies on the future marriage of technology and collaboration to enable the benefits of such knowledge to be universally enjoyed. Bathymetric and hydrospatial sciences is yet another knowledge gap that will be bridged, and global communities will be empowered by better understanding and assisting in the preservation of the health of our oceans and for continued sustainable use of our oceans for many generations unless it is stopped.

Learning algorithms for hydrographic mapping, the accuracy of these depth measurements remains inferior to that achieved using acoustic equipment (Saeidi et al., 2023; Pike et al., 2019). Among acoustic devices, the multi-beam echo sounder (MBES) has gained significant attention in national ports over the last decade. The volume of data captured by MBES is exponentially higher than that of single-beam echo sounders (SBES), providing continuous seabed coverage, which accelerates depth measurement and reduces field operation times (Costa et al., 2009).

References

Araujo, A. A., Hedley, N. (2023). Bathymetric data visualization – A review of current methods, practices and emerging interface opportunities. The *International Hydrographic Review, 29*(2), pp. 150–163. https://doi.org/10.58440/ihr-29-2-a29

Cheng, F., Chi, B., Lindsey, N. J., Dawe, T. C. and Ajo-Franklin, J. B. (2021). Utilizing distributed acoustic sensing and ocean bottom fiber optic cables for submarine structural characterization. *Scientific reports, 11*(1), 5613.

Constantinoiu, L.-F., Bernardino, M. and Rusu, E. (2023). Autonomous Shallow Water Hydrographic Survey Using a Proto-Type USV. *Journal of Marine Science and Engineering, 11*(4), 799.

Corcoran, F. and Parrish, C. E. (2023). DORSL-FIN: A Self-supervised Neural Network for Recovering Missing Bathymetry from ICESat-2. *Photogrammetric Engineering & Remote Sensing, 89*(9), 561-575.

Dery, P. J. (2024). *West Africa Coastal Areas Resilience Investment Project 2*. World Bank Group. https://projects.worldbank.org/en/projects-operations/procurement-detail/OP00305223 (accessed 13 August 2024).

Ekelund, A. (2023). Rising tides: exploring the expanding horizons of bathymetric Lidar applications. *Hydro International*. https://www.hydro-international.com/content/article/

rising-tides-exploring-the-expanding-horizons-of-bathymetric-lidar-applications (accessed 21 March 2025).

Ferreira, I. O., Andrade, L. C. d., Teixeira, V. G. and Santos, F. C. M. (2022). State of art of bathymetric surveys. *Boletim de Ciências Geodésicas, 28*(1), e2022002.

Fu, L. L., Pavelsky, T., Cretaux, J. F., Morrow, R., Farrar, J. T., Vaze, P., Sengenes, P., Vinogradova-Shiffer, N., Sylvestre-Baron, A. and Picot, N. (2024). The surface water and ocean topography mission: A breakthrough in radar remote sensing of the ocean and land surface water. *Geophysical Research Letters, 51*(4), e2023GL107652.

GEBCO (2025a). *General Bathymetric Chart of the Oceans (GEBCO)*. British Oceanographic Data Centre (BODC), National Oceanography Centre, United Kingdom. https://www.gebco.net/ (accessed 21 March 2025).

GEBCO (2025b). *Nippon Foundation/GEBCO Training Program*. British Oceanographic Data Centre (BODC), National Oceanography Centre, United Kingdom. https://www.gebco.net/training/ (accessed 21 March 2025).

Goddard, J. (2025). *Meet the deep-sea explorer with a plan to map the whole ocean floor.* The Times. https://www.thetimes.com/world/us-world/article/the-ocean-floor-map-crust-deep-sxg9s8mn9 (accessed 21 March 2025).

Hains, D., Keating, S. G., Rathnayake, C., Obura, V., Sharma, S. and Hall, S. (2024). Citizen Hydrospatial Sciences – To csB or not to csB, that is the question! *The International Hydrographic Review, 30*(1), pp. 162–170. https://doi.org/10.58440/ihr-30-1-n02

Hains, D., Schiller, L., Ponce, R., Bergmann, M., Cawthra, H. C., Cove, K., Echeverry, P., Gaunavou, L., Kim, S.-P., Lavagnino, A. C., Maschke, J., Mihailov, M. E., Obura, V., Oei, P., Pang, P. Y., Njanaseelan, G. P., Sharma, S. L. (2022). Hydrospatial – update and progress in the definition of this term. *The International Hydrographic Review, 28*, pp. 221–225. https://doi.org/10.58440/ihr-28-n14

Hankin, S., Bermudez, L., Blower, J. D., Blumenthal, B., Casey, K. S., Fornwall, M., Graybeal, J., Guralnick, R. P., Habermann, T. and Howlett, E. (2010). Data management for the ocean sciences—perspectives for the next decade. *Proceedings of OceanObs, 9.*

Hariram, V. (2024). *Bathymetry, the Future Potential of Ocean Mapping, and the Seafloor Revolution*. Available at SSRN 4977191.

IHO (2021a). *Data Centre for Digital Bathymetry.* International Hydrographic Organization, Monaco. https://iho.int/en/data-centre-for-digital-bathymetry (accessed 14 Januar 2025).

IHO (2021b). *IHO Capacity Building Strategy* (ed. 0.3). IHO Publication P-7, International Hydrographic Organization, Monaco. https://iho.int/uploads/user/Inter-Regional%20Coordination/CBSC/MISC/Capacity_Building_Strategy_2021_ver05.pdf

IHO (2023). *Annual Report 2023* (ed. 1.0). International Hydrographic Organization, Monaco. https://iho.int/uploads/user/pubs/periodical/P7_2023_EN.pdf

IHO (2024a). IHO and EC cooperation in third countries – A proposal for hydrographic capacity development. IHO. International Hydrographic Organization, Monaco. https://iho.int/uploads/user/Inter-Regional%20Coordination/IENWG%20and%20EC%20-%20IHO%20Cooperation/IENWG14/IENWG14_2024_WT4.1A_EN_A%20proposal%20for%20hydrographic%20capacity%20development.pdf (accessed 14 Januar 2025).

IHO (2024b). IHO Crowdsourced Bathymetry Initiative. International Hydrographic Organization, Monaco. https://iho.int/en/iho-crowdsourced-bathymetry-initiative

Jakobsson, M., Mohammad, R., Karlsson, M., Salas-Romero, S., Vacek, F., Heinze, F., Bringensparr, C., Castro, C. F., Johnson, P. and Kinney, J. (2024). The International Bathymetric Chart of the Arctic Ocean Version 5.0. *Scientific Data*, 11(1), 1420.

Kyoko, O. (2024). *Advances in Bathymetric Technology and Ocean Floor Geoscience*. Ocean Policy Research Institute. https://www.spf.org/opri/en/newsletter/575_2.html (accessed 21 March 2025).

Long, J., Zhang, H. and Zhao, J. (2023). A comprehensive deep learning-based outlier removal method for multibeam bathymetric point cloud. *IEEE Transactions on Geoscience and Remote Sensing, 61*, pp. 1–22.

Midford, P. and Østhagen, A. (2024). The East China Sea: A Case of Ocean Geopolitics and Maritime Conflict. *East Asia*, pp. 1–32.

National Research Council (2015). *Sea Change: 2015–2025 Decadal Survey of Ocean Sciences.* Washington, DC: The National Academies Press. https://doi.org/10.17226/21655

Ouellette, G., Fargo, K., Charry, H. (2023). Satellite computed bathymetry assessment – Developing satellite LiDAR methods to enhance coastal bathymetry coverage. *The International Hydrographic Review, 29*(2), pp. 208–212. https://doi.org/10.58440/ihr-29-2-n05

Reithmeier, M., Laut, I., Gawehn, M., Kleih, C., Schneider von Deimling, J., Hartmann, K. (2024). Improving global coastal bathymetry from waves – Introducing scalable processing and post-processing workflows for 100 m resolution grids. *The International Hydrographic Review, 30*(2), pp. 30–43. https://doi.org/10.58440/ihr-30-2-a18

Thomas, N., Pertiwi, A. P., Traganos, D., Lagomasino, D., Poursanidis, D., Moreno, S. and Fatoyinbo, L. (2021). Space-borne cloud-native satellite-derived bathymetry (SDB) models using ICESat-2 and Sentinel-2. *Geophysical Research Letters,* 48(6), e2020GL092170.

Trice, A., Robbins, C., Philip, N. and Rumsey, M. (2021). *Challenges and opportunities for ocean data to advance conservation and management*. Ocean Conservancy: Washington, DC, USA.

UNESCO-IOC (2024). Ocean Decade Bathymetry Data Sharing Guideline. *The Ocean Decade Series, 58.* UNESCO, Paris.

Wu, Z., Mao, Z. and Shen, W. (2021). Integrating multiple datasets and machine learning algorithms for satellite-based bathymetry in seaports. *Remote Sensing, 13*(21), 4328.

Zhang, Q., Chai, H., Wang, M., Sun, S. and Liu, Y. (2024). Station-based SDB correction for GPS triple-frequency observations and its application on relative positioning. *Measurement Science and Technology, 35*(11), 116312.

IHO

International
Hydrographic
Organization